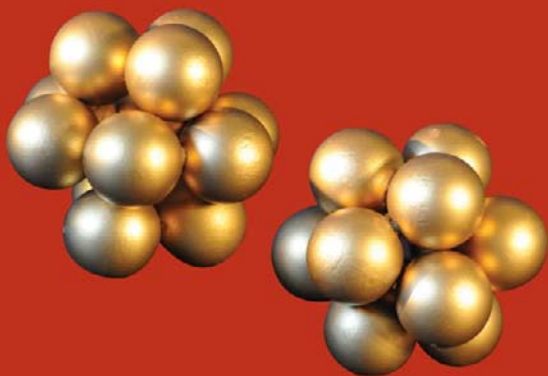


IUCr TEXTS IN CRYSTALLOGRAPHY • 12

The Basics of Crystallography and Diffraction

Third Edition

CHRISTOPHER HAMMOND



INTERNATIONAL UNION OF CRYSTALLOGRAPHY
OXFORD SCIENCE PUBLICATIONS



INTERNATIONAL UNION OF CRYSTALLOGRAPHY TEXTS ON CRYSTALLOGRAPHY

IUCr BOOK SERIES COMMITTEE

J. Bernstein, *Israel*
G. R. Desiraju, *India*
J. R. Helliwell, *UK*
T. Mak, *China*
P. Müller, *USA*
P. Paufler, *Germany*
H. Schenk, *The Netherlands*
P. Spadon, *Italy*
D. Viterbo (*Chairman*), *Italy*

IUCr Monographs on Crystallography

- 1** *Accurate molecular structures*
A. Domenicano, I. Hargittai, editors
- 2** *P.P. Ewald and his dynamical theory of X-ray diffraction*
D.W.J. Cruickshank, H.J. Juretschke, N. Kato, editors
- 3** *Electron diffraction techniques, Vol. 1*
J.M. Cowley, editor
- 4** *Electron diffraction techniques, Vol. 2*
J.M. Cowley, editor
- 5** *The Rietveld method*
R.A. Young, editor
- 6** *Introduction to crystallographic statistics*
U. Shmueli, G.H. Weiss
- 7** *Crystallographic instrumentation*
L.A. Aslanov, G.V. Fetisov, J.A.K. Howard
- 8** *Direct phasing in crystallography*
C. Giacovazzo
- 9** *The weak hydrogen bond*
G.R. Desiraju, T. Steiner
- 10** *Defect and microstructure analysis by diffraction*
R.L. Snyder, J. Fiala and H.J. Bunge
- 11** *Dynamical theory of X-ray diffraction*
A. Authier
- 12** *The chemical bond in inorganic chemistry*
I.D. Brown
- 13** *Structure determination from powder diffraction data*
W.I.F. David, K. Shankland, L.B. McCusker, Ch. Baerlocher, editors
- 14** *Polymorphism in molecular crystals*
J. Bernstein

- 15 *Crystallography of modular materials*
G. Ferraris, E. Makovicky, S. Merlino
- 16 *Diffuse x-ray scattering and models of disorder*
T.R. Welberry
- 17 *Crystallography of the polymethylene chain: an inquiry into the structure of waxes*
D.L. Dorset
- 18 *Crystalline molecular complexes and compounds: structure and principles*
F. H. Herbstein
- 19 *Molecular aggregation: structure analysis and molecular simulation of crystals and liquids*
A. Gavezzotti
- 20 *Aperiodic crystals: from modulated phases to quasicrystals*
T. Janssen, G. Chapuis, M. de Boissieu
- 21 *Incommensurate crystallography*
S. van Smaalen
- 22 *Structural crystallography of inorganic oxysalts*
S.V. Krivovichev
- 23 *The nature of the hydrogen bond: outline of a comprehensive hydrogen bond theory*
G. Gilli, P. Gilli
- 24 *Macromolecular crystallization and crystal perfection*
N.E. Chayen, J.R. Helliwell, E.H. Snell

IUCr Texts on Crystallography

- 1 *The solid state*
A. Guinier, R. Julien
- 4 *X-ray charge densities and chemical bonding*
P. Coppens
- 7 *Fundamentals of crystallography, second edition*
C. Giacovazzo, editor
- 8 *Crystal structure refinement: a crystallographer's guide to SHELXL*
P. Müller, editor
- 9 *Theories and techniques of crystal structure determination*
U. Shmueli
- 10 *Advanced structural inorganic chemistry*
Wai-Kee Li, Gong-Du Zhou, Thomas Mak
- 11 *Diffuse scattering and defect structure simulations: a cook book using the program DISCUS*
R. B. Neder, T. Proffen
- 12 *The basics of crystallography and diffraction, third edition*
C. Hammond
- 13 *Crystal structure analysis: principles and practice, second edition*
W. Clegg, editor

The Basics of Crystallography and Diffraction

Third Edition

Christopher Hammond

*Institute for Materials Research
University of Leeds*

INTERNATIONAL UNION OF CRYSTALLOGRAPHY

OXFORD

UNIVERSITY PRESS

OXFORD

UNIVERSITY PRESS

Great Clarendon Street, Oxford OX2 6DP

Oxford University Press is a department of the University of Oxford.
It furthers the University's objective of excellence in research, scholarship,
and education by publishing worldwide in

Oxford New York

Auckland Cape Town Dar es Salaam Hong Kong Karachi
Kuala Lumpur Madrid Melbourne Mexico City Nairobi New Delhi
Shanghai Taipei Toronto

With offices in

Argentina Austria Brazil Chile Czech Republic France Greece
Guatemala Hungary Italy Japan Poland Portugal Singapore
South Korea Switzerland Thailand Turkey Ukraine Vietnam

Oxford is a registered trade mark of Oxford University Press
in the UK and in certain other countries

Published in the United States
by Oxford University Press Inc., New York

© Christopher Hammond 2009

First edition (1997)
Second edition (2001)
Third edition (2009)

The moral rights of the author have been asserted
Database right Oxford University Press (maker)

All rights reserved. No part of this publication may be reproduced,
stored in a retrieval system, or transmitted, in any form or by any means,
without the prior permission in writing of Oxford University Press,
or as expressly permitted by law, or under terms agreed with the appropriate
reprographics rights organization. Enquiries concerning reproduction
outside the scope of the above should be sent to the Rights Department,
Oxford University Press, at the address above

You must not circulate this book in any other binding or cover
and you must impose the same condition on any acquirer

British library catalogue in Publication Data
Data available

Library of Congress Cataloging in Publication Data
Data available

Typeset by Newgen Imaging Systems (P) Ltd., Chennai, India
Printed in the UK
on acid-free paper by
CPI Antony Rowe, Chippenham, Wiltshire

ISBN 978-0-19-954644-2 (Hbk) ISBN 978-0-19-954645-9 (Pbk)

1 3 5 7 9 10 8 6 4 2

Preface to the First Edition (1997)

This book has grown out of my earlier *Introduction to Crystallography* published in the Royal Microscopical Society's Microscopy Handbook Series (Oxford University Press 1990, revised edition 1992). My object then was to show that crystallography is not, as many students suppose, an abstruse and 'difficult' subject, but a subject that is essentially clear and simple and which does not require the assimilation and memorization of a large number of facts. Moreover, a knowledge of crystallography opens the door to a better and clearer understanding of so many other topics in physics and chemistry, earth, materials and textile sciences, and microscopy.

In doing so I tried to show that the ideas of symmetry, structures, lattices and the architecture of crystals should be approached by reference to everyday examples of the things we see around us, and that these ideas were not confined to the pages of textbooks or the models displayed in laboratories.

The subject of diffraction flows naturally from that of crystallography because by its means—and in most cases only by its means—are the structures of materials revealed. And this applies not only to the interpretation of diffraction patterns but also to the interpretation of images in microscopy. Indeed, diffraction patterns of objects ought to be thought of as being as 'real', and as simply understood, as the objects themselves. One is, to use the mathematical expression, simply the transform of the other. Hence, in discussing diffraction, I have tried to emphasize the common aspects of the phenomena with respect to light, X-rays and electrons.

In Chapter 1 (Crystals and crystal structures) I have concentrated on the simplest examples, emphasizing how they are related in terms of the occupancy of atomic sites and how the structures may be changed by faulting. Chapter 2 (Two-dimensional patterns, lattices and symmetry) has been considerably expanded, partly to provide a firm basis for understanding symmetry and lattices in three dimensions (Chapters 3 and 4) but also to address the interests of students involved in two-dimensional design. Similarly in Chapter 4, in discussing point group symmetry, I have emphasized its practical relevance in terms of the physical and optical properties of crystals.

The reciprocal lattice (Chapter 6) provides the key to our understanding of diffraction, but as a *concept* it stands alone. I have therefore introduced it separately from diffraction and hope that in doing so these topics will be more readily understood. In Chapter 7 (The diffraction of light) I have emphasized the geometrical analogy with electron diffraction and have avoided any quantitative analysis of the amplitudes and intensities of diffracted beams. In my experience the (sometimes lengthy) equations which are required cloud students' perceptions of the basic geometrical conditions for constructive and destructive interference—and which are also of far more practical importance with respect, say, to the resolving power of optical instruments.

Chapter 8 describes the historical development of the geometrical interpretation of X-ray diffraction patterns through the work of Laue, the Braggs and Ewald. The diffraction of X-rays and electrons from single crystals is covered in Chapter 9, but only in the case of X-ray diffraction are the intensities of the diffracted beams discussed.

This is largely because structure factors are important but also because the derivation of the interference conditions between the atoms in the motif can be represented as

nothing more than an extension of Bragg's law. Finally, the important X-ray and electron diffraction techniques from polycrystalline materials are covered in Chapter 10.

The Appendices cover material that, for ease of reference, is not covered in the text. Appendix 1 gives a list of items which are useful in making up crystal models and provides the names and addresses of suppliers. A rapidly increasing number of crystallography programs are becoming available for use in personal computers and in Appendix 2 I have listed those which involve, to a greater or lesser degree, some 'self learning' element. If it is the case that the computer program will replace the book, then one might expect that books on crystallography would be the first to go! That day, however, has yet to arrive. Appendix 3 gives brief biographical details of crystallographers and scientists whose names are asterisked in the text. Appendix 4 lists some useful geometrical relationships.

Throughout the book the mathematical level has been maintained at a very simple level and with few minor exceptions all the equations have been derived from first principles. In my view, students learn nothing from, and are invariably dismayed and perplexed by, phrases such as 'it can be shown that'—without any indication or guidance of *how* it can be shown. Appendix 5 sets out all the mathematics which are needed.

Finally, it is my belief that students appreciate a subject far more if it is presented to them not simply as a given body of knowledge but as one which has been gained by the exertions and insight of men and women perhaps not much older than themselves. This therefore shows that scientific discovery is an activity in which they, now or in the future, can participate. Hence the justification for the historical references, which, to return to my first point, also help to show that science progresses, not by being made more complicated, but by individuals piecing together facts and ideas, and seeing relationships where vagueness and uncertainty existed before.

Preface to the Second Edition (2001)

In this edition the content has been considerably revised and expanded not only to provide a more complete and integrated coverage of the topics in the first edition but also to introduce the reader to topics of more general scientific interest which (it seems to me) flow naturally from an understanding of the basic ideas of crystallography and diffraction.

Chapter 1 is extended to show how some more complex crystal structures can be understood in terms of different faulting sequences of close-packed layers and also covers the various structures of carbon, including the fullerenes, the symmetry of which finds expression in natural and man-made forms and the geometry of polyhedra.

In Chapter 2 the figures have been thoroughly revised in collaboration with Dr K. M. Crennell including additional 'familiar' examples of patterns and designs to provide a clearer understanding of two-dimensional (and hence three-dimensional) symmetry. I also include, at a very basic level, the subject of non-periodic patterns and tilings which also serves as a useful introduction to quasiperiodic crystals in Chapter 4.

Chapter 3 includes a brief discussion on space-filling (Voronoi) polyhedra and in Chapter 4 the section on space groups has been considerably expanded to provide the reader with a much better starting-point for an understanding of the Space Group representation in Vol. A of the *International Tables for Crystallography*.

Chapters 5 and 6 have been revised with the objective of making the subject-matter more readily understood and appreciated.

In Chapter 7 I briefly discuss the human eye as an optical instrument to show, in a simple way, how beautifully related are its structure and its function.

The material in Chapters 9 and 10 of the first edition has been considerably expanded and re-arranged into the present Chapters 9, 10 and 11. The topics of X-ray and neutron diffraction from ordered crystals, preferred orientation (texture or fabric) and its measurement are now included in view of their importance in materials and earth sciences.

The stereographic projection and its uses is introduced at the very end of the book (Chapter 12)—quite the opposite of the usual arrangement in books on crystallography. But I consider that this is the right place: for here the usefulness and advantages of the stereographic projection are immediately apparent whereas at the beginning it may appear to be merely a geometrical exercise.

Finally, following the work of Prof. Amand Lucas, I include in Chapter 10 a simulation by light diffraction of the structure of DNA. There are, it seems to me, two landmarks in X-ray diffraction: Laue's 1912 photograph of zinc blende and Franklin's 1952 photograph of DNA and in view of which I have placed these 'by way of symmetry' at the beginning of this book.

Preface to Third Edition (2009)

I have considerably expanded Chapters 1 and 4 to include descriptions of a much greater range of inorganic and organic crystal structures and their point and space group symmetries. Moreover, I now include in Chapter 2 layer group symmetry—a topic rarely found in textbooks but essential to an understanding of such familiar things as the patterns formed in woven fabrics and also as providing a link between two- and three-dimensional symmetry. Chapters 9 and 10 covering X-ray diffraction techniques have been (partially) updated and include further examples but I have retained descriptions of older techniques where I think that they contribute to an understanding of the geometry of diffraction and reciprocal space. Chapter 11 has been extended to cover Kikuchi and EBSD patterns and image formation in electron microscopy. A new chapter (Chapter 13) introduces the basic ideas of Fourier analysis in X-ray crystallography and image formation and hence is a development (requiring a little more mathematics) of the elementary treatment of those topics given in Chapters 7 and 9. The Appendices have been revised to include polyhedra in crystallography in order to complement the new material in Chapter 1 and the biographical notes in Appendix 3 have been much extended.

It may be noticed that many of the books listed in 'Further Reading' are very old. However, in many respects, crystallography is a 'timeless' subject and such books to a large extent remain a valuable source of information.

Finally, I have attempted to make the Index sufficiently detailed and comprehensive that a reader will readily find those pages which contain the information she or he requires.

Acknowledgements

In the preparation of the successive editions of this book I have greatly benefited from the advice and encouragement of present and former colleagues in the University of Leeds who have appraised and discussed draft chapters or who have materially assisted in the preparation of the figures. In particular, I wish to mention Dr Andrew Brown, Professor Rik Brydson, Dr Tim Comyn, Dr Andrew Scott and Mr David Wright (Institute for Materials Research); Dr Jenny Cousens and Professor Michael Hann (School of Design); Dr Peter Evennett (formerly of the Department of Pure and Applied Biology); Dr John Lydon (School of Biological Sciences); the late Dr John Robertson (former Chairman of the IUCr Book Series Committee) and the late Dr Roy Shuttleworth (formerly of the Department of Metallurgy).

Dr Pam Champness (formerly of the Department of Earth Sciences, University of Manchester) read and advised me on much of the early draft manuscript; Mrs Kate Crennell (formerly Education Officer of the BCA) prepared several of the figures in Chapter 2; Professor István Hargittai (of the Budapest University of Technology and Economics) advised me on the work, and sought out biographical material, on A I Kitaigorodskii; Professor Amand Lucas (of the University of Namur and Belgian Royal Academy) allowed me to use his optical simulation of the structure of DNA and Dr Keith Rogers (of Cranfield University) advised me on the Rietveld method. Ms Melanie Johnstone and Dr Sonke Adlung of the Academic Division, Oxford University Press, have guided me in overall preparation and submission of the manuscript.

Many other colleagues at Leeds and elsewhere have permitted me to reproduce figures from their own publications, as have the copyright holders of books and journals. Individual acknowledgements are given in the figure captions.

I would like to thank Miss Susan Toon and Miss Claire McConnell for word processing the manuscript and for attending to my constant modifications to it and to Mr David Horner for his careful photographic work.

Finally, I recall with gratitude the great influence of my former teachers, in particular Dr P M Kelly and the late Dr N F M Henry.

The structure and content of the book have developed out of lectures and tutorials to many generations of students who have responded, constructively and otherwise, to my teaching methods.

C.H.

*Institute for Materials Research
University of Leeds
Leeds, LS2 9JT
July 2008*

Contents

<i>X-ray photograph of zinc blende</i> (Friedrich, Knipping and von Laue, 1912)	xiv
<i>X-ray photograph of deoxyribonucleic acid</i> (Franklin and Gosling, 1952)	xv

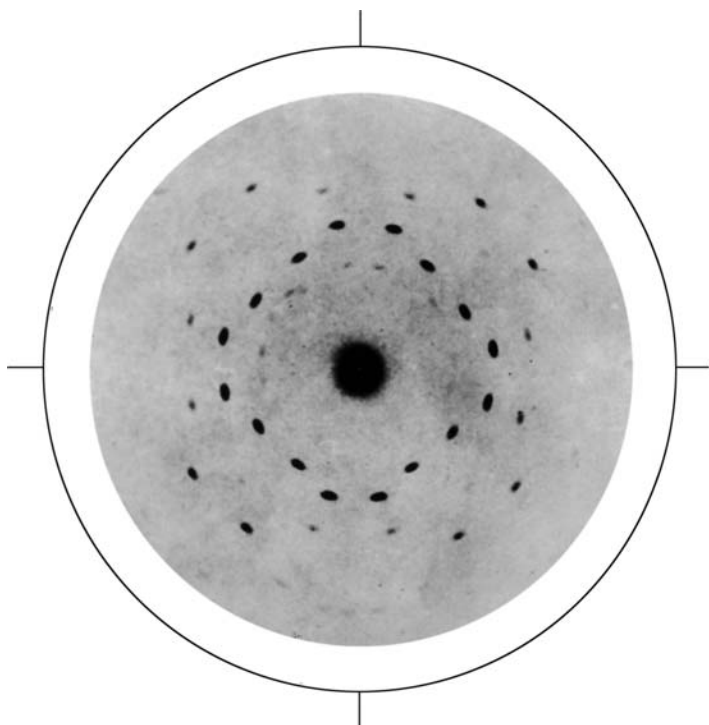
1	Crystals and crystal structures	1
1.1	The nature of the crystalline state	1
1.2	Constructing crystals from close-packed hexagonal layers of atoms	5
1.3	Unit cells of the hcp and ccp structures	6
1.4	Constructing crystals from square layers of atoms	9
1.5	Constructing body-centred cubic crystals	10
1.6	Interstitial structures	11
1.7	Some simple ionic and covalent structures	18
1.8	Representing crystals in projection: crystal plans	19
1.9	Stacking faults and twins	21
1.10	The crystal chemistry of inorganic compounds	26
1.10.1	<i>Bonding in inorganic crystals</i>	27
1.10.2	<i>Representing crystals in terms of coordination polyhedra</i>	29
1.11	Introduction to some more complex crystal structures	31
1.11.1	<i>Perovskite (CaTiO_3), barium titanate (BaTiO_3) and related structures</i>	31
1.11.2	<i>Tetrahedral and octahedral structures—silicon carbide and alumina</i>	33
1.11.3	<i>The oxides and oxy-hydroxides of iron</i>	35
1.11.4	<i>Silicate structures</i>	37
1.11.5	<i>The structures of silica, ice and water</i>	43
1.11.6	<i>The structures of carbon</i>	46
	Exercises	53
2	Two-dimensional patterns, lattices and symmetry	55
2.1	Approaches to the study of crystal structures	55
2.2	Two-dimensional patterns and lattices	56
2.3	Two-dimensional symmetry elements	58
2.4	The five plane lattices	61
2.5	The seventeen plane groups	64
2.6	One-dimensional symmetry: border or frieze patterns	65
2.7	Symmetry in art and design: counterchange patterns	65
2.8	Layer (two-sided) symmetry and examples in woven textiles	73
2.9	Non-periodic patterns and tilings	77
	Exercises	80

3	Bravais lattices and crystal systems	84
3.1	Introduction	84
3.2	The fourteen space (Bravais) lattices	84
3.3	The symmetry of the fourteen Bravais lattices: crystal systems	88
3.4	The coordination or environments of Bravais lattice points: space-filling polyhedra	90
	Exercises	95
 4	 Crystal symmetry: point groups, space groups, symmetry-related properties and quasiperiodic crystals	 97
4.1	Symmetry and crystal habit	97
4.2	The thirty-two crystal classes	99
4.3	Centres and inversion axes of symmetry	100
4.4	Crystal symmetry and properties	104
4.5	Translational symmetry elements	107
4.6	Space groups	111
4.7	Bravais lattices, space groups and crystal structures	118
4.8	The crystal structures and space groups of organic compounds	121
	4.8.1 <i>The close packing of organic molecules</i>	122
	4.8.2 <i>Long-chain polymer molecules</i>	124
4.9	Quasiperiodic crystals or crystalloids	126
	Exercises	130
 5	 Describing lattice planes and directions in crystals: Miller indices and zone axis symbols	 131
5.1	Introduction	131
5.2	Indexing lattice directions—zone axis symbols	132
5.3	Indexing lattice planes—Miller indices	133
5.4	Miller indices and zone axis symbols in cubic crystals	136
5.5	Lattice plane spacings, Miller indices and Laue indices	137
5.6	Zones, zone axes and the zone law, the addition rule	139
	5.6.1 <i>The Weiss zone law or zone equation</i>	139
	5.6.2 <i>Zone axis at the intersection of two planes</i>	139
	5.6.3 <i>Plane parallel to two directions</i>	140
	5.6.4 <i>The addition rule</i>	140
5.7	Indexing in the trigonal and hexagonal systems: Weber symbols and Miller-Bravais indices	141
5.8	Transforming Miller indices and zone axis symbols	143
5.9	Transformation matrices for trigonal crystals with rhombohedral lattices	146
5.10	A simple method for inverting a 3×3 matrix	147
	Exercises	149

6	The reciprocal lattice	150
6.1	Introduction	150
6.2	Reciprocal lattice vectors	150
6.3	Reciprocal lattice unit cells	152
6.4	Reciprocal lattice cells for cubic crystals	156
6.5	Proofs of some geometrical relationships using reciprocal lattice vectors	158
6.5.1	<i>Relationships between \mathbf{a}, \mathbf{b}, \mathbf{c} and \mathbf{a}^*, \mathbf{b}^*, \mathbf{c}^*</i>	158
6.5.2	<i>The addition rule</i>	159
6.5.3	<i>The Weiss zone law or zone equation</i>	159
6.5.4	<i>d-spacing of lattice planes (hkl)</i>	160
6.5.5	<i>Angle ρ between plane normals ($h_1k_1l_1$) and ($h_2k_2l_2$)</i>	160
6.5.6	<i>Definition of \mathbf{a}^*, \mathbf{b}^*, \mathbf{c}^* in terms of \mathbf{a}, \mathbf{b}, \mathbf{c}</i>	161
6.5.7	<i>Zone axis at intersection of planes ($h_1k_1l_1$) and ($h_2k_2l_2$)</i>	161
6.5.8	<i>A plane containing two directions $[u_1v_1w_1]$ and $[u_2v_2w_2]$</i>	161
6.6	Lattice planes and reciprocal lattice planes	161
6.7	Summary	163
	Exercises	164
7	The diffraction of light	165
7.1	Introduction	165
7.2	Simple observations of the diffraction of light	167
7.3	The nature of light: coherence, scattering and interference	172
7.4	Analysis of the geometry of diffraction patterns from gratings and nets	174
7.5	The resolving power of optical instruments: the telescope, camera, microscope and the eye	181
	Exercises	190
8	X-ray diffraction: the contributions of Max von Laue, W. H. and W. L. Bragg and P. P. Ewald	192
8.1	Introduction	192
8.2	Laue's analysis of X-ray diffraction: the three Laue equations	193
8.3	Bragg's analysis of X-ray diffraction: Bragg's law	196
8.4	Ewald's synthesis: the reflecting sphere construction	198
	Exercises	202
9	The diffraction of X-rays	203
9.1	Introduction	203
9.2	The intensities of X-ray diffracted beams: the structure factor equation and its applications	207

9.3	The broadening of diffracted beams: reciprocal lattice points and nodes	215
9.3.1	<i>The Scherrer equation: reciprocal lattice points and nodes</i>	216
9.3.2	<i>Integrated intensity and its importance</i>	220
9.3.3	<i>Crystal size and perfection: mosaic structure and coherence length</i>	220
9.4	Fixed θ , varying λ X-ray techniques: the Laue method	221
9.5	Fixed λ , varying θ X-ray techniques: oscillation, rotation and precession methods	223
9.5.1	<i>The oscillation method</i>	223
9.5.2	<i>The rotation method</i>	225
9.5.3	<i>The precession method</i>	226
9.6	X-ray diffraction from single crystal thin films and multilayers	229
9.7	X-ray (and neutron) diffraction from ordered crystals	233
9.8	Practical considerations: X-ray sources and recording techniques	237
9.8.1	<i>The generation of X-rays in X-ray tubes</i>	238
9.8.2	<i>Synchrotron X-ray generation</i>	239
9.8.3	<i>X-ray recording techniques</i>	240
	Exercises	240
10	X-ray diffraction of polycrystalline materials	243
10.1	Introduction	243
10.2	The geometrical basis of polycrystalline (powder) X-ray diffraction techniques	244
10.3	Some applications of X-ray diffraction techniques in polycrystalline materials	252
10.3.1	<i>Accurate lattice parameter measurements</i>	252
10.3.2	<i>Identification of unknown phases</i>	253
10.3.3	<i>Measurement of crystal (grain) size</i>	256
10.3.4	<i>Measurement of internal elastic strains</i>	256
10.4	Preferred orientation (texture, fabric) and its measurement	257
10.4.1	<i>Fibre textures</i>	258
10.4.2	<i>Sheet textures</i>	259
10.5	X-ray diffraction of DNA: simulation by light diffraction	262
10.6	The Rietveld method for structure refinement	267
	Exercises	269
11	Electron diffraction and its applications	273
11.1	Introduction	273
11.2	The Ewald reflecting sphere construction for electron diffraction	274
11.3	The analysis of electron diffraction patterns	277
11.4	Applications of electron diffraction	280

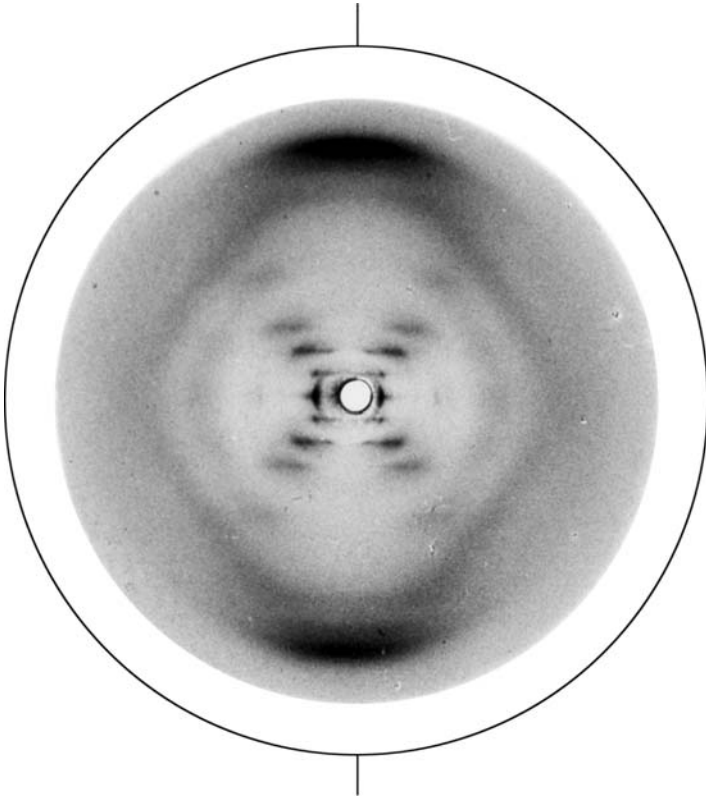
11.4.1	<i>Determining orientation relationships between crystals</i>	280
11.4.2	<i>Identification of polycrystalline materials</i>	281
11.4.3	<i>Identification of quasiperiodic crystals</i>	282
11.5	Kikuchi and electron backscattered diffraction (EBSD) patterns	283
11.5.1	<i>Kikuchi patterns in the TEM</i>	283
11.5.2	<i>Electron backscattered diffraction (EBSD) patterns in the SEM</i>	287
11.6	Image formation and resolution in the TEM	288
	Exercises	292
12	The stereographic projection and its uses	296
12.1	Introduction	296
12.2	Construction of the stereographic projection of a cubic crystal	299
12.3	Manipulation of the stereographic projection: use of the Wulff net	302
12.4	Stereographic projections of non-cubic crystals	305
12.5	Applications of the stereographic projection	308
12.5.1	<i>Representation of point group symmetry</i>	308
12.5.2	<i>Representation of orientation relationships</i>	310
12.5.3	<i>Representation of preferred orientation (texture or fabric)</i>	311
	Exercises	314
13	Fourier analysis in diffraction and image formation	315
13.1	Introduction—Fourier series and Fourier transforms	315
13.2	Fourier analysis in crystallography	318
13.3	Analysis of the Fraunhofer diffraction pattern from a grating	323
13.4	Abbe theory of image formation	328
Appendix 1	Computer programs, models and model-building in crystallography	333
Appendix 2	Polyhedra in crystallography	339
Appendix 3	Biographical notes on crystallographers and scientists mentioned in the text	349
Appendix 4	Some useful crystallographic relationships	382
Appendix 5	A simple introduction to vectors and complex numbers and their use in crystallography	385
Appendix 6	Systematic absences (extinctions) in X-ray diffraction and double diffraction in electron diffraction patterns	392
	Answers to Exercises	401
	Further Reading	414
	Index	421



X-ray photograph of zinc blende

One of the eleven 'Laue Diagrams' in the paper submitted by Walter Friedrich, Paul Knipping and Max von Laue to the Bavarian Academy of Sciences and presented at its Meeting held on June 8th 1912—the paper which demonstrated the existence of internal atomic regularity in crystals and its relationship to the external symmetry.

The X-ray beam is incident along one of the cubic crystal axes of the (face-centred cubic) ZnS structure and consequently the diffraction spots show the four-fold symmetry of the atomic arrangement about the axis. But notice also that the spots are not circular in shape—they are elliptical; the short axes of the ellipses all lying in radial directions. William Lawrence Bragg realized the great importance of this seemingly small observation: he had noticed that slightly divergent beams of light (of circular cross-section) reflected from mirrors also gave reflected spots of just these elliptical shapes. Hence he went on to formulate the Law of Reflection of X-Ray Beams which unlocked the door to the structural analysis of crystals.



X-ray photograph of deoxyribonucleic acid

The photograph of the 'B' form of DNA taken by Rosalind Franklin and Raymond Gosling in May 1952 and published, together with the two papers by J. D. Watson and F. H. C. Crick and M. H. F. Wilkins, A. R. Stokes and H. R. Wilson, in the 25 April issue of *Nature*, 1953, under the heading 'Molecular Structure of Nucleic Acids'.

The specimen is a fibre (axis vertical) containing millions of DNA strands roughly aligned parallel to the fibre axis and separated by the high water content of the fibre; this is the form adopted by the DNA in living cells. The X-ray beam is normal to the fibre and the diffraction pattern is characterised by four lozenges or diamond-shapes outlined by fuzzy diffraction haloes and separated by two rows or arms of spots radiating outwards from the centre. These two arms are characteristic of helical structures and the angle between them is a measure of the ratio between the width of the molecule and the repeat-distance of the helix. But notice also the sequence of spots along each arm; there is a void where the fourth spot should be and this 'missing fourth spot' not only indicates that there are two helices intertwined but also the separation of the helices along the chain. Finally, notice that there are faint diffraction spots in the two side lozenges, but not in those above and below, an observation which shows that the sugar-phosphate 'backbones' are on the outside, and the bases on the inside, of the molecule.

This photograph provided the crucial experimental evidence for the correctness of Watson and Crick's structural model of DNA—a model not just of a crystal structure but one which shows its inbuilt power of replication and which thus unlocked the door to an understanding of the mechanism of transmission of the gene and of the evolution of life itself.

This page intentionally left blank

Crystals and crystal structures

1.1 The nature of the crystalline state

The beautiful hexagonal patterns of snowflakes, the plane faces and hard faceted shapes of minerals and the bright cleavage fracture surfaces of brittle iron have long been recognized as external evidence of an internal order—evidence, that is, of the patterns or arrangements of the underlying building blocks. However, the nature of this internal order, or the form and scale of the building blocks, was unknown.

The first attempt to relate the external form or shape of a crystal to its underlying structure was made by Johannes Kepler* who, in 1611, wrote perhaps the first treatise on geometrical crystallography, with the delightful title, ‘A New Year’s Gift or the Six-Cornered Snowflake’ (*Strena Seu de Nive Sexangula*).¹ In this he speculates on the question as to why snowflakes always have six corners, never five or seven. He suggests that snowflakes are composed of tiny spheres or globules of ice and shows, in consequence, how the close-packing of these spheres gives rise to a six-sided figure. It is indeed a simple experiment that children now do with pennies at school. Kepler was not able to solve the problem as to why the six corners extend and branch to give many patterns (a problem not fully resolved to this day), nor did he extend his ideas to other crystals. The first to do so, and to consider the structure of crystals as a general problem, was Robert Hooke* who, with remarkable insight, suggested that the different shapes of crystals which occur—rhombs, trapezia, hexagons, etc.—could arise from the packing together of spheres or globules. Figure 1.1 is ‘Scheme VII’ from his book *Micrographia*, first published in 1665. The upper part (Fig. 1) is his drawing, from the microscope, of ‘Crystalline or Adamantine bodies’ occurring on the surface of a cavity in a piece of broken flint and the lower part (Fig. 2) is of ‘sand or gravel’ crystallized out of urine, which consist of ‘Slats or such-like plated Stones ... their sides shaped into **Rhombs**, **Rhomboeids** and sometimes into **Rectangles** and **Squares**’. He goes on to show how these various shapes can arise from the packing together of ‘a company of bullets’ as shown in the inset sketches A–L, which represent pictures of crystal structures which have been repeated in innumerable books, with very little variation, ever since. Also implicit in Hooke’s sketches is the *Law of the Constancy of Interfacial Angles*; notice that the solid lines which outline the crystal faces are (except for the last sketch, L) all at 60° or 120° angles which clearly arise from the close-packing of the spheres. This law was first stated by Nicolaus Steno,* a near contemporary of Robert Hooke in 1669, from simple

* Denotes biographical notes available in Appendix 3.

¹ *The Six-Cornered Snowflake*, reprinted with English translation and commentary by the Clarendon Press, Oxford, 1966.

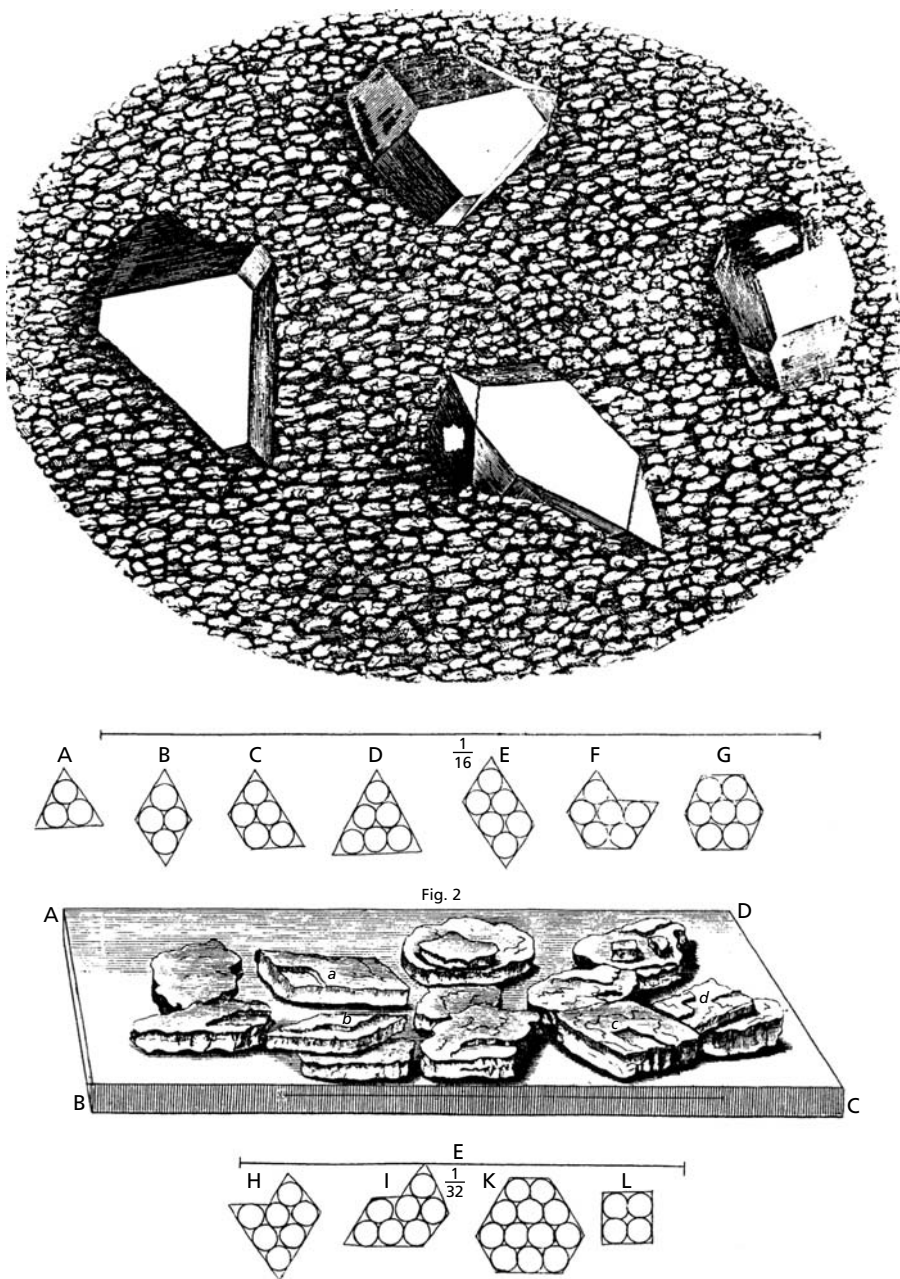


Fig. 1.1. ‘Scheme VII’ (from Hooke’s *Micrographia*, 1665), showing crystals in a piece of broken flint (Upper—Fig. 1), crystals from urine (Lower—Fig. 2) and hypothetical sketches of crystal structures A–L arising from the packing together of ‘bullets’.

observations of the angles between the faces of quartz crystals, but was developed much more fully as a general law by Rome de L'Isle* in a treatise entitled *Cristallographie* in 1783. He measured the angles between the faces of carefully-made crystal models and proposed that each mineral species therefore had an underlying 'characteristic primitive form'. The notion that the packing of the underlying building blocks determines both the shapes of crystals and the angular relationships between the faces was extended by René Just Haüy.* In 1784 Haüy showed how the different forms (or habits) of dog-tooth spar (calcite) could be precisely described by the packing together of little rhombs which he called 'molécules intégrantes' (Fig. 1.2). Thus the connection between an internal order and an external symmetry was established. What was not realized at the time was that an internal order could exist even though there may appear to be no external evidence for it.

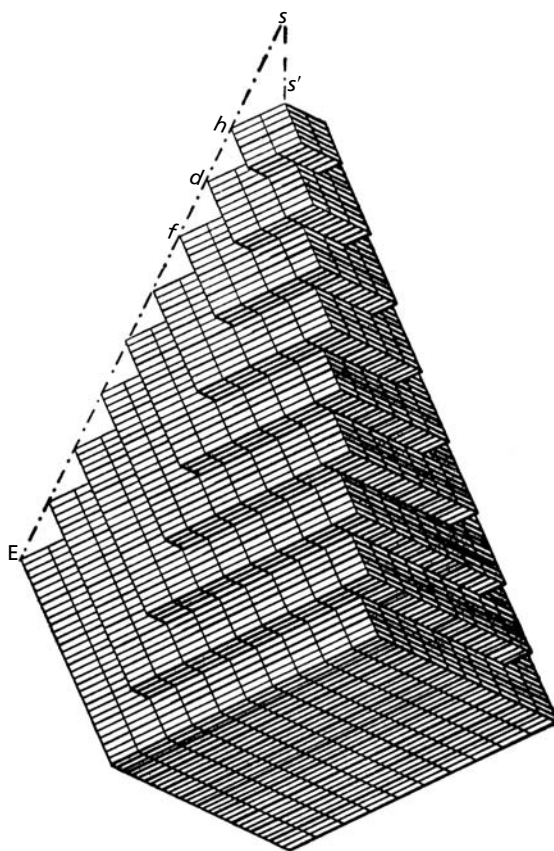


Fig. 1.2. Haüy's representation of dog-tooth spar built up from rhombohedral 'molécules intégrantes' (from *Essai d'une théorie sur la structure des cristaux*, 1784).

* Denotes biographical notes available in Appendix 3.

It is only relatively recently, as a result primarily of X-ray and electron diffraction techniques, that it has been realized that most materials, including many biological materials, are crystalline or partly so. But the notion that a lack of external crystalline form implies a lack of internal regularity still persists. For example, when iron and steel become embrittled there is a marked change in the fracture surface from a rough, irregular 'grey' appearance to a bright faceted 'brittle' appearance. The change in properties from tough to brittle is sometimes vaguely thought to arise because the structure of the iron or steel has changed from some undefined amorphous or noncrystalline 'grey' state to a 'crystallized' state. In both situations, of course, the crystalline structure of iron is unchanged; it is simply the fracture processes that are different.

Given our more detailed knowledge of matter we can now interpret Hooke's spheres or 'bullets' as atoms or ions, and Fig. 1.1 indicates the ways in which some of the simplest crystal structures can be built up. This representation of atoms as spheres does not, and is not intended, to show anything about their physical or chemical nature. The diameters of the spheres merely express their nearest distances of approach. It is true that these will depend upon the ways in which the atoms are packed together, and whether or not the atoms are ionized, but these considerations do not invalidate the 'hard sphere' model, which is justified, not as a representation of the *structure* of atoms, but as a representation of the structures arising from the *packing together* of atoms.

Consider again Hooke's sketches A–L (Fig. 1.1). In all of these, except the last, L, the atoms are packed together *in the same way*; the differences in shape arise from the different crystal boundaries. The atoms are packed in a *close-packed hexagonal* or honeycomb arrangement—the most compact way which is possible. By contrast, in the *square* arrangement of L there are larger voids or gaps (properly called **interstices**) between the atoms. This difference is shown more clearly in Fig. 1.3, where the boundaries of the (two-dimensional) crystals have been left deliberately irregular to emphasize the point

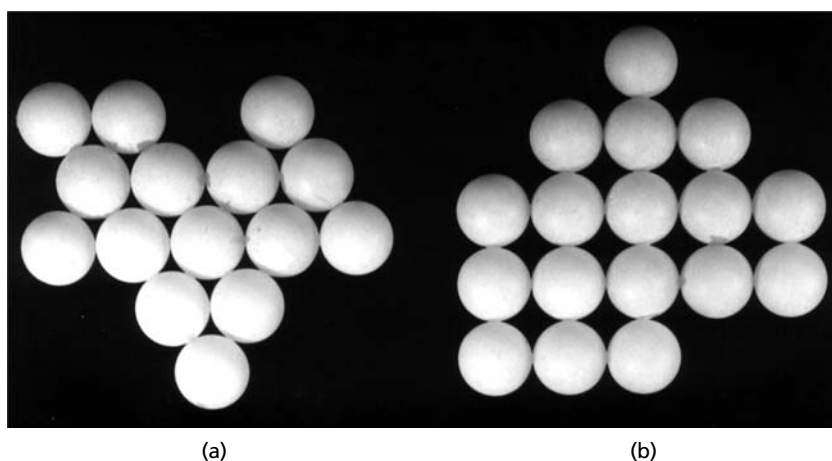


Fig. 1.3. Layers of 'atoms' stacked (a) in hexagonal and (b) in square arrays.

that is the internal regularity, hexagonal, or square, not the boundaries (or external faces) which defines the structure of a crystal.

Now we shall extend these ideas to three dimensions by considering not one, but many, layers of atoms, stacked one on top of the other. To understand better the figures which follow, it is very helpful to make models of these layers (Fig. 1.3) to construct the three-dimensional crystal models (see Appendix 1).

1.2 Constructing crystals from close-packed hexagonal layers of atoms

The simplest way of stacking the layers is to place the atom centres directly above one another. The resultant crystal structure is called the **simple hexagonal structure**. There are, in fact, no examples of elements with this structure because, as the model building shows, the atoms in the second layer tend to slip into the ‘hollows’ or interstices between the atoms in the layer below. This also accords with energy considerations: unless electron orbital considerations predominate, layers of atoms stacked in this ‘close-packed’ way generally have the lowest (free) energy and are therefore most stable.

When a third layer is placed upon the second we see that there are two possibilities: when the atoms in the third layer slip into the interstices of the second layer they may either end up directly above the atom centres in the first layer or directly above the unoccupied interstices between the atoms in the first layer.

The geometry may be understood from Fig. 1.4, which shows a plan view of atom layers. A is the first layer (with the circular outlines of the atoms drawn in) and B is the second layer (outlines of the atoms not shown for clarity). In the first case the third layer goes directly above the A layer, the fourth layer over the B layer, and so on; the stacking sequence then becomes ABABAB ... and is called the **hexagonal close-packed (hcp) structure**. The packing of idealized hard spheres predicts a ratio of interlayer atomic spacing to in-layer atomic spacing of $\sqrt{(2/3)}$ (see Exercise 1.1) and although interatomic forces cause deviations from this ratio, metals such as zinc, magnesium and the low-temperature form of titanium have the hcp structure.

In the second case, the third layer of atoms goes above the interstices marked C and the sequence only repeats at the fourth layer, which goes directly above the first layer.

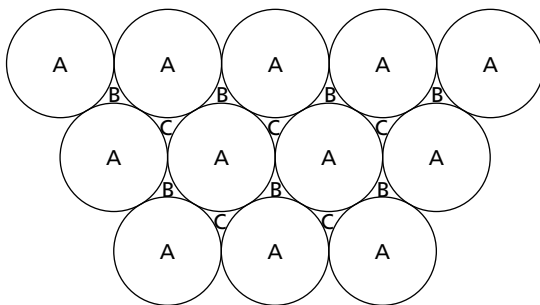


Fig. 1.4. Stacking sequences of close-packed layers of atoms. A—first layer (with outlines of atoms shown); B—second layer; C—third layer.

The stacking sequence is now ABCABC ... and is called the **cubic close-packed (ccp) structure**. Metals such as copper, aluminium, silver, gold and the high-temperature form of iron have this structure. You may ask the question: 'why is a structure which is made up of a three-layer stacking sequence of hexagonal layers called *cubic* close packed?' The answer lies in the shape and symmetry of the unit cell, which we shall meet below.

These labels for the layers A, B, C are, of course, arbitrary; they could be called OUP or RMS or any combination of three letters or figures. The important point is not the labelling of the layers but their **stacking sequence**; a two-layer repeat for hcp and a three-layer repeat for ccp. Another way of 'seeing the difference' is to notice that in the hcp structure there are open channels perpendicular to the layers running through the connecting interstices (labelled C in Fig. 1.4). In the ccp structure there are no such open channels—they are 'blocked' or obstructed because of the ABCABC ... stacking sequence.

Although the hcp and the ccp are the two most common stacking sequences of close-packed layers, some elements have crystal structures which are 'mixtures' of the two. For example, the actinide element americium and the lanthanide elements praseodymium, neodymium and samarium have the stacking sequence ABACABAC ... a four-layer repeat which is essentially a combination of an hcp and a ccp stacking sequence. Furthermore, in some elements with nominally ccp or hcp stacking sequences nature sometimes 'makes mistakes' in model building and faults occur during crystal growth or under conditions of stress or deformation. For example, in a (predominantly) ccp crystal (such as cobalt at room temperature), the ABCABC ... (ccp) type of stacking may be interrupted by layers with an ABABAB ... (hcp) type of stacking. The extent of occurrence of these **stacking faults** and the particular combinations of ABCABC ... and ABABAB ... sequences which may arise depend again on energy considerations, with which we are not concerned. What is of crystallographic importance is the fact that stacking faults show how one structure (ccp) may be transformed into another (hcp) and vice versa. They can also be used in the representation of more complicated crystal structures (i.e. of more than one kind of atom), as explained in Sections 1.6 and 1.9 below.

1.3 Unit cells of the hcp and ccp structures

A simple and economical method is now needed to represent the hcp and ccp (and of course other) crystal structures. Diagrams showing the stacked layers of atoms with irregular boundaries would obviously look very confused and complicated—the greater the number of atoms which have to be drawn, the more complicated the picture. The models need to be 'stripped down' to the fewest numbers of atoms which show the essential structure and symmetry. Such 'stripped-down' models are called the **unit cells** of the structures.

The unit cells of the simple hexagonal and hcp structures are shown in Fig. 1.5. The similarities and differences are clear: both structures consist of hexagonal close-packed layers; in the simple hexagonal structure these are stacked directly on top of each other, giving an AAA ... type of sequence, and in the hcp structure there is an interleaving layer nestling in the interstices of the layers below and above, giving an ABAB ... type of sequence.

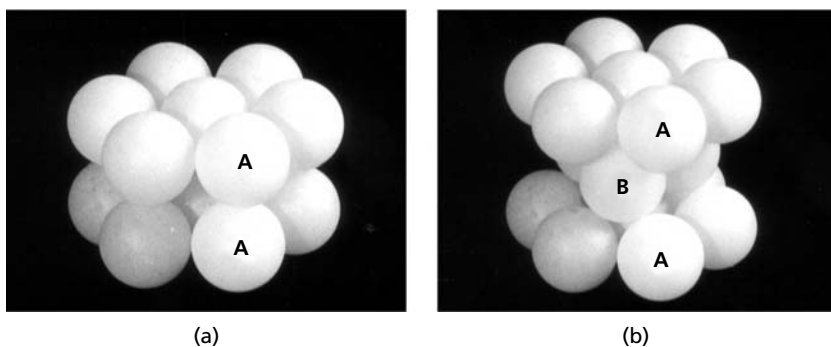


Fig. 1.5. Unit cells (a) of the simple hexagonal and (b) hcp structures.

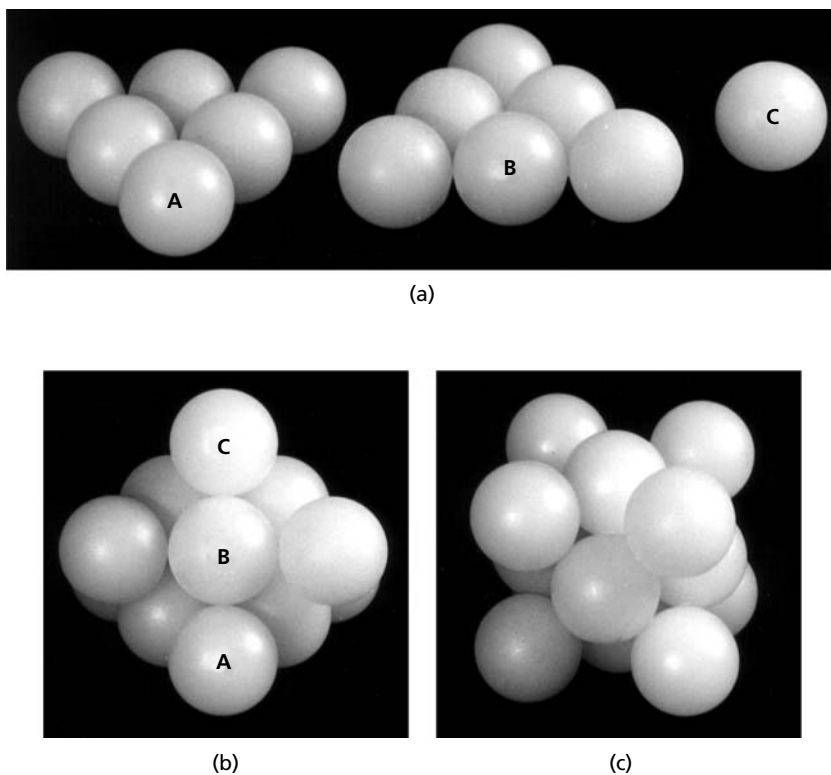


Fig. 1.6. Construction of the cubic unit cell of the ccp structure: (a) shows three close-packed layers A, B and C which are stacked in (b) in the 'ABC...' sequence from which emerges the cubic unit cell which is shown in (c) in the conventional orientation.

The unit cell of the ccp structure is not so easy to see. There are, in fact, two possible unit cells which may be identified, a cubic cell described below (Fig. 1.6), which is almost invariably used, and a smaller rhombohedral cell (Fig. 1.7). Figure 1.6(a) shows three close-packed layers separately—two triangular layers of six atoms (identical to one of Hooke's sketches in Fig. 1.1)—and a third layer stripped down to just one atom. If we stack these layers in an ABC sequence, the result is as shown in Fig. 1.6(b): it is a cube with the bottom corner atom missing. This can now be added and the unit cell of the ccp structure, with atoms at the corners and centres of the faces, emerges. The unit cell is usually drawn in the 'upright' position of Fig. 1.6(c), and this helps to illustrate a very important point which may have already been spotted whilst model building with the close-packed layers. The close-packed layers lie perpendicular to the body diagonal of the cube, but as there are four different body diagonal directions in a cube, there are therefore four different sets of close-packed layers—not just the one set with which we started. Thus three further close-packed layers have been automatically generated by the ABCABC... stacking sequence. This does not occur in the hcp structure—try it and see! The cubic unit cell, therefore, shows the **symmetry** of the ccp structure, a topic which

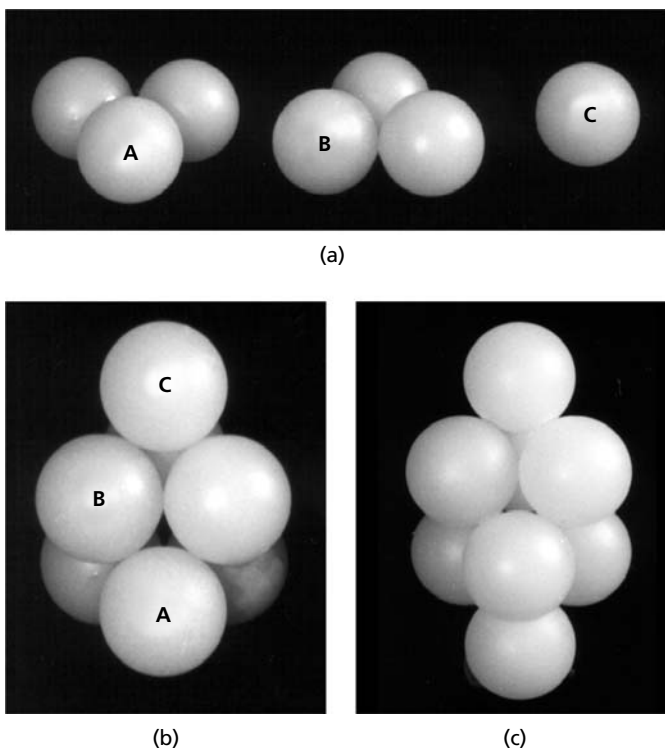


Fig. 1.7. Construction of the rhombohedral unit cell of the ccp structure: the close-packed layers (a) are again stacked (b) in the 'ABC...' sequence but the resulting rhombohedral cell (c) does not reveal the cubic symmetry.

will be covered in Chapter 4. The alternative rhombohedral unit cell of the ccp structure may be obtained by ‘stripping away’ atoms from the cubic cell such that there are only eight atoms left—one at each of the eight corners—or it may be built up by stacking triangular layers of only three atoms instead of six (Fig. 1.7). Unlike the larger cell, this does not obviously reveal the cubic symmetry of the structure and so is much less useful.

1.4 Constructing crystals from square layers of atoms

It will be noticed that the atoms in the cube faces of the ccp structure lie in a square array like that in Fig. 1.3(b) and the ccp structure may be constructed by stacking these layers such that alternate layers lie in the square interstices marked X in Fig. 1.8(a). The models show how the four close-packed layers arise like the faces of a pyramid (Fig. 1.8(b)). If, on the other hand, the layers are all stacked directly on top of each other, a **simple cubic structure** is obtained (Fig. 1.8(c)). This is an uncommon structure for the same reason as the simple hexagonal one is uncommon. An example of an element with a simple cubic structure is α -polonium.

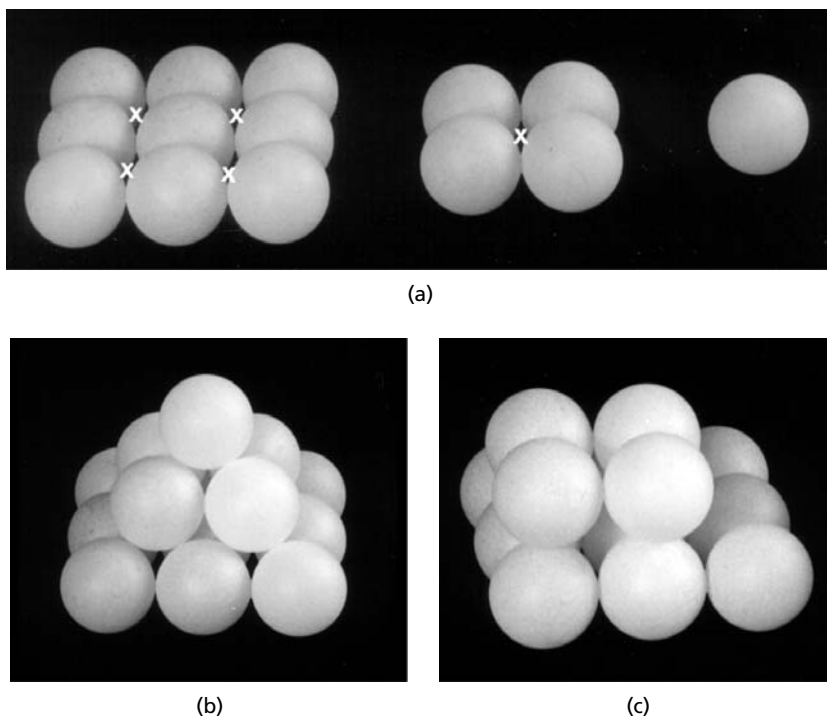


Fig. 1.8. (a) ‘Square’ layers of atoms with interstices marked X; (b) stacking the layers so that the atoms fall into these interstices, showing the development of the close-packed layers; (c) stacking the layers directly above one another, showing the development of the simple cubic structure.

1.5 Constructing body-centred cubic crystals

The important and commonly occurring **body-centred cubic (bcc)** structure differs from those already discussed in that it cannot be constructed either from hexagonal close-packed or square-packed layers of atoms (Fig. 1.3). The unit cell of the bcc structure is shown in Fig. 1.9. Notice how the body-centring atom ‘pushes’ the corner ones apart so that, on the basis of the ‘hard sphere’ model of atoms discussed above, they are not ‘in contact’ along the edges (in comparison with the simple cubic structure of Fig. 1.8(c), where they are in contact). In the bcc structure the atoms are in contact only along the body-diagonal directions. The planes in which the atoms are most (not fully) closely packed is the face-diagonal plane, as shown in Fig. 1.9(a), and in plan view, showing more atoms, in Fig. 1.9(b). The atom centres in the next layer go over the interstices marked B, then the third layer goes over the first layer, and so on—an ABAB ... type of stacking sequence. The interstices marked B have a slight ‘saddle’ configuration, and model building will suggest that the atoms in the second layer might slip a small distance to one side or the other (indicated by arrows), leading to a distortion in the cubic structure. Whether such a situation can arise in real crystals, even on a small scale, is still a matter of debate. Metals such as chromium, molybdenum, the high-temperature form of titanium and the low-temperature form of iron have the bcc structure.

Finally, notice the close similarity between the layers of atoms in Figs 1.3(a) and 1.9(b). With only small distortions, e.g. closing of the gaps in Fig. 1.9(b), the two layers become geometrically identical and some important $\text{bcc} \rightleftharpoons \text{ccp}$ and $\text{bcc} \rightleftharpoons \text{hcp}$ transformations are thought to occur as a result of distortions of this kind. For example, when iron is quenched from its high-temperature form (ccp above 910°C) to transform to its low-temperature (bcc) form, it is found that the set of the close-packed and closest-packed layers and close-packed directions are approximately parallel.

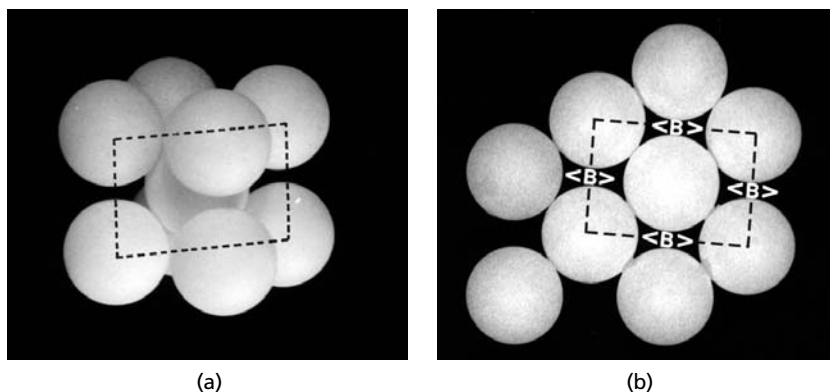


Fig. 1.9. (a) Unit cell of the bcc structure, showing a face-diagonal plane in which the atoms are most closely packed; (b) a plan view of this ‘closest-packed’ plane of atoms; the positions of atoms in alternate layers are marked B. The arrows indicate possible slip directions from these positions.

1.6 Interstitial structures

The different stacking sequences of one size of atom discussed in Sections 1.2 and 1.5 are not only useful in describing the crystal structures in many of the elements, where all the atoms are identical to one another, but can also be used to describe and explain the crystal structures of a wide range of compounds of two or more elements, where there are atoms of two or more different sizes. In particular, they can be applied to those compounds in which ‘small’ atoms or cations fit into the interstices between ‘large’ atoms or anions. The different structures of very many compounds arise from the different numbers and sizes of interstices which occur in the simple hexagonal, hcp, ccp, simple cubic and bcc structures and also from the ways in which the small atoms or cations distribute themselves among these interstices. These ideas can, perhaps, be best understood by considering the types, sizes and numbers of interstices which occur in the ccp and simple cubic structures.

In the ccp structure there are two types and sizes of interstice into which small atoms or cations may fit. They are best seen by fitting small spheres into the interstices between two-close-packed atom layers (Fig. 1.4). Consider an atom in a B layer which fits into the hollow or interstice between three A layer atoms: beneath the B atom is an interstice which is surrounded at equal distances by four atoms—three in the A layer and one in the B layer. These four atoms surround or ‘**coordinate**’ the interstice in the shape of a tetrahedron, hence the name **tetrahedral interstice** or **tetrahedral interstitial site**, i.e. where a small interstitial atom or ion may be situated. The position of one such site in the ccp unit cell is shown in Fig. 1.10(a) and diagrammatically in Fig. 1.10(b).

The other interstices between the A and B layers (Fig. 1.4) are surrounded or coordinated by six atoms, three in the A layer and three in the B layer. These six atoms surround the interstice in the shape of an octahedron; hence the name **octahedral interstice** or **octahedral interstitial site**. The positions of several atoms or ions in octahedral sites in a ccp unit cell are shown in Fig. 1.10(c) and diagrammatically, showing one octahedral site, in Fig. 1.10(d).

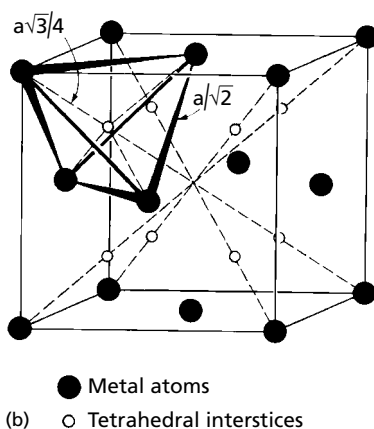
Now the diameters, or radii, of atoms or ions which can just fit into these interstices may easily be calculated on the basis that atoms or ions are spheres of fixed diameter—the ‘hard sphere’ model. The results are usually expressed as a **radius ratio**, r_X/r_A ; the ratio of the radius (or diameter) of the interstitial atoms, X, to that of the large atoms, A, with which they are in contact. In the ccp structure, r_X/r_A for the tetrahedral sites is 0.225 and for the octahedral sites it is 0.414. These radius ratios may be calculated with reference to Fig. 1.11. Figure 1.11(a) shows a tetrahedron, as in Fig. 1.10(b) outlined within a cube; clearly the centre of the cube is also the centre of the tetrahedron. The face-diagonal of the cube, or edge of the tetrahedron, along which the A atoms are in contact is of length $2r_A$. Hence the cube edge is of length $2r_A \cos 45 = \sqrt{2}r_A$ and the body-diagonal is of length $\sqrt{6}r_A$. The interstitial atom X lies at the mid-point of the body diagonal and is in contact with a corner atom A.

Hence $r_X + r_A = \frac{1}{2}\sqrt{6}r_A = 1.225r_A$; whence $r_X = 0.225r_A$.

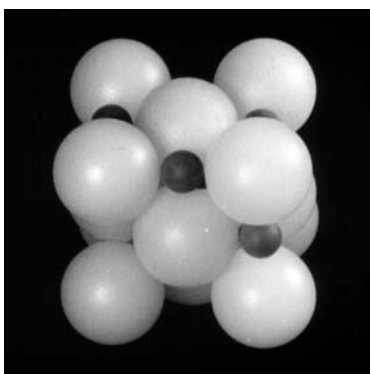
Figure 1.11(b) shows a plan view of the square of four A atoms in an octahedron surrounding an interstitial atom X. The edge of the square, along which the A atoms



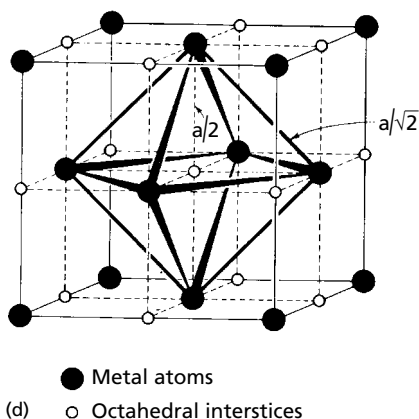
(a)



(b)



(c)



(d)

Fig. 1.10. (a) An atom in a tetrahedral interstitial site, $r_X/r_A = 0.225$ within the ccp unit cell and (b) geometry of a tetrahedral site, showing the dimensions of the tetrahedron in terms of the unit cell edge length a . (c) Atoms or ions in some of the octahedral interstitial sites, $r_X/r_A = 0.414$ within the ccp unit cell and (d) geometry of an octahedral site, showing the dimensions of the octahedron in terms of the unit cell edge length a . (From *The Structure of Metals*, 3rd edn, by C. S. Barrett and T. B. Massalski, Pergamon, 1980.)

are in contact, is of length $2r_A$ and the diagonal along which the X and A atoms are in contact is of length $2\sqrt{2}r_A$.

Hence $2r_X + 2r_A = 2\sqrt{2}r_A$; whence $r_X = 0.414r_A$.

In the simple cubic structure (Fig. 1.8(c)) there is an interstice at the centre of the unit cell which is surrounded by the eight atoms at the corners of the cube (Fig. 1.12(a)), hence the name **cubic interstitial site**. Caesium chloride, CsCl, has this structure, as shown diagrammatically in Fig. 1.12(b). The radius ratio for this site may be calculated in a similar way to that for the tetrahedral site in the ccp structure. In this case the atoms

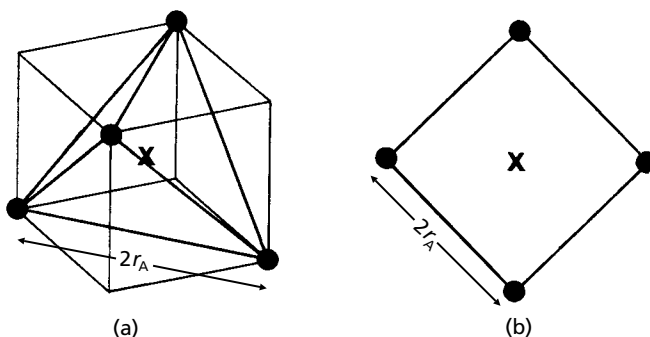


Fig. 1.11. (a) A tetrahedral interstitial site X within a tetrahedron of four A atoms (shown as small filled circles for clarity) outlined within a cube, (b) A plan view of an octahedral interstitial site X with four surrounding A atoms (plus one above and one below X). The centres of the A atoms are shown as solid circles for clarity.

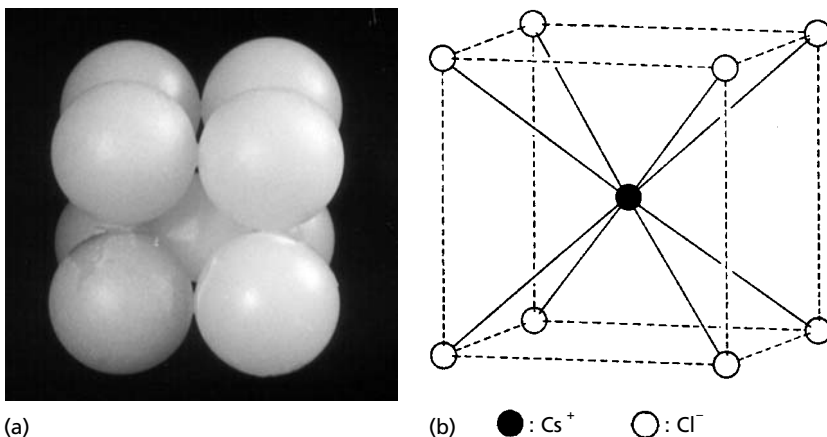


Fig. 1.12. (a) Cubic interstitial site, $r_X/r_A = 0.732$, within the simple cube unit cell and (b) the CsCl structure (ions not to scale).

are in contact along the cube edge, which is of length $2r_A$ and the body diagonal, along which the atoms A and X are in contact, is of length $2\sqrt{3}r_A$.

Hence $r_X + r_A = \frac{1}{2}2\sqrt{3}r_A$; whence $r_X = 0.732r_A$.

As well as being of different relative sizes, there are different numbers, or proportions, of these interstitial sites. For both the octahedral sites in ccp, and the cubic sites in the simple cubic structure, the proportion is one interstitial site to one (large) atom or ion, but for the tetrahedral interstitial sites in ccp the proportion is two sites to one atom. These proportions will be evident from model building or, if preferred, by geometrical reasoning. In the simple cubic structure (Fig. 1.12) there is one interstice per unit cell (at the centre) and eight atoms at each of the eight corners. As each corner atom or ion

is 'shared' by seven other cells, there is therefore one atom per cell—a ratio of 1:1. In the unit cell of the ccp structure (Fig. 1.10(c)), the octahedral sites are situated at the midpoints of each edge and in the centre. As each edge is shared by three other cells there are four octahedral sites per cell, i.e. twelve edges divided by four (number shared), plus one (centre). There are also four atoms per cell, i.e. eight corners divided by eight (number shared), plus six faces divided by two (number shared), again giving a ratio of 1:1. The tetrahedral sites in the ccp structure (Fig. 1.10(a) and (b)) are situated between a corner and three face-centring atoms, i.e. eight tetrahedral sites per unit cell, giving a ratio of 1:2.

It is a useful exercise to determine also the types, sizes and proportions of interstitial sites in the hcp, bcc and simple hexagonal structures. The hcp structure presents no problem; for the 'hard sphere' model with an interlayer to in-layer atomic ratio of $\sqrt{(2/3)}$ (Section 1.2) the interstitial sites are identical to those in ccp. It is only the distribution or 'stacking sequence' of the sites, like that of the close-packed layers of atoms, which is different.

In the bcc structure there are octahedral sites at the centres of the faces and mid-points of the edges (Figs 1.13(a) and (b)) and tetrahedral sites situated between the centres of the faces and mid-points of each edge (Figs 1.13(c) and (d)). Note, however, that both the octahedron and tetrahedron of the coordinating atoms do not have edges of equal length. The octahedron, for example, is 'squashed' in one direction and two of the coordinating atoms are closer to the centre of the interstice than are the other four.

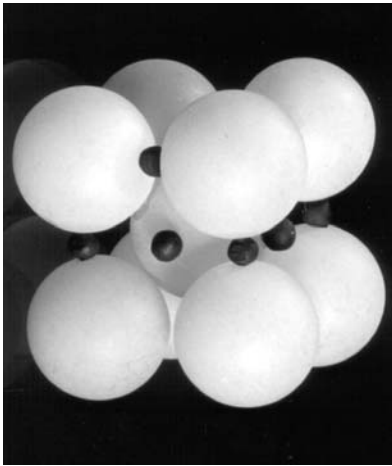
It is very important to take this into account since the radius ratios are determined by the A atoms which are closer to the centre of the interstitial site and not those which are further away. For the octahedral interstitial site the four A atoms which are further away lie in a square (Fig. 1.13(b)), just as the case for those surrounding the octahedral interstitial site in the ccp structure (Fig. 1.10(d)), but it is not these atoms, but the two atoms in the 'squashed' direction in Fig. 1.13(b) which determine the radius ratio. These are at a closer distance $a/2$ from the interstitial site where a is the cube edge length. Since in the bcc structure the atoms are in contact along the body diagonal, length $\sqrt{3}a$, then $4r_A = \sqrt{3}a$.

Hence $r_X + r_A = a/2 = 2r_A/\sqrt{3}$, whence $r_X = 0.154r_A$.

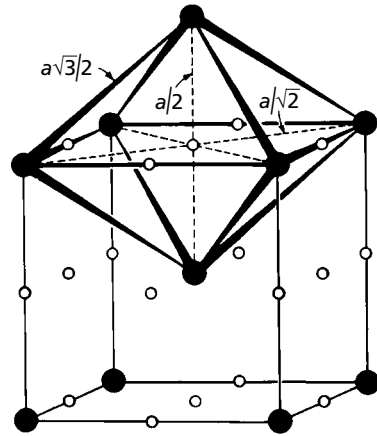
This is a very small site—smaller than the tetrahedral interstitial site (Fig. 1.13(c) and (d))—which has a radius ratio, $r_X/r_A = 0.291$ (see Exercise 1.2).

In the simple hexagonal structure the interstitial sites are coordinated by six atoms—three in the layer below and three in the layer above (Fig. 1.5(a)). It is the same coordination as for the octahedral interstitial sites in the ccp structure except that in this case the surrounding six atoms lie at the corners of a prism with a triangular base, rather than an octahedron, and the radius ratio is larger, $r_X/r_A = 0.527$ (see Exercise 1.3).

The radius ratios of interstitial sites and their proportions provide a very rough guide in interpreting the crystal structures of some simple, but important, compounds. The first problem, however, is that the 'radius' of an atom is not a fixed quantity but depends on its state of ionization (i.e. upon the nature of the chemical bonding in a compound) and coordination (the number and type of the surrounding atoms or ions). For example, the atomic radius of Li is about 156 pm but the ionic radius of the Li^+ cation is about 60 pm. The atomic radius of Fe in the ccp structure, where each atom is surrounded by twelve

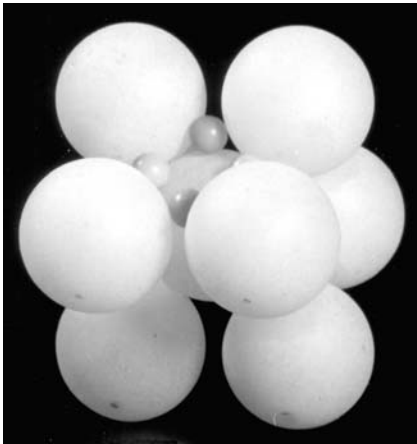


(a)

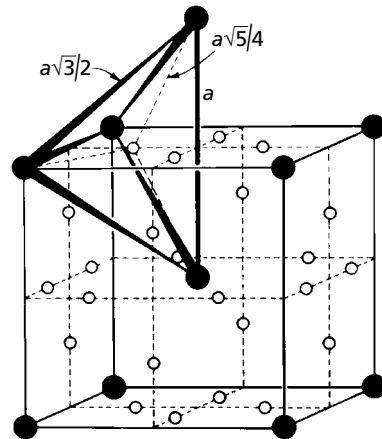


● Metal atoms

○ Octahedral interstices



(c)



● Metal atoms

○ Tetrahedral interstices

Fig. 1.13. (a) Octahedral interstitial sites, $r_X/r_A = 0.154$, (b) geometry of the octahedral interstitial sites, (c) tetrahedral interstitial sites $r_X/r_A = 0.291$, and (d) geometry of the tetrahedral interstitial sites in the bcc structure, (b) and (d) show the dimensions of the octahedron and tetrahedron in terms of the unit cell edge length a (from Barrett and Massalski, loc. cit.).

others, is about 258 pm but that in the bcc structure, where each atom is surrounded by eight others, is about 248 pm—a contraction in going from twelve- to eight-fold coordination of about 4 per cent.

Metal hydrides, nitrides, borides, carbides, etc., in which the radius ratio of the (small) non-metallic or metalloid atoms to the (large) metal atoms is small, provide

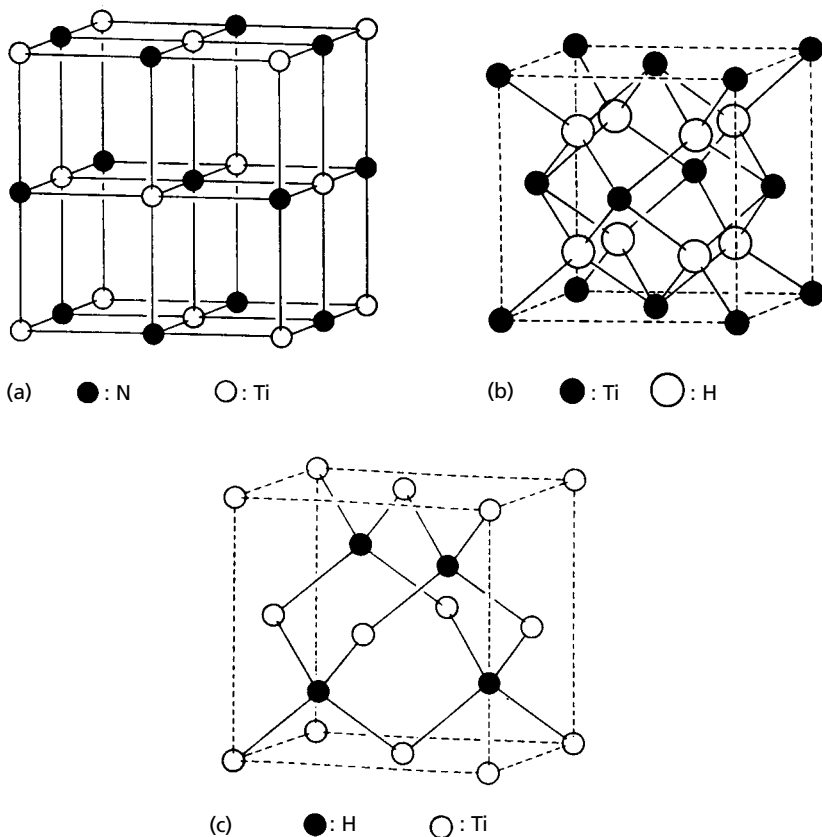


Fig. 1.14. (a) TiN structure (isomorphous with NaCl), (b) TiH₂ structure (isomorphous with CaF₂) and (c) TiH structure (isomorphous with sphalerite or zinc blende, ZnS or gallium arsenide, GaAs) (from *An Introduction to Crystal Chemistry*, 2nd edn, by R. C. Evans, Cambridge University Press, 1964).

good examples of interstitial compounds. However, in almost all of these compounds the interstitial atoms are ‘oversize’ (in terms of the exact radius ratios) and so, in effect, ‘push apart’ or separate the surrounding atoms such that they are no longer strictly close-packed although their pattern or distribution remains unchanged. For example, Fig. 1.14(a) shows the structure of TiN; the nitrogen atoms occupy all the octahedral interstitial sites and, because they are oversize, the titanium atoms are separated but still remain situated at the corners and face centres of the unit cell. This is described as a **face-centred cubic (fcc) array**, rather than a ccp array of titanium atoms, and TiN is described as a **face-centred cubic structure**. This description also applies to all compounds in which some of the atoms occur at the corners and face centres of the unit cell. The ccp structure may therefore be regarded as a special case of the fcc structure in which the atoms are in contact along the face diagonals.

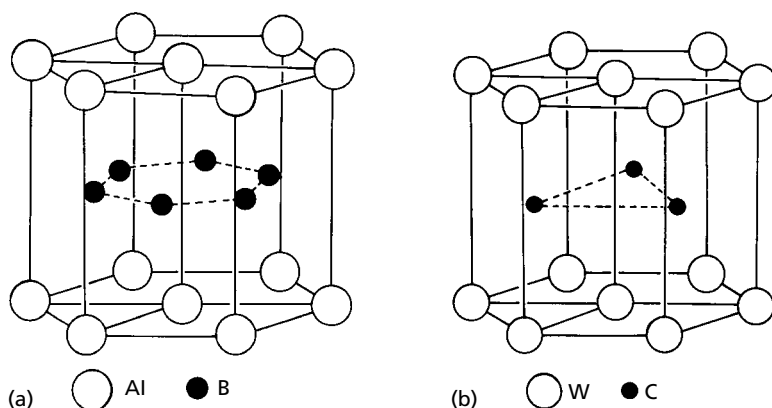


Fig. 1.15. (a) AlB_2 structure, (b) WC structure.

In TiH_2 (Fig. 1.14(b)), the titanium atoms are also in an fcc array and the hydrogen atoms occupy all the tetrahedral sites, the ratio being of course 1:2. In TiH (Fig. 1.14(c)) the hydrogen atoms are again situated in the tetrahedral sites, but only half of these sites are occupied. Notice that in these interstitial compounds the fcc arrangement of the titanium atoms is *not* the same as their arrangement in the elemental form which is bcc (high temperature form) or hcp (low temperature form). In fact, interstitial *compounds* based on a bcc packing of metal atoms are not known to exist; bcc metals such as vanadium, tungsten or iron (low temperature form) form interstitial compounds in which the metal atoms are arranged in an fcc pattern (e.g. VC), a simple hexagonal pattern (e.g. WC) or more complicated patterns (e.g. Fe_3C). Hence although as mentioned in Section 1.2, no elements have the simple hexagonal structure in which the close-packed layers are stacked in an AAA... sequence directly on top of one another (Fig. 1.5(a)), the metal atoms in some metal carbides, nitrides, borides, etc., are stacked in this way, the carbon, nitrogen, boron, etc., atoms being situated in some or all of the interstices between the metal atoms. The interstices are halfway between the close-packed (or nearly close-packed) layers and are surrounded or coordinated by six atoms—not, however, as described above in the form of an octahedron but in the form of a triangular prism. In the AlB_2 structure all these sites are occupied (Fig. 1.15(a)) and in the WC structure only half are occupied (Fig. 1.15(b)).

However, although there are no bcc interstitial *compounds* as such, interstitial elements can enter into the interstitial sites in the bcc structure to a limited extent to form what are known as *interstitial solid solutions*. One very important example in metallurgy is that of carbon in the distorted octahedral interstitial sites in iron, a structure called *ferri-rite*. The radius ratio of carbon to iron, $r_{\text{C}}/r_{\text{Fe}}$, is about 0.6, much greater than the radius ratio calculated above according to the ‘hard sphere’ model and the solubility of carbon is thus very small—1 carbon atom in about 200 iron atoms. The carbon atoms ‘push apart’ the two closest iron atoms and distort the bcc structure in a non-uniform or a *uniaxial* way—and it is this uniaxial distortion which is ultimately the origin of the hardness of

steel. In contrast, a much greater amount of carbon can enter the (uniform) octahedral interstitial sites in the ccp (high temperature) form of iron (called austenite)—1 carbon atom in about 10 iron atoms. The carbon atoms are still oversized, but the distortion is a uniform expansion and the hardening effect is much less.

1.7 Some simple ionic and covalent structures

The ideas presented in Section 1.6 above can be used to describe and explain the crystal structures of many simple but important ionic and covalent compounds, in particular many metal halides, sulphides and oxides. Although the metal atoms or cations are smaller than the chlorine, oxygen, sulphur, etc. atoms or anions, radius ratio considerations are only one factor in determining the crystal structures of ionic and covalent compounds and they are not usually referred to as interstitial compounds even though the pattern or distribution of atoms in the unit cells may be exactly the same. For example, the TiN structure (Fig. 1.14(a)) is isomorphous with the NaCl structure. Similarly, the TiH_2 structure (Fig. 1.14(b)) is identical to the Li_2O structure and the TiH structure (Fig. 1.14(c)) is isomorphous with ZnS (zinc blende or sphalerite) and GaAs (gallium arsenide) structure.

Unlike the fcc NaCl or TiN structure, structures based on an hcp packing of ions or atoms with all the octahedral interstitial sites occupied only occur in a distorted form. The frequently given example is nickel arsenide (niccolite, NiAs). The arsenic atoms are stacked in the ABAB ... hcp sequence but with an interlayer spacing rather larger than that for close packing (see answer to Exercise 1.1) and the Ni atoms occupy all the (distorted) octahedral interstitial sites. These are all 'C' sites between the ABAB ... layers (see Fig. 1.4) and so the nickel atoms are stacked one above the other in a simple hexagonal packing sequence (Fig. 1.5(a))—they approach each other so closely that they are, in effect, nearest neighbours. Several sulphides (TeS, CoS, NiS, VS) all have the NiAs structure but there are no examples of oxides.

For a similar reason, structures based on the hcp packing of ions or atoms with all the tetrahedral sites occupied do not occur; there is no (known) such hcp interstitial structure corresponding to the fcc Li_2O structure. This is a consequence of the distribution of tetrahedral sites which occur in 'pairs' perpendicular to the close packed planes, above and below which are either A or B layer atoms. The separation of these sites is only one-quarter the hexagonal unit cell height (see Exercise 1.1) and both sites cannot be occupied by interstitial ions or atoms at the same time. However, half the interstitial sites can be occupied, one example of such a structure being wurtzite, the hexagonal form of ZnS, described below.

The differences in stacking discussed in Sections 1.2 and 1.6 also explain the different crystal structures or different crystalline polymorphs sometimes shown by one compound. As mentioned above, zinc blende has an fcc structure, the sulphur atoms being stacked in the ABCABC ... sequence. In wurtzite, the other crystal structure or polymorph of zinc sulphide, the sulphur atoms are stacked in the hexagonal ABABAB ... sequence, giving a hexagonal structure. In both cases the zinc atoms occupy half the tetrahedral interstitial sites between the sulphur atoms. As in the case of cobalt, stacking faults may arise during crystal growth or under conditions of deformation, giving rise to 'mixed' sphalerite-wurtzite structures.

Examples of ionic structures based on the simple cubic packing of anions are CsCl and CaF_2 (fluorite). In CsCl all the cubic interstitial sites are occupied by caesium cations (Fig. 1.12(b)) but in fluorite only half the sites are occupied by the calcium cations. The resulting unit cell is not just one simple cube of fluorine anions, but a larger cube with a cell side double that of the simple cube and containing therefore $2 \times 2 \times 2 = 8$ cubes, four of which contain calcium cations and four of which are empty.

The distribution of the small calcium cations in the cubic sites is such that they form an fcc array and the fluorite structure can be represented alternatively as an fcc array of calcium cations with all the tetrahedral sites occupied by fluorine anions. It is identical, in terms of the distribution of ionic sites, to the structure of TiH_2 or Li_2O (Fig. 1.14(b)), except that the positions of the cations and anions are reversed; hence Li_2O is said to have the *antifluorite* structure. However, these differences, although in principle quite simple, may not be clear until we have some better method of representing the atom/ion positions in crystals other than the sketches (or clinographic projections) used in Figs. 1.10–1.15.

1.8 Representing crystals in projection: crystal plans

The more complicated the crystal structure and the larger the unit cell, the more difficult it is to visualize the atom or ion positions from diagrams or photographs of models—atoms or ions may be hidden behind others and therefore not seen. Another form of representation, the **crystal plan** or **crystal projection**, is needed, which shows precisely the atomic or ionic positions in the unit cell. The first step is to specify axes x , y and z from a common origin and along the sides of the cell (see Chapter 5). By convention the ‘back left-hand corner’ is chosen as the origin, the z -axis ‘upwards’, the y -axis to the right and the x -axis ‘forwards’, out of the page. The atomic/ionic positions or coordinates in the unit cell are specified as fractions of the cell edge lengths in the order x , y , z . Thus in the bcc structure the atomic/ionic coordinates are (000) (the atom/ion at the origin) and $\left(\frac{1}{2}\frac{1}{2}\frac{1}{2}\right)$ (the atom/ion at the centre of the cube). As all eight corners of the cube are *equivalent positions* (i.e. any of the eight corners can be chosen as the origin), there is no need to write down atomic/ionic coordinates (100), (110), etc.; (000) specifies *all* the corner atoms, and the two-coordinates (000) and $\left(\frac{1}{2}\frac{1}{2}\frac{1}{2}\right)$ represent the two atoms/ions in the bcc unit cell. In the fcc structure, with four atoms/ions per unit cell, the coordinates are (000), $\left(\frac{1}{2}\frac{1}{2}0\right)$, $\left(\frac{1}{2}0\frac{1}{2}\right)$, $\left(0\frac{1}{2}\frac{1}{2}\right)$.

Crystal projections or plans are usually drawn perpendicular to the z -axis, and Fig. 1.16(a) and (b) are plans of the bcc and fcc structure, respectively. Note that only the z coordinates are indicated in these diagrams; the x and y coordinates need not be written down because they are clear from the plan. Similarly, no z coordinates are indicated for all the corner atoms because all eight corners are equivalent positions in the structure, as mentioned above.

Figure 1.16(c) shows a projection of the antifluorite (LiO_2) structure; the oxygen anions in the fcc positions and the lithium cations in all the tetrahedral interstitial sites with z coordinates one-quarter and three-quarters between the oxygen anions are clearly shown. Notice that the lithium cations are in a simple cubic array, i.e. equivalent to

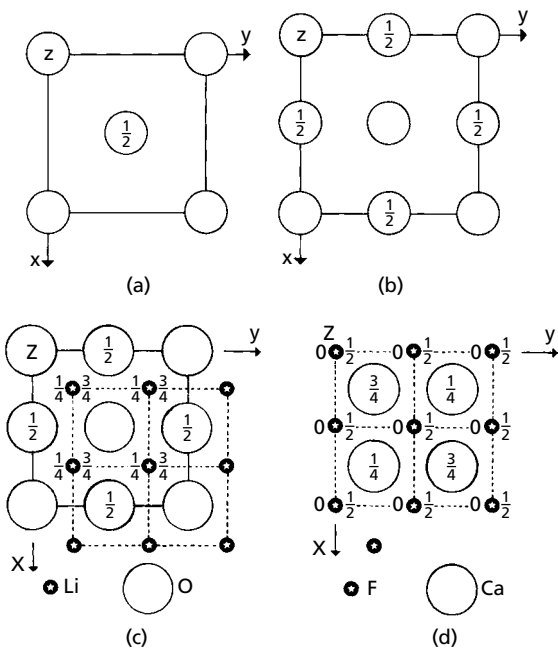


Fig. 1.16. Plans of (a) bcc structure, (b) ccp or fcc structure, (c) Li_2O (antifluorite) structure, (d) CaF_2 (fluorite) structure.

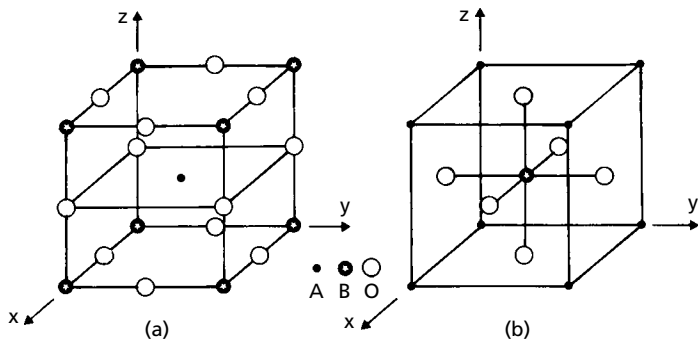


Fig. 1.17. Alternative unit cells of the perovskite ABO_3 structure.

the fluorine anions in the fluorite structure. The alternative fluorite unit cell, made up of eight simple cubes (see Section 1.7), is drawn by shifting the origin of the axes in Fig. 1.16(c) to the ion at the $\left(\frac{1}{4} \frac{1}{4} \frac{1}{4}\right)$ site and relabelling the coordinates. The result is shown in Fig. 1.16(d).

Sketching crystal plans helps you to understand the similarities and differences between structures; in fact, it is very difficult to understand them otherwise! For example,

Fig. 1.17(a) and (b) show the same crystal structure (perovskite, CaTiO_3). They look different because the origins of the cells have been chosen to coincide with different atoms/ions.

1.9 Stacking faults and twins

As pointed out in Sections 1.2 and 1.7, the close packing of atoms (in metals and alloys) and anions (in ionic and covalent structures) may depart from the ABCABC ... (ccp or fcc) or ABAB ... (hcp or hexagonal) sequences: ‘nature makes mistakes’ and may do so in a number of ways. First, stacking faults may occur during crystallization from the melt or magma: second, they may occur during the solid state processes or recrystallization, phase transitions and crystal growth (i.e. during the heating and cooling of metals and alloys, ceramics and rocks); and third, they may occur during deformation. The mechanisms of faulting have been most widely studied, and are probably most easily understood in the simple case of metals in which there is no (interstitial) distribution of cations to complicate the picture. It is a study of considerable importance in metallurgy because of the effects of faulting on the mechanical and thermal properties of alloys—strength, work-hardening, softening temperatures and so on. However, this should not leave the impression that faulting is of lesser importance in other materials.

Consider first the ccp structure (or, better, have your close-packed raft models to hand). Three layers are stacked ABC (Fig. 1.4). Now the next layer should again be A; instead place it in the B layer position, where it fits equally well into the ‘hollows’ between the C layer atoms. This is the only alternative choice and the stacking sequence is now ABCB. Now, when we add the next layer we have two choices: either to place it in an A layer or in a C layer position. Now continue with our interrupted ABC ... stacking sequence. In the first case we have the sequence ABCBABC ... and in the second sequence ABCBCABC ... In both cases it can be seen that there are layers which are in an hcp type of stacking sequence—but is there any difference between them, apart from the mere labelling of atom layers? Yes, there is a difference, which may be explained in two ways. If you examine the first sequence you will see that it is as if the mis-stacked B layer had been *inserted* into the ABCABC ... sequence and this is called an *extrinsic* stacking fault, whereas in the second case it is as if an A layer had been *removed* from the ABCABC ... sequence, and this is called an *intrinsic* stacking fault. However, this explanation, although it is the basis of the names *intrinsic* and *extrinsic*, is not very satisfactory. In order to understand better the distinction between stacking faults of different types (and indeed different stacking sequences in general), a completely different method of representing stacking sequences needs to be used.

You will recall (Section 1.2) that the labels for the layers are arbitrary and that it is the stacking *sequence* which is important; clearly then, some means of representing the sequence, rather than the layers themselves, is required. This requirement has been provided by F.C.Frank* and is named after him—the Frank notation. Frank proposed that each step in the stacking sequence $A \rightarrow B \rightarrow C \rightarrow A \dots$ should be represented

* Denotes biographical notes available in Appendix 3.

by a little ‘upright’ triangle Δ , and that each step in the stacking sequence, $C \rightarrow B \rightarrow A \rightarrow C \dots$ should be represented by a little ‘inverted’ triangle ∇ . Here are some examples, showing both the ABC... etc. type of notation for the layers and the Frank notation for the sequence of stacking of the layers. Note that the triangles come *between* the close packed layers, representing the stacking *sequence* between them.

A B C A B C A B C	C B A C B A C B A	Two fcc sequences
$\Delta \Delta \Delta \Delta \Delta \Delta \Delta \Delta$	$\nabla \nabla \nabla \nabla \nabla \nabla \nabla \nabla$	
A B A B A B A B	C B C B C B C B	Two hcp sequences
$\Delta \nabla \Delta \nabla \Delta \nabla \Delta \nabla$	$\nabla \Delta \nabla \Delta \nabla \Delta \nabla$	
A B C B A B C	A B C B C A B C	Extrinsic (left) and intrinsic (right) stacking faults
$\Delta \Delta \nabla \nabla \Delta \Delta$	$\Delta \Delta \Delta \nabla \Delta \Delta \Delta$	

Notice that the ccp (or fcc) stacking sequence is represented either by a sequence of upright triangles, or by a sequence of inverted ones—you could of course convert one to the other by simply turning your stack of close-packed layers upside down. However, the distinction is less arbitrary than this. An fcc crystal may grow, or be deformed (as explained below), such that the stacking sequence reverses, as indicated in Fig. 1.18 which shows the close-packed layers ‘edge on’ and both their ABC... etc. and Δ or ∇ labels. Such a crystal is said to be twinned and the twin plane is that at which the stacking sequence reverses. Note that the crystal on one side of the twin plane is a mirror reflection of the other, just like the pair of hands in Fig. 4.5(b).

The hcp stacking sequence is represented by alternate upright and inverted triangles—and the sequence is unchanged if the stack of close-packed layers is turned upside down. Hence twinning on the close-packed planes is not possible in the hcp structure—it is as

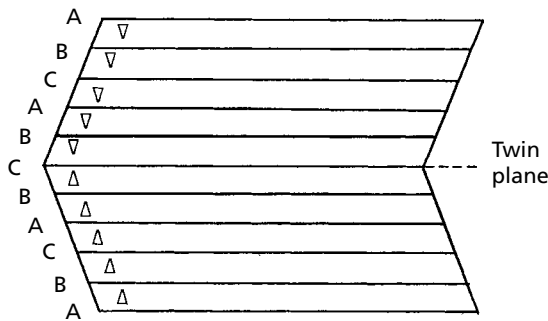


Fig. 1.18. Representation of the close-packed layers of a twinned fcc crystal indicating the atom layers ‘edge on’. Notice that the stacking sequence reverses across the twin plane, such that the crystal on one side of the twin plane is a mirror reflection of the other.

if the backs and palms of your hands were identical, in which case, of course, your right hand would be indistinguishable from your left!

The Frank notation shows very well the distinction between extrinsic and intrinsic stacking faults; in the former case there are two inversions from the fcc stacking sequence, and in the latter case, one.

So far we have only considered stacking of close-packed layers of atoms and stacking faults in terms of the simple ‘hard sphere’ model. This model, given the criterion that the atoms should fit into the ‘hollows’ of the layers below (Fig. 1.4), would indicate that any stacking sequence is equally likely. We know that this is not the case—the fact that (except for the occurrence of stacking faults) the atoms, for example, of aluminium, gold, copper, etc., form the ccp structure, and zinc, magnesium etc., form the hcp structure, indicates that other factors have to be considered. These factors are concerned with the minimization of the energies of the nearest and second nearest neighbour configuration of atoms round an atom. It turns out that it is the configuration of the second nearest neighbours which determines whether the most stable structure is ccp or hcp. In one metal (cobalt) and in many alloys (e.g. α -brass) the energy differences between the two configurations is less marked and varies with temperature. Cobalt undergoes a phase change $\text{ccp} \rightleftharpoons \text{hcp}$ at 25°C , but the structure both above and below this temperature is characterized by many stacking faults. In α -brass the occurrence of stacking faults (and twins) increases with zinc content.

A detailed consideration of the stability of metal structures properly belongs to solid state physics. However, in practice we need to invoke some parameter which provides a measure of the occurrence of stacking faults and twins, and this is provided by the concept of the stacking fault energy (units mJ m^{-2}); it is simply the increased energy (per unit area) above that of the normal (unfaulted) stacking sequence. Hence the lower the stacking fault energy, the greater the occurrence of stacking faults. On this basis the energy of a twin boundary will be about half that of an intrinsic stacking fault, and the energy of an extrinsic stacking fault will be about double that of an intrinsic stacking fault.

As mentioned above, stacking faults, and the concept of stacking fault energy, play a very important role in the deformation of metals. During deformation—rolling, extrusion, forging and so on—the regular, crystalline arrangement of atoms is not destroyed. Metals do not, as was once supposed, become amorphous. Rather, the deformation is accomplished by the gliding or sliding of close-packed layers over each other. The overall gliding directions are those in which the rows of atoms are close-packed, but, as will also be evident from the models, the layers glide in a zig-zag path, from ‘hollow to hollow’ and passing across the ‘saddle-points’ between them. This is shown in Fig. 1.19, which is similar to Fig. 1.4, but re-drawn showing fewer atoms for simplicity. The overall glide direction of the B layer is along a close-packed direction, e.g. left to right, but the path from one B position to the next is over the saddle-points via a C position, as shown by the arrows. But the B layer may stop at a C position (partial slip), in which case we have an (intrinsic) stacking fault (Exercise 1.7). This partial slip is represented by the arrows or vectors $\text{B} \rightarrow \text{C}$ or $\text{C} \rightarrow \text{B}$.

Extrinsic stacking faults, twins and the $\text{ccp} \rightarrow \text{hcp}$ transformation may be accomplished by mechanisms involving the partial slip of close-packed layers. The mechanism

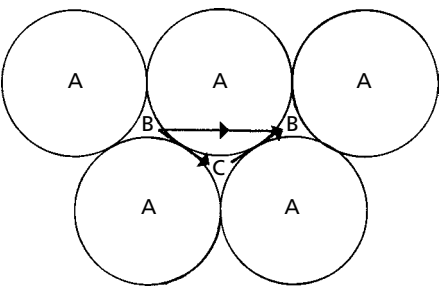


Fig. 1.19. On deformation, a B layer atom glides not in a straight line, e.g. $B \rightarrow B$ (left to right) but in two steps via a C site across the ‘saddle points’ between the underlying A layer atoms, i.e. $B \rightarrow C$ (first step), $C \rightarrow B$ (second step).

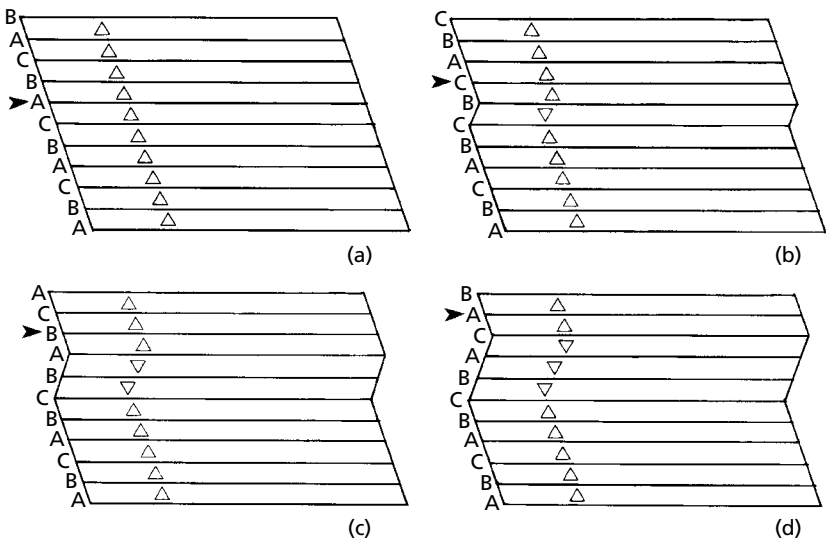


Fig. 1.20. (a)–(d) the sequence of faulting in a ccp (or fcc) crystal which leads to the formation of a twinned crystal as in Fig. 1.18. In Fig. 1.20(a) the close-packed layer to be faulted is an ‘A’ layer (arrowed) which in Fig. 1.20(b) becomes a ‘B’ layer and the layers above are relabelled accordingly; then the next layer above (the ‘C’ layer, arrowed) is faulted to become an ‘A’ layer (Fig. 1.20(c)) and so on.

for the generation of a twinned crystal by deformation is illustrated sequentially in Fig. 1.20. Figure 1.20(a) shows the close packed layers of a single fcc crystal ‘edge on’. Let us now slip an A layer (arrowed) into the sites of the B layer atoms (partial slip), as shown in Fig. 1.20(b). In doing so all the layers above the A layer move too: $B \rightarrow C$; $C \rightarrow A$; $A \rightarrow B$ and so on. Figure 1.20(b) also shows these re-labelled layers of atoms. Now let us slip the next layer up (arrowed), $C \rightarrow A$; and again $A \rightarrow B$, $B \rightarrow C$ and so on (Fig. 1.20(c)). Again, slip the third layer up (arrowed) and re-label the layers—as shown in Fig. 1.20(d). As we can see we will ultimately generate the

twinned crystal as shown in Fig. 1.18. This mechanism for deformation-twin formation may appear to be complicated; it occurs in practice (as in nearly all material deformation processes) through the movement of (partial) *dislocations*, a subject of great importance in materials science. The arrows in Fig. 1.19 represent the slip vectors for dislocations passing through the crystal; a slip vector such as $B \rightarrow B$, in which the stacking sequence is unchanged, represents the passage of a *whole dislocation*; a slip vector such as $B \rightarrow C$ or $C \rightarrow B$ in which, as described above, the stacking sequence is changed, represents the passage of a *partial dislocation*. Such whole and partial dislocations also occur in bcc metal (and other) crystals. In the particular example above (Fig. 1.19) the partial dislocation vectors $B \rightarrow C$ and $C \rightarrow B$ (which lie in the close-packed slip plane) are called *Shockley partials*, after William Shockley* who first identified them.

The twinned crystal shown diagrammatically in Fig. 1.18 is just one particular example of very general phenomenon, which occurs in crystals with much more complex structures and in which the two parts of the twinned crystal may not simply be related by reflection across the twin plane (reflection twins). In general a twinned crystal is one in which the two parts are related to each other by a rotation (usually, but not necessarily, 180°) about some particular direction called a *twin axis*. For example, we could create the twinned crystal in Fig. 1.18 by folding the figure 180° along the dashed line (the twin axis) which lies in the twin plane; alternatively we could ‘cut’ the single crystal in Fig. 1.20(a) in two along the *c* layer and create the twinned crystal by rotating the upper half 180° about a vertical direction (another twin axis) which in this case is normal to the twin plane. In our crystal all these actions (reflection in the twin plane, rotation 180° about an axis in the twin plane, rotation 180° about an axis normal to the twin plane) are all equivalent, but this is not necessarily the case as we will discover when we have learned about the symmetry of crystals.

Some examples of twinned crystals from geology and metallurgy are shown in Fig. 1.21. The left–right-hand character of the twinned crystal in Fig. 1.21(a) is easily seen; in practice the twins may be interpenetrated and twinning may occur not just in one but in several different planes, as shown in Figs 1.21(b) and (c). In metals and alloys, the presence of twins may be seen in polished and etched surfaces (Fig. 1.21(d)). Old cast brass doorknobs provide a good and homely example. The stacking fault energy of α -brass ($\text{Cu} \sim 30\% \text{ Zn}$) is very low (30 mJ m^{-2}) and almost all the grains or crystals will contain twins. The corrosive contact of human hands reveals the irregular outlines or boundaries between the grains and also the perfectly straight lines or traces of the twin boundaries which terminate (unlike scratches) at the grain boundaries, as shown in Fig. 1.21(d).

Twinning is very common in minerals, frequently occurring as a result of phase transitions during cooling. They may be observed, like the brass, on the polished surfaces of minerals, where they may give rise to beautiful iridescent textures as a result of the diffraction and interference of light (Chapter 7). They may be more readily seen in petrographic thin sections under the polarizing light microscope. For the petrologist they constitute one of the most important means of mineral identification.

* Denotes biographical notes available in Appendix 3.

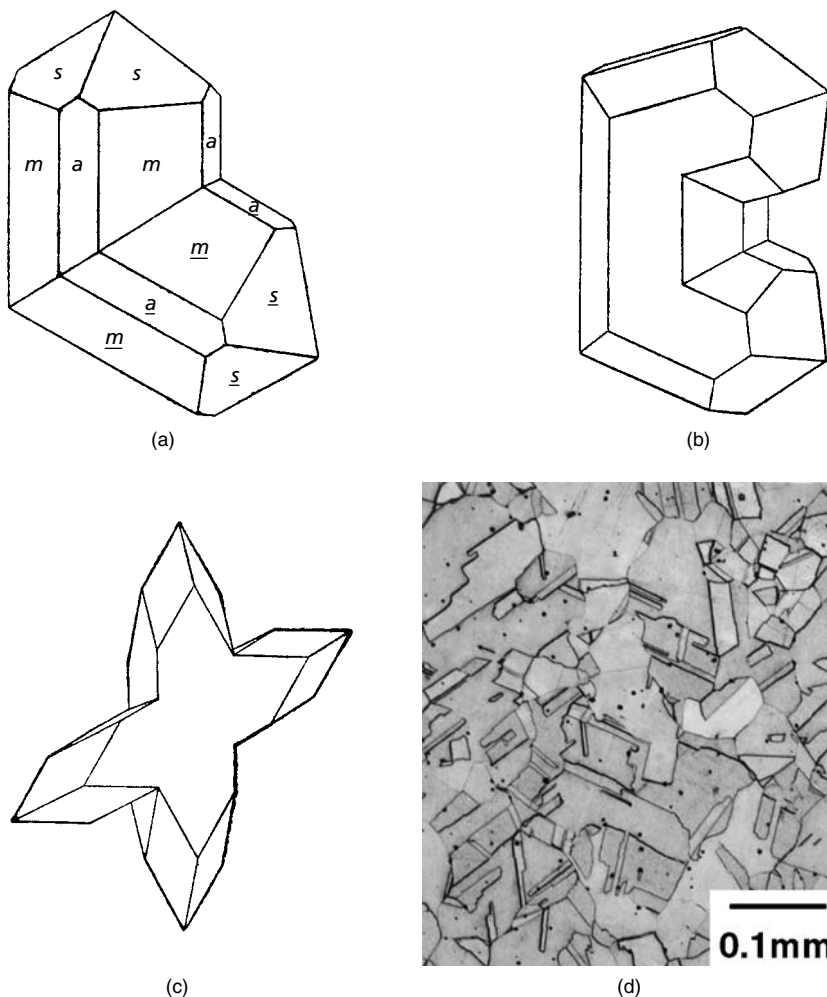


Fig. 1.21. Examples of twinned crystals: (a) rutile (TiO_2) twinned on a $\{101\}$ plane (from Rutley's *Elements of Mineralogy*, 25th edn, revised by H. H. Read, George Allen and Unwin Ltd, 1962); (b) multiple twinning in rutile (from *Introduction to Crystallography*, 3rd edn, by F. C. Phillips, Longmans, 1963); (c) interpenetrant twin in mercurous chloride (Hg_2Cl_2), twin plane $\{101\}$ (from F. C. Phillips loc. cit); (d) a photomicrograph of the etched surface of α -brass showing grain boundaries and (straight-sided) annealing twins, twin plane $\{111\}$.

1.10 The crystal chemistry of inorganic compounds

The newcomer to crystallography is often dismayed by the daunting level of complexity, or immensity of all the different crystal structures—not only inorganic but also organic. The subject may seem to depend so much on rote-learning and the committing to memory of a vast number of facts. The subject is certainly immense, but it is not arbitrary, and the

rules or criteria determining the simplest structures described in the preceding sections are the stepping-stones to an understanding of more complex structures.

We will consider the types of bonding which apply to inorganic crystals and the main differences to organic crystals (which are considered in more detail in Chapter 4). We have already seen how crystals may be represented as plans or projections (Section 1.8); now we will see how they can be represented in terms of coordination polyhedra, which lead naturally to a (brief) discussion of Pauling's rules which describe the conditions for the stability (and therefore the existence of) predominantly ionic crystal structures. Then, in Section 1.11, we describe some rather more complex crystal structures which either illustrate the principles we have already learned or for their own intrinsic interest and topolity.

1.10.1 Bonding in inorganic crystals

So far in this book we have described some simple crystal structures solely in geometrical terms—i.e. the various arrangements in which ions and atoms of different sizes can pack together. Now we must consider the forces which hold the ions and atoms together. This is of course a subject of profound importance in physical chemistry and we can only summarize, in a very simple way, the main features of the bonding mechanisms.

In inorganic crystals, the dominant bonding forces are *ionic* or *heteropolar bonds* and *covalent* or *homopolar bonds*, with lesser contributions from van der Waals and hydrogen bonds.

Ionic bonding dominates in inorganic crystals as a result of the high *electronegativity difference* between the atomic species—the (positive) metal cations on the one hand and the (negative) F^- , Cl^- , O^{2-} anions on the other. The simple compounds $NaCl$, $CsCl$ and CaF_2 which we have already described are examples of almost 'pure' ionic bonding. Moreover, the ionic bond is non-directional, an important characteristic which it shares with the *metallic bond* which is the dominant cohesive force in metals with a high conductivity: the positive metal ions are held together by a 'sea' of conduction electrons which are wholly non-localized, i.e. the electrons are not bound to individual atoms.

As the electronegativity difference between the atomic species decreases, the covalent bond begins to dominate: the bonding electrons are 'shared' between the atoms instead of being transferred between the atomic orbitals. In sulphides, e.g. ZnS , the bonding is partly covalent. Unlike the ionic bond, the covalent bond is directional, the configuration around the atoms corresponds to, or arises from, the configuration of the atomic orbitals. An example of 'pure' covalent bonding is diamond (the hardest material known), described in more detail in Section 1.11.6. The carbon atoms in diamond are tetrahedrally coordinated, corresponding to the pattern of the sp^3 orbitals. The metallic bond, mentioned above, may be regarded as a 'special case' of a covalent bond—an atom shares electrons with its nearest neighbours and the empty orbitals permit the flow of conduction electrons. In many inorganic compounds, the bonding is a 'mixture' of (dominantly) ionic and (dominantly) covalent bonding. For example, in calcite, $CaCO_3$, the bonding between the Ca^{2+} and $(CO_3)^{2-}$ ions is dominantly ionic but the bonds which hold the $(CO_3)^{2-}$ groups together is dominantly covalent. The structure of calcite strongly resembles that

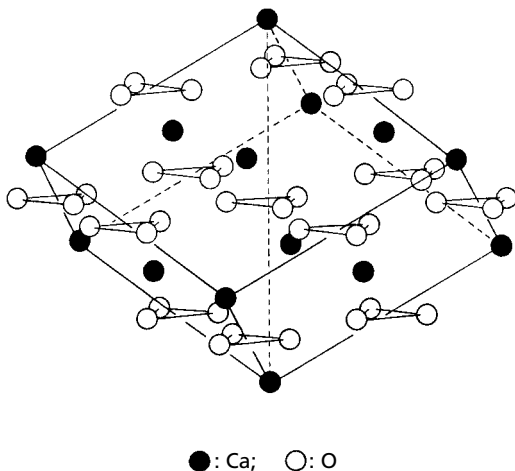


Fig. 1.22. The rhombohedral structure of calcite, CaCO_3 . The cell shown is not the smallest unit cell but corresponds to the cleavage rhombohedra which occur in natural crystals of calcite. The smallest unit cell may be outlined by linking together the eight innermost Ca^{2+} ions, following the pattern shown in Figure 1.7(c). (From *An Introduction to Crystal Chemistry*, 2nd Edn, by R. C. Evans, Cambridge University Press, 1964.)

of NaCl, except that the presence of the planar $(\text{CO}_3)^{2-}$ groups, all orientated the same way, parallel to the ABCABC ... stacking sequence (see Fig. 1.6(b)), ‘distorts’ the cubic symmetry, or shape of the unit cell, to rhombohedral as shown in Fig. 1.22.

It is the high strength of ionic and covalent bonds which gives rise to the most characteristic mechanical property of inorganic compounds—their high hardness. However, many inorganic compounds are highly anisotropic in their mechanical properties, being ‘strong’ in some directions and ‘weak’ in others. Examples are the ‘layer-structure’ phyllosilicates, talc and mica (see Section 1.11.4) and graphite (see Section 1.11.6). Within the layers the ions/atoms are strongly ionically or covalently bonded, but the layers are only held together by much weaker *van der Waals* bonds which arise from the continuously changing dipole moments within atoms or molecules. An analogous situation applies to solid *organic* compounds; the atoms in the molecules themselves are strongly covalently bonded but the molecules are held together by weak *van der Waals* bonds and solid organic compounds are, in comparison, generally soft materials.

The concept of a molecule, introduced above, is of course fundamental in chemistry, but it can be an obstacle in understanding the arrangements and proportions of atoms and ions in inorganic compounds in the solid state. For example, it is not possible to identify a ‘molecule’ of NaCl in a crystal (Fig. 1.14(a)); each Na ion is bonded equally to six surrounding Cl ions and vice versa; the Na and Cl ions are not ‘paired’ to each other in any special way. W. L. Bragg records (in *The Development of X-ray Analysis*) that his chemical colleagues were loath to give up the idea of molecules in inorganic compounds and even as late as 1927, Henry E. Armstrong, an eminent chemist, published the following letter in *Nature*.

‘Poor Common Salt’

“Some books are lies frae to end” says Burns. Scientific (save the mark) speculation would seem to be on the way to this state!... Prof. W.L. Bragg asserts that “In sodium chloride there appear to be no molecules represented by NaCl. The equality in number of sodium and chlorine atoms is arrived at by a chess-board pattern of these atoms; it is a result of geometry and not of a pairing-off of the atoms.”

This statement is more than repugnant to common sense. It is absurd to the n .th degree, not chemical cricket. Chemistry is neither chess nor geometry, whatever X-ray physics may be. Such unjustified aspersion of the molecular character of our most necessary condiment must not be allowed any longer to pass unchallenged... It were time that chemists took charge of chemistry once more and protected neophytes against the worship of false gods; at least taught them to ask for something more than chess-board evidence.

However, perhaps the letter was written with a pinch of salt!

In addition, many inorganic compounds are *non-stoichiometric*. FeO, for example, which has the same structure as NaCl, rarely has the exact formula FeO, but a smaller proportion of Fe than in the ratio 1:1. This simply indicates the existence of vacant Fe^{2+} lattice sites and equal numbers of Fe^{3+} ions on other sites to ensure electrical neutrality and does not indicate a distinct chemical compound (see Section 1.11.3).

However, as mentioned above, the concept of a molecule is of vital importance in understanding the structures of solid *organic* compounds. The strong covalent bonds which bind together the carbon, nitrogen, oxygen, etc. atoms within the organic molecule, and which cause it to retain its identity when the compound is melted, dissolved, or even vaporized, are much stronger than the van der Waals bonds between the molecules in the solid state. The symmetries of the crystal structures which occur are, to a first approximation, determined by the overall shape or envelope of the molecules and the ways in which they pack together in the most efficient manner. However, we defer any further consideration of organic compounds until Chapter 4 when we have learned about symmetry, lattices and the methods needed to describe the geometry of crystals.

1.10.2 Representing crystals in terms of coordination polyhedra²

As we have seen in Sections 1.6 and 1.7, inorganic crystal structures may be described in terms of (small) atoms or cations, surrounded, or coordinated by, (large) atoms or anions. An alternative and very fruitful way of representing such structures is to concentrate attention on the coordinating polyhedra themselves rather than the individual atoms situated at their corners. We can then view the crystal structure as a pattern of linked polyhedra, without our view being obscured, as it were, by the large atoms or ions themselves.

The most important coordination polyhedra in inorganic crystals are the tetrahedron, $r_X/r_A = 0.225$; the octahedron, $r_X/r_A = 0.414$ (see Section 1.6) and the cubeoctahedron and hexagonal cubeoctahedron, $r_X/r_A = 1.000$, all of which occur in close-packed

² See Appendix 2 – Polyhedra in crystallography.

structures. The last two polyhedra represent the pattern of 12 atoms surrounding, or co-ordinating, an atom in face-centred and hexagonal close-packing respectively.

The polyhedra may be separate or linked together in various ways – corner-to-corner, edge-to-edge, face-to-face or in various combinations. Geometrically, the possibilities are almost endless, but in terms of the stability of inorganic crystals, they are not. The criteria which govern the stability, and hence possible structures, in (dominantly) ionic crystals, were set out by Linus Pauling* in a series of empirical rules. Essentially, these rules express the requirement for a charge balance between a cation and its surrounding polyhedron of anions and also between an anion and the cations that immediately surround it. The chemical law of valency is satisfied not by ‘pairing off’ individual anions and cations but by a ‘sharing’, or distribution of (say) the positive charge of a cation among the surrounding polyhedron of anions. This is further evidence of the

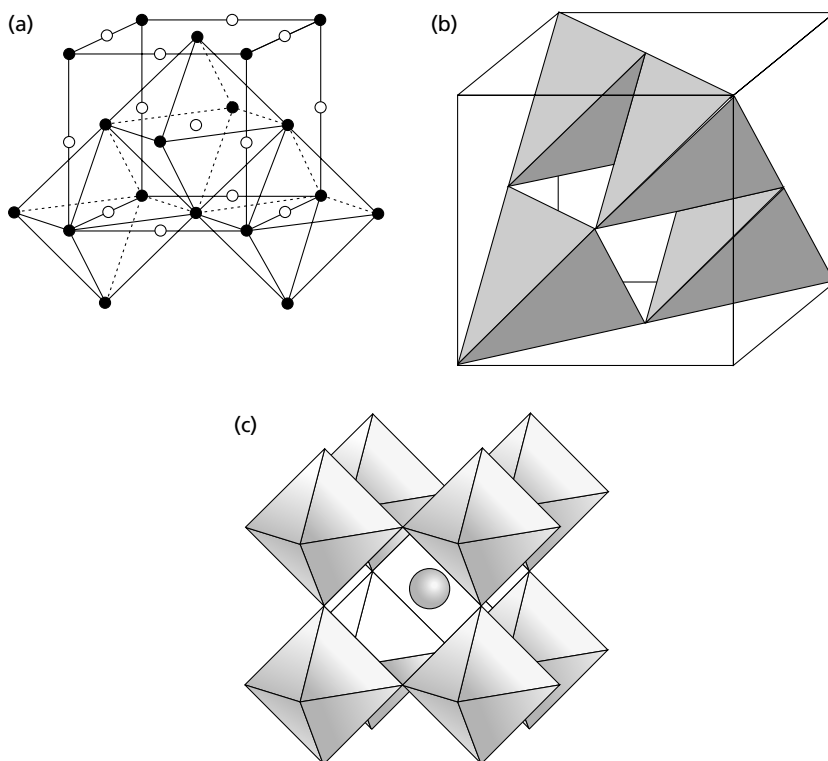


Fig. 1.23. Co-ordination polyhedra in three simple crystal structures: (a) edge-sharing octahedra in sodium chloride; (b) corner-sharing tetrahedra in zinc blende; and (c) corner-sharing octahedra and the (central) cubeoctahedron in perovskite. (From *An Introduction to Mineral Sciences* by Andrew Putnis, Cambridge University Press, 1992.)

* Denotes biographical notes available in Appendix 3.

non-existence of identifiable ‘molecules’ in inorganic ionic structures. Pauling’s rules also determine, or limit, the ways in which the polyhedra can be linked together. The octahedra and cubeoctahedra surrounding larger and weaker cations may share corners, edges or even faces, but the tetrahedra surrounding the smaller and more highly positive cations tend only to share corners, such that the cations are as far apart as possible. We have already encountered this aspect of Pauling’s rules in our discussion (Section 1.7) of the ‘non-existence’ of hcp structures in which all the tetrahedral sites are filled; the sites occur in pairs with the tetrahedra arranged face-to-face and the cations are too close to ensure stability. This also applies to the (Si,Al) O_4 tetrahedra which comprise the building blocks of the silicate minerals (see Section 1.11.4), the tetrahedra are isolated or share one, two, three or four corners, never edges or faces. However, this is not true of all synthesized ceramic materials. The new nitrido-silicates and sialons are based on the linkage of (Si, Al)(N, O) $_4$ (predominantly SiN $_4$) tetrahedra which share edges as well as corners and in addition, Si is octahedrally coordinated by N.

Figure 1.23 shows the coordination polyhedra in three simple crystal structures: (a) the edge-sharing octahedra in sodium chloride, NaCl; (b) the corner-sharing tetrahedra in zinc blende, ZnS; and (c) the corner-sharing octahedra and the central cubeoctahedron in perovskite, CaTiO $_3$. The unit cell shown is the same as that in Fig. 1.17(a).

1.11 Introduction to some more complex crystal structures

1.11.1 *Perovskite (CaTiO $_3$), barium titanate (BaTiO $_3$) and related structures*

Perovskite is an important ‘type’ mineral (in the same way as sodium chloride, NaCl) and is the basis of many technologically important synthetic ceramics in which the Ca is replaced by Ba, Pb, K, Sr, La or Co and the Ti by Sn, Fe, Zr, Ta, Ce or Mn. The general formula is ABO $_3$ (see Fig. 1.17), the A ion being in the large cubeoctahedral sites and the B ion being in the smaller octahedral sites (Fig. 1.23(c)). In perovskite itself, A is the divalent ion and B the tetravalent ion. This however is not a necessary restriction; trivalent ions can, for example, occupy both A and B sites; all that is needed is an aggregate valency of six to ensure electrical neutrality. It is, in short, a working out of Pauling’s rules again. Of much greater importance are the sizes of these ions because they lead, separately or in combination, to different distortions of the cubic cell. In perovskite itself, the Ca cation is ‘too small’ for the large cubeoctahedral site and so the surrounding octahedra tilt, in opposite senses relative to one another, to reduce the size of the cubeoctahedral site. This is shown diagrammatically in Fig. 1.24(a). The unit cell is now larger, as outlined by the solid lines, the unit cell repeat distance now being between the similarly oriented octahedra (see Section 2.2). The symmetry is tetragonal, rather than cubic. The tilts are also slightly out of the plane of the projection which further reduces the symmetry to orthorhombic (see Chapter 3 for a description of these non-cubic structures).

In barium titanate, BaTiO $_3$, the Ti cation is ‘too small’ for the octahedral site and shifts slightly off-centre within the octahedron (Fig. 1.24(b)); the cubic unit cell is distorted to tetragonal. These shifts may occur along any of the three cube-edge directions such that a

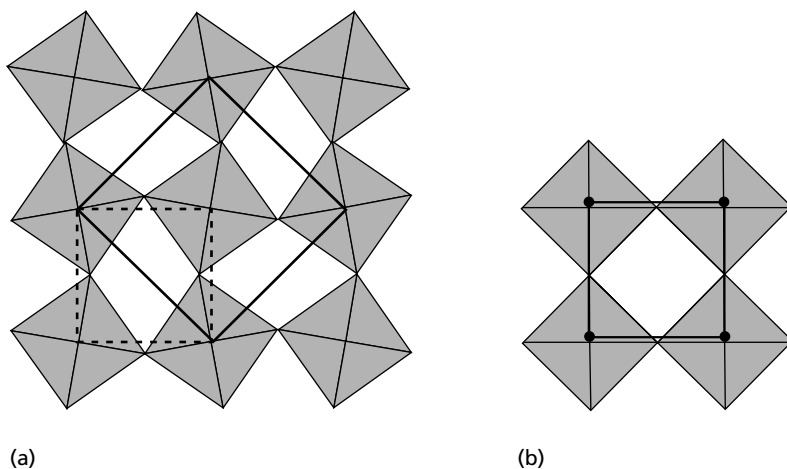


Fig. 1.24. Two modifications to the perovskite structure: (a) octahedra tilted in opposite senses, the cubic cell is outlined by dashed lines and the tetragonal cell by full lines; (b) displacements of the B cations from the centres of the octahedra resulting in a distortion of the original cubic cell to a tetragonal unit cell (full lines). (From *An Introduction to Mineral Sciences* by Andrew Putnis, Cambridge University Press, 1992.)

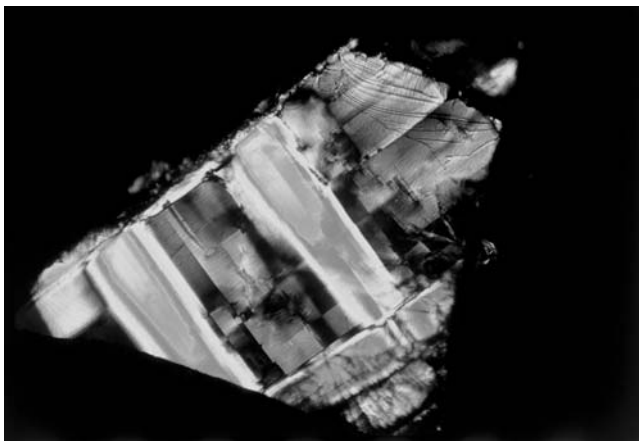


Fig. 1.25. A polarized-light micrograph (crossed polars) of a single crystal of barium titanate which reveals the domains in each of which the tetragonal distortion is in a different cube-edge direction.

single crystal of BaTiO_3 may be divided into *domains*; within each domain, the shift is in the same direction (Fig. 1.25) (the idea of domains is discussed, with respect to ordered crystals, in Section 9.7). The consequence is that within a crystal (or within a domain) there is a net movement of charge, resulting in a structure with a dipole moment, and this spontaneous electrical polarization leads to the property of *ferroelectricity* which is of

such great importance in many electronic devices and is the basis of much research on the titanates—some of which are antiferroelectric (e.g. PbZrO_3), ferromagnetic (e.g. $\text{LaCo}_{0.2}\text{Mn}_{0.8}\text{O}_3$) or antiferromagnetic (e.g. LaFeO_3). Barium titanate itself undergoes further transformations at lower temperatures (to orthorhombic and rhombohedral forms) which are, as with the tetragonal form, ferroelectric.

At higher temperatures (120°C for barium titanate), due to the increased thermal movement of the atoms, these structures revert to the cubic forms. This is an example of a *displacive transformation*: no bonds are broken. Such displacive transformations also characterize the ‘high temperature’ (α) and ‘low temperature’ (β) forms of quartz, tridymite and cristobalite (see Section 1.11.5) and also relate the polymorphous forms of many *organic* compounds—the structures only differing in the way in which the molecules are packed together under the influence of the weak van der Waals forces.

1.11.2 Tetrahedral and octahedral structures—silicon carbide and alumina

Consider, for example, the crystal structures which consist of close-packed or nearly close-packed layers of large atoms or ions with the smaller atoms or ions occupying some or all of the tetrahedral interstitial sites. Zinc blende and wurtzite are two such structures (Section 1.7) which are re-drawn in Fig. 1.26 so as to emphasize the

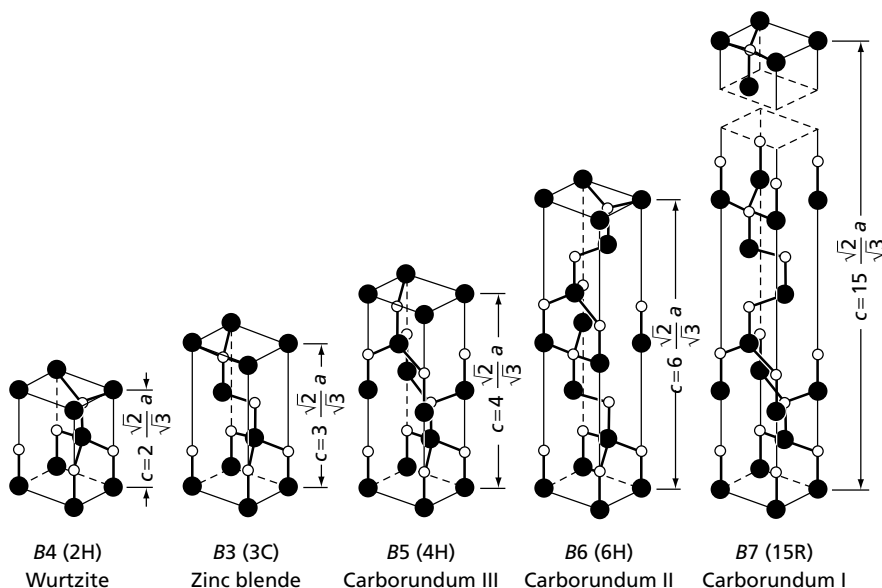


Fig. 1.26. Five common tetrahedral structure types. The bracketed symbols refer to the number of layers in the repeat sequence and the structure type: H (hexagonal), C (cubic) and R (rhombohedral) (after E. Parthe, *Crystal Chemistry of Tetrahedral Structures*, Gordon and Breach, New York, 1964, reproduced from *The Structure of Metals*, 3rd edn, C. S. Barrett and T. B. Massalski, Pergamon, 1980).

$\Delta\Delta\Delta\Delta \dots$ Stacking of the Zn (or S) atoms in zinc blende and the $\Delta\nabla\Delta\nabla \dots$ stacking of the Zn (or S) atoms in wurtzite. Many carbides, including silicon carbide, SiC, also possess such close-packed structures with the carbon atoms occupying the tetrahedral sites and the metal or metalloid atoms stacked in various combinations of $\Delta\Delta\Delta\Delta \dots$ and $\Delta\nabla\Delta\nabla \dots$. Figure 1.26 shows five structures or *polytypes* of silicon carbide (B3–B7) in which the silicon atoms are represented as solid spheres and the carbon atoms as small open spheres. The low-temperature form, β -SiC (B3) has the fcc structure, isomorphous with zinc blende. There are a number of high-temperature polytypes known collectively as α -SiC, the simplest structure of which, B4, is isomorphous with wurtzite. The other polytypes of α -SiC, three of which (B5, B6, B7) are shown in Fig. 1.26, have more complex stacking sequences, resulting in longer unit cell repeat distances.

For example, the stacking sequence in B5 (Carborundum III) is (reading up) ABA-CABAC giving a four-layer repeat distance. In the Frank notation this is represented as $\Delta\nabla\nabla\Delta\Delta\nabla\nabla \dots$ i.e. by inversions in the stacking sequence every two layers, rather than every layer as in B4, the wurtzite structure. Similarly, for B6 (Carborundum II) the stacking sequence is ABCACBA \dots giving a six-layer repeat distance which in the Frank notation is $\Delta\Delta\Delta\nabla\nabla\nabla \dots$ i.e. an inversion every three layers.

Figure 1.27 shows an alternative representation of the polytypes of SiC showing (for clarity) only the close-packed layers of the metalloid (Si) atoms. The number below each polytype refers to the number of layers in the unit cell repeat distance and the letter refers to the type of unit cell (C—cubic; H—hexagonal; R—rhombohedral). All these polytypes of silicon carbide should not be thought of as distinct ‘species’, rather they should be regarded as interrelated as a result of different sequences of stacking faults and the transformations $\beta \rightleftharpoons \alpha$ SiC appear, from electron microscopy evidence, to occur as the result of the passage of partial dislocations across the close-packed planes in the same way as for the generation of a twinned crystal, as shown in Fig. 1.20. For example 6H, a common form of α -SiC, may be regarded as a ‘microtwinning’ form of 3C, the three-layer thick twins being generated by the passage of three partial dislocations on successive close-packed planes as shown in Fig. 1.20(d).

In aluminium oxide, Al_2O_3 , the large oxygen anions occur in close-packed or nearly close packed layers with the aluminium cations occupying two-thirds of the octahedral interstitial sites. We now have an added complexity; not only may the oxygen anions be packed in different sequences but also the aluminium cations may be distributed differently throughout the interstitial sites—i.e. there may be different distributions of the one-third ‘empty’ sites. In the well-characterized form, α - Al_2O_3 (corundum—isomorphous with α - Fe_2O_3), the oxygen anions are stacked in the hcp ABAB \dots stacking sequence and the aluminium cations between them are stacked in a rhombohedral sequence in exactly the same pattern as the carbon atoms in the rhombohedral form of graphite (see Fig. 1.37(b)). Hence the structure of α - Al_2O_3 is rhombohedral with a six-layer unit cell repeat distance of oxygen anions. The other polytypes of alumina, called the transition aluminas, are not so well characterized, particularly with respect to the distribution of the aluminium cations. A common form, γ - Al_2O_3 is based on an ABCABC \dots (fcc) stacking of oxygen anions with a distribution of aluminium cations which gives rise to a maghemite structure, described in Section 1.11.3.

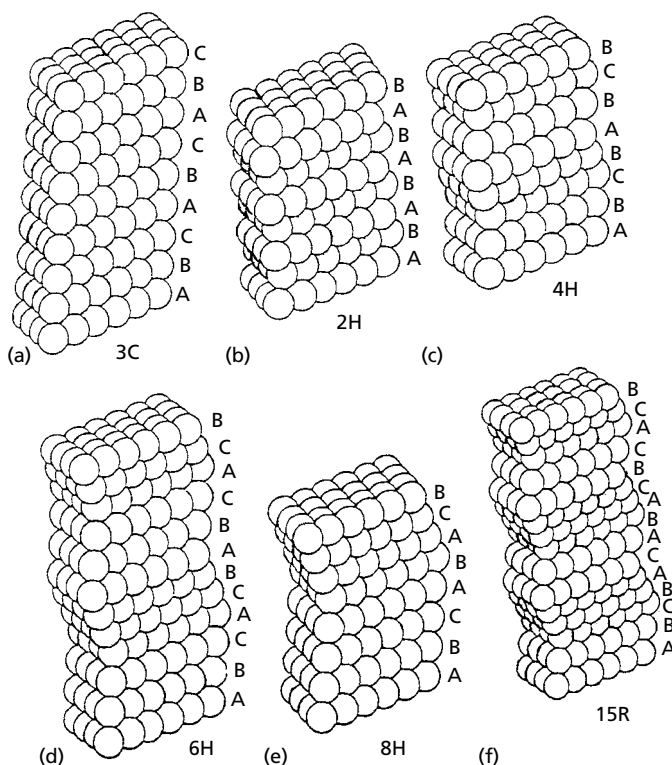


Fig. 1.27. The crystal structures of six SiC polytypes. 3C is β -SiC, the fcc low temperature form and the others with 2, 4, 6 and 8-layer repeat hexagonal cells or a 15-layer repeat rhombohedral cell are the α -SiC high temperature forms (from *Ceramic Microstructures* by W. E. Lee and W. M. Rainforth, Chapman & Hall, 1994).

1.11.3 The oxides and oxy-hydroxides of iron

Iron is remarkable for the range of oxides and hydroxides which can be formed and is one of the few elements which form compounds intermediate between these two—the oxy-hydroxides, the crystal structures of which are also of interest, and we will now describe them (as far as we are able) and trace their interrelationships.

We will begin with the simplest oxide, wustite, ferrous oxide, FeO and consider the structural changes which take place in the progressive oxidation of FeO to Fe₃O₄ (ferroso-ferric oxide) and Fe₂O₃ (ferric oxide). FeO has the NaCl structure—the Fe²⁺ ions are situated in the octahedral interstitial sites between the oxygen anions³. However, FeO is rarely stoichiometric but has vacant Fe²⁺ sites in the face-centred cubic

³ The terms 'anion' and 'cation' are used when we want to draw specific attention to the charge on the ionic species, otherwise the more general term 'atom' is used—it being understood that the term encompasses both neutral and charged species.

structure, electrical neutrality being preserved by the presence of equal numbers of Fe^{3+} ions (some of which are situated in the tetrahedral interstitial sites). The 'oxidation' of FeO to Fe_3O_4 proceeds, not by the 'addition' of oxygen atoms to the structure, but by the migration of Fe atoms to the surface (to combine with atmospheric oxygen there)—to a first approximation the close-packed oxygen atoms in the original FeO structure remain undisturbed. Within the structure the Fe^{2+} ions are progressively replaced by Fe^{3+} ions, half of which are situated in the tetrahedral interstitial sites. The structure of Fe_3O_4 (magnetite) thus formed is that of an *inverse spinel* with the general formula AB_2O_3 in which the 'A' tetrahedral sites are occupied by Fe^{3+} ions and the 'B' octahedral sites by equal numbers of Fe^{3+} and Fe^{2+} ions. Fe_3O_4 is therefore better represented by the formula $\text{Fe}^{3+}(\text{Fe}^{3+}\text{Fe}^{2+})\text{O}_4$. However, the occupancy of the interstitial sites is not random, but ordered such that the unit cell of Fe_3O_4 has twice the side-edge (eight times the volume) of the original FeO unit cell and contains 32 O^{2-} ions, 8 Fe^{2+} ions and 16 Fe^{3+} ions.

The distinction between an 'inverse' and a 'normal' spinel (both bad names!) is simple: spinel is the mineral MgAl_2O_4 . The Mg^{2+} ions occupy the 'A' tetrahedral sites and the Al^{3+} ions occupy the 'B' octahedral sites—with regard to the 'A' sites only the inverse of Fe_3O_4 . Again, we see that the occupancies of the interstitial sites are determined not simply by the valencies of the ions but also their sizes. Figure 1.28 shows a projection, or crystal plan of the spinel structure (see Section 1.8), split into two halves to make the atom/ion positions more clear.

As oxidation proceeds further the remaining eight Fe^{2+} ions in the unit cell are replaced by two-thirds of their number by Fe^{3+} ions (i.e. to maintain electrical neutrality) giving a total of $16 + 5\frac{1}{3} = 21\frac{1}{3}$ Fe^{3+} ions, 32 O^{2-} ions and the overall composition Fe_2O_3 . Except for a small reduction in volume (on account of the increased number of vacant lattice sites) the large cubic unit cell is unchanged. The structure is called maghemite, $\gamma\text{-Fe}_2\text{O}_3$ and is isostructural with the $\gamma\text{-Al}_2\text{O}_3$ structure (see Section 1.11.2).

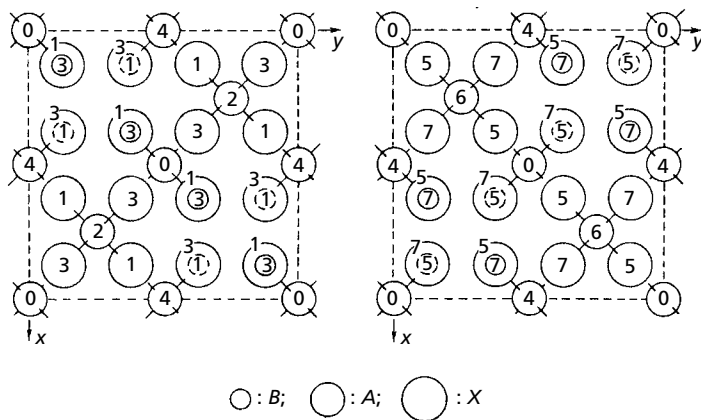


Fig. 1.28. Plan view of the unit cell of the cubic spinel structure AB_2X_4 projected on to a plane perpendicular to a cube axis. The heights of the atoms are indicated in units of one-eighth the cubic cell edge length. For clarity, the upper and lower halves of the cell are shown separately and only the tetrahedral coordination of the A ions is indicated. (From *Crystal Chemistry*, 2nd Edn, by R. C. Evans, Cambridge University Press, 1966.)

However, γ -Fe₂O₃ (like γ -Al₂O₃) is not the stable structural form and its conversion to α -Fe₂O₃ (haematite) occurs essentially by the rearrangement of the oxygen atoms from the fcc to the hcp stacking sequence.

Similar relationships exist in the oxy-hydroxides in which iron is in the Fe³⁺ (ferric) form. The formulae are best written FeO·OH (rather than Fe₂O₃·H₂O) to emphasize the replacement of oxygen ions by hydroxyl, (OH)⁻ groups rather than the presence in the structure of discrete ‘molecules’ of water. In γ -FeO·OH (lepidocrocite), the oxygen and hydroxyl ions are *approximately* cubic close-packed and in α -FeO·OH (goethite), they are *approximately* hexagonal close-packed. The deviation from perfect close-packing arises from the formation of directed hydrogen bonds between the hydroxyl groups in different layers; the structures are not cubic or hexagonal but have orthorhombic symmetry (see Chapter 3). On heating, these oxy-hydroxide structures dehydrate to γ -Fe₂O₃ and α -Fe₂O₃, respectively.

Lepidocrocite and goethite are not the only oxy-hydroxides which occur. Of perhaps more biological or technological importance is ferrihydrite, a poorly crystallized mineral which is ubiquitous across the Earth’s surface. It is a common product of weathering of iron-bearing minerals and of the microbial oxidation of ferrous ions and doubtless of the rusting of iron itself.

The determination of its crystal structure and composition is a matter of considerable difficulty because of the very small crystallite size, typically in the range 2–10 nm. However, it appears that the oxygen-hydroxyl groups are arranged in an hcp (2H, 4H or 6H) stacking sequence (see Fig. 1.27), i.e. closer to goethite than lepidocrocite and possibly isostructural with a natural alumina hydrate phase, akdaleite. The composition is commonly given as Fe₅(OH)₈·4H₂O but the water content appears to depend on particle size.

Ferrihydrite is an example of a naturally occurring *nanocrystalline* material—upon which a whole new science and technology is now being built. Their importance consists in the simple fact that at these sizes a large proportion of the atoms or ions are at, or near, the surface and the conditions for the stability of the structures are found to be (as might be expected) quite different at the centres of the crystals and at their surfaces.

Such nano-sized crystals of ferrihydrite also appear to constitute the inorganic ‘core’ of the ferritin molecule—the iron storage molecule that occurs principally within the liver. The core is enclosed within a protein ‘shell’ (Fig. 1.29) which has a cubic symmetry not found in any inorganic crystals (see Chapter 4).

The mechanisms by which iron leaves and enters the ferritin molecule, and how it is taken up, and released, from the ferrihydrite, are matters of much research. But undoubtedly the crystallography—the valency and distribution of iron ions across the interstitial sites both at and below the crystal surfaces—will emerge as factors of great importance.

1.11.4 Silicate structures

Silicates—which constitute by far the most important minerals in the earth’s crust—are based on the different ways in which SiO₄ tetrahedra⁴ may be joined together, each

⁴ The SiO₄ tetrahedra may be referred to more generally as Si–O tetrahedra since, as described in subsections (a)–(g), the silicon–oxygen ratio depends on how they are linked.

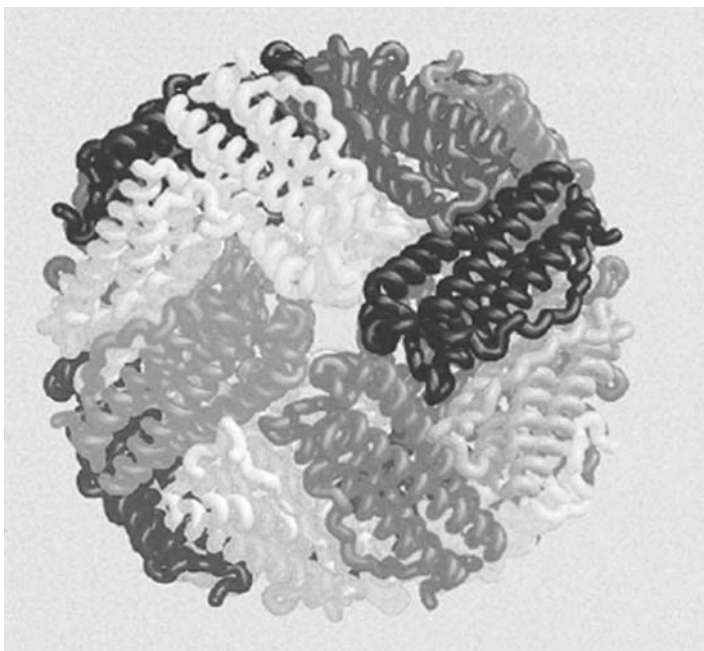


Fig. 1.29. The cubic (point group 432) structure of the ferritin protein shell viewed along a cube axis. (From *Mineralization in Ferritin: An Efficient Means of Iron Storage* by N Dennis Chasteen and Pauline M Harrison, *Journal of Structural Biology* **126**, 182–, 1999.)

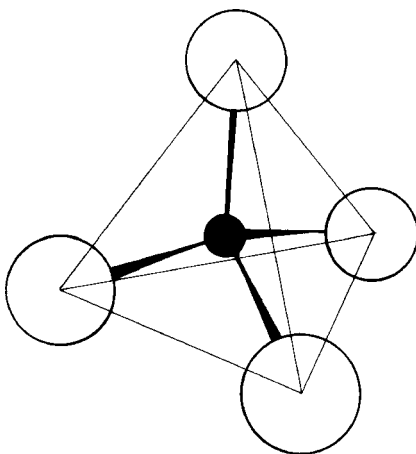
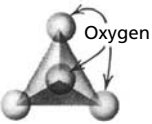

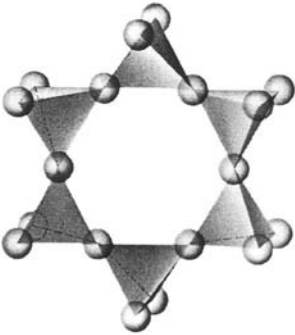
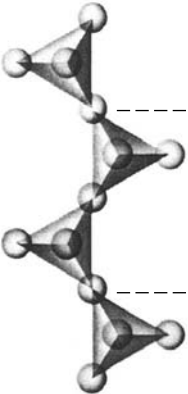


Fig. 1.30. A perspective of the SiO_4 tetrahedron. The oxygen anions at the corners of the tetrahedron are nearly close packed, as shown in the models, e.g. in Fig. 1.7 (the radius of the oxygen anion, $r_n = 0.132 \text{ nm}$ and that of the silicon cation, $r_x = 0.039 \text{ nm}$, give a radius ratio, $r_x/r_n = 0.296$, slightly larger than the ideal value $r_x/r_n = 0.225$, Fig. 1.10(a) and (b)).

tetrahedron being made up of four oxygen anions with the silicon cation in the tetrahedral interstice in the centre (Fig. 1.30). Silicate chemistry is based on the linking of the SiO_4 tetrahedra, i.e. whether they occur separately, or whether they are linked by common oxygen anions to form chains, rings, sheets or complete frameworks. This provides the initial basis for the classification of silicate structures. If the Si–O bond is considered to be purely ionic, there are four positive charges associated with each silicon cation and two negative charges associated with each oxygen anion; hence there are four net negative charges associated with each SiO_4 tetrahedron. The ‘charge balance’ in silicates may be achieved in seven possible ways (see Fig. 1.31):

- (a) Separate SiO_4 tetrahedra (*nesosilicates*): the charge balance (four net negative charges) is achieved with metal cations, e.g. Mg^{2+} , Fe^{2+} , which also link the tetrahedra together. Typical minerals are forsterite, $\text{Mg}_2(\text{SiO}_4)$, or fayalite, $\text{Fe}_2(\text{SiO}_4)$, the end-members of the olivine group, $\text{MgFe}(\text{SiO}_4)$.
- (b) Two tetrahedra linked together sharing one oxygen anion (*sorosilicates*): the Si:O ratio is now Si_2O_7 giving six net negative charges which are balanced with metal cations. Typical minerals are melilite, $\text{Ca}_2\text{Mg}(\text{Si}_2\text{O}_7)$, or hemimorphite, $\text{Zn}_4(\text{OH})\text{H}_2\text{O}(\text{Si}_2\text{O}_7)$.
- (c) Three or more tetrahedra linked together to form rings, each tetrahedron sharing two oxygen anions (*cyclosilicates*): the Si:O ratio is Si_nO_{3n} , where n is the number of tetrahedra in the ring. A typical mineral is beryl, with a ring of six tetrahedra, $\text{Be}_3\text{Al}_2(\text{Si}_6\text{O}_{18})$.
- (d) Many tetrahedra linked together to form single chains (*inosilicates*): each tetrahedron shares two oxygen anions, as in the ring structures above, and which therefore give rise to the same Si:O ratio. This is the basis of the group of minerals called the pyroxenes. Typical examples are enstatite, $\text{Mg}_2(\text{Si}_2\text{O}_6)$, or diopside, $\text{CaMg}(\text{Si}_2\text{O}_6)$.
- (e) Tetrahedra linked together to form double chains (*inosilicates*), each tetrahedron sharing alternately two and three oxygen anions, giving the Si:O ratio Si_4O_{11} . This is the basis of the group of minerals called the amphiboles. Typical examples are anthophyllite, $\text{Mg}_7(\text{OH})_2(\text{Si}_4\text{O}_{11})_2$, or tremolite, $\text{Ca}_3\text{Mg}_5(\text{OH})_2(\text{Si}_4\text{O}_{11})_2$.
- (f) Tetrahedra linked together to form sheets (*phyllosilicates*), each tetrahedron sharing three oxygen anions giving the Si: O ratio Si_2O_5 . This is the basis of the micas, chlorites and the clay minerals.
- (g) Tetrahedra linked together such that all the oxygen anions are shared giving a three-dimensional framework (*tectosilicates*). The Si:O ratio is now SiO_2 and there is an overall charge balance without the necessity of any linking cations.

Figure 1.31 shows the arrangements of SiO_4 tetrahedra in these seven silicate structures. However, having established the basic pattern there are very important complications both in the chemistry and the arrangements of the tetrahedra which must not be overlooked. In all the silicates, and in the chain, sheet and framework silicates in particular, the silicon in the centre of the tetrahedron can be substituted by aluminium—a trivalent rather than a tetravalent ion. For each such substitution an additional positive charge by way of a ‘linking cation’ is required. All sheet silicates or phyllosilicates show

Class	Arrangement of SiO ₄ tetrahedra (central Si ⁴⁺ not shown)	Unit composition	Mineral example
(a) Nesosilicates		(SiO ₄) ⁴⁻	Olivine, (Mg, Fe) ₂ SiO ₄
(b) Sorosilicates		(Si ₂ O ₇) ⁶⁻	Hemimorphite Zn ₄ Si ₂ O ₇ (OH)·H ₂ O
(c) Cyclosilicates		(Si ₆ O ₁₈) ¹²⁻	Beryl, Be ₃ Al ₂ Si ₆ O ₁₈
(d) Inosilicates (single chain)		(Si ₂ O ₆) ⁴⁻	Pyroxene e.g. Enstatite, MgSiO ₃

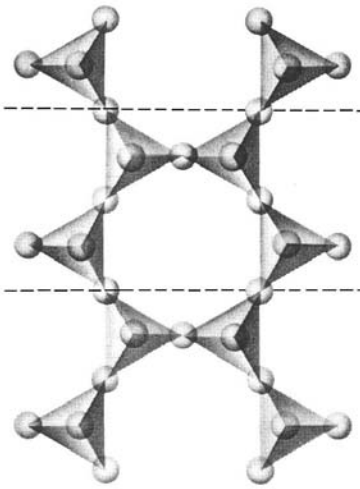
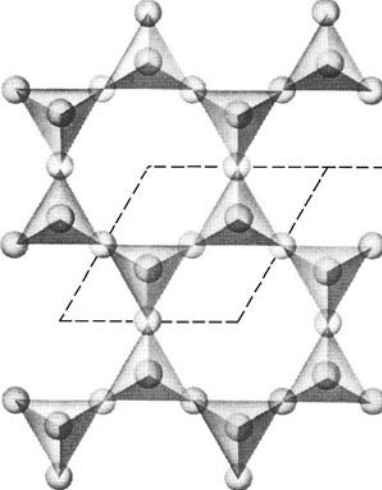
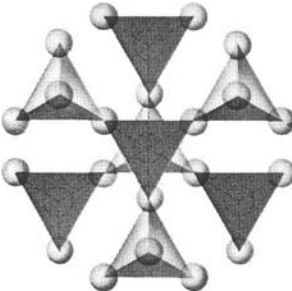
<p>(e) Inosilicates (double chain)</p>		$(\text{Si}_4\text{O}_{11})^{6-}$	<p>Amphibole e.g. Anthophyllite, $\text{Mg}_7\text{Si}_8\text{O}_{22}(\text{OH})_2$</p>
<p>(f) Phyllosilicates</p>		$(\text{Si}_2\text{O}_5)^{2-}$	<p>Mica e.g. Phlogopite, $\text{KMg}_3(\text{AlSi}_3\text{O}_{10})(\text{OH})_2$</p>
<p>(g) Tectosilicates</p>		$(\text{SiO}_2)^0$	<p>High cristobalite, SiO_2</p>

Fig. 1.31. The arrangements of the SiO_4 tetrahedra and Si:O ratios in the seven main types of silicate structures, with examples of typical minerals (from *Manual of Mineralogy*, 21st edn, by C. Klein and C. S. Hurlbut Jr., John Wiley & Sons Inc., 1993).

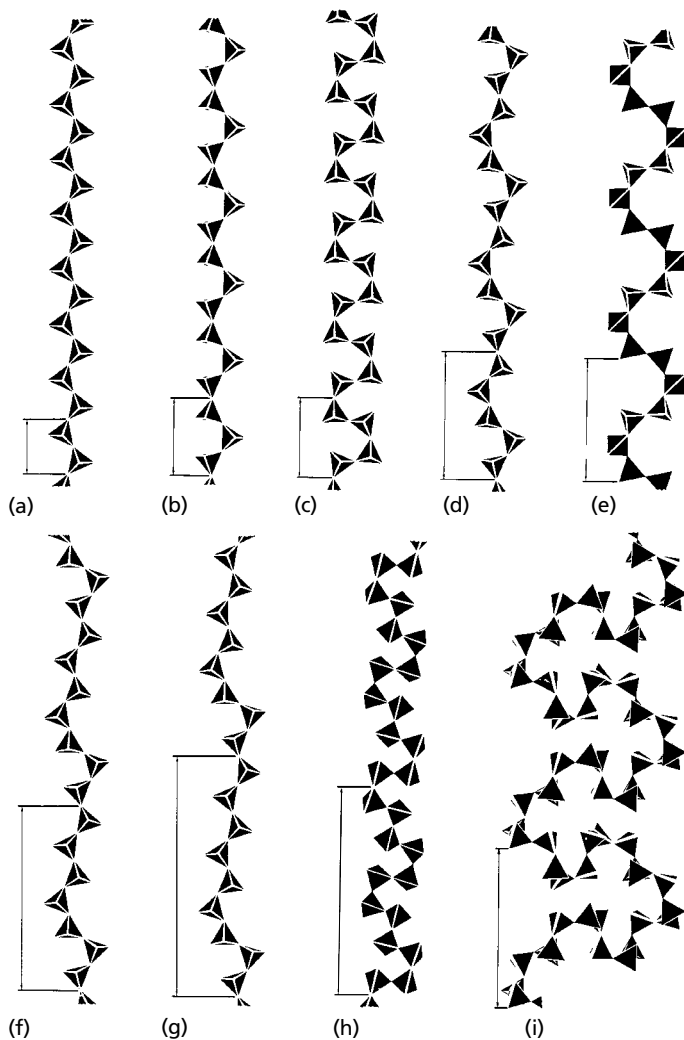


Fig. 1.32. The arrangements of the tetrahedra in the inosilicates. They are described (in German) according to the number of the tetrahedra in the repeat distance: a (zweier); b (dreier); c (vierer); d (fünfer); e (sechser); f (siebener); g (neuner); h (zwölfer); i (24er) (from *Structural Chemistry of Silicates* by F. Liebau, Springer-Verlag, 1985).

such substitution to a greater or lesser extent, for example phlogopite in which one silicon is replaced by one aluminium cation giving the formula $\text{KMg}_3(\text{OH})_2(\text{Si}_3\text{AlO}_{10})$. In framework silicates (tectosilicates), substitution gives rise to an important new class of minerals—the feldspars, the most abundant minerals in the earth's crust, e.g. albite, $\text{Na}(\text{Si}_3\text{AlO}_8)$, or orthoclase, $\text{K}(\text{Si}_3\text{AlO}_8)$ (one silicon cation substituted), or anorthite, $\text{Ca}(\text{Si}_2\text{Al}_2\text{O}_8)$ (two silicon cations substituted).

With respect to the arrangements of the tetrahedra, one example—that of the inosilicates—will suffice to show the principles involved. Figure 1.32 shows nine possible patterns (a)–(i) or conformations of the (unbranched) single chains, giving rise to different repeat distances as indicated: (a) (the simplest—known as *zweier* single chains because there are two tetrahedra in the repeat distance) is that for diopside and enstatite; (b) (drier single chains with three tetrahedra in the repeat distance) is that for wollastonite, $\text{Ca}_3(\text{Si}_3\text{O}_9)$, and so on.

Clearly, there are also many possible arrangements of the tetrahedra in the cyclosilicates, phyllosilicates and tectosilicates, and it is these which give rise (in part) to the many structural differences in silicate minerals. For example, in the tectosilicates the three different crystallographic forms of silica—quartz, tridymite and cristobalite—simply correspond to different ways in which the SiO_4 tetrahedra are linked together.

1.11.5 The structures of silica, ice and water

Of the three structural forms of silica—quartz, tridymite and cristobalite (not counting the high-pressure forms, coesite and stishovite)—quartz is by far the most common and is structurally stable at ambient temperatures, whereas tridymite is stable between 857 and 1470 °C and cristobalite is stable from 1470 °C to the melting point. At ambient temperatures, these latter two forms of silica are therefore metastable but they do not transform to quartz because in order to do so, a rearrangement of the linking of the SiO_4 tetrahedra needs to take place—in short, a *reconstructive* phase transformation must occur in contrast to a *displacive* transformation in which atomic bonds are not broken. However, displacive transformations occur in all three forms of silica by small rotations of the SiO_4 tetrahedra, giving rise to the ‘more open, high temperature’ β forms and the ‘more closed, low temperature’ α forms. This is illustrated, for quartz, in Fig. 1.33. Figure 1.33(b) is a plan view or projection of the hexagonal β -quartz structure perpendicular to the *c*-axis. For simplicity, only the Si atoms are indicated and their relative heights along the *c*-axis: white (0), grey (1/3) and black (2/3). Figure 1.33(a) is the corresponding projection for α -quartz; the structure is ‘twisted’ but no bonds are broken. The symmetry also changes from hexagonal to trigonal, as will be described in Section 3.3.

However, it is worth noticing at this stage one very important structural feature of quartz: the silicon atoms (and hence the SiO_4 tetrahedra) are arranged in a helical pattern along the *c*-axis. If we imagine a spiral staircase in the centre of a hexagon then the steps go: 0, 1/3, 2/3 ... in a clockwise fashion giving rise to a left-handed screw or helix. Now, we can interchange the positions of the grey and black atoms such that the steps go 0, 1/3, 2/3 ... in an anticlockwise fashion giving rise to a right-handed screw or helix. In short, quartz (both α and β) has two forms, one ‘left-handed’ and one ‘right-handed’ and is an example of an *enantiomorphous crystal structure* (see Table 3.1 and Section 4.5).

Quartz is the densest structural form (not counting the high-pressure form, coesite), ($\sim 2.66 \text{ g/cm}^3$); tridymite and cristobalite have much more ‘open’ structures ($\sim 2.33 \text{ g/cm}^3$). In their β forms, these two structures are similar to those of wurtzite and zinc blende (the two structural forms of zinc sulphide), respectively, the SiO_4 tetrahedra being in the positions of the Zn and S atoms. More specifically, they correspond to the

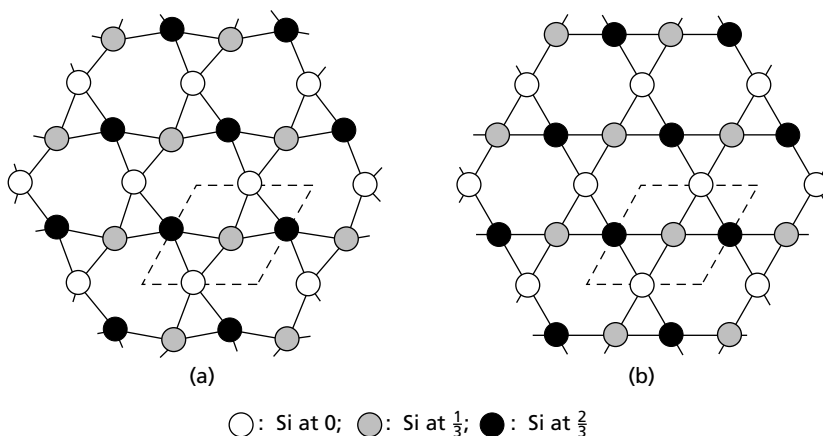


Fig. 1.33. (a) Plan of the trigonal structure of α -quartz and (b) plan of the hexagonal structure of β -quartz. Only the silicon atoms are shown, the oxygen atoms are tetrahedrally arranged about those of silicon. The structures are clearly related by a displacive (shear) transformation. (From *Crystal Chemistry*, 2nd Edn, by R.C. Evans, Cambridge University Press, 1966.)

two structural forms of diamond shown in Fig. 1.36 (Section 11.1.6). Figure 1.36(a) shows the (common) face-centred cubic form of diamond; the positions of the carbon atoms correspond to the positions of the silicon atoms in β -cristobalite. If we now add the oxygen atoms half-way in between the silicon atoms then we generate the complete β -cristobalite structure. Similarly, Fig. 1.36(b) shows the (uncommon) hexagonal form of diamond (Lonsdaleite); the carbon atoms correspond to the positions of the silicon atoms in β -tridymite and by adding the oxygen atoms half-way in between as before, we generate the complete β -tridymite structure. In the α forms of these structures there are small deviations from the cubic and hexagonal symmetries which give rise to lower-symmetry enantiomorphous crystal forms.

Quartz is the best-known and most readily recognized mineral (as a visit to any 'rock-shop' will show). Its common name is rock-crystal and it was thought by the ancients to be a form of ice, frozen so hard that it did not melt. It was described in detail by Strabo (d. AD 24), the Greek geographer who travelled widely throughout the Roman empire, recording the geology and mining operations. He gave it the name *Krystallos*, which is Greek for ice, and from which our word crystal is derived. The notion that rock-crystal was a form of ice has a long history and persisted as late as the seventeenth century, but what is very curious is that the structures of ice and water *do* have strong resemblances to those of silica as described below.

In structural terms, the water molecule may be regarded as a sphere, or rather a spherical envelope or radius 1.38 Å, with the large oxygen atom in the centre and two (small) hydrogen atoms 'embedded' within it (Fig. 1.34).

These hydrogen atoms may be supposed to occupy two corners of a tetrahedron, the other two corners being empty. However, it is not the location of the hydrogen atoms which is important, but rather that the corners of the tetrahedron are oppositely charged,

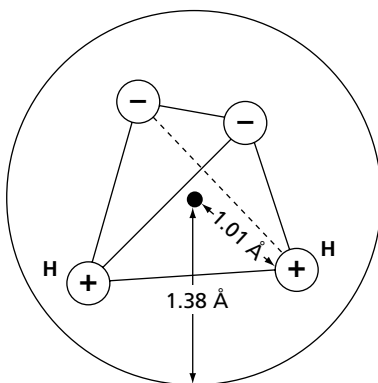


Fig. 1.34. The tetrahedral distribution of charge on the water molecule and its effective radius (1.38 Å). (From *Crystal Chemistry*, 2nd Edn, by R. C. Evans, Cambridge University Press, 1966.)

as indicated in Fig. 1.34. The water molecule, although it is neutral, is nevertheless polar and the crystal structures of ice which arise are determined by the ways in which these spherical, polar molecules, pack together. They are *not* close-packed, rather they form tetrahedrally coordinated networks as in silica. In the common form of ice (ice-I_h) the pattern of H₂O molecules is similar to that of the SiO₄ tetrahedra in β -tridymite except that the hydrogen atoms are not disposed symmetrically between pairs of oxygen atoms as indicated in Fig. 1.35(a) (Fig. 1.35(b) shows a model of an ice-I_h snowflake crystal). When water is frozen at very low temperatures, a structure (ice-I_c) corresponding to β -cristobalite is formed (and there are, as with silica, high pressure forms as well).

In liquid water, from about 4 °C to 150 °C (water II), the molecules are of course in a state of flux, but at any moment small regions (10~100 molecules in size) are arranged in a β -quartz-like arrangement, denser, of course than the β -tridymite arrangement in ice. Only at very high temperatures (> 150 °C) and pressures do the molecules approach random close-packing as in a liquid metal (water III).

Between 0 °C and 4 °C, as is known, the density of water increases. This is considered to arise from the slow breakdown of the less-dense tridymite-like arrangement (water I) to the more-dense quartz-like arrangement (water II). Above 4 °C, normal thermal expansion is dominant.

Water is unique. It owes its properties—high melting and boiling points, latent heat of boiling, etc.—to the divalency of oxygen, the polar nature of the molecules and the hydrogen bonding between them. The distribution of charge, and the positions of the hydrogen atoms (in both ice and water—Figs. 1.34 and 1.35(a)) is not fixed: the hydrogen atom in any one bond may be associated with either of the two oxygen atoms each side of it to give the alternative configurations O-H · · O or O · · H-O. In other words, there is a multiplicity of ways in which a hydrogen atom can be arranged. In contrast, in H₂S the sulphur atom is insufficiently electronegative to form hydrogen bonds and H₂S has a low specific heat, a low boiling point (−62 °C) and forms close-packed structures, like metals.

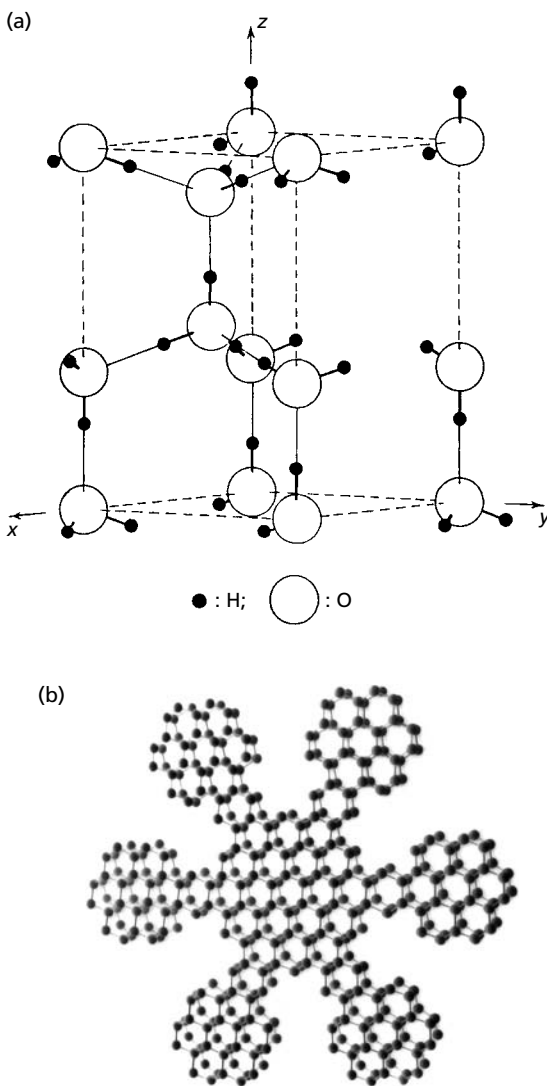


Fig. 1.35. (a) The hexagonal structure of ice-I_h. The distribution of the hydrogen atoms is arbitrary. (b) A model of an ice (ice-I_h) crystal. The spheres represent water molecules tetrahedrally linked in the hexagonal β -tridymite-like structure.

1.11.6 The structures of carbon

Of all the elements in the periodic table, only carbon and sulphur are capable of forming elemental rings or chains whose stability is independent of length. However, the chains formed by sulphur (with a higher valency than two), and those formed by silicon, immediately below carbon in the periodic table, are thermally unstable and

only short-length chain compounds are possible. Hence only carbon is capable of forming the complex ring- and long-chain compounds which are the prerequisite of life itself: the 'sulphur man' and 'silicon man' must remain figments of the imagination!

We will briefly survey only those structures of carbon itself, partly for their own intrinsic interest and partly because they serve to illustrate some of the basic ideas we have already met. These are diamond, graphite, 'mesophase', the fullerenes or 'bucky balls' and nanotubes.

In diamond the basic structural unit is a carbon atom linked to four equidistant neighbours in a tetrahedral coordination, which arises, in chemical terms, from the sp^3 hybridization of the carbon atom. There are, however, two ways in which the tetrahedra can be linked together. In by far the commonest form of diamond the tetrahedra are linked together to generate a cubic structure, the pattern of carbon atoms being precisely the same as that in TiH (Fig. 1.14), or sphalerite or zinc blende, the cubic form of ZnS. The analysis of this structure (by W. H. and W. L. Bragg in 1913) was indeed one of the earliest triumphs of the X-ray diffraction technique. In the other, rare form of diamond, called Lonsdaleite, after Kathleen Lonsdale*, the tetrahedra are linked together to generate an hexagonal structure, the pattern of carbon atoms being precisely the same as that in wurtzite, the hexagonal form of ZnS (Section 1.7). These structures are shown in Fig. 1.36.

In graphite, the carbon atoms are linked together to form plane hexagonal nets or graphene layers (sp^2 hybridization), the layers being stacked upon one another and held together by weak (van der Waals) forces. As in the case of our close-packed layers of metal atoms, the layers are not stacked immediately over each other (to give a simple hexagonal structure) but are again displaced in either of two ways. In the commonest form of graphite they are stacked in an ABAB sequence as in the hcp structure—carbon atoms in the 'B' layers lying immediately above and below the hexagonal hollows of the 'A' layers either side (Fig. 1.37(a)). This stacking pattern is precisely the same as that of the cells in the two sides of a honeycomb—the corners of the cells on one side corresponding with the centres of the cells on the other side.⁵

In the uncommon form of graphite the layers are stacked in an ABCABC... sequence as in the ccp structure (Figs. 1.37(b)) and this is designated the rhombohedral form of graphite on the basis of the simplest unit cell which can be drawn (see Fig. 1.7(c)). However, just as in the case of metals 'stacking faults' doubtless occur particularly when we shear the graphene layers over each other as we do when we write with a pencil! It is also possible for the layers to be stacked in parallel layers but in a random orientation (with no correlation between the atoms in each layer) and this so-called turbostratic form appears to arise as an intermediate stage in the graphitization of pitch or some polymer precursors.

Plan views of the stacking of the layers in the hexagonal and rhombohedral graphite structures are shown in Fig. 1.37. These structures are related to the hexagonal and cubic diamond structures respectively as shown in Exercise 1.10.

* Denotes biographical notes available in Appendix 3.

⁵ The dividing walls between the two sides of the honeycomb are not flat but are faceted at angles corresponding to those between the close-packed layers of atoms in the ccp structure (Section 1.3), and this arrangement can be shown to result in the most economical use of beeswax.

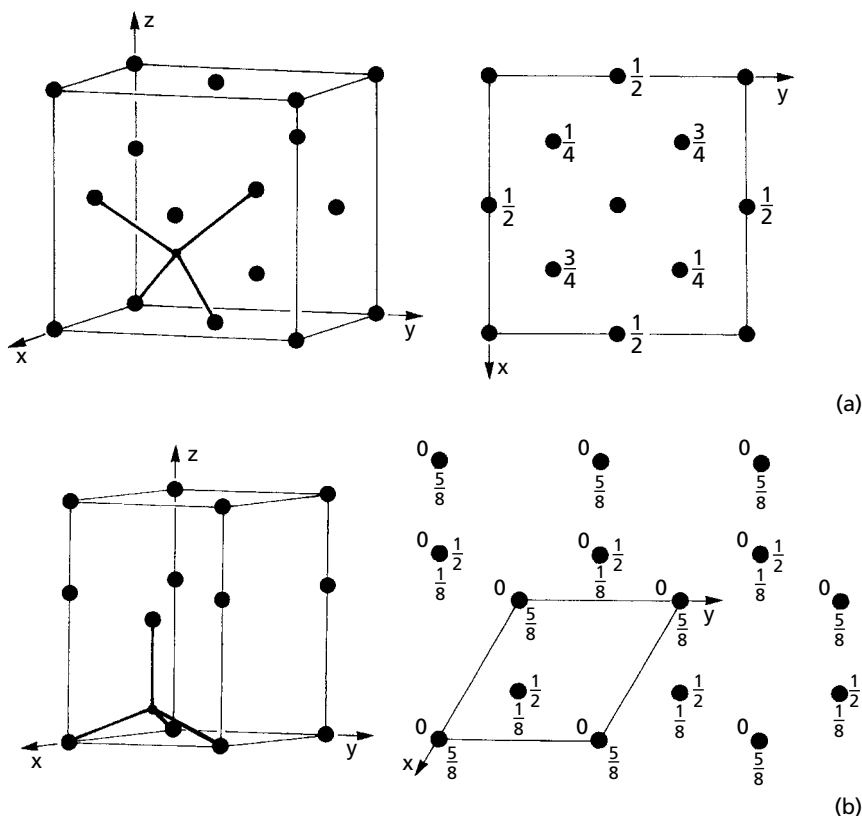


Fig. 1.36. (a) The cubic and (b) hexagonal structures of diamond in clinographic projection (left) and in plan view (right). In both cases the carbon atoms are linked to four others in tetrahedral coordination but the arrangement of the tetrahedra differs. The *pattern* of atom sites is precisely the same as in the cubic (sphalerite) and hexagonal (wurtzite) forms of ZnS. (From *Crystalline Solids* by D. McKie and C. McKie, Nelson, 1975.)

Perhaps the most remarkable of the structures of carbon—remarkable, that is, for having been discovered so late—are the fullerenes or colloquially ‘bucky balls’. These were postulated as an act of scientific imagination by D. E. H. Jones (who wrote under the pen-name Daedalus) in 1966, but their actual existence and structures were not established until 1985 by H. W. Kroto, R. W. Smalley, and their co-workers. If a hexagon is replaced by a pentagon in a graphite-like net then, as model-building shows in a most immediate way, the net assumes a dome-like shape (Fig. 1.38). This principle was applied in engineering design by the American architect and polymath R. Buckminster Fuller*—the distribution of pentagons and hexagons in the structure determining, of course, the

* Denotes biographical notes available in Appendix 3.

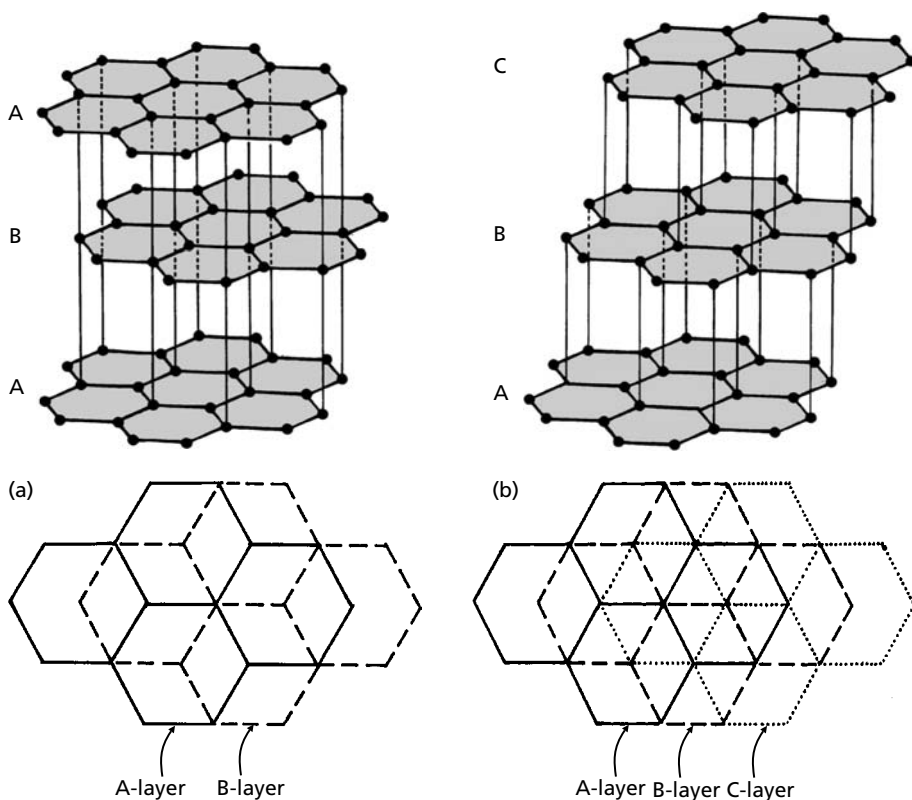
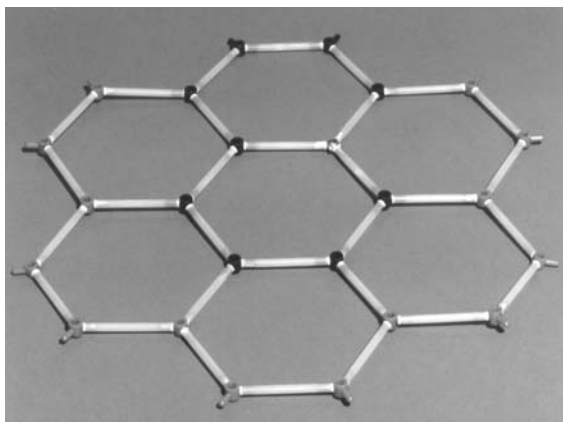


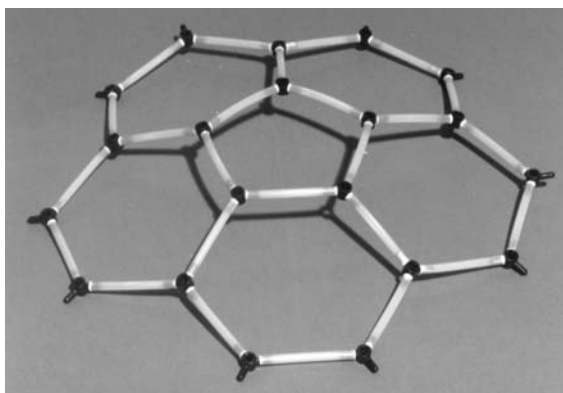
Fig. 1.37. (a) The hexagonal (layer sequence ABAB ...) and (b) the rhombohedral (layer sequence ABCABC ...) structures of graphite. These are shown (below) in plan view with the layers shown 'offset' for clarity. A-layer—full lines; B-layer—dashed lines and C-layer—dotted lines.

overall shape and stability of what he called a geodesic dome⁶. In order to create a complete closed sphere precisely 12 pentagons are needed and the smallest, simplest sphere consists of 12 pentagons only, without any hexagons. The shape or polyhedron which is formed is called a pentagonal dodecahedron (Fig. 1.39(a)) and is one of the five 'perfect' polyhedra, or Platonic solids since all the 12 pentagonal faces and all the 20 vertices or 'corners' where the carbon atoms are situated are identical. [The other Platonic solids are the cube (6 square faces, 8 vertices, Fig. 4.2(a)), the octahedron (8 triangular faces, 6 vertices, Fig. 4.2(b)), the tetrahedron (4 triangular faces, 4 vertices,

⁶ A geodesic, meaning 'earth dividing', is the shortest distance between two points across the surface of a sphere—just as a straight line is the shortest distance between two points in a plane. A geodesic is part of the circumference of what is called a great circle (see Chapter 12), a circle which has its centre at the centre of the sphere and which divides the sphere into two equal halves. In the design of geodesic domes, the constructional struts, the 'geodesics', follow the lines of great circles such that the stresses are distributed evenly. The edges of the Platonic, and many other polyhedra, also follow the lines of great circles (see Appendix 2).



(a)



(b)

Fig. 1.38. Model-building with simple linked straws or sticks, (a) The plane graphite-like or graphene net formed by linking hexagons and (b) the dome-like net formed when a hexagon is replaced by a pentagon.

Fig. 4.2(c)), and the icosahedron, Fig. 1.39(b) (20 triangular faces, 12 vertices)]. Hence, the simplest and smallest of the ‘bucky-balls’ consists of 20 carbon atoms. It is called dodecahedrene, but it has not been isolated and is doubtless thermally unstable.

As an increasing number of hexagons are included in the structure a family of fullerenes of increasing thermal stability and an increasing number of carbon atoms is developed (Fig. 1.40). The most interesting of these is Buckminsterfullerene itself with 60 carbon atoms (C_{60}) consisting of 12 pentagons separated from each other by 20 hexagons (Fig. 1.40 (a)) precisely in the same way as a football (or US soccer ball). This polyhedron is called a truncated icosahedron and is one of the thirteen ‘semi-regular’ or Archimedean polyhedra in which every face is a regular polygon, though not all faces are of the same kind. In crystals of C_{60} the spheres arrange themselves in an fcc pattern

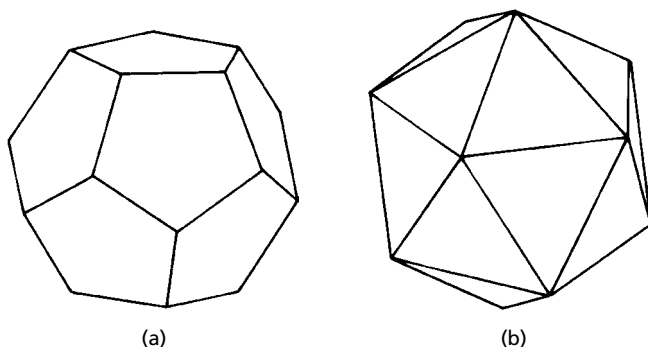


Fig. 1.39. (a) the pentagonal dodecahedron (12 pentagonal faces) and (b) the icosahedron (20 triangular faces)—two of the five ‘perfect’ or ‘Platonic’ polyhedra (the others being the cube, the octahedron and the tetrahedron—see Fig. 4.2 and Appendix 2).

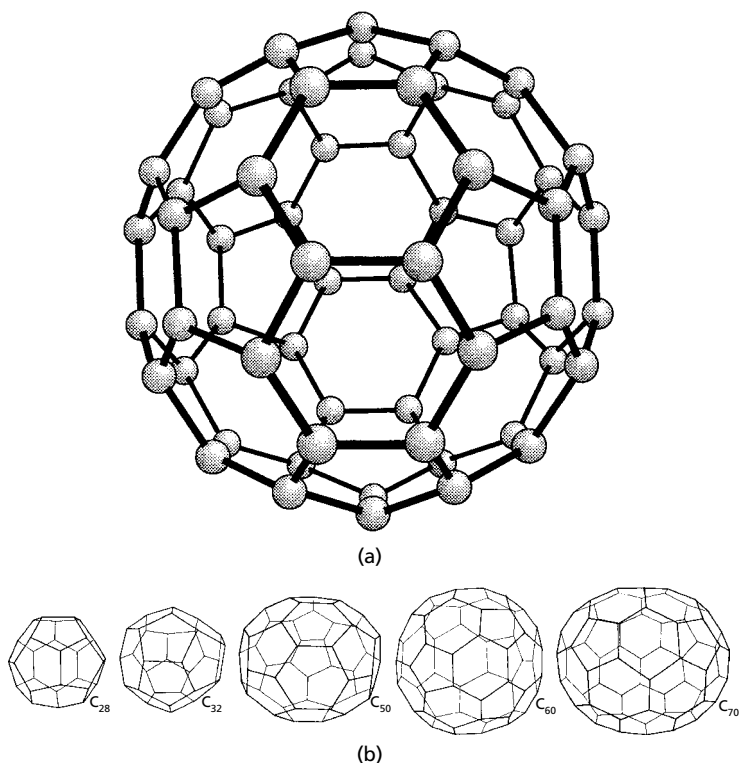


Fig. 1.40. (a) Buckminsterfullerene, C_{60} , consisting of 12 pentagonal and 20 hexagonal faces (from *Perfect Symmetry* by Jim Baggott, Oxford University Press, 1994) and (b) fullerenes C_{28} – C_{70} all of which have 12 pentagonal faces and an increasing number of hexagonal faces (from *Science* **242**, 1142, 1988: reproduced by courtesy of Prof. Sir Harry Kroto).

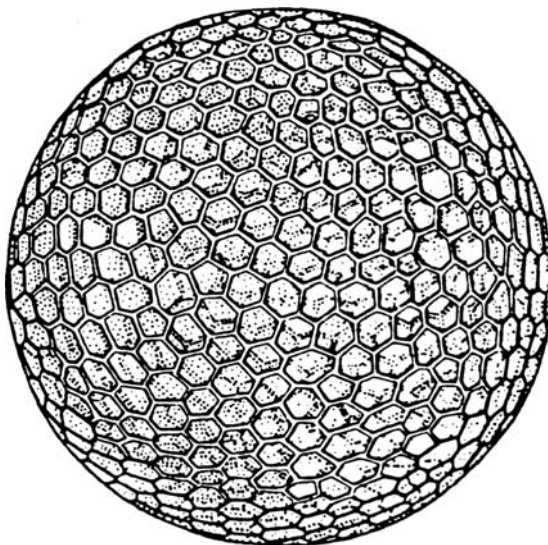


Fig. 1.41. The siliceous skeleton of *Aulonia hexagona*, a deep sea-water radiolarian, drawn by E. Haeckel (from 'On Growth and Form' by D'Arcy Wentworth Thompson, Cambridge University Press, 1942).

but doubtless faulting can also occur. The next fullerene, C_{70} , with 70 carbon atoms, has the shape of a Rugby ball (US football) and fullerenes with much larger numbers of carbon atoms also occur. These structures have their counterparts in the structures of the spherical skeletons of the radiolaria (deep sea-water creatures) where pentagons (and octagons and heptagons) occur in a predominantly hexagonal network (Fig. 1.41). Here we see nature obeying the dictates of geometry both on an atomic and on a biological scale!

Finally, the graphene layers may not lie flat as in graphite, but may 'roll up' with the edges joined together to form carbon 'nanotubes'. These may consist of a single rolled-up layer (single walled nanotubes) or many such tubes, one inside the other (multi-walled nanotubes) the spacing between the graphene layers being rather larger than that for graphite. These structural forms of carbon were first identified by Iijima in 1991 and Bethune et al. in 1993, but again were suggested as a possible form of carbon by D.E.H. Jones in 1972. The tubes may also be 'capped' with fullerene hemispheres, to form close-ended nanotubes.

Carbon nanotubes also exhibit different geometries or patterns depending upon the orientations of the carbon hexagons with respect to the tube axis. Figure 1.42 shows nanotube models made from sheets depicting graphene layers rolled up in different ways and overlapped such that the hexagons match along the join. In Fig. 1.42(a) the carbon atoms show an 'armchair' pattern along the axis of the tube; in Fig. 1.42(b) a 'zig-zag' pattern and (perhaps of most interest) in Fig. 1.42(c) the carbon hexagons form a helical pattern along the axis of the tube. Clearly, there are many more helices possible, of different pitches, both right and left handed. These different patterns are not

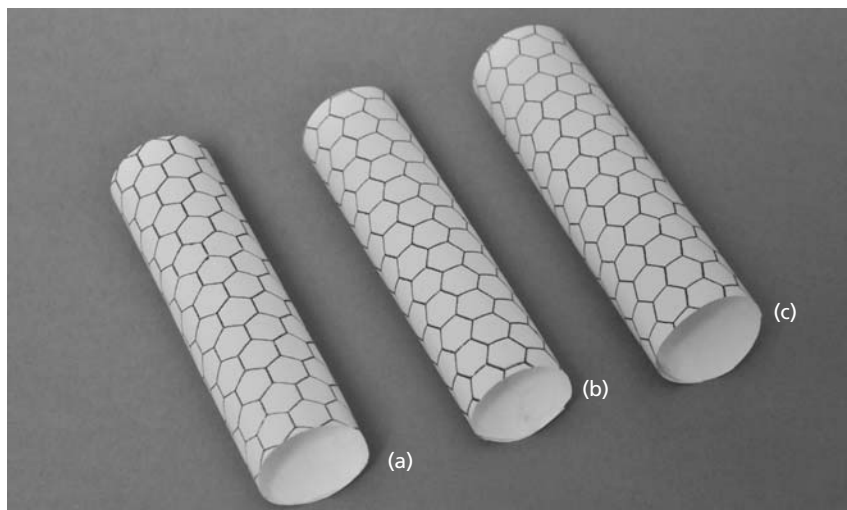


Fig. 1.42. Models of single-walled carbon nanotubes showing different orientations of the graphene cells along the tube axis (a) ‘armchair’, (b) ‘zig-zag,’ and (c) helical conformations.

just of crystallographic model-making interest but give rise to entirely different thermal, conductivity and strength properties and which make carbon nanotubes of such potential importance in nanotechnology.

A note on boron nitride—boron and nitrogen, which occur each side of carbon in the periodic table, form BN compounds with striking similarities to those of carbon described above. The boron and nitrogen atoms are linked alternately in a planar (sp^2) conformation, giving rise to graphite-like structures, or in a tetrahedral (sp^3) conformation giving diamond-like structures—the latter possess very high hardness and melting-points and are of great importance in materials engineering. It is not known whether BN also exhibits Buckminster fullerene structures—this may be unlikely in view of the necessity for adjacent boron or nitrogen atoms in the 5-ring components. However, open-ended ‘nanotube’ structures, which do not require 5-ring components, may occur.

Exercises

- 1.1 With reference to Fig. 1.5(b) or Fig. 1.11(a), determine the c/a ratio for the hcp structure. (*Hint: a is equal to d , the atomic diameter and edge length of the tetrahedron, and c is twice the height of the tetrahedron. Determine also the height of the tetrahedron above the triangular base.*)
- 1.2 Determine the radius ratio, r_X/r_A , for the tetrahedral interstitial sites in the bcc structure.
- 1.3 Determine the radius ratio, r_X/r_A , for the six-fold coordinated interstitial site in the simple hexagonal structure.
- 1.4 Examine your crystal models and find:
 - (a) the number of different (non-parallel) close-packed planes and close-packed directions in the ccp and hcp structures; and
 - (b) the number of closest-packed planes and close-packed directions in the bcc structure.

- 1.5 In the deformation of ccp and bcc metals, slip generally occurs on the close- or closest-packed planes and in close-packed directions. Each combination of slip plane and direction is called a **slip system**. How many slip systems are there in these metals?
- 1.6 Draw a plan or crystal projection of the hcp structure perpendicular to the z - or c -axis. Assign axes x and y (at 120° to each other) and outline a primitive hexagonal cell (one atom at each corner and one within the cell). What are the atomic coordinates of the atoms in the cell?
- 1.7 Referring to Figs. 1.26 or 1.27(a) or (b), express the stacking sequences in the β -SiC structures B7(15R) and 8H in the Frank notation.
- 1.8 With reference to Fig. 1.20, show that an hcp structure may be generated from a ccp structure by faulting *alternate* close-packed planes.
- 1.9 Draw crystal plans of the perovskite structure shown in Fig. 1.17, relocate the origin of one cell, relabel the ionic coordinates and show that these two cells do represent the same crystal structure.
- 1.10 Make ball-and-stick models of the cubic-diamond (Fig. 1.36(a)) and rhombohedral-graphite (Fig. 1.37(b)) structures. Notice that in the diamond structure the carbon atoms lie in 'puckered' layers perpendicular to the body-diagonal directions of the cube. If we (physically or in imagination) make the atoms in these layers coplanar and also lengthen the bonds between them, then we have the rhombohedral form of graphite. A similar relationship exists between the hexagonal-diamond (Fig. 1.36(b)) and hexagonal-graphite (Fig. 1.37(a)) structures.
- 1.11 Express the stacking sequence of the close-packed layers in the element americium (Section 1.2) in terms of the Frank notation.
- 1.12 Make a graphene layer (print a pattern of hexagons on transparency film or a piece of paper) and roll it up in the ways shown in Fig. 1.42 to make different crystallographic forms of carbon nanotubes.

Two-dimensional patterns, lattices and symmetry

2.1 Approaches to the study of crystal structures

In Chapter 1 we developed an understanding of simple crystal structures by first considering the ways in which atoms or ions could pack together and then introducing smaller atoms or ions into the interstices between the larger ones. This is a pragmatic approach as it not only provides us with an immediate and straightforward understanding of the atomic/ionic arrangements in some simple compounds, but also suggests the ways in which more complicated compounds can be built up.

However, it is not a systematic and rigorous approach, as all the possibilities of atomic arrangements in all crystal structures are not explored. The rigorous, and essentially mathematical approach is to analyse and classify the geometrical characteristics of quite general two-dimensional patterns and then to extend the analysis to three dimensions to arrive at a completely general description of all the patterns to which atoms or molecules or groups of atoms or molecules might conform in the crystalline state.

These two distinct approaches—or strands of crystallographic thought—are apparent in the literature of the nineteenth and early twentieth centuries. In general, it was the metallurgists and chemists, such as Tammann* and Pope,* who were the pragmatists, and the theoreticians and geometers, such as Fedorov* and Schoenflies,* who were the analysts. It might be thought that the analytical is necessarily superior to the pragmatic approach because its generality and comprehensiveness provides a much more powerful starting point for progress to be made in the discovery and interpretation of the crystal structures of more and more complex substances. But this is not so. It was, after all, the simple models of sodium chloride and zinc blende of Pope (such as we also constructed in Chapter 1) that helped to provide the Braggs* with the necessary insight into crystal structures to enable them to make their great advances in the interpretation of X-ray diffraction photographs. In the same way, 40 years later, the discovery of the structure of DNA by Watson and Crick was based as much upon structural and chemical knowledge and intuition, together with model building, as upon formal crystallographic theory.

However, a more general appreciation of the different patterns into which atoms and molecules may be arranged is essential, because it leads to an understanding of the important concepts of symmetry, motifs and lattices. The topic need not be pursued rigorously—in fact it is unwise to do so because we might quickly ‘lose sight of the wood for the trees!’ The essential ideas can be appreciated in two dimensions, the subject of

* Denotes biographical notes available in Appendix 3.

this chapter. The extension to three dimensions (Chapters 3 and 4) which relates to ‘real crystal structures’, should then present no conceptual difficulties.

2.2 Two-dimensional patterns and lattices

Consider the pattern of Fig. 2.1 (a), which is made up of the letter **R** repeated indefinitely. What does **R** represent? Anything you like—a ‘two-dimensional molecule’, a cluster of atoms or whatever. Representing the ‘molecule’ as an **R**, an *asymmetric* shape, is in effect representing an *asymmetric* molecule. We shall discuss the different types or elements of symmetry in detail in Section 2.3 below, but for the moment our general everyday knowledge is enough. For example, consider the symmetry of the letters **R M S**. **R** is asymmetrical. **M** consists of two equal sides, each of which is a reflection or mirror image of the other, there is a **mirror line** of symmetry down the centre indicated by the letter m, thus **M_m**. There is no mirror line in the **S**, but if it is rotated 180° about a point in its centre, an identical **S** appears; there is a **two-fold rotation axis** usually called a **diad axis** at the centre of the **S**. This is represented by a little lens-shape at \cdot the axis of rotation: **S**.

In Fig. 2.1(a) **R**, the repeating ‘unit of pattern’ is called the **motif**. These motifs may be considered to be situated at or near the intersections of an (imaginary) grid. The grid is called the **lattice** and the intersections are called **lattice points**.

Let us now draw this underlying lattice in Fig. 2.1(a). First we have to decide where to place each lattice point in relation to each motif: anywhere will do—above, below, to one side, in the ‘middle’ of the motif—the only requirement is that the *same* position with respect to the motif is chosen every time. We shall choose a position a little below the motif, as shown in Fig. 2.1(b). Now there are an infinite number of ways in which the

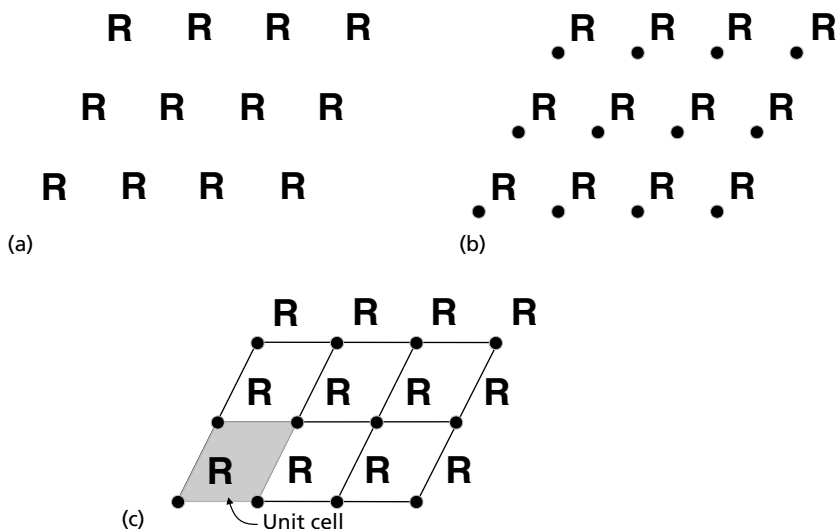


Fig. 2.1. (a) A pattern with the motif **R**, (b) with the lattice points indicated and (c) the lattice and a unit cell outlined. (Drawn by K. M. Crennell.)

lattice points may be ‘joined up’ (i.e. an infinite number of ways of drawing a lattice or grid of lines through lattice points). In practice, a grid is usually chosen which ‘joins up’ adjacent lattice points to give the lattice as shown in Fig. 2.1(c), and a unit cell of the lattice may also be outlined. Clearly, if we know (1) the size and shape of the unit cell and (2) the motif which each lattice point represents, including its orientation with respect to the lattice point, we can draw the whole pattern or build up the whole structure indefinitely. The unit cell of the lattice and the motif therefore define the whole pattern or structure. This is very simple: but observe an importance consequence. Each motif is identical and, for an infinitely extended pattern, the environment (i.e. the spatial distribution of the surrounding motifs, and their orientation) around each motif is identical. This provides us with the definition of a lattice (which applies equally in two and three dimensions): *a lattice is an array of points in space in which the environment of each point is identical*. Again it should be stressed that by environment we mean the spatial distribution and orientation of the surrounding points.

Like all simple definitions (and indeed ideas), this definition of a lattice is often not fully appreciated; there is, to use a colloquial expression, ‘more to it than meets the eye!’ This is particularly the case when we come to three-dimensional lattices (Chapter 4), but, for the two-dimensional case, consider the patterns of points in Fig. 2.2 (which should be thought of as extending infinitely). Of these only (a) and (d) constitute a lattice; in (b) and (c) the points are certainly in a *regular* array, but the surroundings of each point are *not* all identical.

Figures 2.2(a) and (d) represent two two-dimensional lattice types, named **oblique** and **rectangular**, respectively, in view of the shapes of their unit cells. But what is the distinction between the oblique and rectangular lattices? Surely the rectangular lattice is just a special case of the oblique, i.e. with a 90° angle?

The distinction arises from different symmetries of the two lattices, and requires us to extend our everyday notions of symmetry and to classify a series of symmetry elements.

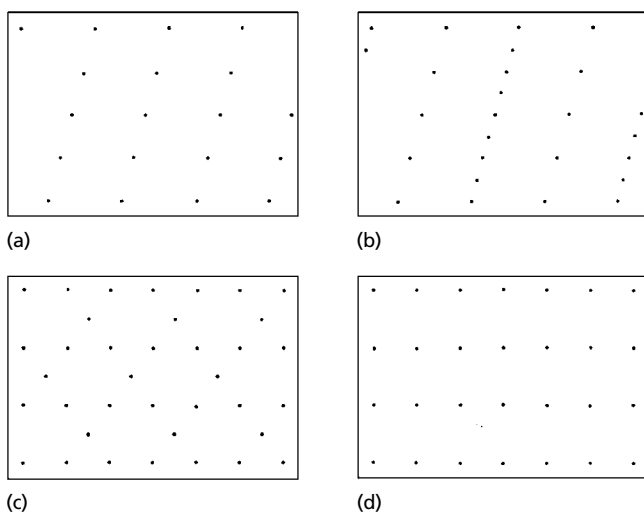


Fig. 2.2. Patterns of points. Only (a) and (d) constitute lattices.

This precise knowledge of symmetry can then be applied to both the motif and the lattice and will show that there are a limited number of patterns with different symmetries (only seventeen) and a limited number of two-dimensional lattices (only five).

2.3 Two-dimensional symmetry elements

The clearest way of developing the concept of symmetry is to begin with an asymmetrical 'object'—say the **R** of Fig. 2.1—then to add successively mirror lines and axes of symmetry and to see how the **R** is repeated to form different patterns or groups. The different patterns or groups of **R**s which are produced correspond, of course, to objects or projections of molecules (i.e. 'two-dimensional molecules') with different symmetries which are not possessed by the **R** alone.

The patterns or groups which arise and which as explained below are of concern in crystallography are shown in Fig. 2.3. On the left are the patterns of **R**s, in the centre are decorative motifs with the same symmetry, and on the right are projections of molecules. Figure 2.3(1) shows the **R** 'on its own' and, as an example, the asymmetrical projection of the CHFCIBr molecule. Figure 2.3(2) shows 'right-' and 'left'-handed **R**s reflected in the 'vertical' mirror line between them. This pair of **R**s has the same mirror symmetry as the projection of the *cis*-difluoroethene molecule. Now add another 'horizontal' mirror line as in Fig. 2.3(3). A group of four **R**s (two right- and two left-handed) is produced. This group has the same symmetry as the projection of the ethene molecule.

The **R** may be repeated with a diad (two-fold rotation) axis, as in Fig. 2.3(4). The two **R**s (both right handed) have the same symmetry as the *trans*-difluoroethene molecule. Now look back to the group of **R**s in Fig. 2.3(3); notice that they also are related by a diad (two-fold rotation axis) at the intersection of the mirror lines: the action of reflecting the **R**s across two perpendicular mirror lines 'automatically' generates the two-fold symmetry as well. This effect, where the action of two symmetry elements generates another, is quite general as we shall see below.

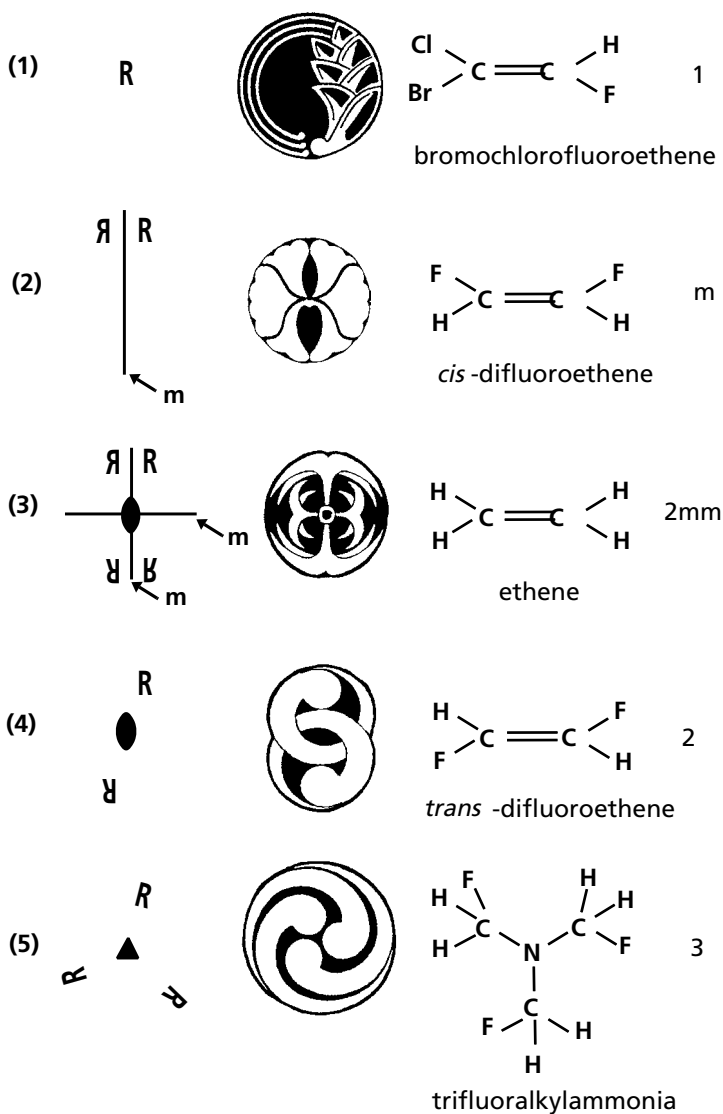
Mirror lines and diad axes of symmetry are just two of the symmetry elements that occur in two dimensions. In addition there are three-fold rotation or **triad** (3) axes (represented by a little triangle, ▲), four-fold rotation or **tetrad** (4) axes (represented by a little square, ■), and six-fold (6) or **hexad** axes (represented by a little hexagon, ●). Asymmetrical objects are represented as having a one-fold or **monad** (1) axis of symmetry (for which there is no little symbol)—which means in effect that one 360° rotation brings the object into coincidence with itself.

Figure 2.3(5) shows the **R** related by a triad (three-fold) axis. The projection of the trifluoroalkylammonia molecule also has this same symmetry. Now add a 'vertical' mirror line as in Fig. 2.3(6). Three more left-handed **R**s are generated, and at the same time the **R**s are mirror related not just in the vertical mirror line but also in two lines inclined at 60° as shown; another example of additional symmetry elements (in this case mirror lines) being automatically generated.

This procedure (of generating groups of **R**s which represent motifs with different symmetries) may be repeated for tetrad (four-fold) axes (Fig. 2.3(7)); plus mirror lines (Fig. 2.3(8)); for hexad (six-fold) axes (Fig. 2.3(9)); plus mirror lines (Fig. 2.3(10)). Notice that not only do these axes of symmetry 'automatically' generate mirror lines at

90° (for tetrads) and 60° (for hexads) but also 'interleaving' mirror lines at 45° and 30° as well.

The ten arrangements of **R**s (and the corresponding two-dimensional motifs or projections of molecules) are called the **ten two-dimensional crystallographic or plane point groups**, so called because all the symmetry elements—axes (perpendicular to the page) and mirror lines (in the page)—pass through a point. The ten plane point groups are labelled with 'shorthand' symbols which indicate, as shown in Fig. 2.3, the symmetry elements present: 1 for a monad (no symmetry), *m* for one mirror line, *mm* (or *2mm*) for two



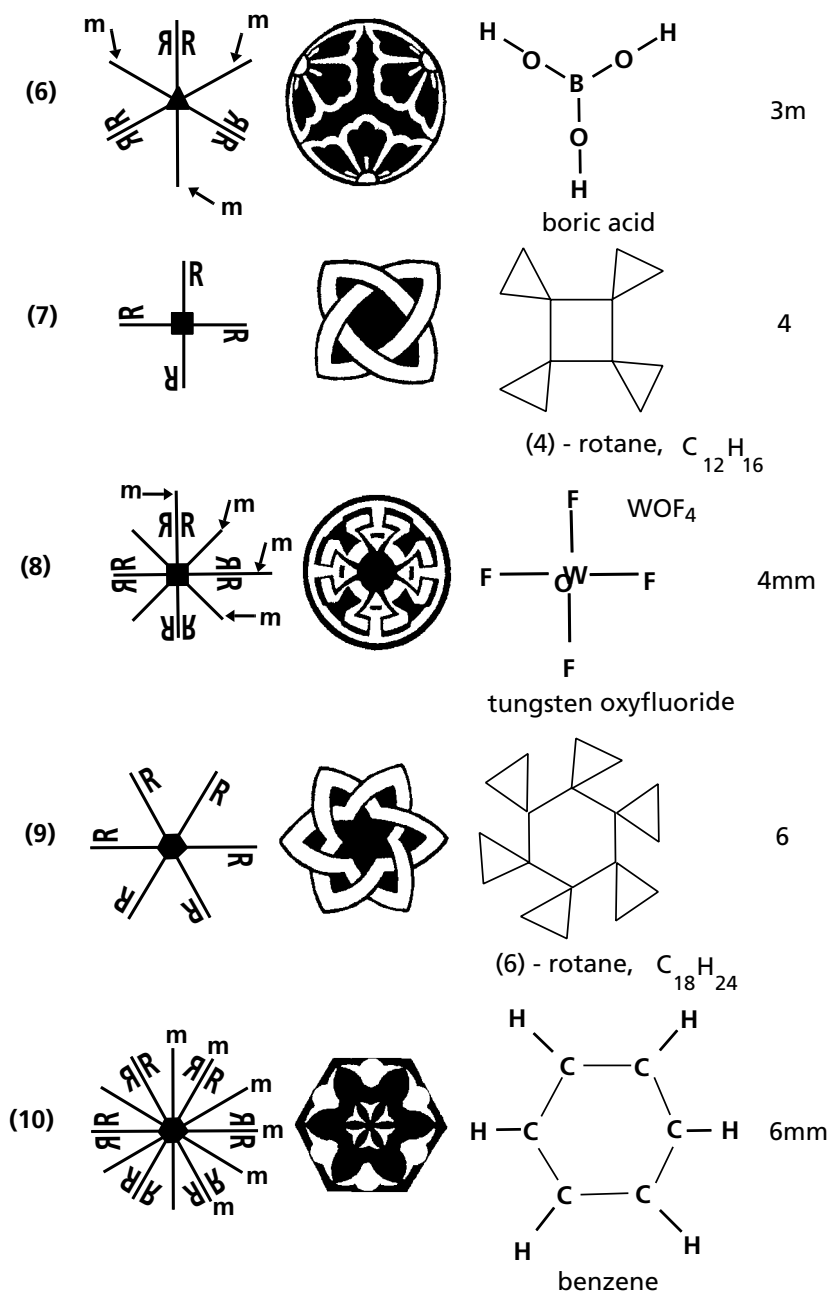


Fig. 2.3. The ten plane point groups showing left to right, the symmetry which arises based on an asymmetrical object **R**; examples of motifs; examples of molecules and ions (drawn as projections) and the point group symbols. (Drawn by K. M. Crennell.)

mirror lines (plus diad), 2 for a diad, 3 for a triad, $3m$ for a triad plus three mirror lines, 4 for a tetrad, $4mm$ for a tetrad plus four mirror lines, 6 for a hexad and $6mm$ for a hexad plus six mirror lines (the extra ‘ m ’ in the symbols referring to the ‘interleaving’ mirror lines).

Now, in deriving these ten plane point groups we have ignored groups of **R**s with fivefold (**pentad**), seven-fold (**heptad**) etc. axes of symmetry with and without mirror lines. Such plane point groups are certainly possible and are widely represented in nature—the pentagonal symmetry of a starfish for example. However, what makes the ten plane point groups in Fig. 2.3 special or distinctive is that *only* these combinations of axes and mirror lines can occur in regular repeating patterns in two dimensions as is explained in Sections 2.4 and 2.5 below. Hence they are properly called the two-dimensional *crystallographic* point groups as indicated above. Patterns with pentagonal symmetry are necessarily non-repeating, non-periodic or ‘incommensurate’ and consequently have in the past been rather overlooked by crystallographers. However, with the realization that groups of atoms (or viruses) can form ‘quasicrystals’ with five-fold symmetry elements (see Section 4.9), the study of non-periodic two-dimensional patterns has become of increasing interest and importance (see Section 2.9). A simple way at this stage of ‘seeing the difference’ is to compare, for example, the arrangement of six lattice points equally spaced around a central lattice point (hexagons) with the arrangement of five ‘lattice’ points equally spaced around a central point (pentagons). In the former case the arrangement of points can be put together to form a lattice (a pattern or *tiling* of hexagons with ‘no gaps’ and ‘no overlaps’). In the latter case the points cannot be put together to form a lattice—there are always ‘gaps’ or ‘overlaps’ between the tiling of pentagons. Try it and see!

2.4 The five plane lattices

Having examined the symmetries which a two-dimensional motif may possess we can now determine how many two-dimensional or plane lattices there are. We will do this by building up patterns from the ten motifs in Fig. 2.3 with the important condition that the symmetry elements possessed by the single motif must also extend throughout the whole pattern. This condition is best understood by way of a few examples. Consider the asymmetrical motif **R** (Fig. 2.3(1)); there are no symmetry elements to be considered and the **R** may be repeated in a pattern with an oblique unit cell (i.e. the most asymmetrical) arrangement of lattice points. Now consider the motif which possesses one ‘vertical’ mirror line of symmetry (Fig. 2.3(2)). This mirror symmetry must extend throughout the whole pattern from motif to motif which means that the lattice must be rectangular. There are two possible arrangements of lattice points which fulfil this requirement: a simple rectangular lattice and a centred rectangular lattice as shown in Fig. 2.4(a).

These rectangular lattices also possess ‘horizontal’ mirror lines of symmetry corresponding to the motif with the two sets of mirror lines as shown in Fig. 2.3(3). Now consider the motifs with tetrad (four-fold) symmetry (Figs 2.3(7) and (8)). This four-fold symmetry must extend to the surrounding motifs which means that they must be arranged in a square pattern giving rise to a square lattice (Fig. 2.4(a)).

Altogether, five two-dimensional or plane lattices may be worked out, as shown in Fig. 2.4(a). They are described by the shapes of the unit cells which are drawn between

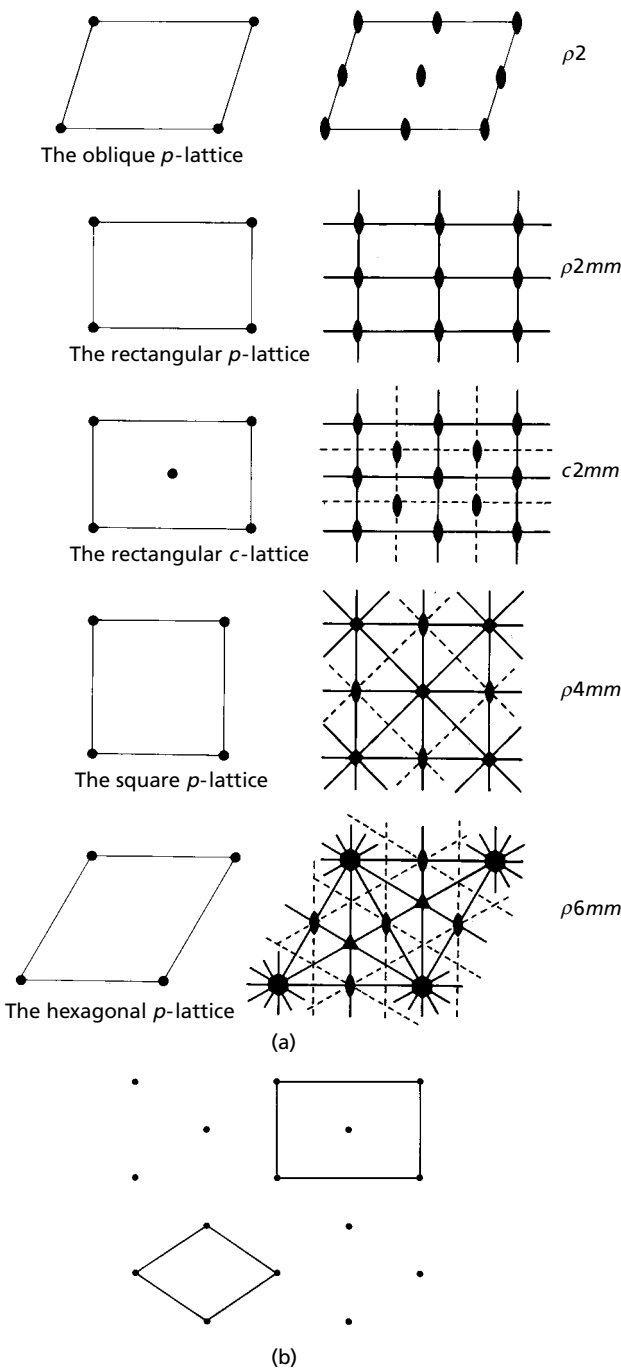


Fig. 2.4. (a) Unit cells of the five plane lattices, showing the symmetry elements present (heavy solid lines indicate mirror lines, dashed lines indicate glide lines) and their plane group symbols (from *Essentials of Crystallography*, by D. McKie and C. McKie, Blackwell, 1986). (b) The rectangular c lattice, showing the alternative primitive (rhombic p or diamond p) unit cell.

lattice points—oblique p , rectangular p , rectangular c (which is distinguished from rectangular p by having an additional lattice point in the centre of the cell), square p and hexagonal p . Notice again that additional symmetry elements are generated ‘in between’ the lattice points as shown in Fig. 2.4(a) (right). For example, in the square lattice there is a tetrad at the centre of the cell, diads halfway along the edges and vertical, horizontal and diagonal mirror lines as well as the tetrads situated at the lattice points.

All two-dimensional patterns must be based upon one of these five plane lattices; no others are possible. This may seem very surprising—surely other shapes of unit cells are possible? The answer is ‘yes’, a large number of unit cell shapes are possible, but the pattern of lattice points which they describe will always be one of the five of Fig. 2.4(a). For example, the rectangular c lattice may also be described as a rhombic p or diamond p lattice, depending upon which unit cell is chosen to ‘join up’ the lattice points (Fig. 2.4(b)). These are just two alternative descriptions of the *same* arrangement of lattice points. So the choice of unit cell is arbitrary: *any* four lattice points which outline a parallelogram can be joined up to form a unit cell. In practice we take a sensible course and mostly choose a unit cell that is as small as possible—or ‘primitive’ (symbol p)—which does not contain other lattice points within it. Sometimes a larger cell is more useful because the axes joining up the sides are at 90° . Examples are the rhombic or diamond lattice which is identical to the rectangular centred lattice described above and, to take an important three-dimensional case, the cubic cell (Fig. 1.6(c)) which is used to describe the ccp structure in preference to the primitive rhombohedral cell (Fig. 1.7(c)).

Now as there are ten point group symmetries which a motif can possess, it may be thought that there are therefore only ten different types of two-dimensional patterns, distributed among the five plane lattices. However, there is a complication: the combination of a point group symmetry with a lattice can give rise to an additional symmetry element called a **glide line**. Consider the two patterns in Fig. 2.5, both of which have a rectangular lattice. In Fig. 2.5(a) the motif has mirror symmetry as in Fig. 2.3(2); it consists of a

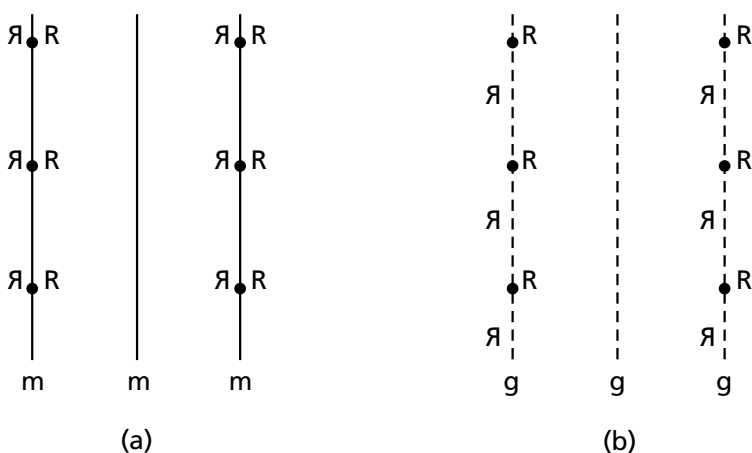


Fig. 2.5. Patterns with (a) reflection symmetry and (b) glide-reflection symmetry. The mirror lines (m) and glide lines (g) are indicated.

pair of right- and left-handed **R**s. In Fig. 2.5(b) there is still a reflection—still pairs of right- and left-handed **R**s—but one set of **R**s has been translated, or glided half a lattice spacing. This symmetry is called a **reflection glide** or simply a **glide line of symmetry**. Notice that glide lines also arise automatically in the centre of the unit cell of Fig. 2.5(b) as do mirror lines in Fig. 2.5(a). Glide lines are, of course, as familiar to us as mirror lines; they represent the pattern of our footprints in the snow when we walk in a straight line!

The presence of the glide lines also has important consequences regarding the symmetry of the motif. In Fig. 2.5(a) the motif has mirror symmetry but in Fig. 2.5(b) it does not: the pair of right- and left-handed **R**s is asymmetric. It is the repetition of the translational symmetry elements—the glide lines—that determines the overall rectangular symmetry of the pattern. The glide lines which are present in the five plane lattices are shown (in addition to the axes and mirror lines of symmetry) in Fig. 2.4(a).

2.5 The seventeen plane groups

Glide lines give seven more two-dimensional patterns, giving seventeen in all—the seventeen **plane groups**. On a macroscopic scale the glide symmetry in a crystal would appear as simple mirror symmetry—the shift between the mirror-related parts of the motif would only be observable in an electron microscope which was able to resolve the individual mirror-related parts of the motif, i.e. distances of the order of 0.5–2 Å (50–200 pm).

The seventeen plane groups are shown in Fig. 2.6(a). They are labelled by ‘shorthand’ symbols which indicate the type of lattice (*p* for primitive, *c* for centred) and the symmetry elements present, *m* for mirror lines, *g* for glide lines, 4 for tetrads and so on. The symmetry elements within a unit cell are shown in Fig. 2.6(b). It is a good exercise in recognizing the symmetry elements present in the 17 plane groups to lay a sheet of tracing paper over Fig. 2.6(a), to indicate the positions of the axes, mirror and glide lines of symmetry in an (arbitrary) unit cell and then to compare your ‘answers’ with those shown in Fig. 2.6(b).

It is essential to practice recognizing the motifs, symmetry elements and lattice types in two-dimensional patterns and therefore to find to which of the seventeen plane groups they belong. Any regular patterned object will do—wallpapers, fabric designs, or the examples at the end of this chapter. Figure 2.7 indicates the procedure you should follow. Cover up Fig. 2.7(b) and examine only Fig. 2.7(a); it is a projection of molecules of $\text{C}_6\text{H}_2(\text{CH}_3)_4$. You should recognize that the molecules or groups of atoms are *not* identical in this two-dimensional projection. The motif is a *pair* of such molecules and this is the ‘unit of pattern’ that is repeated. Now look for symmetry elements and (using a piece of tracing paper) indicate the positions of all of these on the pattern. Compare your pattern of symmetry elements with those shown in Fig. 2.7(b). If you did not obtain the same result you have not been looking carefully enough! Finally, insert the lattice points—one for each motif. Anywhere will do, but it is convenient to have them coincide with a symmetry element, as has been done in Fig. 2.7(b). The lattice is clearly oblique and the plane group is $p2$ (see Fig. 2.6).

Another systematic way of identifying a plane pattern is to follow the ‘flow diagram’ shown in Fig. 2.8. The first step is to identify the highest order of rotation symmetry

present, then to determine the presence or absence of reflection symmetry and so on through a series of ‘yes’ and ‘no’ answers, finally identifying one of the seventeen plane patterns whose plane group symbols are indicated ‘in boxes’, corresponding to those given in Fig. 2.6.

2.6 One-dimensional symmetry: border or frieze patterns

Identifying the number of one-dimensional patterns provides us with a good exercise in applying our more general knowledge of plane patterns. It is also a useful exercise in that it tells us about the different types of patterns that can be designed for the borders of wallpapers, edges of dress fabrics, friezes and cornices in buildings, and so on.

In plane patterns the symmetry operations and symmetry elements are (clearly) repeated in a plane; in one-dimensional patterns they can only be repeated in or along a line—i.e. the line or long direction of the border or frieze. This restriction immediately rules out all rotational symmetry elements with the exception of diads: two-fold symmetry alone can be repeated in a line: three-, four-, and six-fold symmetry elements require the repetition of a motif in directions other than the line of the border. For the same reason glide-reflection lines of symmetry, other than that along the line of the border, are ruled out. Mirror lines of symmetry are restricted to those along, and perpendicular to, the line of the border.

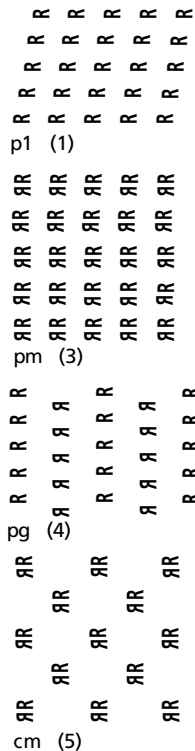
These restrictions result in seven one-dimensional groups, shown in Fig. 2.9. It is a good and satisfying exercise for you to derive these from first principles as outlined above. It is also useful to compare Fig. 2.9 with Fig. 2.6; the bracketed symbols in Fig. 2.9 indicate from which plane pattern the one-dimensional pattern may be derived. Notice that in one case two one-dimensional patterns—these with ‘horizontal’ and ‘vertical’ mirror planes—are derived from one plane pattern (*pm*). This is because the mirror lines in the plane group *pm* can be oriented either along, or perpendicular to, the line of the one-dimensional pattern.

Figure 2.23 (see Exercise 2.6) also shows examples of some of the border patterns. You can practice recognizing such patterns either by overlaying the pattern with a piece of tracing paper, and indicating the positions of the diads, mirror and glide lines as described above for plane patterns or by following the flow diagram (Fig. 2.10).

2.7 Symmetry in art and design: counterchange patterns

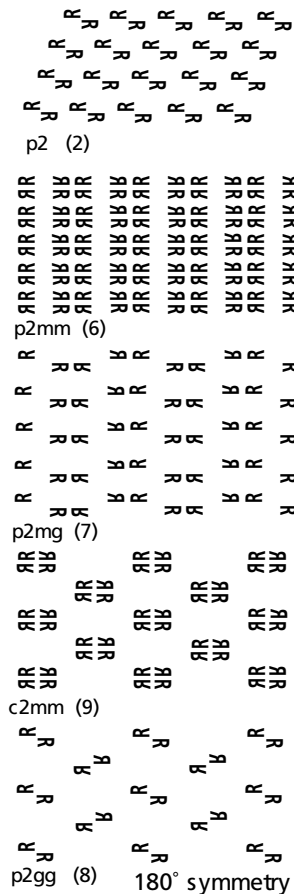
We have a rich inheritance of plane and border patterns in printed and woven textiles, wallpapers, bricks and tiles which have been designed and made by countless craftsmen and artisans in the past ‘without benefit of crystallography’. The question we may now ask is: ‘Have all the seventeen plane groups and seven one-dimensional groups been utilized in pattern design or are some patterns and some symmetries more evident than others? If so, is there any relationship between the preponderance or absence of certain types of symmetry elements in patterns and the civilization or culture which produced them?’

(a)

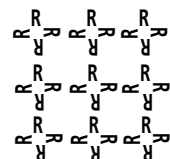
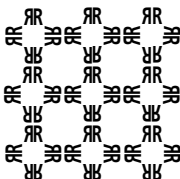
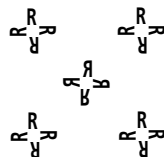


no axial symmetry

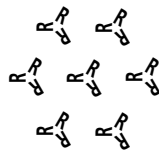
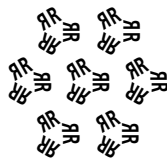
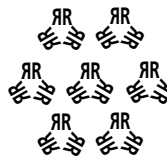
The Seventeen Plane Groups



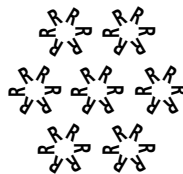
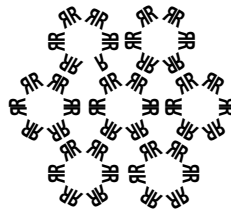
180° symmetry

 $p4$ (10) $p4mm$ (11) $p4gm$ (12)

90° symmetry

 $p3$ (13) $p31m$ (14) $p3m1$ (15)

120° symmetry

 $p6$ (16) $p6mm$ (17)

60° symmetry

Notes:

Each group has a symbol and a number in ().

The symbol denotes the lattice type (primitive or centered), and the major symmetry elements

The numbers are arbitrary, they are those of the International Tables Vol.1, pp 58 – 72

(Drawn by K.M.Crennell)

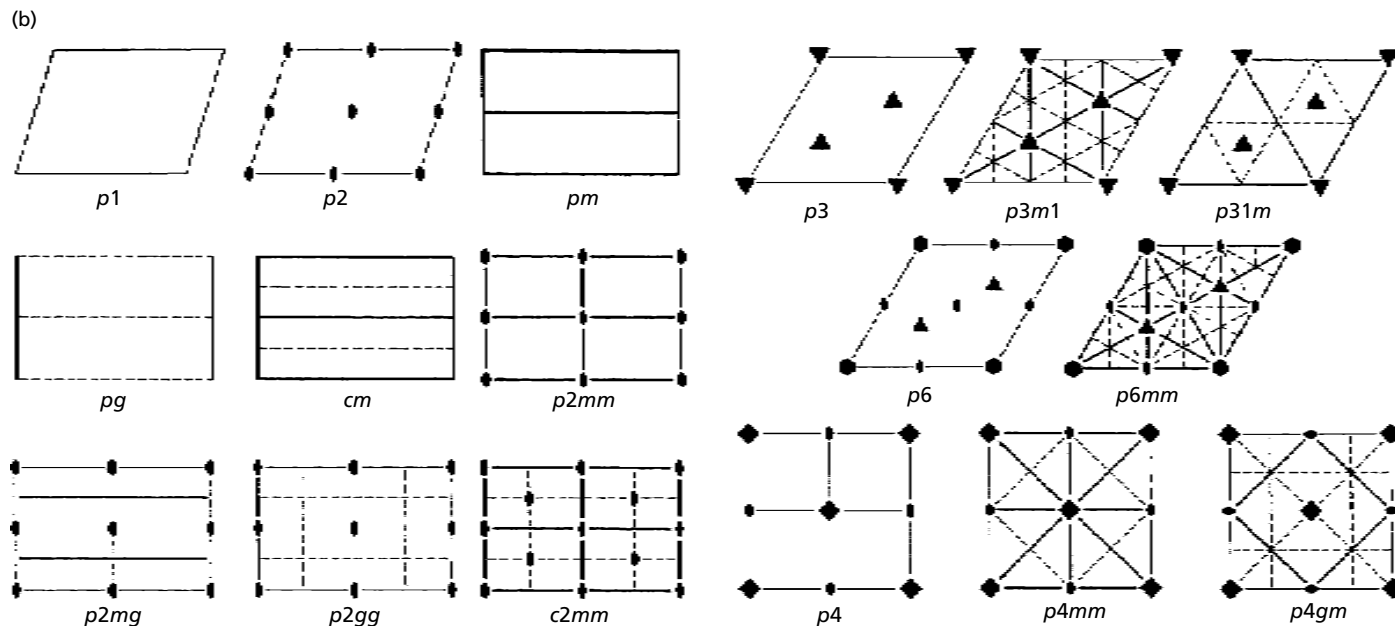


Fig. 2.6. (a) The seventeen plane groups (from *Point and Plane Groups* by K. M. Crennell). The numbering 1–17 is that which is arbitrarily assigned in the International Tables. Note that the ‘shorthand’ symbols do not necessarily indicate all the symmetry elements which are present in the patterns, (b) The symmetry elements outlined within (conventional) unit cells of the seventeen plane groups, heavy solid lines and dashed lines represent mirror and glide lines respectively (from *Manual of Mineralogy* 21st edn, by C. Klein and C. S. Hurlbut, Jr., John Wiley, 1999).

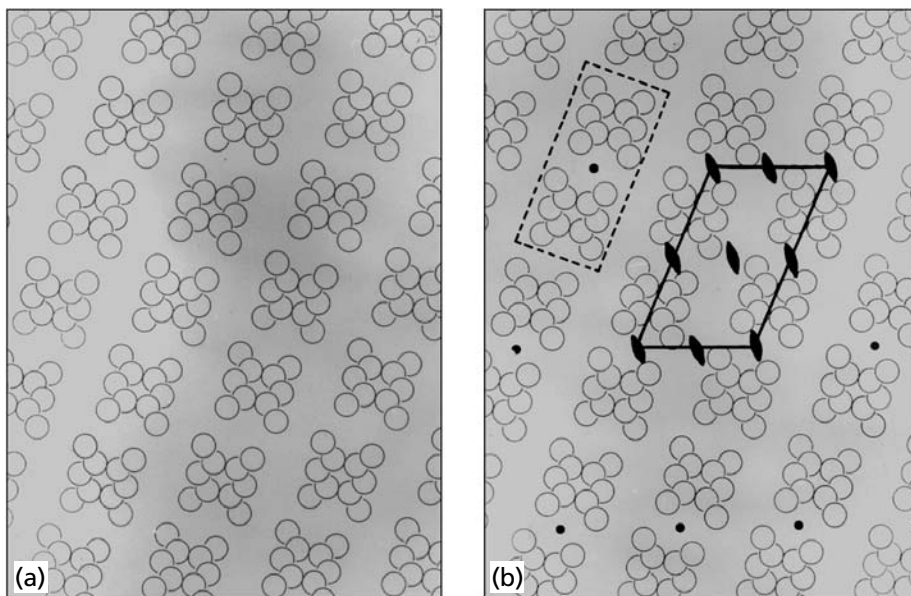


Fig. 2.7. Projection (a) of the structure of $C_6H_2(CH_3)_4$ (from *Contemporary Crystallography*, by M. J. Buerger, McGraw-Hill, 1970), with (b) the motif, lattice and symmetry elements indicated.

Questions such as these have exercised the minds of archaeologists, anthropologists and historians of art and design. They are, to be sure, questions more of cultural than crystallographic significance, but patterns play such a large part in our everyday experience that a crystallographer can hardly fail to be absorbed by them, just as he or she is absorbed by the three-dimensional patterns of crystals.

The study of plane and one-dimensional patterns (and indeed three-dimensional (space) patterns) is complicated by the question of colour—‘real’ colours in the case of plane and one-dimensional patterns, or colours representing some property, such as electron spin direction or magnetic moment, in space patterns (Chapter 4). Colour changes may also be analysed in terms of symmetry elements in which colours are alternated in a systematic way. Clearly, the greater the number of colours, the greater the complexity. The simplest cases to consider are two-colour (e.g. black and white) patterns. Figure 2.11 shows the generation of plane motifs through the operation of what are called counterchange or colour symmetry elements,¹ which are distinguished from ordinary (rotation) axes and mirror lines of symmetry by a prime superscript. For example, the operation of a $2'$ axis is a twice repeated rotation of an asymmetric object by 180° plus a colour change at each rotation; the operation of an m' mirror line is a reflection plus colour change. Altogether there are eleven counterchange point groups (Fig. 2.11) compared

¹ These are a special case of what are sometimes known as *anti-symmetry* elements, which relate the symmetry of opposites—black/white in this case. But the word anti-symmetry itself conveys no clear meaning.

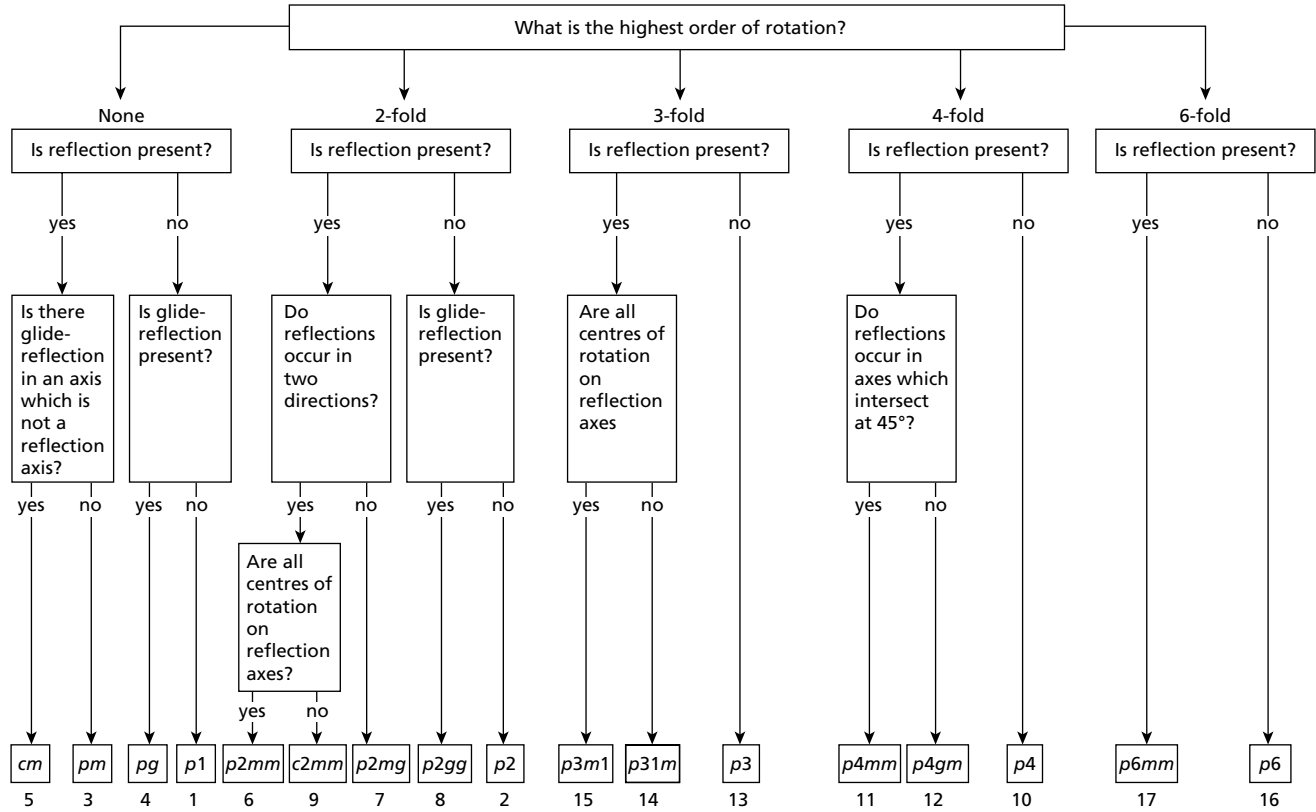


Fig. 2.8. Flow diagram for identifying one of the seventeen plane patterns (redrawn from *The Geometry of Regular Repeating Patterns* by M. A. Hann and G. M. Thomson, the Textile Institute, Manchester, 1992). The numbering is that which is arbitrarily assigned in the International Tables (see Fig 2.6).

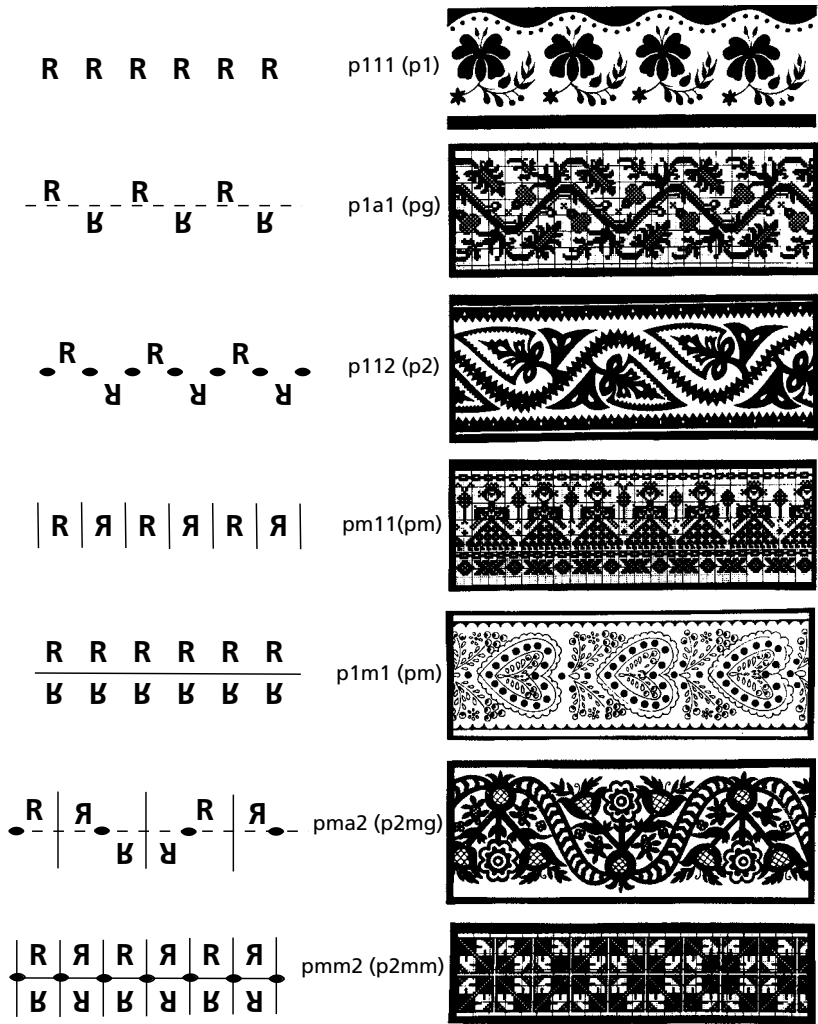


Fig. 2.9. (Left) the seven one-dimensional groups or classes of border or frieze patterns (drawn by K. M. Crennell); (solid lines indicate mirror lines, dashed lines (symbol a) indicate glide lines and \bullet symbols indicate diads); (centre) their symmetry symbols and (bracketed) the plane point groups from which they are derived; and (right) examples of Hungarian needlework border patterns (from *Symmetry Through the Eyes of a Chemist* 3rd edn. by M. and I. Hargittai, Springer, New York and London 2008).

with the ten plane point groups (Fig. 2.3). Note that there are **no** counterchange point groups corresponding to the plane point groups with only odd-numbered axes of symmetry (the monad and the triad), but that there are in each case two possible counterchange point groups corresponding to the plane point groups with symmetry $2mm$, $4mm$ and $6mm$.

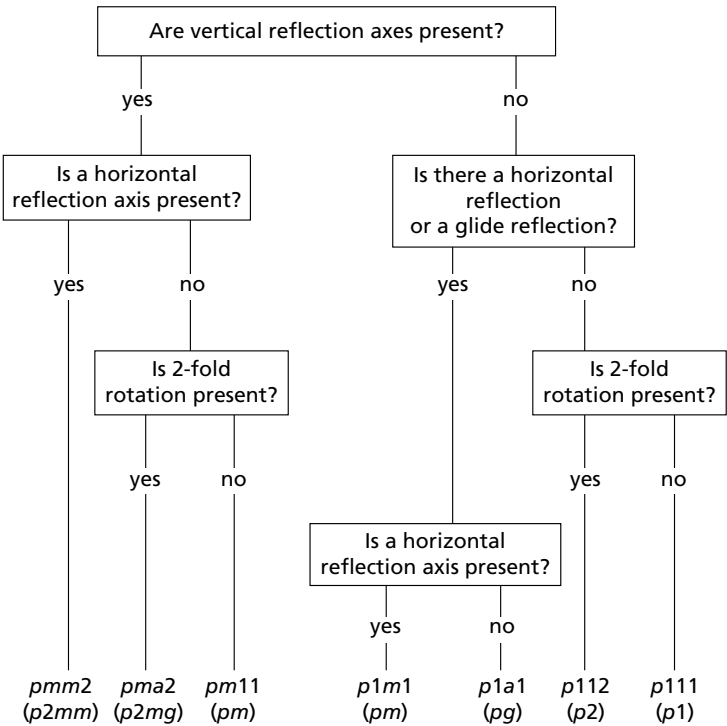


Fig. 2.10. Flow diagram for identifying one of the seven border patterns (from *The Geometry of Regular Repeating Patterns*, loc. cit.).

The derivation of the counterchange one- and two-dimensional patterns also involves the operation of a g' glide line which involves a reflection plus a translation of half a lattice spacing **plus** a colour change and gives (to extend our footprint analogy) a sequence of black/white (i.e. right/left footprints).

Accounting for two-colour symmetry gives rise to a total of forty-six (rather than seventeen) plane patterns and seventeen (rather than seven) one-dimensional patterns. Figure 2.12 shows an example of plane group pattern $p2gg$ (No. 8—see Fig. 2.6(a), (b)) and the two possible counterchange patterns (symbols $p2' gg'$ and $p2g' g'$) which are based upon it.

Probably the most influential and pioneering study of patterns was *The Grammar of Ornament* by Owen Jones, first published in 1856.² Owen Jones attempted to categorize both plane and border patterns in terms of the different cultures that produced them, and although the symmetry aspects of patterns are touched on in the most fragmentary

² Owen Jones. *The Grammar of Ornament*, Day & Sons Ltd., London, reprinted by Studio Editions, London (1986).

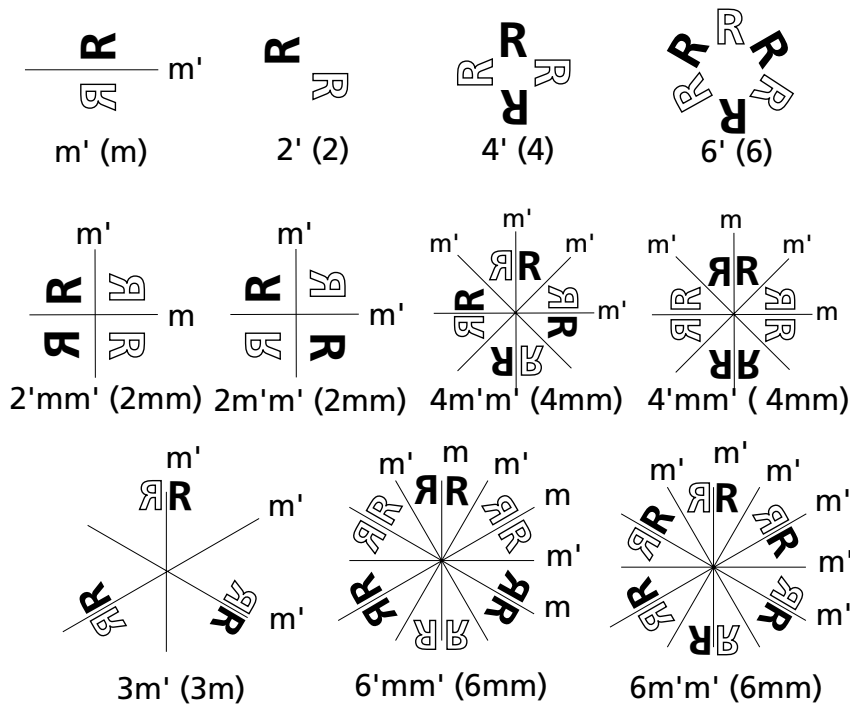


Fig. 2.11. The eleven counterchange (black/white) point groups and (bracketed) the point group symbols for the plane point groups to which they correspond (see Fig. 2.3). The counterchange symmetry elements are denoted by prime superscripts. (Drawn by K. M. Crennell.)

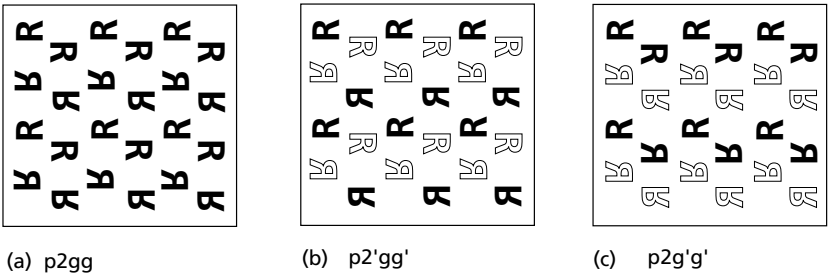


Fig. 2.12. (a) Plane group $p2gg$ and (b) and (c) the two counterchange plane groups $p2'gg'$ and $p2g'g'$ respectively which are based upon it. (Drawn by K. M. Crennell.)

way, there is no doubt that the superb illustrations and encyclopaedic character of the book provided later writers with material which could be classified and analysed in crystallography terms. Perhaps the best known of these was M. C. Escher (1898–1971) who drew inspiration for his drawings of tessellated figures from visits to the Alhambra

in the 1930s, and also presumably from Owen Jones' chapter on 'Moresque Ornament' in which he describes the Alhambra as 'the very summit of Moorish art, as the Parthenon is of Greek art'. Escher's patterns encompass all the seventeen plane groups, eleven of which are represented in the Alhambra.

More recent work has identified clear preponderances of certain plane symmetry groups, and the absences of others.³ For example, nearly 50% of traditional Javanese batik (wax-resist textile) patterns belong to plane group $p4mm$ (Fig. 2.6), others, such as $p3$, $p3m1$, $p31m$ and $p6$ are wholly absent. In Jacquard-woven French silks of the last decade of the nineteenth century, nearly 80% of the patterns belong to plane group pg . In Japanese textile designs of the Edo period *all* plane groups are represented, with a marked preponderance for groups $p2mm$ and $c2mm$. What these differences mean, or tell us about the cultures which gave rise to them, is, as the saying goes, 'another question'.

In X-ray crystallography crystal structures are frequently represented as two-dimensional projections (electron density maps—see Section 13.2). The beauty and variety of these patterns led Dr Helen Megaw*, a crystallographer at Birkbeck College, London, to suggest that they be made the basis for the design of wallpapers and fabrics in the same way that William Morris used flowers and birds in his pattern designs. Her suggestion eventually bore fruit in the work of the *Festival Pattern Group* of the 1951 Festival of Britain and the production of a remarkable variety of patterned wallpapers, carpets and fabrics based upon crystal structures as diverse as haemoglobin, insulin and apophyllite. These patterns, recently republished,⁴ provide a rich source of material for plane group recognition.

2.8 Layer (two-sided) symmetry and examples in woven textiles

Woven textiles consist of interlacing warp 'north-south' threads and weft 'east-west' threads. The various combinations of interlacings, which give rise to the different patterns of cloths, are very wide indeed, ranging from the simplest 'single cloth', plain weave fabric, where individual warp and weft threads pass over and under each time (Fig. 2.13), to more complex cloth structures. Common structures include twills (e.g. Fig. 2.14), herringbones, sateens, etc. Clearly, there are symmetry relationships between the 'face' and 'back' of such woven fabrics and the study of such relationships introduces us to what are known as *layer-symmetry groups* or classes.

We will not describe all the layer-symmetry groups or classes (of which there are a total of 80) but just some of the general principles of their construction. Readers who wish to follow this topic further should refer to the book by Shubnikov and Koptsik or

* Denotes biographical notes available in Appendix 3.

³ M. A. Hann. *Symmetry of Regular Repeating Patterns: Case Studies from various cultural settings*. Journal of the Textile Institute (1992), Vol. 83, pp. 579–580.

⁴ L. Jackson. *From Atoms to Patterns, Crystal Structure Designs from the 1951 Festival of Britain*. Richard Dennis Publications, Shepton Beauchamp, Somerset (2008).

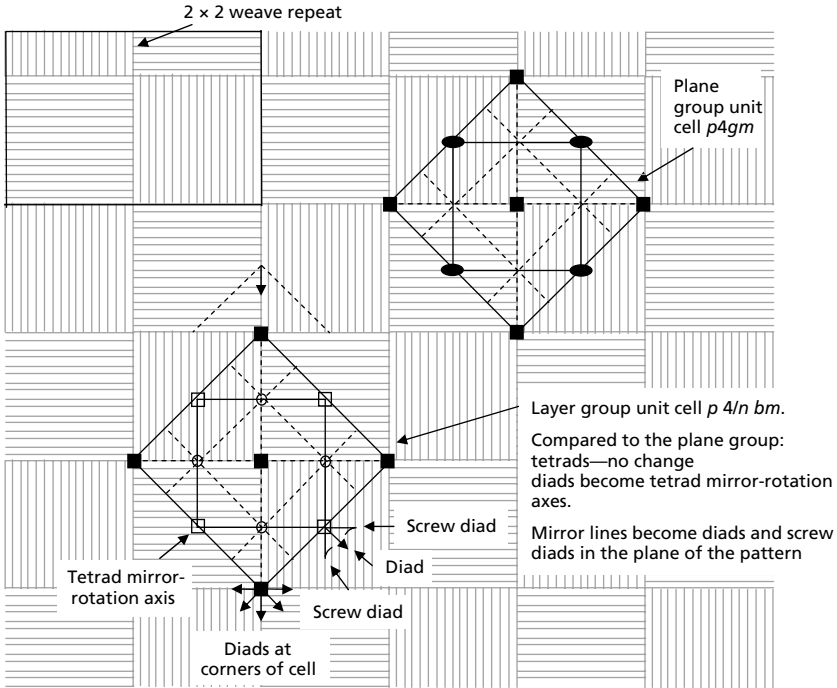


Fig. 2.13. Diagrammatic representation of a plain weave and (superimposed) the plane group unit cell $p4gm$ (see also Fig. 2.6) and the layer-symmetry group unit cell $p4/nbm$. Note the differences between the symmetry elements in these unit cells: the diads and mirror lines in $p4gm$ become tetrad mirror-rotation axes and screw diads respectively (in the plane) in $p4/nbm$. (Drawn by C. McConnell.)

the papers by Scivier and Hann.⁵ However, we may note here that the 80 layer-symmetry groups are sub-groups of the 230 space groups (Section 4.6) and that the 17 plane groups are, in turn, sub-groups of the 80 layer-symmetry groups.

Because of the structural restrictions imposed by the warp and weft character, the five plane groups with three or six fold symmetry are not applicable to woven fabrics and, correspondingly, neither are 16 of the 80 layer-symmetry groups.

As we have seen, in describing the 17 plane groups we are restricted to rotation axes perpendicular to the plane and reflection (mirror) and glide lines of symmetry within the plane. In describing layer-symmetry groups further symmetry elements or operations are required which relate the 'face' and 'back' of the fabric. These are (i) rotation-reflection (mirror-rotation) axes of symmetry perpendicular to the plane which consist of a rotation plus a reflection in the plane. These symmetry operations correspond to the black/white counterchange point groups (Fig. 2.11) in which the symbol **R** is now

⁵ J.A. Scivier and M.A. Hann The application of symmetry principles to the classification of fundamental simple weaves, *Ars Textrina* **33**, 29 (2000) and Layer symmetry in woven textiles, *Ars Textrina* **34**, 81 (2000).

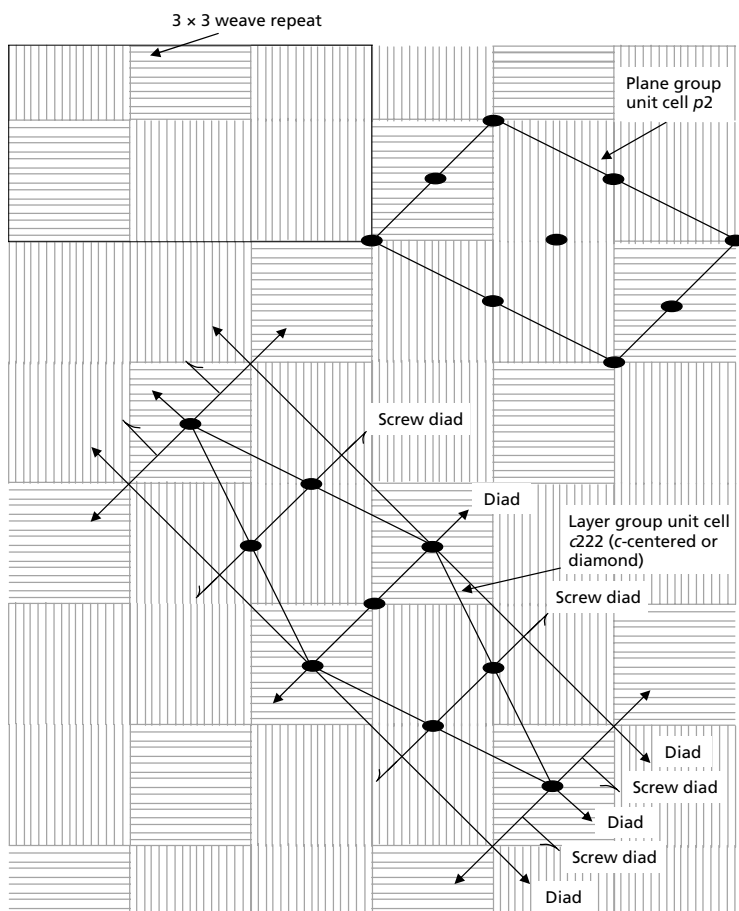


Fig. 2.14. Diagrammatic representation of a twill weave with a 3×3 repeat and (superimposed) the plane group unit cell $p2$ and the layer-symmetry group unit cell $c222$. Note the differences between these unit cells: $c222$ is a rectangular c-centred or ‘diamond’ unit cell (see Fig. 2.4) and contains diads and screw diads lying in the plane of the pattern. (Drawn by C. McConnell.)

understood to have two sides—black on the face and white on the back. Again, because of the structural restrictions imposed by woven fabrics, only two such rotation-reflection axes are applicable— $2'$ and $4'$ (Fig. 2.11). (ii) Diad axes lying *within* the plane—both the simple diad axes which we have already met and also *screw diad* axes which involve a rotation plus a translation (like glide lines) of half a lattice spacing (screw diad axes are but one example of screw axes which we shall meet in our description of three-dimensional symmetry and space groups). In both cases, because the axes lie in the plane, they ‘turn over’ the black face of the **R** to its white face. The operations of these in-plane axes are shown in Fig. 2.15. Notice that the operation of the diad is identical to that of the counterchange mirror line m' (Fig. 2.11). (iii) Planes (not lines) of symmetry coinciding

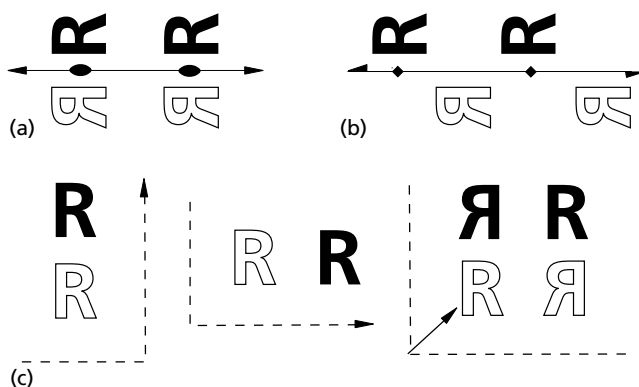


Fig. 2.15. The additional symmetry operations for the 52 layer-symmetry groups applicable to woven fabrics (plus the counterchange symmetry operations $2'$ and $4'$ (Fig. 2.11). The 'face' and 'back' of the **R** symbols are shown here as black and white, respectively.

(a) Operation of an in-plane diad axis (double arrow-head) (identical to counterchange symmetry element m' —see Fig. 2.11) and (b) an in-plane screw diad axis (single arrow-head). (c) Operation of in-plane glide planes (dashed lines) for three different orientations of the glide directions—along the axes and diagonally. (Drawn by K. M. Crennell.)

with the plane; both reflection (mirror) planes (which are not applicable to woven textiles because the back of the cloth is not identical to the front⁶) and glide-reflection planes (which are applicable to woven textiles). These symmetry operations are also shown in Fig. 2.15.

We will now apply these ideas to the plain weave and twill illustrated in Figs 2.13 and 2.14. The 'weave repeat' is the smallest number of warp and weft threads on which the weave interlacing can be represented; it is a 2×2 square for the plain weave (Fig. 2.13) and a 3×3 square for this example of a twill weave (Fig. 2.14). It is important to note that these weave repeat squares *do not* correspond with the unit cells of the plane patterns. These unit cells and the plane group symmetry elements are also shown in Figs 2.13 and 2.14. As can be seen, the plain weave has plane symmetry $p4gm$ and the twill plane symmetry $p2$ (see Fig. 2.6).

Figures 2.13 and 2.14 also show the unit cells and layer symmetry elements for these two weaves and the standard notation (which we will not describe in detail) which goes with them. Notice that for the plain weave that the unit cell is identical to that for the plane group symmetry but for the twill it is different—the primitive (p) lattice becomes a centred (c) or diamond lattice. Notice also that the layer-group symmetry of the plain weave is much more 'complicated' than that of the twill. It includes tetrad rotation-reflection axes perpendicular to the plane as well as diads and screw diads within the plane. The twill, by contrast, has no mirror lines of symmetry at all.

⁶ This restriction further reduces (by 12) the number of layer-symmetry groups applicable to woven textiles, leaving a total of $80 - 16 - 12 = 52$. Still a lot!



Fig. 2.16. Operation of a tetrad rotation-reflection axis showing an **R** superimposed on a 'float' of the plain weave fabric (Fig. 2.13). The operations of reflection-rotation are of course repeated three times. (Drawn by K. M. Crennell.)

Finally, look carefully at the positions of the tetrad rotation-reflection axes in the centres of the plain weave warp and weft 'floats'. These axes help us to visualize the relation between the face and back of the fabric: for example, rotate a warp float 90° and we have a weft float, reflect it (black to white) and you have the weft float in the back face of the fabric as shown in Fig. 2.16.

2.9 Non-periodic patterns and tilings

Johannes Kepler was the first to show that pentagonal symmetry would give rise to a pattern which was non-repeating. Figure 2.17 is an illustration from perhaps his greatest work *Harmonices mundi* (1619) which shows in the figures captioned 'Aa' and 'z' a pattern or tiling of pentagons, pentagonal stars and 10 and 16-sided figures which radiate out in pentagonal symmetry from a central point. Grünbaum and Shephard⁷ have shown how the tiling 'Aa' can be extended indefinitely giving long-range orientational order but the pattern does not repeat and cannot be identified with any of the seventeen plane groups (Fig. 2.6). A. L. Mackay⁸ has shown how a regular, but non-periodic pattern, can be built up from regular pentagons in a plane with the triangular gaps covered by pieces cut from pentagons, which he describes with the title (echoing Kepler) *De nive quinquangula*—on the pentagonal snowflake.

These are but two examples of non-periodic or 'incommensurate' tilings, the mathematical basis of which was largely developed by Roger Penrose and are generally named after him. Figure 2.18 shows how a Penrose tiling may be constructed by linking together edge-to-edge 'wide' and 'narrow' rhombs or diamond-shaped tiles of equal edge lengths. The angles between the edges of the tiles (as shown in Fig. 2.18(a)) are not arbitrary but arise from pentagonal symmetry as shown in Fig. 2.18(b) (where the tiles are shown shaded in relation to a pentagon); nor are they linked together in an arbitrary fashion but according to local 'matching rules', shown in Fig. 2.18(a) by little triangular 'pegs' and 'sockets' along the tile edges. These are omitted in the resultant tiling (Fig. 2.18(c)), partly for clarity and partly because their work in constructing the pattern is done. (An

⁷ B. Grünbaum and G. C. Shephard. *Tilings and Patterns: An Introduction*. W. H. Freeman, New York, 1989.

⁸ A. L. Mackay. *De nive quinquangula*. *Physics Bulletin* 1976, p. 495.

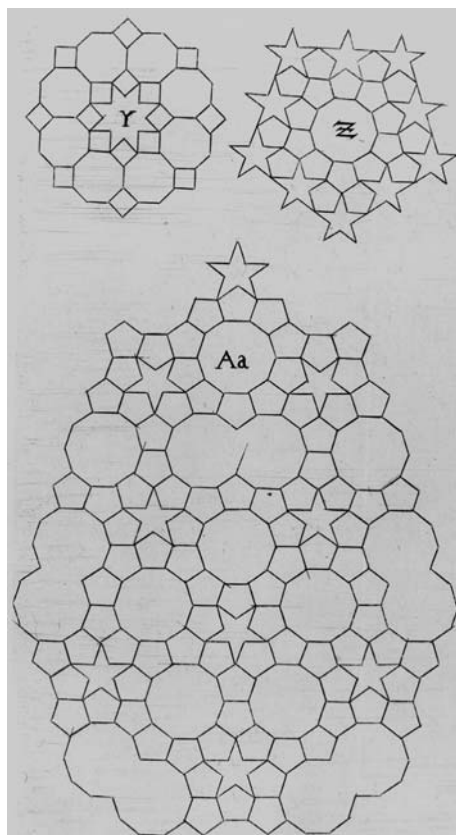


Fig. 2.17. Non-periodic tiling patterns ‘z’ and ‘Aa’ (from *Harmonices Mundi* by Johannes Kepler, 1619, reproduced from the copy in the Brotherton Library, University of Leeds, by courtesy of the Librarian).

alternative of showing how the tiles must be fitted together is to colour or shade them in three ways and then to match the colours, like the pegs and sockets, along the tile edges.) The tiling can be viewed as a linkage of little cubes where we see three cube faces; the ‘front’ and ‘top’ faces (represented by the ‘wide’ diamonds) and ‘side’ face (represented by the ‘narrow’ diamond).

The mathematical analysis of non-repeating patterns is rather difficult (especially in three-dimensions—see Section 4.9), but we can perhaps understand their essential ‘incommensurate’ properties by way of a one-dimensional analogy or example. Consider a pattern made up of a row of arrows and a row of stars extending right and left from an origin O . If the spacings of the arrows and stars are in a ratio of whole numbers then, depending on the values of these numbers, the pattern will repeat. Figure 2.19(a) shows a simple case where the ratio of spacings is $3/2$ and the pattern repeats (i.e. the arrows and stars coincide) every third arrow or second star. If, however, the spacings of

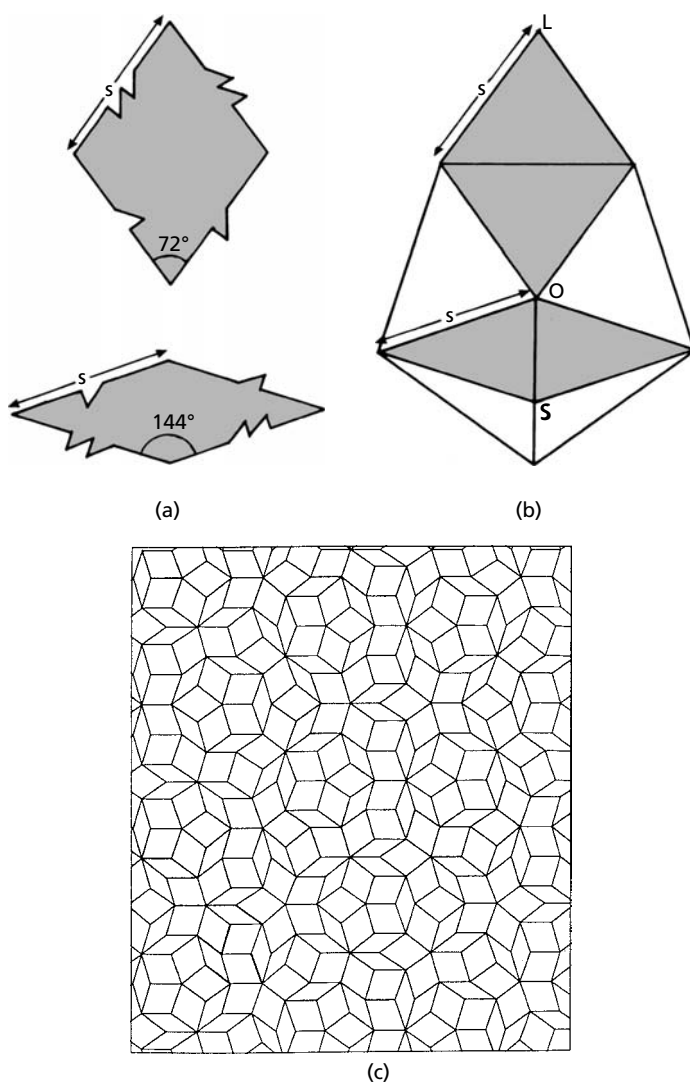


Fig. 2.18. (a) The two types ('wide' and 'narrow') tiles for the construction of a Penrose tiling. The triangular 'pegs' and 'sockets' along the tile edges indicate how they should be linked together edge-to-edge. (b) The geometry of the tiles in relation to a pentagon. The ratio OL/s (wide tile) $= s/OS$ (narrow tile) $= (\sqrt{5} - 1)/2 = 1.618 \dots$ (c) shows the resultant tiling (pegs and sockets omitted for clarity) (reproduced by courtesy of Prof. Sir Roger Penrose).

the arrows and stars cannot be expressed as a ratio of whole numbers, in other words if the ratio is an *irrational* number, then the pattern will never repeat—the arrows and stars will never come into coincidence. Figure 2.19(b) shows an example where the ratio of spacings is $\sqrt{2} = 1.414213 \dots$ an irrational number, like π , where there

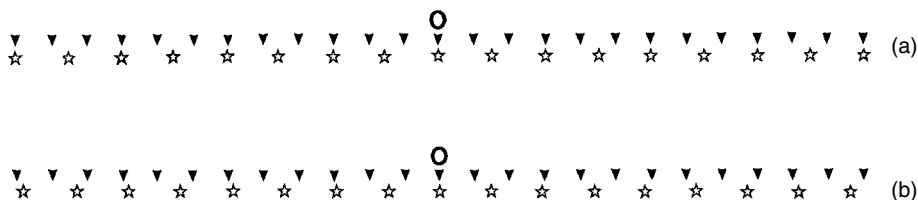


Fig. 2.19. One-dimensional examples of (a) a periodic pattern and (b) a non-periodic pattern. In (a) the pattern repeats every third arrow and second star, in (b) the ratio of the spacings is $\sqrt{2}$ and the pattern never repeats.

is ‘no end’ to the number of decimal places and no cyclic repetition of the decimal numbers.⁹

In Penrose five-fold or pentagonal tiling it turns out (Fig. 2.18(b)) that the ratio of the diagonal OL to the edge length s (for the wide tile) and the ratio of the edge length s to the diagonal OS (for the narrow tile) are also both equal to an irrational number $(\sqrt{5} + 1)/2 = 1.618034 \dots$ called the *Golden Mean* or *Golden Ratio*. The Golden Ratio also applies to a rectangle whose sides are in the ratio $(\sqrt{5} + 1)/2 : 1$; if a square is cut off such a rectangle, then the rectangle which remains also has sides which are in this ratio, i.e. $(\sqrt{5} + 1)/2 - 1 : 1 = 1 : (\sqrt{5} + 1)/2$. The Golden Ratio also occurs as the convergence of the ratio of successive terms in the so-called *Fibonacci series* of numbers where each term is the sum of the preceding two. Any number can be used to ‘start off’ a Fibonacci series, e.g. 1, 1, 2, 3, 5, 8, 13, 21, 34 \dots or 3, 3, 6, 9, 15, 24, 39, 63 \dots Not only is the Golden Ratio a subject of mathematical interest, but it is also of relevance in architectural proportion and spiral growth in animals and plants (e.g. the spirals traced out in the head of a sunflower). However, this is a subject which we must regretfully now leave.

Exercises

- 2.1 Lay tracing paper over the plane patterns in Fig. 2.6. Outline a unit cell in each case and indicate the positions of all the symmetry elements within the unit cell. Notice in particular the differences in the distribution of the triad axes and mirror lines in the plane groups $p31m$ and $p3m1$.
- 2.2 Figure 2.20 is a design by M. C. Escher. Using a tracing paper overlay, indicate the positions of all the symmetry elements. With the help of the flow diagram (Fig. 2.8), determine the plane lattice type.

⁹ The discovery that some numbers are irrational is one of the triumphs of Greek mathematics. The proof that $\sqrt{2}$ is irrational, which is generally attributed to Pythagoras, may be expressed as follows. Suppose that $\sqrt{2}$ can be expressed as a/b where a and b are whole numbers which have no common factor (if they had, we could simply remove it). Hence $\sqrt{2}b = a$ and squaring $2b^2 = a^2$. Now $2b^2$ is an even number, hence a^2 is also an even number and, since the square of an even number is even, a is an even number. Now an even number can be expressed as $2 \times (\text{any number})$, i.e. $a = 2c$. Squaring again $a^2 = 4c^2 = 2b^2$, hence $2c^2 = b^2$ and, for the same reason as before, since $2c^2$ is an even number then b is an even number. So, both a and b are even and have a common factor 2 which contradicts our initial hypothesis which therefore must be false.

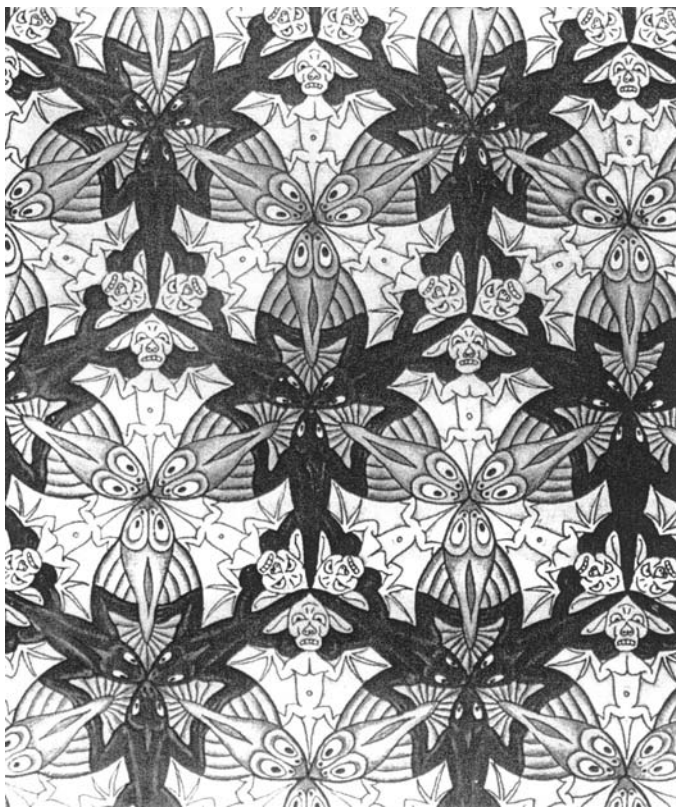


Fig. 2.20. A plane pattern (from *Symmetry Aspects of M. C. Escher's Periodic Drawings*, 2nd edn, by C. H. MacGillavry. Published for the International Union of Crystallography by Bohn, Scheltema and Holkema, Utrecht, 1976).

- 2.3 Figure 2.21 is a projection of the structure of FeS_2 (shaded atoms Fe, unshaded atoms S). Using a tracing paper overlay, indicate the positions of the symmetry elements, outline a unit cell and, with the help of the flow diagram in Fig. 2.8, determine the plane pattern type.
- 2.4 Figure 2.22 is a design by M. C. Escher. Can you see that the two sets of men are related by glide lines of symmetry? Draw in the positions of these glide lines, and determine the plane lattice type.
- 2.5 Determine (with reference to Fig. 2.11) the counterchange (black–white) point group symmetry of a chessboard.
- 2.6 Figure 2.23 shows examples of border or frieze patterns from *The Grammar of Ornament* by Owen Jones. Using a tracing paper overlay, indicate the positions of the symmetry elements and, with the help of the flow diagram (Fig. 2.10), determine the one-dimensional lattice types.
- 2.7 Figure 2.24(a) is a ‘wood block floor’ or ‘herringbone’ pattern with plane group symmetry $p2gg$. Using a tracing-paper overlay (and with the help of Fig. 2.6(b) and the flow chart, Fig. 2.8), locate the positions of the diad axes and glide lines. Now place your tracing paper

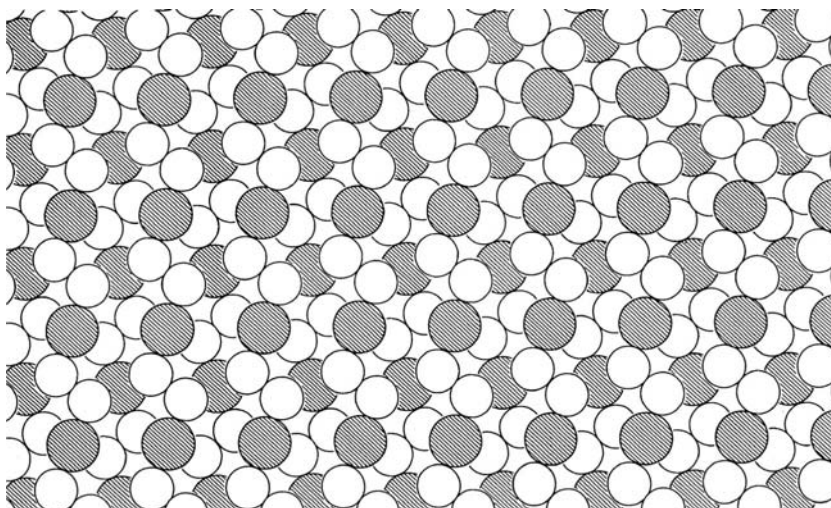


Fig. 2.21. A projection of the structure of marcasite, FeS_2 (from *Contemporary Crystallography* by M. J. Buerger, McGraw-Hill, New York, 1970).

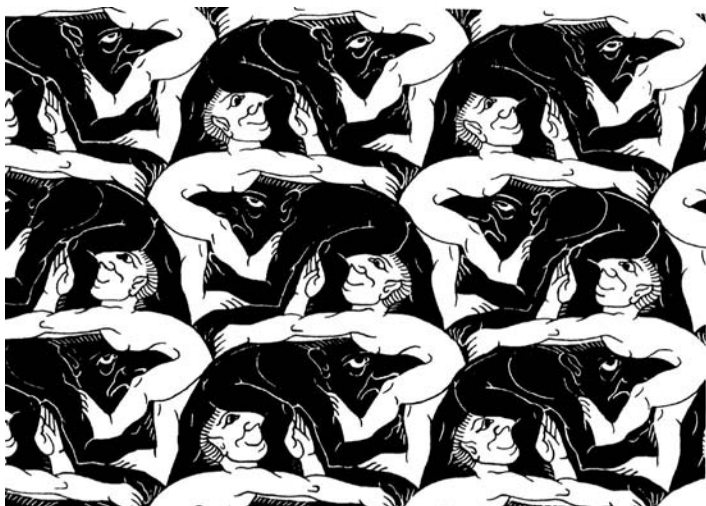


Fig. 2.22. A plane pattern (from C. H. MacGillavry, loc. cit.).

over the counterchange pattern (Fig. 2.24(b)) and determine which of the symmetry elements become counterchange ($2'$ or g') symmetry elements. To which of the counterchange patterns shown in Fig. 2.12 does this pattern belong?

- 2.8 The symmetry of border pattern $pma2$ ($p2mg$) (Fig. 2.9) consists of a glide line a (or g) along the length of the border with vertical mirror lines and diad axes in between. Derive

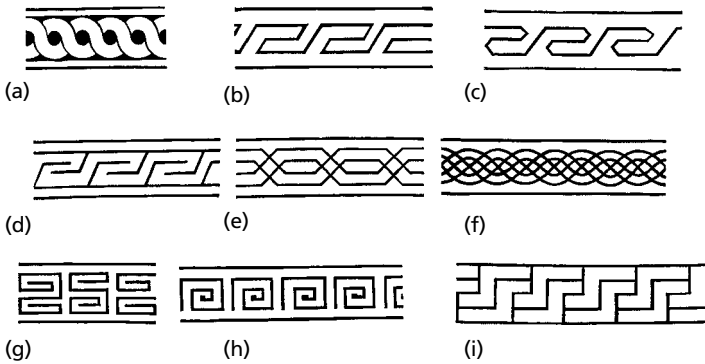


Fig. 2.23. Examples of border or frieze patterns (from *The Grammar of Ornament* by Owen Jones, Day & Son, London 1856, reprinted by Studio Editions, London, 1986). a, b, Greek; c, d, Arabian; e, Moresque; f, Celtic; g, h, Chinese; i, Mexican.

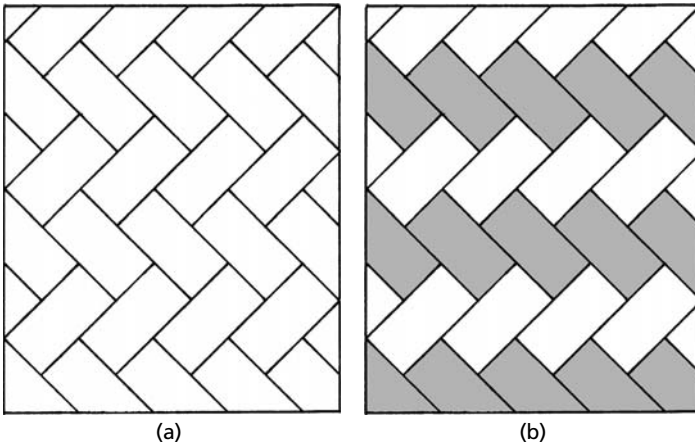


Fig. 2.24. 'Wood block floor' or 'herringbone brickwork' patterns (a) with all blocks the same colour, and (b) with alternating black and white blocks.

the two-colour (black and white) counterchange patterns based upon $pma2$ by replacing, in turn, the glide lines, mirror lines and diad axes by the counterchange symmetry elements g' , m' and $2'$.

Bravais lattices and crystal systems

3.1 Introduction

The definitions of the motif, the repeating ‘unit of pattern’, and the lattice, an array of points in space in which each point has an identical environment, hold in three dimensions exactly as they do in two dimensions. However, in three dimensions there are additional symmetry elements that need to be considered: both **point symmetry elements** to describe the symmetry of the three-dimensional motif (or indeed any crystal or three-dimensional object) and also **translational symmetry elements**, which are required (like glide lines in the two-dimensional case) to describe all the possible patterns which arise by combining motifs of different symmetries with their appropriate lattices. Clearly, these considerations suggest that the subject is going to be rather more complicated and ‘difficult’; it is obvious that there are going to be many more three-dimensional patterns (or space groups) than the seventeen two-dimensional patterns (or plane groups or the eighty two-sided patterns—Chapter 2), and to work through all of these systematically would take up many pages! However, it is not necessary to do so; all that is required is an understanding of the principles involved (Chapter 2), the operation and significance of the additional symmetry elements, and the main results. These main results may be stated straight away. The additional point symmetry elements required are centres of symmetry, mirror planes (instead of lines) and inversion axes; the additional translational symmetry elements are glide planes (instead of lines) and screw axes. The application and permutation of all symmetry elements to patterns in space give rise to 230 **space groups** (instead of seventeen plane groups) distributed among fourteen space lattices (instead of five plane lattices) and thirty-two point group symmetries (instead of ten plane point group symmetries).

In this chapter the concept of space (or Bravais) lattices and their symmetries is discussed and, deriving from this, the classification of crystals into seven systems.

3.2 The fourteen space (Bravais) lattices

The systematic work of describing and enumerating the space lattices was done initially by Frankenheim* who, in 1835, proposed that there were fifteen in all. Unfortunately for Frankenheim, two of his lattices were identical, a fact first pointed out by Bravais* in 1848. It was, to take a two-dimensional analogy, as if Frankenheim had failed to notice

* Denotes biographical notes available in Appendix 3.

(see Fig. 2.4(b)) that the rhombic or diamond and the rectangular centred plane lattices were identical! Hence, to this day, the fourteen space lattices are usually, and perhaps unfairly, called Bravais lattices.

The unit cells of the Bravais lattices are shown in Fig. 3.1. The different shapes and sizes of these cells may be described in terms of three cell edge lengths or axial distances,

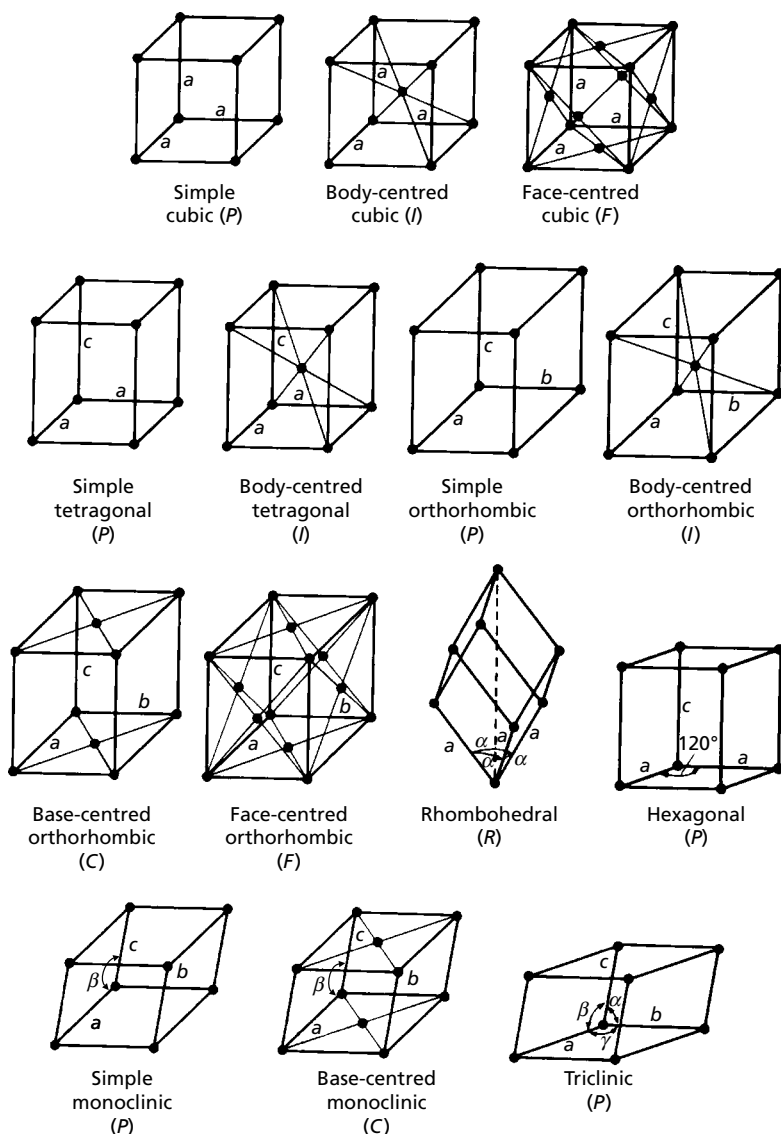


Fig. 3.1. The fourteen Bravais lattices (from *Elements of X-Ray Diffraction*, (2nd edn), by B. D. Cullity, Addison-Wesley, 1978).

a , b , c , or lattice vectors \mathbf{a} , \mathbf{b} , \mathbf{c} and the angles between them, α , β , γ , where α is the angle between \mathbf{b} and \mathbf{c} , β the angle between \mathbf{a} and \mathbf{c} , and γ the angle between \mathbf{a} and \mathbf{b} . The axial distances and angles are measured from one corner to the cell, i.e. a common origin. It does not matter where we take the origin—any corner will do—but, as pointed out in Chapter 1, it is a useful convention (and helps to avoid confusion) if the origin is taken as the ‘back left-hand corner’ of the cell, the a -axis pointing forward (out of the page), the b -axis towards the right and the c -axis upwards. This convention also gives a right-handed axial system. If any one of the axes is reversed (e.g. the b -axis towards the left instead of the right), then a left-handed axial system results. The distinction between them is that, like left and right hands, they are mirror images of one another and cannot be brought into coincidence by rotation.

The drawings of the unit cells of the Bravais lattices in Fig. 3.1 can be misleading because, as shown in Chapter 2, it is the *pattern* of lattice points which distinguishes the lattices. The unit cells simply represent arbitrary, though convenient, ways of ‘joining up’ the lattice points. Consider, for example, the three cubic lattices; cubic P (for *Primitive*, one lattice point per cell, i.e. lattice points only at the corners of the cell), cubic I (for ‘*Innenzentrierte*’, which is German for ‘body-centred’, an additional lattice point at the centre of the cell, giving two lattice points per cell) and cubic F (for *Face-centred*, with additional lattice points at the centres of each face of the cell, giving four lattice points per cell). It is possible to outline alternative primitive cells (i.e. lattice points only at the corners) for the cubic I and cubic F lattices, as is shown in Fig. 3.2. As mentioned in Chapter 1, these primitive cells are not often used (1) because the inter-axial angles are not the convenient 90° (i.e. they are not orthogonal) and (2) because they do not reveal very clearly the cubic symmetry of the cubic I and cubic F lattices. (The symmetry of the Bravais lattices, or rather the point group symmetries of their unit cells, will be described in Section 3.3.)

Similar arguments concerning the use of primitive cells apply to all the other centred lattices. Notice that the unit cells of two of the lattices are centred on the ‘top’ and ‘bottom’ faces. These are called base-centred or C -centred because these faces are intersected by the c -axis.

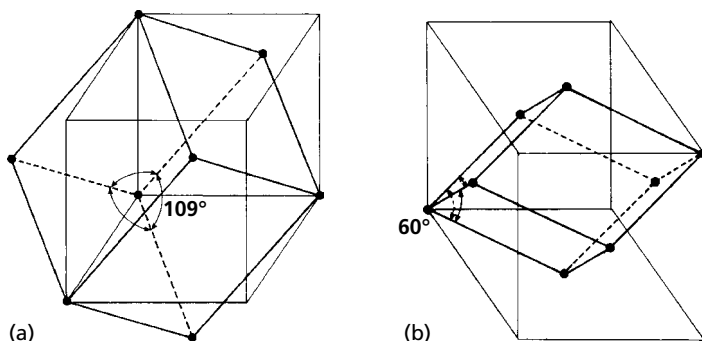


Fig. 3.2. (a) The cubic I and (b) the cubic F lattices with the primitive rhombohedral cells and inter-axial angles indicated.

The Bravais lattices may be thought of as being built up by stacking ‘layers’ of the five plane lattices, one on top of another. The cubic and tetragonal lattices are based on the stacking of square lattice layers; the orthorhombic *P* and *I* lattices on the stacking of rectangular layers; the orthorhombic *C* and *F* lattices on the stacking of rectangular centred layers; the rhombohedral and hexagonal lattice on the stacking of hexagonal layers and the monoclinic and triclinic lattices on the stacking of oblique layers. These relationships between the plane and the Bravais lattices are easy to see, except perhaps for the rhombohedral lattice. The rhombohedral unit cell has axes of equal length and with equal angles (α) between them. Notice that the layers of lattice points, perpendicular to the ‘vertical’ direction (shown dotted in Fig. 3.1) form triangular, or equivalently, hexagonal layers. The hexagonal and rhombohedral lattices differ in the ways in which the hexagonal layers are stacked. In the hexagonal lattice they are stacked directly one on top of the other (Fig. 3.3(a)) and in the rhombohedral lattice they are stacked such that the next two layers of points lie above the triangular ‘hollows’ or interstices of the layer below, giving a three layer repeat (Fig. 3.3(b)). These hexagonal and rhombohedral stacking sequences have been met before in the stacking of close-packed layers (Chapter 1); the hexagonal lattice corresponds to the simple hexagonal AAA... sequence and the rhombohedral lattice corresponds to the fcc ABCABC... sequence.

Now observant readers will notice that the rhombohedral and cubic lattices are therefore related. The primitive cells of the cubic *I* and cubic *F* lattices (Fig. 3.2) are rhombohedral—the axes are of equal length and the angles (α) between them are equal. As in the two-dimensional cases, what distinguishes the cubic lattices from the rhombohedral is their symmetry. When the angle α is 90° we have a cubic *P* lattice, when it is 60° we have a cubic *F* lattice and when it is 109.47° we have a cubic *I* lattice (Fig. 3.2). Or, alternatively, when the hexagonal layers of lattice points in the rhombohedral lattice are spaced apart in such a way that the angle α is 90° , 60° or 109.47° , then cubic symmetry results.

Finally, compare the orthorhombic lattices (all sides of the unit cell of different lengths) with the tetragonal lattices (two sides of the cell of equal length). Why are there

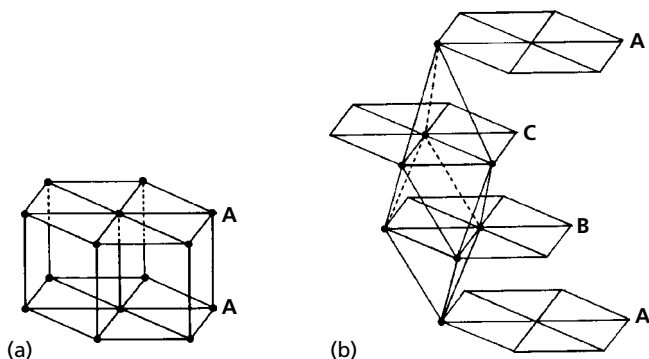


Fig. 3.3. Stacking of hexagonal layers of lattice points in (a) the hexagonal lattice and (b) the rhombohedral lattice.

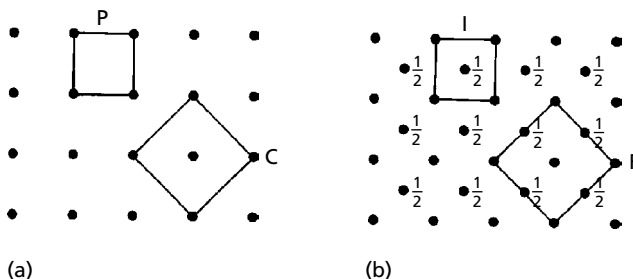


Fig. 3.4. Plans of tetragonal lattices showing (a) the tetragonal $P = C$ lattice and (b) the tetragonal $I = F$ lattice.

four orthorhombic lattices, P , C , I and F , and only two tetragonal lattices, P and I ? Why are there not tetragonal C and F lattices as well? The answer is that there *are* tetragonal C and F lattices, but by redrawing or outlining different unit cells, as shown in Fig. 3.4, it will be seen that they are identical to the tetragonal P and I lattices, respectively. In short, they represent no new arrangements of lattice points.

3.3 The symmetry of the fourteen Bravais lattices: crystal systems

The unit cells of the Bravais lattices may be thought of as the ‘building blocks’ of crystals, precisely as Haüy envisaged (Fig. 1.2). Hence it follows that the habit or external shape, or the observed symmetry of crystals, will be based upon the shapes and symmetry of the Bravais lattices, and we now have to describe the point symmetry of the unit cells of the Bravais lattices just as we described the point symmetry of plane patterns and lattices. The subject is far more readily understood if simple models are used (Appendix 1).

First, mirror lines of symmetry become mirror planes in three dimensions. Second, axes of symmetry (diads, triads, tetrads and hexads) also apply to three dimensions. The additional complication is that, whereas a plane motif or object can only have one such axis (perpendicular to its plane), a three-dimensional object can have several axes running in different directions (but always through a point in the centre of the object).

Consider, for example, a cubic unit cell (Fig. 3.5(a)). It contains a total of nine mirror planes, three parallel to the cube faces and six parallel to the face diagonals. There are three tetrad (four-fold) axes perpendicular to the three sets of cube faces, four triad (three-fold) axes running between opposite cube corners, and six diad (two-fold) axes running between the centres of opposite edges. This ‘collection’ of symmetry elements is called the **point group symmetry** of the cube because all the elements—planes and axes—pass through a point in the centre.

Why should there be these particular numbers of mirror planes and axes? It is because all the various symmetry elements operating at or around the point must be consistent with one another. Self-consistency is a fundamental principle, underlying all the two-dimensional plane groups, all the three-dimensional point groups and all the space groups

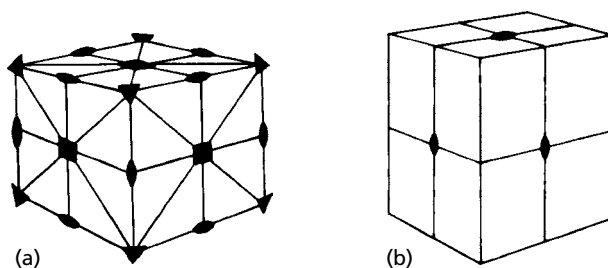


Fig. 3.5. The point symmetry elements in (a) a cube (cubic unit cell) and (b) an orthorhombic unit cell.

that will be discussed in Chapter 4. If there are two diad axes, for example, then they *have* to be mutually orthogonal, otherwise chaos would result; by the same token they also *must* generate a third diad perpendicular to both of them. It is the necessity for self-consistency which governs the construction of every one of the different combinations of symmetry, controlling the nature of each combination; it is this, also, which limits the total numbers of possible combinations to quite definite numbers such as thirty-two, in the case of the crystallographic point groups (the crystal classes), the fourteen Bravais lattices, and so on.

The cubic unit cell has more symmetry elements than any other: its very simplicity makes its symmetry difficult to grasp. More easy to follow is the symmetry of an orthorhombic cell. Figure 3.5(b) shows the point group symmetry of an orthorhombic unit cell. It contains, like the cube, three mirror planes parallel to the faces of the cell but no more—mirror planes do not exist parallel to the face diagonals. The only axes of symmetry are three diads perpendicular to the three faces of the unit cell.

In both cases it can be seen that the point group symmetry of these unit cells (Figs 3.5(a) and 3.5(b)) is independent of whether the cells are centred or not. All three cubic lattices, *P*, *I* and *F*, have the same point group symmetry; all four orthorhombic lattices, *P*, *I*, *F* and *C*, have the same point group symmetry and so on. This simple observation leads to an important conclusion: it is not possible, from the observed symmetry of a crystal, to tell whether the underlying Bravais lattice is centred or not. Therefore, in terms of their point group symmetries, the Bravais lattices are grouped, according to the shapes of their unit cells, into seven **crystal systems**. For example, crystals with cubic *P*, *I* or *F* lattices belong to the **cubic system**, crystals with orthorhombic *P*, *I*, *F* or *C* lattices belong to the **orthorhombic system**, and so on. However, a complication arises in the case of crystals with a hexagonal lattice. One might expect that all crystals with a hexagonal lattice should belong to the hexagonal system, but, as shown in Chapter 4, the external symmetry of crystals may not be identical (and usually is not identical) to the symmetry of the underlying Bravais lattice. Some crystals with a hexagonal lattice, e.g. α -quartz, do not show hexagonal (hexad) symmetry but have triad symmetry. (see Fig. 1.33a, Section 1.11.5) Such crystals are assigned to the **trigonal system** rather than to the hexagonal system. Hence the trigonal system includes crystals with both hexagonal and rhombohedral Bravais lattices. There is yet another problem which is particularly associated with the trigonal system, which is that the rhombohedral unit cell outlined

in Figs 3.1 and 3.3 is not always used—a larger (non-primitive) unit cell of three times the size is sometimes more convenient. The problem of transforming axes from one unit cell to another is addressed in Chapter 5.

The crystal systems and their corresponding Bravais lattices are shown in Table 3.1. Notice that there are no axes or planes of symmetry in the **triclinic system**. The only symmetry that the triclinic lattice possesses (and which is possessed by all the other lattices) is a **centre of symmetry**. This point symmetry element and inversion axes of symmetry are explained in Chapter 4.

3.4 The coordination or environments of Bravais lattice points: space-filling polyhedra

So far we have considered lattices as patterns of points in space in which each lattice point has the same environment in the same orientation. This approach is complete and sufficient, but it fails to stress, or even make clear, the fact that each of these environments is distinct and characteristic of the lattices themselves.

We need therefore a method of clearly and unambiguously defining what we mean by ‘the environment’ of a lattice point. One approach (which we have used already in working out the sizes of interstitial sites) is to state this in terms of ‘coordination’—the numbers and distances of nearest neighbours. For example, in the simple cubic (cubic *P*) lattice each lattice point is surrounded by six other equidistant lattice points; in the bcc (cubic *I*) lattice each lattice point is surrounded by eight equidistant lattice points—and so on. This is satisfactory, but an alternative and much more fruitful approach is to consider the environment or domain of each lattice point in terms of a polyhedron whose faces, edges and vertices are equidistant between each lattice point and its nearest neighbours. The construction of such a polyhedron is illustrated in two dimensions for simplicity in Fig. 3.6. This is a plan view of a simple monoclinic (monoclinic *P*) lattice with the *b* axis perpendicular to the page. The line labelled ① represents the edge or trace of a plane perpendicular to the page and half way between the central lattice point 0 and its neighbour 1. All points lying in this plane (both in the plane of the paper and above and below) are therefore equidistant between the two lattice points 0 and 1. We now repeat the process for the other lattice points 2, 3, 4, etc., surrounding the central lattice point. The planes ①, ②, ③ etc. form the six ‘vertical’ faces of the polyhedron and in three dimensions, considering the lattice points ‘above’ and ‘below’ the central lattice point 0, the polyhedron for the monoclinic *P* lattice is a closed prism, shown shaded in plan in Fig. 3.6. Each lattice point is surrounded by an identical polyhedron and they all fit together to completely fill space with no gaps in between.

In this example (of a monoclinic *P* lattice) the edges of the polyhedron are where the faces intersect and represent points which are equidistant between the central lattice point and *two* other surrounding lattice points. Similarly, the vertices of the polyhedron represent points which are equidistant between the central lattice point and *three* other surrounding points. However, for lattices of higher symmetry this correspondence does not hold. If, for example, we consider a cubic *P* lattice, square in plan, and follow the procedure outlined above, we find that the polyhedron is (as expected) a cube, but the edges of which are equidistant between the central lattice point and *three* surrounding

Table 3.1 The seven crystal systems, their corresponding Bravais lattices and symmetries

System	Bravais lattices	Axial lengths and angles	Characteristic (minimum) symmetry	Non-centrosymmetric point groups		Centrosymmetric point groups ^(a)
				Enantiomorphous ^(b)	Non-enantiomorphous ^(c)	Non-enantiomorphous ^(c)
Cubic	<i>PIF</i>	$a = b = c$ $\alpha = \beta = \gamma = 90^\circ$	4 triads equally inclined at 109.47°	23, 432	$\bar{4}3m$	$m\bar{3}, m\bar{3}m$
Tetragonal	<i>PI</i>	$a = b \neq c$ $\alpha = \beta = \gamma = 90^\circ$	1 rotation tetrad or inversion Tetrad	$4^P, 422$	$\bar{4}, 4mm^P, \bar{4}2m$	$4/m, 4/mmm$
Orthorhombic	<i>PICF</i>	$a \neq b \neq c$ $\alpha = \beta = \gamma = 90^\circ$	3 diads equally inclined at 90°	222	$mm2^P$	mmm
Trigonal	<i>PR</i>	$a = b = c$ $\alpha = \beta = \gamma \neq 90^\circ$	1 rotation triad or inversion triad (= triad + centre of symmetry)	$3^P, 32$	$3m^P$	$\bar{3}, \bar{3}m$
Hexagonal	<i>P</i>	$a = b \neq c$ $\alpha = \beta = 90^\circ, \gamma = 120^\circ$	1 rotation hexad or inversion hexad (= triad + perp. mirror plane)	$6^P, 622$	$\bar{6}, 6mm^P, \bar{6}m2$	$6/m, 6/mmm$
Monoclinic	<i>PC</i>	$a \neq b \neq c$ $\alpha = \gamma = 90^\circ \neq \beta \geq 90^\circ$	1 rotation diad or inversion diad (= perp. mirror plane)	2^P	m^P	$2/m$
Triclinic	<i>P</i>	$a \neq b \neq c$ $\alpha \neq \beta \neq \gamma = 90^\circ$	None	1^P		$\bar{1}$

^(a) All the crystals which possess a centre of symmetry and/or a mirror plane are non-enantiomorphous.

^(b) The eleven enantiomorphous point groups are those which do not possess a plane or a centre of symmetry. Hence enantiomorphous crystals can exist in right- or left-handed forms.

^(c) Eleven of the twenty-one non-enantiomorphous point groups are centrosymmetric. Crystals which have a centre of symmetry do not exhibit certain properties, e.g. the piezoelectric effect.

The ten polar point (non-centrosymmetric) groups (indicated by a superscript P) possess a unique axis not related by symmetry. They are equally divided between the enantiomorphous point groups (1, 2, 3, 4, 6) and non-enantiomorphous point groups ($m, mm2, 3m, 4mm, 6mm$).

Trigonal crystals are divided into those which are represented by the hexagonal *P* lattice and those which are represented by the rhombohedral *R* lattice.

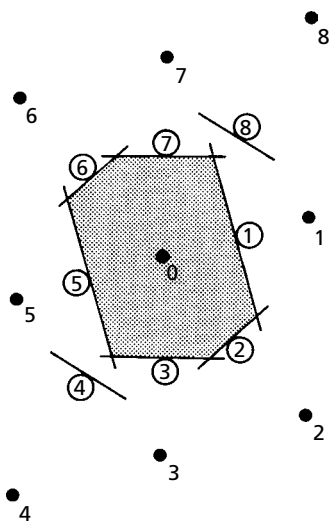


Fig. 3.6. The Voronoi polyhedron (Dirichlet region or Wigner-Seitz cell) for a monoclinic P lattice (plan view, b axis perpendicular to the page). The lines ①, ② etc. represent the edges or traces of planes which are equidistant between the central lattice point 0 and the surrounding or coordinating lattice points 1, 2, etc. The resulting Voronoi polyhedron is outlined in this two-dimensional section by the shaded area.

lattice points and the vertices of which are equidistant between the central lattice point and *seven* surrounding lattice points.

The polyhedra constructed in this way and which represent the domains around each lattice point have various names: Dirichlet regions or Wigner-Seitz cells or Voronoi* polyhedra. There are altogether 24 such space-filling polyhedra corresponding to the 14 Bravais lattices; it is not a simple one-to-one correspondence in all cases because the shape of the polyhedron may depend upon the ratios between the axial lengths and angles and whether the Bravais lattice is centred or not. For example, Fig. 3.7(a) and (b) shows the two polyhedra for the tetragonal I lattice; Fig. 3.7(a) for the case where the axial ratio, c/a , is less than one and Fig. 3.7(b) for the case where it is greater than one.

The space-filling polyhedra for the cubic P , I and F lattices are particularly interesting. For the cubic P lattice it is simply a cube of edge-length equal to the spacing between nearest lattice points (Fig. 3.7(c)). For the cubic I lattice it is a truncated octahedron (Fig. 3.7(d)), the eight hexagonal faces corresponding to the eight nearest neighbours at the corners of the cube and the six square faces corresponding to the six next-nearest neighbours at the centres of the surrounding cubes. For the cubic F lattice it is a rhombic dodecahedron (Fig. 3.7(e)), the twelve diamond-shaped faces corresponding to the twelve nearest neighbours. (see Appendix 2).

* Denotes biographical notes available in Appendix 3.

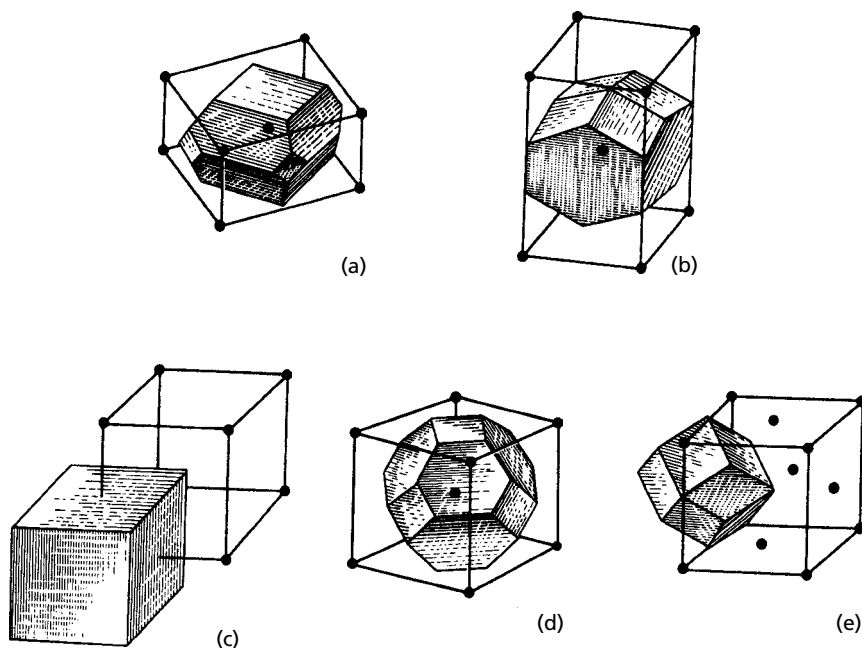


Fig. 3.7. Examples of domains or Voronoi polyhedra outlined around single lattice points (a) tetragonal *I* lattice, $c/a < 1$; (b) tetragonal *I* lattice, $c/a > 1$; (c) cubic *P* lattice; (d) cubic *I* lattice and (e) cubic *F* lattice (from *Modern Crystallography* by B. K. Vainshtein, Academic Press, 1981).

It is of interest to compare the space-filling polyhedra for the fcc (cubic *F*) and hcp close-packing. These are shown in Fig. 3.8(a) and (b) respectively with the positions of the ABC and ABA atom layers indicated. If the 'central' atom is considered to be a B-layer then the 'bottom' three diamond-shaped faces correspond to the coordination of the three A-layer atoms below, the six 'vertical' diamond-shaped faces correspond to the coordination of the six surrounding B-layer atoms and the 'top' three diamond-shaped faces correspond to the coordination of the C-layer atoms for cubic close-packing (Fig. 3.8(a)) or the A-layer atoms for hexagonal close-packing (Fig. 3.8(b)). The polyhedron in Fig. 3.8(a) is a rhombic dodecahedron (as in Fig. 3.7(e)) and in Fig. 3.8(b) it is a trapezohedron (see also Appendix 2).

The truncated octahedron (the Voronoi polyhedron for the cubic *I* lattice) is of particular interest and is also an Archimedean polyhedron (see Appendix 2). It represents the 'special case' polyhedron for the tetragonal *I* lattice when the c/a ratio changes from <1 to >1 (compare Figs 3.7(a), (b) and (d)). More importantly, it is the space-filling solid with *plane* faces which has the largest volume-to-surface-area ratio and therefore *approximates* to the shapes of grains in annealed polycrystalline metals or ceramics or the cells in soap-bubble foams (Fig. 3.9). However, the angles between the faces and edges do not satisfy the equilibrium requirements for grain boundary energy (e.g. in two-dimensions the grain boundaries must meet at 120°). If, following Lord Kelvin, we

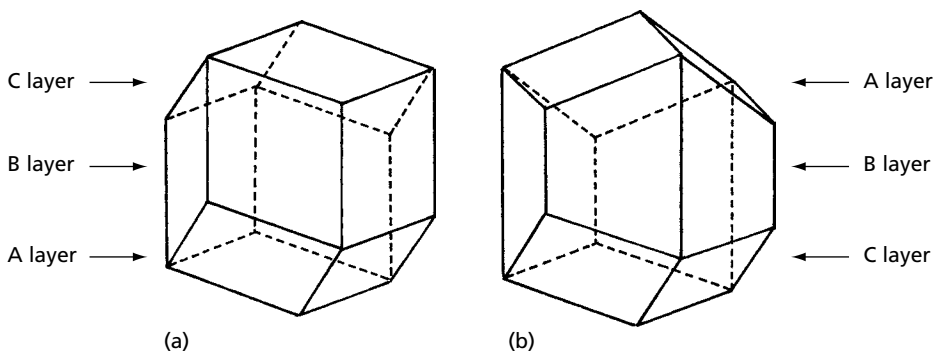


Fig. 3.8. Space filling polyhedra (a) for cubic close-packing (rhombic dodecahedron) and (b) for hexagonal close-packing (trapezohombic dodecahedron).

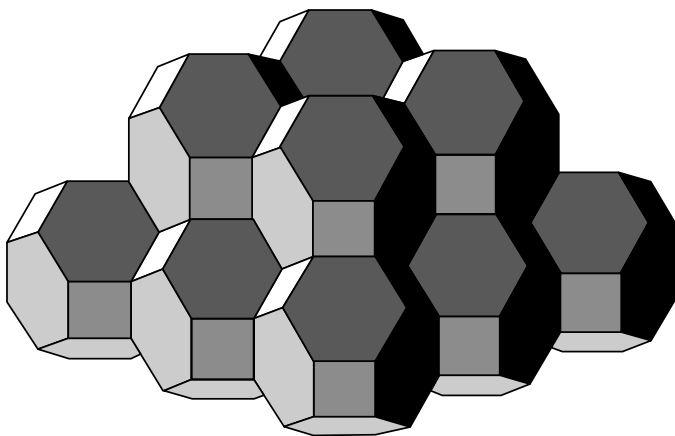


Fig. 3.9. Space-filling by an assembly of truncated octahedra. These polyhedra have 14 faces (6 square plus 8 hexagonal) and are arranged at the points of a cubic I lattice. (From *Symmetry* by Hermann Weyl, Princeton University Press, 1952.)

(partly) accommodate these requirements by allowing the surfaces and edges to bow in or out, we obtain a (space-filling) solid with curved surfaces and edges called an α -tetrakaidecahedron. This, however, does not represent the ‘last word’ in the geometry of grain boundaries. If we relax the condition that all the polyhedra have an equal number of faces, then a space-filling structure with a slightly larger volume to surface area ratio can be built up consisting of pentagonal dodecahedra and 14-sided polygons consisting of 12 pentagonal faces and 2 hexagonal faces¹ (‘ C_{24} ’ in fullerene notation).

¹ D. Weire (ed.) *The Kelvin Problem: Foam Structures of Minimal Surface Area*. Taylor & Francis, London and Bristol, Pa (1996).

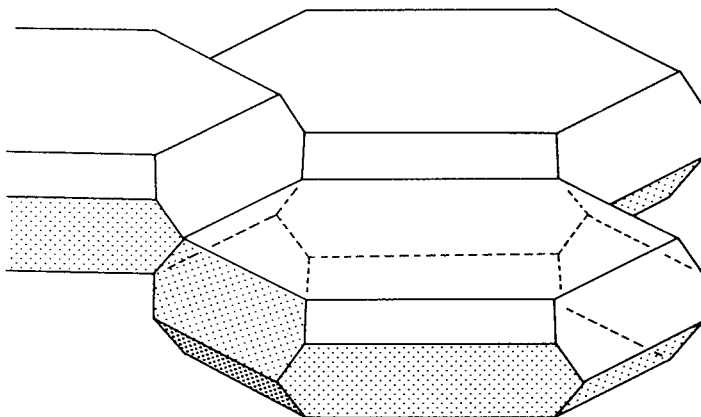


Fig. 3.10. Epidermal cells in mammalian skin which have the shapes of flattened tetrakaidecahedra arranged in vertical columns (compare with Fig. 3.9). (Illustration by courtesy of Professor Honda, Hyogo University, Japan.)

However, in practice, grains and the cells of soap-films are irregular in shape and size, although they do have on average about fourteen faces, like tetrakaidecahedra. In biological structures, the cells in the epidermis (the outer layer) of mammalian skin have also been shown to have the shape of intersecting flattened tetrakaidecahedra arranged in neat vertical columns (Fig. 3.10). In this case the edges are no longer equal in length; two of the eight hexagonal faces (parallel to the surface of the skin) are large and all the other faces are small and elongated. These epidermal cells are of course space-filling but have much smaller volume-to-surface area ratios.

The Voronoi approach to the partitioning of space may also be applied to the analysis of crystal *structures*, in which one alternative is to draw the planes equidistant between the outer radii of atoms or ions and not their centres—the sizes of the polyhedra being a measure of the relative sizes of the atoms or ions. All the polyhedra (now of different sizes and shapes) are space-filling. It may also be used in entirely non-crystallographic situations to determine, for example, the catchment areas for an irregular distribution of schools; pupils whose homes are on the dividing lines between the irregular polyhedra being equidistant from two schools and those whose homes are at the vertices being equidistant from three schools.

Exercises

- 3.1 The drawings in Fig. 3.11 show patterns of points distributed in orthorhombic-shaped unit cells. Identify to which (if any) of the orthorhombic Bravais lattices, *P*, *C*, *I* or *F*, each pattern of points corresponds.
(*Hint*: It is helpful to sketch plans of several unit cells, which will show more clearly the patterns of points, and then to outline (if possible) a *P*, *C*, *I* or *F* unit cell.)
- 3.2 The unit cells of several **orthorhombic** structures are described below. Draw *plans* of each and identify the Bravais lattice, *P*, *C*, *I* or *F*, in each case.
 - (a) One atom per unit cell located at $(x'y'z')$.

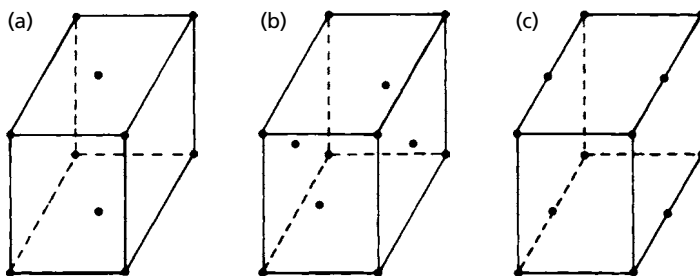


Fig. 3.11. Patterns of points in orthorhombic unit cells.

(b) Two atoms per unit cell of the *same* type located at $(0\frac{1}{2}0)$ and $(\frac{1}{2}0\frac{1}{2})$.

(c) Two atoms per unit cell, one type located at $(00z')$ and $(\frac{1}{2}\frac{1}{2}z')$ and the other type at $(00(\frac{1}{2} + z'))$ and $(\frac{1}{2}\frac{1}{2}(\frac{1}{2} + z'))$.

(Hint: Draw plans of several unit cells and relocate the origin of the axes, x' , y' , z' should be taken as small (non-integral) fractions of the cell edge lengths.)

3.3 What are the shapes of the Voronoi polyhedra which correspond to the rhombohedral Bravais lattice?

(Hint: recall that the three cubic lattices are 'special cases' of the rhombohedral lattice in which the inter-axial angle α is 90° (cubic P), 60° (cubic F) or 109.47° (cubic I).)

Crystal symmetry: point groups, space groups, symmetry-related properties and quasiperiodic crystals

4.1 Symmetry and crystal habit

As indicated in Chapter 3, the system to which a crystal belongs may be identified from its observed or external symmetry. Sometimes this is a very simple procedure. For example, crystals which are found to grow or form as cubes obviously belong to the cubic system: the external point symmetry of the crystal and that of the underlying unit cell are identical. However, a crystal from the cubic system may not grow or form with the external shape of a cube; the unit cells may stack up to form, say, an octahedron, or a tetrahedron, as shown in the models constructed from sugar-cube unit cells (Fig. 4.1). These are just two examples of a very general phenomenon throughout all the crystal systems: only very occasionally do crystals grow with the same shape as that of the underlying unit cell. The different shapes or **habits** adopted by crystals are determined by chemical and physical factors which do not, at the moment, concern us; what does concern us as crystallographers is to know how to recognize to which system a crystal belongs even though its habit may be quite different from, and therefore conceal, the shape of the underlying unit cell.

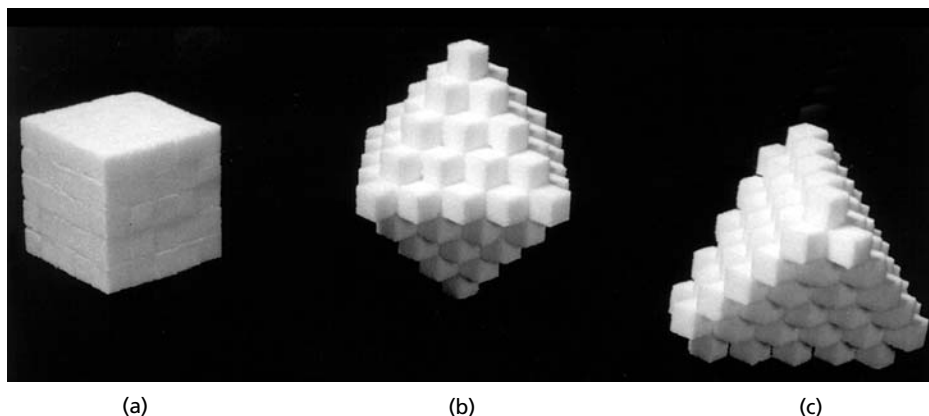


Fig. 4.1. Stacking of ‘sugar-cube’ unit cells to form (a) a cube, (b) an octahedron and (c) a tetrahedron. Note that the cubic cells in all three models are in the same orientation.

The clue to the answer lies in the point group symmetry of the crystal. Consider, for example, the symmetry of the cubic crystals which have the shape or habit of a cube, an octahedron or a tetrahedron (Figs 4.1 and 4.2) or construct models of them (Appendix 1). The cube and octahedron, although they are different shapes, possess the same point group symmetry. The tetrahedron, however, has less symmetry: only six mirror planes instead of nine: only three diads running between opposite edges (i.e. along the directions perpendicular to the cube faces in the underlying cubes) and, as before, four triads running through each corner. The common, unchanged symmetry elements are the four (equally inclined) triads, and it is the presence of these four triads which

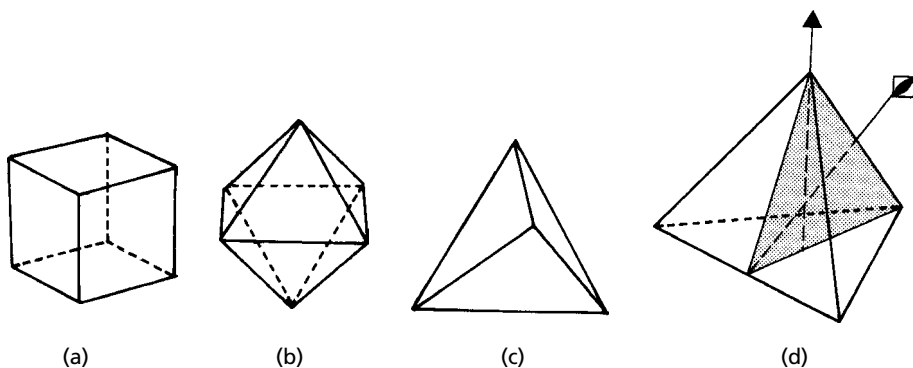


Fig. 4.2. (a) A cube, (b) an octahedron and (c) a tetrahedron drawn in the same orientation as the models in Fig. 4.1. (d) A tetrahedron showing the positions of one variant of the point symmetry elements: mirror plane (shaded) ($\times 6$), triad ($\times 4$) and inversion tetrad (which includes a diad) ($\times 3$).

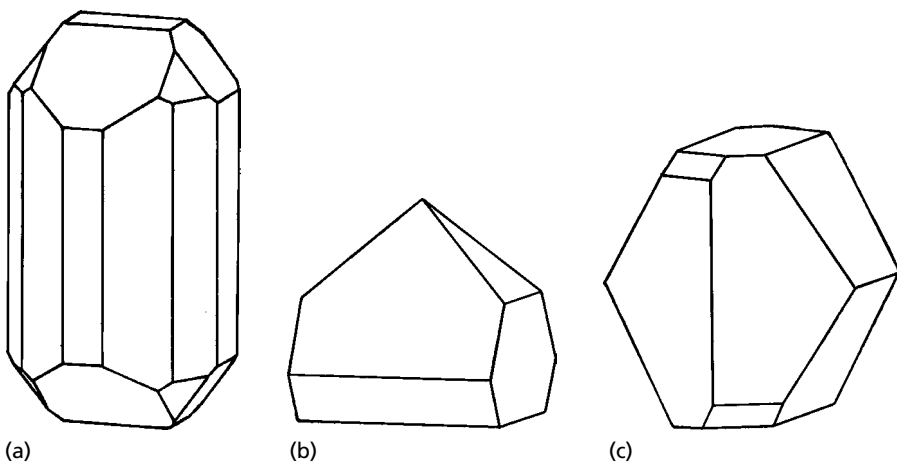


Fig. 4.3. Orthorhombic crystals (a) anglesite PbSO_4 (mmm), (b) struvite $\text{NH}_4\text{MgPO}_4 \cdot 6\text{H}_2\text{O}$ ($mm2$), (c) asparagine $\text{C}_4\text{H}_4\text{O}_3(\text{NH}_2)_2$ (222) (from *Introduction to Crystallography*, 3rd edn, by F. C. Phillips, Longmans 1963).

characterizes crystals belonging to the cubic system. Cubic crystals usually possess additional symmetry elements—the most symmetrical cubic crystals being those with the full point group symmetry of the underlying unit cell. But it is the four triads—not the three tetrads or the nine mirror planes—which are the ‘hallmark’ of a cubic crystal.

Similar considerations apply to all the other crystal systems. For example, Fig. 4.3 shows three orthorhombic crystals. Figure 4.3(a) shows a crystal with the full symmetry of the underlying unit cell—three perpendicular mirror planes and three perpendicular diads. Figure 4.3(b) shows a crystal with only two mirror planes and one diad along their line of intersection. Figure 4.3(c) shows a crystal with three perpendicular diads but no mirror planes.

4.2 The thirty-two crystal classes

The examples shown in Figs 4.1–4.3 are of crystals with different point group symmetries: they are said to belong to different **crystal classes**. Crystals in the same class have the same point group symmetry, so in effect the terms are synonymous. Notice that crystals in the same class do not necessarily have the same shape. For example, the cube and octahedron are obviously different shapes but belong to the same class because their point group symmetry is the same.

In two dimensions (Chapter 2) we found that there were ten plane point groups; in three dimensions there are thirty-two three-dimensional point groups. One of the great achievements of the science of mineralogy in the nineteenth century was the systematic description of the thirty-two point groups or crystal classes and their division into the seven crystal systems. Particular credit is due to J. F. C. Hessel,* whose contributions to the understanding of point group symmetry were unrecognized until after his death. The concept of seven different types or shapes of underlying unit cells then links up with the concept of the fourteen Bravais lattices; in other words, it establishes the connection between the external crystalline form or shape and the internal molecular or atomic arrangements.

It is not necessary to describe all the thirty-two point groups systematically; only the nomenclature for describing their important distinguishing features needs to be considered. This requires a knowledge of additional symmetry elements—centres and inversion axes.

Finally, we come to a ‘practical’ problem, which those of us who collect minerals or who grow crystals from solutions will immediately recognize. Our crystals are rarely uniformly developed, like those in Figs 4.2 or 4.3, but are irregular in appearance, with faces of different size and shape and from which it is almost impossible to recognize any point symmetry elements at all. Figure 4.4 shows examples of quartz crystals in which the corresponding faces are developed to different extents. It is this problem which hindered the development of crystallography until the discovery of the Law of Constancy of Interfacial Angles (Section 1.1) which enables us to focus on the underlying crystal symmetry rather than being diverted by the contingencies of crystal growth.

* Denotes biographical notes available in Appendix 3.

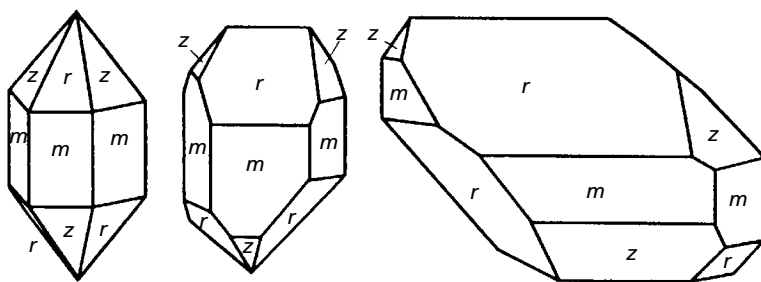


Fig. 4.4. Three quartz crystals with corresponding faces developed differently (from *Modern Crystallography* by B.K. Vainshtein, Springer-Verlag, 1981).

4.3 Centres and inversion axes of symmetry

If a crystal, or indeed any object, possesses a **centre of symmetry**, then any line passing through the centre of the crystal connects equivalent faces, or atoms, or molecules. A familiar example is a right hand and a left hand placed palm-to-palm but with the fingers pointing in opposite directions, as in Fig. 4.5(a). Lines joining thumb to thumb or fingertip to fingertip all pass through a centre of symmetry between the hands. When the hands are placed palm-to-palm but with the fingers pointing in the same direction, as in prayer, then there is no centre of symmetry but a **mirror (or reflection) plane of symmetry** instead, as in Fig. 4.5(b).

Notice the important relationship between these two symmetry elements: a centre of symmetry (Fig. 4.5(a)) *plus* a rotation of 180° (of one hand) is equivalent to a mirror plane of symmetry (Fig. 4.5(b)). Conversely, a mirror plane of symmetry *plus* a rotation of 180° (about an axis perpendicular to the mirror plane) is equivalent to a centre of symmetry. In short, centres and mirror planes of symmetry relate objects which (like hands) do not themselves possess these symmetry elements; conversely objects which themselves possess these symmetry elements do not occur in either right or left-handed forms (see Table 3.1).

In two dimensions a centre of symmetry is equivalent to diad symmetry. (See, for example, the motif and plane molecule shown in Fig. 2.3(4), which may be described as showing diad symmetry or a centre of symmetry.) In three dimensions this is not the case, as an inspection of Fig. 4.5(a) will show.

Inversion axes of symmetry are rather difficult to describe (and therefore difficult for the reader to understand) without the use of the stereographic projection—a method of representing a three-dimensional pattern of planes in a crystal on a two-dimensional plan. This topic is covered in Chapter 12 and the representation of symmetry elements in detail in Section 12.5.1. Geographers have the same problem when trying to represent the surface of the Earth on a two-dimensional map, and they too make use of the stereographic projection. In atlases, the circular maps of the world (usually with the north or south poles in the centre) are often stereographic projections.

Inversion axes are *compound* symmetry elements, consisting of a rotation followed by an inversion. For example, as described in Chapter 2, the operation of a tetrad

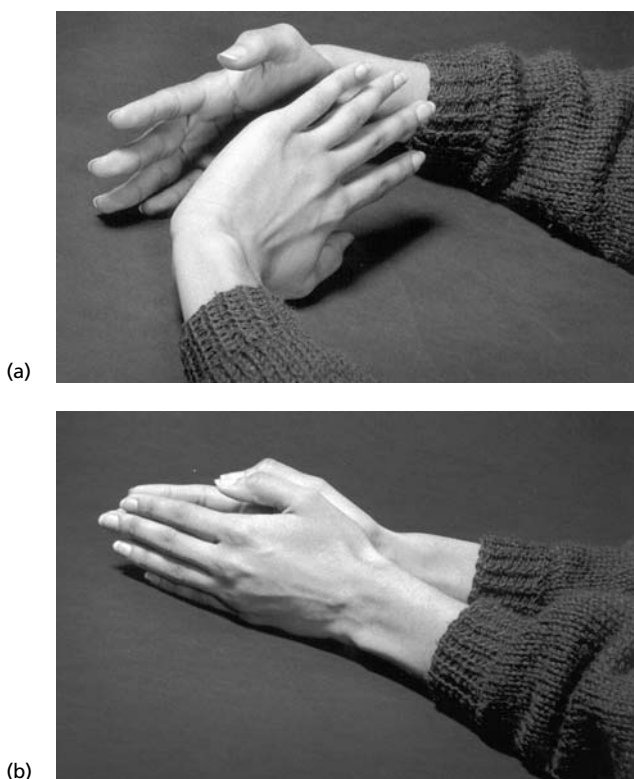


Fig. 4.5. Right and left hands (a) disposed with a centre of symmetry between them and (b) disposed with a mirror plane between them.

(fourfold) rotation axis is to repeat a crystal face or pattern every 90° rotation, e.g. in two dimensions giving four repeating **R**s or the four-fold pattern of faces in a cube. The operation of an inversion tetrad, symbol $\bar{4}$ or $\bar{4}$, is to repeat a crystal face or pattern every 90° rotation-plus-inversion through a centre. What results is a four-fold pattern of faces around the inversion axis, but with each alternate face inverted. Examples of a crystal and an object with inversion tetrad axes are shown in Figs 4.6(a) and (b). The tennis ball has, in fact, the same point group symmetry as the crystal. Notice that when it is rotated 90° about the axis indicated, the 'downwards' loop in the surface pattern is replaced by an 'upwards' loop. Another 90° rotation brings a 'downwards' loop and so on for the full 360° rotation. Notice also that the inversion tetrad includes a diad, as is indicated by the diad (lens) symbol in the inversion tetrad (open square) symbol, $\bar{4}/2$ or $\bar{4}$.

Finally, compare the symmetry of the tetragonal crystal in Fig. 4.6(a) with that of the tetrahedron (Fig. 4.2(d)): the diad axes which we recognized passing through the centres of opposite edges in the tetrahedron are, in fact, inversion tetrad axes or, to develop one of the points made in Section 4.1, stacking the cubes into the form of a tetrahedron reduces the symmetry element along the cube axis directions from rotation to inversion tetrad.

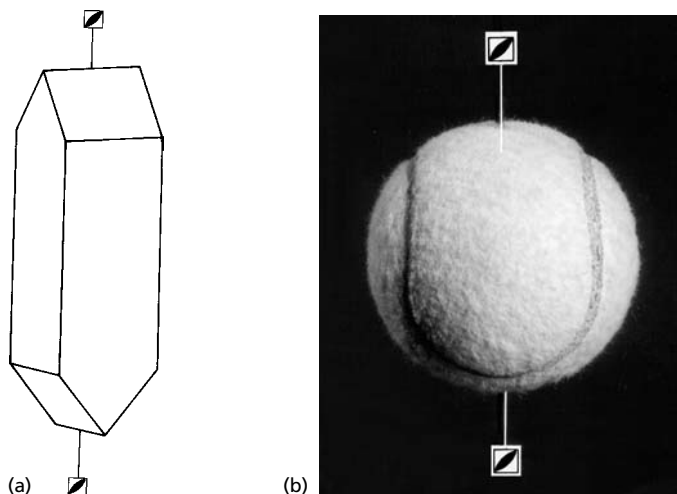


Fig. 4.6. Examples of a crystal and an object which have inversion tetrad axes (both point group $\bar{4}2m$). (a) Urea $\text{CO}(\text{NH}_2)_2$ and (b) a tennis ball.

There are also inversion axes corresponding to rotation monads diads, triads and hexads. The operation of an inversion hexad, for example, is a rotation of 60° plus an inversion, this compound operation being repeated a total of six times until we return to the beginning. However, for a beginner to the subject, these axes may perhaps be regarded as being of lesser importance than the inversion tetrad because they can be represented by combinations of other (better-understood) symmetry elements.

An inversion monad, symbol \circ or $\bar{1}$ is equivalent to a centre of symmetry.

An inversion diad, symbol $\bar{2}$ is equivalent to a perpendicular mirror plane.

An inversion triad, symbol Δ or $\bar{3}$ is equivalent to a triad plus a centre of symmetry—which is the symmetry of a rhombohedral lattice (see Fig. 3.1). Notice that the ‘top’ three faces of the rhombohedron are related to the ‘bottom’ three faces by a centre of symmetry.

An inversion hexad, symbol $\bar{6}$ or $\bar{6}$ is equivalent to a triad plus a perpendicular mirror plane.

Again, these equivalences are best understood with the use of the stereographic projection (Chapter 12). The important point is that only inversion tetrads are unique (i.e. they cannot be represented by a combination of rotation axes, centres of symmetry or mirror planes) and therefore need to be considered separately.

The point group symmetries of the thirty-two classes are described by a ‘short-hand’ notation or **point group symbol** which lists the main (but not necessarily all) symmetry elements present. For example, the presence of centres of symmetry is not recorded because they may arise ‘automatically’ from the presence of other symmetry elements, e.g. the presence of an inversion triad axis mentioned above. This notation for the thirty-two crystal classes or point groups, and their distribution among the seven crystal

systems, is fully worked out in the *International Tables for Crystallography* published for the International Union of Crystallography and in F. C. Phillips' *Introduction to Crystallography*. Altogether there are five cubic classes, three orthorhombic classes, three monoclinic classes and so on. They are all listed in Table 3.1 (p. 91). The order in which the symmetry elements are written down in the point group symbol depends upon the crystal system.

In the cubic system the first place in the symbol refers to the axes parallel to, or planes of symmetry perpendicular to, the x -, y - and z -axes, the second refers to the four triads or inversion triads and the third the axes parallel to, or planes of symmetry perpendicular to, the face diagonal directions. Hence the point group symbol for the cube or the octahedron—the most symmetrical of the cubic crystals—is $4/m\bar{3}2/m$. This full point group symbol is usually (and rather unhelpfully) contracted to $m\bar{3}m$ because the operation of the four triads and nine mirror planes (three parallel to the cube faces and six parallel to the face diagonals) 'automatically' generates the three tetrads, six diads, and a centre of symmetry. The symbol for the tetrahedron is $\bar{4}3m$, the $\bar{4}$ referring to the three inversion tetrad axes along the x -, y - and z -axes together with the m referring to the face-diagonal mirror planes. The least symmetric cubic class has point group symbol 23, i.e. it only has diads along the x -, y - and z -axes and the characteristic four triads.

In the orthorhombic system the three places in the point group symbol refer to the symmetry elements associated with the x -, y - and z -axes. The most symmetrical class (Fig. 4.3(a)), which has the full point group symmetry of the underlying orthorhombic unit cell (Fig. 3.5), has the full point group symbol $2/m2/m2/m$, but this is usually abbreviated to mmm because the presence of the three mirror planes perpendicular to the x -, y - and z -axes 'automatically' generates the three perpendicular diads. The other two classes are $mm2$ (Fig. 4.3(b))—a diad along the intersection of two mirror planes—and 222 (Fig. 4.3(c))—three perpendicular diads.

In the monoclinic system the point group symbol simply refers to the symmetry elements associated with the y -axis. This may be a diad (class 2), an inversion diad (equivalent to a perpendicular mirror plane (class $\bar{2}$ or m)), or a diad plus a perpendicular mirror plane (class $2/m$).

In the tetragonal, hexagonal and trigonal systems, the first position in the point group symbol refers to the 'unique' z -axis. For example, the tetragonal crystals in Fig. 4.6 have point group symmetry $\bar{4}2m$; $\bar{4}$ referring to the inversion tetrad along the z -axis, 2 referring to the diads along the x - and y -axes and m to the mirror planes which bisect the x - and y -axes (which you will find by examining the model!). One of the trigonal classes has point group symbol 32 (not to be confused with cubic class 23!), i.e. a single triad along the z -axis and (three) perpendicular diads.

Not all classes are of equal importance; in two of them (432 and $\bar{6} = 3/m$) there may be no examples of inorganic crystals at all! On the other hand, the two monoclinic classes m and $2/m$ contain about 50 per cent of all inorganic crystalline materials on a 'crystal counting' basis, including feldspar, the commonest mineral in nature, and many other economically important minerals. As for the crystals of organic compounds, class $2/m$ is by far the most important, while crystals of biologically important substances which contain chiral (right- or left-handed enantiomorphic molecules) have a predilection for class 2. The commonest class in any system is the **holosymmetric** class, i.e. the class

which shows the highest symmetry. The holosymmetric cubic class $m\bar{3}m$, the most symmetrical of all, contains only a few per cent of all crystals on this basis, but these also include many materials and ceramics of economic and commercial importance.

It is a great help in an understanding of point group symmetry simply to identify the symmetry elements of everyday objects such as clothes pegs, forks, pencils, tennis balls, pairs of scissors, etc. Or, one step further, you could make models showing the point group symmetries of all the 32 crystal classes as described in Appendix 1.

A note on alternating or rotation-reflection axes

These compound symmetry elements were used by Schoenflies in his derivation of the 230 space groups. They are used in the description of layer-symmetry (Section 2.8) but are otherwise little used today. They consist of rotation plus a **reflection** in a plane perpendicular to the axis, rather than an **inversion**. Hence a monad alternating axis is equivalent to a perpendicular mirror plane (or inversion diad); a diad alternating axis is equivalent to a centre of symmetry (or inversion monad); a triad alternating axis is equivalent to an inversion hexad; a tetrad alternating axis is equivalent to an inversion tetrad and a hexad alternating axis is equivalent to an inversion triad.

4.4 Crystal symmetry and properties

The quantities which are used to describe the properties of materials are, as we know, simply represented as *coefficients*, i.e. as one measured (or measurable) quantity divided by another. For example, the property (coefficient) of electrical conductivity is given by the amount of electrical current flowing between two points (which may be measured in various ways) divided by the electrical potential gradient; the pyroelectric effect—the property of certain crystals of developing electrical polarization when the temperature is changed—is given by the polarization divided by the temperature change; the heat capacity is given by the quantity of heat absorbed or given out divided by the temperature change, and so on.

In many (in fact most) cases the measured quantities depend on direction and are called **vectors**.¹ In the examples above, electrical current flow, potential gradient and polarization are all vectors. The other quantities in the examples above, temperature change, quantity of heat, do not depend on direction and are called **scalars**.

The important point is that, in those cases where one or more of the measured quantities vary with direction, so also do the crystal properties; they are said to be *anisotropic* (from the Greek tropos, direction or turn; (an)iso, (not the) same). Anisotropy clearly arises because the arrangements of atoms in crystals vary in different directions—you would intuitively *expect* crystals to be anisotropic, the only exceptions being those properties (the heat capacity) which are direction independent. You would also intuitively expect cubic crystals to be ‘less anisotropic’ than, say, monoclinic ones because of their greater symmetry, and this intuition would also be correct. For many properties, but not all, cubic crystals are isotropic—the property (and property coefficient) is direction

¹ See Appendix 5.

independent. In the example given above, cubic crystals are isotropic with respect to electrical conductivity. They are also isotropic with regard to the pyroelectric effect, i.e. cubic crystals do not exhibit electrical polarization when the temperature is changed; the pyroelectric coefficient is zero. But cubic crystals are not isotropic with respect to all properties. For example, their elastic properties, which determine the mechanical properties of stiffness, shear and bulk moduli, are direction dependent and these are very important factors with respect to the properties of metals and alloys.

Hence, one major use of point groups is in relating crystal symmetry and properties; as the external symmetry of crystals arises from the symmetry of the internal molecular or atomic arrangements, so also do these in turn determine or influence crystal properties. Some examples have already been alluded to. For example, the pyroelectric effect cannot exist in a crystal possessing a centre of symmetry, and the pyroelectric polarization can only lie along a direction in a crystal that is *unique*, in the sense that it is not repeated by any symmetry element. There are only ten point groups or crystal classes which fulfil these conditions and they are called the **ten polar point groups**:

1	2	3	4	6
<i>m</i>	<i>mm2</i>	<i>3m</i>	<i>4mm</i>	<i>6mm</i> .

Hence, pyroelectricity or the pyroelectric effect can only occur in these ten polar point groups or classes.

A very closely related property to pyroelectricity, and of great importance in electro-ceramics, is ferroelectricity. A ferroelectric crystal, like a pyroelectric crystal, can also show polarization, but in addition the direction of polarization may be reversed by the application of an electric field. Most ferroelectric crystals have a transition temperature (Curie point) above which their symmetry is non-polar and below which it is polar.

One such example is barium titanate, BaTiO_3 , which has the perovskite structure (Fig. 1.17). Above the Curie temperature barium titanate has the fully symmetric cubic structure, point group $m\bar{3}m$, but below the Curie temperature, when the crystal becomes ferroelectric, distortions occur—a small expansion occurs along one cell edge and small contractions along the other two, changing the crystal system symmetry from cubic to tetragonal and the point group symmetry from $m\bar{3}m$ to $4mm$. As the temperature is further lowered below the Curie point, further distortions occur and the point group symmetry changes successively to $mm2$ and $3m$ —all of them, of necessity, being polar point groups (see Section 1.11.1).

Another very important crystal property is piezoelectricity—the development of an electric dipole when a crystal is stressed, or conversely, the change of shape of a crystal when it is subjected to an electrical field. At equilibrium the applied stress will be centrosymmetrical, so if a crystal is to develop a dipole, i.e. develop charges of opposite sign at opposite ends of a line through its centre, it cannot have a centre of symmetry. There are twenty-one non-centrosymmetric point groups (Table 3.1), all of which, except one, point group 432, may exhibit piezoelectricity. It is the presence of the equally inclined triads, tetrads and diads in this cubic point group which in effect cancel out the development of a unidirectional dipole.

The optical properties of crystals—the variation of refractive index with the vibration and propagation direction of light (double refraction or birefringence), the variation of

refractive index with wavelength or colour of the light (dispersion), or the associated variations of absorption of light (pleochroism)—are all symmetry dependent. The complexity of the optical properties increases as the symmetry decreases. Cubic crystals are optically isotropic—the propagation of light is the same in all directions and they have a single refractive index. Tetragonal, hexagonal and trigonal crystals are characterized by two refractive indices. For light travelling in a direction *perpendicular* to the principal (tetrad, hexad or triad) axis, such crystals exhibit two refractive indices—one for light vibrating along the principal axis, and another for light vibrating in a plane perpendicular to the principal axis. For light travelling *along* the principal axis (and therefore vibrating in the planes parallel to it), the crystal exhibits only one refractive index, and therefore behaves, for this direction only, as an optically isotropic crystal. Such crystals are called *uniaxial* with respect to their optical properties, and their principal symmetry axis is called the *optic axis*. Crystals belonging to the remaining crystal systems—orthorhombic, monoclinic and triclinic—are characterized by three refractive indices and two, not one, optic axes. Hence they are said to be biaxial since there are two, not one, directions for the direction of propagation of light in which they appear to be optically isotropic. It should be noted, however, that unlike uniaxial crystals, there is no simple relationship between the two optic axes of biaxial crystals and the principal symmetry elements; nor are they fixed, but vary as a result of dispersion, i.e. the variations in the values of the refractive indices with wavelength.

Finally, there is the phenomenon or property of optical activity or rotatory polarization, which should not be confused with double refraction. It is a phenomenon in which, in effect, the vibrational direction of light rotates such that it propagates through the crystal in a helical manner either to the right (dextrorotatory) or the left (laevorotatory). Now right-handed and left-handed helices are distinct in the same way as a right and left hand (Fig. 4.5) or the two parts of a twinned crystal (Fig. 1.18) and therefore optical activity would be expected to occur only in those crystals which occur in right-handed or left-handed forms, i.e. those which do not possess a mirror plane or a centre (or inversion axis) of symmetry. Such crystals are said to be enantiomorphous and there are altogether eleven enantiomorphous classes or point group symmetries (Table 3.1).

A famous example is tartaric acid (Fig. 4.7). In 1848 Louis Pasteur* first noticed these two forms ‘hemihedral to the right’ and ‘hemihedral to the left’ under the microscope and, having separated them, found that their solutions were optically active in opposite senses.

The study of enantiomorphism, or chirality, from the Greek word *chiros*, meaning hand, is becoming increasingly important. Louis Pasteur, as a result of his work on tartaric acid, was the first to suggest that the molecules themselves could be chiral—i.e. that they could exist in either right-handed or left-handed forms. The basic constituents of living things are chiral, including the amino acids² present in proteins, the nucleotides present in nucleic acids and the DNA double helix itself. But *only one* enantiomorph is ever found in nature—only L-amino acids are present in proteins and only D-nucleotides are

* Denotes biographical notes available in Appendix 3.

² Except glycine, the simplest amino acid.

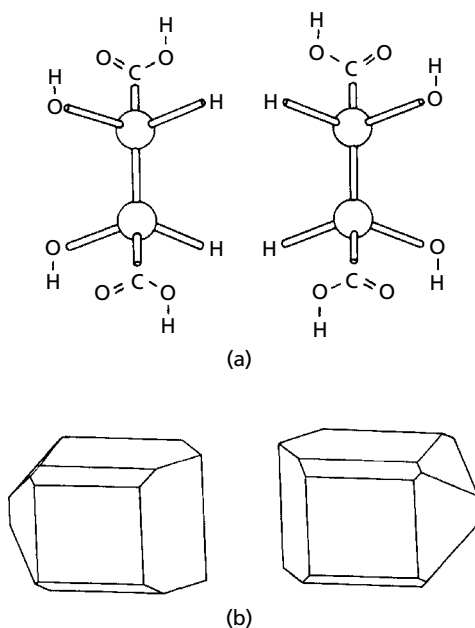


Fig. 4.7. (a) Left- and right-handed forms of tartaric acid molecules (from *Crystals: their Role in Nature and Science* by C. W. Bunn, Academic Press, New York, 1964); and (b) the left- and right-handed forms of tartaric acid crystals (from F. C. Phillips, loc. cit.).

present in nucleic acids (L stands for laevo—or left-rotating, and D stands for dextro—or right-rotating). Why this should be so is one of the mysteries surrounding the origin of life itself and for which many explanations or hypotheses have been offered. If, as many hypotheses suppose, it was the result of a chance event which was then consolidated by growth, then we might reasonably suppose that on another planet such as ours the *opposite* event might have occurred and that there exist living creatures, in every way like ourselves, but who are constituted of D-amino acids and L-nucleotides!

However, to return to earth, once our basic chirality has been established, the D- and L- (enantiomorphous) forms of many substances, including drugs in particular, may have very different chemical and therapeutic properties. For example, the molecule asparagine (Fig 4.3(c)) occurs in two enantiomorphous forms, one of which tastes bitter and the other sweet. Thalidomide also; the right-handed molecule of which acts as a sedative but the left-handed molecule of which gave rise to birth defects. Hence chiral separation, and the production of enantiomorphically pure substances, is of major importance.

4.5 Translational symmetry elements

The thirty-two point group symmetries (Table 3.1) may be applied to three-dimensional patterns just as the ten plane point group symmetries are applied to two-dimensional patterns (Chapter 2). As in two dimensions where translational symmetry elements or

glide lines arise, so also in three dimensions do **glide planes** and also **screw axes** arise. It is only necessary to state the symmetry properties of patterns that are described by these translational symmetry elements. Glide planes are the three-dimensional analogues of glide lines; they define the symmetry in which mirror-related parts of the motif are shifted half a lattice spacing. In Fig. 2.5(b) the figures are related by glide lines, which can easily be visualized as glide-plane symmetry. Glide planes are symbolized as a , b , c (according to whether the translation is along the x -, y - or z -axes), n or d (diagonal or diamond glide—special cases involving translations along more than one axis).

Screw axes (for which there is no two-dimensional analogue—except for screw diads which arise in layer-symmetry patterns (see Section 2.8))—essentially describe helical patterns of atoms or molecules, or the helical symmetry of motifs. Several types of helices are possible and they are all based upon different combinations of rotation axes and translations. Figure 4.8 shows the possible screw axes (the direction of translation out of the plane of the page) with the heights \mathbf{R} of the asymmetrical objects represented as fractions of the lattice repeat distance (compare to Fig. 2.3). Screw axes are represented in writing by the general symbol N_m, N representing the rotation (2, 3, 4, 6) and the subscript m representing the pitch in terms of the number of lattice translation or repeat

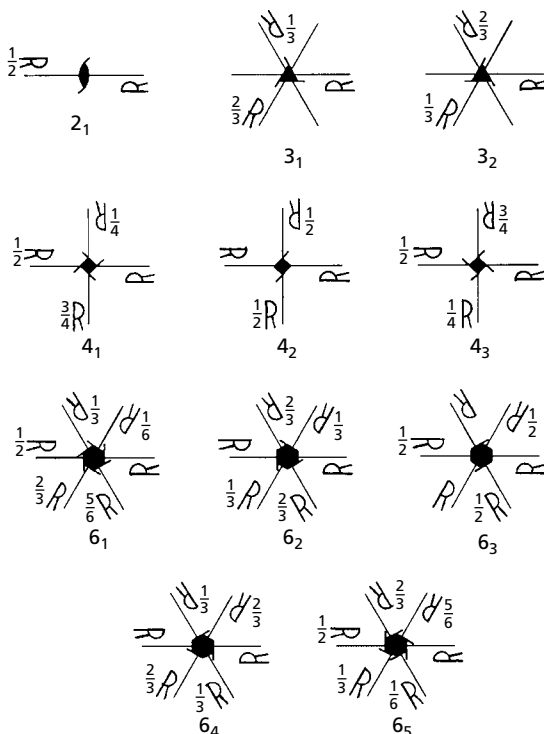


Fig. 4.8. The operation of screw axes on an asymmetrical motif, \mathbf{R} . The fractions indicate the 'heights' of each motif as a fraction of the repeat distance.

distances for one complete rotation of the helix. m/N therefore represents the translation for each rotation around the axis. Thus the 4_1 screw axis represents a rotation of 90° followed by a translation of $\frac{1}{4}$ of the repeat distance, which repeated three times brings **R** to an identical position but displaced one lattice repeat distance; the 4_3 screw axis represents a rotation of 90° followed by a translation of $\frac{3}{4}$ of the lattice repeat distance, which repeated three times gives a helix with a pitch of three lattice repeat distances. This is equivalent to the 4_1 screw axis but of opposite sign: the 4_1 axis is a right-handed helix and 4_3 axis is a left-handed helix. In short they are enantiomorphs of each other. Similarly the 3_1 and 3_2 axes, the 6_1 and 6_5 axes, and the 6_2 and 6_4 axes are enantiomorphs of each other. In diagrams, screw axes are represented by the symbol for the rotation axis with little 'tails' indicating (admittedly not very satisfactorily) the pitch and sense of rotation (see Fig. 4.8). Screw axes have, of course, their counterparts in nature and design—the distribution of leaves around the stem of a plant, for example, or the pattern of steps in a spiral (strictly helical) staircase. Figure 4.9 shows two such examples. Figure 4.10 shows the 6_3 screw hexads which occur in the hcp structure; notice that they run parallel to the c -axis and are located in the 'unfilled' channels which occur in the hcp structure. They do not pass through the atom centres of either the A layer or the B layer atoms; these are the positions of the triad (not hexad) axes in the hcp structure.

Just as the external symmetry of crystals does not distinguish between primitive and centred Bravais lattices, so also it does not distinguish between glide and mirror planes, or screw and rotation axes. For example, the six faces of an hcp crystal show hexad, six-fold symmetry, whereas the underlying structure possesses only screw hexad, 6_3 , symmetry.

In many crystals, optical activity arises as a result of the existence of enantiomorphous screw axes. For example, in α -quartz (enantiomorphous class 32), the SiO_2 structural units which are not themselves asymmetric, are arranged along the c -axis (which is also the optic axis) in either a 3_1 or a 3_2 screw orientation (see Figure 1.33(a), Section 1.11.5). This gives rise to the two enantiomorphous crystal forms of quartz (class 32, Fig. 4.11).

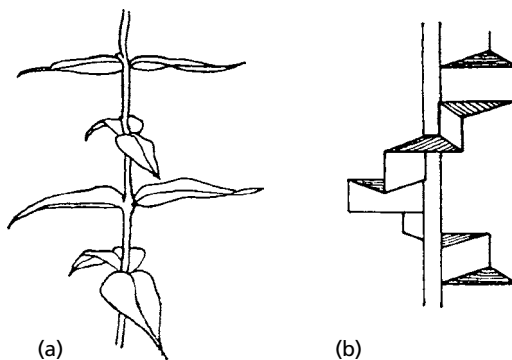


Fig. 4.9. (a) The 4_2 screw axis arrangement of leaves round a stem of pentstemon (after Walter Crane); and (b) a 6_1 screw axis spiral (helical) staircase (from *The Third Dimension in Chemistry* by A. F. Wells, Clarendon Press, Oxford, 1968).

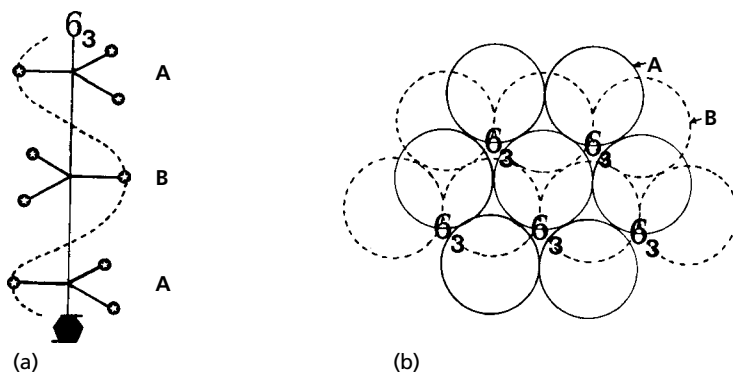


Fig. 4.10. (a) A screw hexad (6_3) axis; and (b) location of these axes in the hcp structure. Notice that they pass through the 'unfilled channels' between the atoms in this structure.

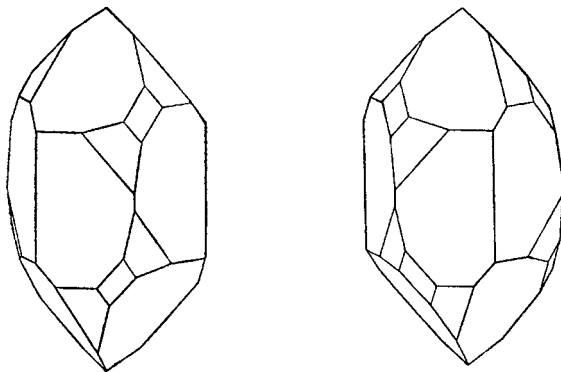


Fig. 4.11. The enantiomorphic (right- and left-handed) forms of quartz. The optic axis is in the vertical (long) direction in each crystal (from F. C. Phillips, loc. cit.).

The plane of polarization of plane-polarized light propagating along the optic axis is rotated to right or left, the angle of rotation depending on the wavelength of the light and the thickness of the crystal. This is not, to repeat, the same phenomenon as birefringence; for the light travelling along the optic axis the crystal exhibits (by definition) one refractive index. If the 3_1 or 3_2 helical arrangement of the SiO_2 structural units in quartz is destroyed (e.g. if the crystal is melted and solidified as a glass), the optical activity will also be destroyed.

However, in other crystals such as tartaric acid (Fig. 4.7) and its derivatives, the optical activity arises from the asymmetry—the lack of a mirror plane or centre of symmetry—of the molecule itself (Fig. 4.7(a)). In such cases the optical activity is not destroyed if the crystal is melted or dissolved in a liquid. The left or right handedness of the molecules, even though they are randomly orientated in a solution, is communicated at least in part, to the plane-polarized light passing through it. Unlike quartz, in which

the optical activity depends on the direction of propagation of the light with respect to the optic axis, the optical activity of a solution such as tartaric acid is unaffected by the direction of propagation of the light. In summary, the optical activity of solutions arises from the asymmetry of the molecule itself; the optical activity which is shown in crystals, but not their solutions or melts, arises from the enantiomorphic screw symmetry of the arrangement of molecules in the crystal.

4.6 Space groups

In Section 2.4 it is shown how the seventeen possible two-dimensional patterns or plane groups (Fig. 2.6) can be described as a combination of the five plane lattices with the appropriate point and translational symmetry elements. Similarly, in three dimensions, it can be shown that there are 230 possible three-dimensional patterns or **space groups**, which arise when the fourteen Bravais lattices are combined with the appropriate point and translational symmetry elements. It is easy to see why there should be a substantially larger number of space groups than plane groups. There are fourteen space lattices compared with only five plane lattices, but more particularly there is a greater number of combinations of point and translational symmetry elements in three dimensions, particularly the presence of inversion axes (point) and screw axes (translational) which do not occur in two-dimensional patterns.

The first step in the derivation of 230 space groups was made by L. Sohncke* (who also first introduced the notion of screw axes and glide planes described in Section 4.5). Essentially, Sohncke relaxed the restriction in the definition of a Bravais lattice—that the environment of each point is identical—by considering the possible arrays of points which have identical environments when viewed from *different* directions, rather than from the *same* direction as in the definition of a Bravais lattice. This is equivalent to combining the fourteen Bravais lattices with the appropriate translational symmetry elements, and gives rise to a total of sixty-five space groups or Sohncke groups.

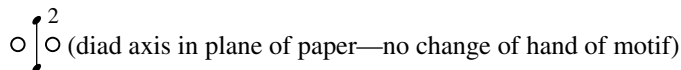
The second, final, step was to account for inversion axes of symmetry which gives rise to a further 165 space groups. They were first worked out by Fedorov* in Moscow in 1890 (who drew heavily on Sohncke's work) and independently by Schoenflies* in Göttingen in 1891 and Barlow* in London in 1894—an example of the frequently occurring phenomenon in science of progress being made almost at the same time by people approaching a problem entirely independently.

The 230 space groups are systematically drawn and described in the *International Tables for Crystallography* Volume A, which is based upon the earlier *International Tables for X-ray Crystallography* Vol. 1 compiled by N. F. M. Henry* and Kathleen Lonsdale*—a work of great crystallographic scholarship. The space groups are arbitrarily numbered 1 to 230, beginning with triclinic crystals of lowest symmetry and ending with cubic crystals of highest symmetry. There are two space group symbols, one due to Schoenflies* used in spectroscopy and the other, which is now generally adopted in crystallography, due to Hermann* and Mauguin.*

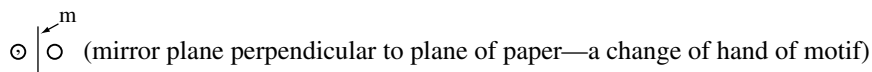
* Denotes biographical notes available in Appendix 3.

The Hermann–Mauguin space group symbol consists first of all of a letter *P*, *I*, *F*, *R*, *C*, *B* or *A* which describes the Bravais lattice type (Fig. 3.1) (the alternatives *C*, *B* or *A* being determined as to whether the unit cell axes are chosen such that the *C*, *B* or *A* faces are centred); then a statement, rather like a point group symbol, of the essential (not all) symmetry elements present. For example, the space group symbol *Pba*2 represents a space group which has a primitive (*P*) Bravais lattice and whose point group is *mm*2 (the *a* and *b* glide planes being simple mirror planes in point group symmetry). This is one of the point groups of the orthorhombic system (Fig. 4.3) and the lattice type is orthorhombic *P*. Similarly, space group *P*6₃/*mmc* has a primitive (*P*) (hexagonal) Bravais lattice with point group symmetry 6/*mmm*.

The space group itself is represented by means of two diagrams or projections, one showing the symmetry elements present and the other showing the operation of these symmetry elements on an asymmetric ‘unit of pattern’ represented by the circular symbol \bigcirc and its mirror-image by \odot : a circle with a comma inside. These symbols, which may represent an asymmetric molecule, a group of molecules, or indeed any asymmetrical structural unit, correspond to the **R** and **A** of our two-dimensional patterns. The choice of a *circle* to represent an *asymmetric* object might be thought to be inadequate—surely a symbol such as **R** or, better still, a right hand would be more appropriate? In a sense it would, but there would then arise a serious problem of typography, of clearly and unambiguously representing the operation of all the symmetry elements in the projection. For example, in the case where a mirror plane lies *in* the plane of projection a right hand (palm-down) would be mirrored by a left hand (palm-up)—and the problem would be to represent clearly these two superimposed hands in a plan view. In the case of a circle this situation is easily represented by \bigoplus —a circle divided in the middle with the mirror-image indicated in one half. Similarly, the use of a symbol such as **R** would lead to ambiguity. For example, a diad axis *in* the plane of projection would rotate an **R** 180° out of the plane of projection into an **A**—which would be indistinguishable from an **R** reflected to an **A** in a mirror plane perpendicular to the plane of projection—i.e. as for mirror-lines in the two-dimensional case. In the case of a circle there is no such ambiguity; in the former case we have



and in the latter case

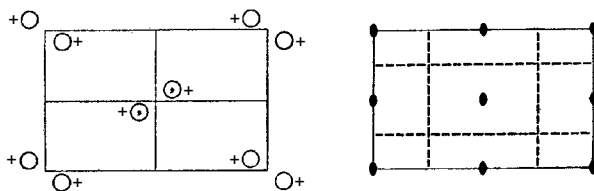


The representation of space groups and some, but not all of the associated crystallographic information, is best described by means of four examples *Pba*2 (No. 32), *P*2₁/*c* (No. 14), *P*6₃/*mmc* (No. 194) and *P*4₁2₁2 (No. 92).

Figure 4.12, from the *International Tables for X-ray Crystallography*, shows space group No. 32, *Pba*2 with the Hermann–Mauguin and Schoenflies symbols shown top left and the point group and crystal system top right. The two diagrams are projections in the *x* – *y* plane, the right-hand one shows the symmetry elements present—the diads parallel to the *z*-axis at the corners, edges and centre of the unit cell and the *a* and *b* glide planes shown as dashed lines in between. It would be perfectly possible to draw the

$Pba2$
 C_{2v}^8

No. 32

 $Pba2$ mmm Orthorhombic

Origin on 2

Number of positions,
Wyckoff notation,
and point symmetry

Co-ordinates of equivalent positions

Conditions limiting
possible reflections

4 c 1 $x, y, z; \bar{x}, \bar{y}, z; \frac{1}{2} - x, \frac{1}{2} + y, z; \frac{1}{2} + x, \frac{1}{2} - y, z.$

General:

 hkl : No conditions $0kl$: $k = 2n$ $h0l$: $h = 2n$ hkl : No conditions $h00$: $(h = 2n)$ $0k0$: $(k = 2n)$ $00l$: No conditions

2 b 2 $0, \frac{1}{2}, z; \frac{1}{2}, 0, z.$

Special: as above, plus

2 a 2 $0, 0, z; \frac{1}{2}, \frac{1}{2}, z.$

hkl : $h+k = 2n$

Symmetry of special projections

 (001) pgg ; $a' = a, b' = b$ (100) $pm1$; $b' = b/2, c' = c$ (010) $p1m$; $c' = c, a' = a/2$

Fig. 4.12. Space group $Pba2$ (No. 32) (from the *International Tables for X-ray Crystallography*).

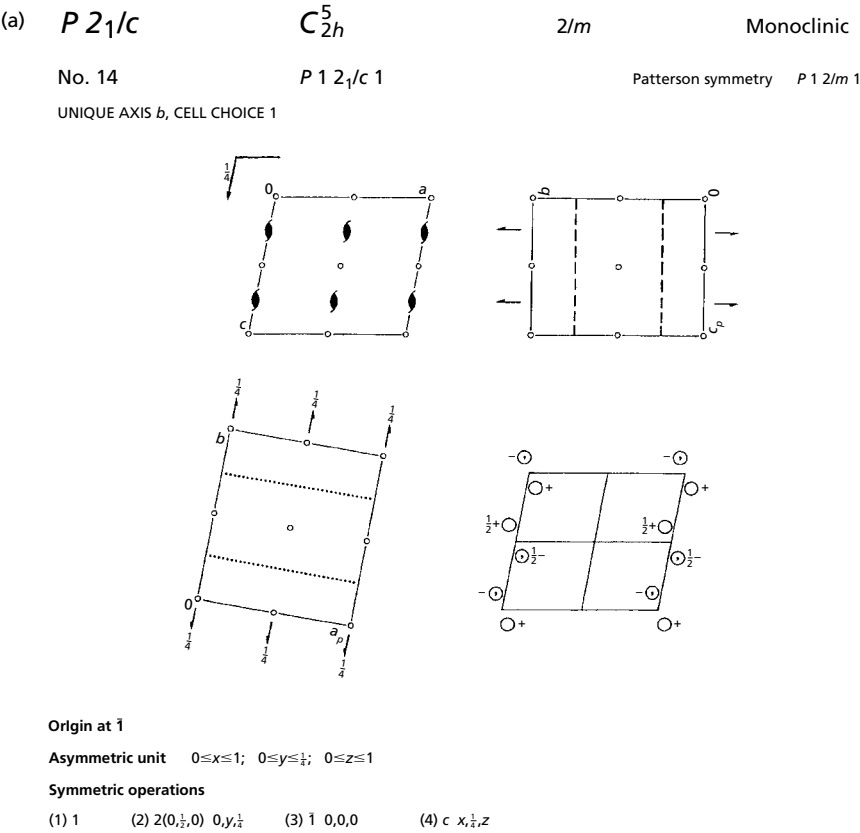
origin of the unit cell at an intersection of the glide planes—but to choose it, as shown, at a diad axis is more convenient, hence the note ‘origin on 2’.

In the left-hand diagram the \bigcirc is placed at (small) fractions, x, y, z of the cell edge lengths away from the origin, the z parameter or ‘height’ being represented by a plus (+) sign. This is called a ‘general equivalent position’ because the \bigcirc does not lie on any of the symmetry elements present and the resulting pattern is known as the set of ‘general equivalent positions’. The coordinates of these positions are listed below together with the total number of them, 4, the ‘Wyckoff letter’, c and the symbol 1 for a monad, indicating the asymmetry of the \bigcirc (and its glide plane image \odot).

If the pattern unit \bigcirc were to be placed not in a general position but in a ‘special position’, on a diad axis in this example, then a simpler pattern results. The four asymmetric pattern units ‘merge together’ to give two units with diad symmetry and these are called ‘special equivalent positions’. There are in fact two possibilities, denoted by the Wyckoff letters a and b and their co-ordinates are listed in the table on the left. The Wyckoff letters are purely arbitrary, like the numbering of the space groups themselves.

The table on the right lists the conditions (on the Laue indices hkl) limiting possible reflections, those not meeting these conditions being known as *systematic absences* in X-ray diffraction. These topics are covered in Chapter 9 and Appendix 6. Finally, the ‘symmetry of special projections’ shows the plane groups corresponding to the space group projected on different planes (just as in our projections of crystal structures in Chapter 2). For example, the projection on the (001) plane (which is that of the diagrams) corresponds to plane groups pgg (or $p2gg$ —see Fig. 2.6).

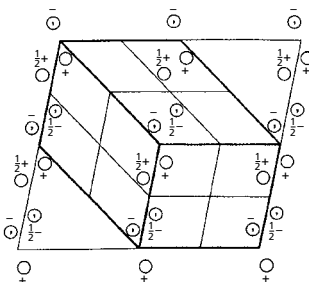
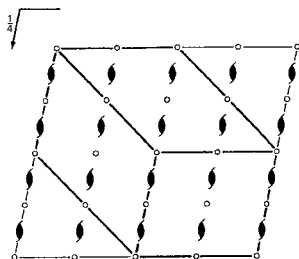
Figure 4.13 is extracted from the entry for the most frequently occurring space group No. 14 ($P2_1/c$) in the *International Tables for Crystallography* in which two choices for the unique axis b or c (parallel to the (screw) diad axes) and three choices of unit cell are available. Figure 4.13(a) shows the usual choice of the b (or y -axis) parallel to the (screw) diad axes as indicated by the monoclinic point group symbol $2/m$ (see Section 4.3) and ‘cell choice 1’. The pattern of general equivalent positions is shown in the lower right diagram and the symmetry elements (screw diads, centres of symmetry and glide planes) are shown in three different projections. The centres of symmetry are indicated by small circles, the glide planes by dashed or dotted lines depending as to whether the



(b) $P 2_1/c$ C_{2h}^5 $2/m$

Monoclinic

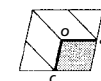
No. 14

UNIQUE AXIS b , DIFFERENT CELL CHOICES $P 12_1/c 1$ UNIQUE AXIS b , CELL CHOICE 1Origin at $\bar{1}$ Asymmetric unit $0 \leq x \leq 1; 0 \leq y \leq \frac{1}{2}; 0 \leq z \leq 1$ Generators selected (1); $t(1,0,0)$; $t(0,1,0)$; $t(0,0,1)$; (2); (3)

Positions

Multiplicity,
Wyckoff letter,
Site symmetry

Coordinates

4 e 1 (1) x, y, z (2) $\bar{x}, y + \frac{1}{2}, \bar{z} + \frac{1}{2}$ (3) $\bar{x}, \bar{y}, \bar{z}$ (4) $x, \bar{y} + \frac{1}{2}, z + \frac{1}{2}$ 2 d $\bar{1}$ $\frac{1}{2}, 0, \frac{1}{2}$ $\frac{1}{2}, \frac{1}{2}, 0$ 2 c $\bar{1}$ $0, 0, \frac{1}{2}$ $0, \frac{1}{2}, 0$ 2 b $\bar{1}$ $\frac{1}{2}, 0, \frac{1}{2}$ $\frac{1}{2}, \frac{1}{2}, \frac{1}{2}$ 2 a $\bar{1}$ $0, 0, 0$ $0, \frac{1}{2}, \frac{1}{2}$ 

Reflection conditions

General:

 $h0l: l = 2n$ $0k0: k = 2n$ $00l: l = 2n$

Special: as above, plus

 $hkl: k + l = 2n$ $hkl: k + l = 2n$ $hkl: k + l = 2n$ $hkl: k + l = 2n$

Fig. 4.13. Space group $P2_1/c$ (No. 14) (from the *International Tables for Crystallography*), (a) unique axis b , cell choice 1, (b) unique axis b , different cell choices.

glide direction is in, or perpendicular to, the plane of the diagram, and similarly the screw diad axes normal to or in the plane of the projection are indicated by \bullet or single-headed arrow symbols respectively. Figure 4.13(b) shows the three possible cell choices and the tables of the coordinates of the general and special equivalent positions (with their Wyckoff letters running from bottom to top) and the reflection conditions as before.

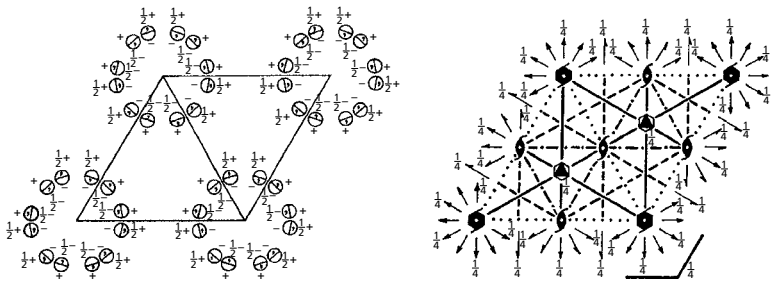
Figure 4.14 is extracted from the entry for space group $P6_3/mmc$, No. 194 in the *International Tables for X-ray Crystallography*; this is the space group for the hcp metals (Fig. 1.5(b)), AlB_2 , WC (Fig. 1.15) and wurtzite (Figs 1.26 and 1.36(b)). Notice that there is a greater number of special equivalent positions (Wyckoff letters running from a to k) than in the two lower-symmetry space groups we have just looked at and

$P6_3/mmc$
 D_{6h}^4

No. 194

$P6_3/m2/m2/c$

$6/mmm$ Hexagonal



Origin at centre ($\bar{3}m1$)

Number of positions, Wyckoff notation, and point symmetry			Co-ordinates of equivalent positions			Conditions limiting possible reflections	
General:							
24	<i>l</i>	1	$x, y, z; \bar{y}, x-y, z; y-x, \bar{x}, z; \bar{y}, \bar{x}, z; x, x-y, z; y-x, y, z; \bar{x}, \bar{y}, z; y, y-x, z; x-y, x, z; y, x, z; \bar{x}, y-x, z; x-y, \bar{y}, z;$ $\bar{x}, y, \frac{1}{2}+z; y, y-x, \frac{1}{2}+z; x-y, x, \frac{1}{2}+z; x, y, \frac{1}{2}-z; \bar{y}, x-y, \frac{1}{2}-z; y-x, \bar{x}, \frac{1}{2}-z;$ $y, x, \frac{1}{2}+z; \bar{x}, y-x, \frac{1}{2}+z; x-y, \bar{y}, \frac{1}{2}+z;$ $\bar{y}, \bar{x}, \frac{1}{2}-z; x, x-y, \frac{1}{2}-z; y-x, y, \frac{1}{2}-z.$			<i>hkil</i> : No conditions <i>hh2h̄l</i> : <i>l</i> =2 <i>n</i> <i>hh0l</i> : No conditions	
Special: as above, plus							
12	<i>k</i>	<i>m</i>	$x, 2x, z; 2\bar{x}, \bar{x}, z; x, \bar{x}, z; \bar{x}, 2\bar{x}, \bar{z}; 2x, x, \bar{z}; \bar{x}, x, \bar{z};$ $\bar{x}, 2\bar{x}, \frac{1}{2}+z; 2x, \bar{x}, \frac{1}{2}+z; \bar{x}, x, \frac{1}{2}+z;$ $x, 2x, \frac{1}{2}-z; 2\bar{x}, \bar{x}, \frac{1}{2}-z; x, \bar{x}, \frac{1}{2}-z.$			} no extra conditions	
12	<i>j</i>	<i>m</i>	$x, y, \frac{1}{4}; \bar{y}, x-y, \frac{1}{4}; y-x, \bar{x}, \frac{1}{4}; \bar{y}, \bar{x}, \frac{1}{4}; x, x-y, \frac{1}{4}; y-x, y, \frac{1}{4};$ $\bar{x}, \bar{y}, \frac{3}{4}; y, y-x, \frac{3}{4}; x-y, x, \frac{3}{4}; y, x, \frac{3}{4}; \bar{x}, x-y, \frac{3}{4}; x-y, \bar{y}, \frac{3}{4}.$				
12	<i>i</i>	2	$x, 0, 0; 0, x, 0; \bar{x}, \bar{x}, 0; x, 0, \frac{1}{2}; 0, x, \frac{1}{2}; \bar{x}, \bar{x}, \frac{1}{2};$ $\bar{x}, 0, 0; 0, \bar{x}, 0; x, x, 0; \bar{x}, 0, \frac{1}{2}; 0, \bar{x}, \frac{1}{2}; x, x, \frac{1}{2}.$			<i>hkil</i> : <i>l</i> =2 <i>n</i>	
6	<i>h</i>	<i>mm</i>	$x, 2x, \frac{1}{4}; 2\bar{x}, \bar{x}, \frac{1}{4}; x, \bar{x}, \frac{1}{4}; \bar{x}, 2\bar{x}, \frac{3}{4}; 2x, x, \frac{3}{4}; \bar{x}, x, \frac{3}{4}.$			no extra conditions	
6	<i>g</i>	<i>2/m</i>	$\frac{1}{2}, 0, 0; 0, \frac{1}{2}, 0; \frac{1}{2}, \frac{1}{2}, 0; \frac{1}{2}, 0, \frac{1}{2}; 0, \frac{1}{2}, \frac{1}{2}; \frac{1}{2}, \frac{1}{2}, \frac{1}{2}.$			<i>hkil</i> : <i>l</i> =2 <i>n</i>	
4	<i>f</i>	<i>3m</i>	$\frac{1}{3}, \frac{2}{3}, z; \frac{2}{3}, \frac{1}{3}, \bar{z}; \frac{2}{3}, \frac{1}{3}, \frac{1}{2}+z; \frac{1}{3}, \frac{2}{3}, \frac{1}{2}-z.$			<i>hkil</i> : If <i>h</i> - <i>k</i> =3 <i>n</i> , then <i>l</i> =2 <i>n</i>	
4	<i>e</i>	<i>3m</i>	$0, 0, z; 0, 0, \bar{z}; 0, 0, \frac{1}{2}+z; 0, 0, \frac{1}{2}-z;$			<i>hkil</i> : <i>l</i> =2 <i>n</i>	
2	<i>d</i>	$\bar{6}m2$	$\frac{1}{3}, \frac{2}{3}, \frac{3}{4}; \frac{2}{3}, \frac{1}{3}, \frac{1}{4}.$			} <i>hkil</i> : If <i>h</i> - <i>k</i> =3 <i>n</i> , then <i>l</i> =2 <i>n</i>	
2	<i>c</i>	$\bar{6}m2$	$\frac{1}{3}, \frac{2}{3}, \frac{1}{4}; \frac{2}{3}, \frac{1}{3}, \frac{3}{4}.$				
2	<i>b</i>	$\bar{6}m2$	$0, 0, \frac{1}{4}; 0, 0, \frac{3}{4}.$			} <i>hkil</i> : <i>l</i> =2 <i>n</i>	
2	<i>a</i>	$\bar{3}m$	$0, 0, 0; 0, 0, \frac{1}{2}.$				

Fig. 4.14. Space group $P6_3/mmc$ (No. 194) (from the *International Tables for X-ray Crystallography*).

that the coordinates of the pattern units are much reduced—from 24 for the general case to 2 for positions with Wyckoff letters a , b , c , d . In hcp metals the A and B layer atoms (Fig. 1.5(b)) are in the special equivalent positions denoted by Wyckoff letters c and d . Notice that if the origin of the unit cell is shifted so as to coincide with one of these atoms then their coordinates become (000) , $(\frac{2}{3} \frac{1}{3} \frac{1}{2})$ and (000) , $(\frac{1}{3} \frac{2}{3} \frac{1}{2})$ (see Exercise 1.6 and Section 9.2, Example 4). Finally, having studied Fig. 4.14 it is a good test of your powers of observation to turn back to Fig. 4.10(b) and fill in all the symmetry elements in addition to the 6_3 axes already indicated.

Figure 4.15 is extracted from the entry for space group $P4_12_12$ (No. 92) in the *International Tables for Crystallography*, Volume A. This space group contains principally 4_1 (screw tetrad) axes of symmetry but no glide, mirror planes or inversion axes of

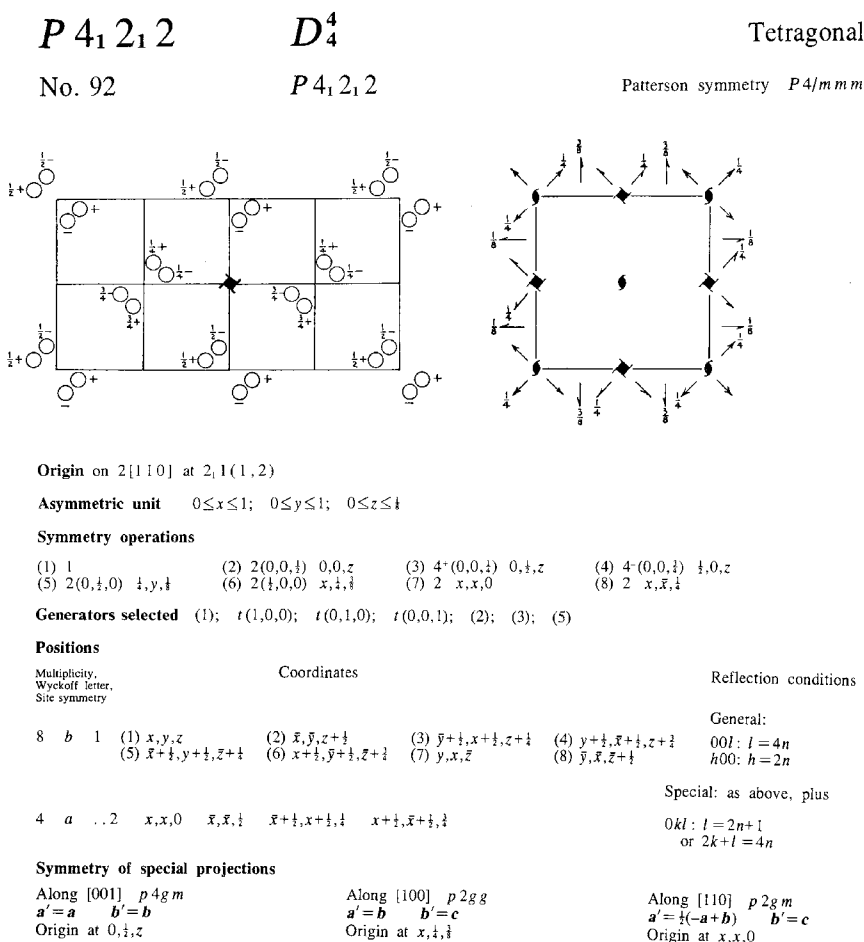


Fig. 4.15. Space group $P4_12_12$ (No. 92) (from the *International Tables for Crystallography*, Volume A—partly redrawn and data relating to sub-groups omitted).

symmetry. It is enantiomorphous with space group $P4_32_12$ (No. 96). In the left-hand diagram two neighbouring cells are drawn to show clearly the operation of the 4_1 (right-handed) screw axes along the cell edges. To these two space groups belong the α (low-temperature) form of cristobalite (see Section 1.11.5) in which the distortion from the high temperature β (cubic) form gives rise to the enantiomorphous tetragonal forms.

4.7 Bravais lattices, space groups and crystal structures

In the simple cubic, bcc and ccp structures of the elements, the three cubic lattices (Fig. 3.1) have exactly the same arrangement of lattice points as the atoms, i.e. in these examples the motif is just one atom. In more complex crystals the motif consists of more than one atom and, to determine the Bravais lattice of a crystal, it is necessary first to identify the motif and then to identify the arrangement of the motifs. In crystals consisting of two or more different types of atoms this procedure may be quite difficult, but fortunately simple examples best illustrate the procedure and the principles involved. For example, in NaCl (isomorphous with TiN; see Fig. 1.14(a)), the motif is one sodium and one chlorine ion and the motifs are arranged in an fcc array. Hence the Bravais lattice of NaCl and TiN is cubic F .

In Li_2O (isomorphous with TiH_2 ; see Fig. 1.14(b)) the motif is one oxygen and two lithium atoms; the motifs are arranged in an fcc array and the Bravais lattice of these compounds is cubic F . In ZnS (isomorphous with TiH ; see Fig. 1.14(c)) the motif is one zinc and one sulphur atom; again, these are arranged in an fcc array and Bravais lattice of these compounds is cubic F . All the crystal structures illustrated in Fig. 1.14 have the cubic F Bravais lattice. They are called face-centred cubic structures not because the arrangements of atoms are the same—clearly they are not—but because they all have the cubic F lattice.

In CsCl (Fig. 1.12(b)), the motif is one caesium and one chlorine ion; the motifs are arranged in a simple cubic array and the Bravais lattice is cubic P . To be sure, the arrangement of ions in CsCl (and compounds isomorphous with it) is such that there is an ion or atom at the body-centre of the unit cell, but the Bravais lattice is *not* cubic I because the ions or atoms at the corners and centre of the unit cell are different. Nor, for the same reason, should CsCl and compounds isomorphous with it be described as having a body-centred cubic structure.

In the case of hexagonal structures the arrangements of lattice points in the hexagonal P lattice (Fig. 3.1) corresponds to the arrangement of atoms in the simple hexagonal structure (Fig. 1.5(a)) and *not* the hcp structure (Fig. 1.5(b)). In the simple hexagonal structure the environment of all the atoms is identical and the motif is just one atom. In the hcp structure the environment of the atoms in the A and B layers is different. The motif is a pair of atoms, i.e. an A layer and a B layer atom per lattice point. The environment of these pairs of atoms (as for the pairs of ions or atoms in the NaCl, or CsCl or ZnS structures) is identical and they are arranged on a simple hexagonal lattice. Notice that in these examples the motif is either asymmetric or has a mirror plane or centre of symmetry. These are further instances of the situation which we found in two-dimensional patterns (Section 2.5). It is the repetition of the motif by the lattice which generates the crystal structures.

The space groups of the simple cubic bcc and ccp structures of the elements are those of maximum symmetry, namely $Pm\bar{3}m$, $Im\bar{3}m$ and $Fm\bar{3}m$, and in which the atoms are all at the special positions 000 etc. Similarly, CsCl (Fig. 1.12(b)) and the cubic forms of perovskite CaTiO_3 (Fig. 1.17) or barium titanate BaTiO_3 , in which all the atoms are in special positions, also belong to space group $Pm\bar{3}m$. All these space groups or structures have a centre of symmetry (at the origin) as indicated by the inversion triad axis, $\bar{3}$, symbol.

In all the examples above, the (special) atom positions are fixed or ‘pinned down’ by the symmetry elements. For example, in the CaF_2 (fluorite) or Li_2O (antifluorite) structures the space group, as with fcc metals, is of maximum symmetry $Fm\bar{3}m$ (point group $m\bar{3}m$) and the symmetry elements fix the positions of the atoms in their special positions precisely as shown in Figs 1.16(c) and (d). For example, an atom or ion must either be evenly bisected by a mirror plane or must be arranged in pairs equidistant each side of it: it cannot occupy an ‘in between’ position because the mirror symmetry would be violated. It is in crystals of lower symmetry that the positions of the atoms is not completely fixed. The ‘classic’ example is the structure of iron pyrites, FeS_2 , which at first glance might be thought to have the same structure as CaF_2 , the S atoms situated precisely at the centres of the tetrahedral sites co-ordinated by the Fe atoms. But this is not so: the S atoms do not lie in the centres of the tetrahedra but are shifted in a body-diagonal (triad axis) direction; in short, they lie in general positions in the structure. The geometry, just for one S atom, is shown in Figure 4.16. Within the whole unit cell the shifts of the S atoms are towards different ‘empty’ corners, preserving the cubic symmetry but reducing the space group symmetry from $Fm\bar{3}m$ to $Pa\bar{3}$ (point group symmetry reduced from $m\bar{3}m$ to $m\bar{3}$ (or $2/m\bar{3}$)).³

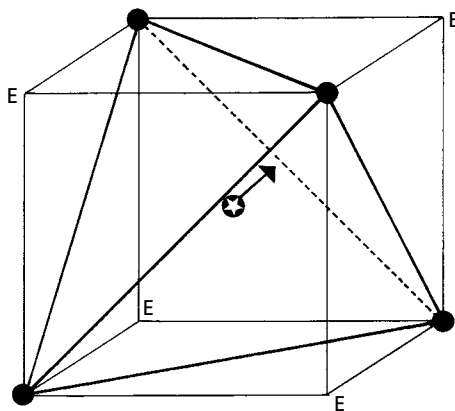


Fig. 4.16. A tetrahedral site in FeS_2 outlined within a cube. The Fe atoms are situated at four corners of the cube, the other four corners are ‘empty’ (denoted by E). The S atom (starred) is shifted from the centre of the tetrahedron/cube towards one of the four ‘empty’ corners as indicated by the arrow.

³ See Appendix 1 for illustrative models of the five cubic point groups.

The ‘amount’ of shift of the S atoms in FeS₂, a single parameter, was deduced by W. L. Bragg in 1913 from the intensities of the X-ray reflections. It was the first structure to be analysed in which the atom positions are not fixed by the symmetry and provided Bragg, as he records long afterwards ‘with the greatest thrill’.⁴ Today of course the number of parameters required to be determined for the far more complex inorganic and especially organic crystals runs into the thousands and constitutes the major task in crystal structure determination.

Zinc blende, ZnS, and isomorphous structures such as TiH (Fig. 1.14(c)) and the technologically important gallium arsenide, GaAs, have the cubic $F\bar{4}3m$ Bravais lattice, the atoms are again in special positions but the structure does not have a centre of symmetry; the space group in this case is $F\bar{4}3m$. This lack of a centre of symmetry, which is the origin, or crystallographic basis of the important electrical and physical properties in these structures, may be visualized with reference to Fig. 1.14(c). The TiH, ZnS or GaAs atoms are arranged in pairs in the body-diagonal directions of the cube (symbolized by $\langle 111 \rangle$ —see Section 5.2) and the sequence of the atoms is either, e.g. $\bullet\bullet\bullet$ GaAs $\bullet\bullet\bullet$ GaAs $\bullet\bullet\bullet$ GaAs $\bullet\bullet\bullet$, or the reverse, i.e. $\bullet\bullet\bullet$ AsGa $\bullet\bullet\bullet$ AsGa $\bullet\bullet\bullet$ AsGa $\bullet\bullet\bullet$. The body-diagonal directions are *polar* axes and the faces on the opposite sides of the crystal are terminated either by Ga or by As atoms.

In silicon, germanium and the common (cubic) form of diamond (see Section 1.11.6), the pattern of the atoms is the same as in ZnS or GaAs but of course all the atoms are of the same type (see Fig. 1.36). The body-diagonal directions are no longer polar because the sequence of pairs of atoms, e.g. $\bullet\bullet\bullet$ SiSi $\bullet\bullet\bullet$ SiSi $\bullet\bullet\bullet$ SiSi $\bullet\bullet\bullet$, is obviously the same either way. These structures are centro-symmetric, the centres of symmetry lying half-way between the pairs of atoms. The space group in these cases is $Fd\bar{3}m$, the d referring to the special type of glide plane. Graphite and hcp metals, as mentioned above, belong to space group $P6_3/mmc$, as does also wurtzite, the hexagonal form of ZnS (Fig. 1.26) and the common crystal structure of ice (see Section 1.11.5) in which the oxygen atoms lie in the same atomic positions as the carbon atoms in the hexagonal form of diamond (Fig. 1.36(b)) and in which the H atoms are between (but not equidistant between) neighbouring O atoms.

There are (Table 3.1) eleven enantiomorphous point groups (i.e. without a centre or mirror plane of symmetry) and upon which are based the 65 space groups first derived by L. Sohncke and in which there are eleven enantiomorphous pairs. We have already noticed the enantiomorphous pair for α -cristobalite ($P4_12_12$ and $P4_32_12$) based on the tetragonal point group 422. The others of particular interest are those for α -quartz ($P3_121$ and $P3_221$) based on the trigonal point group 32 and for β -quartz ($P6_222$ and $P6_422$) based on the hexagonal point group 622.

Not all the 230 space groups are of equal importance; for many of them there are no examples of real crystals at all. About 70% of the elements belong to the space groups $Fm\bar{3}m$, $Im\bar{3}m$ and $Fd\bar{3}m$ (all based on point group $m\bar{3}m$), $F\bar{4}3m$ (based on point group $\bar{4}3m$) and $6_3/mmc$ (based on point group 6/ mmm). Over 60% of organic and

⁴ W. L. Bragg *The development of X-ray analysis*, Proc. Roy. Soc. **A262**, 145 (1961).

inorganic crystals belong to space groups $P2_1/c$, $C2/c$, $P2_1$, $P\bar{1}$, $Pbca$ and $P2_12_12_1$ and of these space group $P2_1/c$ (based on point group $2/m$, Fig. 4.12) is by far the commonest (see Table 4.1, p. 125).

4.8 The crystal structures and space groups of organic compounds

As mentioned in Section 1.10.1, the stability of inorganic molecules arises primarily from the strong, directed, covalent bonds which bind the atoms together. In comparison, the forces which bind organic molecules together are weak (in the liquid or solid states) or virtually non-existent (as in the gaseous state). The strongest of the intermolecular forces are hydrogen bonds, which link polar groups (as in water or ice, Section 1.11.5) or hydroxyl groups as in sugars. Indeed, organic crystals in which hydrogen bonds dominate are hard and rigid, like inorganic crystals. The remaining intermolecular forces are short-range and are generally described as van der Waals bonds. Apart from residual polarity, organic molecules are generally electrically neutral, and intermolecular ionic bonds, such as occur between atoms or groups of atoms in ionic crystals, do not exist.

The crystal structures which occur (if they occur at all) are largely determined by the ways in which the molecules pack together most efficiently: it is the ‘organic equivalent’ of Robert Hooke’s packing together of ‘bullets’ described at the very beginning of this book—except of course that organic molecules have far more complex shapes, or envelopes, than simple spheres.

As described below, it is from such packing considerations that the space groups of organic crystals can be predicted. However, it should be recognized at the outset that the determination of the space group provides little information on the positions of the atoms within the molecules themselves and which, particularly in macromolecules, are nearly all in general positions. The importance of crystallization (apart from its role in purification) lies in the fact that the structure of organic molecules may then be investigated by X-ray diffraction techniques: the space group determines the geometry of the pattern but it is the intensities of the X-ray reflections which ultimately determine the atom positions (see Chapters 6–10 and Chapter 13).

However, there is a further desideratum. Organic molecules which constitute living tissue—proteins, DNA, RNA—do not generally occur *in vivo* as crystals but are separated in an aqueous environment. The process of crystallization may not only reduce or eliminate the aqueous environment but may also distort the molecules away from their free-molecule geometry. An historically important example is the structure of DNA (see Section 10.5). Only when the parallel-orientated strands of DNA are examined in the wet or high-humidity condition (the B form) does the double-helical structure correspond to that which occurs *in vivo*. In the low-humidity or ‘dry’ condition (the A form) the repeat distance and conformation of the helices is changed—but at the same time giving rise to much sharper diffraction patterns. F.H.C. Crick realized that the transformation was in effect displacive rather than reconstructive (see Section 1.11.5) and that from the A form the double helical B form could be deduced.

4.8.1 *The close packing of organic molecules*

The first detailed analysis of the close (and closest) packing of organic molecules was made by A.I. Kitaigorodskii* who predicted the possible space groups arising from the close packing of 'molecules of arbitrary form'.⁵ He proceeded on the principle that all the molecules were in contact, none interpenetrated, but rather that the 'protrusions' of one molecule fitted into the 'recesses' of a neighbouring molecule such that the amount of empty space was the least possible. He found, in summary, that the deviations from close-packing were small and that (as in the close-packing of spheres) a twelve-fold coordination was the general rule. No assumptions were made as to the nature of the intermolecular forces—the analysis is purely geometrical and must of course be modified when, for example, hydrogen bonding between molecules is taken into account.

The crystallographic interest of the analysis lies in its development from plane group symmetry (Section 2.5) to layer-group symmetry (Section 2.8) and then to space-group symmetry (Section 4.7). We shall follow these steps in outline (omitting the details of the analysis).

For plane molecules (or motifs) of arbitrary form having point group symmetry 1, 2 or m (see Fig. 2.3) it turns out that the requirement of close or closest-packing limits the plane groups to those with either oblique or rectangular unit cells (see Fig. 2.6). Figure 4.17 shows four examples to illustrate the motifs of 'arbitrary form' and the packing principles involved.

We now consider molecules or motifs which are three-dimensional, i.e. having 'top' and 'bottom' faces (as represented in Section 2.8, Fig. 2.15 by black and white **R**'s).

As in the two-dimensional case, such motifs can only be arranged with a minimum of empty space in layers in which the unit cells are oblique (total 7) or rectangular (total 41), i.e. a total of 48 out of the 80 possible layer symmetry groups (see Section 2.8). However, there are further restrictions. Layer symmetry groups with horizontal mirror planes are unsuitable for the close packing of such motifs since such planes would double the layers and cause protrusions to fall on protrusions and recesses on recesses. Similarly, horizontal glide planes parallel to, or mirror planes perpendicular to, the axes of rectangular cells lead to four-fold, not six-fold coordination in the plane. Taking all these restrictions into account we are left with only ten layer symmetry groups which allow six-fold coordination close packing within the plane. These ten groups are shown in Fig. 4.18 where the black and white triangles indicate the 'top' and 'bottom' faces of the 'molecules of arbitrary form'.

Now we need to stack these layers upon each other to create a close-packed structure. Four of these layers are polar—the molecules all face the same way (all black triangles, Fig. 4.18 (a), (d), (f), (i)), represented diagrammatically in Fig. 4.19(a). The rest are non-polar, (Fig. 4.19(b)) and clearly only these non-polar layers can in principle give rise to close packing. Further, the presence of diad axes normal to the layers prohibit the close-packing of arbitrary shapes which just leaves us with layer-symmetry groups

* Denotes biographical notes available in Appendix 3.

⁵ A.I. Kitaigorodskii *Organic Chemical Crystallography*, USSR Academy of Sciences, Moscow, 1955; Eng. Trans (revised) Consultants Bureau Enterprises, New York, 1961.

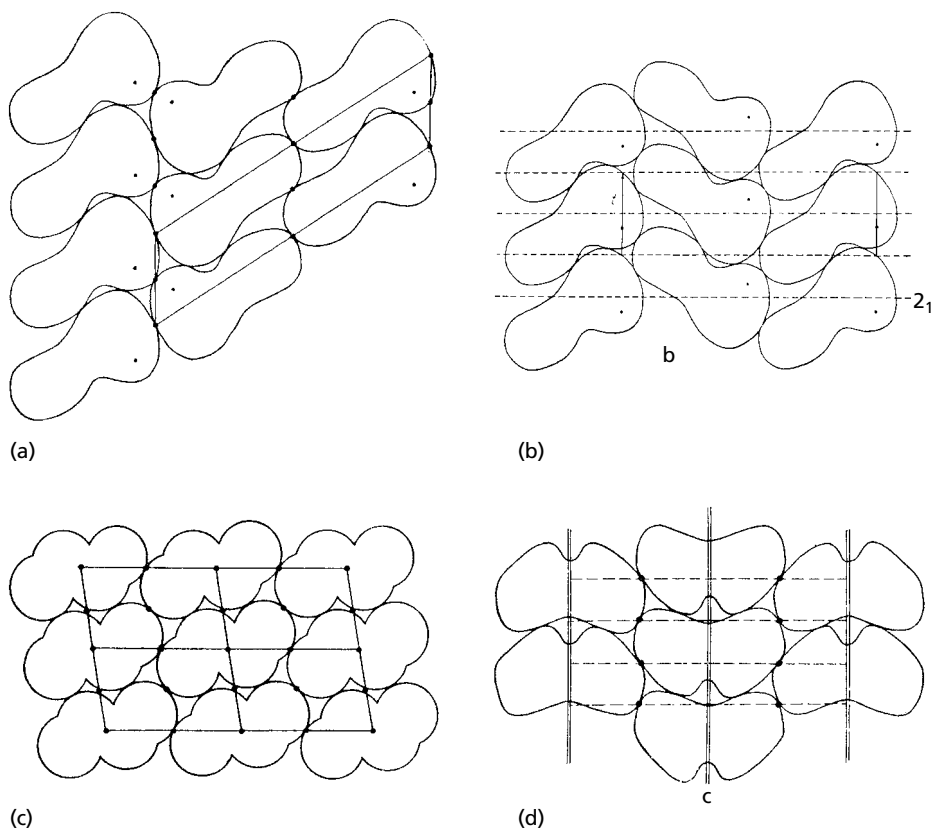


Fig. 4.17. Close-packing of two-dimensional motifs of 'arbitrary form' in oblique and rectangular unit cells. Motifs with point group symmetry 1 (a) and (b), 2 (c) and m (d) (from *Organic Chemical Crystallography* by A.I. Kitaigorodskii, Consultants Bureau, New York, 1961).

b, c, g and h (Fig. 4.18). Finally Kitaigorodskii concludes that close-packing can be achieved with molecules with monad symmetry (1) or a centre of symmetry ($\bar{1}$) but that for molecules with diad (2) or a single mirror plane (m) symmetry there is a reduction in full packing density; such structures he called 'limitingly close packed'.⁵ Finally, he established those space groups which he termed 'permissible'. The space groups thus derived are listed in Table 4.1.

It is of interest to compare these predicted space groups with those of the molecular solids listed in the *Cambridge Structural Database* which (in 1999) had a total of 186,074 entries. Of this number, eight space groups account for 84% of all the entries, viz. $P2_1/c$ (36%), $P\bar{1}$ (17.6%), $P2_12_12_1$ (10.2%), $C2/c$ (7.0%), $P2_1$ (5.7%), $Pbca$ (4.1%), $Pnma$ (1.7%) and $Pna2_1$ (1.7%). All these space groups are included in Table 4.1—a remarkable predictive achievement when one considers how little chemistry was involved!

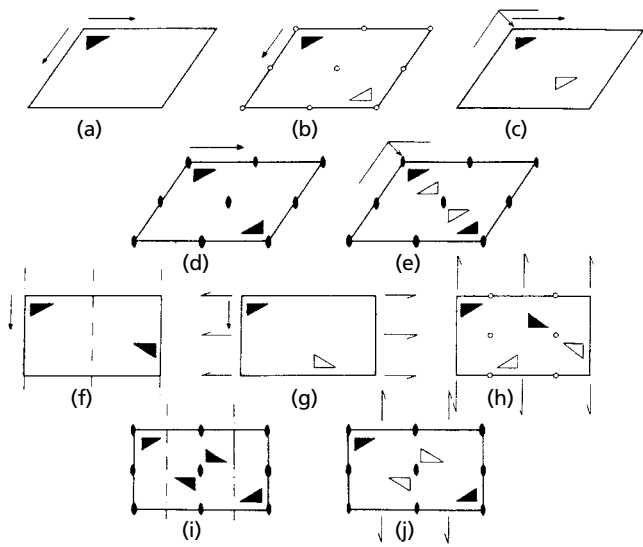


Fig. 4.18. Representation of the ten symmetry groups allowing coordination close packing of three-dimensional motifs in a plane. Single-headed arrows indicate in-plane screw diads, dashed lines indicate vertical mirror planes (from *Macromolecular Physics*, Volume 1, by B. Wunderlich, Academic Press, New York and London, 1973).

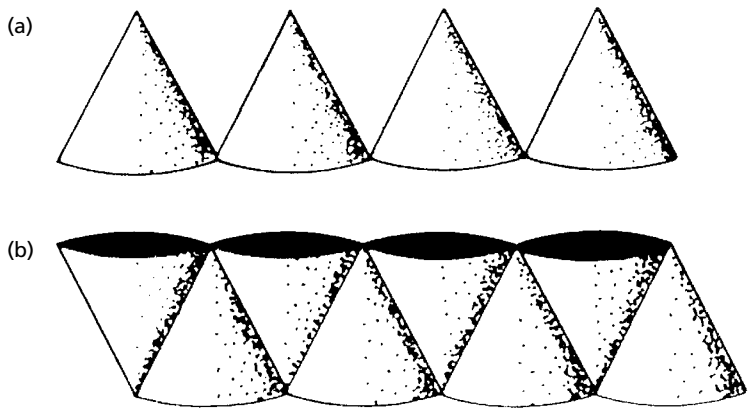


Fig. 4.19. Representation using a cone as a motif of the packing of (a) polar and (b) non-polar layers (from *Macromolecular Physics*, Volume 1, by B. Wunderlich, Academic Press, New York and London, 1973).

4.8.2 Long-chain polymer molecules

The crystal structures and space groups formed by long-chain polymer molecules are also in accord with the principles outlined above.

In the case of *atactic* polymers (i.e. those in which the side-groups are large and/or randomly distributed along the chain), crystal structures rarely occur—the side-groups keep the chains well apart—hence the name atactic. Crystal structures only occur in *tactic* polymers in which the side-groups are regularly distributed on one side of the chain (*isotactic*) or alternatively each side (*syndiotactic*). We shall consider just two polymers—polyethylene (polythene) and isotactic polypropylene (polypropene).

Polyethylene $n(\text{CH}_2)$ is the simplest polymer, made up of a planar zig-zag chain of carbon atoms, each carbon tetrahedrally coordinated to two hydrogen atoms. Two crystal structures occur, polyethylene I (orthorhombic, space group $Pnam$ —equivalent to $Pnma$ by change of axes) and polyethylene II (monoclinic, space group $C2/m$). Polyethylene I is the common, stable form and the arrangement of the chains in the unit cell is shown in Fig. 4.20(a). The zig-zag planes of the chains are at 45° to the unit cell axes and are so arranged that the protrusions of one chain fit into the ‘hollow’ or recess formed by three neighbouring chains as is also shown in Fig. 4.20(a) by the outlines or the envelopes of the molecules. Screw diad axes of symmetry run in the directions of all three axes in the unit cell—principally along and through the centres of the chains.

Table 4.1 Space groups for closest, limitingly and permissible close packing.

Motif symmetry	Closest packed	Limitingly close packed	Permissible
1	$P\bar{1}$, $P2_1$, $P2_1/c$, $Pca2_1$, $Pna2_1$, $P2_12_12_1$	None	$P1$, C_2 , $P2_12_12_1$, $Pbca$
$\bar{1}$	$P\bar{1}$, $P2_1/c$, $C2/c$, $Pbca$	None	$Pccn$
2	None	$C2/c$, $P2_12_12_1$, $Pbcn$	$C2$, $Aba2$
m	None	$Pmc2_1$, $Cmc2_1$, $Pnma$	C_m , $P2_1/m$, $Pmn2_1$, $Abm2$, $Ima2$, $Pbcm$

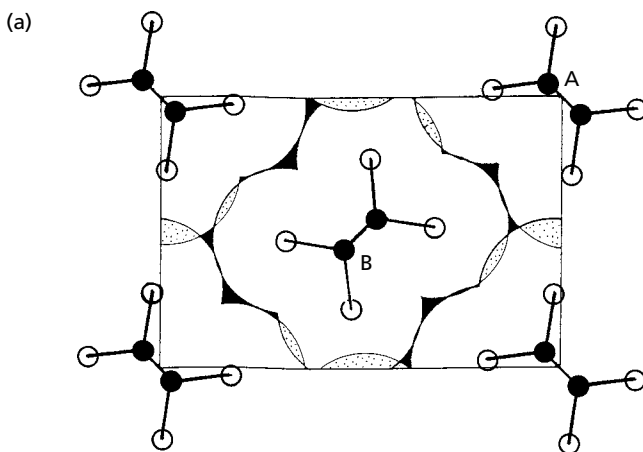


Fig. 4.20. (continued)

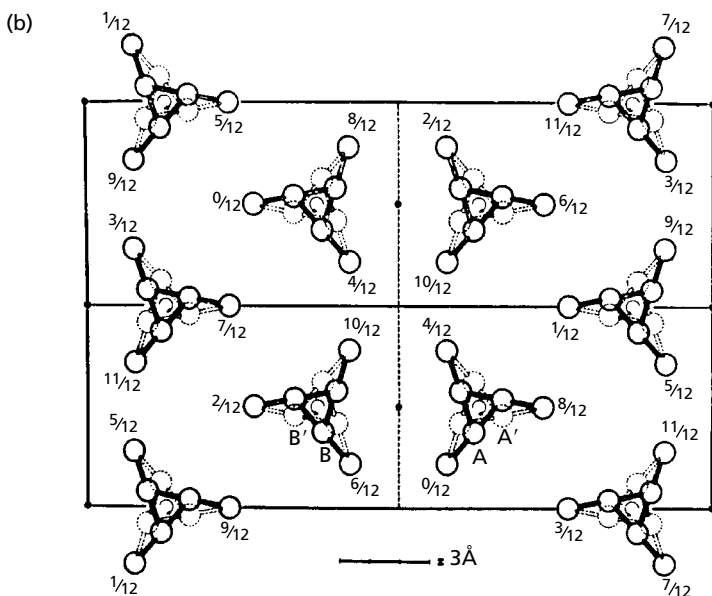


Fig. 4.20. Projections of polymer unit cells perpendicular to the chain axes. (a) Polyethylene, space group $Pnam$, the centres of the carbon and hydrogen atoms in the planar zig-zag chains are shown by black and open circles respectively; the envelopes of the molecules show clearly the close packing (from *Macromolecular Physics*, Volume 1, by B. Wunderlich, Academic Press, New York and London, 1973). (b) Isotactic polypropylene, space group $P2_1/c$; the senses of the helices are indicated by the \odot and \ominus symbols (from *Structure and properties of isotactic polypropylene* by G. Natta and P. Corradini, *Nuovo Cimento*, Suppl. to Vol **15** 1, 40, 1960).

In polypropylene (polypropene), $n(\text{CH}_2\text{-CHCH}_3)$, the CH_3 side-groups approach too closely for the backbone to remain planar and their efficient packing results in the backbone being twisted into a helical conformation, both right and left handed. In isotactic polypropylene the crystal structure is monoclinic and the space group is $P2_1/c$ —the commonest space group of all. Figure 4.20(b) shows a projection of the unit cell perpendicular to the chain axes. The packing together of the helices is dictated by the intermeshing of the CH_3 side-groups and this occurs most efficiently when the rows of helices along the c -axis are alternatively right and left handed as shown in Fig. 4.20(b). The packing is, in fact, very close to hexagonal, like a bundle of pencils, and an hexagonal unit cell may also occur. (Figure 10.11(b) shows a fibre photograph of isotactic polypropylene and Exercise 10.4 shows how the orientation of the chains in the unit cell may be determined.)

4.9 Quasiperiodic crystals or crystalloids

The 230 space groups represent all the possible combinations of symmetry elements, and therefore all the possible patterns which may be built up by the repetition, without

any limit, of the structural units of atoms and molecules which constitute crystals. But real crystals are finite and the atoms or molecules at their surfaces obviously do not have the same environment as those inside. Moreover, crystals nucleate and grow not according to geometrical rules as such but according to the local requirements of atomic and molecular packing, chemical bonding and so on. The resulting repeating pattern or space group is the usual consequence of such requirements, but it is not a necessary one. We will now consider some such cases where ‘crystals’ nucleate and grow such that the resulting pattern of atoms or molecules is non periodic and does not conform to any of the 230 space groups—in short the three-dimensional analogy to the non-periodic patterns and tilings discussed in Section 2.9. But first we need to adopt a new name for such structures and, following Shechtman⁶ can call them *quasiperiodic crystals* or materials, or following Mackay⁷ call them *crystalloids*.

We will start ‘where we began’ in Section 1.1 of this book by model-building with equal size closely packed spheres. In the ccp structure, as we have seen, each sphere is surrounded or coordinated by 12 others as shown in Fig. 4.21(a). The polyhedron formed around the central sphere is a cubeoctahedron. It is one of the thirteen semi-regular or Archimedean solids (see Sections 3.4 and Appendix 2). However, even though all the spheres are close-packed, they are not all *evenly distributed* around the central sphere the interstices between them are different: some ‘square’, some ‘triangular’.

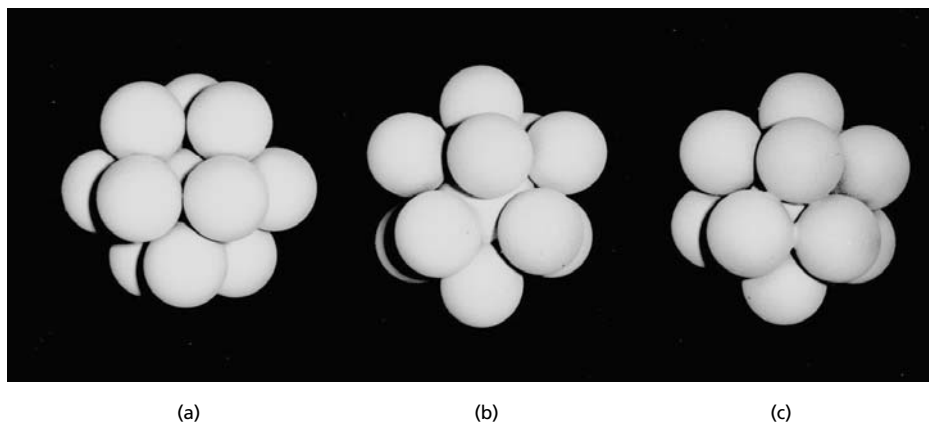


Fig. 4.21. (a) The close packing of 12 spheres around a central sphere as in the ccp structure. The solid is a cubeoctahedron; note that the spheres are not *evenly* distributed round the central sphere, some of the interstices are square, some triangular, (b) The twelve spheres shifted to obtain an *even* distribution; note that the spheres are surrounded by, but not in contact with, five others. (c) The spheres brought together such that they are now in contact; the central sphere is now $\sim 10\%$ smaller. The solid now has the 20 triangular faces of an icosahedron (see also note on pp. 129–30).

⁶ D. Shechtman, I. Blech, D. Gratias and J. W. Cahn. ‘Metallic phase with long-range orientational order and no translational symmetry.’ *Phys. Rev. Lett.* **53**, 1951 (1984).

⁷ A. L. Mackay. *Phys. Bull.* p. 495 (1976).

Now, we can shift the spheres around the central sphere to obtain an even distribution and as we see (Fig. 4.21(b)), this occurs when each sphere is surrounded by (but not now touching) five others and with ‘open’ triangular interstices between them. (This operation is best carried out by making the central sphere out of soft modelling clay and using pegs sticking from the spheres into the clay to keep them in place.) Finally, we can squeeze the whole model (i.e. compress the central sphere) in our cupped hands to bring all the spheres into contact and make a close-packed shell of 12 spheres as shown in Fig. 4.21(c). We have created icosahedral packing because the solid has the 20 triangular faces of an icosahedron. The central sphere or interstice now has a radius some 10% smaller than the 12 surrounding spheres.

The icosahedron can be extended by adding a second, then a third shell of spheres, the spheres succeeding each other to give cubic close packing on each of the 20 triangular faces (Fig. 4.22). Icosahedral packing is not the densest packing (cubeoctahedral packing is the densest), nor is it crystallographic packing—the non-repeating pattern of the shells of spheres constitutes a crystalloid with point group symmetry $\bar{2}35$ indicating the presence of 30 two-fold, 20 three-fold and 12 five-fold axes of symmetry. It is, however, an extremely stable structure (the spheres naturally ‘lock’ together during the squeezing operation) and it is the basis of Buckminster Fuller’s construction of geodesic domes (Section 1.11.6) as well as being characteristic of many virus structures (e.g. the polio virus) which makes them so indestructible.

Icosahedral structures also occur in several metallic alloys, in particular those based on aluminium with copper, iron, ruthenium, manganese, etc. These quasiperiodic crystals were first recognised (in an Al-25% Mn alloy) from the ten-fold symmetry of their electron diffraction patterns (i.e. five-fold symmetry) plus a centre of symmetry resulting from diffraction—Friedel’s law—see Section 9.2). Many such quasiperiodic crystals,

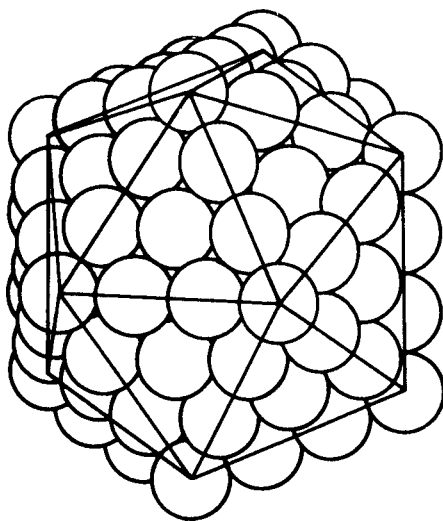


Fig. 4.22. Icosahedral packing of spheres showing close-packing on each of the 20 triangular faces (from ‘A dense non-crystallographic packing of equal spheres’, by A. L. Mackay, *Acta. Cryst.* **15**, 916, 1962).

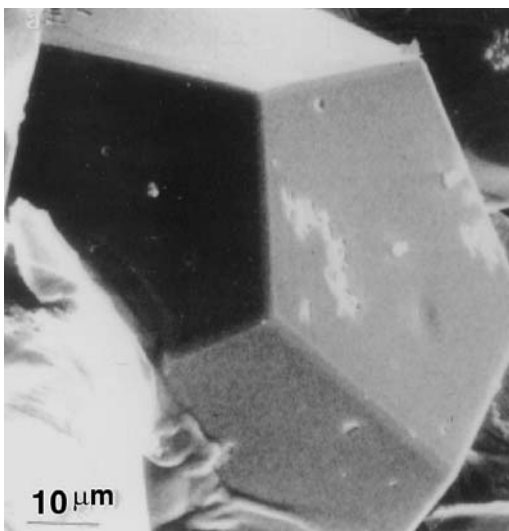


Fig. 4.23. A quasicrystal of a 63% Al, 25% Cu-11% Fe alloy showing pentagonal dodecahedral faces (from ‘A stable quasicrystal in Al-Cu-Fe system’ by An-Pang Tsai, Akihisa Inoue and Tsuyoshi Masumoto, *Jap. J. Appl. Phys.* **26**, 1505, 1987).

formed by rapid solidification from the melt, are metastable and revert to crystalline structures on heating, but stable quasiperiodic crystals as large as a few millimetres in size have been prepared. Figure 4.23 is a scanning electron micrograph of a 63% Al-25% Cu-11% Fe alloy quasicrystal showing the existence of beautiful pentagonal dodecahedral faces. The pentagonal arrangement of atoms in such a face can be revealed by scanning tunnelling microscopy of carefully prepared surfaces and Fig. 4.24 shows such a (Fourier filtered) image of the quasicrystalline alloy $\text{Al}_{70}\text{Pd}_{21}\text{Mn}_9$. Icosahedral shells of atoms may also occur as the motif within crystal structures. For example, the alloy MoAl_{12} consists of Mo atoms surrounded by icosahedral shells of 12 Al atoms, the icosahedra themselves being packed together in a bcc array.

Icosahedral groups of molecules also occur in a number of gas hydrates which can be crystallized in the form of highly hydrated solids, called clathrates. For example, chlorine hydrate, $\text{Cl}_2\text{H}_2\text{O}$, has a body-centred cubic structure at the centre and corners of which the water molecules are arranged at the corners of pentagonal dodecahedra—an arrangement analogous to dodecahedrene (see Section 1.11.6). Further water molecules occupy the interstices between four such dodecahedra and the chlorine molecules are ‘imprisoned’ within this framework—hence the name clathrate, meaning latticed or screened.

A note on the transformation from crystallographic to quasiperiodic atom packing

The transformation from the cubeoctahedron to the icosahedron (Fig 4.21 and the front cover illustration of this book) may be described in another way. In cubic close-packing

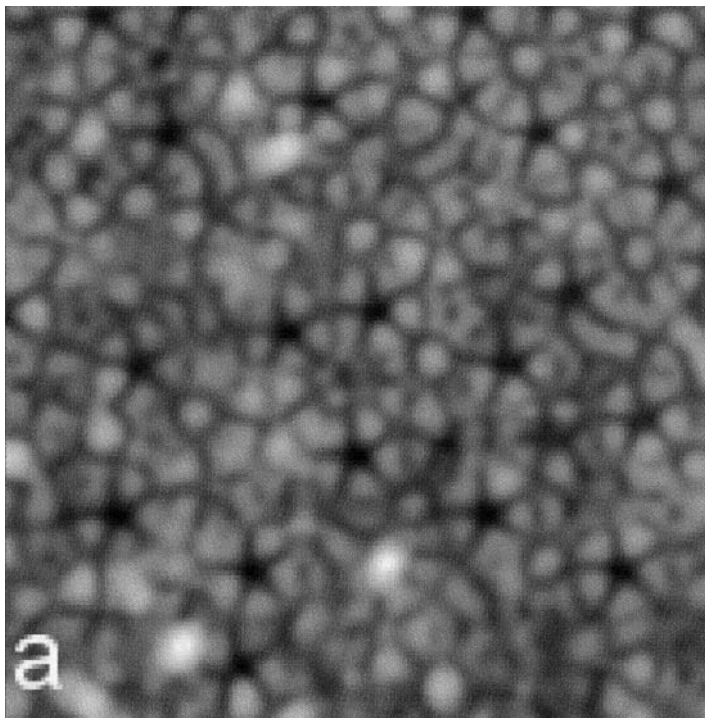


Fig. 4.24. Image (10 nm \times 10 nm) of a surface of the alloy $\text{Al}_{70}\text{Pd}_{21}\text{Mn}_9$ showing the five-fold ‘dark star’ quasiperiodic pattern. (Photograph by courtesy of Prof. Ronan McGrath, University of Liverpool.)

the ‘middle’ ring of six atoms is *planar* with a group of three close-packed atoms above and three below. In icosahedral packing the corresponding ring of six atoms is *puckered* (resulting in a $\sim 10\%$ smaller central cavity) with again three close-packed atoms above and three below. Hence, the transformation may proceed by such small displacive atom movements.

Exercises

4.1 Draw the space group $Pba2$ with the pattern unit \bigcirc at the following positions:

- on the b glide plane, i.e. at $(x'\frac{1}{4}z')$;
- at the intersections of the a and b glide planes, i.e. at $(\frac{1}{4}\frac{1}{4}z')$;
- on a diad axis through the origin, i.e. at $(00z')$;
- on a diad axis through the mid-points of the cell edges, i.e. at $(\frac{1}{2}0z')$.

Hence, show that only (c) and (d) constitute special positions.

4.2 Make and examine the crystal models of NaCl, CsCl, diamond, ZnS (sphalerite), ZnS (wurtzite), Li_2O or CaF_2 (fluorite), CaTiO_3 (perovskite). Identify the Bravais lattice and describe the motif of each structure.

Describing lattice planes and directions in crystals: Miller indices and zone axis symbols

5.1 Introduction

In previous chapters we have described the distributions of atoms in crystals, the symmetry of crystals, and the concept of Bravais lattices and unit cells. We now introduce what are essentially shorthand notations for describing directions and planes in crystals (whether or not they correspond to axes or planes of symmetry). The great advantages of these notations are that they are short, unambiguous and easily understood. For example, the direction (or zone axis) symbol for the ‘corner-to-corner’ (or triad axis) directions in a cube is simply $\langle 111 \rangle$. The plane index (or Miller index) for the faces of a cube is simply $\{100\}$ or of an octahedron $\{111\}$ (Fig. 4.1). The various faces and the directions of their intersections in crystals such as those illustrated in Fig. 4.3 can also be precisely described using these notations. Without them one would have to resort to carefully scaled drawings or projections.

Now direction symbols and plane indices are based upon the crystal axes or lattice vectors which outline or define the unit cell (see Section 3.2) and the only ambiguities which can arise occur in those cases in which different unit cells may be used. For example, crystals with the cubic F Bravais lattice may be described in terms of the ‘conventional’ face-centred cell (Fig. 1.6) or in terms of the primitive rhombohedral cell (Fig. 1.7). Because the axes are different, the direction symbols and plane indices will also be different. Hence it is important to know (1) which set of crystal axes, or which unit cell, is being used and (2) how to change or transform direction symbols and plane indices when the set of crystal axes or the unit cell is changed. This topic is covered in Section 5.8. It is a serious problem only in the case of the trigonal system for crystals with a rhombohedral lattice where there are two almost equally ‘popular’ unit cells—unlike, say, the rhombohedral cells for the cubic F and cubic I lattices which are rarely used. In addition, in the trigonal and hexagonal systems it is possible to introduce, because of symmetry considerations, a fourth axis, giving rise to ‘Miller-Bravais’ plane indices and ‘Weber’ direction symbols, each of which consist of four, rather than three, numbers. This topic is covered in Section 5.7, but first the concept of a zone and zone axis needs to be explained, a topic which is covered in more detail in Section 5.6.

A **zone** may be defined as ‘a set of faces or planes in a crystal whose intersections are all parallel’. The common direction of the intersections is called the **zone axis**. All directions in crystals are zone axes, so the terms ‘direction’ and ‘zone axis’ are

synonymous. So much for the definition. The concept of a zone is readily understood by examining an ordinary pencil. The six faces of a pencil all form or lie in a zone because they all intersect along one direction—the pencil lead direction—which is the zone axis for this set of faces. The number of faces in a zone is not restricted and the faces need not be crystallographically equivalent. For example, the edges of a pencil may be shaved flat to give a 12-sided pencil, i.e. an additional six faces in the zone. Or consider an orthorhombic crystal (Fig. 3.5(b)), or a matchbox. Each crystal axis is the zone axis for four faces, or two crystallographically equivalent pairs of faces. Each face lies in two zones; for example, the ‘top’ and ‘bottom’ faces of Fig. 3.5(b) lie in the zones which have the x - and y -directions as zone axes. In general, a face or plane in a crystal belongs to a whole ‘family’ of zones, the zone axes of which lie in or are parallel to the face.

Verbal definitions are frequently rather clumsy in relation to the simple concepts which they seek to express. Take a piece of paper and draw on it some parallel lines. Fold the paper along the lines—and there you have a zone!

5.2 Indexing lattice directions—zone axis symbols

First, the direction whose symbol is to be determined must pass through the origin of the unit cell. Consider the unit cell shown in Fig. 5.1, which has unit cell edge vectors **a**, **b**, **c** (which are not necessarily orthogonal or equal in length)¹. The steps for determining the zone axis symbol for the direction OL are as follows. Write down the coordinates of a point—any point—in this direction—say P—in terms of fractions of the lengths a , b and c , respectively. The coordinates of P are $\frac{1}{2}$, 0, 1. Now express these fractions as the ratio of whole numbers and insert them into [square] brackets without commas; hence [102]. This is then the direction or zone axis symbol for OL. Notice that if we had chosen a

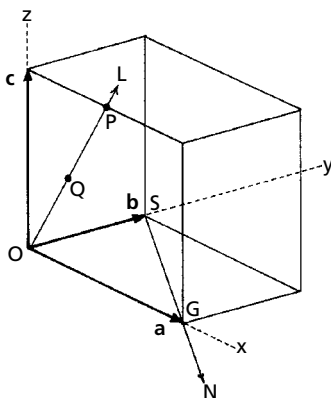


Fig. 5.1. Primitive unit cell of a lattice defined by unit cell vectors **a**, **b**, **c**. OL and SN are directions [102] and $[1\bar{1}0]$ respectively.

¹ See Appendix 5 for a simple introduction to vectors.

different point along OL—say Q—with coordinates $\frac{1}{4}, 0, \frac{1}{2}$, we would have obtained the same result.

Now consider the direction SN. To find its direction symbol the origin must be shifted from O to S. Proceeding as before (e.g. finding the coordinates of G with respect to the origin at S) gives the direction symbol $[1\bar{1}0]$ (pronounced one bar-one oh), the bar or minus sign referring to a coordinate in the negative sense along the crystal axis.

Directions in crystals are, of course, vectors, which may be expressed in terms of components on the three unit cell edge or ‘base’ vectors **a**, **b** and **c**. In the above example the direction OL is written

$$\mathbf{r}_{102} = 1\mathbf{a} + 0\mathbf{b} + 2\mathbf{c}.$$

The general symbol for a direction is $[uvw]$ or, written as a vector,

$$\mathbf{r}_{uvw} = u\mathbf{a} + v\mathbf{b} + w\mathbf{c}.$$

The direction symbols for the unit cell edge vectors **a**, **b** and **c** are $[100]$, $[010]$ and $[001]$, and very often these symbols are used in preference to the terms *x*-axis, *y*-axis and *z*-axis.

5.3 Indexing lattice planes—Miller indices

First, for reasons which will be apparent shortly, the lattice plane whose index is to be determined must not pass through the origin of the unit cell, or rather the origin must be shifted to a corner of the cell which does not lie in the plane. Consider the unit cell in Fig. 5.2 (identical to Fig. 5.1 but drawn separately to avoid confusion). We shall determine the index of the lattice plane which is shaded and outlined by the letters RMS. It is important first to realize that this plane extends indefinitely through the crystal; the shaded area is simply that portion of the plane that lies within the unit cell of Fig. 5.2. It is also important to realize that we are not just considering *one* plane but a whole *family* of identical, parallel planes passing through the crystal. The next plane ‘up’ in

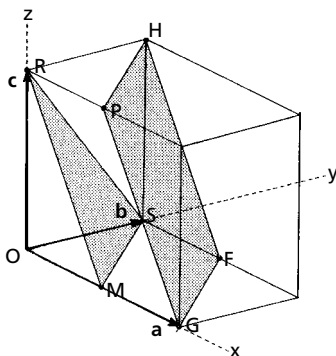


Fig. 5.2. Primitive unit cell (identical to Fig. 5.1), showing the first two planes, RMS and PGFH, in the family. These planes are shaded within the confines of the unit cell.

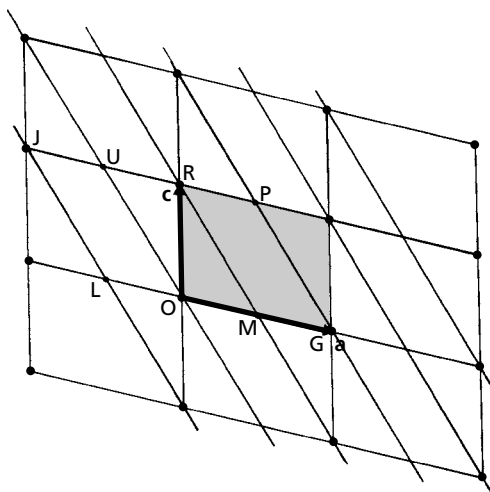


Fig. 5.3. Sketch of Fig. 5.2 with the **a** and **c** unit cell vectors in the plane of the paper (**b** into the plane of the paper) showing traces JL, UO, RM, PG of a family of planes.

the family is also shaded within the confines of the unit cell and is outlined by the letters PGFH. There is a whole succession of such planes, including one which passes through the origin of the unit cell and they all pass through successive 'layers' of lattice points, hence the name, lattice planes.

A two-dimensional sketch (Fig. 5.3) of Fig. 5.2, with the *x*- and *z*-axes in the plane of the paper, and showing the traces of these planes extending into neighbouring cells, will make this clear. Figure 5.3 also shows that all the planes in the family are identical in that they contain the same number or sequence of lattice points.

For RMS, the plane in the family nearest the origin, write down the *intercepts* of the plane on the axes or unit cell vectors **a**, **b**, **c**, respectively; they are $\frac{1}{2}a, 1b, 1c$. Expressed as fractions of the cell edge lengths we have $\frac{1}{2}, 1, 1$. Now take the *reciprocals* of these fractions, and put the whole numbers into (round) brackets without commas; hence (211). This is the **Miller index** of the plane, so-called after the crystallographer, W. H. Miller,* who first devised the notation. Proceeding similarly for the next plane in the family, PGFH (and considering its extension beyond the confines of the unit cell), we have intercepts $1a, 2b, 2c$, which expressed as fractions becomes $1, 2, 2$; the reciprocals of which are $1, \frac{1}{2}, \frac{1}{2}$, which expressed as whole numbers again gives the Miller index (211). The plane through the origin, OU (Fig. 5.3), has intercepts 0, 0, 0 which gives an indeterminate 'Miller index' ($\infty\infty\infty$), but this is merely expressive of the fact that another corner of the unit cell must be selected as the origin. The plane JL (Fig. 5.3) in the same family lies on the opposite side of the origin from RM and has intercepts $-\frac{1}{2}a, -1b, -1c$, which gives the Miller index ($\bar{2}\bar{1}\bar{1}$) (pronounced bar-two, bar-one, bar-one),

* Denotes biographical notes available in Appendix 3.

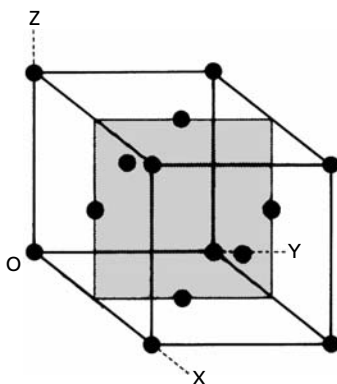


Fig. 5.4. A cubic F unit cell showing (shaded) the first plane from the origin of a family of planes perpendicular to the x -axis but with interplanar spacing $a/2$.

the bar signs simply being expressive of the fact that the planes are recorded from the opposite (negative axis) side of the origin.

The general index for a lattice plane is (hkl) , i.e. (working backwards), the first plane in the family from the origin makes intercepts a/h , b/k , c/l on the axes. This provides us with an alternative method for determining the Miller index of a family of planes. Count the number of planes intercepted in passing from one corner of the unit cell to the next. For the family of planes (hkl) the first plane intercepts the x -axis at a distance a/h , the second at $2a/h$, and so on; i.e. a total of h planes are intercepted in passing from one corner of the unit cell to the next along the x -axis. Similarly, k planes are intercepted along the y -axis and l planes along the z -axis.

Miller indices apply not only to lattice planes, as sketched in Figs. 5.2 and 5.3, but also to the external faces of crystals, where the origin is conventionally taken to be at the centre of the crystal. The intercepts of a crystal face will be many millions of lattice spacings from the origin, depending of course on the size of the crystal but the *ratios* of the fractional intercepts, and therefore the Miller indices, will be simple whole numbers as before. This is sometimes expressed as ‘The Law of Rational Indices’, the germ of which can be traced back to Hailū—see, for example, his representation of the relationship between the crystal faces and the unit cell in dog-tooth spar (Fig. 1.2).

When a crystal plane lies parallel to an axis its intercept on that axis is infinity, the reciprocal of which is zero. For example, the ‘front’ face of a crystal, i.e. the face which intersects the x -axis only and is parallel to the y - and z -axes, has Miller index (100) ; the ‘top’ face, which intersects the z -axis is (001) and so on. It is useful to remember that a zero Miller index means that the plane (or face) is parallel to the corresponding unit cell axis.

Although Miller indices never include fractions they may, when used to describe lattice planes, have common factors and this occurs when the unit cell is non-primitive. Consider, for example, the lattice planes perpendicular to the x -axis in the cubic F unit cell (Fig. 5.4). Because of the presence of the face-centring lattice points, lattice planes

are intersected every $\frac{1}{2}a$ distance along the x -axis. The first lattice plane in the family, shown shaded in Fig. 5.4, makes fractional intercepts $\frac{1}{2}, \infty, \infty$, on the x -, y - and z -axes. The Miller index of this family of planes is therefore (200). To refer to them as (100) would be to ignore the ‘interleaving’ lattice planes within the unit cell². This distinction does not apply to the Miller indices of the external crystal faces, which are many millions of lattice planes from the origin.

The procedure described above for defining plane indices may seem rather odd—why not simply express indices as fractional intercepts without taking reciprocals? The Law of Rational Indices gives half a clue, but the full significance can only be appreciated in terms of the reciprocal lattice (Chapter 6).

5.4 Miller indices and zone axis symbols in cubic crystals

Miller indices and zone axis symbols may be used to express the symmetry of crystals. This applies to crystals in all the seven systems, but the principles are best explained in relation to cubic crystals because of their high symmetry.

The positive and negative directions of the crystal axes x, y, z can be expressed by the direction symbols (Section 5.2) as $[100]$, $[\bar{1}00]$, $[010]$, $[0\bar{1}0]$, $[001]$, $[00\bar{1}]$. Because, in the cubic system, the axes are crystallographically equivalent and interchangeable, so also are all these six direction symbols. They may be expressed collectively as $\langle 100 \rangle$, the (triangular) brackets implying all six permutations or variants of 1, 0, 0. Similarly, the triad axis corner-to-corner directions are expressed as $\langle 111 \rangle$, of which there are eight (four pairs) of variants, namely, $[11\bar{1}]$, $[\bar{1}\bar{1}1]$; $[1\bar{1}1]$, $[\bar{1}1\bar{1}]$; $[\bar{1}11]$, $[1\bar{1}\bar{1}]$; $[111]$, $[\bar{1}\bar{1}\bar{1}]$. The diad axis (edge-to-edge) directions are $\langle 110 \rangle$, of which there are twelve (six pairs) of variants. For the general direction $\langle uvw \rangle$ there are forty-eight (twenty-four pairs) of variants.

A similar concept can be applied to Miller indices. The six faces of a cube (with the origin at the centre) are (100), $(\bar{1}00)$, (010), $(0\bar{1}0)$, (001), $(00\bar{1})$. These are expressed collectively as planes ‘of the form’ $\{100\}$, i.e. in $\{\text{curly}\}$ brackets. Again, for the general plane $\{hkl\}$ there are forty-eight (twenty-four pairs) of variants.

In cubic crystals, directions are perpendicular to planes with the same numerical indices; for example, the direction $[111]$ is perpendicular to the plane (111), or equivalently it is parallel to the normal to the plane (111). This parallelism between directions and normals to planes with the same numerical indices does not apply to crystals of lower symmetry except in special cases. This will be made clear by considering Figs 5.5(a) and (b), which show plans of unit cells perpendicular to the z -axis of a cubic and an orthorhombic crystal. The traces of the (110) plane and $[110]$ direction are shown in each case. Clearly, the (110) plane and $[110]$ direction are only perpendicular to each other in the cubic crystal. In the orthorhombic crystal it is only in the special cases, e.g. (100) planes and $[100]$ directions, that the directions are perpendicular to planes of the same numerical indices.

² In face-centred cells the Miller indices (hkl) describing lattice planes must be all odd or all even (see Appendix 6). The common factor 2 (as in the example, Fig. 5.4) arises when they are all even.

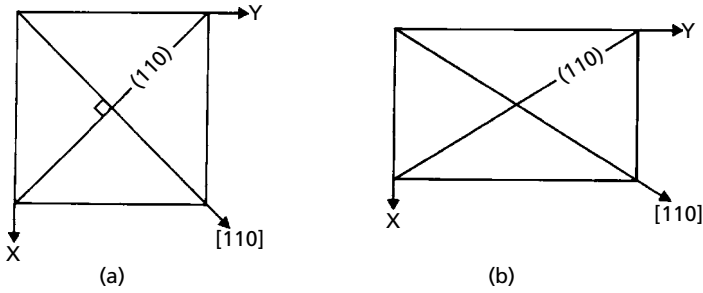


Fig. 5.5. Plans of (a) cubic and (b) orthorhombic unit cells perpendicular to the z -axis, showing the relationships between planes and zone axes of the same numerical indices.

5.5 Lattice plane spacings, Miller indices and Laue indices

The calculation for lattice plane spacings (also called interplanar spacings or d -spacings), d_{hkl} , is simple in the case of crystals with orthogonal axes. Consider Fig. 5.6, which shows the first plane away from the origin in a family of (hkl) planes. As there is another plane in the family passing through the origin, the lattice plane spacing is simply the length of the normal ON . Angle $AON = \alpha$ (angle between normal and x -axis) and angle $ONA = 90^\circ$. Hence

$$OA \cos \alpha = ON \quad \text{or} \quad (a/h) \cos \alpha = d_{hkl} \quad \text{or} \quad \cos \alpha = \left(\frac{h}{a}\right) d_{hkl}.$$

Given that β and γ (not shown in Fig. 5.6) are the angles between ON and the y - and z -axes, respectively, then

$$\cos \beta = \left(\frac{k}{b}\right) d_{hkl} \quad \text{and} \quad \cos \gamma = \left(\frac{l}{c}\right) d_{hkl}.$$

For orthogonal axes $\cos^2 \alpha + \cos^2 \beta + \cos^2 \gamma = 1$ (Pythagoras' theorem), hence

$$\left(\frac{h}{a}\right)^2 d_{hkl}^2 + \left(\frac{k}{b}\right)^2 d_{hkl}^2 + \left(\frac{l}{c}\right)^2 d_{hkl}^2 = 1.$$

For a cubic crystal $a = b = c$, hence

$$\frac{1}{d_{hkl}^2} = \frac{h^2 + k^2 + l^2}{a^2}.$$

Finally, since $\cos \alpha = (h/a)d_{hkl}$, $\cos \beta = (k/a)d_{hkl}$ and $\cos \gamma = (l/a)d_{hkl}$ the ratios of the direction cosines $\cos \alpha : \cos \beta : \cos \gamma$ for a cubic crystal equals the ratios of the Miller indices $h : k : l$.

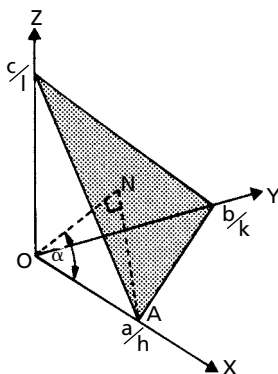


Fig. 5.6. Intercepts of a lattice plane (hkl) on the unit cell vectors \mathbf{a} , \mathbf{b} , \mathbf{c} . $ON = d_{hk} =$ interplanar spacing.

The concept of lattice planes and interplanar spacings is the basis of the concept of the reciprocal lattice (Chapter 6) and also Bragg's law (Chapter 8)—an equation which every schoolboy (or schoolgirl) knows!

$$n\lambda = 2d_{hkl} \sin \theta$$

where n is the order of reflection, λ is the wavelength, d_{hkl} is the lattice plane spacing and θ is the angle of incidence/reflection to the lattice planes. However, it is very important, when using Bragg's law, to distinguish between lattice planes and **reflecting planes**.

Except in the cases of non-primitive cells discussed above (Section 5.3), indices for lattice planes do not have common factors. However, the indices for reflecting planes frequently do have common factors. They are sometimes called **Laue indices** and are usually written without brackets. Their relationship with Miller indices for lattice planes is best illustrated by way of an example. Apply Bragg's law to the (111) lattice planes in a crystal:

$$\text{first-order reflection } (n = 1): 1\lambda = 2d_{111} \sin \theta_1$$

$$\text{second-order reflection } (n = 2): 2\lambda = 2d_{111} \sin \theta_2, \text{ etc.}$$

Now the order of reflection is written on the right-hand side, i.e. for the second-order reflection ($n = 2$)

$$1\lambda = 2 \left(\frac{d_{111}}{2} \right) \sin \theta_2.$$

This suggests that second-order reflections from the (111) lattice planes of d -spacing d_{111} can be regarded as first-order reflections from planes of half the spacing, $d_{111}/2$. Halving the intercepts implies doubling the indices, so these planes are called 222 (no brackets) of d -spacing $d_{222} = d_{111}/2$. These 222 planes are imaginary in the sense that only half of them pass through lattice points, but they are a useful fiction in the sense that the order of

reflection, n in Bragg's law, can be omitted. Continuing the above example, third-order reflections from the (111) lattice planes can be regarded as first-order reflections from the 333 reflecting planes (only a third of which in a family pass through lattice points). As mentioned above, these unbracketed indices are sometimes called Laue indices or reflection indices.

However, it should be pointed out that, in practice, when analysing X-ray or electron diffraction patterns, crystallographers very often do not make this distinction between Miller indices and Laue indices, but simply refer, for example, to 333 reflections (no brackets) from (333) 'planes' (with brackets). This should not lead to any confusion, except perhaps in the case of centred lattices where lattice planes may have common factors. For example, the 200 reflecting planes in the cubic F lattice (Fig. 5.4) are also the (200) lattice planes, but the 200 reflecting planes in the cubic P lattice refer to second-order reflections from the (100) lattice planes.

5.6 Zones, zone axes and the zone law, the addition rule

The concept of a zone has been introduced in Section 5.1. In this section some useful geometrical relationships are listed, the proofs of which are given in Section 6.5, in which use is made of reciprocal lattice vectors. It is possible, of course, to prove the relationships given below without making use of the concept of the reciprocal lattice, but the proofs tend to be long, tedious and not very obvious.

5.6.1 The Weiss* zone law or zone equation

If a plane (hkl) lies in a zone $[uvw]$ (i.e. if the direction $[uvw]$ is parallel to the plane (hkl)), then




$$hu + kv + lw = 0.$$

5.6.2 Zone axis at the intersection of two planes

The line or direction of intersection of two planes in a zone ($h_1k_1l_1$) and ($h_2k_2l_2$) gives the zone axis, $[uvw]$, where

$$u = (k_1l_2 - k_2l_1); \quad v = (l_1h_2 - l_2h_1); \quad w = (h_1k_2 - h_2k_1).$$

To remember these relationships, use the following 'memogram':

h_1	k_1	l_1	h_1	k_1	l_1
h_2	k_2	l_2	h_2	k_2	l_2
					
u		v		w	

* Denotes biographical notes available in Appendix 3.

Write down the indices twice and strike out the first and last pairs. Then u is given by cross-multiplying, i.e.

$$u = (\text{plus } k_1l_2 \text{ minus } k_2l_1),$$

and similarly for v and w .

5.6.3 Plane parallel to two directions

To find the plane lying parallel to two directions $[u_1v_1w_1]$ and $[u_2v_2w_2]$, write down the ‘memogram’

u_1	v_1	\diagdown	$-$	w_1	\diagup	$-$	u_1	\diagdown	$-$	v_1	w_1
u_2	v_2	\diagup	$+$	w_2	\diagdown	$+$	u_2	\diagup	$+$	v_2	w_2
			h			k			l		

and proceed as above, i.e. $h = (v_1w_2 - v_2w_1)$, etc.

5.6.4 The addition rule

Consider two planes $(h_1k_1l_1)$ and $(h_2k_2l_2)$ lying in zone. Then the index of another plane (HKL) in the zone lying between these planes is given by $H = (mh_1 + nh_2)$; $K = (mk_1 + nk_2)$; $L = (ml_1 + nl_2)$, where m and n are small whole numbers.

The rule enables us to work out the indices of ‘in-between’ planes in zones. Consider, for example, the plane marked P in Fig. 5.7, which lies both in the zone containing (100) and (011) and the zone containing (101) and (110). We need a choose values of m and n such that adding the pairs of indices as above gives the same result for (HKL) . This is

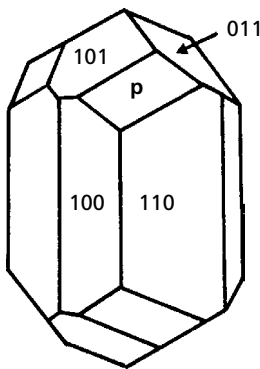


Fig. 5.7. A monoclinic crystal (class m) in which the face P lies in two zones, one containing (101) and (110), the other containing (011) and (100).

much more easily done than said! The plane is (211), i.e.

$$(101) + (110) = (211) \quad (m = 1, n = 1)$$

and

$$(011) + 2(100) = (211) \quad (m = 1, n = 2).$$

5.7 Indexing in the trigonal and hexagonal systems: Weber symbols and Miller-Bravais indices

As shown in Section 3.3, the rhombohedral and hexagonal lattices both consist of hexagonal layers of lattice points which in the rhombohedral lattice are ‘stacked’ in the ABCABC... sequence (Fig. 3.3(b)) and in the hexagonal lattice are ‘stacked’ in the AAA... sequence (Fig. 3.3(a)). In both cases, it is convenient to outline unit cells using the easily recognized hexagonal layers as the ‘base’ of the cells and with the z -axis (or \mathbf{c} vector) perpendicular thereto. However, at least three choices of unit cell are commonly made and these are illustrated in the case of the hexagonal lattice in Fig. 5.8 (the corresponding unit cells of the rhombohedral lattice differ only insofar as they contain additional lattice points of the B and C layers at fractional distances of $\frac{1}{3}$ and $\frac{2}{3}$ of the unit edge length along the z -axis).

Figure 5.8(a) shows the primitive hexagonal unit cell, the smallest that can be chosen with the x - and y -axes at 120° . However, this is often inconvenient in that it does not reveal the hexagonal symmetry of the lattice. For example, all the (pencil) faces parallel to the z -axis are crystallographically equivalent or of the same form, but their indices differ in type as shown—some have indices of the type $(1\bar{1}0)$ and some have indices of the type (100) . To overcome this problem a *fourth* axis—the u -axis—is inserted at 120° to both the x - and y -axes, as shown in Fig. 5.8(b). These are called Miller-Bravais axes

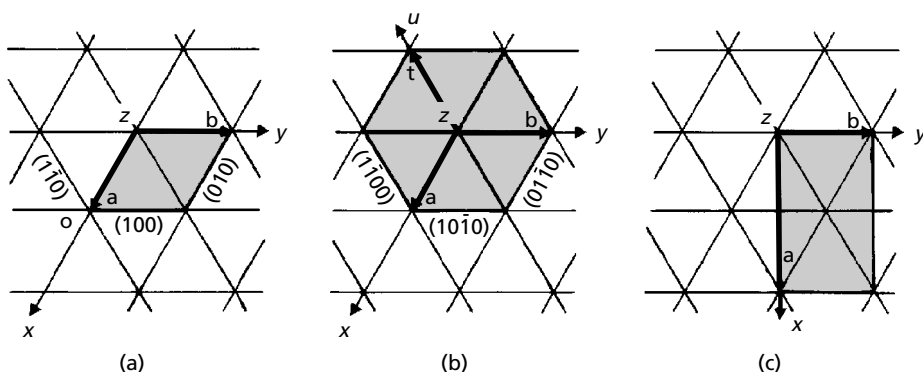


Fig. 5.8. Hexagonal net of the hexagonal P lattice showing (shaded) (a) primitive hexagonal unit cell with the traces of the six prism faces indexed $\{hkl\}$, (b) hexagonal (four-index) unit cell with the traces of the six prism faces indexed $\{hkil\}$, (c) orthohexagonal (Base or C -centred) unit cell. The z -axis is out of the plane of the page.

x, y, u, z (or vectors **a, b, t, c**) and the indices of the lattice planes, called **Miller–Bravais indices**, now consist of four numbers (hkl). The indices for the pencil faces are shown in Fig. 5.8(b) and they are all of the same form $\{10\bar{1}0\}$. Notice that, in all cases the sum of the first three numbers is zero, i.e. $h+k+i=0$. As therefore $i=-(h+k)$, is sometimes simply represented as a dot, i.e. $\{hk.l\}$. However, this unnecessary abbreviation should be discouraged, as it defeats the object of using Miller–Bravais axes in the first place.

Similarly, zone axis symbols, sometimes called **Weber* symbols**, consist of four numbers $\langle UVTW \rangle$. However, determining these numbers (i.e. determining the components of a vector using four base vectors in three-dimensional space) is not straightforward. We cannot convert to 4-index Weber symbols $\langle UVTW \rangle$ from 3-index zone axis symbols $\langle uvw \rangle$ by ‘adding’ the third symbol T such that $T=-(u+v)$ as we did for the i index in Miller–Bravais indices. We need to derive the relationship between $\langle UVTW \rangle$ and $\langle uvw \rangle$ as follows. For a vector specified in both systems to be identical:

$$u\mathbf{a} + v\mathbf{b} + w\mathbf{c} = U\mathbf{a} + V\mathbf{b} + T\mathbf{t} + W\mathbf{c}.$$

Since the x, y and u axes are at 120° to each other, the vector sum, $\mathbf{a} + \mathbf{b} + \mathbf{t} = 0$. Substituting for $\mathbf{t} = -(\mathbf{a} + \mathbf{b})$,

$$u\mathbf{a} + v\mathbf{b} + w\mathbf{c} = U\mathbf{a} + V\mathbf{b} - T(\mathbf{a} + \mathbf{b}) + W\mathbf{c}, \text{ i.e.}$$

$$u\mathbf{a} + v\mathbf{b} + w\mathbf{c} = (U - T)\mathbf{a} + (V - T)\mathbf{b} + W\mathbf{c}.$$

Hence we obtain the identities:

$$u = (U - T); \quad v = (V - T); \quad w = W.$$

To obtain the identities for the reverse transformation we impose the condition that $U + V + T = 0$ (in the same way that $h + k + i = 0$ for Miller–Bravais indices).

Eliminating T the identities become:

$$u = 2U + V; \quad v = U + 2V; \quad w = W$$

and by adding/subtracting the first two equations we obtain:

$$U = 1/3(2u - v); \quad V = 1/3(2v - u); \quad T = -1/3(u + v); \quad W = w.$$

On this basis the zone axis symbols for the x -, y - and u -axes are $[2\bar{1}\bar{1}0]$, $[\bar{1}2\bar{1}0]$ and $[\bar{1}\bar{1}20]$ respectively.

When using Miller–Bravais indices and Weber symbols the zone law $hu + kv + lw = 0$ becomes (using the above identities)

$$h(U - T) + k(V - T) + lW = 0$$

$$\text{i.e. } hU + kV - (h + k)T + lW = 0$$

* Denotes biographical notes available in Appendix 3.

and since $i = -(h + k)$ the zone law for Miller–Bravais axes becomes:

$$hU + kV + iT + lW = 0.$$

In order to find the Weber symbol $[U\ V\ T\ W]$ for the zone axis along the intersection of two planes $(h_1\ k_1\ i_1\ l_1)$ and $(h_2\ k_2\ i_2\ l_2)$, first find $[u\ v\ w]$ using the ‘memogram’ in Section 5.6.2 and then find $[U\ V\ T\ W]$ using the above identities. Alternatively (and more conveniently), use the following ‘memogram’:

$(2h_1+k_1)$	(h_1+2k_1)	l_1
$(2h_2+k_2)$	(h_2+2k_2)	l_2
	U	W

Write down the indices twice and strike out the first and last pairs. Then U is given by cross-multiplying, i.e.

$$U = (h_1 + 2k_1)l_2 - (h_2 + 2k_2)l_1$$

and similarly for V and W . T is simply $-(U + V)$. Conversely, the plane $(h\ k\ i\ l)$ lying parallel to two directions $[U_1\ V_1\ T_1\ W_1]$ and $[U_2\ V_2\ T_2\ W_2]$ is found by using a similar ‘memogram’, i.e.

$(2U_1+V_1)$	(U_1+2V_1)	W_1
$(2U_2+V_2)$	(U_2+2V_2)	W_2
	h	l

Another unit cell—the orthohexagonal cell—is shown in Fig. 5.8(c). The ratio of the lengths of the edges, a/b is $\sqrt{3}$. As with the primitive hexagonal cell this does not reveal the hexagonal symmetry of the lattice. This base-centred cell has the advantage that the axes are orthogonal and is particularly useful in showing the relationships between the crystals which have similar structures but where small distortions can change the symmetry from hexagonal to orthorhombic, i.e. in situations in which the ratio a/b is no longer precisely $\sqrt{3}$.

To summarize, great care must be taken in interpreting plane indices and zone axis symbols in the hexagonal and trigonal systems—an index such as (111) could refer to the primitive hexagonal or orthohexagonal unit cell, or it could even refer to the Miller–Bravais hexagonal unit cell and be the contracted form of $(11\bar{2}1)$, i.e. (11.1) , in which the dot may have been omitted in printing!

5.8 Transforming Miller indices and zone axis symbols

As mentioned in Section 3.3, different choices of axes (i.e. different unit cells) are frequently encountered in trigonal crystals with the rhombohedral Bravais lattice and it

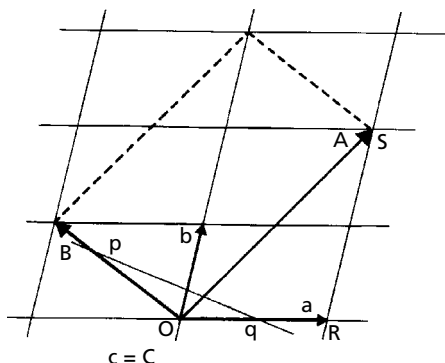


Fig. 5.9. Alternative unit cells in a lattice defined by unit cell vectors \mathbf{a} , \mathbf{b} , \mathbf{c} and \mathbf{A} , \mathbf{B} , \mathbf{C} .

is therefore important to know how to transform Miller indices and zone axis symbols from one axis system to the other. The appropriate matrix equations or **transformation matrices** are given in Section 5.9. However, the concept and derivation of transformation matrices are best understood by way of an easily visualized, in effect, ‘two-dimensional’ example (Fig. 5.9) in which one of the axes (out of the plane of the paper) is common to both cells.

Figure 5.9 shows a plan view of a lattice with two possible unit cells outlined by vectors \mathbf{a} , \mathbf{b} , \mathbf{c} and \mathbf{A} , \mathbf{B} , \mathbf{C} . The common vectors $\mathbf{c} = \mathbf{C}$ lie out of the plane of the paper. The unit cell vectors \mathbf{A} , \mathbf{B} , \mathbf{C} can be expressed as components of \mathbf{a} , \mathbf{b} , \mathbf{c} :

$$\mathbf{A} = 1\mathbf{a} + 2\mathbf{b} + 0\mathbf{c}$$

$$\mathbf{B} = \bar{1}\mathbf{a} + 1\mathbf{b} + 0\mathbf{c}$$

$$\mathbf{C} = 0\mathbf{a} + 0\mathbf{b} + 1\mathbf{c}.$$

Now there are two ways of writing these three equations in matrix form; the vectors may either be written as column matrices:

$$\begin{pmatrix} \mathbf{A} \\ \mathbf{B} \\ \mathbf{C} \end{pmatrix} = \begin{pmatrix} 1 & 2 & 0 \\ \bar{1} & 1 & 0 \\ 0 & 0 & 1 \end{pmatrix} \begin{pmatrix} \mathbf{a} \\ \mathbf{b} \\ \mathbf{c} \end{pmatrix}$$

or as row matrices:

$$(\mathbf{A} \mathbf{B} \mathbf{C}) = (\mathbf{a} \mathbf{b} \mathbf{c}) \begin{pmatrix} 1 & \bar{1} & 0 \\ 2 & 1 & 0 \\ 0 & 0 & 1 \end{pmatrix}.$$

Notice that the rows and columns of the 3×3 matrix are transposed.

Let (hkl) and $[uvw]$ be the Miller indices and zone axis symbols referred to the primitive unit cell \mathbf{a} , \mathbf{b} , \mathbf{c} and (HKL) and $[UVW]$ be the Miller indices and zone axis symbols referred to the ‘large’ unit cell \mathbf{A} , \mathbf{B} , \mathbf{C} (which has three lattice points per cell).

Consider first the transformation between the indices (hkl) and (HKL) . Figure 5.9 shows the trace pq of the first plane from the origin in a family of planes in the lattice. By definition, the intercepts of this plane are a/h on the \mathbf{a} lattice vector, A/H on the \mathbf{A} lattice vector, b/k on the \mathbf{b} lattice vector and B/K on the \mathbf{B} lattice vector. Or, recall the equivalent definition that h is the number of planes intersected along the \mathbf{a} lattice vector, H is the number intersected along the \mathbf{A} lattice vector, and so on; h is the number intersected along \mathbf{a} (i.e. 0 to R) and $2k$ is the number intersected along $2\mathbf{b}$ (i.e. R to S). Hence, $h + 2k$ is the total number of planes intersected along $\mathbf{1a} + 2\mathbf{b}$ (i.e. O to S) and, as $\mathbf{A} = \mathbf{1a} + 2\mathbf{b}$, then this number is the H index. Hence

$$H = 1h + 2k + 0l$$

$$K = \bar{1}h + 1k + 0l$$

$$L = 0h + 0k + 1l,$$

and the indices transform in the same way as the unit cell vectors, and again can be written in matrix form as column matrices or row matrices. We shall choose the *row* matrix form, viz.

$$(HKL) = (hkl) \begin{pmatrix} 1 & \bar{1} & 0 \\ 2 & 1 & 0 \\ 0 & 0 & 1 \end{pmatrix}.$$

The relationship between $[uvw]$ and $[UVW]$ may be derived as follows. A vector \mathbf{r} in the lattice is written in terms of its components on the two sets of lattice vectors, i.e.

$$\mathbf{r} = u\mathbf{a} + v\mathbf{b} + w\mathbf{c} = U\mathbf{A} + V\mathbf{B} + W\mathbf{C}.$$

Substituting for \mathbf{A} , \mathbf{B} and \mathbf{C} :

$$u\mathbf{a} + v\mathbf{b} + w\mathbf{c} = U(\mathbf{1a} + 2\mathbf{b} + 0\mathbf{c}) + V(\bar{1}\mathbf{a} + 1\mathbf{b} + 0\mathbf{c}) + W(0\mathbf{a} + 0\mathbf{b} + 1\mathbf{c}).$$

Collecting terms together for u , v and w gives

$$u = 1U + \bar{1}V + 0W$$

$$v = 2U + 1V + 0W$$

$$w = 0U + 0V + 1W.$$

Writing the zone axis symbols as *column* matrices gives

$$\begin{pmatrix} u \\ v \\ w \end{pmatrix} = \begin{pmatrix} 1 & \bar{1} & 0 \\ 2 & 1 & 0 \\ 0 & 0 & 1 \end{pmatrix} \begin{pmatrix} U \\ V \\ W \end{pmatrix}.$$

Hence the *same* 3×3 matrix relates plane indices written as *row* matrices from the primitive to ‘large’ unit cell and zone axis symbols written as *column* matrices from the ‘large’ to the primitive unit cell.

The reverse relationships are found from the inverse of the matrix. The procedures for inverting a matrix and for finding its determinant may be found in many A-level mathematics textbooks. A simple ‘memogram’ method for a 3×3 matrix is given in Section 5.10. For this example the inverse matrix is given by

$$\begin{pmatrix} 1 & \bar{1} & 0 \\ 2 & 1 & 0 \\ 0 & 0 & 1 \end{pmatrix}^{-1} = \frac{1}{3} \begin{pmatrix} 1 & 1 & 0 \\ \bar{2} & 1 & 0 \\ 0 & 0 & 3 \end{pmatrix};$$

hence

$$(hkl) = (HKL) \frac{1}{3} \begin{pmatrix} 1 & 1 & 0 \\ \bar{2} & 1 & 0 \\ 0 & 0 & 3 \end{pmatrix}$$

and

$$\begin{pmatrix} U \\ V \\ W \end{pmatrix} = \frac{1}{3} \begin{pmatrix} 1 & 1 & 0 \\ \bar{2} & 1 & 0 \\ 0 & 0 & 3 \end{pmatrix} \begin{pmatrix} u \\ v \\ w \end{pmatrix}.$$

Finally, note that the determinant of the matrix equals 3 (and its inverse equals $\frac{1}{3}$), the ratio of the volumes, or number of lattice points, in the unit cells.

In transforming indices and zone axis symbols from one set of crystal axes to another it is usually best to work from first principles as above because it is very easy to fall into error by using a transformation matrix without knowing which conventions for writing lattice planes and directions are being used.

5.9 Transformation matrices for trigonal crystals with rhombohedral lattices

Figure 5.10 shows a plan view of hexagonal layers of lattice points stacked in the rhombohedral ABC ... sequence. (See also Fig. 3.3(b).) (To avoid confusion only the A hexagonal layers are outlined.) The (primitive) rhombohedral unit cell with equi-inclined lattice vectors **a**, **b**, **c** is outlined, as is a unit cell of a non-primitive hexagonal unit cell with lattice vectors **A** and **B** at 120° to each other and **C** perpendicular to the plan view. Proceeding as described in Section 5.8,

$$(HKL) = (hkl) \begin{pmatrix} 1 & 0 & 1 \\ \bar{1} & 1 & 1 \\ 0 & \bar{1} & 1 \end{pmatrix}; \quad \begin{pmatrix} u \\ v \\ w \end{pmatrix} = \begin{pmatrix} 1 & 0 & 1 \\ \bar{1} & 1 & 1 \\ 0 & \bar{1} & 1 \end{pmatrix} \begin{pmatrix} U \\ V \\ W \end{pmatrix}$$

$$(hkl) = (HKL) \begin{pmatrix} \frac{2}{3} & \bar{\frac{1}{3}} & \bar{\frac{1}{3}} \\ \frac{1}{3} & \frac{1}{3} & \frac{2}{3} \\ \frac{1}{3} & \frac{1}{3} & \frac{1}{3} \end{pmatrix}; \quad \begin{pmatrix} U \\ V \\ W \end{pmatrix} = \begin{pmatrix} \frac{2}{3} & \bar{\frac{1}{3}} & \bar{\frac{1}{3}} \\ \frac{1}{3} & \frac{1}{3} & \frac{2}{3} \\ \frac{1}{3} & \frac{1}{3} & \frac{1}{3} \end{pmatrix} \begin{pmatrix} u \\ v \\ w \end{pmatrix},$$

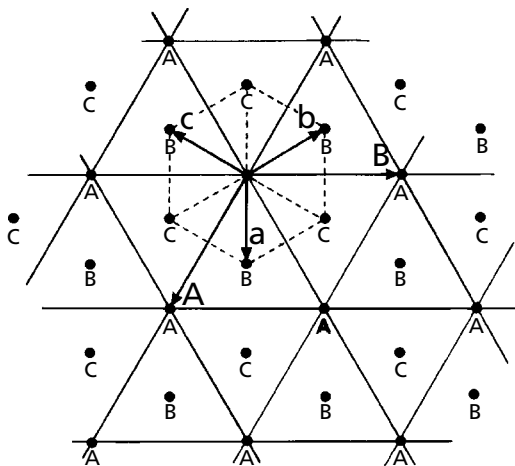


Fig. 5.10. A plan view of the hexagonal layers of lattice points, **A**, **B** and **C**, in the rhombohedral lattice. The rhombohedral unit cell (equally inclined lattice vectors **a**, **b** and **c** out of the plane of the paper from an **A** to a **B** layer lattice point) and the triple hexagonal unit cell (lattice vectors **A**, **B** and **C** perpendicular to the plan view) are outlined.

where (HKL) , $[UVW]$ and (hkl) , $[uvw]$ refer to the Miller indices and zone axes symbols for the hexagonal and rhombohedral unit cells, respectively. Note that the determinants of these two matrices are 3 and $\frac{1}{3}$, respectively, i.e. equal to the ratios of the number of lattice points in the two cells. Hence the hexagonal unit cell is known as a triple hexagonal cell because it contains three lattice points per cell. Note also that it is possible to choose the hexagonal **A** and **B** axes differently (e.g. rotated 60° to those shown in Fig. 5.10); this will give rhombohedral unit cells that are mirror-related, sometimes known as ‘obverse’ and ‘reverse’ unit cells.

5.10 A simple method for inverting a 3×3 matrix

This method has the advantage that we do not need to memorize a sign convention. We will use the matrix derived in Section 5.8 as an example:

Step 1: Write out the matrix (top left) and repeat it three times as if it were the ‘motif’ of a pattern, thus:

$$\begin{array}{cccccc}
 1 & \bar{1} & 0 & 1 & \bar{1} & 0 \\
 2 & \boxed{1} & 0 & 2 & 1 & 0 \\
 0 & \boxed{0} & 1 & 0 & 0 & 1 \\
 1 & \bar{1} & 0 & 1 & \bar{1} & 0 \\
 2 & 1 & 0 & 2 & 1 & 0 \\
 0 & 0 & 1 & 0 & 0 & 1
 \end{array}$$

Step 2: Find the co-factor for each term. We will start with the term 1 in the first row and first column. ‘Look down’ towards the right (as indicated by the arrow) at the group of four terms (shown inside the dashed box)

1	0
0	1

Cross-multiply these terms following the ‘memogram’ procedure (Section 5.6),

i.e.

1	0
0	1

The result, 1, is the co-factor. Repeat this procedure for all the other terms—for each term ‘look down’ towards the right, identify the group of four terms and cross-multiply them. For example, for $\bar{1}$, the second term in the first row, the group of four terms is

0	2
1	0

 and the cofactor is $\bar{2}$.

Step 3: Write down, following the above procedure, the matrix of co-factors, which is:

$$\begin{matrix} 1 & \bar{2} & 0 \\ 1 & 1 & 0 \\ 0 & 0 & 3 \end{matrix}$$

Step 4: The determinant, det, of the matrix is the sum of the terms in *any* row or *any* column multiplied by their co-factors. For example, for the first row:

$$\det = 1.1 + 1.2 + 0.0 = 3$$

and for the second row:

$$\det = 2.1 + 1.1 + 0.0 = 3$$

and for the second column:

$$\det = 1.2 + 1.1 + 0.0 = 3$$

(repeating in this way serves as a useful cross-check to see that you have not made any mistakes, particularly with signs).

Step 5: The inverse of the matrix is found by transposing the matrix of co-factors (i.e. interchanging rows and columns) and by dividing by the determinant, hence:

$\frac{1}{3} \begin{pmatrix} 1 & 1 & 0 \\ \bar{2} & 1 & 0 \\ 0 & 0 & 3 \end{pmatrix}$

which is
the inverse
of the matrix

$\begin{pmatrix} 1 & \bar{1} & 0 \\ 2 & 1 & 0 \\ 0 & 0 & 1 \end{pmatrix}.$

Exercises

- 5.1 Write down the Miller indices and zone axis symbols for the slip planes and slip directions in fcc and bcc crystals. (See also Exercise 1.5.)
- 5.2 Which of the directions $[010]$, $[432]$, $[\bar{2}10]$, $[23\bar{1}]$, if any, lie parallel to the plane (115) ? Which of the planes (112) , (321) , $(911\bar{2})$, $(\bar{1}\bar{1}1)$, if any, lie parallel to the direction $[1\bar{1}\bar{1}]$?
- 5.3 Write down the planes whose normals are parallel to directions with the same numerical indices in the triclinic, monoclinic and tetragonal systems.
- 5.4 Using the ‘memograms’ on pp. 139 and 140, find the plane which lies parallel to the directions $[131]$ and $[0\bar{1}1]$. Find the plane which lies parallel to the directions $[102]$ and $[\bar{1}11]$. Find the direction which lies parallel to the intersection of the planes (342) and $(10\bar{3})$. Find the direction which lies parallel to the intersection of the planes $(21\bar{3})$ and (110) . Check your answers by using the zone law.
- 5.5 An orthorhombic crystal (cementite, Fe_3C) has unit cell vectors (or lattice parameters) of lengths $a = 452$ pm, $b = 508$ pm, $c = 674$ pm.
 - (a) Find the d -spacings of the following families of planes: (101) , (100) , (111) and (202) .
 - (b) Find the angles α , β , γ (Fig. 5.6) between the normal to the plane (111) and the three crystal axes.
 - (c) Find the angles p , q , r between the $[111]$ direction and the three crystal axes. Briefly explain why these angles are not the same as those in (b).
- 5.6 Figure 3.2 shows the cubic I and cubic F lattices and the corresponding primitive rhombohedral unit cells. Study these figures carefully, then close the book and redraw them for yourself—to ensure that you understand the geometries of the cells in each case. Assign unit cell vectors \mathbf{A} , \mathbf{B} , \mathbf{C} to the primitive rhombohedral cells and unit cell vectors \mathbf{a} , \mathbf{b} , \mathbf{c} to the cubic I and cubic F cells and derive the transformation matrices for indices $(hkl) \rightleftharpoons (HKL)$ and direction symbols $[UVW] \rightleftharpoons [uvw]$ in each case.
- 5.7 Draw the directions (zone axes) $[001]$, $[010]$, $[210]$, $[110]$ in a hexagonal unit cell, and determine their Weber zone axis symbols, $\langle UVTW \rangle$.
- 5.8 Using the ‘memograms’ on p. 143, find the direction (Weber symbol) $[U\ V\ T\ W]$ which lies parallel to the intersection of planes $(1\ 2\ \bar{3}\ 1)$ and $(0\ \bar{1}\ 1\ 2)$. Find the plane $(h\ k\ i\ l)$ which lies parallel to the directions $[3\ \bar{1}\ \bar{2}\ 1]$ and $[1\ 0\ \bar{1}\ 2]$. Check your answers by using the zone law for Miller–Bravais axes.
- 5.9 In an hcp crystal, sketch the traces of the (0002) and $\{10\bar{1}1\}$ planes in a $\langle 11\bar{2}0 \rangle$ zone. Note the near-hexagonal arrangement of these planes around the zone axis. Determine the value of the axial ratio c/a , for which the arrangement of these planes is exactly hexagonal.

The reciprocal lattice

6.1 Introduction

The **reciprocal lattice** is often regarded by students of physics as a geometrical abstraction, comprehensible only in terms of vector algebra and difficult diffraction theory. It is, in fact, a very simple concept and therefore a very important one. It provides a simple geometrical basis for understanding not only the geometry of X-ray and electron diffraction patterns but also the behaviour of electrons in crystals—reciprocal space being essentially identical to ‘ k -space’.

The concept of the reciprocal lattice may be approached in two ways. First, reciprocal lattice unit cell vectors may be defined in terms of the (direct) lattice unit cell vectors **a**, **b**, **c**, and the geometrical properties of the reciprocal lattice developed therefrom. This is certainly an elegant approach, but it very often fails to provide the student with an immediate understanding of the relationships, for example, between the reciprocal lattice of a crystal and the diffraction pattern. The second approach, which is the one adopted in this chapter, is much less elegant. It develops the notion that families of planes in crystals can be represented simply by their normals, which are then specified as (reciprocal lattice) vectors and which can then be used to define a pattern of (reciprocal lattice) points, each (reciprocal lattice) point representing a family of planes. The advantage of this approach is that it accentuates the connections between families of planes in the crystals, Bragg’s law and the directions of the diffracted or reflected beams.

The notion that crystal axes can be defined in terms of the *normals* to crystal faces belongs to Bravais* (1850) who called them ‘polar axes’ (not to be confused with current usage of the term which means axes or directions whose ends are not related by symmetry). However, the credit for the development of this idea to the concept of the reciprocal lattice, and the application of this concept to the analysis of X-ray diffraction patterns, belongs to P. P. Ewald,* whose story is told in Section 8.1 and Appendix 3.

A study of the reciprocal lattice does require an elementary knowledge of vectors, their symbolism and some simple rules governing their manipulation (vector algebra). If you are unfamiliar with these topics, or wish to refresh your memory, Appendix 5 provides all the information you will require in order to follow the rest of this chapter.

6.2 Reciprocal lattice vectors

Consider a family of planes in a crystal (for example, those in Figs 5.2 or 5.3). Geometrically, the planes can be specified by two quantities: (1) their orientation in the crystal and (2) their d -spacings. Now, the orientation of the planes is given or defined

* Denotes biographical notes available in Appendix 3.

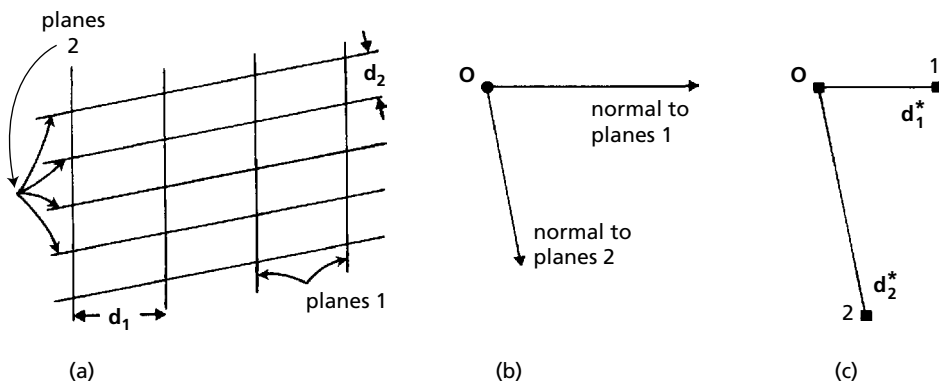


Fig. 6.1. (a) Traces of two families of planes 1 and 2 (perpendicular to the plane of the paper), (b) the normals to these families of planes drawn from a common origin and (c) definition of these planes in terms of the reciprocal (lattice) vectors \mathbf{d}_1^* and \mathbf{d}_2^* , where $\mathbf{d}_1^* = K/d_1$, $\mathbf{d}_2^* = K/d_2$, K being a constant.

by the direction of their normals. In Fig. 6.1(a) two families of planes, simply labelled 'planes 1' and 'planes 2', are sketched 'edge on'. Notice that the planes do not have the same d -spacings and are not at right angles to one another—in short we are starting with a completely general case. In Fig. 6.1(b) the normals to these planes are drawn from a common origin and these specify the orientation of the planes but as yet give no information about their d -spacings. Now the d -spacings, d_1 and d_2 need to be specified. An 'obvious' way of doing this might be to make the lengths of the normals directly proportional to the d -spacings, i.e. by expressing them as *vectors* with moduli equal to $K \times (d\text{-spacing})$ where K is a proportionality constant. However, this is *not* the way; instead, we make the lengths or the moduli of the vectors *inversely* proportional to the d -spacings, i.e. equal to $K/d\text{-spacing}$ (where K is a proportionality constant, taken as unity or, in X-ray or electron diffraction, as λ , the X-ray electron wavelength), i.e. a *longer* vector, indicating a *smaller* d -spacing. The reason for making the moduli of the vectors inversely proportional to the d -spacings will be apparent shortly (recall also the inversion of the intercepts in the definition of Miller indices). These vectors are called **reciprocal (lattice) vectors**, symbols \mathbf{d}_1^* and \mathbf{d}_2^* , and are shown in Fig. 6.1(c). The 'end points' of the vectors (called reciprocal lattice points) are labelled 1 and 2, corresponding to the planes which they represent, and are usually denoted by little squares (as in Fig. 6.1(c)) instead of arrow-heads. Reciprocal lattice vectors have dimensions of $1/\text{length}$ (for $K = 1$), i.e. reciprocal Ångströms, \AA^{-1} , or reciprocal picometres, pm^{-1} . For example, if $d_1 = 0.5 \text{ \AA}$, the length or modulus of \mathbf{d}_1^* (for $K = 1$) is

$$|\mathbf{d}_1^*| = \frac{1}{0.5 \text{ \AA}} = 2 \text{ \AA}^{-1}.$$

This completes the simple definition of reciprocal lattice vectors. But, like all simple concepts, it is capable of great development, which will be done for particular examples in the sections below. But first we need to show that the points do indeed form a grid or lattice—we have so far only two such points (plus an origin) in Fig. 6.1(c). Let us

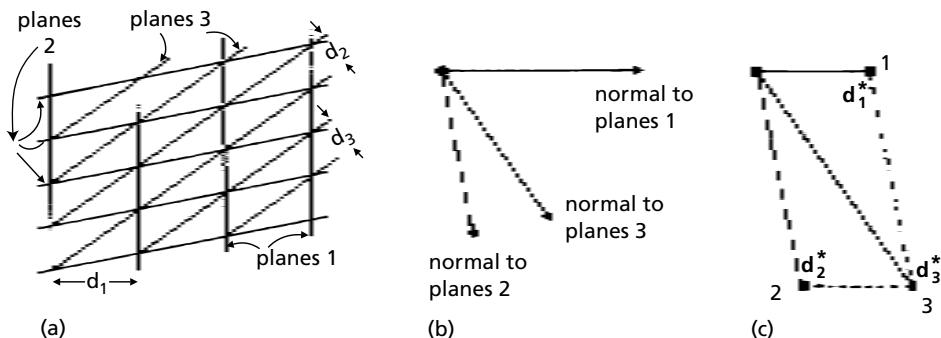


Fig. 6.2. As Fig. 6.1, showing in Fig. 6.2(a) a third set of intersecting planes (planes 3), their normals in Fig. 6.2(b) and their reciprocal lattice vectors in Fig. 6.2(c). Note that $\mathbf{d}_1^* + \mathbf{d}_2^* = \mathbf{d}_3^*$ and that the reciprocal lattice points do form a lattice.

therefore add a third set of planes—‘planes 3’ to Fig. 6.1(a), as shown separately for clarity in Fig. 6.2(a). All the planes have common points of intersection. Figure 6.2(b) shows in addition the normal to planes 3 and Fig. 6.2(c) shows the reciprocal lattice vector \mathbf{d}_3^* and reciprocal lattice point 3. Without any calculations or measurement we can see intuitively that the reciprocal lattice points 1, 2 and 3 do indeed form a lattice as indicated by the dashed lines and that, by vector addition, $\mathbf{d}_1^* + \mathbf{d}_2^* = \mathbf{d}_3^*$. If you are not immediately convinced (and even if you are), it is worthwhile sketching some planes (of arbitrary spacings and orientations) as in Fig. 6.2(a) and then proceeding to draw their reciprocal lattice vectors as in Fig. 6.2(c). But first a practical note. In drawing crystals, and in sketching crystal planes, we have to use a ‘map scale’ in ‘direct space’, choosing a scale to fit our piece of paper, e.g. 1 Å equals 1 cm. So also when drawing reciprocal lattice vectors we have to use a quite separate ‘map scale’ in ‘reciprocal space’, e.g. 1 Å⁻¹ equals 1 cm or 10 cm or 1 inch, as convenient. Strictly speaking we should add ‘scale bars’ to drawings of crystals and crystal planes as we do for micrographs, giving the scale of the drawing in terms of Å or nm or μm, as appropriate, and quite different ‘scale bars’ to drawings of reciprocal lattices (as we ought to do for diffraction patterns) giving the scale of the reciprocal lattice/diffraction pattern in terms of reciprocal units; Å⁻¹, or nm⁻¹ or μm⁻¹ as appropriate.

The five plane lattices (Fig. 2.4(a)) also have their reciprocal lattice counterparts as is shown in Fig. 6.3—a comparison which further emphasizes the reciprocal relationships between them. The unit cells of the plane lattices are specified by the lattice vectors \mathbf{a} and \mathbf{b} and the unit cells of the reciprocal lattices are specified by the reciprocal lattice vectors \mathbf{a}^* and \mathbf{b}^* , as explained in Section 6.3 below.

6.3 Reciprocal lattice unit cells

To avoid the pitfalls of making hasty assumptions about the relationships between reciprocal and (direct) lattice vectors, a monoclinic crystal will be used as an example. First, we shall draw the reciprocal lattice vectors in a section perpendicular to the y -axis

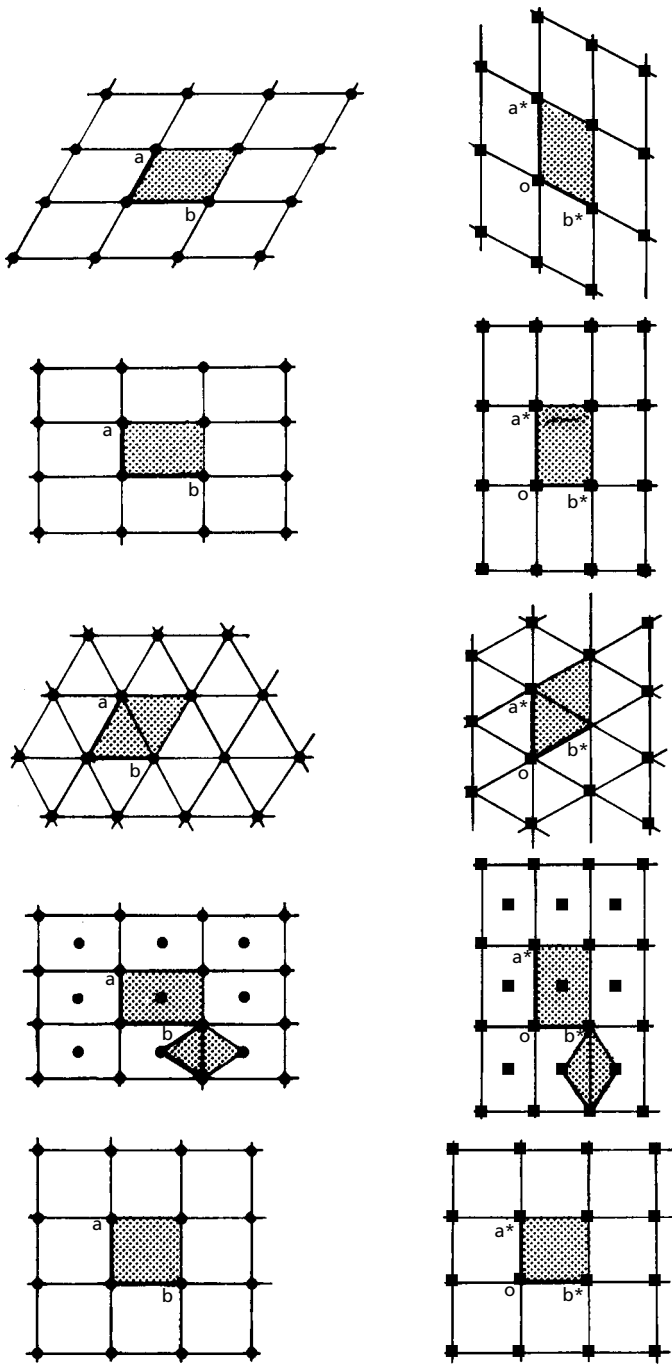


Fig. 6.3. The five plane lattices (left) and plane reciprocal lattices (right) indicating the corresponding unit cells, lattice vectors \mathbf{a} and \mathbf{b} and reciprocal lattice vectors \mathbf{a}^* and \mathbf{b}^* .

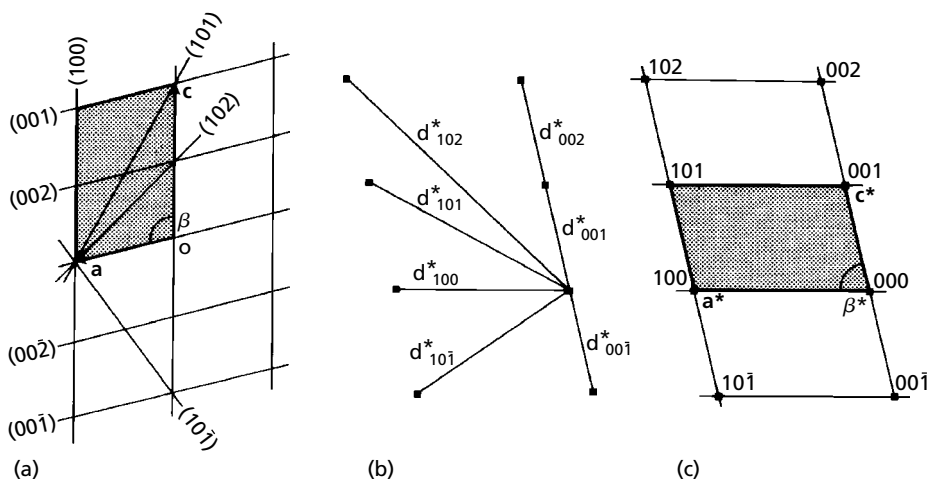


Fig. 6.4. (a) Plan of a monoclinic P unit cell perpendicular to the y -axis with the unit cell shaded. The traces of some planes of type $\{h0l\}$ (i.e. parallel to the y -axis) are indicated, (b) the reciprocal (lattice) vectors, \mathbf{d}^*_{hkl} for these planes and (c) the reciprocal lattice defined by these vectors. Each reciprocal lattice point is labelled with the indices of the plane it represents and the unit cell is shaded. The angle β^* is the complement of β .

(i.e. containing the \mathbf{a} and \mathbf{c} lattice vectors) from which we will find the reciprocal lattice unit cell vectors \mathbf{a}^* and \mathbf{c}^* . This then enables us to express reciprocal lattice vectors in this section in terms of their components on these unit cell vectors. It is then a simple step to extend these ideas to three dimensions.

Figure 6.4(a) shows a section of a monoclinic P lattice through the origin and perpendicular to the y -axis or \mathbf{b} unit cell vector. The section of the unit cell is outlined by the lattice vectors \mathbf{a} and \mathbf{c} at the obtuse angle β and also the traces of some planes of the type $\{h0l\}$ (i.e. those planes parallel to the y -axis). In Fig. 6.4(a), (and Fig. 6.7(a)) no distinction is made between Miller indices and Laue indices—the indices of the planes are all put in brackets whether or not they all pass through lattice points.

Figures 6.4(b) and (c) show the reciprocal lattice vectors for these planes constructed in the same way as before (Section 6.2), with the reciprocal lattice points labelled with the index of the planes they represent. Note again the reciprocal relationships between the lengths of the vectors and the d_{hkl} -spacings, e.g. the (002) planes with *half* the d -spacing of the (001) planes are represented by a reciprocal lattice point 002 , *twice* the distance from the origin as the reciprocal lattice point 001 . Obviously, 003 will be three times the distance, and so on.

It can be seen that the reciprocal lattice points (the ‘end points’ of the reciprocal lattice vectors) do indeed form a grid or lattice—hence the name. This is emphasized in Fig. 6.4(c), which also shows the **reciprocal lattice unit cell** for this section outlined by reciprocal lattice unit cell vectors \mathbf{a}^* and \mathbf{c}^* , where

$$\mathbf{a}^* = \mathbf{d}^*_{100} \quad \text{and} \quad |\mathbf{a}^*| = 1/d_{100}; \quad \mathbf{c}^* = \mathbf{d}^*_{001} \quad \text{and} \quad |\mathbf{c}^*| = 1/d_{001}.$$

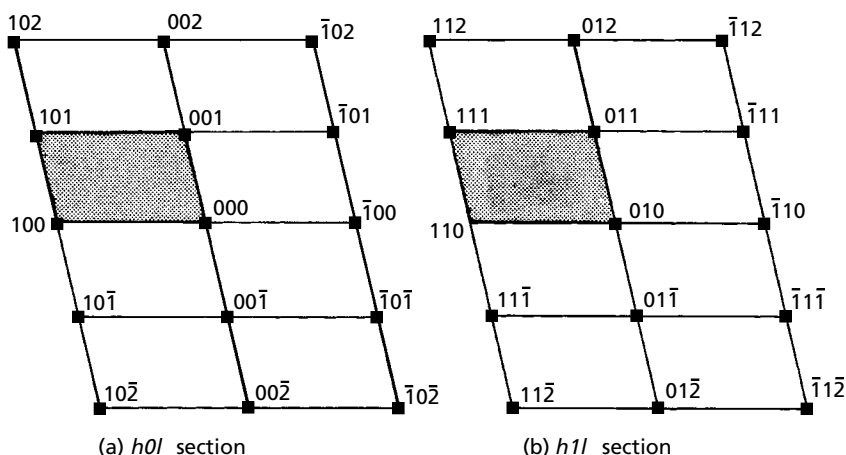


Fig. 6.5. Sections of a monoclinic reciprocal lattice perpendicular to the \mathbf{b}^* vector or y^* -axis, (a) $h0l$ section through the origin 000 , built up by simply extending the section in Fig. 6.4(c); (b) $h1l$ section (representing planes intersecting the y -axis at one lattice vector \mathbf{b}) 'one layer up' along the \mathbf{b}^* axis.

Note that \mathbf{a}^* and \mathbf{c}^* are *not* parallel to \mathbf{a} and \mathbf{c} , respectively, because the normals to the (100) and (001) planes in the monoclinic lattice are not parallel to \mathbf{a} and \mathbf{c} , respectively. Also the angle β^* between \mathbf{a}^* and \mathbf{c}^* is the complement of the angle β .

Figure 6.4(c) shows just part of the reciprocal lattice for the few planes we have labelled in Fig. 6.4(a). It can obviously be extended for many more planes and the reciprocal lattice points labelled by adding indices like coordinates, as is shown in Fig. 6.5(a), with the origin labelled 000 .

These ideas are readily extended to the third dimension; the \mathbf{b}^* vector is perpendicular to the plane of the paper, normal to the (010) planes which are parallel to the plane of the paper, i.e. in the monoclinic system \mathbf{b} is parallel to \mathbf{b}^* and the 010 reciprocal lattice point is 'one step above' 000 out of the plane of the paper. Similarly with all the other reciprocal lattice points whose k index is 1; the 011 reciprocal lattice point is 'one step above' 001 and so on. All these points form another layer, or section of the reciprocal lattice as shown in Fig. 6.5(b). Obviously we can build up as many sections of the reciprocal lattice, representing as many planes in the crystal, as we please; the 'ground floor' layer containing the $h0l$ reciprocal lattice points, the section one step along the \mathbf{b} axis (the 'first floor' layer) containing the $h1l$ reciprocal lattice points and so on.

Now, before expressing these ideas in vector notation, we can reflect on what we have already achieved. First, we are able to represent any set of planes in a crystal by a single reciprocal lattice point: consider how difficult and confusing it would be to have to draw very many different planes in crystal in the same way as in Figs 5.2 or 5.3! Second, the indices (strictly the Laue indices since they have common factors) are represented simply as coordinates of reciprocal lattice points.

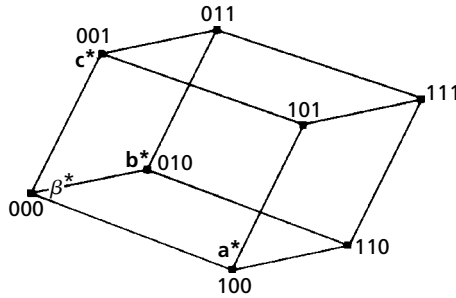


Fig. 6.6. The reciprocal lattice unit cell of a monoclinic *P* crystal defined by reciprocal lattice vectors \mathbf{a}^* , \mathbf{b}^* and \mathbf{c}^* . β^* is the angle between \mathbf{a}^* and \mathbf{c}^* .

In vector notation, the reciprocal lattice vectors can now be expressed in terms of their components of the reciprocal unit cell vectors \mathbf{a}^* , \mathbf{b}^* , \mathbf{c}^* . For example, for the (102) family of planes (Figs 6.4(b) and (c)) $\mathbf{d}_{102}^* = 1\mathbf{a}^* + 0\mathbf{b}^* + 2\mathbf{c}^*$, or, in general,

$$\mathbf{d}_{hkl}^* = h\mathbf{a}^* + k\mathbf{b}^* + l\mathbf{c}^*.$$

Hence, just as direction symbols $[uvw]$ are the components of a vector \mathbf{r}_{uvw} in direct space (Section 5.2), so also plane indices are the components of a vector \mathbf{d}_{hkl}^* in reciprocal space.

It is worth while rewriting these two equations once again to emphasize their importance and what might be called their symmetry:

$$\mathbf{r}_{uvw} = u\mathbf{a} + v\mathbf{b} + w\mathbf{c}$$

(direction symbols are simply the components of a direct lattice vector)

$$\mathbf{d}_{hkl}^* = h\mathbf{a}^* + k\mathbf{b}^* + l\mathbf{c}^*$$

(Laue indices are simply the components of a reciprocal lattice vector).

The reciprocal lattice unit cell of the monoclinic crystal is drawn in Fig. 6.6 in an orientation where the \mathbf{a}^* , \mathbf{b}^* and \mathbf{c}^* unit cell vectors and the reciprocal lattice points at the corners can be seen clearly. Notice that the idea of ‘layers’ of reciprocal lattice points applies (of course) to all orientations, for example the ‘bottom face’ of the cell contains the $hk0$ reciprocal lattice points, the ‘top face’, one step along \mathbf{c}^* contains the $hk1$ reciprocal lattice points—and so on.

6.4 Reciprocal lattice cells for cubic crystals

In crystals with orthogonal axes (cubic, tetragonal, orthorhombic) the reciprocal lattice vectors \mathbf{a}^* , \mathbf{b}^* , \mathbf{c}^* are parallel to \mathbf{a} , \mathbf{b} , \mathbf{c} , respectively. Hence we have the further identities that $\mathbf{a} \cdot \mathbf{b} = 0$, $\mathbf{a}^* \cdot \mathbf{b} = 0$, etc. The reciprocal lattice unit cell of a simple cubic crystal (cubic *P* lattice) is obviously a cube with reciprocal lattice points only at the corners. The reciprocal unit cells of the cubic *I* and cubic *F* lattices also have additional lattice points

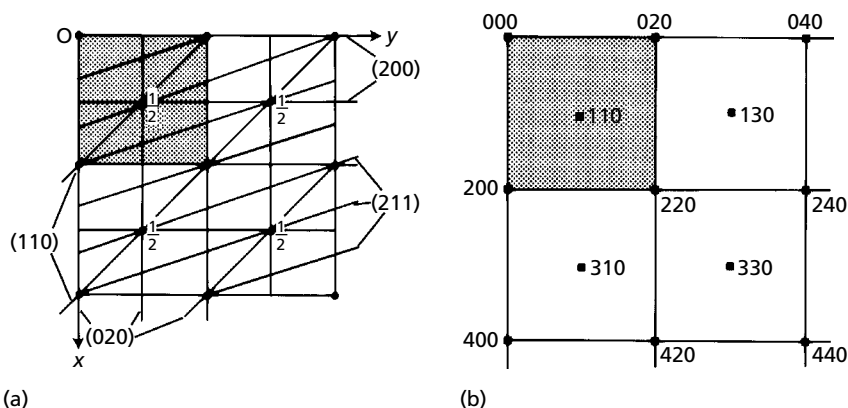


Fig. 6.7. (a) Plan of a cubic I crystal perpendicular to the z -axis and (b) pattern of reciprocal lattice points perpendicular to the z -axis. Note the cubic F arrangement of reciprocal lattice points in this plane.

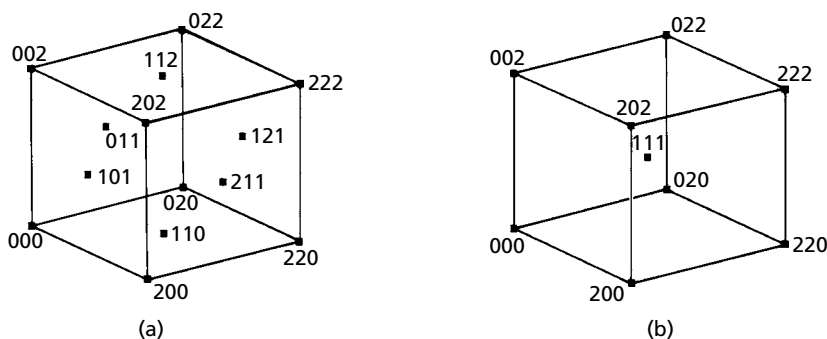


Fig. 6.8. (a) The cubic F reciprocal lattice unit cell of the cubic I (direct) lattice; (b) The cubic I reciprocal lattice cell of the cubic F (direct) lattice.

within the unit cells, i.e. they are also not primitive. This is illustrated for the case of the cubic I lattice in Fig. 6.7, which shows four unit cells with the z -axis perpendicular to the plane of the paper and the traces of several $hk0$ planes (parallel to the z -axis) sketched in. Notice (for example) that in the direction of the x -axis the first set of *lattice* planes encountered is not (100) but (200) because of the presence of the additional lattice points in the centres of the cells (see also Fig. 5.4). Hence the reciprocal lattice vector in this direction is equal to \mathbf{d}_{200}^* not \mathbf{d}_{100}^* ; similarly, in the direction of the y -axis it is \mathbf{d}_{020}^* . In the $[110]$ direction, however, the first set of lattice planes encountered is (110), which gives a reciprocal lattice point in the centre of the face of the cell and the second-order 220 reciprocal lattice point at the corner. Proceeding in this way we find that this section of the reciprocal lattice is *face-centred*. Repeating this procedure in the other sections gives a **face-centred cubic reciprocal lattice (cubic F)** (Fig. 6.8(a)) for the **body-centred cubic (direct) lattice (cubic I)**—the two are reciprocally related. In the same

way, we find that the reciprocal lattice of the face-centred cubic lattice is body-centred (Fig. 6.8(b)).

There is another way of looking at these reciprocal relationships. Recall that the cubic lattices may all be referred to rhombohedral axes (primitive cells) with axial angles at 60° (cubic F), 90° (cubic P), and 109.47° (cubic I) (Section 3.2, Fig. 3.2). The reciprocals of these cells are again rhombohedral cells with axial angles 109.47° (i.e. cubic I), 90° (i.e. cubic P) and 60° (i.e. cubic F), respectively.

Finally, just as we can define the environments around lattice points in terms of Voronoi polyhedra, or Wigner–Seitz cells (Section 3.4), so also can we define the environments around reciprocal lattice points in just the same way and in this case the polyhedra are called *Brillouin zones*. Brillouin zones are useful in describing the energy states of electrons in metallic crystals. For a cubic F crystal, for which the reciprocal lattice is cubic I , the first Brillouin zone is a truncated octahedron and for a cubic I crystal, for which the reciprocal lattice is cubic F , it is a rhombic dodecahedron (see Fig. 3.7(d) and (e) and Appendix 2).

6.5 Proofs of some geometrical relationships using reciprocal lattice vectors

Some useful geometrical relationships stated without proof in Chapter 5 can be proved very simply using the concept of the reciprocal lattice and an elementary knowledge of vector algebra (see Appendix 5). The results are summarized in Appendix 4.

6.5.1 Relationships between \mathbf{a} , \mathbf{b} , \mathbf{c} and \mathbf{a}^* , \mathbf{b}^* , \mathbf{c}^*

Consider, for example, \mathbf{c}^* (Fig. 6.4) and its relationships with \mathbf{a} , \mathbf{b} and \mathbf{c} , which are redrawn for clarity in Fig. 6.9. showing in addition the angle ϕ between \mathbf{c} and \mathbf{c}^* .

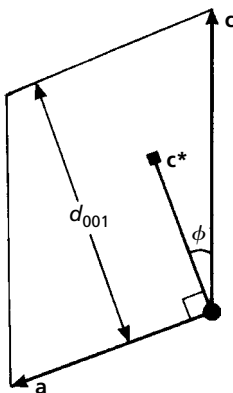


Fig. 6.9. Plan of a monoclinic unit cell perpendicular to the y -axis emphasizing the geometrical relationships between \mathbf{a} , \mathbf{c} and \mathbf{c}^* (see Fig. 6.4 and Section 6.5.1).

Since \mathbf{c}^* is perpendicular to both \mathbf{a} and \mathbf{b} , the scalar (or dot) products are zero, i.e. $\mathbf{c}^* \cdot \mathbf{a} = 0$, $\mathbf{c}^* \cdot \mathbf{b} = 0$ and similarly for \mathbf{a}^* and \mathbf{b}^* , i.e. $\mathbf{a}^* \cdot \mathbf{b} = 0$, $\mathbf{a}^* \cdot \mathbf{c} = 0$, $\mathbf{b}^* \cdot \mathbf{a} = 0$, $\mathbf{b}^* \cdot \mathbf{c} = 0$.

Now consider the scalar product $\mathbf{c} \cdot \mathbf{c}^* = c|\mathbf{c}^*| \cos \phi$. However, since $|\mathbf{c}^*| = 1/d_{001}$ by definition and $c \cos \phi = d_{001}$, then $\mathbf{c} \cdot \mathbf{c}^* = d_{001}/d_{001} = 1$ and similarly for $\mathbf{a} \cdot \mathbf{a}^* = 1$ and $\mathbf{b} \cdot \mathbf{b}^* = 1$.

6.5.2 The addition rule

This rule is simply based on the addition of reciprocal lattice vectors. For example (Fig. 6.4(b)), $\mathbf{d}_{102}^* = \mathbf{d}_{101}^* + \mathbf{d}_{001}^*$ or, in general,

$$\mathbf{d}_{(mh_1+nh_2)(mk_1+nk_2)(ml_1+ml_2)}^* = \mathbf{d}_{m(h_1k_1l_1)}^* + \mathbf{d}_{n(h_2k_2l_2)}^*.$$

6.5.3 The Weiss zone law or zone equation

If a plane (hkl) lies in a zone $[uvw]$, then \mathbf{d}_{hkl}^* is perpendicular to \mathbf{r}_{uvw} , i.e. $\mathbf{d}_{hkl}^* \cdot \mathbf{r}_{uvw} = 0$. Writing \mathbf{d}_{hkl}^* and \mathbf{r}_{uvw} in terms of their components,

$$(h\mathbf{a}^* + k\mathbf{b}^* + l\mathbf{c}^*) \cdot (u\mathbf{a} + v\mathbf{b} + w\mathbf{c}) = 0$$

Hence

$$hu + kv + lw = 0 \quad \text{because } \mathbf{a}^* \cdot \mathbf{a} = 1, \mathbf{a}^* \cdot \mathbf{b} = 0, \text{ etc.}$$

The zone law can be generalized as follows. Consider the condition for a lattice point with coordinates uvw (or with position vector \mathbf{r}_{uvw}) to lie in a lattice plane (hkl) (Fig. 6.10). For the lattice plane passing through the origin, \mathbf{r}_{uvw} is perpendicular to \mathbf{d}_{hkl}^* and hence $hu + kv + lw = 0$ as before. Now consider the n th lattice plane which lies at a perpendicular distance nd_{hkl} from the origin.

The condition for a lattice point to be in this plane is that the component of \mathbf{r}_{uvw} perpendicular to the planes should equal this distance; i.e. $\mathbf{r}_{uvw} \cdot \mathbf{i} = nd_{hkl}$ where \mathbf{i} is a unit vector perpendicular to the planes. Now, since by definition

$$\mathbf{i} = \frac{\mathbf{d}_{hkl}^*}{|\mathbf{d}_{hkl}^*|} = \mathbf{d}_{hkl}^* d_{hkl}$$

then

$$\mathbf{r}_{uvw} \cdot \mathbf{d}_{hkl}^* d_{hkl} = nd_{hkl};$$

hence

$$\mathbf{r}_{uvw} \cdot \mathbf{d}_{hkl}^* = n$$

and, substituting for \mathbf{r}_{uvw} and \mathbf{d}_{hkl}^* as before,

$$hu + kv + lw = n.$$

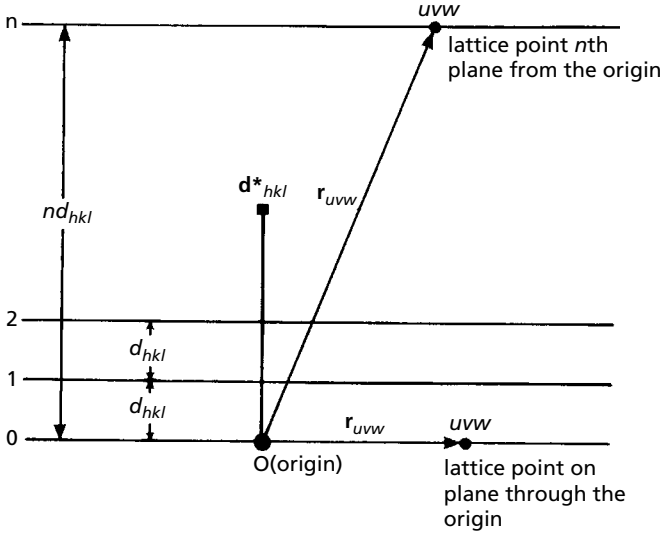


Fig. 6.10. Diagram representing the geometry of the (generalized) zone law. A set of hkl planes are drawn 'edge on'. When a lattice point uvw lies on a plane through the origin then $hu + kv + lw = 0$; when a lattice point lies on the n th plane from the origin then $hu + kv + lw = n$.

6.5.4 d -spacing of lattice planes (hkl)

Recalling (Appendix 5) that the scalar product of a vector multiplied by itself is the modulus squared:

$$\mathbf{d}_{hkl}^* \cdot \mathbf{d}_{hkl}^* = \frac{1}{d_{hkl}^2} = (h\mathbf{a}^* + k\mathbf{b}^* + l\mathbf{c}^*) \cdot (h\mathbf{a}^* + k\mathbf{b}^* + l\mathbf{c}^*).$$

Simple expressions are only obtained for crystals with orthogonal axes (orthorhombic, tetragonal, cubic) where $\mathbf{a}^* \cdot \mathbf{b}^* = 0$, etc., i.e. for orthorhombic crystals;

$$\frac{1}{d_{hkl}^2} = h\mathbf{a}^* \cdot \mathbf{a}^* + k\mathbf{b}^* \cdot \mathbf{b}^* + l\mathbf{c}^* \cdot \mathbf{c}^* = \frac{h^2}{a^2} + \frac{k^2}{b^2} + \frac{l^2}{c^2}$$

$$\text{since } \mathbf{a}^* \cdot \mathbf{a}^* = \frac{1}{a^2}, \text{ etc.}$$

6.5.5 Angle ρ between plane normals ($h_1k_1l_1$) and ($h_2k_2l_2$)

The angle ρ between two vectors \mathbf{a} and \mathbf{b} is given by (Appendix 5):

$$\cos \rho = \frac{\mathbf{a} \cdot \mathbf{b}}{ab}.$$

Hence:

$$\cos \rho = \frac{\mathbf{d}_{h_1 k_1 l_1}^* \cdot \mathbf{d}_{h_2 k_2 l_2}^*}{|\mathbf{d}_{h_1 k_1 l_1}^*| |\mathbf{d}_{h_2 k_2 l_2}^*|}.$$

Again, substituting in terms of components gives a simple expression only for cubic crystals.

6.5.6 Definition of \mathbf{a}^* , \mathbf{b}^* , \mathbf{c}^* in terms of \mathbf{a} , \mathbf{b} , \mathbf{c}

The volume of the unit cell V is given by $\mathbf{a} \cdot (\mathbf{b} \times \mathbf{c})$ (see Appendix 5). Now, as $(\mathbf{b} \times \mathbf{c})$ is a vector parallel to \mathbf{a}^* and of modulus equal to the area of the face of the unit cell defined by \mathbf{b} and \mathbf{c} , then $\mathbf{a}^* = (\mathbf{b} \times \mathbf{c})/V = (\mathbf{b} \times \mathbf{c})/\mathbf{a} \cdot (\mathbf{b} \times \mathbf{c})$, and similarly for \mathbf{b}^* and \mathbf{c}^* . \mathbf{a} , \mathbf{b} and \mathbf{c} can be defined in the same way, i.e. $\mathbf{a} = (\mathbf{b}^* \times \mathbf{c}^*)/V^*$, and similarly for \mathbf{b} and \mathbf{c} , where V^* is the volume of the reciprocal unit cell.

Hence to summarize:

$$\begin{aligned} \mathbf{a}^* &= \frac{\mathbf{b} \times \mathbf{c}}{V}, & \mathbf{b}^* &= \frac{\mathbf{c} \times \mathbf{a}}{V}, & \mathbf{c}^* &= \frac{\mathbf{a} \times \mathbf{b}}{V}, \\ \mathbf{a} &= \frac{\mathbf{b}^* \times \mathbf{c}^*}{V^*}, & \mathbf{b} &= \frac{\mathbf{c}^* \times \mathbf{a}^*}{V^*}, & \mathbf{c} &= \frac{\mathbf{a}^* \times \mathbf{b}^*}{V^*}. \end{aligned}$$

6.5.7 Zone axis at intersection of planes $(h_1 k_1 l_1)$ and $(h_2 k_2 l_2)$

The zone axis is defined by \mathbf{r}_{uvw} , the vector product of

$$\mathbf{d}_{h_1 k_1 l_1}^* \quad \text{and} \quad \mathbf{d}_{h_2 k_2 l_2}^*.$$

Substituting in terms of their components and remembering the identities $\mathbf{a} = (\mathbf{b}^* \times \mathbf{c}^*)/V^*$, etc., gives

$$u\mathbf{a} + v\mathbf{b} + w\mathbf{c} = \mathbf{a}(k_1 l_2 - k_2 l_1) + \mathbf{b}(l_1 h_2 - l_2 h_1) + \mathbf{c}(h_1 k_2 - h_2 k_1)$$

therefore (see Memogram, Section 5.6.2)

$$u = (k_1 l_2 - k_2 l_1); \quad v = (l_1 h_2 - l_2 h_1); \quad w = (h_1 k_2 - h_2 k_1).$$

6.5.8 A plane containing two directions $[u_1 v_1 w_1]$ and $[u_2 v_2 w_2]$

The plane is defined by \mathbf{d}_{hkl}^* , the vector product of $\mathbf{r}_{u_1 v_1 w_1}$ and $\mathbf{r}_{u_2 v_2 w_2}$. Proceeding as above gives (see Memogram, Section 5.6.3)

$$h = (v_1 w_2 - v_2 w_1); \quad k = (w_1 u_2 - w_2 u_1); \quad l = (u_1 v_2 - u_2 v_1).$$

6.6 Lattice planes and reciprocal lattice planes

Just as we have lattice planes passing through lattice points in the ‘direct’ lattice, so also we have planes (or layers) passing through reciprocal lattice points in the reciprocal

lattice. There is, as far as I know, no standard terminology to describe these reciprocal lattice planes or layers nor their spacings (unlike the familiar (hkl) and d_{hkl} for lattice planes) so I will call them $(uvw)^*$ reciprocal lattice planes with spacing r_{uvw}^* —the stars to indicate that they are planes and spacings in reciprocal space. In the case of X-ray diffraction, the reciprocal lattice planes correspond to the layer-lines of spots in oscillation photographs (Fig. 9.17) and in the case of electron diffraction they are called Laue zones—the plane or layer of reciprocal lattice points passing through the origin being called the zero order Laue zone; the next plane or layer ‘up’ from the origin being called the first order Laue zone, and so on (Fig. 11.1).

The spacings r_{uvw}^* of reciprocal lattice planes are defined in a precisely analogous way to that for the spacings of lattice planes, d_{hkl} , so we will write the equations side-by-side to emphasise their ‘symmetry’:

$$r_{uvw}^* = \frac{1}{|\mathbf{r}_{uvw}|} = \frac{1}{|u\mathbf{a} + v\mathbf{b} + w\mathbf{c}|} \quad d_{hkl} = \frac{1}{|\mathbf{d}_{hkl}^*|} = \frac{1}{|h\mathbf{a}^* + k\mathbf{b}^* + l\mathbf{c}^*|}.$$

In short, just as lattice planes (hkl) are, by definition, perpendicular to the reciprocal lattice vector \mathbf{d}_{hkl}^* and of reciprocal spacing, so also are reciprocal lattice planes $(uvw)^*$ perpendicular to the direct lattice vector \mathbf{r}_{uvw} and of reciprocal spacing.

These interrelationships are perhaps best understood by means of a particular example. Figure 6.11(a) shows a plan view (perpendicular to the c -axis) of an orthorhombic crystal. The unit cell, lightly shaded, is outlined by lattice vectors \mathbf{a} and \mathbf{b} . The traces of a particular set of lattice planes, (210) , are indicated by the long dashed lines together

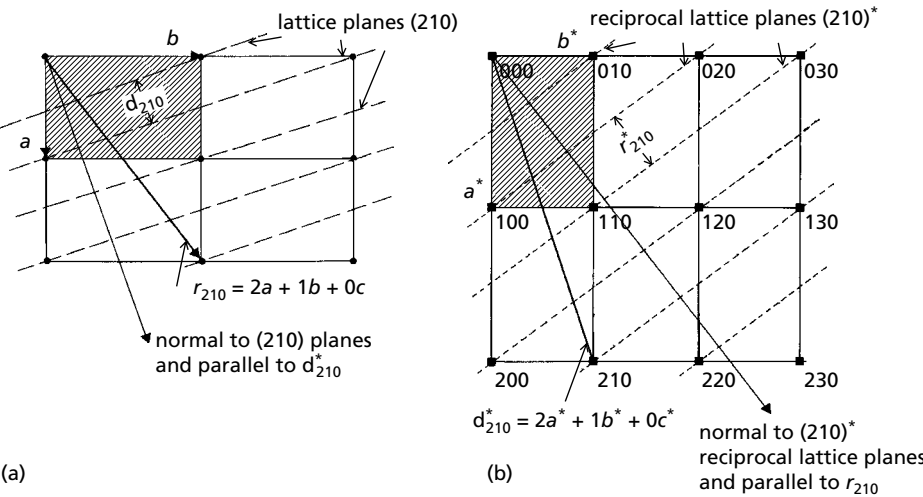


Fig. 6.11. (a) The (direct) lattice of a simple (primitive) orthorhombic crystal with the unit cell shaded, traces of the (210) lattice planes (long dashed lines) and their normal and the lattice vector \mathbf{r}_{210} . (b) The corresponding reciprocal lattice with the unit cell shaded, traces of the $(210)^*$ reciprocal lattice planes or layers (short dashed lines) and their normal (parallel to \mathbf{r}_{210}) and the reciprocal lattice vector \mathbf{d}_{210}^* (parallel to the normal to the lattice planes (210)).

with their normal and also the lattice vector $\mathbf{r}_{210} = (2\mathbf{a} + 1\mathbf{b} + 0\mathbf{c})$. Note that the normal to the lattice planes is *not* parallel to the direction $[210]$ (see Fig. 5.5).

Figure 6.11(b) shows the corresponding plan view of the reciprocal orthorhombic lattice, the unit cell, lightly shaded, being outlined by reciprocal lattice vectors \mathbf{a}^* and \mathbf{b}^* . (In this case, (orthogonal axes) \mathbf{a}^* is parallel to \mathbf{a} and \mathbf{b}^* is parallel to \mathbf{b} .) The traces of the reciprocal lattice planes $(210)^*$ are indicated by the short dashed lines together with their normal and also the reciprocal lattice vector $\mathbf{d}_{210}^* = (2\mathbf{a}^* + 1\mathbf{b}^* + 0\mathbf{c}^*)$. Note, by comparing the diagrams, that \mathbf{d}_{210}^* is (by definition) perpendicular to the lattice planes (210) and that \mathbf{r}_{210} is also (by definition) perpendicular to the reciprocal lattice planes $(210)^*$.

The Weiss zone law or zone equation (Section 6.5.3) also applies to reciprocal lattice planes: for the reciprocal lattice points (hkl) lying in the plane through the origin and perpendicular to the lattice vector \mathbf{r}_{uvw} :

$$hu + kv + lw = 0$$

and for the reciprocal lattice points lying in the n th reciprocal lattice plane from the origin:

$$hu + kv + lw = n.$$

You can easily ‘check’ these equations with reference to Fig. 6.11(b). For example, reciprocal lattice point (130) lies in the fifth plane in zone $[210]$ and $n = 1.2 + 3.1 + 0.0 = 5$. For crystals with orthogonal axes and primitive unit cells, the spacings d_{hkl} (of lattice planes) and the spacings r_{uvw}^* (of reciprocal lattice planes) may be readily calculated (see Section 6.5.4):

$$d_{hkl} = \frac{1}{|\mathbf{d}_{hkl}^*|} = \frac{1}{\sqrt{(h\mathbf{a}^*)^2 + (k\mathbf{b}^*)^2 + (l\mathbf{c}^*)^2}} = \frac{1}{\sqrt{\left(h/a\right)^2 + \left(k/b\right)^2 + \left(l/c\right)^2}}$$

$$r_{uvw}^* = \frac{1}{|\mathbf{r}_{uvw}|} = \frac{1}{\sqrt{(u\mathbf{a})^2 + (v\mathbf{b})^2 + (w\mathbf{c})^2}} = \frac{1}{\sqrt{(ua)^2 + (vb)^2 + (wc)^2}}.$$

For crystals with centred lattices, analogous conditions apply to the symbols $(uvw)^*$ for reciprocal lattice planes as they do to (hkl) for lattice planes. For example, for the cubic F lattice, for which the reciprocal lattice is cubic I (Section 6.4), $u + v + w =$ an even integer.

Now, having completed this chapter, you should feel as confident and familiar with the concept of reciprocal space as you do with direct space—for as we shall see in subsequent chapters, diffraction patterns reveal, or are imperfect images of, the reciprocal lattices of crystals.

6.7 Summary

In this chapter we have developed the reciprocal lattice as a purely geometrical exercise—as simply a method of representing the orientations and spacings of planes in a crystal

and from which the geometrical relationships between planes and directions may be easily worked out. But (as might be expected), the reciprocal lattice has a much greater significance than this. First of all we shall see (in Chapters 8, 9 and 11) how the reciprocal lattice may be used to interpret the geometry of X-ray and electron diffraction patterns. Then we shall see (in Chapters 9 and 10) that reciprocal lattice points may not be ‘points’ but have finite size and shape which is related to the size, shape and strain in ‘real’ (as opposed to ‘infinitely large perfect’) crystals.

Note In the field of electron diffraction reciprocal lattice vectors are often denoted by the symbol \mathbf{g}_{hkl} (no star) rather than \mathbf{d}_{hkl}^* .

Exercises

- 6.1 Derive the [0001] reciprocal lattice section for the hexagonal P lattice and [111] reciprocal lattice sections for the cubic I and cubic F lattices.
- 6.2 Derive expressions for $1/d_{hkl}$ and $\cos \rho$ for orthorhombic crystals.
- 6.3 Do the relationships derived in Section 6.4 apply also to non-cubic centred Bravais lattices and their reciprocal unit cells?
- 6.4 Calculate the reciprocal lattice plane spacing r_{210}^* of the $(210)^*$ planes in a simple cubic (cubic P) crystal of lattice parameter $a = 3\text{\AA}$.

The diffraction of light

7.1 Introduction

As introduced in Chapter 6, the reciprocal lattice is the basis upon which the geometry of X-ray and electron diffraction patterns can be most easily understood and, as we shall see in Chapters 8, 9 and 11, the electron diffraction patterns observed in the electron microscope, or the X-ray diffraction patterns recorded with a precession camera, are simply sections through the reciprocal lattice of a crystal—the pattern of spots on the screen or photographic film and the pattern of reciprocal lattice points in the corresponding plane or section through the crystal are identical.

This also applies to the diffraction of light from ‘two-dimensional crystals’ such as umbrella cloths, net window curtains and the like and in which the warp and weft of the cloth correspond in effect to intersecting lattice planes. The diffraction patterns which we see through umbrellas and curtains are, in effect, the two-dimensional reciprocal lattices of these two-dimensional lattices.

The important point to realize at the outset is that the reciprocal lattice is not merely an elegant geometrical abstraction, or a crystallographer’s way of formally representing lattice planes in crystals or two-dimensional nets, but that it is something we can ‘see for ourselves’. Indeed, in the case of light it is a familiar part of our everyday visual sensations. Furthermore, as explained in Section 7.2 below, when our eyes are relaxed and focused on infinity we see the patterns of spots and streaks around the lights from distant street lamps when viewed through umbrellas and net curtains, or the circles of haze around them on foggy nights quite clearly. Hence, it might be suggested that diffraction patterns constitute our first visual sensations, before we have learned to near-focus upon the world!

The familiarity and ease of demonstration is the main justification or reason for considering the diffraction of light, but there are three others. First, there is a geometrical analogy between light and electron diffraction: in both cases the wave-lengths (of light and electrons) are small in comparison with the spacings of the diffracting objects (the fibre separations in woven fabrics or the lattice spacings in crystals). For example, the wavelength of green light ($\sim 0.5\text{ }\mu\text{m}$) is about $500\times$ smaller than the fibre spacings in nets and fabrics ($\sim 0.25\text{ mm}$); similarly, the wavelength of electrons in a 100kV electron microscope ($\sim 4.0\text{ pm}$) is about $100\times$ smaller than the lattice spacings in crystals ($\sim 0.4\text{ nm}$). In both cases therefore (as explained in Sections 7.4 and 11.2) the diffraction angles are also small and electron diffraction patterns can, at least initially, be interpreted as sections through the reciprocal lattice of the crystal.

The geometry of X-ray diffraction patterns is rather more complicated because the wavelengths of X-rays (~ 0.2 nm) are roughly comparable with the lattice spacings in crystals. Hence the diffraction angles are large (Sections 8.2, 8.3, 8.4 and 9.5) and X-ray diffraction patterns are in a sense ‘distorted’ representations of the patterns of reciprocal lattice points from crystals, the nature of the ‘distortion’ depending upon the particular X-ray technique used.

The second reason for considering the diffraction of light is that it provides a simple basis or analogy for an understanding of how and why the **intensities** of X-ray diffraction beams vary (Section 9.1), **line broadening** and the occurrence of **satellite** reflections (Section 9.6). The analogy is provided by a consideration of the diffraction grating, which is, in effect, a one-dimensional crystal. There are three variables to consider in the diffraction of light from a diffraction grating—the line or slit spacing, the width of each slit and the total number of slits. The slit spacing corresponds to the lattice spacings in crystals and determines the directions of the diffracted beams, or, in short, the geometry of the diffraction patterns. The width of the slits determines, for each diffracted beam direction, the sum total of the interference of all the little Huygens’ wavelets which contribute to the total intensity of the light from each slit (Section 7.4), which is analogous to the sum total of the interference between all the diffracted beams from all the atoms in the motif. In short it is the lattice which determines the *geometry* of the pattern and the motif which determines the *intensities* of the X-ray diffracted beams. The analogy, however, must not be pressed too far because it takes no account of the dynamical interactions between diffracted beams, i.e. the interference effects arising from re-reflection (and re-re-reflection, etc.) of the direct and diffracted/reflected beams as they pass through a crystal. This desideratum is particularly important in the case of electron diffraction. Finally, the total number of slits in a diffraction grating determines the numbers and intensities of the satellite or subsidiary diffraction peaks each side of a main diffraction peak—the greater the number of slits, the greater the numbers and the smaller are the intensities of the satellite peaks. In most X-ray and electron diffraction situations the total number of diffracting planes is so large that satellite peaks are unobservable and of no importance, but in the case of X-ray diffraction from thin film multilayers, consisting not of thousands but only of tens or hundreds of layers, the numbers and intensities of the satellite peaks are important and useful.

Third, it is the diffraction of light which sets a limit, ‘the diffraction limit,’ to the resolving power or limit of resolution of optical instruments, in particular telescopes and microscopes, and is therefore of utmost importance to an understanding of how these instruments work. The diffraction limit however is not unsurmountable and it is an important characteristic of modern microscopical techniques—for example scanning tunnelling, atom force, or near field scanning optical microscopes—that they overcome this limit by virtue of the close approach of a fine probe to a specimen surface.

Finally, to generalize the point made in the first paragraph, the reciprocal relationship between an object and its diffraction pattern is formally expressed by what is known as a Fourier transform, which is a (mathematical) operation which transforms a function containing variables of one type (in our case distances in an object or *displacements*) into a function whose variables are reciprocals of the original type (in our

case $1/\text{displacements}$). The reciprocal lattices which we worked out in Chapter 6 using very simple geometry are, in fact, the Fourier transforms of the corresponding (real) lattices.

In this sense diffraction patterns may be described as ‘visual representations’ or ‘images’ of the Fourier transforms of objects—irrespective as to whether they are generated using light, X-rays or electrons. In the case of light, diffraction patterns are often described as the ‘optical transforms’ of the corresponding objects.

To summarize, in Section 7.4 we derive in a very simple way (emphasizing the physical principles involved) the form of the diffraction pattern of a grating: we consider the conditions for *constructive* interference between the slit separation a —which give us the angles of the principal maxima and then the conditions for *destructive* interference, both across a single slit, width d , and also across the whole grating, width $W = Na$ (where N = the number of slits)—which gives us the angles of the minima for a single slit and the minima between the principal and subsidiary maxima respectively. The analysis may be carried out more rigorously using *amplitude—phase diagrams* and this approach is covered separately in Chapter 13 (Section 13.3).

Finally, we show in Section 7.5 that it is diffraction which determines the limit of resolution of optical instruments—the telescope, microscope and of course the eye. Again, this subject is covered in greater depth, by means of Fourier analysis, in Section 13.4.

7.2 Simple observations of the diffraction of light

The diffraction of light is most easily demonstrated using a laser—the hand-held types which are designed to be used as ‘pointers’ on screens for lecturers are more than adequate and are relatively safe (but you should never look directly at the laser light). Many everyday objects may be used as ‘diffraction gratings’ either in transmission or reflection—fabrics, nets, stockings (transmission) or graduated metal rulers (reflection) and the resultant diffraction patterns may be projected on to a wall or screen. Such experiments will quickly make apparent the inverse or reciprocal relationships between the spacings of the nets, graduations, etc. and the spacings between the diffracted spots. For example, when laser light is reflected from a graduated metal scale or ruler, in addition to the mirror-reflected beam, diffracted beams will be observed on each side; the spacings of these will change as the angle of the surface of the ruler to the laser beam (and hence the apparent spacings between the graduations) is changed, but, more convincingly, when the beam is shifted from the ‘ $\frac{1}{2}$ mm’ to the ‘1 mm’ graduated regions of the ruler, the spacings of the diffraction spots are halved. However, it is probably better to begin with the familiar diffraction patterns which are obtained with a simple point source of light and a piece of fabric with an open weave and which moreover serve to emphasize some important ideas about the angular relationships between the diffracted beams. A point-source of light may in practice be a distant street lamp or, in order to conduct the experiments indoors, a mini torch bulb or a domestic light bulb placed behind a screen with a pinhole (or a fine needle hole) punched into it. Nylon net curtain material is an effective fabric to use—the filaments of nylon which make up the strands are tightly twisted giving sharply defined transparent/opaque boundaries.

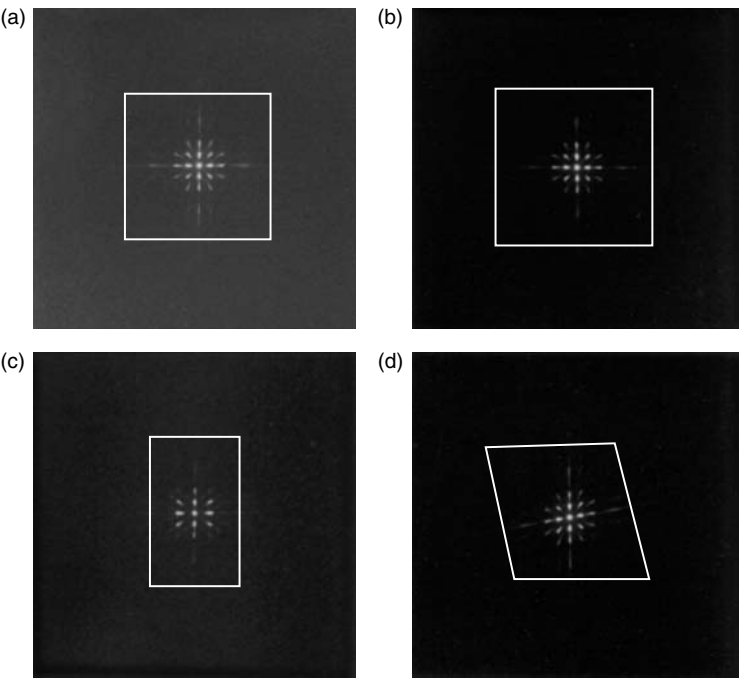


Fig. 7.1. (a) A diffraction pattern from a piece of net curtain with a square weave. The outline of the net is indicated by the white frame. Note that two rows of strong spots and the fainter spots forming a square grid diffraction pattern, (b) The diffraction pattern is identical in scale when the net is brought closer to the observer’s eye. (c) Rotating the net about a vertical axis reduces the effective spacing of the vertical lines of the weave, resulting in diffraction spots in the horizontal direction which are further apart. (d) Shearing or distorting the net such that the strands or lines are no longer at 90° to each other results in a diffraction pattern ‘sheared’ in the opposite sense—the rows of strong diffraction spots remain perpendicular to the lines of the net.

Observe the point source (which should be at least 5 m distant) through the net. The image of the point source will be seen to be repeated to form a grid (or reciprocal lattice) of diffraction spots (Fig. 7.1(a)). In general the spots are of greatest intensity, and are streaked, in directions perpendicular to the lines or strands of the net.

These familiar observations may be supplemented by two more. First the same pattern of spots is seen whether both, or only one, eye is used. Second the size of the pattern—the apparent spacings of the spots—is *independent* of the position of the net. The diffraction pattern appears to be unchanged, irrespective of whether the net is held away from, or close to the eyes (Fig. 7.1(b)).¹ These observations show that the diffraction spots or diffracted beams bear *fixed angular relationships* to the direct beam.

¹ If the light falling on the net is not parallel but is slightly diverging (i.e. the point source is not effectively at infinity), then the apparent spacing of the spots will change slightly as the net is held at different distances from the eyes.

The reciprocal relationship between the net and diffraction pattern may be demonstrated in two ways. First, a net with a finer line spacing will be found to give diffraction spots more widely spaced. If a finer net is not available, the effective spacing of the lines may be decreased by rotating the net such that it is no longer oriented perpendicular to the line of sight to the light (Fig. 7.1(c)). Secondly, the net may be twisted or sheared such that the strands—the weft and the warp—no longer lie in lines at 90° to each other. It will be seen that the rows of strong diffraction spots rotate in such a way that they continue to lie in directions perpendicular to the lines of the net—the grid of diffraction spots is reciprocally related to the sheared lattice (Fig. 7.1(d)).

These reciprocal relationships are analogous to those shown for a set of planes in a zone parallel to the y -axis in a monoclinic crystal (corresponding to the net, Fig. 6.4(a)) and its reciprocal lattice section (corresponding to the diffraction pattern, Fig. 6.4(c)).

The observation that the size of the pattern is independent of the position of the net, and that it is seen to be identical with both eyes, may be explained by reference to Fig. 7.2. The light from a point source radiates out in all directions, but if it is distant then that part incident upon the net is (approximately) parallel.

Figure 7.2 shows a parallel beam of light from a (distant) source with the net held away from the eye (Fig. 7.2(a)) and closer to the eye (Fig. 7.2(b)). One set of diffracted beams from the net is shown. Of all the direct light and diffracted light from the net, only a portion will enter the eye. The portion of the net from which the diffracted light entering the eye originates changes as the net is moved: the further the net is moved away from the eye the greater the contribution from its outer regions (compare Fig. 7.2(a) with

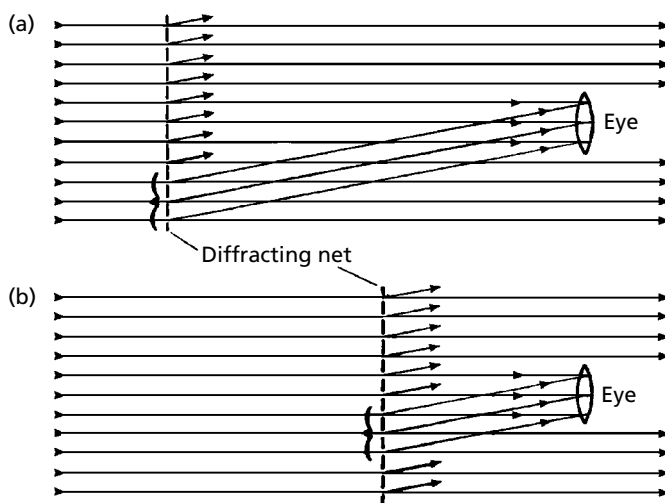


Fig. 7.2. (a) Parallel light (from a distant point source) falls on the net and is diffracted; only one set of diffracted beams is shown. The region of the net contributing to the diffracted light entering the eye of the observer is indicated by brackets, (b) As the net is moved towards the eye, the region of the net which contributes to the diffracted light entering the eye is different. The angular relationship between the direct and diffracted light at the eye remains unchanged.

Fig. 7.2(b)). However, for incident parallel light, irrespective of the position of the net, the angular relationship at the eye between the direct and diffracted beams, and hence the apparent size of the diffraction pattern, remains unchanged. And what is true for one eye is true for both eyes; you do not need to squint, or keep your head still: the diffraction pattern remains unchanged.

When using lasers to observe diffraction, a narrow, parallel beam of monochromatic light is available, as it were, ready made. Hence, unlike the previous situation, the diffraction pattern can be recorded on a screen because the diffracted beams all originate from the same small area of the net which is illuminated by the laser. (In the previous case, Fig. 7.2, because the diffracted beams originate from a large area of the net, they will correspondingly be ‘blurred out’ when they fall on a screen.) Only if most of the incident light is ‘blocked off’ such that only a small area of the net is exposed (or illuminated in the case of a laser) will a (faint) diffraction pattern be recorded. These points are best appreciated by ‘self-modifying’ Fig. 7.2. Remove the ‘eye’ and extend all the arrows showing the diffracted beams: notice how broad is the width of the total beam. Now ‘block off’ all the beams except those passing through a small (bracketed) area of the net and add a screen, in place of the eye, on the right. The direct and diffracted spots will be about equal to the area of the diffracting net (or the diameter of the laser beam), and their separation will increase the more distant is the screen.

The reciprocal relationship between the diffracting object and its diffraction pattern also extends to the shapes and sizes of the diffracting apertures (the ‘holes’ in the net) as well as their spacings. However, this is not easy to demonstrate simply without a laser carefully set up on an optical bench, with diffracting apertures of various shapes and sizes and appropriate lenses to focus the diffraction patterns (see Section 7.4 below).

Figure 7.3 shows a sequence of pinholes or apertures and the corresponding diffraction patterns using a laser as a coherent source of light (see Section 7.3). Figures 7.3(a)–(c) show the diffraction patterns (right) from the simplest apertures (left)—single pinholes of various sizes (which may be simply made by punching holes in thin aluminium foil and observing the diffraction pattern on a screen in a darkened room). The diffraction patterns consist of a central disc (of diameter greater than the geometrical shadow of the pinhole) surrounded by much fainter (and sometimes difficult to see) annuli or rings; notice that the diameters of the disc and rings decrease as the diameter of the aperture increases. Figure 7.3(d) shows the diffraction pattern (right) from a rectangular net or lattice (left) of 20 (4 by 5) of the smallest apertures. There are three things to notice about this net and its associated diffraction pattern. First, the reciprocal relationship between the unit cell of the net and that of the diffraction pattern (see also Fig. 7.1(c)); second the intensities of the diffraction spots which vary in the same way as the intensities of the central disc and rings from a single aperture (Fig. 7.3(a)), and third that there are faint spots, or subsidiary maxima, between the main diffraction spots. Finally, Fig. 7.3(e) shows the diffraction pattern (right) from a square net of many small apertures (left). The diffraction spots all lie within the region of the large central disc from a single small aperture and the subsidiary maxima between the main diffraction spots are no longer evident.

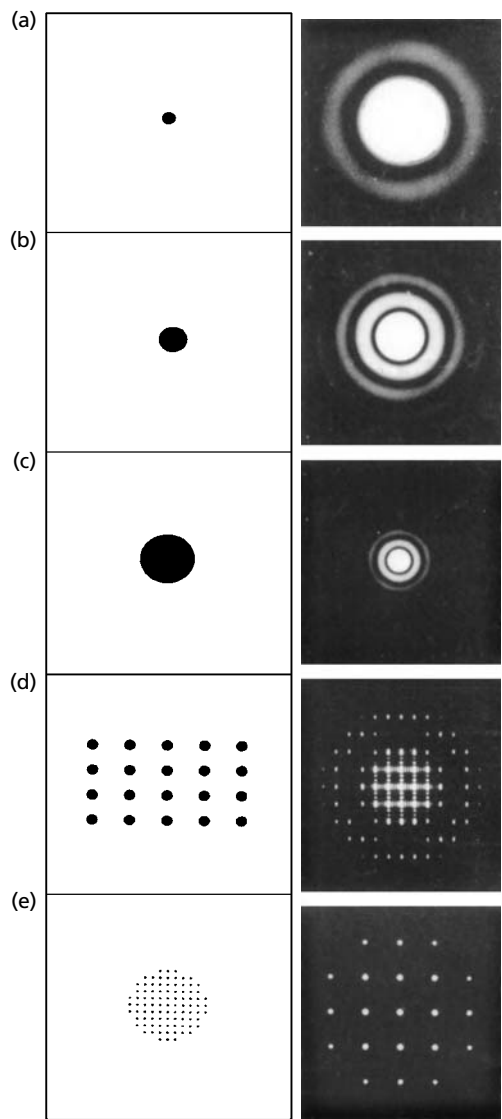


Fig. 7.3. Diffracting apertures (reproduced as black dots on a white background) (left) and their corresponding diffraction patterns (or optical transforms) (right) taken using a laser, (a), (b) and (c) show the diffraction patterns (Airy discs and surrounding haloes or rings) from circular apertures of increasing diameters, (d) shows the diffraction pattern from a 4×5 net of small apertures (as in (a)). Note the reciprocal relationship between the net and the diffraction pattern, the 2×3 number of subsidiary peaks in each direction and the overall variation in intensity of the diffraction pattern in accordance with that for a single aperture (a), (e) shows that for a net of many apertures the subsidiary maxima are not discernible. (From *Atlas of Optical Transforms* by G. Harburn, C. A. Taylor and T. R. Welberry, Bell and Hyman, 1983, an imprint of HarperCollins.)

7.3 The nature of light: coherence, scattering and interference

In the previous section we surveyed the phenomenon of diffraction: the pattern of beams which occur when light passes through pinholes and nets or is reflected from graduated rulers. We examined the conditions under which diffraction patterns can be observed either by looking at a point source of light through a net, or when using a laser, by projection onto a screen. Finally we observed the inverse or reciprocal relationship between the diffracting object and the diffraction pattern. All these observations need to be explained and given a quantitative basis (Section 7.4), but before doing so we need to know something of the nature of light itself and the notions of coherence, scattering and interference.

The nature of light is expressed through the ‘working models’ which seek to describe it. Physics provides us with two such models—light as ‘particles’ (photons or quanta) and light as waves. These working models are not contradictory or opposed; rather they express different aspects of the quantum-mechanical interpretation of light and matter. Visible light occupies a very small part of the whole spectrum of electromagnetic radiation, with a wavelength range from about 400 nm (violet-blue) to about 700 nm (red). In the range below we have ultraviolet ($\sim 400\text{ nm}$ – 1 nm), X-rays ($\sim 10\text{ nm}$ – 10 pm), and the very shortest, γ -rays ($\sim 10\text{ pm}$ – 10 fm). In the range above we have infrared ($\sim 700\text{ nm}$ – 1 mm), microwaves ($\sim 1\text{ mm}$ – 500 mm) and, the very longest, radio waves ($\sim 500\text{ mm}$ – 100 km).

Light (in common with all other electromagnetic radiation) has both wave-like and particle-like character which are linked by an equation of great simplicity—Planck’s equation: $E = hc/\lambda$, where E is the energy of the photon (a particle-like quantity), c is the velocity of light ($\sim 3 \times 10^8\text{ ms}^{-1}$), λ is the wavelength (a wave-like quantity) and h is the Planck constant ($6.6256 \times 10^{-34}\text{ J s}$). Notice that the smaller is the wavelength, the higher is the energy of the photon—a matter of great physiological and practical importance: we are all continuously bathed in radio waves with no ill effects, but a short exposure to X-rays or γ -rays results in severe damage to our body tissues. Light obviously occupies an important niche in between.

Matter—electrons, protons, particles of any sort—also has wave-like as well as particle-like character, which are similarly linked by de Broglie’s equation, $\lambda = h/mv$, where m and v are the mass and velocity of the particle respectively and λ is the wavelength. As before, the ‘linking constant’ between the particle-like and wave-like character is h , the Planck constant.

The notion that light has both particle-like and wave-like character reaches back to the seventeenth century and the work of Isaac Newton* and Christiaan Huygens*. Newton has been represented as the advocate of the particle or ‘corpuscular’ theory of light and Huygens the advocate of the wave theory of light. Certainly Huygens’ simple and elegant interpretation of reflection and refraction in terms of wavefronts made up of the envelopes of secondary waves or wavelets, which was taken up and extended by Thomas Young* and Augustin Jean Fresnel* early in the nineteenth century, has been far more

* Denotes biographical notes available in Appendix 3.

fruitful than Newton's corpuscular theory. However, it is clear from his own writings that Newton himself was undecided. In his great work *Opticks* there are a number of *Queries* which represent his reflections on his life's work on the properties of light. In Query 13 he asks:

Do not several sorts of Rays make Vibrations of several bignesses, which according to their bignesses excite Sensations of several Colours?

and in Query 17:

considering the lastingness of Motions excited in the bottom of the Eye by Light, are they not of a vibrating nature?

Light originates from the transitions of electrons which occur within excited atoms, excited by virtue of being at a high temperature, as in lamp filaments and the Sun, or by stimulated emission, as in a laser. The physics of the processes in either case does not concern us; the important point is that each atom emits a wavetrain for a period of time (about 10^{-8} s for lamp filaments; or from about 10^{-12} s for pulsed lasers to indefinite times for continuous lasers). In the former cases the wave is therefore not infinite in extent, but begins and ends, like a group of ripples moving outward from a point where a stone has been thrown into a pond. It is called a *wavetrain* or a *photon*, so leading back, in a sense, to the corpuscles of Newton. The length of each wavetrain depends on the velocity of light, 3×10^8 ms⁻¹ in air, and the period of emission; for lamp filaments a wavetrain is typically about 3 m long (3×10^8 ms⁻¹ $\times 10^{-8}$ s) and for lasers from about 0.3 mm long (3×10^8 ms⁻¹ $\times 10^{-12}$ s) to much longer lengths (for 'continuous' lasers).

For lamp filaments there are, in general, no phase relationships between the individual wavetrains; they overlap and follow on each other's heels without any registration between the individual 'peaks' and 'troughs'. Furthermore, the vibration directions of each wavetrain will be more or less random—and the light is said to be **natural** or **unpolarized**.

Light from an extended source is said to be **incoherent**. Interference will occur spasmodically as it were, between the peaks and troughs of adjacent similarly polarized wavetrains, but the net effect is zero. Coherence, the condition which gives rise to clearly defined diffraction beams, is only achieved by a point source, a small part of an extended source (which condition is fulfilled by the distant street lamp) or by a laser. The condition for coherence may be illustrated by an example. Consider a distant light source shining on two slits (or pinholes). Figure 7.4 shows the arrangement with a point source, a wavetrain 'on its way' and at its arrival *at the same time* at the slits. The slits, in turn, will act as secondary waves or sources of light according to Huygens' construction—the peaks and troughs of the waves being 'in step' with each other. As the waves spread out they meet and interfere—where peak meets peak or trough meets trough we have reinforcement or constructive interference, and where peak meets trough we have cancellation or destructive interference. In Section 7.4 we shall determine the particular angles or directions in which constructive and destructive interference occur. The important point to note now is that the geometrical conditions for interference which apply to just *one* wavetrain apply to *all* the wavetrains, and the resultant pattern of light and dark on the screen is the diffraction pattern. The words 'diffraction pattern' are a very inadequate description of the physical processes which are involved and the words or

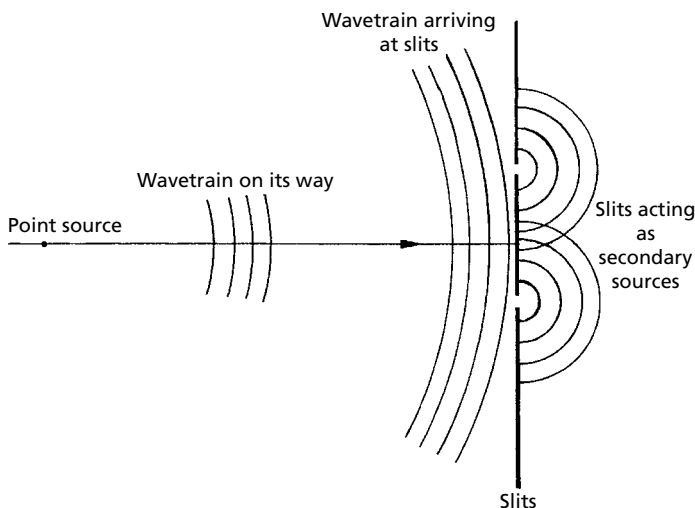


Fig. 7.4. A diagram of a distant light source emitting coherent wavetrains. When one of these strikes a screen which has adjacent slits, the slits act as secondary sources of light according to Huygens' construction, which then meet and interfere (from *Qualitative Polarized Light Microscopy* by P. C. Robinson and S. Bradbury, Oxford University Press/Royal Microscopical Society, 1992).

phrase 'diffraction (or scattering)-followed-by-interference-between-the-diffracted (or scattered)-beams-pattern' would be more accurate, albeit rather long-winded!

Now consider the situation when the slits are illuminated by separate light sources, or by an extended source. *Separate* sets of wavetrains from different parts of the source will arrive independently at the slits and thus the secondary waves emanating from each slit will bear no relationship with each other. To be sure, when 'peak meets peak' constructive interference will occur and where 'peak meets trough' destructive interference will occur—but these effects will be quite random in space and will cancel out: the light in this situation is said to be *incoherent*. Laser light, by contrast, is highly coherent.

7.4 Analysis of the geometry of diffraction patterns from gratings and nets

We will now analyse the diffraction phenomena described in Section 7.1 by considering the constructive and destructive interference conditions for all the scattered waves which emerge from nets and apertures of different sizes, shapes and spacings. We will do this step-by-step by first considering diffraction from a grating, which consists of a set of parallel lines engraved or photographed on to a glass or a polished metal plate. Diffraction occurs when light passes through the transparent 'slits' between the lines, or when it is reflected from the metal 'strips'. The constructive and destructive interference conditions in each case are identical, but it is much easier to draw the transmission case because the incident and diffracted beams do not overlap. This situation is analogous to the ray diagrams used in light microscopy; it is simpler to demonstrate image formation in

transmitted light microscopy by showing light passing from the condenser and through the specimen and objective lens to the eyepiece rather than light passing in two directions through the condenser/objective lens as it is reflected from the specimen as in reflected light microscopy.

The conditions for constructive/destructive interference from a set of parallel slits will, fairly obviously (ignoring end effects), be the same all along their length and the diffraction pattern will be a series of light/dark bands (corresponding to constructive and destructive interference conditions, respectively) running parallel to the slits. A net may be regarded as a two-dimensional grating, with a criss-cross pattern of slits, or two gratings superimposed upon each other with their slits running in different directions. Each grating will give rise to its own diffraction pattern of light/dark bands, but the net effect is that constructive interference will only occur when the light bands intersect and reinforce—giving rise to the observed diffraction peaks or spots. Hence, consideration of the, in effect, ‘one-dimensional diffraction’ case of a grating will lead us to a complete analysis of the ‘two-dimensional diffraction’ case of a net.

First we will consider diffraction from a grating made up of very narrow or thin slits spaced distance a apart in which each slit is the source of just one Huygens’ wavelet across its width; from this we will determine the conditions for constructive interference and therefore the directions of the diffracted beams. By simply extending the analysis to two dimensions we will demonstrate the reciprocal relationship between the diffracting net and the positions of the spots in the diffraction pattern. Then we shall consider diffraction from a wide aperture—a circular hole or wide slit which is the source of not one but many Huygens’ wavelets and we shall see that this modifies the intensities, but does not change the positions, of the diffracted spots. Finally we shall consider gratings or nets of limited extent and will show how this leads to the occurrence of subsidiary peaks or spots.

Figure 7.5 shows just part of a diffraction grating—a one-dimensional net—consisting of many narrow slits distance a apart. The incident light is shown as parallel beams from

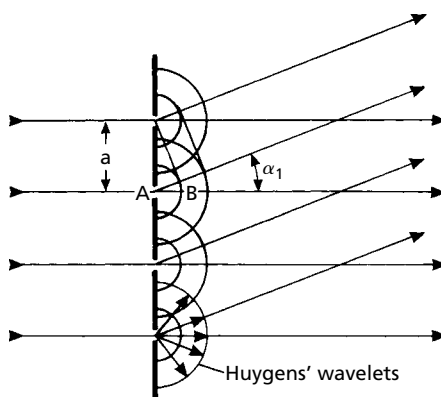


Fig. 7.5. A set of lines in the net acts as a diffraction grating, each slit acting as the source of a single set of Huygens’ wavelets. The diffracted beam is drawn for a path difference of one wavelength.

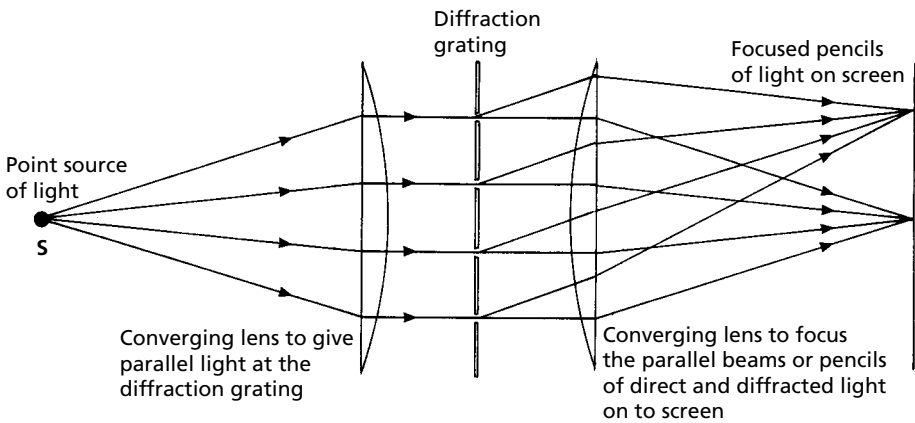


Fig. 7.6. A plane wavefront (parallel light) incident upon a grating may be achieved by inserting a lens (left) with the point source at its focus. Conversely, the parallel ‘pencils’ of the direct and diffracted light may be sharply focused onto a screen or photographic plate by inserting another lens (right). (Compare with Fig. 7.5.)

a distant source (i.e. a plane wavefront). This special case is sometimes called the case of Fraunhofer* diffraction as opposed to the case of Fresnel* diffraction in which the source is not distant and the wavefront is an arc, as shown in Fig. 7.4. Of course they are not different ‘types’ of diffraction, it is simply that Fraunhofer diffraction is simpler to treat mathematically. However, Fresnel diffraction may in practice be ‘converted’ to Fraunhofer diffraction by inserting a converging (positive) lens into the light beam with the point source at its focus and from which of course emerges parallel light (Fig. 7.6).

Each narrow slit (Fig. 7.5) acts as a *single* source of Huygens’ wavelets spreading out in all directions. Constructive interference occurs in those directions where the path difference (AB) between adjacent slits equals a whole number of wavelengths, i.e.

$$AB = n\lambda = a \sin \alpha_n$$

where a = the line (or lattice) spacing and α_n = the diffracted angle for the n th order diffracted beam. Since $\lambda \approx 0.5 \mu\text{m}$ and typically $a \approx 0.5\text{--}2 \text{ mm}$, then, as pointed out in Section 7.1, the diffraction angles are small (because $a \gg \lambda$) and $\sin \alpha_n \approx \alpha_n$. Hence, for the first few visible diffraction orders $AB = n\lambda = a\alpha_n$, from which the angle $\alpha_n = n\lambda/a$: here we have the reciprocal relationship between the diffraction angles, α_n , and lattice spacing, a .

The screen on which the diffracted beams fall (not shown in Fig. 7.5) should be a long distance from the grating compared with its width—and of course the further it is away the greater is the separation between the beams. This may, in practice, be rather inconvenient, but the inconvenience may be overcome by placing a converging (positive)

* Denotes biographical notes available in Appendix 3.

lens after the grating and placing the screen at its focal point such that the ‘pencils’ or parallel light of the direct and diffracted beams are sharply focused there (Fig. 7.6). The presence of such a lens does not modify in any way our understanding of the diffraction and interference phenomena at the grating and is best ‘left out’ of diagrams because it may appear to complicate the ray paths unnecessarily.

Figure 7.7(a) shows diagrammatically the diffraction pattern from such a grating—a central maximum or peak with the first, second, third order, etc. diffracted beams each

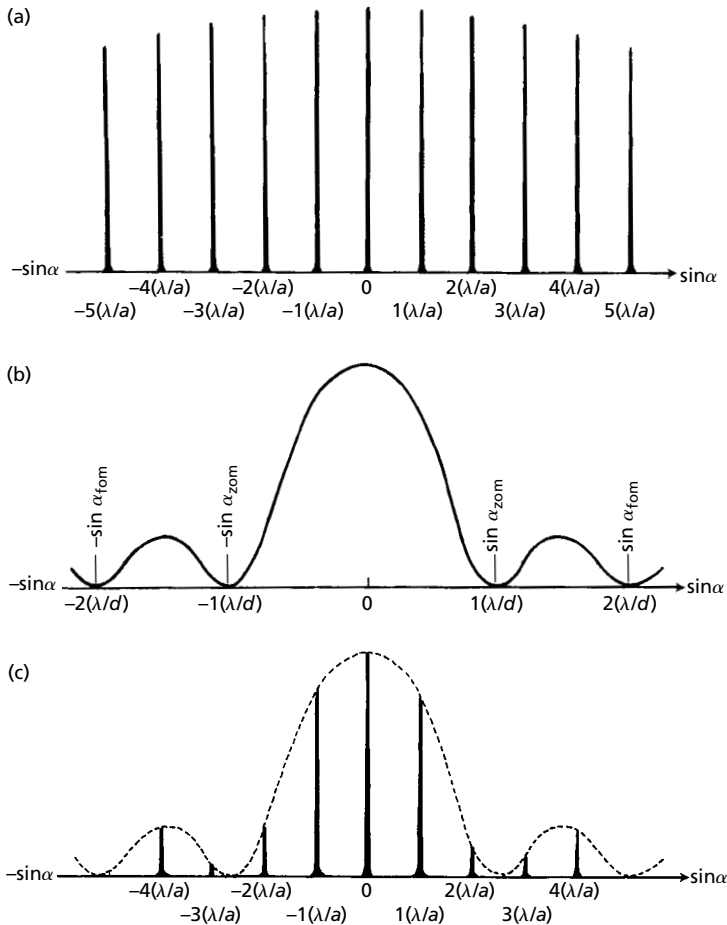


Fig. 7.7. Diagrams of the diffraction patterns from gratings and a single slit as a function of angle α ; the intensities of the peaks are represented only qualitatively. (a) The diffracted beams for a narrow-slit grating of spacing a . Constructive interference occurs at $\sin \alpha_n$ angles of $\pm n(\lambda/a)$ where n = the order of the diffracted beams ($n = 0$ represents the direct beam), (b) The diffraction profile for a single slit of width d . Destructive interference occurs at $\sin \alpha$ angles $1(\lambda/d)$ (zero order minimum), $2(\lambda/d)$ (first order minimum), etc. (c) For a wide-slit grating (slit-width d , slit spacing a) the intensities of the diffracted beams Fig. 7.7(a) are modulated by the intensity profile for a single slit Fig. 7.7(b).

side. Their intensity decreases because as the angle α_n increases the screen is further away from the diffraction grating.

This analysis of diffraction from a grating—a one-dimensional net—may readily be extended to the other set of lines in the net spaced, say, distance b apart, giving a second set of diffracted beams whose diffraction angles are again reciprocally related to b , the observed diffraction spots forming, as stressed before, the two-dimensional reciprocal lattice of the two-dimensional net (Figs 7.1(c) and 7.3(d) and (e)).

Now, the practical requirements for narrow slits which are the source of just one Huygens' wavelet are difficult if not impossible to achieve. Not only must the slit width be a small fraction of the wavelength of light, but it must also be equally thin—otherwise it will be, in effect, not a slit but a little rectangular tunnel—rather like the narrow openings in castle walls! Furthermore, the narrower (and thinner) are the slits, the smaller is the intensity of light.

In practice, therefore, slits are wide, which means that they are the source of many Huygens' wavelets, as shown in Fig. 7.8(a). The problem now is to sum all the contributions of all the wavelets. This may be carried out analytically or graphically by means of amplitude-phase diagrams, which are explained in Chapter 13 (Section 13.3). However, we shall use a simplified approach, which is quite adequate and emphasizes the principles involved.

In the forward (direct beam) direction, all the wavelets are in phase and interfere constructively. At increasing angles to the direct beam the wavelets become progressively

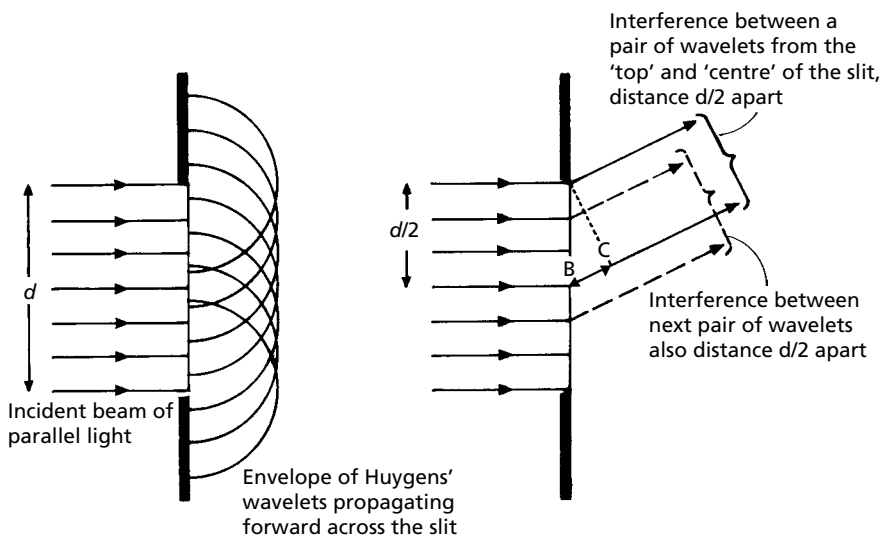


Fig. 7.8. Showing (a) a wide slit as the source of many Huygens' wavelets (shown propagating in the forward direction) and (b) the condition for destructive interference for the zero order peak. For the pair of wavelets separated by distance $d/2$ —one at the 'top' edge and one at the 'centre' of the slit (shown bracketed)—destructive interference occurs when the path difference $BC = \lambda/2$. Similarly for the next pair down (indicated by dashed lines and brackets), and so on for pairs of wavelets across the whole slit.

more out of step; they begin to interfere destructively and the intensity falls: we need to work out the angle at which it falls to zero. Now consider a pair of wavelets; one wavelet at the ‘top edge’ of the slit and the other at the centre of the slit (Fig. 7.8(b)); when the path difference between them is $\lambda/2$ ‘trough meets peak’ and total destructive interference occurs. Hence from Fig. 7.8(b),

$$BC = \lambda/2 = d/2 \sin \alpha_{\text{zom}}$$

i.e.

$$\lambda = d \sin \alpha_{\text{zom}}$$

where d is the slit width and α_{zom} is the angle at which total destructive interference of the direct (zero order) peak occurs, i.e. zero order *minimum*, α_{zom} .

Now consider the next pair of wavelets again distance $d/2$ apart, one just below that at the top edge and one just below that at the centre, as shown by dashed lines in Fig. 7.8(b). The condition for destructive interference between this pair of wavelets will be the same—and so on for all the pairs of wavelets across the whole slit. Hence the above condition for total destructive interference applies to the *whole* slit and gives the angle at which the intensity of the direct or zero order beam or the ‘central maximum’ falls to zero. Notice that the equation ‘looks’ the same as that for constructive interference *between* the slits; the difference is of course that in the former case only two Huygens’ wavelets needed to be considered, one from each slit.

As the angle increases further there will be some net constructive interference, giving a first order diffracted beam but of much smaller intensity than the zero order beam. The next condition for total destructive interference may be found by again considering the condition for destructive interference between a pair of wavelets, one wavelet at the ‘top edge’ of the slit as before and the other a *quarter* of the slit width from the top. Again, when the path difference between them is $\lambda/2$, destructive interference occurs. Continuing as before, i.e. considering pairs of such wavelets across the whole slit width, it is seen that this is again the condition for total destructive interference of all the wavelets across the slit, i.e. for the first order zero or minimum

$$\lambda/2 = (d/4) \sin \alpha_{\text{fom}}, \quad \text{i.e. } 2\lambda = d \sin \alpha_{\text{fom}}$$

where α_{fom} is the angle for first order destructive interference (*first order minimum* α_{fom}). Note that $\sin \alpha_{\text{fom}} = 2(\lambda/d) = 2 \sin \alpha_{\text{zom}}$, i.e. for small angles where $\sin \alpha \approx \alpha$, the first order minimum occurs at twice the angle of the zero order minimum.²

The diffraction pattern from a single slit is therefore a central maximum with much fainter bands of half the width of the central maximum on each side. It is represented diagrammatically in Fig. 7.7(b). The diffraction pattern from a circular hole or aperture

² The angle for maximum *constructive* interference for the first order diffracted beam cannot be determined precisely by such a simple approach as we have used. It turns out that the peak is slightly asymmetrical—the peak does not lie at an angle half way between α_{zom} and α_{fom} but is displaced slightly to a lower angle (see Section 13.3).

is, correspondingly, a central disc surrounded by much fainter rings or haloes, as shown in Figs 7.3(a)–(c). The disc is called the Airy disc because its diameter was worked out precisely by Sir George Airy.* His calculation for the angle α_{zom} of the zero order minimum, which takes into account the circular symmetry of a round hole or aperture, only differs from our simple calculation by a factor of 1.22, i.e. $1.22\lambda = d \sin \alpha_{\text{zom}}$. A close approximation to the Airy factor can be obtained by comparing the diffraction pattern from a circular aperture diameter d , to a rectangular aperture of the same area, one side of which is length d and the other side of length $\pi/4 d$. In comparison with the circular aperture, the narrower rectangular aperture gives rise to an Airy disc which is wider in the reciprocal ratio, i.e. $4/\pi = 1.27$ —a value which is only 4% different from the Airy factor 1.22. The Airy disc is of immense importance in optics since it determines the limit of resolution of telescopes and microscopes, as explained in Section 7.5.

Now we have to consider the diffraction patterns from a grating with wide slits (width d) separated a distance a apart. The result is simply the combination of the narrow-slit diffraction pattern (Fig. 7.7(a)) and the single wide-slit diffraction pattern (Fig. 7.7(b)). The resultant is shown in Fig. 7.7(c). Notice that the angles at which the diffraction peaks occur are unchanged and are determined solely by the slit spacing a , but that their intensities are modulated by the intensity profile of a single slit of width d .

Finally, we have to consider the situation in which the diffraction grating is of limited extent, consisting of a limited number of slits. If W is the width of the grating and N is the number of slits, then $W = Na$. We simply consider the whole grating as a very wide slit, then work out the conditions for destructive interference as before. The sines of the angles are simply

$$1(\lambda/W), 2(\lambda/W), 3(\lambda/W), \dots \quad \text{or} \quad \frac{1}{N}(\lambda/a), \frac{2}{N}(\lambda/a), \frac{3}{N}(\lambda/a) \dots$$

Each of the diffracted peaks or ‘principal maxima’ will no longer be ‘sharp’, as indicated in Figs 7.7(a) and (c), but will be broadened and surrounded by fringes or ‘subsidiary maxima’. The number of fringes increases with N and their intensities decrease with N , such that they are generally not detectable for large N values.

Figure 7.9 shows the zero, first and second order principal maxima and the subsidiary maxima from a grating with N slits. Note that the (half) angular widths of the principal maxima, and the angular widths of the subsidiary maxima, are simply equal to $1/N$ of the angular separation of the principal maxima. This leads to the simple result that there are $(N-2)$ subsidiary maxima between the principal maxima, as shown in Fig. 7.9. The proof is as follows. The first minimum of the zero order principal maximum (the direct beam) occurs at angle $1/N(\lambda/a)$, the second minimum at $2/N(\lambda/a)$ and so on. Altogether therefore, going from the zero to the first order principal maximum which occurs at angle $1(\lambda/a)$, there will be $(N-1)$ subsidiary minima, the $(N-1)$ th minimum defining, in effect, the first minimum of the first order principal maximum. Hence, between the $(N-1)$ minima there will be $(N-2)$ subsidiary maxima.

* Denotes biographical notes available in Appendix 3.

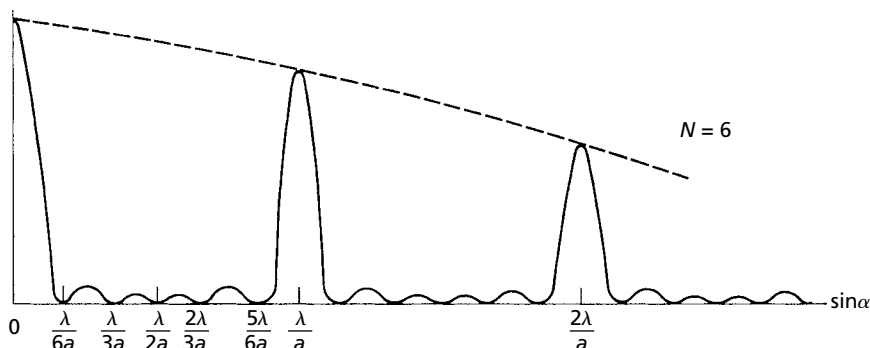


Fig. 7.9. Diagram of the diffraction pattern from a grating (drawn on one side of the direct beam) consisting of N narrow slits of spacing a . Between the principal maxima there are $(N - 2)$ subsidiary maxima or fringes. The diagram is drawn for $N = 6$. The dashed line shows the intensity profile for a single narrow slit (modified from *Optics* by E. Hecht and A. Zajac, Addison-Wesley, 1980).

Figure 7.9 is drawn for $N = 6$ and shows the principal maxima at $\sin \alpha$ angles $1(\lambda/a)$, $2(\lambda/a)$, the subsidiary minima at $\sin \alpha$ angles $1/6(\lambda/a)$, $2/6(\lambda/a)$, $3/6(\lambda/a)$, $4/6(\lambda/a)$ and $5/6(\lambda/a)$ and the $(N - 2) = 4$ subsidiary maxima.

All these considerations—the sizes and numbers of diffracting apertures—may be extended to the two-dimensional case of nets, as shown in Figs 7.3(d) and (e). The intensities of the diffraction peaks are modulated by the intensity profiles of the Airy disc and its surrounding fainter rings or haloes and the numbers of subsidiary maxima between the principal maxima are two less than the number of apertures in each direction—and clearly will become insignificant as the number of apertures becomes large. Hence, although we have not determined quantitatively the light intensity distribution in the diffraction patterns from nets, the main features that we noted in Section 7.2 are now explained.

7.5 The resolving power of optical instruments: the telescope, camera, microscope and the eye

One of the most important and useful applications of the study of diffraction is the determination of the resolving power of optical instruments, in particular the telescope and the microscope. By resolving power we mean the ability to distinguish points with small angular separations, such as stars in the telescope, or points which are small distances apart as in the microscope. In both cases the customary term *resolving power* is better expressed by the more precise term *limit of resolution*; either an angular limit of resolution as in the telescope or a distance limit of resolution as in the microscope. In either case the resolving power is a term reciprocally related to the limit of resolution.

There are several other factors which determine the limit of resolution of optical instruments, in particular lens defects, such as spherical and chromatic aberration, and coma. To a large extent these can be eliminated by appropriate lens design or the use of reflecting elements: mirrors have almost wholly replaced lenses as the principal element

in astronomical telescopes and, except for the difficulties in manufacture, could partially replace objective lenses in microscopes. But the limit of resolution is ultimately limited by diffraction—either at the aperture of the telescope or microscope or at closely spaced features in the microscope.

Consider first the limit of resolution of a telescope. Parallel rays from a distant point source—a star—enter the aperture, diameter d , and are focused by the objective lens on to a screen, photographic plate or the focal plane of the eyepiece. As explained in Section 7.4, the image of the distant point source is not a point, but an Airy disc (surrounded by haloes of decreasing intensity), as shown in Figs 7.3(a)–(c) and Fig. 7.10. Now consider light from another star; again its image is an Airy disc, as also shown in Fig. 7.10. The net intensity in the image plane is the sum of the intensities of the two discs (and their haloes). As the angular separation between the stars decreases their Airy discs overlap and the limit of resolution is the point at which the net intensity does not show

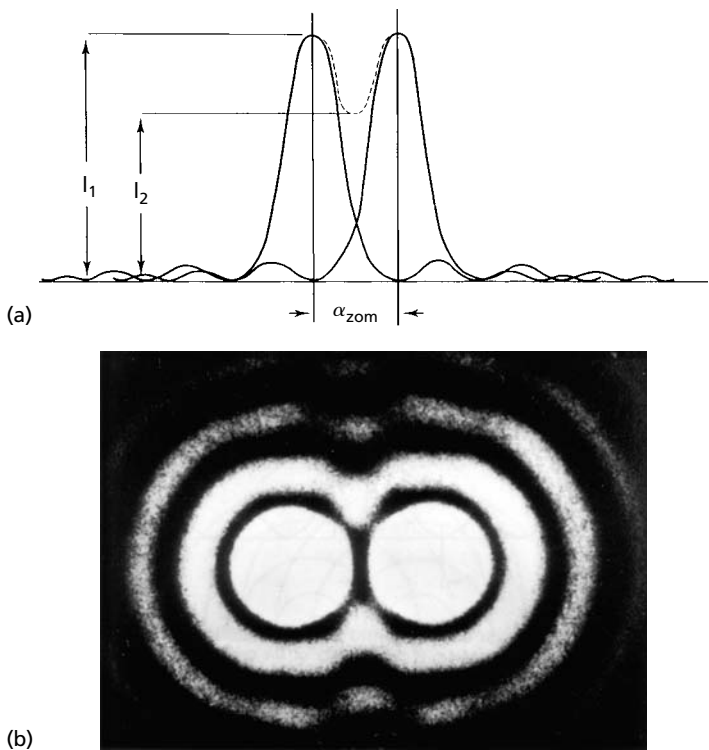


Fig. 7.10. (a) The intensity profile of an Airy disc pattern of two points separated by an angle which just satisfies the Rayleigh criterion for resolution. (Note that the centre of one disc falls on the zero order minimum of the other.) The overall intensity profile is indicated by the dotted line and the minimum, I_2 , is about 85% of the maximum, I_1 . (b) Photograph of two point sources which are clearly resolved (angular separation of Airy discs $\approx 2\alpha_{zom}$, i.e. about double the Rayleigh limit) (from *An Introduction to the Optical Microscope*, 2nd edn, by S. Bradbury, Oxford University Press/Royal Microscopical Society, 1989).

a discernible decrease between the central maxima of the Airy discs. Determining this point is a matter of some difficulty, but the criterion proposed by Lord Rayleigh* is most generally adopted. The Rayleigh criterion is that the centre of one Airy disc should coincide with the zero order minimum of the adjacent Airy disc. This criterion is shown in Fig. 7.10(a). The net intensity profile shows a small dip of about 85% of the maxima each side—which is easily discernible by the eye or detectable by a photographic plate. Hence the angular resolution of a telescope is α_{zom} , the zero order minimum angle for destructive interference, i.e. referring to Section 7.4:

$$\text{limit of resolution} = \alpha_{\text{zom}} \approx \sin \alpha_{\text{zom}} = \frac{1.22\lambda}{d}.$$

Clearly, the greater is the aperture of a telescope, the smaller is the limit of resolution and this explains why astronomical telescopes in particular are constructed with objective mirrors with as large a diameter as possible.

These considerations are also relevant to an estimation of the limit of resolution of cameras in which the diameter x of the Airy disc depends, additionally, on the focal length of the telescope or camera objective, f , the radius or half-diameter $x/2$ being given approximately by $x/2 = f \sin \alpha_{\text{zom}}$ (Fig. 7.11). Substituting from above gives $x = 2.44\lambda(f/d)$. The ratio (f/d) is called the f -number and is the important number engraved on camera lenses and the like. For blue-green light $\lambda \approx 0.5 \mu\text{m}$ and therefore x is *roughly* equal to f -number expressed as micrometres. ‘Stopping down’ a camera lens (i.e. increasing f -number) means increasing the size of the Airy disc. How important this is (in comparison with other factors such as the depth of field) depends upon the relation between the size of the Airy disc and the ‘grain size’ of the photographic film or pixel size of the CCD. Clearly, deterioration in image sharpness will only begin to occur when the Airy disc becomes (roughly) equal to the grain or pixel size.

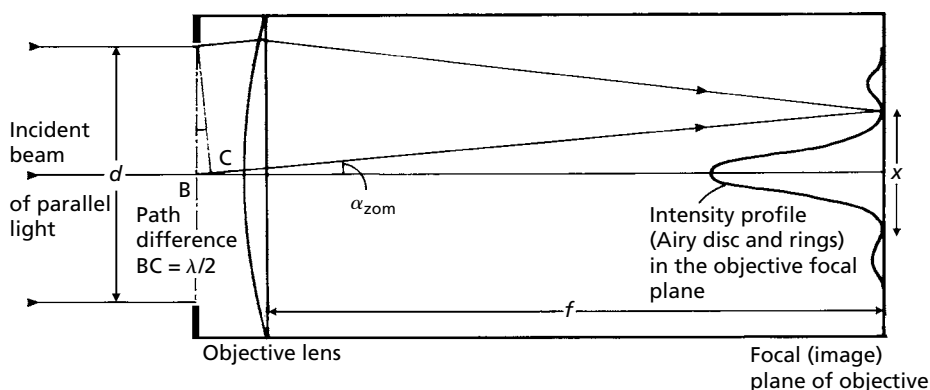


Fig. 7.11. The formation of the Airy disc in the focal plane of a telescope or camera. The half-diameter $x/2$ (shown much exaggerated) is given by $f \sin \alpha_{\text{zom}}$. (Compare with Fig. 7.8(b)).

* Denotes biographical notes available in Appendix 3.

The diffraction-limited resolution of a microscope can be treated in two ways. First, it may be treated in the same way as for a telescope or camera—by considering the separation between the Airy discs of two closely spaced points of light and situated close to the front focal plane of the objective rather than (as in the telescope or camera) a long distance away. In so doing a simplifying assumption is made that the light from the two point sources is incoherent (just as in the case of two stars) and hence interference between them can be neglected (see Section 7.3). The assumption is generally invalid—microscopical specimens do not consist of independent points of light of different intensities across their surfaces. It is more reasonable to assume that the specimen is illuminated with *coherent* light and that interference occurs between the light waves diffracted at the light/dark regions across the specimen surface.³ This leads us to the second way of treating the diffraction-limited resolution of the microscope which was first developed by Ernst Abbe,* the optical designer for Carl Zeiss.

It turns out from a rigorous analysis that the expressions for the limit of resolution are closely identical irrespective of the assumptions made about the illumination or self-illumination of the specimen. We shall follow both approaches, not least because they serve as useful applications of the diffraction theory we have already learned.

The first approach is represented in Fig. 7.12 which shows two such points of light and their Airy disc images—an axial point (solid lines) and an off-axis point (dashed lines). In a microscope the plane in which the Airy disc images occur is called the primary image plane—the plane which is ‘observed’ in the eyepiece.

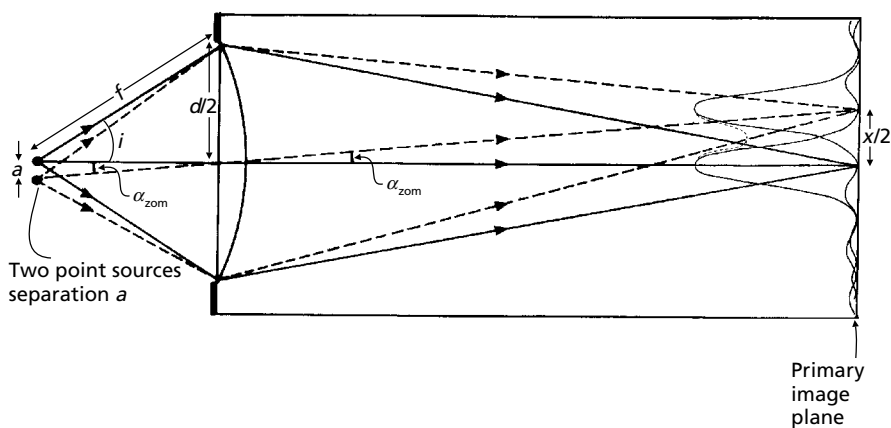


Fig. 7.12. The limit of resolution in a microscope for two points of light separated by distance a and which subtend angle α_{zom} at the objective lens. At this angle the zero order minimum of the Airy disc of one point source corresponds with the central maximum of the Airy disc of the adjacent point source. The sources are situated at a distance from the objective lens close to f , the focal length.

³ The condition for incoherent illumination is closely approached in the case of fluorescence microscopy. Otherwise, in the usual Köhler illumination arrangement (in which each point in the light source gives rise to a parallel pencil of rays at the specimen as in Fig 7.6), the illumination is coherent.

* Denotes biographical notes available in Appendix 3.

Just as in a telescope, the limit of resolution is given when the angular separation between the two point sources, $\alpha_{\text{zom}} = 1.22\lambda/d$ (see Fig. 7.11). We now have to express this limit in terms of a , the separation of the two point sources and i , the semi-angle subtended by the objective lens at the point-sources. Let f be the focal length of the objective lens as indicated in Fig. 7.12, then $\sin i = d/2f$ and $\alpha_{\text{zom}} \approx a/f$. Hence $\alpha_{\text{zom}} = 1.22\lambda/d = a/f$ from which $a = 1.22\lambda/(f/d)$. Substituting $(f/d) = 1/2 \sin i$ we obtain

$$\text{limit of resolution} = a = \frac{1.22\lambda}{2 \sin i} = \frac{0.61\lambda}{\sin i}.$$

In the case of microscope objectives of very small focal length (i.e. 'high power' objectives), the space between the specimen and front element of the lens may be filled with a drop of oil, of refractive index n , which is simply the ratio of the wavelength λ of light in air (or vacuum) to the wavelength λ' in the oil, i.e. by definition $n = \lambda/\lambda'$. Substituting this factor gives:

$$\text{limit of resolution} = a = \frac{0.61\lambda'}{\sin i} = \frac{0.61\lambda}{n \sin i}.$$

The second approach, due to Ernst Abbe, is as follows: in order for the microscope to form an image of the specimen (i.e. in order to resolve the slits or lines of a grating), at least two beams (usually the direct beam and the first order diffracted beam) should enter the objective lens. This situation is shown in Fig. 7.13. The specimen/grating is illuminated with a parallel beam of light (from a distant source or a sub-stage condenser in which the aperture diaphragm is almost fully closed) and the first order diffracted beams (on either side of the direct beam) are just collected by the objective lens.

These parallel beams are then focused by the objective lens to give diffraction spots which are situated, as shown, in its back focal plane (a screen placed here would record

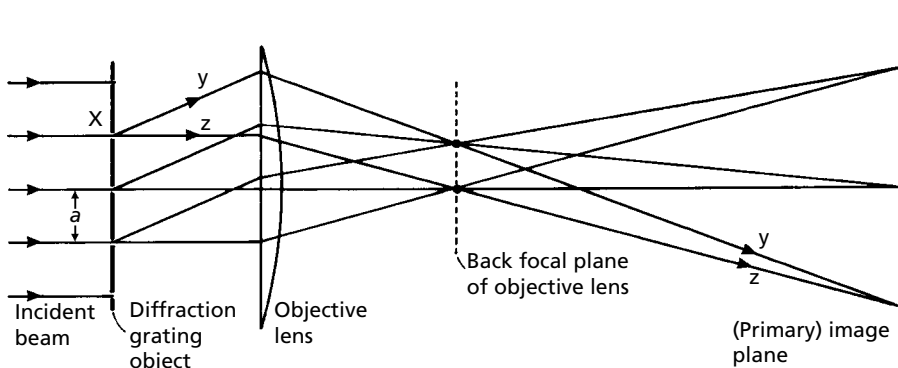


Fig. 7.13. Image formation in the light microscope. The direct and diffracted beams enter the objective lens and are focused to form a diffraction pattern in its (back) focal plane (compare with Fig. 7.6). The rays 'continue on their way' to form an image by the recombination of the diffracted light, e.g. incident ray **X** is separated into **z** (direct) and **y** (diffracted) light; these two rays recombine in the image plane.

this diffraction pattern, just as shown in Fig. 7.6). However, the beams or rays continue on their way and intersect, as shown, to form the (primary) image, (which is then magnified by the eyepiece or photographic projection lens). The important point is that the image is formed by the *recombination* of light which was *separated* at the specimen by diffraction. Consider, for example, the incident beam marked X (Fig. 7.13); this is separated by diffraction into z (direct beam) and y (diffracted beam). These two beams then contribute to the separate (zero and first order) diffraction spots, but then continue on their way to be reunited or recombined and, as Abbe pointed out, it is this recombination that constitutes an image. The greater the number of diffracted beams which are collected by the objective lens and thence recombined, the closer the image approximates to the object, but the limit of resolution is determined by the criterion that at least two beams should enter the objective.

Hence, for the case of normal incidence, in which the direct and two first order beams enter the objective lens (Fig. 7.14(a)), the limit of resolution is simply obtained from the

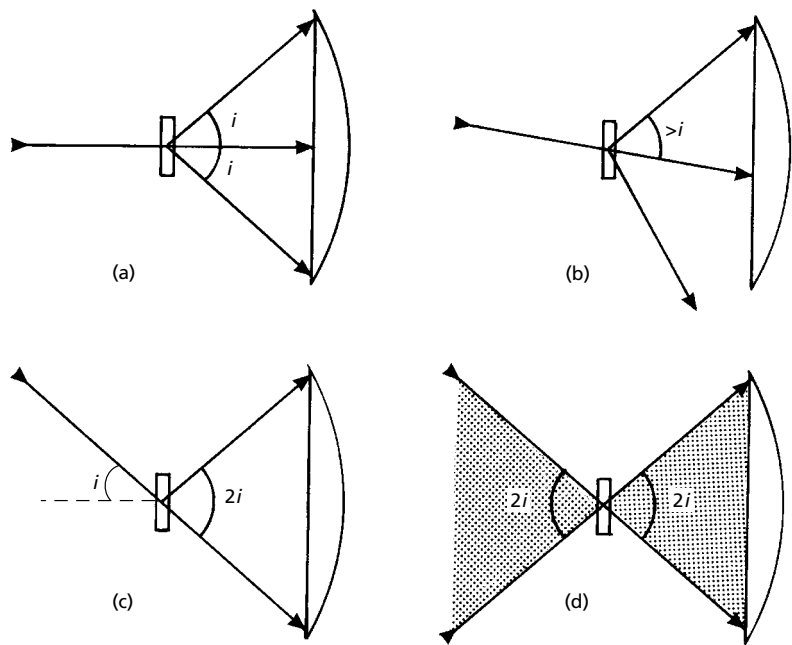


Fig. 7.14. The Abbe criterion for the limit of resolution of an objective lens of (semi-angular) aperture i . (a) normal incidence, parallel light (condenser diaphragm closed down); the direct and two first-order beams at angle i enter the objective and contribute to the image; (b) as (a) but a slightly inclined incident parallel beam, the direct beam and just one first-order beam enter the objective lens but at an angle greater than i ; (c) as (b) but the incident beam is inclined at the maximum angle i ; it passes inside one edge of the objective lens and one diffracted beam at angle $2i$ passes inside the opposite edge; (d) the practical arrangement; the condenser diaphragm is opened to admit a convergent cone of light on to the specimen (in practice rather less than $2i$) to admit direct and diffracted light to the objective over a whole range of angles.

equation derived in Section 7.4, i.e. $1\lambda = a \sin \alpha_1 = a \sin i$, i.e. the limit of resolution $a = \lambda / \sin i$, where i is the semi-angle of the objective lens subtended at the specimen which is set equal to α_1 the angle between the direct and first order diffracted beams.

This equation may be modified in two ways. First, Fig. 7.13 shows an *overfilled* case in which, because the incident beam is normal to the specimen and axial with the microscope, *two* first-order diffracted beams, as well as the direct or zero order beam, enter the objective. This situation is sketched for emphasis in Fig. 7.14(a). However, if the incident beam is inclined to the axis of the microscope as shown in Fig. 7.14(b), then the first order beam on one side of the direct beam is lost but a first order beam on the other side of the direct beam of greater diffraction angle can enter the objective lens. The extreme or limiting case arises when the incident beam is inclined at angle i to the microscope axis (Fig. 7.14(c)), in which case the direct or zero order beam just passes inside one edge of the objective lens and one first order diffracted beam, now at twice the angle, $2i$ to the direct beam, just passes inside the opposite edge. The Abbe criterion is still satisfied because two beams (zero order and first order) enter the objective lens and are recombined to form an image in the same way as shown in Fig. 7.13.

We must now work out the path difference for this inclined case. The geometry is shown in detail in Fig. 7.15, which should be compared with that for normal incident light shown in Fig. 7.5. The path difference between the direct and first order diffracted beam is now $AB + BC = 1\lambda$ for constructive interference, i.e. $a \sin i + a \sin i = 2a \sin i$. This equation, it should be noted, is identical to the Bragg equation (see Section 8.3) since both describe the same geometrical conditions: in both cases the incident and diffracted

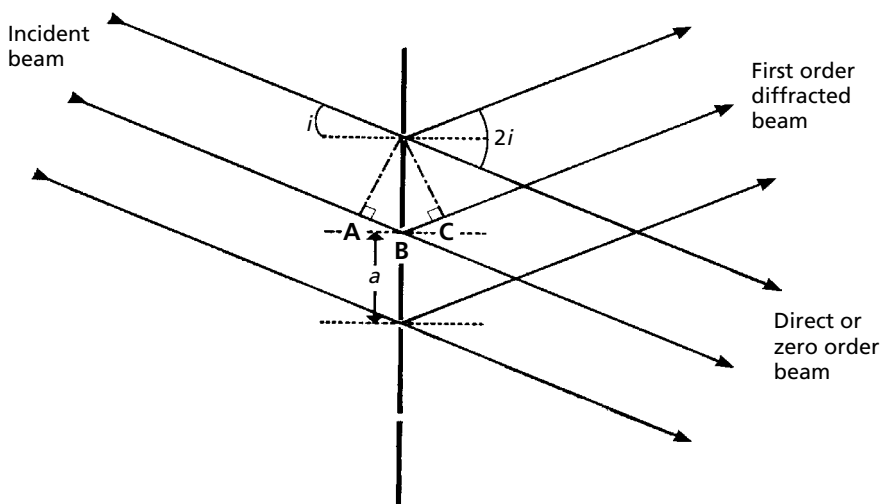


Fig. 7.15. The geometry for constructive interference when the incident and diffracted beams make equal angle i to the diffraction grating. For constructive interference (first order) the path difference = $AB + BC = a \sin i + a \sin i = 2a \sin i = 1\lambda$. This condition is equivalent to Bragg's law where a is the interplanar spacing d and i is θ , the Bragg angle.

beams are at the same angle to the diffraction grating or lattice planes (i.e. $i = \theta$) and the grating spacing a corresponds to the interplanar spacing d .

Rearranging the equation gives:

$$\text{limit of resolution} = a = \frac{\lambda}{2 \sin i} = \frac{0.5\lambda}{\sin i},$$

which differs from our previous equation by a factor of 0.5.

Second, the space between the specimen and the front element of the objective lens may be filled with oil of refractive index n . Proceeding as before:

$$\text{limit of resolution} = a = \frac{0.5\lambda'}{\sin i} = \frac{0.5\lambda}{n \sin i}.$$

In practice we do not in general illuminate the specimen with a single parallel inclined beam as shown in Fig. 7.14(c), but we open the aperture diaphragm of the condenser lens to give a highly convergent beam on the specimen of semi-angle i (in practice slightly less) as shown in Fig. 7.14(d). This is analogous, in terms of illumination, to the case of the point sources of light radiating out in all directions as described above and the equations for the limit of resolution which we have derived—one for incoherent illumination (diffraction at the objective aperture) and the other for coherent illumination (diffraction at the specimen)—are, except for the Airy factor 1.22, precisely the same. As mentioned above, a much more rigorous analysis also predicts closely identical solutions.

The important quantity in the equations $n \sin i$ was called by Abbe the **numerical aperture**, **NA** and fulfils, in effect, the same role with respect to the microscope as does the aperture d of the objective lens (or mirror) with respect to the telescope. To summarize:

$$\text{Angular-limit of resolution of a telescope} = \alpha_{\text{zom}} = \frac{1.22\lambda}{d}$$

$$\text{Distance-limit of resolution of a microscope} = a = \frac{0.61\lambda}{\text{NA}} \text{ or } \frac{0.5\lambda}{\text{NA}}.$$

The concept of numerical aperture $\text{NA} = n \sin i$ is of enormous importance in optics. It is closely related to the f -number, the ratio of focal length/aperture, (f/d) of a lens. Referring again to Fig. 7.12, since $\sin i = d/2f$ then $(f/d) = 1/2 \sin i$ since $\sin i = \text{NA}/n$,

$$f\text{-number, } (f/d) = \frac{n}{2} \text{NA}.$$

The Abbe criterion applies equally to light microscopes and electron microscopes. The enormous decrease in the limit of resolution obtainable in the transmission electron microscope arises because of the much smaller values of λ for electrons (typically 4 pm for 100 kV instruments compared with light (typically 500 nm)). This (approximate) 100 000 decrease is however offset because of the high inherent spherical aberrations in electron lenses which limit NA values to the order of 0.01 compared with NA values up to 1.4 for oil immersion light objectives.

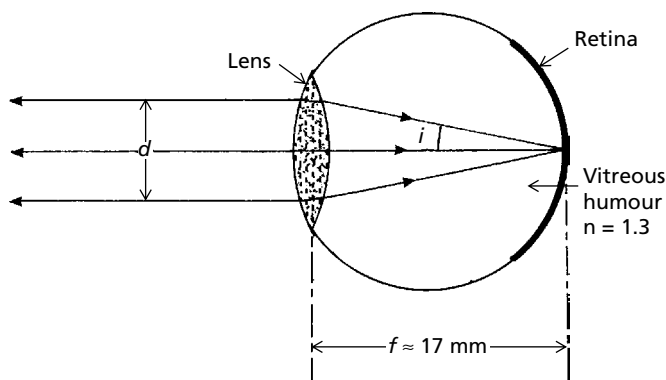


Fig. 7.16. The components of the eye (a) considered as a telescope or camera (light path to the right), the retina being the image plane. The angular-limit of resolution (for $d = 3 \text{ mm}$) = 0.77 min of arc or 0.07 mm at the near distance of 250 mm . (b) The eye considered as a water-immersion microscope objective (light path to the left), the retina being the object plane. The numerical aperture $\text{NA} = 0.115$ and the distance-limit of resolution = $2.9 \mu\text{m}$ (see text for calculations). These values correspond (a) for visual acuity of $\approx 0.1 \text{ mm}$ at 250 mm and (b) to the spacing of the central retinal cone cells.

Finally, we may apply these ideas to those most important and precious optical instruments—our eyes.

We may treat the eye either as a telescope or camera to determine the angular-limit of resolution between two distant points, or as a microscope, with the direction of the light in effect reversed, to determine the distance-limit of resolution at the retina, the space between the objective (eye) lens and the retina (corresponding to the microscope object or specimen-plane) being filled with liquid (the vitreous humour) of refractive index n (see Fig. 7.16).

If we take $f = 17 \text{ mm}$, $n = 1.3$, d (the diameter of the pupil) $\approx 3 \text{ mm}$ (which varies of course roughly in the range $1 \sim 4 \text{ mm}$ depending on the intensity of the light) and λ (for green light) $\approx 0.55 \mu\text{m}$, then the f -number of the eye is $(17/3) \text{ mm} = 5.67$ and the numerical aperture NA is $1.3/2(5.67) = 0.115$.

Substituting these values of λ and d into the expression for the angular-limit of resolution α_{zom} gives $0.22 \times 10^{-3} \text{ rads}$ or 0.77 min of arc which is close to that for normal vision ($\sim 1 \text{ min of arc}$ or 0.07 mm at the near distance of 250 mm).

Similarly, substitution of these values of λ and d into the expression for the distance-limit of resolution a at the retina gives $2.9 \mu\text{m}$ —which is approximately equal to the spacing of our visual receptors (the cone cells) in the central part (the *fovea centralis*) of our retina. In short, our eyes have evolved, as we should expect, with a perfect balance between the sizes of their physiological components.

A note on light and radio telescopes

It is of interest to compare the performance of light and radio telescopes with regard to the observation of extragalactic objects. The equation for the angular-limit of resolution,

$\alpha_{\text{zom}} = \frac{1.22\lambda}{d}$, applies (approximately) equally to radio telescopes where d is now the diameter of the paraboloidal receiving dish and λ is in the range 5 cm upwards. For $\lambda = 1$ m and $d = 100$ m we obtain $\alpha_{\text{zom}} = 0.012$ rads = 42 min of arc—a resolution inferior to that of the human eye. However, it should be noted that substantially decreased limits of resolution are obtained by interferometric techniques, i.e. by linking the signals from widely spaced radio telescopes. Resolutions down to a thousandth of an arc second or so are obtainable using the technique of *very long baseline interferometry* (VLBI). This is superior to anything that can be presently obtained using optical telescopes. Radio telescopes also have the advantage of using larger area collecting dishes than is currently possible with optical telescopes. They therefore enable very faint radio sources to be detected.

Exercises

7.1 Figure 7.17(a) shows a net with a single twin and the corresponding diffraction pattern (optical transform) and Fig. 7.17(b) shows a net with several twins and the corresponding diffraction

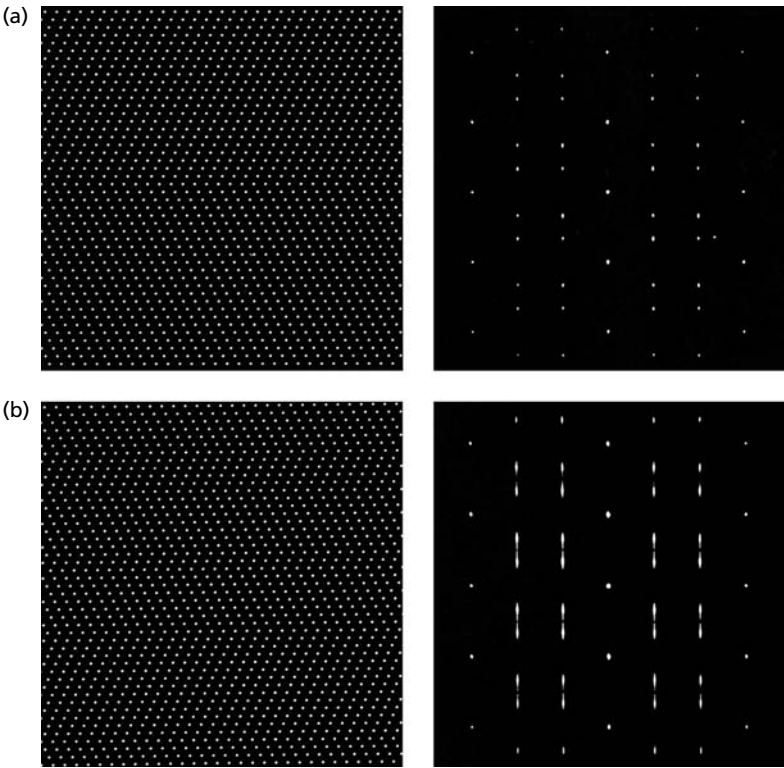


Fig. 7.17. (a) A net with a single twin, and (b) a net with several twins and their corresponding diffraction patterns (from *Atlas of Optical Transforms* by G. Harburn, C. A. Taylor and T. R. Welberry, Bell & Hyman, 1983, an imprint of HarperCollins).

pattern (see Figs. 1.18, 1.21 and 4.4(b)). Using a tracing paper overlay on the diffraction pattern in Fig. 7.17(a), outline the reciprocal lattice unit cells of the two twin orientations and note those reciprocal lattice points which are common to both twin orientations.

The diffraction pattern in Fig. 7.17(b) is similar to that in Fig. 7.17(a) except that some of the spots are streaked in a direction perpendicular to the twin plane. Explain this streaking qualitatively after you have read Section 9.3.

- 7.2 With reference to Fig. 7.7(c), describe the diffraction pattern which you would obtain with a diffraction grating in which the slit width d is equal to half the slit spacing a .

X-ray diffraction: the contributions of Max von Laue, W. H. and W. L. Bragg and P. P. Ewald

8.1 Introduction

The experimental technique which has been of the greatest importance in revealing the structure of crystals is undoubtedly X-ray diffraction.

The story of the discovery of X-ray diffraction in crystals by Laue,* Friedrich and Knipping in Munich in 1912 and the development of the technique by W. H. Bragg* and W. L. Bragg* in Leeds and Cambridge in the years preceding the First World War is well known. But why did the Braggs make such rapid advances in the analysis of X-ray diffraction photographs in comparison with Laue and his co-workers? An important factor in the answer seems to be that Laue envisaged crystals in terms of a three-dimensional network of rows of atoms and based his analysis on the notion that the crystal behaved, in effect, as a three-dimensional diffraction grating. This approach is not wrong, but it is in practice rather clumsy or protracted. On the other hand, the Braggs (and here the credit must go to W. L. Bragg, the son) envisaged crystals in terms of layers or planes of atoms which behaved in effect as reflecting planes (for which the angle of incidence equals the angle of reflection), strong ‘reflected’ beams being produced when the path differences between reflections from successive planes in a family is equal to whole number of wavelengths. This approach is not correct in a physical sense—planes of atoms do not reflect X-rays as such—but it is correct in a geometrical sense and provides us with the beautifully simple expression for the analysis of crystal structure:

$$n\lambda = 2d_{hkl} \sin \theta,$$

where λ is the wavelength, n is the order of reflection, d_{hkl} is the lattice plane spacing and θ is the angle of incidence/reflection to the planes.

What led W. L. Bragg to this novel perception of the diffraction? Simply his observation of the elliptical shapes of the diffraction spots, which he noticed were also characteristic of the reflections from mirrors of a pencil-beam of light (see the Laue photograph on p. xiv). Only connect!

* Denotes biographical notes available in Appendix 3.

Finally, we come to the contribution of P. P. Ewald,* a physicist who never achieved the recognition that was his due. The story is briefly recorded in his autobiographical sketch in *50 Years of X-ray Diffraction*. Ewald was a 'doctorand'—a research student working in the Institute of Theoretical Physics in the University of Munich under Professor A. Sommerfeld. The subject of his thesis was 'To find the optical properties of an anisotropic arrangement of isotropic oscillators'. In January 1912, while he was in the final stages of writing up his thesis, he visited Max von Laue, a staff member of the Institute, to discuss some of the conclusions of his work. Ewald records that Laue listened to him in a slightly distracted way and insisted first on knowing what was the distance between the oscillators in Ewald's model; perhaps $1/500$ or $1/1000$ of the wavelength of light, Ewald suggested. Then Laue asked 'what would happen if you assumed very much shorter waves to travel through the crystal?' Ewald turned to Paragraph 6, Formula 7, of his thesis manuscript, saying 'this formula shows the results of the superposition of all wavelets issuing from the resonators. It has been derived without any neglect or approximation and is therefore valid also for short wave-lengths.' Ewald copied the formula down for Laue shortly before taking his leave, saying that he, Laue, was welcome to discuss it. Laue's question, of course, arose from his intuitive insight that if X-rays were waves and not particles, with wavelengths very much smaller than light, then they might be diffracted by such an array of regularly spaced oscillators.

The next Ewald heard of Laue's interest was through a report which Sommerfeld gave in June 1912 on the successful Laue–Friedrich–Knipping experiments. He realized that the formula which he had copied down for Laue, and which Laue had made no use of, provided the obvious way of interpreting the geometry of the diffraction patterns—by means of a construction which he called the reciprocal lattice and a sphere determined by the mode of incidence of the X-rays on the crystal (the Ewald or reflecting sphere). Ewald's interpretation of the geometry of X-ray diffraction was not published until 1913, by which time rapid progress in crystal structure analysis had already been made by W. H. and W. L. Bragg in Leeds and Cambridge.

8.2 Laue's analysis of X-ray diffraction: the three Laue equations

Laue's analysis of the geometry of X-ray diffraction patterns has been referred to in Section 8.1. What follows is a much simplified treatment which does not take into consideration Laue's interpretation of the origin of the diffracted waves from irradiated crystals.

Consider a simple crystal in which the motif is one atom and the atoms are simply to be regarded as scattering centres situated at lattice points. The more general situation in which the motif consists of more than one atom and in which the different scattering amplitudes of the atoms and the path differences between the atoms have to be taken into account is discussed in Section 9.2. The crystal may be considered to be built up of rows

* Denotes biographical notes available in Appendix 3.

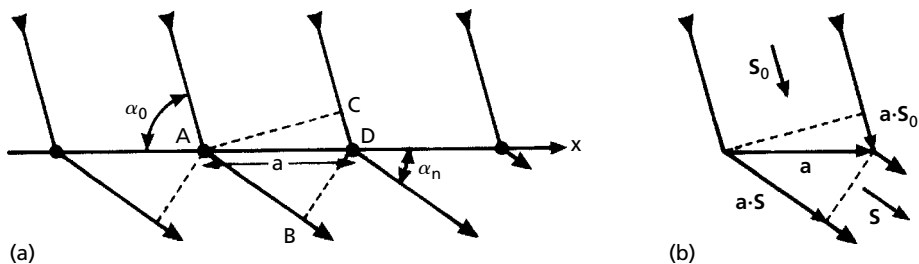


Fig. 8.1. (a) Diffraction from a lattice row along the x -axis. The incident and diffracted beams are at angles α_0 and α_n to the row respectively. The path difference between the diffracted beams $= (AB - CD)$. (b) The incident and diffracted beam directions and the path difference between the diffracted beams as expressed in vector notation.

of atoms in three dimensions: rows of atoms of spacing a along the x -axis, of spacing b along the y -axis and of spacing c along the z -axis. Consider first of all the condition for constructive interference for the waves scattered from the row of atoms along the x -axis—which may simply be reduced to a consideration of the path differences between waves scattered from adjacent atoms in the row (Fig. 8.1(a)).

For constructive interference the path difference $(AB - CD)$ must be a whole number of wavelengths, i.e.

$$(AB - CD) = a(\cos \alpha_n - \cos \alpha_0) = n_x \lambda$$

where α_n , α_0 are the angles between the diffracted and incident beams to the x -axis, respectively, and n_x is an integer (the order of diffraction).

This equation, known as the first Laue equation, may be expressed more elegantly in vector notation. Let s , s_0 be unit vectors along the directions of the diffracted and incident beams, respectively, and let a be the translation vector from one lattice point (or atom position) to the next (Fig. 8.1(b)). The path difference $a(\cos \alpha_n - \cos \alpha_0)$ may be represented by the scalar product $a \cdot s - a \cdot s_0 = a \cdot (s - s_0)$. Hence the first Laue equation may be written

$$a(\cos \alpha_n - \cos \alpha_0) = a \cdot (s - s_0) = n_x \lambda.$$

Now Fig. 8.1 is misleading in that it only shows the diffracted beam at angle α_n below the atom row—but the same path difference obtains if the diffracted beam lies in the plane of the paper at angle α_n above the atom row—or indeed *out of the plane of the paper* at angle α_n to the atom row. Hence all the diffracted beams with the same path difference occur at the same angle to the atom row, i.e. the diffracted beams of the same order all lie on the surface of a cone—called a Laue cone—centred on the atom row with semi-apex angle α_n . This situation is illustrated in Fig. 8.2 which shows just three Laue cones with semi-apex angle α_0 (zero order, $n_x = 0$), semi-apex angle α_x (first order, $n_x = 1$) and semi-apex angle α_2 (second order, $n_x = 2$). Clearly there will be a whole set of such cones with semi-apex angles α_n varying between 0° and 180° .

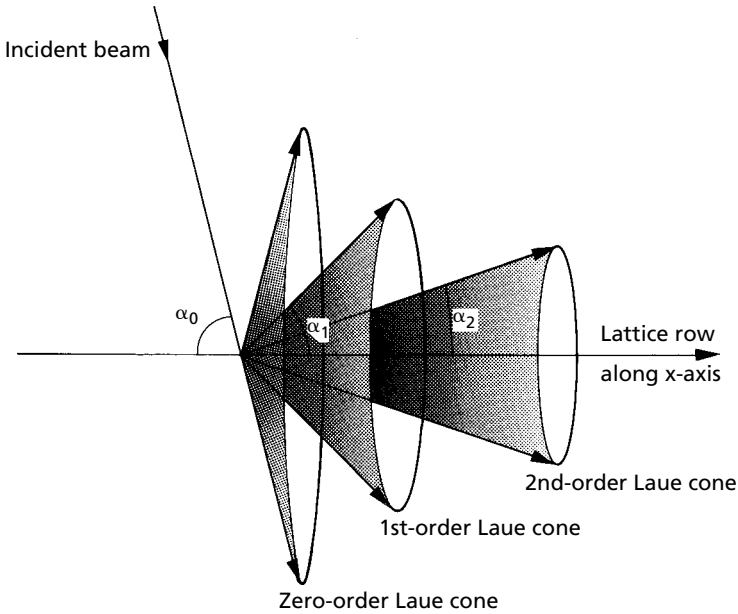


Fig. 8.2. Three Laue cones representing the directions of the diffracted beams from a lattice row along the x -axis with 0λ ($n_x = 0$), 1λ ($n_x = 1$) and 2λ ($n_x = 2$) path differences. The corresponding Laue cones for $n_x = -1$, $n_x = -2$ etc. lie to the left of the zero order Laue cone.

The analysis is now repeated for the atom row along the y -axis, giving the second Laue equation:

$$b(\cos \beta_n - \cos \beta_0) = \mathbf{b} \cdot (\mathbf{s} - \mathbf{s}_0) = n_y \lambda,$$

and for the atom row along the z -axis giving the third Laue equation:

$$c(\cos \gamma_n - \cos \gamma_0) = \mathbf{c} \cdot (\mathbf{s} - \mathbf{s}_0) = n_z \lambda,$$

where the angles β_n , β_0 , γ_n , γ_0 and the integers n_y and n_z are defined in the same way as for α_n , α_0 and n_x .

Now, for constructive interference to occur simultaneously from all three atom rows, all three Laue equations must be satisfied simultaneously. This is equivalent to the geometrical condition that diffracted beams only occur in those directions along which three Laue cones, centred along the x -, y - and z -axes, intersect. Each diffracted beam may be identified by three integers n_x , n_y and n_z which, as pointed out above, represent the order of diffraction from each of the atom rows. We shall find in Section 8.3 that these integers are simply h , k and l Laue indices (see Section 5.5) of the reflecting planes in the crystal.

8.3 Bragg's analysis of X-ray diffraction: Bragg's law

Laue's analysis is in effect an extension of the idea of a diffraction grating to three dimensions. It suffers from the severe practical disadvantage that in order to calculate the directions of the diffracted beams, a total of six angles α_n , α_0 , β_n , β_0 and γ_n , γ_0 , three lattice spacings a , b and c , and three integers n_x , n_y and n_z need to be determined. As discussed in Section 5.5, W. L. Bragg envisaged diffraction in terms of reflections from crystal planes giving rise to the simple relationship (Bragg's law, derived below):

$$n\lambda = 2d_{hkl} \sin \theta.$$

It can be seen immediately, by comparing the Laue equations with Bragg's law, that the number of variables needed to calculate the directions of the diffracted beams are much reduced.

Bragg's law may be derived with reference to Fig. 8.3(a) which shows (as for the derivation of the Laue equations) a simple crystal with one atom at each lattice point. The path difference between the waves scattered by atoms from adjacent (hkl) lattice planes of spacings d_{hkl} is given by

$$(AB + BC) = (d_{hkl} \sin \theta + d_{hkl} \sin \theta) = 2d_{hkl} \sin \theta.$$

Hence for constructive interference:

$$n\lambda = 2d_{hkl} \sin \theta,$$

where n is an integer (the order of reflection or diffraction).

As explained in Section 5.5, n is normally incorporated into the lattice plane symbol, i.e.

$$\lambda = 2 \left(\frac{d_{hkl}}{n} \right) \sin \theta = 2d_{nh\ nk\ nl} \sin \theta$$

where $nh\ nk\ nl$ are the Laue indices for the reflecting planes of spacing d_{hkl}/n . In other words, to repeat the important point made in Section 5.5, n is not written separately but

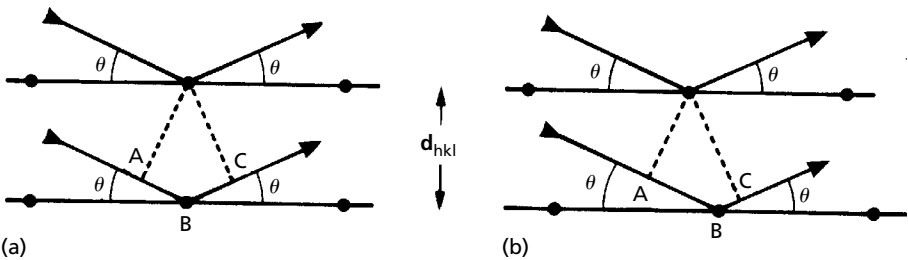


Fig. 8.3. (a) Bragg's law for the case of a rectangular grid, i.e. $AB = BC = d_{hkl} \sin \theta$; the path difference $(AB + BC) = 2d_{hkl} \sin \theta$. (b) Bragg's law for the general case in which $AB \neq BC$. Again, the path difference $(AB + BC) = d_{hkl} \sin \theta$.

is represented as the common factor in the Laue indices. For example a *third* order reflection from the (111) lattice planes (Miller indices—in parentheses) is represented as a *first* order reflection from the 333 planes (Laue indices—no parentheses), the 333 planes having 1/3rd the spacing of the (111) planes.

Figure 8.3(a) represents a particularly simple geometrical situation in which the lattice is shown as a rectangular grid and the atoms are symmetrically disposed with respect to the incident and diffracted beam, i.e. $AB = BC$. With reference to the diffraction of light this corresponds to the case in which the incident and diffracted beams make equal angles to the diffraction grating—i.e. the situation shown in Fig. 7.15 where the angle i corresponds to θ and the slit spacing a corresponds to d_{hkl} . Figure 8.3(b) shows a more general situation in which the lattice is not rectangular and the distance AB does not equal BC . However, the sum $(AB + BC)$ is unchanged and is again equal to $2d_{hkl} \sin \theta$ (see Exercise 8.3). The important point is that Bragg's law applies irrespective of the positions of the atoms in the planes; it is solely the spacing between the planes which needs to be considered. It follows as a corollary that the path difference between the waves scattered by the atoms in the same plane is zero—i.e. all the waves scattered from the same plane interfere constructively. This is *only* the case (to emphasize the significance of Bragg's law once more) when the angle of incidence to the planes equals the angle of reflection. Finally, note that (unlike the Laue equations), Bragg's law is wholly represented in two dimensions: the incident and diffracted beams and the normal to the reflecting planes (Fig. 8.3) all lie in a plane—i.e. the plane of the paper.

Bragg's law may also be expressed in vector notation. Again, let \mathbf{s}, \mathbf{s}_0 be unit vectors along the directions of the diffracted and incident beams, then (with reference to Fig. 8.4) the vector $(\mathbf{s} - \mathbf{s}_0)$ is parallel to \mathbf{d}_{hkl}^* , the reciprocal lattice vector of the reflecting planes. Comparing the moduli of these vectors $|\mathbf{s} - \mathbf{s}_0| = 2 \sin \theta$ and $|\mathbf{d}_{hkl}^*| = 1/d_{hkl}$, it is seen from Bragg's law that their ratio is simply λ . Hence Bragg's law may be written:

$$\frac{(\mathbf{s} - \mathbf{s}_0)}{\lambda} = \mathbf{d}_{hkl}^* = h\mathbf{a}^* + k\mathbf{b}^* + l\mathbf{c}^*.$$

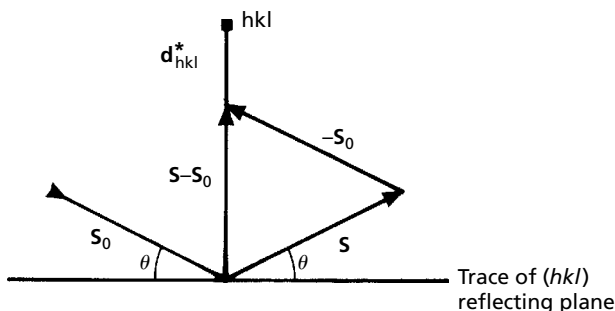


Fig. 8.4. Bragg's law expressed in vector notation. Vectors $(\mathbf{s} - \mathbf{s}_0)$ and \mathbf{d}_{hkl}^* are parallel and the ratio of the moduli is λ . Hence Bragg's law is expressed as $(\mathbf{s} - \mathbf{s}_0)/\lambda = \mathbf{d}_{hkl}^*$.

Hence constructive interference occurs, or Bragg's law is satisfied, when the vector $(\mathbf{s} - \mathbf{s}_0)/\lambda$ coincides with the reciprocal lattice vector \mathbf{d}_{hkl}^* of the reflecting planes.

The vector form of Bragg's law may be combined with each of the three Laue equations: i.e. for the first Laue equation:

$$\mathbf{a} \cdot (\mathbf{s} - \mathbf{s}_0) = n_x \lambda = \mathbf{a} \cdot \mathbf{d}_{hkl}^* \cdot \lambda = \mathbf{a} \cdot (h\mathbf{a}^* + k\mathbf{b}^* + l\mathbf{c}^*)\lambda.$$

Hence $n_x = h$ (since $\mathbf{a} \cdot \mathbf{a}^* = 1$, $\mathbf{a} \cdot \mathbf{b}^* = 0$, etc), and similarly $n_y = k$ and $n_z = l$ for the other Laue equations. The integers n_x , n_y and n_z of the Laue equations are simply the Laue indices h , k , l of the reflecting planes.

Bragg's law, like Newton's laws, and all such uncomplicated expressions in physics, is deceptively simple. Its applicability and relevance to problems in X-ray and electron diffraction only unfold themselves gradually (to teachers and students alike!). Newton was once asked how he made his great discoveries: he replied 'by always thinking unto them'. The student of crystallography could do no better with respect to Bragg's law!

8.4 Ewald's synthesis: the reflecting sphere construction

Ewald's synthesis is a geometrical formulation or expression of Bragg's law which involves the reciprocal lattice and a 'sphere of reflection'. It is best illustrated and understood by way of an example. Consider a crystal with the (hkl) reflecting planes (Laue indices) at the correct Bragg angle (Fig. 8.5). The reciprocal lattice vector \mathbf{d}_{hkl}^* is also shown. Now draw a sphere (the reflecting or Ewald sphere) of radius $1/\lambda$ (where λ is the X-ray wavelength) with the crystal at the centre. Since Bragg's law is satisfied it may be shown that the vector \mathbf{OB} (from the point where the direct beam exits from the sphere to the point where the diffracted beam exits from the sphere) is identical to \mathbf{d}_{hkl}^* : i.e. from the triangle AOC, $|\mathbf{OC}| = (1/\lambda) \sin \theta = (1/2) |\mathbf{d}_{hkl}^*| = 1/2d_{hkl}$, i.e. $\lambda = 2d_{hkl} \sin \theta$. Hence, if the origin of the reciprocal lattice is shifted from the centre of the sphere (A) to the point where the direct beam exits from the sphere (O), then $\mathbf{OB} = \mathbf{d}_{hkl}^*$ and Bragg's law is equivalent to the statement that the reciprocal lattice point for the reflecting planes (hkl) should intersect the sphere; the diffracted beam direction being given by the vector \mathbf{AB} —i.e. the line from the centre of the sphere to the point where the reciprocal lattice point \mathbf{d}_{hkl}^* intersects the sphere. Conversely, if the reciprocal lattice point does not intersect the sphere then Bragg's law is not satisfied and no diffracted beams occur. Finally, note the equivalence of the Ewald reflecting sphere construction to the vector form of Bragg's law $\frac{(\mathbf{s} - \mathbf{s}_0)}{\lambda} = (\mathbf{k} - \mathbf{k}_0) = \mathbf{d}_{hkl}^*$ (Section 8.3). The vector $\mathbf{AO} = \mathbf{k}_0$, the vector $\mathbf{AB} = \mathbf{k}$ and again the origin of \mathbf{d}_{hkl}^* is shifted from A to O (Fig. 8.5).¹

Figure 8.5 shows the construction of just one reflecting plane and one reciprocal lattice point. It is a simple matter to extend it to all the reciprocal lattice points in a crystal. Figure 8.6(a) shows a section of the reciprocal lattice of a monoclinic crystal

¹ An alternative vector notation, widely used in transmission electron microscopy (Chapter 11), is to write $\mathbf{k}_0 = \mathbf{s}_0/\lambda$ and $\mathbf{k} = \mathbf{s}/\lambda$. Hence Bragg's law in vector notation is $\mathbf{k} - \mathbf{k}_0 = \mathbf{d}_{hkl}^* = h\mathbf{a}^* + k\mathbf{b}^* + l\mathbf{c}^*$. The advantage of this notation is that the moduli of \mathbf{k}_0 and \mathbf{k} are equal to the radius of the Ewald reflecting sphere (see Section 8.4). Further, the symbol \mathbf{g}_{hkl} (no star) is widely used instead of \mathbf{d}_{hkl}^* .

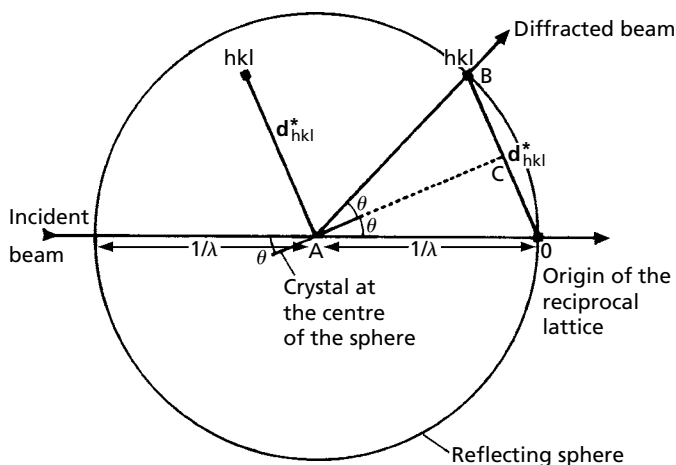


Fig. 8.5. The Ewald reflecting sphere construction for a set of planes at the correct Bragg angle. A sphere (the Ewald or reflecting sphere) is drawn, or radius $1/\lambda$ with the crystal at the centre. The vector \mathbf{OB} is identical to \mathbf{d}_{hkl}^* . The origin of the reciprocal lattice is fixed at O and the reciprocal lattice point hkl intersects the sphere at the exit point of the diffracted beam.

perpendicular to the \mathbf{b}^* reciprocal lattice vector (i.e. the y-axis—see Fig. 6.5(a)). All the reciprocal lattice points in this section have indices of the form $h0l$. An incident X-ray beam is directed along the \mathbf{a}^* reciprocal lattice vector (i.e. along a direction in the crystal perpendicular to the y- and z-axes—see Fig. 6.4(a)). The centre of the reflecting sphere is at a distance $1/\lambda$ from the origin of the reciprocal lattice along the line of the incident beam: note again that the origin of the reciprocal lattice is *not* at the centre of the sphere but is at the point where the direct beam exits from the sphere.

In the section shown, Fig. 8.6(a), the reflecting sphere intersects the 201 reciprocal lattice point: hence the only plane for which Bragg's law is satisfied is the (201) plane and the direction of the 201 reflected beam is as indicated.

Figure 8.6(a) only shows one layer or section of the reciprocal lattice (through the origin) and a (diametral) section of the reflecting sphere. But the reciprocal lattice sections above and below the plane of the page need to be taken into account and also the smaller non-diametral sections of the reflecting sphere which intersect them. Fig. 8.6(b) shows the 'next layer above' or $h1l$ section of the reciprocal lattice (see Fig. 6.5(b)) and the smaller, non-diametral section of the reflecting sphere which it intersects. Notice that this section of the sphere does *not* pass through 010 (the reciprocal lattice point immediately 'above' the origin 000). The sphere intersects the $21\bar{1}$ reciprocal lattice point, hence the $(21\bar{1})$ plane also satisfies Bragg's law and the direction of the $21\bar{1}$ reflected beam is from the centre of the sphere (which is *not* the point in the centre of this smaller circle but the point in the centre of the sphere in the reciprocal lattice section below—Fig. 8.6(a)) and the $21\bar{1}$ reciprocal lattice point. The reflected beam direction therefore cannot be drawn in Fig. 8.6(b) because it is directed upwards, out of the plane of the page.

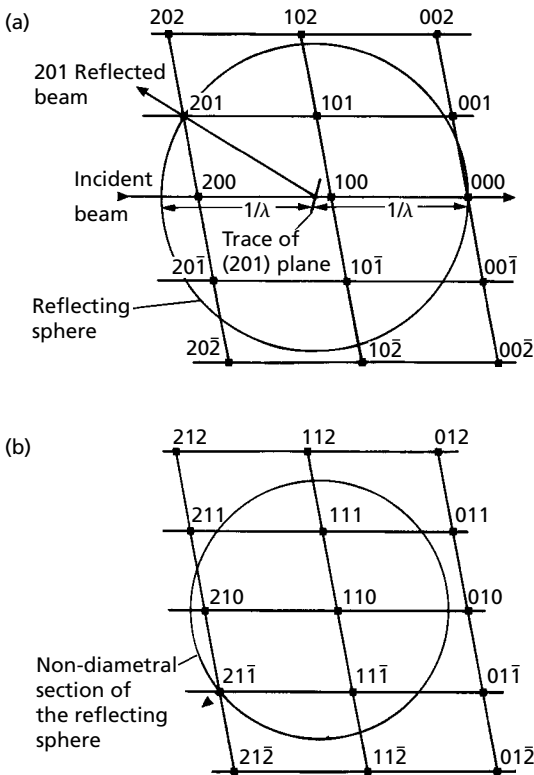


Fig. 8.6. The Ewald reflecting sphere construction for a monoclinic crystal in which the incident X-ray beam is directed along the a^* reciprocal lattice vector, (a) Shows the $h0l$ reciprocal lattice section (through the origin and perpendicular to the b^* reciprocal lattice vector or y -axis—see Fig. 6.5(a) and a diametral section of the reflecting sphere radius $1/\lambda$. The 201 reciprocal lattice point intersects the sphere and the direction of the 201 reflected beam is indicated, (b) Shows the $h1l$ reciprocal lattice section (i.e. the layer ‘above’ the $h0l$ section—see Fig. 6.5(b)) and the smaller, non-diametral section of the reflecting sphere. The $21\bar{1}$ reciprocal lattice point intersects the sphere, the direction of the $21\bar{1}$ reflected beam is ‘upwards’ from the centre of the sphere (in the $h0l$ section below) through the $21\bar{1}$ reciprocal lattice point as indicated by the arrow-head.

Clearly, the construction can be extended to other reciprocal lattice sections, i.e. through the $h2l$, $h3l$, etc. sections (above); the $h\bar{1}l$, $h\bar{2}l$, $h\bar{3}l$ etc. sections (below) and so on. The further the reciprocal lattice section is from the origin, the smaller is the section of the reflecting sphere which it intersects. In the example above, the sphere only intersects the $h0l$ section (Fig. 8.6(a)), the $h1l$ section (Fig. 8.6(b)) and the $h\bar{1}l$ section (below), but no more. Hence only these sections, and the reciprocal lattice points within them, need to be considered.

In Fig. 8.6 the relative sizes of the reciprocal lattice and the sphere happen to be such that just one reciprocal lattice point in each section intersects the sphere. Clearly if the diameter of the sphere were made a little larger (i.e. the X-ray wavelength was

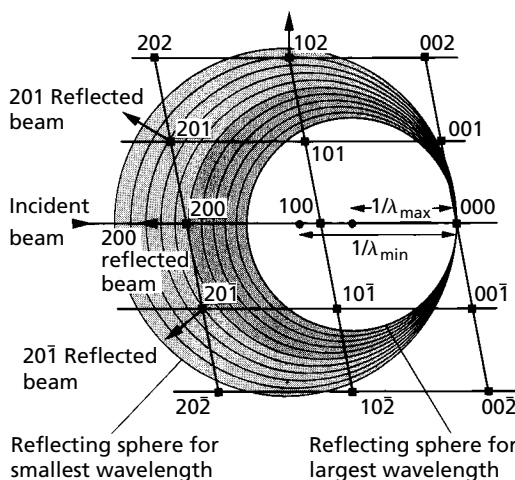


Fig. 8.7. The Ewald reflecting sphere construction for the $h0l$ reciprocal lattice section of the monoclinic crystal shown in Fig. 8.6(a) for the 'white' X-radiation, i.e. for a range of wavelengths from the smallest (largest sphere) to the largest (smallest sphere) giving rise to a 'nest' of spheres (shaded region) all passing through the origin. The 102, 201, 200 and $20\bar{1}$ reciprocal lattice points lying within this region satisfy Bragg's law, each for the particular wavelength or sphere which they intersect. The directions of the reflected beams from these planes are indicated by the arrows.

made a little smaller) then no reciprocal lattice points would intersect the sphere and no planes in the crystal would be at the correct Bragg angle for reflection; if the diameter of the sphere were continuously made larger (or smaller) than that shown in Fig. 8.6 then other planes would reflect as their reciprocal lattice points successively intersected the sphere. This is the basis of Laue's original X-ray experiment; 'white' X-radiation was used which contains a range of wavelengths, which correspond to a range or 'nest' of spheres of different diameters. Any plane whose reciprocal lattice point falls within this range will therefore satisfy Bragg's law for one particular wavelength.

The situation is illustrated in Fig. 8.7, again for the $h0l$ reciprocal lattice section of the monoclinic crystal shown in Fig. 8.6(a). The shaded region indicates a 'nest' of spheres with diameters in the wavelength range from largest wavelength (smallest sphere diameter) to smallest wavelength (largest sphere diameter). All the planes whose reciprocal lattice points lie within this region satisfy Bragg's law for the particular sphere on which they lie.

The Laue technique is unique in that it utilizes white X-radiation. All the others utilize monochromatic or near-monochromatic (K_α) X-radiation. In order to obtain diffraction, therefore, the crystal and the sphere (of a fixed diameter) must be moved relative to one another; whenever a reciprocal lattice point touches the sphere then 'out shoots' a diffracted (or reflected) beam from the centre of the sphere in a direction through the reciprocal lattice point. As described in Chapter 9 there are several ways in which these relative movements may be achieved in practice and several ways in which the diffracted beams may be recorded. The crystal may be oscillated (oscillation method), precessed

(precession method), the film may be arranged cylindrically round the crystal or flat, it may be stationary or it may be moved in some way as in the Weissenberg method (in which the cylindrical film movement is linked to the oscillation of the crystal) or, as in the precession method, precessed with the crystal. The geometry of these X-ray diffraction methods may *appear* to be complicated, but the basis of them all—the Ewald reflecting sphere construction—is the same.

Exercises

- 8.1 Compare Figs 7.5 and 8.3; both show conditions for constructive interference, one for light at a diffraction grating with line spacing a (Fig. 7.5) and one for X-rays reflected from planes of spacing d_{hkl} (Fig. 8.3). Show that the equations describing the conditions for constructive interference in each case ($n\lambda = a \sin \alpha_n$ and $n\lambda = 2d_{hkl} \sin \theta$) are equivalent.
- 8.2 Iron (bcc, $a = 0.2866$ nm (2.866 \AA)) is irradiated with $\text{CrK}\alpha$ X-radiation ($\lambda = 0.2291$ nm (2.291 \AA)). Find the indices $\{hkl\}$ and d -spacings of the planes which give rise to X-ray reflections.
(Note: In body-centred lattices, reflection from planes for which $(h + k + l)$ does *not* equal an even integer are forbidden (see Appendix 6).)
(Hint: Prepare a table listing the indices and d -spacings of the allowed reflecting planes in order of decreasing d -spacings and determine the θ angles for reflection using Bragg's law.)
- 8.3 It is stated without proof with respect to Bragg's law that when the atoms are not symmetrically disposed to the incident and reflected beams (Fig. 8.3(b)), the path difference $(AB + BC) = 2d_{hkl} \sin \theta$. Prove, using very simple geometry, that this is indeed the case.

The diffraction of X-rays

9.1 Introduction

In Chapter 8, the Laue equations and Bragg's law were derived on the basis that single atoms, of unspecified scattering power, were situated at each lattice point. Now we need to consider the physics of the scattering process. Since it is almost exclusively the electrons in atoms which contribute to the scattering of X-rays we have to sum the contributions to the scattered amplitude of all the electrons in all the atoms in the crystal, a problem which may be approached step-by-step. First the scattering amplitude of a single electron and the variation in scattering amplitude with angle is determined. Then the scattering amplitude of an atom is determined by summing the contributions from all Z electrons (where Z = the atomic number of the atom)—the summation taking into account the path or phase differences between all the Z scattered waves. The result of this analysis is expressed by a simple number, f , the **atomic scattering factor**, which is the ratio of the scattering amplitude of the atom divided by that of a single (classical) electron, i.e.

$$\text{atomic scattering factor } f = \frac{\text{amplitude scattered by atom}}{\text{amplitude scattered by a single electron}}.$$

At zero scattering angle, all the scattered waves are in phase and the scattered amplitude is the simple sum of the contribution from all Z electrons, i.e. $f = Z$. As the scattering angle increases, f falls below Z because of the increasingly destructive interference effects between the Z scattered waves. Atomic scattering factors f are plotted as a function of angle (usually expressed as $\sin \theta/\lambda$). Figure 9.1 shows such a plot for the oxygen anion O^{2-} , the neon atom Ne , and the silicon cation Si^{4+} —all of which contain 10 electrons. When $\sin \theta/\lambda = 0$, $f = 10$ but with increasing angle f falls below 10. The extent to which it does depends upon the relative sizes of the atoms or ions; the silicon cation is small, hence the phase differences are small and the destructive interference between the scattered waves is least—and conversely for the large oxygen anion.

The scattering amplitude of a unit cell is determined by summing the scattering amplitudes, f , from all the atoms in the unit cell (equivalent, in the case of a primitive unit cell), to all the atoms in the motif. Again, the summation must take into account the path or phase differences between all the scattered waves and is again expressed by a dimensionless number, F_{hkl} , the **structure factor**, i.e.

$$\text{structure factor } F_{hkl} = \frac{\text{amplitude scattered by the atoms in the unit cell}}{\text{amplitude scattered by a single electron}}.$$

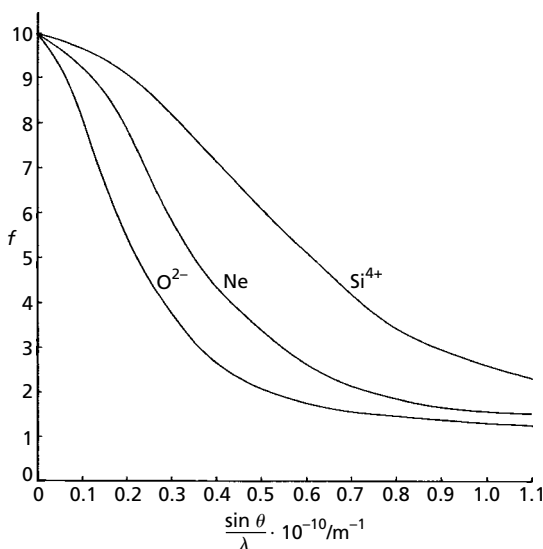


Fig. 9.1. The variation in atomic scattering factor f with scattering angle (expressed as $\sin \theta / \lambda$) for atoms and ions with ten electrons. Note that the decrease in f is greatest for the (large) O^{2-} anion and least for the (small) Si^{4+} cation.

F_{hkl} must not only express the amplitude of scattering from a reflecting plane with Laue indices hkl but must also express the phase angle of the scattered wave, an important concept which is explained in Section 9.2 below. F_{hkl} is therefore not a simple number, like f , but is represented as a vector or mathematically as a complex number (see Appendix 5).

Crystal structure determination is a two-part process: (a) the determination of the size and shape of the unit cell (i.e. the lattice parameters) from the geometry of the diffraction pattern and (b) the determination of the lattice type and distribution of the atoms in the structure from the (relative) intensities of the diffraction spots. Part (a) is in principle a straightforward process; part (b) is not, because films and counters record intensities which are proportional to the *squares* of the amplitudes. The square of a complex number, F_{hkl} is always real (i.e. a simple number) and hence the information about the phase angles of the diffracted beams is lost. A major problem in crystal structure determination is, in effect, the recovery of this phase information and requires for its solution as much insight and intuition as mathematical and crystallographic knowledge. A graphic account of the problems involved in the epoch-making determination of the structure of DNA is given by one of those most closely involved, James D. Watson, in his book *The Double Helix* (see Further Reading).

The distinction between the direction-problem and intensity-problem of diffracted beams from crystals has its corollary in the diffraction of light from diffraction gratings, which may be expressed as follows. A (primitive) crystal with one atom per lattice point (Fig. 9.2(a)) may be regarded as being analogous to a 'narrow slit' diffraction

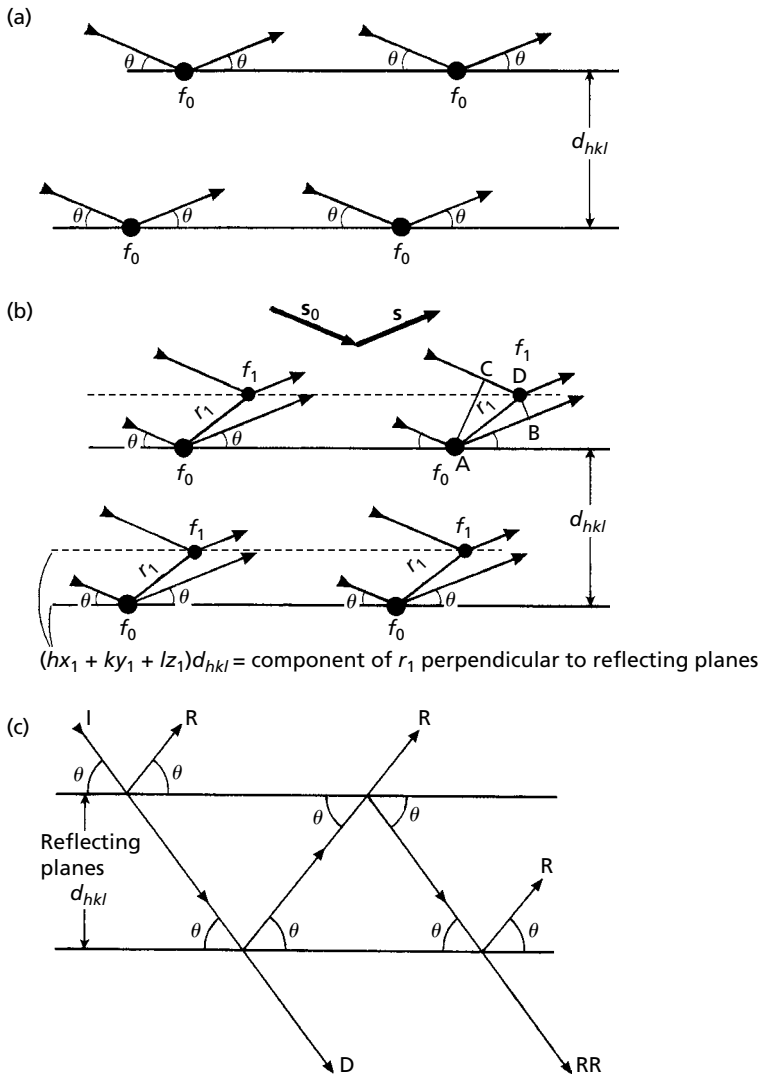


Fig. 9.2. (a) Part of a crystal lattice with atoms with atomic scattering factor f_0 , situated at each lattice point, and a particular set of (hkl) planes through the lattice points. Incident/reflected beams at the Bragg angle θ to these planes are indicated by the arrows. (b) As for (a), but with another atom with atomic scattering factor f_1 defined by position vector r_1 . The path difference (shown for simplicity for one motif) is given by $(AB - CD)$, s and s_0 are unit vectors along the reflected and incident beam directions and the component of r_1 perpendicular to the (hkl) planes is also indicated. (c) The process of reflection and re-reflection for a single incident beam I ; as it passes through the crystal at the Bragg angle θ it is (partially) reflected by each successive plane. The reflected beams R are then re-reflected from the 'undersides' of the planes giving rise to beams RR with interfere *destructively* with the direct beam D . Clearly, the process is repeated for all the beams throughout the crystal.

grating in which each slit can be regarded as the source of a single Huygens' wavelet which propagates uniformly in all directions (Fig. 7.5). Only the interference effects of light emanating from different slits (equivalent to single atoms at lattice points) need to be taken into account and these determine the directions of the diffracted beams (Section 7.4). The intensities of the diffracted beams are proportional to the squares of the scattered amplitudes of the Huygens' wavelets (for light) or the squares of the atomic scattering factors of the single atoms (for X-rays).

A (primitive) crystal with a motif consisting of more than one atom (Fig. 9.2(b)) may be regarded as being analogous to a 'wide slit' diffraction grating in which the interference effects from all the atoms in the motif may be regarded as being analogous to the interference effects between all the Huygens' wavelets distributed *across* each slit. Of course, the problem is rather more complicated because the atoms in the motif do not all lie in a plane or surface as do the Huygens' wavelets, but the principle—of summing the contributions with respect to phase differences—is the same.

As shown in Section 7.4 and Fig. 7.7, the diffraction pattern from a wide-slit diffraction grating may be expressed as that from a narrow-slit grating in which the intensities of the diffracted beams are modulated by the intensity distribution predicted to occur from a single wide slit. Similarly, in the case of X-ray diffraction from crystals it is the structure factor, F_{hkl} , which expresses the interference effects from all the atoms in the unit cell and which modulates, in effect, the intensities of the diffracted beams.

The final step is to sum the contributions from all the unit cells in the crystal. This is a difficult problem because we have to take into account the fact that the incident X-ray beam is attenuated as it is successively scattered by the atoms in the crystal—such that atoms 'deeper down' in the crystal encounter smaller amounts of incident radiation. Furthermore, the reflected beams also propagate through the crystal at the Bragg angle θ (see Fig. 9.2(c)) and are hence 're-reflected' in a direction parallel to that of the incident beam. These re-reflected beams then interfere destructively¹ with the incident or direct beam, attenuating it still further. This is covered in a comprehensive analysis, known as the dynamical theory of X-ray diffraction because it takes into account the dynamical interactions between the direct, reflected and re-reflected, etc., beams. It is much simpler to consider the case in which the size of the crystal is sufficiently small such that the attenuation of the direct beam is negligible and the intensities of the diffracted beams are small in comparison with the direct beam.² This case is fairly readily achieved in X-ray diffraction and enables the observed relative intensities of the diffracted spots to be assumed to be equal to the relative intensities of the squares of the F_{hkl} values.³

¹ When considering the interference between the direct and re-reflected beams, the 180° or π phase difference of the re-reflected beams needs to be taken into account. This complication does not arise when we are considering interference between the reflected or diffracted beams alone.

² The crystal size in this context is better expressed by the notion of coherence length—the dimensions over which the scattering amplitudes from the unit cells can be summed. Crystal imperfections—dislocations, stacking faults, subgrain boundaries—within imperfect single crystals effectively limit or determine the coherence length as well as grain boundaries in perfect crystals (see Section 9.3.3).

³ A number of physical and geometrical factors also need to be taken into account—temperature factor, Lorentz-polarization factor, multiplicity factor, absorption factor, etc. These are described in standard textbooks such as *Elements of X-ray Diffraction* by B. D. Cullity and S. R. Stock, (2001) Addison Wesley.

In electron diffraction, however, dynamical effects are always important and the above assumption cannot be made, but they are an important source of specimen contrast in the electron microscope.

Finally, we have to consider the connection between the diffraction pattern and the type of unit cell (whether it is centred or not) and the symmetry elements present. It turns out that the presence of the centring lattice points and translational symmetry elements (glide planes and screw axes—see Section 4.5) results in ‘zero intensity’ or *systematically absent* reflections from certain planes with Laue indices hkl . This topic, and that of *double diffraction*, which is of particular importance in the case of electron diffraction, are discussed in Appendix 6.

9.2 The intensities of X-ray diffracted beams: the structure factor equation and its applications

We shall begin by considering the simplest case of a primitive crystal with just one atom at each lattice point. Figure 9.2(a) shows part of such a crystal with atoms with atomic scattering factor f_0 at each lattice point (the subscript 0 indicating that each atom is at an origin). Consider an X-ray beam incident at the correct Bragg angle θ in a particular set of lattice planes (hkl) as indicated. For all the atoms lying in one plane the path differences between the reflected beams are zero, and for the atoms lying in successive planes spaced d_{hkl} , $2d_{hkl}$ etc. apart the path differences are λ , 2λ , etc. (Fig. 8.3). In all cases constructive interference occurs and the total scattered amplitude (relative to that of a single electron—see Section 9.1) is simply the sum of the atomic scattering factors. Hence, since we have a primitive crystal with one lattice point and therefore one atom per unit cell, the scattered amplitude from one cell, F_{hkl} , is simply equal to the atomic scattering factor, f_0 .

Now consider a crystal with a motif consisting of two atoms, one at the origin with atomic scattering factor f_0 , as before and another with atomic scattering factor f_1 at a distance from the origin defined by vector \mathbf{r}_1 (Fig. 9.2(b)); \mathbf{r}_1 is called a **position vector** because it specifies the position of an atom within the unit cell. It may be expressed in terms of its components or fractional atomic coordinates along the unit cell vectors \mathbf{a} , \mathbf{b} , \mathbf{c} in the same way as for a lattice vector \mathbf{r}_{uvw} , i.e. $\mathbf{r}_1 = x_1\mathbf{a} + y_1\mathbf{b} + z_1\mathbf{c}$; the important difference being that the components $x_1y_1z_1$ are *fractions* of the cell edge lengths, whereas the components uvw of a lattice vector \mathbf{r}_{uvw} are *integers*.

The path difference (P.D.) between the waves scattered by these two atoms is AB – CD (Fig. 9.2(b)), which, expressed in vector notation, is:

$$\text{P.D.} = \text{AB} - \text{CD} = \mathbf{r}_1 \cdot \mathbf{s} - \mathbf{r}_1 \cdot \mathbf{s}_0 = \mathbf{r}_1 \cdot (\mathbf{s} - \mathbf{s}_0)$$

where \mathbf{s} , \mathbf{s}_0 are unit vectors along the direction of the reflected and incident beams, respectively. Two substitutions can be made in this equation. First, \mathbf{r}_1 may be expressed in terms of its components and second (since Bragg’s law is satisfied) the vector $(\mathbf{s} - \mathbf{s}_0)$ may be expressed in terms of λ and \mathbf{d}_{hkl}^* (see Section 8.3), i.e.

$$(\mathbf{s} - \mathbf{s}_0) = \lambda \mathbf{d}_{hkl}^* = \lambda (h\mathbf{a}^* + k\mathbf{b}^* + l\mathbf{c}^*).$$

Hence

$$\text{P.D.} = \lambda(x_1 \mathbf{a} + y_1 \mathbf{b} + z_1 \mathbf{c}) \cdot (h\mathbf{a}^* + k\mathbf{b}^* + l\mathbf{c}^*)$$

multiplying out, and remembering the identities $\mathbf{a} \cdot \mathbf{a}^* = 1$, etc., $\mathbf{a} \cdot \mathbf{b}^* = 0$, etc.:

$$\text{P.D.} = \lambda(hx_1 + ky_1 + lz_1).$$

This equation is another manifestation of the Weiss zone law (Section 6.5.3); in this case the *number* within the brackets $(hx_1 + ky_1 + lz_1)$ represents the component of \mathbf{r}_1 perpendicular to the lattice planes as a fraction of the interplanar spacing, d_{hkl} (Fig. 9.2(b)). It is clearly the important number with respect to constructive/destructive interference conditions; when for example $(hx_1 + ky_1 + lz_1) = 0$ (the two atoms lying within the (hkl) planes), complete constructive interference occurs and when $(hx_1 + ky_1 + lz_1) = 0.5$ (the second atom lying halfway between the (hkl) planes), destructive interference occurs, which is complete when the atomic scattering factors of the two atoms in the motif are equal.

In general, in adding the contributions of the two atoms, we need to use a vector-phase diagram in which the lengths or moduli of the vectors are proportional to the atomic scattering factors of the atoms, and the phase angle between them, ϕ_1 , is equal to $2\pi/\lambda$ (P.D.), i.e. in the above case

$$\phi_1 = 2\pi(hx_1 + ky_1 + lz_1).$$

This is shown in Fig. 9.3(a). The resultant is the structure factor, F_{hkl} .

The analysis may be simply extended to any number of atoms in the motif with position vectors $\mathbf{r}_1, \mathbf{r}_2, \mathbf{r}_3$ etc. and phase angles (referred to the origin) ϕ_1, ϕ_2, ϕ_3 etc. The resultant, F_{hkl} is found by adding all the vectors, representing the atomic scattering factors of all the atoms, as shown in Fig. 9.3(b). Note that the phase angles, ϕ , are all measured with respect to the origin (horizontal line in Fig. 9.3); they are *not* the angles

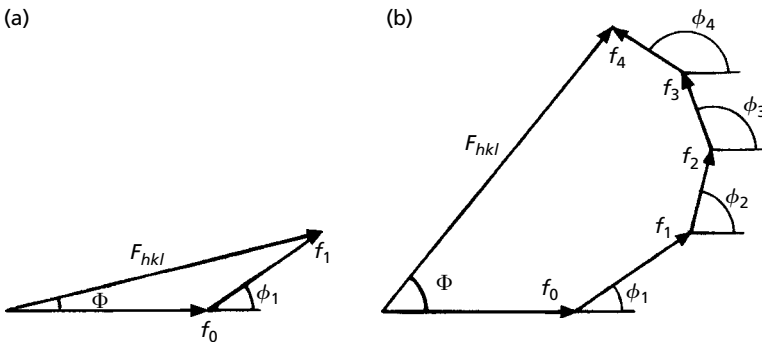


Fig. 9.3. Vector-phase diagrams for obtaining F_{hkl} . The atomic scattering factors f_1, f_2, \dots are represented as vectors with phase angles ϕ_1, ϕ_2, \dots with respect to a wave scattered from the origin: (a) result for two atoms and (b) result for several atoms.

between the vectors. Note also that, although for simplicity we began with an atom at the origin, there need not be one there. The length or *modulus* of the vector F_{hkl} represents the resultant amplitude of the scattered or reflected beam and the angle Φ which it makes with the horizontal line is the resultant phase angle.

Adding vectors graphically in this way is obviously not very convenient; in practice vector-phase diagrams, such as Fig. 9.3, are substituted by Argand diagrams in which F_{hkl} is represented as a complex number (see Appendix 5), i.e.

$$F_{hkl} = \sum_{n=0}^{n=N} f_n \exp 2\pi i(hx_n + ky_n + lz_n)$$

where f_n is the atomic scattering factor and $2\pi(hx_n + ky_n + lz_n)$ is the phase angle ϕ_n of the n th atom in the motif with fractional coordinates (x_n, y_n, z_n) .

Many students are deterred at first sight of equations such as this. It is important to realize that it *merely* represents an analytical way of adding vectors ‘top to tail’, the convenience and ease of which is soon appreciated by way of a few examples.

Example 1: CsCl structure (Fig. 1.12). The (x_n, y_n, z_n) values are (000) for Cl, atomic scattering factor f_{Cl} and $(\frac{1}{2}, \frac{1}{2}, \frac{1}{2})$ for Cs, atomic scattering factor f_{Cs} . Substituting these two terms in the equation:

$$\begin{aligned} F_{hkl} &= f_{\text{Cl}} \exp 2\pi i(h \cdot 0 + k \cdot 0 + l \cdot 0) + f_{\text{Cs}} \exp 2\pi i\left(h \frac{1}{2} + k \frac{1}{2} + l \frac{1}{2}\right) \\ &= f_{\text{Cl}} + f_{\text{Cs}} \exp \pi i(h + k + l). \end{aligned}$$

Two situations may be identified: when $(h + k + l) = \text{even integer}$, $\exp \pi i$ (even integer) $= 1$, hence $F_{hkl} = f_{\text{Cl}} + f_{\text{Cs}}$ and when $(h + k + l) = \text{odd integer}$, $\exp \pi i$ (odd integer) $= -1$, hence $F_{hkl} = f_{\text{Cl}} - f_{\text{Cs}}$. These two situations may be simply represented on the Argand diagram as shown in Fig. 9.4. Note that in both cases F_{hkl} is a real number; the imaginary component is zero. This arises because CsCl has a centre of symmetry at the origin, as explained below.

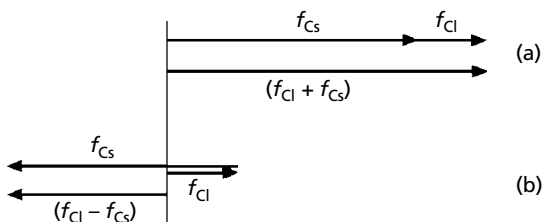


Fig. 9.4. Argand diagrams for F_{hkl} for CsCl (a) $(h + k + l) = \text{even integer}$, $F_{hkl} = f_{\text{Cl}} + f_{\text{Cs}}$; (b) $(h + k + l) = \text{odd integer}$, $F_{hkl} = f_{\text{Cl}} - f_{\text{Cs}}$.

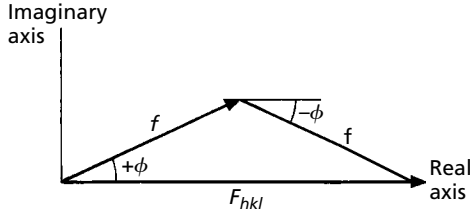


Fig. 9.5. The Argand diagram for a centrosymmetric crystal. The phase angle $+\phi$ for the atom at (xyz) is equal and opposite to the phase angle $-\phi$ for the atom at $(\bar{x}\bar{y}\bar{z})$, hence F_{hkl} is real.

Example 2: bcc metal structure. The atomic coordinates are (000) , $(\frac{1}{2} \frac{1}{2} \frac{1}{2})$ —the same as for CsCl—but the atomic scattering factors are equal. Proceeding as before we find that when $(h + k + l) = \text{odd integer}$, F_{hkl} is zero (see Appendix 6).

Example 3: A crystal with a centre of symmetry at the origin. This is an important case because the structure factor for all reflections is real (as in Examples 1 and 2).

For every atom with fractional coordinates (xyz) and phase angle $+\phi$ there will be an identical one on the *opposite* side of the origin with fractional coordinates $(\bar{x}\bar{y}\bar{z})$ and phase angle $-\phi$. For these two atoms:

$$\begin{aligned} F_{hkl} &= f \exp 2\pi i(hx + ky + lz) + f \exp 2\pi i(h\bar{x} + k\bar{y} + l\bar{z}) \\ &= f \exp 2\pi i(hx + ky + lz) + f \exp -2\pi i(hx + ky + lz). \end{aligned}$$

The second term is the complex conjugate of the first, hence the sine terms cancel and

$$F_{hkl} = 2f \cos 2\pi(hx + ky + lz)$$

as shown graphically in Fig. 9.5.

Example 4: hcp metal structure. Here we have a choice of unit cells (Fig. 5.8). It is best to refer to the primitive hexagonal cell, Fig. 5.8(a), which contains two identical atoms, atomic scattering factor f . We also have a choice of origin. We can choose a cell with one atom at the origin (000) (an A-layer atom) and the other with fractional atomic coordinates $(\frac{1}{3} \frac{2}{3} \frac{1}{2})$ (a B-layer atom), Fig. 9.6. In this case the origin is *not* at a centre of symmetry. Alternatively, we can place the origin at a centre of symmetry which are at positions equidistant between an A-layer and a *next nearest* B-layer atom (not, it should be noted between adjacent A and B-layer atoms). One such choice of origin is also shown in Fig. 9.6 and the fractional atomic coordinates in the cell become $(\frac{1}{3} \frac{2}{3} \frac{3}{4})$ and $(\frac{2}{3} \frac{1}{3} \frac{1}{4})$ (equivalent to $(\frac{1}{3} \frac{2}{3} \frac{1}{4})$). These correspond to the fractional atomic coordinates denoted by Wyckoff letter d in space group $P6_3/mmc$ (Fig. 4.14).

It is a useful exercise to apply the structure factor equation to both of these choices of origin. First we choose the origin at an A-layer atom. Substituting coordinates (000)

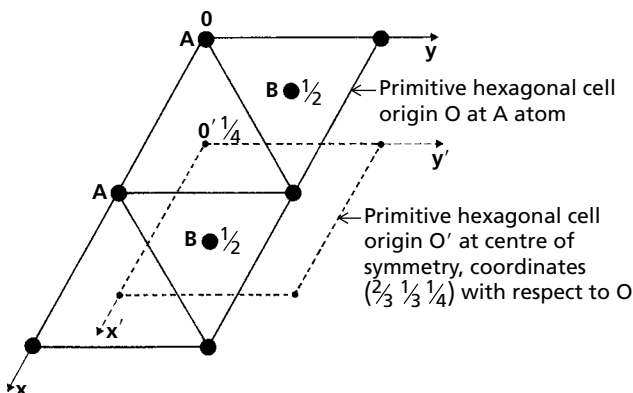


Fig. 9.6. hcp metal structure, centres of A and B layer atoms as indicated. The origin of the primitive hexagonal cell may be chosen at an atom position (solid lines) or at centre of symmetry (dashed lines).

and $(\frac{1}{3}, \frac{2}{3}, \frac{1}{2})$ in the equation:

$$F_{hkl} = f \exp 2\pi i(h0 + k0 + l0) + f \exp 2\pi i \left(h\frac{1}{3} + k\frac{2}{3} + l\frac{1}{2} \right) \\ = f \left(1 + \exp 2\pi i \left(h\frac{1}{3} + k\frac{2}{3} + l\frac{1}{2} \right) \right).$$

Now let us apply this to some particular (hkl) planes, e.g. $(002) \equiv (0002)$; $(100) \equiv (10\bar{1}0)$ and $(101) \equiv (10\bar{1}1)$:

$$F_{002} = f(1 + \exp 2\pi i) = 2f$$

$$F_{100} = f \left(1 + \exp \frac{2}{3}\pi i \right) = f \left(1 + \cos \frac{2}{3}\pi + i \sin \frac{2}{3}\pi \right) = f(0.5 + i0.866)$$

$$F_{101} = f \left(1 + \exp 2\pi i \left(\frac{1}{3} + \frac{1}{2} \right) \right) = f \left(1 + \cos \frac{5}{3}\pi + i \sin \frac{5}{3}\pi \right) = f(1.5 - i0.866).$$

These results are shown graphically in Fig. 9.7. Note that F_{100} and F_{101} are complex numbers.

The intensities I_{hkl} of X-ray beams are proportional to their amplitudes squared, or F_{hkl} multiplied by its complex conjugate F_{hkl}^* (see Appendix 5). For the hcp metal example above:

$$I_{002} = 2f \cdot 2f = 4f^2$$

$$I_{100} = f(0.5 + i0.866)f(0.5 - i0.866) = f^2$$

$$I_{101} = f(1.5 - i0.866)f(1.5 + i0.866) = 3f^2.$$

Again, it should be stressed that I_{hkl} is a real number, the phase information expressed in F_{hkl} is lost.

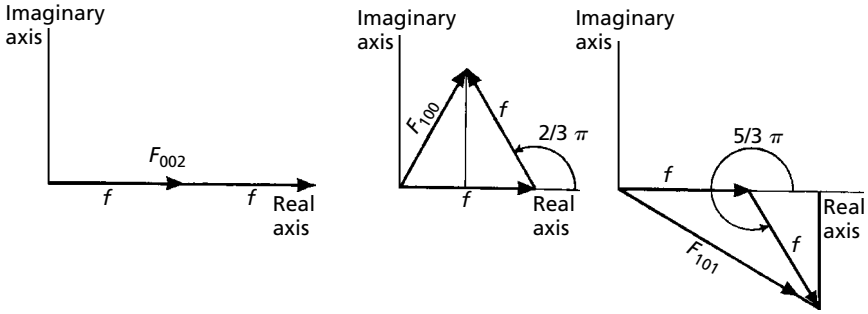


Fig. 9.7. Argand diagrams for an hcp metal for (left to right) F_{002} , F_{100} and F_{101} showing also how these structure factors are obtained graphically by vector addition. The origin is not at the centre of symmetry.

For the origin at a centre of symmetry we use the simplified equation (Example 3) and coordinates ($\frac{1}{3}$ $\frac{2}{3}$ $\frac{3}{4}$).

$$F_{hkl} = 2f \cos 2\pi \left(h^1/3 + k^2/3 + l^3/4 \right).$$

Again, for the particular (hkl) planes (002), (100) and (101) we have:

$$F_{002} = 2f \cos 3\pi = 2f; \quad I_{002} = 4f^2$$

$$F_{100} = 2f \cos 2\pi/3 = f; \quad I_{100} = f^2$$

$$F_{101} = 2f \cos \pi^{13}/6 = \sqrt{3}/2f; \quad I_{101} = 3f^2.$$

Note that the structure factors are real and (of course) the intensities are the same as those obtained in the previous case.

Example 5: Non-centrosymmetric crystal: Friedel's Law and anomalous scattering. It follows from Example 3 that the diffraction pattern from a centrosymmetric crystal is also centrosymmetric. However, except for the case of anomalous scattering discussed below, even if a crystal does not possess a centre of symmetry, the diffraction pattern will still be centrosymmetric. This is known as Friedel's law which may be proved with reference to the Argand diagram in Fig. 9.8(a). We have to show that the intensity of the reflection from the hkl planes, i.e. I_{hkl} is equal to that from the $\bar{h}\bar{k}\bar{l}$ planes, i.e. $I_{\bar{h}\bar{k}\bar{l}}$.

As can be seen, $F_{\bar{h}\bar{k}\bar{l}}$ is the complex conjugate of F_{hkl} ; i.e. $F_{\bar{h}\bar{k}\bar{l}} = F_{hkl}^*$ and similarly $F_{hkl} = F_{\bar{h}\bar{k}\bar{l}}^*$.

$$\text{Hence } I_{hkl} = F_{hkl} \cdot F_{hkl}^* = F_{\bar{h}\bar{k}\bar{l}}^* \cdot F_{hkl} = I_{\bar{h}\bar{k}\bar{l}}.$$

The presence of a centre of symmetry in the diffraction pattern means that non-centrosymmetric crystals cannot be distinguished from those with a centre of symmetry. There are eleven centrosymmetric point groups (Table 3.1, page 91) and hence eleven symmetries which diffraction patterns can possess. These are called the eleven

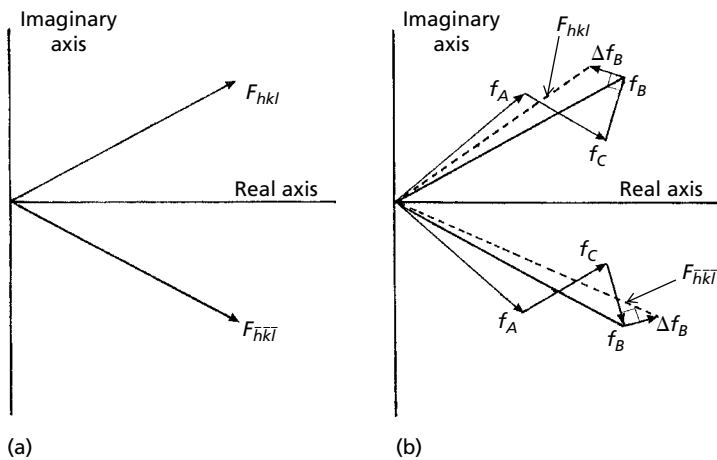


Fig. 9.8. Argand diagram for a non-centrosymmetric crystal: (a) no anomalous scattering; (b) anomalous scattering for atom B (see Fig 9.9).

Table 9.1 The eleven Laue point groups or crystal classes.

Crystal system	Laue point group and centrosymmetric point group	Non-centrosymmetric point groups belonging to the Laue point group	
Cubic	$m\bar{3}m$	432	$\bar{4}3m$
(two Laue point groups)	$m\bar{3}$	23	
Tetragonal	$4/mmm$	422	$4mm$ $\bar{4}2m$
(two Laue point groups)	$4/m$	4	$\bar{4}$
Orthorhombic	mmm	222	$mm2$
Trigonal	$\bar{3}m$	32	$3m$
(two Laue point groups)	$\bar{3}$	3	
Hexagonal	$6/mmm$	622	$6mm$ $\bar{6}m2$
(two Laue point groups)	$6/m$	6	$\bar{6}$
Monoclinic	$2/m$	2	m
Triclinic	$\bar{1}$	1	

Laue groups and are identified by the corresponding point group symbol of the centrosymmetric point group. They are listed in Table 9.1.

Friedel’s law holds so long as the phases of the scattered waves are those expected for scattering at the atomic centres, i.e. precisely at the positions specified by the fractional atomic coordinates $(x_n \ y_n \ z_n)$. However, if the energy of the incident X-rays is just sufficient to displace the innermost K-electrons from their orbitals, i.e. if the wavelength is just below the K-absorption edge wavelength of an atom, then the phase of the scattered wave differs from that expected from scattering at the atomic centre. It is as if the atom were displaced and the sense of the displacement depends on whether the reflection is

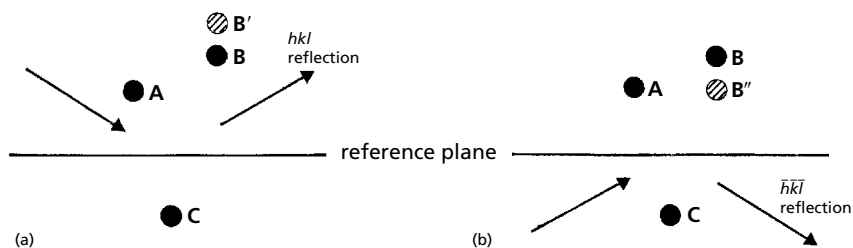


Fig. 9.9. Representation of anomalous scattering of atom labelled B: (a) hkl reflection, B displaced to B'; and (b) $\bar{h}\bar{k}\bar{l}$ reflection, B displaced to B''.

from the 'top' or 'underside' of the reflecting planes. This is the condition for anomalous scattering. Figure 9.9 (due to W.L. Bragg) shows the geometry involved for just three atoms, A, B and C, one of which, B, scatters anomalously.

For the hkl reflection, Fig. 9.9(a), B scatters as if it were situated at B' and for the $\bar{h}\bar{k}\bar{l}$ reflection, Fig. 9.9(b), B scatters as if it were at B''. The resultant amplitudes, obtained by combining the effects of all the atoms, will clearly be different.

The effect may also be represented in the Argand diagram; the alteration of phase of an anomalously scattering atom is equivalent to combining the normal f of the atom with a vector Δf at right angles to it as shown in Fig. 9.8(b), where the resultant structure factors F_{hkl} and $F_{\bar{h}\bar{k}\bar{l}}$ which are now different, are shown by the dashed lines.

Anomalous scattering (or absorption) can be 'put to use' to distinguish centrosymmetric and non-centrosymmetric point groups. In particular it can be used to distinguish the right and left-handed (dextro and laevo) crystals in the enantiomorphic point groups—e.g. tartaric acid (Fig. 4.6, page 107). In so doing a salt is synthesized which contains an anomalously scattering atom for the X-ray wavelength used. The first such experiments were carried out by J. M. Bijvoet* using crystals of sodium rubidium tartrate. It is very fortunate (even chances!) that the dextro- and laevo-configurations thus determined agree with those of chemical convention—otherwise all the dextro- and laevo-conventions would have had to be interchanged.

To summarize, these simple examples show how the amplitude, F_{hkl} , and hence the intensity, I_{hkl} , of the reflected X-ray beam from a set of hkl planes can be calculated from the simple 'structure factor' equation on p. 209; all we need to know are the positions of the atoms in the unit cell (the $x_n y_n z_n$ values) and their atomic scattering factors, f_n . The great importance of the equation is that it can be applied, as it were, 'the other way round': by measuring the intensities of the reflections from several sets of planes (the more the better), the positions of the atoms in the unit cell can be determined. This is the basis of crystal structure determination, which has developed and expanded since the pioneering work of the Braggs, so that, at the time of writing, some 400 000 different crystal structures are known. Many of these are very complex, for example protein crystals in which the motif may consist of several thousand atoms. Again, it

* Denotes biographical notes available in Appendix 3.

should be emphasized that the procedures are invariably not straightforward because the phase information in going from the F_{hkl} to the (measured) I_{hkl} values is lost, e.g. as in Example 4, Fig. 9.7. This is called the **phase problem** in crystal structure determination, which may be understood with reference to Fig. 9.3(b). All F_{hkl} vectors with the same modulus or amplitude will give the same observed intensity I_{hkl} ; the value of the phase angle Φ , which is an essential piece of information in the vector-phase diagram, is lost. In short, we do not know in which direction the vector F_{hkl} ‘points’, e.g. as in Fig. 9.7. In some cases (as in Example 4), the problem is simply solved if we are able to arrange the origin to coincide with a centre of symmetry in the crystal in which case, as shown in Example 3, Fig. 9.5, the phase angle ϕ is zero and the structure factor F_{hkl} is a real number with no imaginary component. However, in the many cases where the crystal does not possess a centre of symmetry, we must resort to more subtle procedures, the details of which are beyond the scope of this book. One method is to arrange a heavy atom (possibly substituted in the crystal structure for a light atom) to be at the origin. Then, in terms of our vector-phase diagram (Fig. 9.3(b)), f_0 is so large that it dominates the contributions of all the other atoms such that the phase angles Φ for all the F_{hkl} values are small and therefore can more easily be guessed at. In all cases the structure factor equation is expressed as it were in a ‘converse’ form (or transform of that on p. 209 in which atomic positions (expressed as electron (X-ray scattering) density) are expressed in terms of the F_{hkl} values of the reflections.

The notion of *electron density* provides a much more realistic representation of atomic structure. Atoms, which are detected by X-rays from the scattering of their constituent electrons, have a finite size and the atomic coordinates essentially represent those positions where the amount of scattering (the electron density) is the highest. In our two-dimensional plan views (Section 1.8) we may therefore represent the atoms as hills—a contour map of electron density; the ‘higher the hill’ the greater the atomic scattering factor of the atom. These ideas, which involve the application of Fourier analysis, are introduced in Chapter 13, but it is a subject of great complexity which is covered in more detail in those books on crystal structure determination which are listed in Further Reading.

9.3 The broadening of diffracted beams: reciprocal lattice points and nodes

In Chapter 8 we treated diffraction in a purely geometrical way, incident and reflected beams being represented by single lines implying perfectly narrow, parallel beams and reflections only at the Bragg angles. Of course, in practice, such ‘ideal’ conditions do not occur; X-ray beams have finite breadth and are not perfectly parallel to an extent depending upon the particular experimental set-up. Such *instrumental factors* give rise to broadening of the reflected X-ray beams: the reflections peak at the Bragg angles and decrease to zero on either side. However, broadening is not solely due to such instrumental factors but much more importantly also arises from the crystallite size, perfection and state of strain in the specimen itself. The measurement of such broadening (having accounted for the contribution of the instrumental factor) can then provide information on such specimen conditions.

We now consider the effects of crystal size on the broadening and peak intensity of the reflected beams, which lead to the Scherrer equation (Section 9.3.1) and the notion of integrated intensity (Section 9.3.2). In Section 9.3.3 we consider the imperfection (or mosaic structure) of real crystals. The effect of lattice strain on broadening is covered in Section 10.3.4.

9.3.1 *The Scherrer equation: reciprocal lattice points and nodes*

In Section 7.4 we found that when the number N of lines in a grating, or the number of apertures in a net, were limited, the principal diffraction maxima were broadened and surrounded by much fainter subsidiary maxima. These phenomena are shown in Fig. 7.3(d) and diagrammatically in Fig. 7.9. Precisely the same considerations apply to X-ray (and electron) diffraction from ‘real’ crystals in which the number of reflecting planes is limited: and the broadening and occurrence of the subsidiary maxima can be derived by similar arguments. This, in turn, leads us to modify our concept of reciprocal lattice *points*, which are not geometrical points, but which have finite size and shape, reciprocally related, as we shall see, to the size and shape of the crystal. There is, as far as I know, no common term to express the fact that reciprocal lattice points do have a finite size and shape, except in special cases such as the reciprocal lattice streaks or ‘**rel-rods**’ which occur in the case of thin plate-like crystals. Reciprocal lattice **nodes** seems to be the closest approximation to a common term.

The broadening of the reflected beams from a crystal of finite extent is derived as follows. Consider a crystal of thickness or dimension t perpendicular to the reflecting planes, d_{hkl} , of interest. If there are m planes then $md_{hkl} = t$. Consider an incident beam bathing the whole crystal and incident at the exact Bragg angle for first order reflection (Fig. 9.10 (a)). For the first two planes labelled 0 and 1, the path difference $\lambda = 2d_{hkl} \sin \theta$; for planes 0 and 2 the path difference is $2\lambda = 4d_{hkl} \sin \theta$ and so on—constructive interference between all the planes occurs right through the crystal. Now consider the interference conditions for an incident and reflected beam deviated a small angle $\delta\theta$ from the exact Bragg angle (Fig. 9.7(b)). For planes 0 and 1 the path difference will be very close to λ as before and there will be constructive interference. However, for planes 0 and 2, 0 and 3, etc. the ‘extra’ path difference will deviate increasingly from 2λ , 3λ etc.—and when it is an additional half-wavelength *destructive* interference between the pair of planes will result.

The condition for destructive interference for the whole crystal is obtained by notionally ‘pairing’ reflections in the same way as we did for the destructive interference of Huygens’ wavelets across a wide slit (Fig. 7.8). Consider the constructive and destructive interference condition between planes 0 and $(m/2)$ (halfway down through the crystal). At the exact Bragg angle θ (Fig. 9.10 (a)), the condition for constructive interference is $(m/2)\lambda = (m/2)2d_{hkl} \sin \theta$. The condition for *destructive* interference at angle $(\theta + \delta\theta)$ is given by $(m/2)\lambda + \lambda/2 = (m/2)2d_{hkl} \sin(\theta + \delta\theta)$. Now this is also the condition for destructive interference between the next pair of planes 1 and $(m/2) + 1$ —and so on through the crystal. This equation gives us, in short, the condition for destructive interference for the *whole* crystal and the angular range $\delta\theta$ (each side of the exact Bragg angle) of the reflected beam.

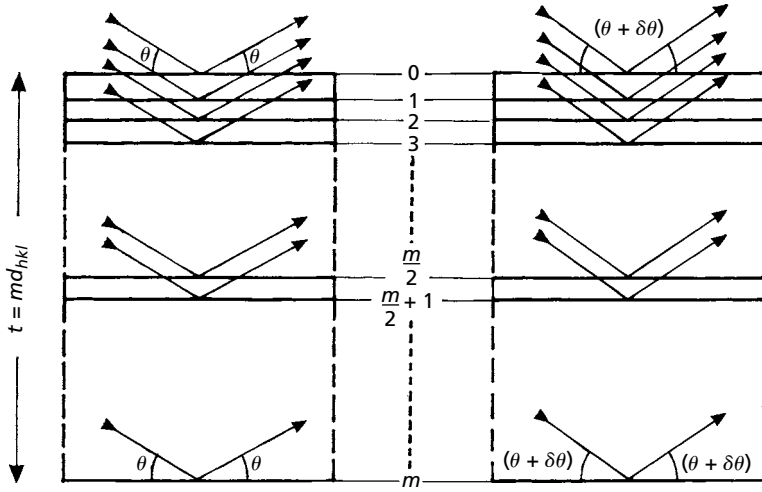


Fig. 9.10. Bragg reflection from a crystal of thickness t (measured perpendicular to the particular set of reflecting planes shown). The whole crystal is bathed in an X-ray beam (a) at the exact Bragg angle θ and (b) at a small deviation from the exact Bragg angle, i.e. angle $(\theta + \delta\theta)$. The arrows represent the incident and reflected beams from successive planes 0, 1, 2, 3 ... $(m/2)$ (half-way down) and ... m (the lowest plane).

Expanding the sine term and making the approximations $\cos \delta\theta = 1$ and $\sin \delta\theta \approx \delta\theta$ gives:

$$(m/2)\lambda + \lambda/2 = (m/2)2d_{hkl} \sin \theta + (m/2)2d_{hkl} \cos \theta \delta\theta.$$

Cancelling the terms $(m/2)\lambda$ and $(m/2)2d_{hkl} \sin \theta$ and substituting $md_{hkl} = t$ gives

$$2\delta\theta = \frac{\lambda}{t \cos \theta} = \frac{2d \sin \theta}{t \cos \theta} = \frac{2 \tan \theta}{m}.$$

This is the basis of the Scherrer* equation which relates the broadening of an X-ray beam to the crystal size t or number of reflecting planes m . The broadening is usually expressed as β , the breadth of the beam at half the maximum peak intensity and in which the angles are measured relative to the direct beam. As indicated in Fig. 9.11, β is approximately equal to $2\delta\theta$, hence

$$\beta = \frac{\lambda}{t \cos \theta} = \frac{2 \tan \theta}{m}.$$

The broadening can be represented in the Ewald reflecting sphere construction in terms of the extension of the reciprocal lattice point to a node of finite size. Figure 9.12 shows

* Denotes biographical notes available in Appendix 3.

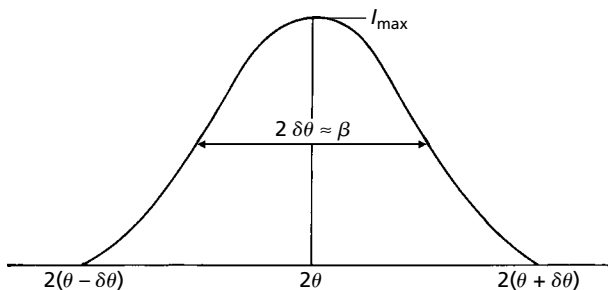


Fig. 9.11. A schematic diagram of a broadened Bragg peak arising from a crystal of finite thickness. The breadth at half the maximum peak intensity, β , is approximately equal to $2\delta\theta$. Note that the angular ' 2θ ' scale is measured in relation to the direct and reflected beams.

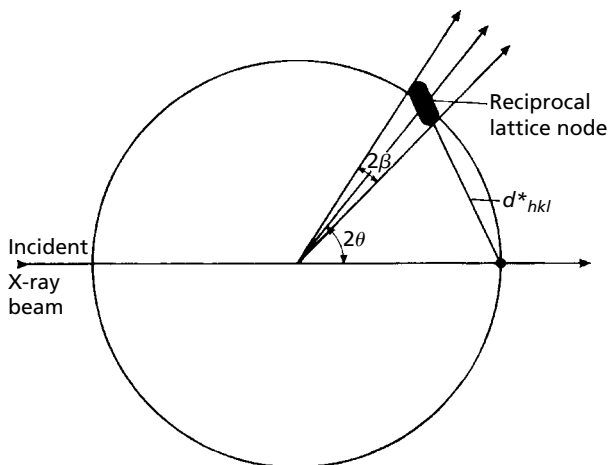


Fig. 9.12. The Ewald reflecting sphere construction for a broadened reflected beam, β , which corresponds to an extension $1/t$ of the reciprocal lattice node.

a diffracted beam (angle 2θ to the direct beam) which is broadened over an angular range $2\beta \approx 4\delta\theta$. This is expressed by extending the reciprocal lattice point into a node of finite length which, as the crystal rotates, intersects the reflecting sphere over this angular range. Let $\delta(d_{hkl}^*)$ represent the extension of the reciprocal lattice point about its mean position. Now since

$$|\mathbf{d}_{hkl}^*| = d_{hkl}^* = \frac{2 \sin \theta}{\lambda};$$

$$\delta(d_{hkl}^*) = \delta \left(\frac{2 \sin \theta}{\lambda} \right) = \frac{2 \cos \theta}{\lambda} \delta\theta.$$

Substituting for $\delta\theta$ from above gives:

$$\delta(d_{hkl}^*) = \frac{2 \cos \theta}{\lambda} \cdot \frac{\lambda}{2t \cos \theta} = \frac{1}{t}$$

i.e. the extension of the reciprocal lattice node is simply the reciprocal of the crystal dimension perpendicular to the reflecting planes. This applies to all the other directions in a crystal with the result that the *shape* of the reciprocal lattice node is reciprocally related to the *shape* of the crystal. For example, in the case of thin, plate-like crystals (e.g. twins or stacking faults), the reciprocal lattice node is a rod or ‘streak’ perpendicular to the plane of the plate.

The extension of the reciprocal lattice node $\delta(d_{hkl}^*)$ may also be expressed as a ratio or proportion of d_{hkl}^* , i.e. since

$$\delta(d_{hkl}^*) = \frac{1}{t} = \frac{1}{md_{hkl}} = \frac{(d_{hkl}^*)}{m},$$

then

$$\frac{\delta(d_{hkl}^*)}{d_{hkl}^*} = \frac{1}{m},$$

i.e. the ratio is simply equal to the reciprocal of the number of reflecting planes, m .

The above is a simplified treatment, both of the Scherrer equation and the extension of reciprocal lattice points into nodes. The Scherrer equation is normally applied to the broadening from polycrystalline (powder) specimens and includes a correction factor K (not significantly different from unity) to account for particle shapes.⁴ Hence the Scherrer equation is normally written:

$$\beta = \frac{K\lambda}{t \cos \theta} = \frac{K\lambda \sec \theta}{t}.$$

Finally, it should be noted that the reciprocal lattice nodes are also surrounded by subsidiary nodes (or satellites, maxima, or fringes) just as in the case of light diffraction from gratings with a finite number of lines (Section 7.4, Fig. 7.9). In most situations these subsidiary nodes are very weak because the number of diffracting planes contributing to the beam is large. However, in the case of X-ray diffraction from specimens consisting of a limited number of diffracting planes, superlattice repeat distances or multilayers, the subsidiary nodes (or satellites, maxima or fringes) are observable and are important in the characterization of the specimen, as described in Section 9.6.

⁴ Note that the observed breadth at half the maximum peak intensity, β_{OBS} , includes additional sources of broadening arising from the experimental set up and instrumentation, β_{INST} , which must be ‘subtracted’ from β_{OBS} in order that β can be determined (see Section 10.3.3).

9.3.2 Integrated intensity and its importance

In Section 9.3.1, we have seen the effect of crystal thickness on broadening. What is its effect on the peak intensity, I_{\max} (Fig. 9.11)? To answer this question we will carry out a ‘thought experiment’. Let us suppose that in our crystal, of thickness t , there are a total of n unit cells each of which contributes a scattering amplitude $|F_{hkl}|$. The total scattered amplitude is therefore $n|F_{hkl}|$ and the total scattered intensity, I_{\max} , is proportional to $n^2|F_{hkl}|^2$. Now let us separate the crystal into two halves, each of thickness $t/2$. The X-ray peaks from each crystal are twice the breadth of that for the single crystal (half the thickness, twice the breadth). The total scattered amplitude from each crystal is $n/2|F_{hkl}|$ and hence the peak intensity is proportional to $n^2/4|F_{hkl}|^2$. Added together, the two crystals give a peak intensity, $I_{\max} = n/2|F_{hkl}|^2$, i.e. *half* that of the single crystal but a peak breadth *twice* that of the single crystal. What is constant and independent of the ‘state of division’—or crystallite size in the specimen—is the *area* under the diffraction peak. This quantity, usually measured in arbitrary units, is called the *integrated intensity* of the reflection or just the *integrated reflection*. It is not a measurement of intensity, but rather a measurement of the total energy of the reflection. Furthermore, except for situations in which dynamical interactions need to be taken into account (i.e. large, perfect crystals in which the reflected beams are comparable in intensity with the direct beam—see Section 9.1), the integrated intensity is a measure of $|F_{hkl}|$ (and of course crystal volume).

9.3.3 Crystal size and perfection: mosaic structure and coherence length

Except for rather special cases there is rarely a continuity of structure throughout the whole volume of a ‘single’ crystal, but rather is separated into ‘blocks’ of slightly varying misorientation (Fig. 9.13(a))—a situation recognized in the early days of X-ray diffraction from the discrepancy between the intensities predicted for ‘perfect’ crystals

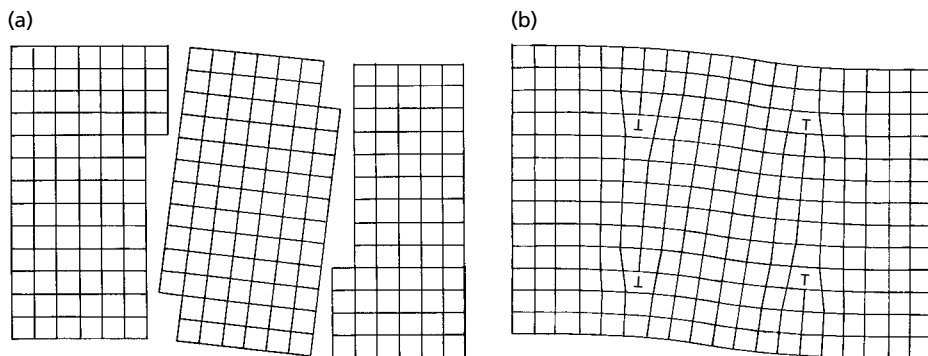


Fig. 9.13. Representation of a single crystal: (a) divided into three mosaic blocks; and (b) the boundaries as ‘walls’ of edge dislocations.

and those actually observed. Ewald termed this a ‘mosaic’ structure—but of course the nature of the mosaic blocks and the boundaries were unknown. It is now evident, from transmission electron microscopy, that crystals contain dislocations which may be distributed uniformly throughout the structure, or arrange themselves (as shown in the simple case in Fig. 9.13(b)), into sub-grain boundaries. However, it remains the case that the relationship between sub-grain size, as measured by electron microscopy, and coherence length or mosaic size, as measured by X-ray broadening, is by no means clear.

In an X-ray experiment, as a crystal is ‘swept’ through its diffracting condition, the individual crystallites of the mosaic structure reflect at slightly different angles and the total envelope of the diffraction profile, or integrated intensity, is the sum of all the separate reflections.

9.4 Fixed θ , varying λ X-ray techniques: the Laue method

X-ray single crystal techniques may be classified into two groups depending upon the way in which Bragg’s law is satisfied experimentally. There are two variables in Bragg’s law— θ and λ —and a series of fixed values, d_{hkl} . In order to satisfy Bragg’s law for any of the d -values, either λ must be varied with θ fixed, or θ must be varied with λ fixed. The former case has only one significant representative—the (original) Laue method and its variants, whereas there are many methods based upon the latter case.

The geometry of the Laue method, in terms of the reflecting sphere construction, has already been explained in Section 8.4. Now we need to consider the practical applications of the technique. The important point to emphasize is that each set of reflecting planes with Laue indices hkl (see Section 8.4) gives rise to just one reflected beam. Of all the white X-radiation falling upon it, a lattice plane with Miller indices (hkl) reflects only that wavelength (or ‘colour’) for which Bragg’s law is satisfied, a reflecting plane of half the spacing with Laue indices $2h\ 2k\ 2l$ reflects a wavelength of half this value, and so on. In other words the reflections from planes such as, for example, (111) (Miller indices for lattice planes) 222, 333, 444, etc. (Laue indices for the parallel reflecting planes) are all superimposed.

The usual practice is to record the back-reflected beams since thick specimens which are opaque to the transmission of X-rays through them can be examined. The set-up showing just one reflected beam in the plane of the paper is shown in Fig. 9.14(a). In analysing the film it is necessary to determine the projection of the normal (or reciprocal lattice vector) of each of the reflecting planes on to the film from each reflection S and then to plot these on a stereographic projection. By measuring the angles between the normals, and then comparing them with lists of angles such as given for cubic crystals in Section A4.4 (Appendix 4), it is possible to identify the reflections. In practice such manual procedures (involving the use of the Greninger net⁵) have largely been replaced

⁵ Greninger nets are prepared for a particular specimen-film distance (e.g. 30 mm), on which are drawn a series of calibrated hyperbolae (for the back reflection case). By measuring the distance between two spots along a hyperbola the angle between the normals, or the reciprocal lattice vectors of the two planes giving rise to these spots, can be obtained.

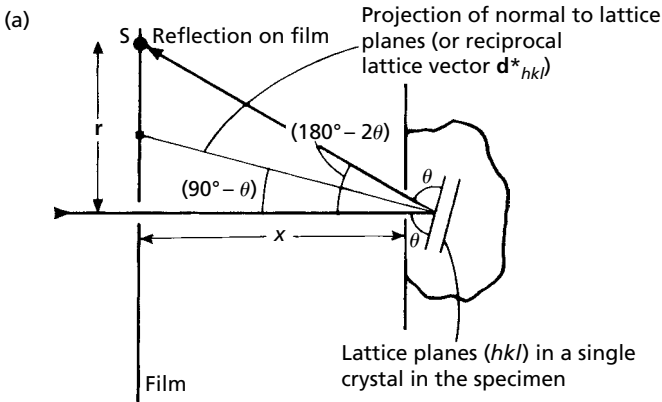


Fig. 9.14. (a) The geometry of the back-reflection Laue method for a particular set of hkl planes in a single crystal. The wavelength of the reflected beam is that for which Bragg's law is satisfied for the particular fixed θ and d_{hkl} value, (b) A back-reflection Laue photograph of a single crystal of aluminium oriented with a $\langle 100 \rangle$ direction nearly parallel to the incident X-ray beam showing the reflections S from many (hkl) planes. They lie on a series of intersecting hyperbolae (close to straight lines in this photograph), each hyperbola corresponding to reflections from planes in a single zone, $[uvw]$. Note the four-fold symmetry of the intersecting zones indicating the $\langle 100 \rangle$ crystal orientation. (Photograph by courtesy of Prof. G. W. Lorimer.)

by computer programs which determine the orientation of the crystal using as input data the positions of spots on the film, film-specimen distance and (assumed) crystal structure.

Hence (back reflection) Laue photographs may be used to determine or check the orientation of single crystals and the orientation relationships between crystals. An example of a Laue photograph is shown in Fig. 9.14(b).

Figure 9.14(a) should be compared with Fig. 8.7. Consider for example the 201 reciprocal lattice point which is situated in the ‘nest’ of spheres representing the wavelength range of the incident ‘white’ X-radiation. Bragg’s law is satisfied for the particular wavelength represented by the sphere which passes through the 201 reciprocal lattice point and the direction of the reflected beam (indicated by the arrow) is from the centre of this sphere (which can be found by construction) and the 201 reciprocal lattice point. This beam makes angle $(180^\circ - 2\theta)$ with the incident beam and the reciprocal lattice vector \mathbf{d}_{201}^* makes angle $(90^\circ - \theta)$ with the incident beam.

9.5 Fixed λ , varying θ X-ray techniques: oscillation, rotation and precession methods

In Section 8.4, Fig. 8.6, we showed the Ewald reflecting sphere construction for the case where the incident X-ray beam was incident along the \mathbf{a}^* reciprocal lattice vector (from the left). Figure 8.6(a) shows the $h0l$ section of the reciprocal lattice through the centre of the sphere and the origin of the reciprocal lattice and Fig. 8.6(b) shows the $h1l$ section of the reciprocal lattice and the smaller (non-diametral) section of the Ewald sphere. For the particular wavelength and particular incident beam direction drawn in Fig. 8.6, only two planes—201 and $21\bar{1}$ satisfy Bragg’s law. Now, instead of varying λ , as in the Laue case (Fig. 8.7), let us change the direction of the incident beam such that it is no longer incident along the \mathbf{a}^* reciprocal lattice vector direction. This variation in the Bragg angle is accomplished in practice by moving the crystal.

9.5.1 *The oscillation method*

Consider the crystal, Fig. 8.6, oscillated say $\pm 10^\circ$ about an axis parallel to the \mathbf{b}^* reciprocal lattice vector (or y -axis), i.e. perpendicular to the plane of the paper. As the crystal is (slowly) oscillated, the angles between the incident beam and hkl planes vary and whenever Bragg’s law is satisfied for a particular plane ‘out shoots’ momentarily a reflected beam. The oscillation of the crystal can be represented by an oscillation of the reciprocal lattice about the origin: imagine a pencil fixed to the crystal perpendicular to the page with its point at the origin of Fig. 8.6(a). As you oscillate the pencil the reciprocal lattice oscillates about the origin but the Ewald sphere remains fixed, centred along the direction of the incident beam from the left: whenever a reciprocal lattice point intersects the sphere ‘out shoots’ a reflected beam.

The relative movement of the sphere and reciprocal lattice is most easily represented, not by drawing the whole reciprocal lattice in its different positions, but by drawing the Ewald sphere at the extreme limits of oscillation say 10° in one direction and 10° in the other. These limits are shown in Fig. 9.15 for (a) the $h0l$ and (b) the $h1l$ reciprocal lattice sections. The shaded regions, called ‘lunes’ because of their shape, represent the regions of reciprocal space through which the surface of the sphere passes as it is oscillated. Only those reciprocal lattice points which lie within these shaded regions give rise to reflected beams.

There are several ways of recording the reflected beams. The simplest is to arrange a cylindrically shaped film coaxially around the crystal (with a hole to allow the exit of the

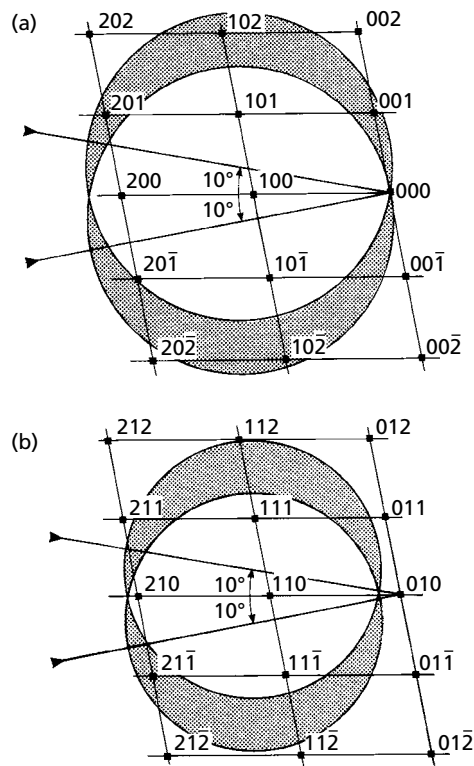


Fig. 9.15. The Ewald reflecting sphere construction for a monoclinic crystal in which the incident X-ray beam is oscillated $\pm 10^\circ$ from the direction of the \mathbf{a}^* reciprocal lattice vector about the $[010]$ direction (y -axis, perpendicular to the plane of the paper). The directions of the X-ray beams and the corresponding surface of the reflecting sphere are shown at the limits of oscillation. Any reciprocal lattice points lying in the regions of reciprocal space through which the reflecting sphere passes (the shaded regions, called ‘lunes’) give rise to reflections, (a) The $h0l$ reciprocal lattice section through the origin and a diametral section of the reflecting sphere and (b) the $h1l$ reciprocal lattice section (i.e. the layer ‘above’ the $h0l$ section) and the smaller, non-diametral section of the reflecting sphere (compare with Fig. 8.6). In these two sections the planes which reflect are $201, 102, 001, 20\bar{1}, 10\bar{2}$ (zero layer line) and $112, 21\bar{1}$ (first layer line above).

incident beam) such that reflections at all angles can be recorded. Now, all the reflected beams from the $h0l$ reciprocal lattice section (Fig. 9.15(a)) lie in the plane of the paper and thus lie in a ring around the film. The reflected beams from the $h1l$ reciprocal lattice section lie in a cone whose centre is the centre of the Ewald sphere and these beams also intersect the film in a ring ‘higher up’ than the ring from the $h0l$ reciprocal lattice section. Figure 9.16(a) shows this geometry for the reflected beams from the $h0l, h1l, h\bar{1}l, h2l$, etc. sections of the reciprocal lattice.

When the film is ‘unwrapped’ and laid flat, the rings of spots appear as lines, called layer lines (Fig. 9.16(b)), the ‘zero layer line’ spots from the $h0l$ reciprocal lattice section

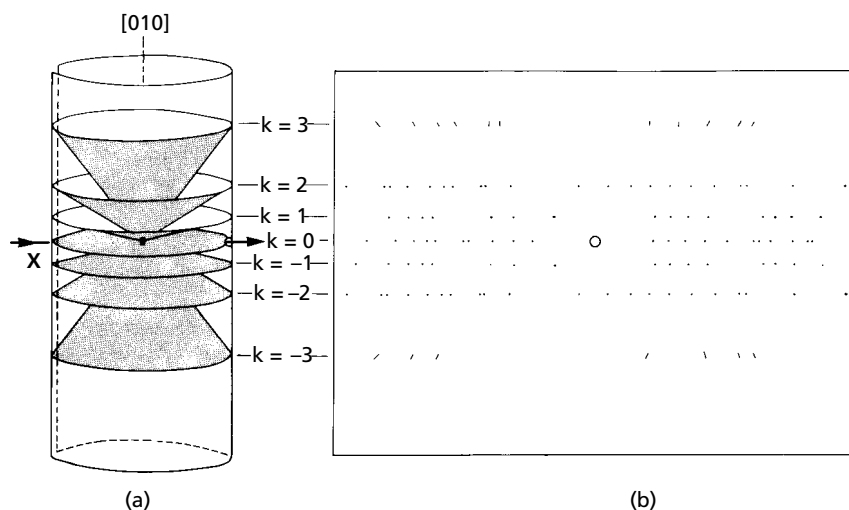


Fig. 9.16. (a) The oscillation photograph arrangement with the crystal at the centre of the cylindrical film. The oscillation axis $[010]$ is co-axial with the film and the reflections from each reciprocal lattice section $(h0l)$, $(h1l)$, $(h\bar{1}l)$, $(h2l)$ etc. lie on cones which intersect the film in circles. **X** indicates the incident beam direction and in (b), showing the cylindrical film 'unwrapped', **O** indicates the exit beam direction through a hole at the centre of the film.

through the centre, the 'first layer line' spots from the $h1l$ reciprocal lattice section next above—and so on for all the reciprocal lattice sections perpendicular to the axis of oscillation.

In practice it is necessary to set up a crystal such that some prominent zone axis is along the oscillation axis, such as, in our case, the $[010]$ axis. This implies that the reciprocal lattice sections or layers perpendicular to the oscillation axis are well defined and give rise to clearly defined layer lines on the film. If, for example, we set a cubic crystal with the z -axis or $[001]$ direction along the axis of oscillation, then the reciprocal lattice sections giving the layer lines would be $hk0$ (zero layer line), $hk1$ (first layer line above) and so on (see Figs 6.7 or 6.8). If on the other hand the crystal was set up in no particular orientation, i.e. no particular reciprocal lattice section perpendicular to the axis of rotation, the layer lines would, correspondingly, hardly be evident.

9.5.2 The rotation method

As the angle of oscillation increases, the Ewald reflecting sphere sweeps to and fro through a greater volume of reciprocal space, the lunes (Fig. 9.15) become larger and overlap and more reflections are recorded. The extreme case is to oscillate the crystal $\pm 180^\circ$ —but this is the same as rotating it 360° , in which case the Ewald reflecting sphere makes a complete circuit round the origin of the reciprocal lattice. As the Ewald sphere sweeps through the reciprocal lattice, a plane will reflect twice: once when it crosses 'from outside to inside' the reflecting sphere and once when it crosses out again, the



Fig. 9.17. A single crystal c -axis rotation photograph of α -quartz showing zero, $hk0$, first order, $hk1$ and $hk\bar{1}$ and second order $hk2$ and $hk\bar{2}$ layer lines. (Photograph by courtesy of the General Electric Company.)

reflections being recorded on opposite sides of the direct beam. Rotation photographs are generally used to determine the orientation of small single crystals. An example is given in Fig. 9.17.

9.5.3 The precession method

This is an ingenious and useful technique invented by M. J. Buerger* by means of which (unlike oscillation and rotation photographs), undistorted sections or layers of reciprocal lattice points may be recorded on a flat film. It is probably easiest to appreciate the geometrical basis of the method by using, as an example, a simple cubic crystal.

Figure 9.18(a) shows an $(h0l)$ section of a simple cubic crystal (drawn with the y -axis or \mathbf{b}^* reciprocal lattice unit cell vector perpendicular to the page). The X-ray beam is incident along the x -axis or \mathbf{a}^* reciprocal lattice unit cell vector and the Ewald reflecting sphere for a particular wavelength is centred about the incident beam direction. The flat film is set perpendicular to the X-ray beam. We are now going to consider the conditions by which we can obtain reflections from the reciprocal lattice points lying in the plane $Ok\bar{l}$ —i.e. the plane through the origin and perpendicular to the x -axis or \mathbf{a}^* reciprocal lattice vector. Figure 9.18(a) shows only one row of these reciprocal lattice points—001, 002, 003, 00 $\bar{1}$, 00 $\bar{2}$, 00 $\bar{3}$, etc.; the others are above and below the plane of the diagram. Now, ignoring for the time being the reciprocal lattice points not lying in this plane $Ok\bar{l}$, let us consider the movements necessary to bring 001, 002, 003, etc. reciprocal lattice points into reflecting positions. Clearly, we need to tilt or rotate the crystal anticlockwise such that first 001, then 002, then 003, etc. successively intersect the sphere. As we do so we tilt or rotate the film anticlockwise by the same angle (the film and crystal rotation mechanisms being coupled together). The 001, 002, 003 reflections then strike the film successively at equally spaced distances from the origin 000. The situation in which 003 is in the reflecting position at a tilt or rotation angle ϕ is drawn in Fig. 9.18(b). Clearly, if we rotate the crystal and film clockwise we would record the

* Denotes biographical notes available in Appendix 3.

$00\bar{1}$, $00\bar{2}$, $00\bar{3}$, etc. reflections on the opposite side of the film from the origin. The result (ignoring reflections from reciprocal lattice points not lying on this row) would be a row of equally spaced spots on the film corresponding to the equally spaced reciprocal lattice points in the row through the origin. These are shown on a plan view of the film (Fig. 9.18(c)), as the vertical row of spots through the centre.

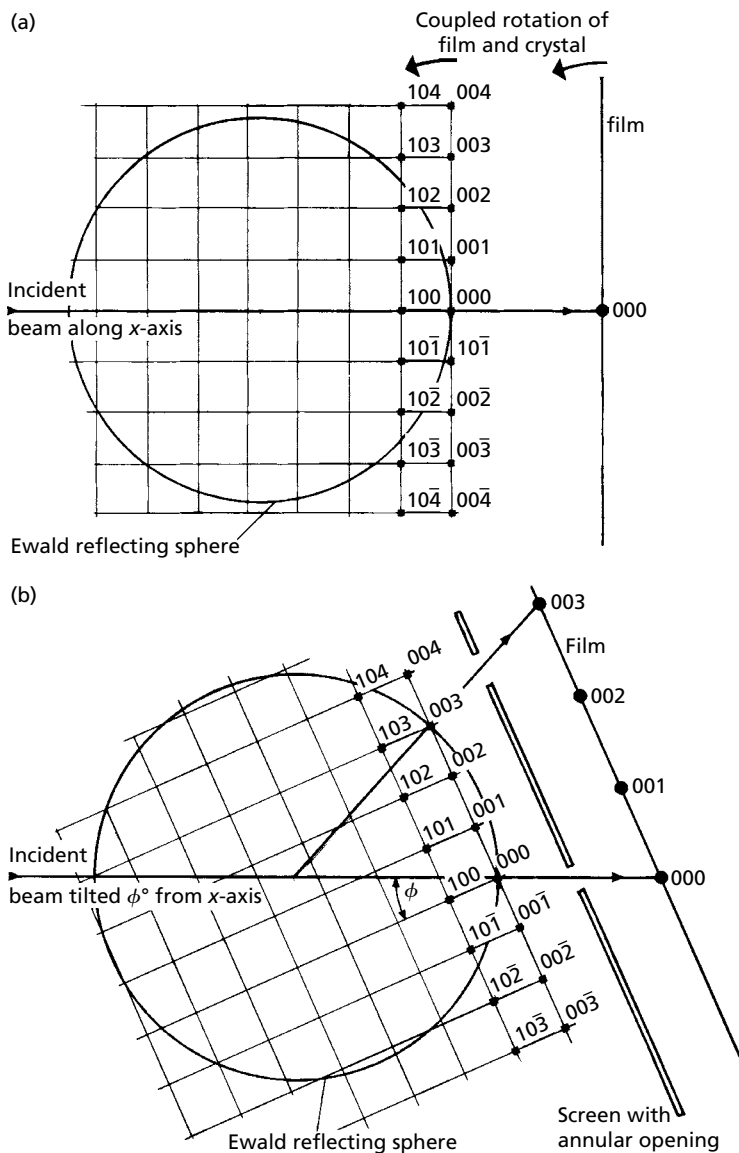


Fig. 9.18. (continued)

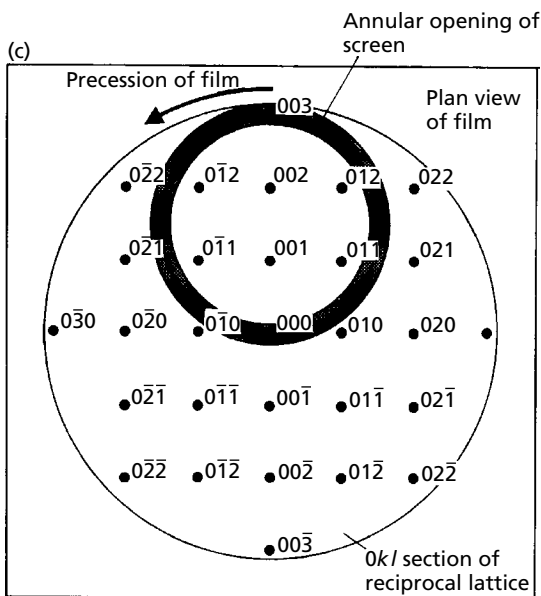


Fig. 9.18. The geometry of the precession method, (a) The incident beam normal to the $Ok\ell$ section of the reciprocal lattice (indicated by the row of reciprocal lattice points 001, 002, 003, etc.). In order to bring these points into reflecting positions the crystal and the film are rotated anti-clockwise as indicated. The situation in which the 003 reciprocal lattice point is in a reflecting position is shown in (b). (c) A plan view of the film at this angle ϕ with the circle representing the intersection of the $Ok\ell$ plane and the reflecting sphere and the projection of the annulus on to the screen. The only reflections to reach the film are those falling within the annulus (shaded region). As the crystal + screen + film are precessed about the angle ϕ the annulus effectively sweeps through the $Ok\ell$ section of the reciprocal lattice as indicated by the arrow and all reciprocal lattice points within the large circle give rise successively to reflections.

Now we have to consider the reciprocal lattice points in the $0kl$ section of the reciprocal lattice which intersect the Ewald reflecting sphere above and below the plane of Fig. 9.18(b). The sphere intersects the reciprocal lattice section $0kl$ in a circle, Fig. 9.18(c); any reciprocal lattice point lying in this circle gives rise to a reflected beam. Now we precess the crystal and the film about the incident beam direction such that the film is always parallel to the $0kl$ reciprocal lattice section (the precession movement means that the x -axis of the crystal rotates about the incident beam direction at the fixed angle ϕ). As we do so the circle moves through the reciprocal lattice section in an arc centred at the origin 000 of the reciprocal lattice, i.e. about the direction of the direct X-ray beam. Hence, in a complete revolution, all the reciprocal lattice points lying within the large circle of Fig. 9.18(c) reflect—and the pattern of spots on the film corresponds to the pattern of reciprocal lattice points in the $0kl$ section of the reciprocal lattice, as shown in Fig. 9.18(c).

Finally, we have to eliminate the complicating effects of the reflections from reciprocal lattice points not lying in the OkI plane through the origin. This is achieved by placing a

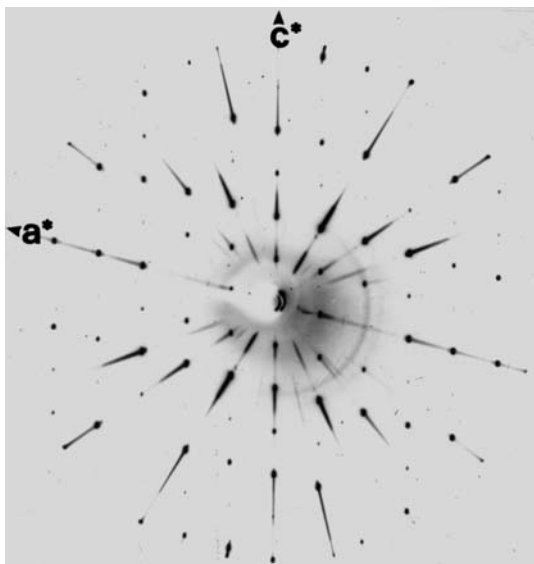


Fig. 9.19. A (zero level) precession photograph of tremolite, $\text{Ca}_2\text{Mg}_5\text{Si}_8\text{O}_{22}(\text{OH})_2$ (monoclinic $C2/m$, $a = 9.84 \text{ \AA}$, $b = 18.05 \text{ \AA}$, $c = 5.28 \text{ \AA}$, $\beta = 104.7^\circ$), showing reflections from the $h0l$ reciprocal lattice section (incident beam along the y -axis). The *orientations* of the reciprocal lattice vectors \mathbf{a}^* and \mathbf{c}^* are indicated. Compare this photograph with the drawing of the $(h0l)$ reciprocal lattice section of a monoclinic crystal (Fig. 6.4(c)). The streaking arises from the presence of a spectrum of X-ray wavelengths in the incompletely filtered $\text{MoK}\alpha$ ($\lambda = 0.71 \text{ \AA}$) X-radiation. (Photograph by courtesy of Dr. J. E. Chisholm.)

screen with an annular opening between the crystal and the film, the size of the annulus being chosen to allow reflections to pass to the screen only from reciprocal lattice points lying in the circle (Fig. 9.18(c)). The screen is indicated in cross-section in Fig. 9.18(b) for the case in which the furthest reciprocal lattice point from the origin which can be recorded is 003. The screen is also linked to the crystal–film precession movements.

The precession method can be modified to record reciprocal lattice sections which do not pass through the origin (non-zero-level photographs), details of which can be found in the books on X-ray diffraction techniques listed in Further Reading. Its main application is in crystal structure determination by measurement of the intensities of the X-ray reflections. Figure 9.19 shows an example of a zero-level photograph (of a reciprocal lattice section passing through the origin) which shows very convincingly the pattern of reciprocal lattice points.

9.6 X-ray diffraction from single crystal thin films and multilayers

Thin films and multilayer specimens are invariably studied using the X-ray diffractometer, the geometrical basis of which is described in detail in Section 10.2.

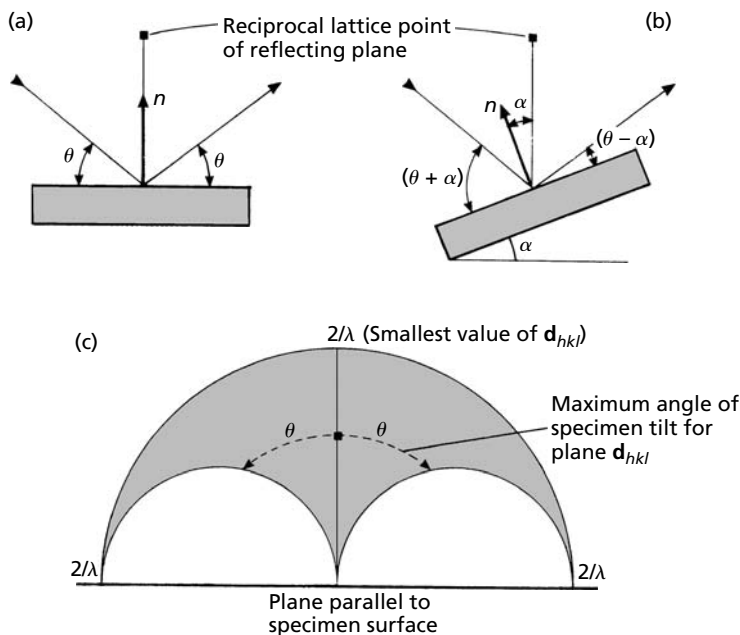


Fig. 9.20. The X-ray diffractometer arrangements for a single crystal. (a) The symmetrical setting: the reciprocal lattice vectors of the reflecting planes are all parallel to the specimen surface normal n . (b) The asymmetrical setting, the reciprocal lattice vectors of the reflecting planes are inclined at angle α to n . (c) The region of reciprocal space (shaded) within which lie the reciprocal lattice points of possible reflecting planes.

The normal arrangement, as used in X-ray powder diffractometry, is the symmetrical (Bragg–Brentano) one in which only the d -spacings of those planes parallel to the specimen surface are recorded. This is achieved by arranging the X-ray source and X-ray detector and their collimating slits such that the incident and reflected beams make equal angles to the specimen surface. The arrangement is shown diagrammatically in Fig. 9.20(a). As the angle θ is varied (either by keeping the specimen fixed and rotating the source and detector in opposite senses as indicated in Figs 10.3(a) and (b), or by keeping the source fixed and rotating the detector at twice the angular velocity of the specimen), reflections occur whenever Bragg's law is satisfied. Clearly, for a single crystal, with only one set of planes parallel to the surface, there will only be one Bragg reflection. For multilayer specimens, which may consist of a sequence of thin crystal films (say, of copper and cobalt) mounted on a single crystal substrate, there will be three Bragg reflections—one from the substrate and one each from the thin films (of different crystal structure).

However, there are more diffraction phenomena to be recorded. First, since the layers are generally thin—of the order of 1–10 nm—the (high angle) Bragg peaks are substantially broadened and this may be used to estimate the thickness of the layers by means of the Scherrer equation (Section 9.3). Second, the repeat distance, or superlattice

wavelength Λ of the layers can be determined from the angles of ‘satellite’ reflections which occur (given a multilayer specimen with a long range structural coherence) on either side of the (high angle) Bragg peaks. The value of Λ may be determined from the equation

$$\Lambda = \frac{\lambda}{2(\sin \theta_2 - \sin \theta_1)}$$

where λ = the X-ray wavelength and $\sin \theta_1$, $\sin \theta_2$ are the Bragg angles of adjacent satellite peaks. This equation may be rearranged to give

$$\frac{1}{\Lambda} = \frac{1}{d_2} - \frac{1}{d_1}$$

where d_1 , d_2 are the notional d -spacings of the satellite peaks. An example of a cobalt-gold multilayer specimen is given in Fig. 9.21(a).

The repeat distance Λ of the layers also gives rise to low-angle Bragg reflections (of the order $2\theta = 2 - 5^\circ$), between which occur a further set of satellite peaks or fringes called Keissig fringes which may be used to determine the total multilayer film thickness $N\Lambda$ using an analogous equation to that above, viz.

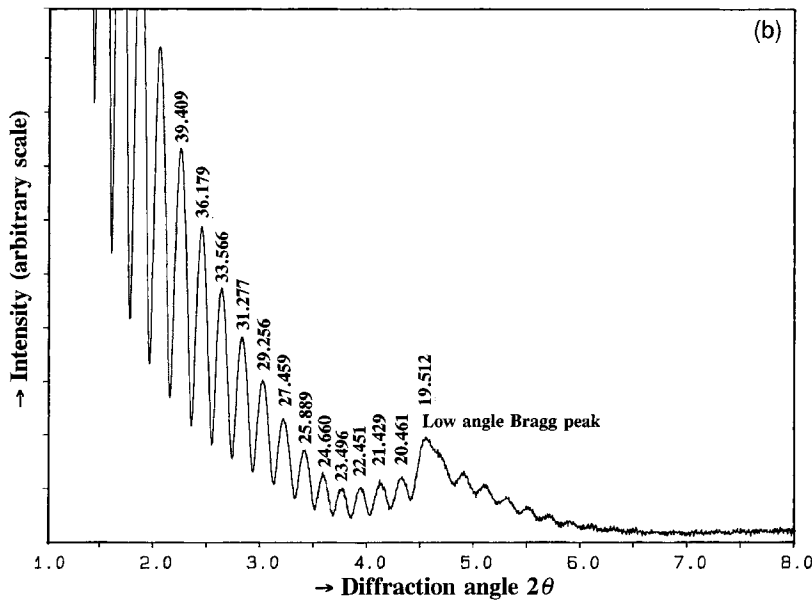
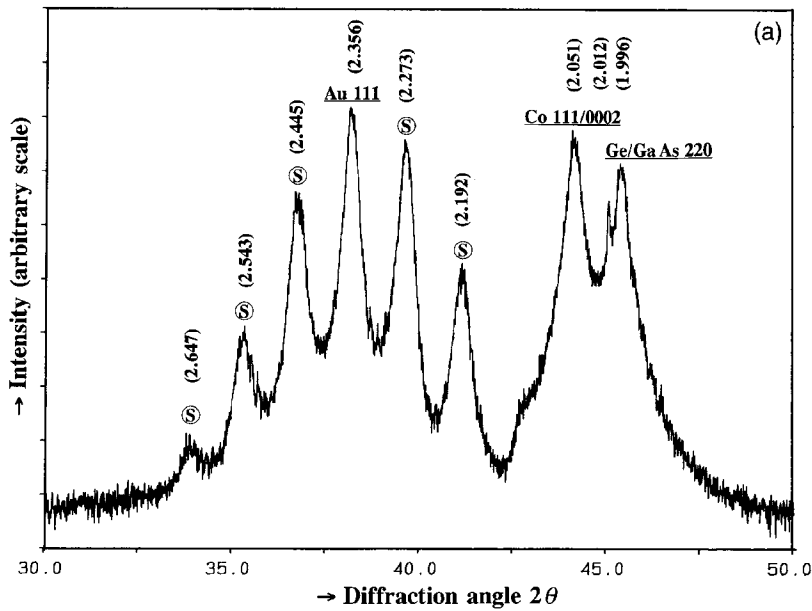
$$\frac{1}{N\Lambda} = \frac{1}{d_{k2}} - \frac{1}{d_{k1}}$$

where d_{k1} , d_{k2} are the notional d -spacings of any pair of adjacent Keissig fringes. An example of a cobalt-copper multilayer specimen is given in Fig. 9.21(b).

The occurrence of the low-angle Bragg peaks and Keissig fringes may be understood by analogy with the diffraction pattern from a limited number N of slits of width a (Section 7.4); Fig. 7.9 shows a particular case for $N = 6$. The principal maxima correspond to the low-angle Bragg peaks in which the slit spacing a corresponds to the repeat distance of the layers, or superlattice wavelength Λ . The subsidiary maxima, of which there are $(N - 2)$ between principal maxima, correspond to the Keissig fringes; by counting the number of Keissig fringes (plus two) between the low-angle Bragg peaks the number of multilayers or superlattice wavelengths N can be determined and by measuring the angles between adjacent fringes the total thickness $N\Lambda$ of the multilayers can be determined using the equation given above. Its validity can be checked by applying it, say, to the subsidiary maxima in Fig. 7.9; for the zero and first order minima the $\sin \alpha \approx \alpha \approx 2\theta$ values are $1(\lambda/6a)$ and $2(\lambda/6a)$. Substituting these values in the above equation gives $N\Lambda = 6a$, the total width of the grating.

In practice in X-ray diffraction the Keissig fringes are most clearly defined between the direct beam (zero order peak) and first low-angle Bragg peak (Fig. 9.21(b)).

The other arrangement used in X-ray diffractometry is the asymmetrical one in which, for any particular Bragg angle (source and detector fixed), the specimen can be rotated such that the incident and diffracted beams make different angles to the specimen surface (the angle between them remaining fixed at 2θ). The arrangement is shown diagrammatically in Figs 9.20(b) and 10.3(c). It has the advantage in that reflections from planes which are not parallel to the surface can be recorded (and is also a useful means of ‘fine



tuning' the angle of the specimen to maximize the intensity of reflections from planes which may not be exactly parallel to the specimen surface). Clearly, the maximum angle of tilt either way is θ , otherwise the surface of the specimen will block or 'cut off' either the incident or the diffracted beam.

The Ewald reflecting sphere construction, which shows the extent to which the symmetrical and asymmetrical techniques sample a volume of reciprocal space, is shown in Fig. 9.20(c). The construction is essentially two-dimensional, since only those planes whose normals lie in the plane of the diagram (co-planar with the incident and reflected beams) can be recorded. In the symmetrical case (Fig. 9.20(a)), the reciprocal lattice points of the reflecting planes lie along a line perpendicular to the specimen surface whose maximum extent corresponds with the reciprocal lattice vector of the plane of smallest d_{hkl} -spacing that can be measured, i.e. that for which $\theta = 90^\circ$; hence $|\mathbf{d}_{hkl}^*| = 2/\lambda$.

In the asymmetrical case (Fig. 9.20(b)) the crystal can be tilted or rotated clockwise or anticlockwise such that the reciprocal lattice vector of the reflecting planes is also tilted or rotated with respect to the specimen surface. The angular range, $\pm\theta$ (limited by specimen cut-off), increases as $|\mathbf{d}_{hkl}^*| = 2 \sin \theta / \lambda$ increases, the maximum being $\pm 90^\circ$ when $\sin \theta = 1$. This is shown as the shaded region in Fig. 9.20(c). Clearly, the choice of the wavelength of the X-radiation may be important, particularly in the asymmetrical case, since it determines which crystal planes in the specimen may, or may not, be recorded.

9.7 X-ray (and neutron) diffraction from ordered crystals

In metal alloys, solid solutions may be of two kinds—*interstitial solid solutions* such as, for example, carbon in iron (see p. 17) and *substitutional solid solutions*, such as, for example, α -brass where zinc atoms substitute for copper atoms in the ccp structure. In some cases complete solid solubility is obtained across the whole compositional range from one pure metal to another—such as, for example, copper and nickel, both

Fig. 9.21. (a) A high angle X-ray diffraction trace ($\text{CuK}\alpha_1$ radiation) from a cobalt–gold multilayer specimen showing the satellite peaks or fringes \textcircled{S} each side of the Au 111 Bragg reflection. The repeat distance Λ of the layers is determined by measuring the (notional) d -spacings d_1 and d_2 of adjacent fringes and using the equation on page 231. The notional d -spacings (\AA) of the fringes and the Au 111 peak are indicated (from which a value of $\Lambda \approx 64 \text{ \AA}$ is obtained). The group of higher angle reflections are from Co 111, Co 0002, the substrate GaAs 110 and the 'buffer' layer Ge 110. (b) A low angle X-ray diffraction trace ($\text{CuK}\alpha_1$ radiation) from a cobalt–copper multilayer specimen showing the low angle Bragg reflection at 4.525° and the Keissig fringes each side. The Bragg peak gives the multilayer or superlattice repeat distance Λ and the number $N - 2$ of Keissig fringes between the Bragg peak and zero angle gives $N\Lambda$, the total thickness. In this example $\Lambda = 19.512 \text{ \AA}$ and $(N - 2) = 22$ (only those fringes from about $2\theta \approx 1.5^\circ$ are shown). Hence the total thickness $N\Lambda = 468.3 \text{ \AA}$. $N\Lambda$ may also be determined by measuring the (notional) d -spacings, d_{K1} and d_{K2} of adjacent Keissig fringes and using the equation on page 231. The notional d -spacings (\AA) of fringes 11 to 22 are indicated, from which values of $N\Lambda$, in fair agreement with that given above (subject to experimental scatter), are obtained.

of which have the ccp structure; but in most alloys the solid solubility is limited and a series of different solid solutions and intermetallic compounds occur across the whole composition range. Copper-zinc alloys for example exhibit a range of such structures or phases: α (ccp, stable up to about 35 at% Zn); β (which is a bcc solid solution stable over a narrow composition range close to equal atomic proportions of copper and zinc and which is also described as the intermetallic compound CuZn); γ (a complex cubic structure); ϵ (a complex hexagonal structure); and finally η (an hep solid solution of copper in zinc). The study of such alloy phases belongs to physical metallurgy; our interest is solely concerned with the arrangements of the atoms.

In some phases, e.g. α -brass, the copper and zinc atoms are randomly distributed amongst the lattice sites and the structure is said to be *disordered*. In others there is a tendency, which increases with decreasing temperature, for the atoms to occupy specific sites. Two situations may be distinguished: *clustering*, where atoms tend to be surrounded by atoms of their own type (such as, for example, solid solutions of zinc in aluminium); and the converse *short range ordering* where atoms tend to be surrounded by atoms of opposite type. β brass provides a simple example of short range ordering; at high temperatures the structure is disordered but as the temperature decreases (to about 460°C), short range ordered regions develop, the copper (or zinc) atoms tending to occur either at the corners or the centres of the bcc unit cell. Below this temperature the short-range ordered regions extend throughout the crystal and impinge. We now have *domains* of *long-range order*. Within each domain the copper and zinc atoms are at the corners or centres of the unit cell and the crystal structure is the same as that for CsCl (Fig. 1.12(b)). The boundaries (called antiphase domain boundaries) are where the ordering 'changes over'—in one domain it is, say, the copper atoms which occupy the centres of the cell and in the other it is the zinc atoms. It is, of course, possible for a single domain to extend across the whole crystal, in which case of course the distinction between corners and centres in the bcc unit cell disappears.

Long-range ordering also occurs in many ccp alloys, of which the copper-gold system provides 'type' examples. For example, at high temperatures the alloy Cu₃Au is disordered but at low temperatures the gold atoms occupy the corners, and the copper atoms the face-centres of the unit cell. In the alloy CuAu the atoms order so as to occupy alternate (002) planes.

The phenomenon of long-range ordering is often described as *superlattice formation*, but this is a bad name because it suggests the existence of lattices other than the 14 Bravais lattices. Ordering rather consists of a *change* of lattice type. For β -brass (Fig. 9.22(a)) it is a change from Cubic *I* to Cubic *P* (the motif, as in CsCl, being Cu + Zn), and for Cu₃Au (Fig. 9.22(b)) it is a change from Cubic *F* to Cubic *P* (the motif being 3Cu + Au). In the case of CuAu (Fig. 9.22(c)), the change is from Cubic *F* to Tetragonal *P* as a consequence of the size difference between the copper and gold atoms, which results in a small reduction in the interlayer spacing perpendicular to the 002 planes giving a *c/a* ratio less than unity.

Long range ordering and antiphase domain boundaries are also characteristic of ferromagnetic (and antiferromagnetic) materials where in each domain it is the magnetic dipoles or moments which are ordered or orientated in a particular direction.

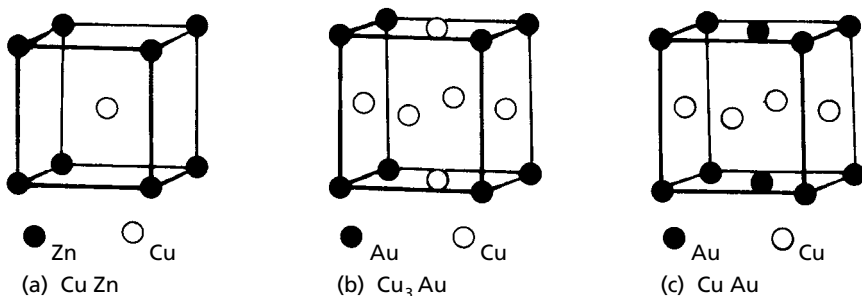


Fig. 9.22. Unit cells of ordered structures, atom positions as indicated, (a) CuZn (bcc structure, cubic *P* lattice), (b) Cu₃Au (ccp structure, cubic *P* lattice), (c) CuAu—the ordering of Cu and Au atoms on alternate 002 planes in the ccp structure results in a reduction of symmetry from a cubic to a tetragonal *P* lattice.

Ordering was one of the earliest phenomena to be detected by X-ray diffraction techniques and provides further simple examples of the application of the structure factor equation (Section 9.2).

Example 6: *Cu₃Au*. For the disordered case the atomic scattering factor for each atom site, f_{Av} , is taken as the weighted average of f_{Cu} , and f_{Au} , i.e. $f_{Av} = 1/4(f_{Au} + 3f_{Cu})$ and the structure factor F_{hkl} is that for an fcc crystal (see Appendix 6), i.e.

$$F_{hkl} = 4 \cdot 1/4(f_{Au} + 3f_{Cu}) = (f_{Au} + 3f_{Cu}) \quad \text{for } h, k, l \text{ all odd or all even}$$

$$F_{hkl} = 0 \quad \text{for } h, k, l \text{ mixed.}$$

For the fully ordered case (Fig. 9.18(b)) the atomic positions $u_n v_n w_n$ for the gold atoms are (000) and for the copper atoms $\left(\frac{1}{2} \frac{1}{2} 0\right)$, $\left(\frac{1}{2} 0 \frac{1}{2}\right)$, $\left(0 \frac{1}{2} \frac{1}{2}\right)$. Hence:

$$\begin{aligned}
 F_{hkl} &= f_{Au} \exp 2\pi i(h \cdot 0 + k \cdot 0 + l \cdot 0) + f_{Cu} 2\pi i \left(h \frac{1}{2} + k \frac{1}{2} + l \cdot 0\right) \\
 &\quad + f_{Cu} \exp 2\pi i \left(h \frac{1}{2} + k \cdot 0 + l \frac{1}{2}\right) + f_{Cu} \exp 2\pi i \left(h \cdot 0 + k \frac{1}{2} + l \frac{1}{2}\right) \\
 &= f_{Au} + f_{Cu} (\exp \pi i(h + k) + \exp \pi i(h + l) + \exp \pi i(k + l)).
 \end{aligned}$$

Hence

$$\begin{aligned}
 F_{hkl} &= (f_{Au} + 3f_{Cu}) \quad \text{for } h, k, l \text{ all odd or all even} \\
 F_{hkl} &= (f_{Au} - f_{Cu}) \quad \text{for } h, k, l \text{ mixed.}
 \end{aligned}$$

Hence, in the ordered case reflections occur when h, k, l are mixed and it is the occurrence of these additional or ‘superimposed’ reflections in the diffraction pattern that gave rise to the term ‘superlattice’. Their intensities, in proportion to the ‘base’ reflections for which h, k, l are all odd or all even, can be estimated by approximating $f \approx Z$; i.e. $f_{\text{Au}} = 79$ and $f_{\text{Cu}} = 29$. Hence:

$$I_{hkl} = F_{hkl} \cdot F_{hkl}^* = (79 + 3.29)^2 = (166)^2 \quad h, k, l \text{ all odd or all even}$$

$$I_{hkl} = F_{hkl} \cdot F_{hkl}^* = (79 - 29)^2 = (50)^2 \quad h, k, l \text{ mixed.}$$

Hence the intensities of the ‘superlattice’ reflections are $50^2/166^2 \times 100\% = 9\%$ of the intensities of the ‘base’ reflections and are easily detectable.

Partial ordering is expressed in terms of the long range order parameter S which is defined in terms of p , the fraction of sites occupied by (in the fully ordered case) the number of ‘right’ atoms and r , the fraction of such sites, whence $S = (p - r)/(1 - r)$. We may apply this equation either to the Au or the Cu atoms. For the Au atoms $r = 0.25$. Suppose, for example that $2/3$ of these sites are occupied by the ‘right’ Au atoms (and $1/3$ by the ‘wrong’ Cu atoms). Then $P = 2/3$ and $S = 0.56$.

For this partially ordered case, for h, k, l mixed indices $F_{hkl} = S(f_{\text{Au}} - f_{\text{Cu}})$ and the intensity of the reflections is proportional to S^2 .

Example 7: CuZn (β -brass). For the disordered case $f_{\text{Av}} = (f_{\text{Cu}} + f_{\text{Zn}})$ and, as for a bcc crystal, reflections only occur when $(h + k + l) = \text{even integer}$. For the fully ordered case we follow the same procedure as for CsCl (Example 1), i.e. $F_{hkl} = f_{\text{Cu}} + f_{\text{Zn}}$ for $(h + k + l) = \text{even integer}$ and $F_{hkl} = f_{\text{Cu}} - f_{\text{Zn}}$ for $(h + k + l) = \text{odd integer}$. Approximating $f_{\text{Cu}} = 29$ and $f_{\text{Zn}} = 30$, the intensities of the ‘superlattice’ reflections are $-1^2/59^2 \times 100\% = 0.03\%$ of the intensities of the ‘base’ reflections and are much too small to be readily detected by X-ray diffraction techniques.

This situation is illustrative of a general problem in X-ray diffraction: since atomic scattering factors are proportional to Z then the positions in the unit cell of atoms of similar atomic number are not easy to determine, nor are the positions of atoms of low atomic number which scatter X-rays very weakly. It is a situation in which **neutron diffraction** finds a ‘niche market’. Unlike X-rays, neutrons in most cases are scattered by the nuclei rather than the electrons in atoms and the scattering amplitudes (expressed as scattering lengths) vary in an irregular way with atomic number. The relatively large scattering amplitudes of, for example, hydrogen and oxygen atoms in comparison with heavy metal atoms enables these atoms to be located within the unit cell and also allows the small distortions which occur below the Curie temperature in ferroelectric perovskite structures (see Sections 8.11.1 and 4.4) to be determined.

Figure 9.23 shows, in a most visually convincing way, the differences between the scattering amplitudes, and therefore the absorptions, of neutrons by hydrogen, oxygen



Fig. 9.23. A neutron radiograph of a rose-stem within a thick-walled lead cylinder. (Photograph by courtesy of Dr Hans Priesmeyer, Christian-Albrechts University, Kiel.)

and heavy metal atoms. It is a neutron radiograph of a rose-stem within a thick-walled lead container; the lead is almost invisible to the neutrons, but the absorption in the rose and stem reveals the delicacy of the flower.

9.8 Practical considerations: X-ray sources and recording techniques

The discovery of X-rays by W. C. Röntgen* at the University of Würzburg in 1895 is a wonderful example of serendipity in science⁶. Röntgen was interested in the nature of cathode rays generated when a high voltage from an induction coil was discharged across a discharge tube and which gave rise to faint luminescence in gases and fluorescence in some crystals placed close to the tube. He enclosed the tube in a light-tight cardboard box (for what experiments we do not know). On discharge of the induction coil he

* Denotes biographical notes available in Appendix 3.

⁶ The word comes from the fairy-tale *The Three Princes of Serendip* 'who were always making discoveries by accidents and sagacity, of things they were not in quest of'. (From the *Shorter Oxford English Dictionary*.)

noticed that, on a table a considerable distance away, a barium platinocyanide crystal (which happened to be there) gave a flash of fluorescence. This clearly was not due to the cathode rays, which would have been absorbed in the glass walls of the tube and in the air, but originated from rays (or particles) emanating from the point where the cathode rays struck the walls of the tube. In a feverish period of work, Röntgen established that the rays travelled in straight lines, were not refracted or diffracted (by optical diffraction gratings), were more strongly absorbed the denser the material through which they passed and could be recorded on photographic plates. He took the very first medical radiograph—a beautiful image of the bones in his wife's hand and clearly showing her wedding ring. Röntgen coined the term 'X-rays'—a term used ever since, even though we now know that they are short-wavelength ($\sim 0.1 \sim 10 \text{ \AA}$) electromagnetic waves.

Modern X-ray tubes are descendants of Röntgen's discharge tube except that the cathode rays (electrons) are provided by a heated filament and the target, or anode, is a heavy metal, typically copper, iron, molybdenum or tungsten. By far the greatest proportion of the energy of the incident electrons is converted into heat (phonons) and hence the anode must be water-cooled or, in the case of micro-focus tubes in which the beam is concentrated into a small area, by also rotating the anode to prevent incipient melting. Heating is a 'nuisance' in X-ray tubes and largely limits the intensity of the beam which can be obtained—but it is also the basis of electron beam melting and welding techniques.

9.8.1 The generation of X-rays in X-ray tubes

As the electrons pass into the anode they suffer collisions with the atoms and are eventually brought to rest. At each collision the loss of energy ΔE gives rise to an X-ray photon of energy hc/λ . The energy losses ΔE have a wide range of values, giving rise to a wide range of λ values. This is the origin of the 'continuous', 'white' or Bremsstrahlung (which is German for braking) radiation.

Figure 9.24 shows a typical X-ray spectrum. Notice that there is a 'cut-off' at a short wavelength called the short-wavelength limit (swl). This arises from electrons which lose all their energy in one single collision, i.e. $\Delta E = eV = hc/\lambda_{\text{swl}}$, where V is the voltage of the X-ray tube and e is the charge on the electron. The intensity of the continuous radiation peaks at a wavelength of about $4/3\lambda_{\text{swl}}$. Superimposed on this continuous radiation are a series of sharp peaks. These arise from electron transitions between energy levels in the atom. The innermost (K -shell) has one (the highest) energy level, the L -shell has three and the M -shell has five such energy levels. If (and only if) the incident electrons have sufficient energy (designated as W_K , the work function), they can 'knock out' an electron from the K -shell. In this situation the incident electrons are strongly absorbed and the corresponding wavelength is called the K absorption edge, designated λ_K . Hence $\lambda_K = hc/W_K$. This ionized state of the atom is short lived and the atom returns to its ground state as a result of the electrons 'tumbling down' from

outer to inner shells, each transition being accompanied by the emission of an X-ray photon of energy, and therefore wavelength, characteristic of the difference between the energy levels. The spectra are designated the K_α -series (for transitions from the L to the K -shell), the K_β -series (for transitions from the M to the K -shell), the L_α -series (for transitions from the M to the L -shell), and so on. The most important, in relation to X-ray diffraction, is the K_α -series. Since there are three energy levels in the L -shell there are three, closely separated K_α wavelengths: K_{α_1} , K_{α_2} and K_{α_3} . These are not equally strong: K_{α_3} is very weak and K_{α_1} is about twice as intense as K_{α_2} . The latter two comprise what is termed the K_α -doublet (Fig. 9.24).

Except for Laue-type experiments, use is generally made only of the K_{α_1} radiation and this is achieved by the use of a crystal monochromator set to reflect only this particular wavelength (and its sub-multiples, i.e. $\lambda_{K_{\alpha_1}} = 2d \sin \theta = 2(\lambda_{K_{\alpha_1}}/2)$, etc.) Older ‘filter’ methods are unable to discriminate between K_{α_1} and K_{α_2} wavelengths.

9.8.2 Synchrotron X-ray generation

Very high intensity X-ray beams, ~ 100 – $10,000$ times more intense than the K_{α_1} radiation from X-ray tubes, are generated in a synchrotron, a type of particle accelerator. Electrons, travelling at velocities close to the speed of light, are confined to travel in near-circular paths in a ‘storage ring’ by the action of magnets placed at intervals around the ring. The ‘synchrotron radiation’, which arises as a result of the continuous inward radial acceleration of the electrons, is outputted tangentially from the ring and covers a wavelength range from infrared to very short X-ray wavelengths. The radiation then

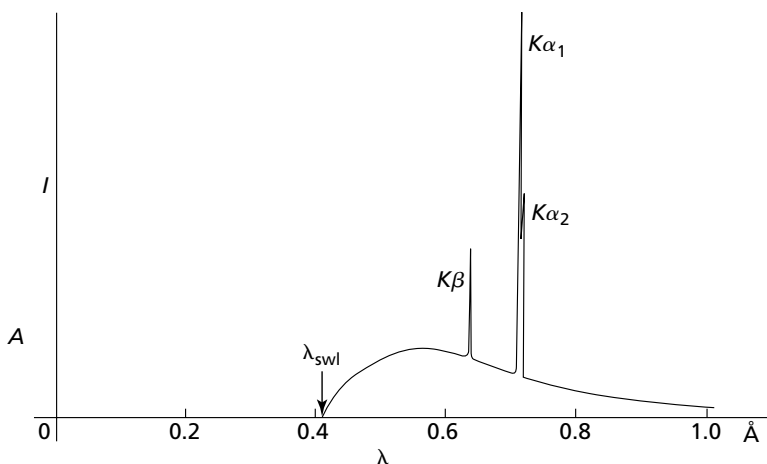


Fig. 9.24. An X-ray spectrum showing the continuous (white) radiation which peaks at about $4/3\lambda_{\text{swl}}$ and the sharp K_{α_1} and K_{α_2} peaks at wavelengths characteristic of the anode element. (From *Contemporary Crystallography* by Martin J. Buerger, McGraw-Hill, 1970.)

passes to a crystal monochromator, set to reflect the particular wavelength required. Apart from the higher intensity, the advantage of synchrotron radiation is that, unlike X-ray tubes where one is restricted to the particular K_{α_1} wavelength of the anode element, the monochromator can be ‘tuned’ to reflect X-rays either well away from the absorption edge of (e.g.) a heavy element in the specimen to minimize absorption effects, or, contrariwise, close to an absorption edge to maximize the effects of anomalous absorption (see Example 5). The radiations also differ in their states of polarization; that from an X-ray tube is almost wholly unpolarized whereas that from a synchrotron is wholly polarized in the plane of the storage ring.

The advent of synchrotron radiation has not only allowed very much smaller crystals to be examined (in the micrometre, rather than tens or hundreds of micrometre range) but has also allowed the examination of very short-lived crystal structures occurring in chemical reactions.

9.8.3 X-ray recording techniques

The recording of X-ray reflections has been revolutionized by the advent of CCD (charge-coupled-device) and position sensitive area detectors and the associated developments in computer software. They represent, in a sense, a return to the older film methods in that they record reflections in the whole of reciprocal space (or that portion intercepted by the detector) simultaneously rather than sequentially as was the case in Bragg’s early X-ray spectrometer or the complex 4-circle goniometers which until recently were dominant in single crystal X-ray work. Similarly, in X-ray powder diffractometry (Section 10.2), scintillation and proportional counters are being superseded by position sensitive detectors although the future of the diffractometer, as an item of hardware, seems secure.

It is of course very easy for a beginner to the subject of X-ray diffraction to be dazzled by the technology: the basic principles remain unchanged irrespective of developments in recording techniques.

Exercises

- 9.1 In the Laue experiment, a bcc crystal, lattice parameter $a = 0.4 \text{ nm}$ (4 \AA) is irradiated in the $[100]$ (or \mathbf{a}^*) direction with an X-ray beam which contains a continuous spectrum of wavelengths in the range between 0.167 nm (1.67 \AA) and 0.25 nm (2.5 \AA). Use the reflecting sphere construction to determine the indices of the planes in the crystal for which Bragg’s law is satisfied and draw the direction of the reflected beam for *one* plane in the $[001]$ zone. (*Hint:* Make a scale drawing of the section of the reciprocal lattice normal to the $[001]$ (or \mathbf{z}^*) direction and which passes through the origin 000 (i.e. the section which contains the $hk0$ reciprocal lattice points as shown in Fig. 6.7(b)). A convenient scale to use between the reciprocal lattice dimensions and A4 size drawing paper is $1 \text{ nm}^{-1} = 0.5 \text{ cm}$ ($1 \text{ \AA}^{-1} = 5.0 \text{ cm}$). Draw a line indicating the $[100]$ direction of the incident beam and draw in the two reflecting spheres representing the limits of the wavelength range. Remember that the origin

of the reciprocal lattice is located at the point where the beam *exits* from the spheres—hence the centres of the spheres are obviously not coincident. Shade in the region of the reciprocal lattice between the two spheres; planes whose reciprocal lattice points lie in this region satisfy Bragg's law. For one reciprocal lattice point in this region, find, by construction, the sphere which it intersects. The direction of the reflected beam is from the centre of this sphere through the reciprocal lattice point, and the radius of the sphere gives the particular wavelength reflected. Draw sections of the reciprocal lattice normal to the $[001]$ (or \mathbf{z}^*) direction and which pass through the $hk1$, $hk2$, $hk\bar{1}$, $hk\bar{2}$, etc. reciprocal lattice points (see Fig. 6.8(a)). In these sections of the reciprocal lattice 'above' and 'below' that through the origin, the sections of the sphere are reducing in size—simple trigonometry will show by how much. Again, planes whose reciprocal lattice points lie in the region between the spheres satisfy Bragg's law.)

- 9.2 In an oscillating crystal experiment the bcc crystal described in Exercise 9.1 is irradiated in the $[100]$ (or \mathbf{a}^*) direction with a monochromatic X-ray beam of wavelength 0.167 nm (1.67 Å). The crystal is then oscillated $\pm 10^\circ$ about the $[001]$ (or \mathbf{z}^*) direction. Find the indices $hk0$ of the planes in the $[001]$ zone which give rise to reflections during the oscillation of the crystal.

(*Hint:* Make a scale drawing of the section of the reciprocal lattice through the origin 000 and normal to the $[001]$ (or \mathbf{z}^*) direction. Draw a line indicating the $[100]$ direction of the incident beam and a single sphere corresponding to the single X-ray wavelength (see Exercise 9.1). Oscillating the crystal (at the centre of the sphere) is equivalent to oscillating the reciprocal lattice (at the origin). The simplest way to represent the relative changes in orientation between the crystal and the X-ray beam is to 'oscillate' the beam. The directions of the beam at the oscillation limits are $\pm 10^\circ$ from the $[100]$ direction in the plane of the reciprocal lattice section. Draw in the reflecting sphere at these limits and shade in the lunes or the regions of reciprocal space through which the surface of the sphere passes. Planes whose reciprocal lattice points lie in these regions reflect the X-ray beam during oscillation.)

- 9.3 The kinetic energy of neutrons emerging in thermal equilibrium from a reactor is given by $3/2 kT$ where k = Boltzmann's constant, $1.38 \times 10^{-23} \text{ JK}^{-1}$ and T is the Kelvin temperature. Given that the (rest) mass M_n of a neutron = $1.67 \times 10^{-27} \text{ kg}$ and Planck's constant $h = 6.63 \times 10^{-34} \text{ Js}$, estimate the wavelength of neutrons in thermal equilibrium at 100°C .
- 9.4 Determine the F_{hkl} values for reflections for the ZnS (zinc blende or sphalerite structure, Fig. 1.14(c)). Show that they fall into three groups: $(h + k + l) = 4n$; $(h + k + l) = 4n + 2$; $(h + k + l) = 2n + 1$.

Hint: ZnS has a cubic F lattice, each lattice point being associated with a motif consisting of one Zn atom at (000) and one S at $(\frac{1}{4} \frac{1}{4} \frac{1}{4})$. F_{hkl} is determined (i) by writing down the reflection condition for cubic F crystal (see Appendix A6) and (ii) by substituting f_{Zn} at (000) and f_{S} at $(\frac{1}{4} \frac{1}{4} \frac{1}{4})$.

- 9.5 In diamond the atom positions are identical to those in ZnS. Hence determine the conditions for reflection in the diamond cubic lattice.

Hint: We may simply proceed as before. However, since all the atoms are now of the same type, diamond has the centrosymmetric point group $m\bar{3}m$, the centres of symmetry lying equidistant between nearest neighbour atoms. We may therefore choose an origin at $(\frac{1}{8} \frac{1}{8} \frac{1}{8})$ —called 'origin choice 2' in space group $Fd\bar{3}m$, No. 227—and use the simplified structure factor equation in Example 3, page 210.

- 9.6 Determine the F_{hkl} values for reflections for the NaCl structure (Fig. 1.14(a)). Show that they fall into two groups: h, k, l all even and h, k, l all odd.
Hint: Proceed as in Exercise 9.4.
- 9.7 In Fig. 9.16, measure the hkl and $hk2$ layer line spacings and hence determine the c -axis repeat distance in α -quartz.
Hint: The photograph was taken using X-rays of wavelength $\lambda = 1.541\text{\AA}$ and a camera of 30 mm radius. To account for the reduced scale of the photograph in printing, multiply your layer-line spacing measurements by a factor 1.33.

X-ray diffraction of polycrystalline materials

10.1 Introduction

The preparation or synthesis of single crystals which are sufficiently large—of the order of a tenth of a millimetre or so—to be studied using the X-ray diffraction methods described in Chapter 9 is often a matter of great experimental difficulty. This is particularly the case for proteins and other complex organic crystals, the preparation of which requires considerable ingenuity and skill. However, in many situations the preparation of large single crystals is neither possible nor desirable. In materials science and petrology, for example, the crystal structures of interest are frequently those of metastable phases which occur on a very fine scale as a result of precipitation (or exsolution) from metal, ceramic or mineral matrices. As such phases grow, either as a result of natural or artificial ageing processes, their crystal structures invariably change as they evolve into more stable phases. These changes are best studied using the electron diffraction techniques outlined in Chapter 11, since electron beams can be focused down to diameters of the order of 1–10 nm, compared with beam diameters of the order of 0.1–1.0 mm for X-rays. Electron diffraction has the further advantage that crystallographic relationships between the phases and the matrices in which they occur can be investigated. Its disadvantage lies in the fact that the accuracy with which d_{hkl} -spacings can be measured is low compared to that for X-ray diffraction.

Polycrystalline or ‘powder’ X-ray diffraction techniques (Section 10.2) were developed by Debye* and Scherrer* and independently by Hull* in the period 1914–1919. They may be classified as ‘fixed λ , varying θ ’ techniques (see Section 9.5) in which the ‘varying θ ’ is achieved by having a sufficiently large number of more-or-less randomly orientated crystals in the specimen such that *some* of the hkl planes in *some* of them will be orientated, by chance, at the appropriate Bragg angles for reflection. All the planes of a given d_{hkl} -spacing reflect at the same 2θ angle to the direct beam and all these reflected beams lie on a cone of semi-angle 2θ about the direct beam. The various ‘powder’ X-ray diffraction techniques may be classified as to the ways in which the cones of diffracted beams are intercepted and recorded. In situations in which the crystals are randomly orientated, the diffracted intensity in the cones will be uniform and hence only part of the cones need to be recorded. This is the case with what might be called the ‘classical’ powder camera and diffractometer techniques (Section 10.3).

* Denotes biographical notes available in Appendix 3.

However, in situations in which the crystals are not randomly orientated the diffracted intensity in the cones will not be uniform and in order to determine the extent of the ‘non-randomness’ the whole, or a large part, of the cones needs to be recorded. In metallurgy and materials science the ‘non-randomness’ of crystals is known as *texture* or *preferred orientation* whereas in earth science it is known as *fabric* or *petrofabric*. (The word texture in earth science has quite a different meaning and refers rather generally to grain shapes and grain size distributions—a different nomenclature which is a possible source of confusion.)

The analysis of preferred orientation (texture or fabric) is important since it almost invariably arises as a consequence of the processes of crystallization and re-crystallization, sintering, extrusion and hot deformation which occur either in the short time-scale in materials processing or in the long time-scale in the earth’s crust and mantle. The simplest experimental techniques are the ‘fibre’ X-ray techniques in which the crystals are orientated with a particular crystallographic direction (or directions) along the fibre axis. In the case of rolled/recrystallized metal sheets or strata in the earth’s crust the analysis is more complicated—in addition to preferred orientation along some reference (e.g. rolling or shear) direction there may also be preferred orientation of the crystals with respect to the plane of the metal sheet or rock strata. Such textures may be represented by stereographic projections referred to as pole figures, fabric or petrofabric diagrams (Section 10.4) or, more quantitatively, by what are known as orientation distribution functions.

Fibre techniques play an essential experimental part in the determination of the structures of long-chain organic molecules in which the aim is to draw out a fibre from a solution which contains a sufficient number of molecules, all perfectly aligned along the fibre axis, and which give rise to reflections of measurable intensity. A simple description of the structure of DNA, which was discovered by such a technique, is given in Section 10.5.

Finally, X-ray (and neutron) powder diffraction techniques are being used increasingly in crystal structure determination, once the sole preserve of single crystal techniques. This has arisen from the necessity of determining the structures of the many materials of technological importance—e.g. clay minerals, ferrihydrites, etc.—which are finely crystalline and/or poorly ordered and which cannot be grown into crystals of large enough size (~ 0.2 mm) to be investigated by single crystal techniques. However, powder techniques are only able to deal with situations in which the structure (depending on its complexity) is known approximately and are thus better described as *structure refinement* techniques. The principal of these—known as the Rietveld method—is outlined in Section 10.6.

10.2 The geometrical basis of polycrystalline (powder) X-ray diffraction techniques

We begin, perhaps rather surprisingly, with a theorem which we learned off-by-heart (or should have done) in our early geometry lessons at school—never imagining that it would ever come in useful! The theorem comes from *The Elements of Euclid*, the mathematics textbook which has remained in print ever since it was first written in

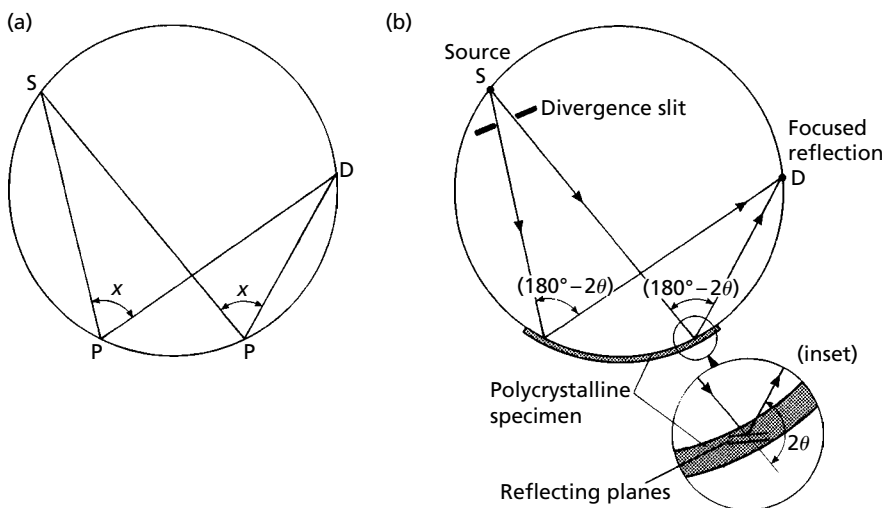


Fig. 10.1. (a) The geometrical basis of X-ray powder diffraction techniques; for two given points S and D on the circle, the angle x at the circumference is constant, irrespective of the position of P. (b) Application to an X-ray focusing camera. S is a source of monochromatic X-rays, the angular spread of which is collimated by a divergence slit to strike a thin layer of a powder specimen on the circumference at P...P. Angle $x = (180^\circ - 2\theta)$, hence any crystal planes in the right orientation for Bragg's law to be satisfied reflect to give a focused beam (as shown in the inset for a particular d_{hkl} -spacing). Note that the reflecting planes are not in general tangential to the circumference of the camera, although in practice they are closely so.

c. 300 B.C. The theorem, which is proved in Proposition 21, Book III of *The Elements*, states that 'the angles in the same segment of a circle are equal to one another'. It follows the other equally well known theorem (Proposition 20) that 'the angle at the centre of a circle is double that of the angle at the circumference on the same base, that is, on the same arc'.

The former theorem is illustrated (without Euclid's proof) in Fig. 10.1(a) and may be simply restated by saying that for any two points S and D on the circumference of a circle, the angle shown as x is constant irrespective of the position of point P. Now let us make use of this geometry in devising an X-ray camera (Fig. 10.1 (b)). Let S be a point or slit source of monochromatic X-rays (the slit being perpendicular to the plane of the paper) and let part of the circumference P...P be 'coated' with a thin film of a polycrystalline specimen.

The X-rays diverge from the source S and in order that they should only strike the specimen we limit or collimate them with a (divergence) slit as shown. Now the angle x is, in terms of Bragg's law, the angle $(180^\circ - 2\theta)$ —and whenever this is the correct Bragg angle for reflection for a particular set of hkl planes, reflections occur from all those crystals in the specimen which are in the right orientation and the reflected beams, as proved by Euclid, all converge to point D. In short D is a point where all the reflected beams for a particular d_{hkl} spacing are focused. Different positions of D on the

circumference correspond to different x , hence different $(180^\circ - 2\theta)$ values. Hence we will have a series of focused diffraction lines, one for each d_{hkl} -spacing in the specimen, around the circumference of the circle.

The Bragg reflecting geometry is shown in detail in the little 'inset' diagram below Fig. 10.1(b) which shows the orientation of the reflecting planes in one part of the specimen and the angle 2θ between the direct and reflected beams. Notice that the reflecting planes are not (except for some particular part of the specimen) tangential to the circumference.

A film placed around the rest of the circumference of the circle will record all the reflected beams and this arrangement is the basis of the Seeman–Bohlin camera and the variants of it devised by Guinier and Hägg. They are called **focusing X-ray methods** because they exploit the focusing geometry of Euclid's circle which is thus called the **focusing circle**.

The focusing geometry can also be used to provide a monochromatic source of X-rays (Fig. 10.2). The source S is now the line focus of an X-ray tube from which a spectrum of X-ray wavelengths (the 'white' radiation with superimposed characteristic wavelengths, $K\alpha_1$, $K\alpha_2$, $K\beta$ etc.) is emitted. A single plate-shaped crystal is cut such that a set of strongly reflecting planes is parallel to the surface. The crystal is curved or bent to a radius of curvature *twice* that of the focusing circle and then (ideally) is shaped or 'hollowed out' such that its inner surface lies along that of the focusing circle. The position of the source S , and hence the angle $(180^\circ - 2\theta)$ is, together with the d_{hkl} spacing of the crystal planes, chosen to reflect, say, only the strong $K\alpha_1$ component of the whole X-ray spectrum which is focused to a point or line D , symmetrical with the source S . D becomes, in

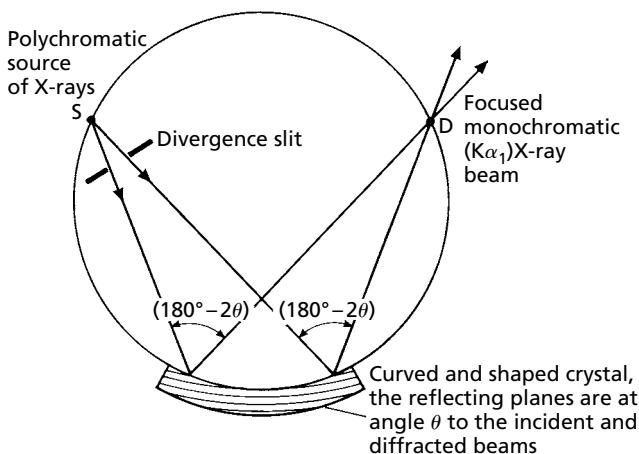


Fig. 10.2. The principle of the X-ray monochromator. The crystal planes are curved to a radius twice that of the focusing circle such that they make the same angle (θ) to the divergent incident beam. The surface of the crystal is also shaped so as to lie precisely on the focusing circle. The source and focus of the reflected beams are symmetrical (i.e. equal distances) with respect to the crystal and θ and the d_{hkl} -spacing of the crystal planes are chosen such that only the strong $K\alpha_1$ X-ray wavelength component is reflected.

effect, the line source of a beam of monochromatic X-rays, which can be used ‘upstream’ of the Seeman–Bohlin camera as the source S of monochromatic X-rays.

The symmetrical arrangement is also made use of in the X-ray diffractometer, which has become by far the most important classical X-ray powder diffraction technique. The diffractometer has become, in effect, the X-ray data acquisition end of a computer in which the data can be stored, analysed, plotted, compared with standard powder data files, etc. The advantages are enormous; the disadvantage, if it can be called such, is that students may simply regard the diffractometer as a ‘black box’ to generate data, without understanding the principles on which the instrument works, nor the parameters underlying the data analysis procedures.

The symmetrical or Bragg–Brentano focusing geometry of the diffractometer is shown in Figs 10.3(a) and (b). As described in Section 9.6, the source of monochromatic X-rays, S (from a monochromator upstream of the diffractometer) is at an equal distance

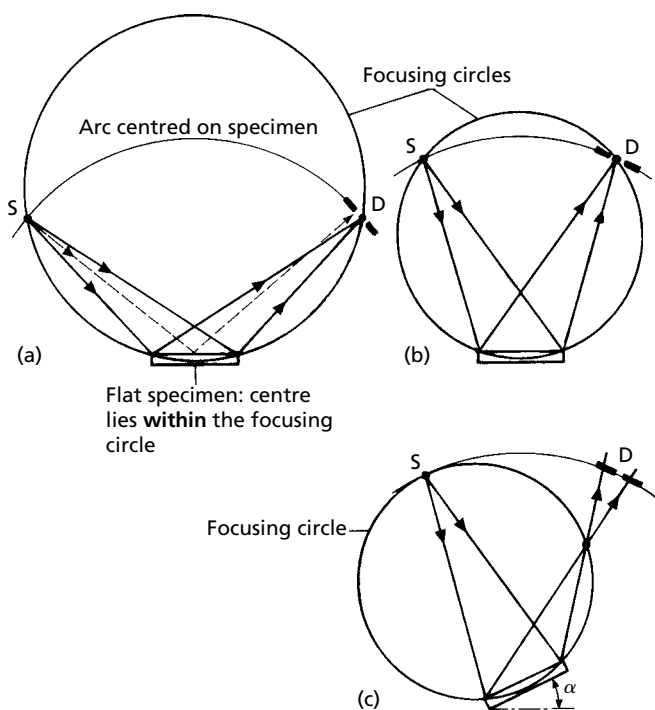


Fig. 10.3. The principle of the X-ray diffractometer. The source–specimen and specimen–detector slit distances are fixed and equal, (a) The situation for a small θ angle and (b) for a large θ angle, the source and detector moving round the arc of a circle centred on the specimen. Notice the change in the diameter of the focusing circle and the fact that, since the specimen is flat, complete focusing conditions are not achieved (dashed line in (a)), (c) An asymmetrical specimen arrangement for the same 2θ angle as in (b), the position and diameter of the focusing circle have changed such that the detector slit is no longer coincident with it. The reflecting planes are now those which make (approximately) angle α to the specimen surface (see Fig. 9.20).

and equal angle to the specimen surface as D, the ‘receiving slit’ of the detector (a proportional counter). The 2θ angle is continuously varied by the source and detector slit tracking round the arc of a circle centred on (and therefore at a fixed distance from) the specimen. Figure 10.3(a) shows the situation at a low θ angle and Fig. 10.3(b) shows the situation at a high θ angle. In some instruments the specimen is fixed and the source and detector slit rotate in opposite senses; in others the source is fixed and the specimen and detector slit rotate in the same sense, the detector slit at twice the angular velocity of the specimen—but the result geometrically is the same.

However, the important point to note is that the polycrystalline specimen as used in a diffractometer is flat, and not curved to fit the circumference of the focusing circle. Focusing therefore is not perfect—the reflected beams from across the whole surface of the specimen do not all converge to the same point: those from the centre converge to a point a little above those from the edges, as shown in Fig. 10.3(a). The diffractometer is hence called a *semi-focusing X-ray method*. In practice the deviation from full focusing geometry is only important (in the symmetrical arrangement) at low θ angles and in which a large width of specimen contributes to the reflected beam. It is not however laziness or experimental difficulty which prevents specimens being made to fit the circumference of the focusing circle, but the fact that, unlike the situation for the Seeman–Bohlin camera, the radius of the focusing circle changes with angle as is shown by a comparison with Figs 10.3(a) and (b).

As pointed out above, in the symmetrical arrangement, in which the specimen surface makes equal angles to the incident and reflected beams, the only crystal planes which contribute to the reflections are those which lie (approximately) parallel to the specimen surface, particularly when the divergence angle of the incident beam, and therefore the irradiated surface of the specimen, is small. In situations in which the d_{hkl} spacings of planes which lie at large angles to the specimen surface need to be measured (e.g. in determining the variation of lattice strains from planes in different orientations), the specimen is rotated as shown in Fig. 10.3(c); the angle of rotation α is of course (approximately) equal to the angle of the reflecting planes to the specimen surface (Fig. 9.20). In doing so, however, the symmetrical Bragg–Brentano focusing geometry is lost; the focusing circle changes both in diameter and position, as shown in Fig. 10.3(c), and the detector slit is no longer at the approximate line of focus, but in this case beyond it where the beam diverges and broadens. This deviation from the focusing geometry may be serious because the observed ‘broadening’ at the detector slit could be misinterpreted as arising from a variation in reflection angle as a result of a variation in lattice strain. The problem may be partially overcome in two ways. First, the detector slit may be moved along a sliding-arm arrangement so as to coincide more precisely with the line of focus. However, this may itself introduce errors in the angular measurements because of the difficulty of achieving a precise radial alignment of the slider. Second, the angular divergence of the incident beam may be restricted to very low values—say 0.25° – 0.5° —such that the broadening of the beam at the detector slit is very small, and this is now the preferred option.

An example of an X-ray diffractometer chart or ‘trace’ for quartz (SiO_2) is given in Fig. 10.4. The d_{hkl} -spacings and relative intensities of the reflections may be used to identify the material, as described in Section 10.3 below.

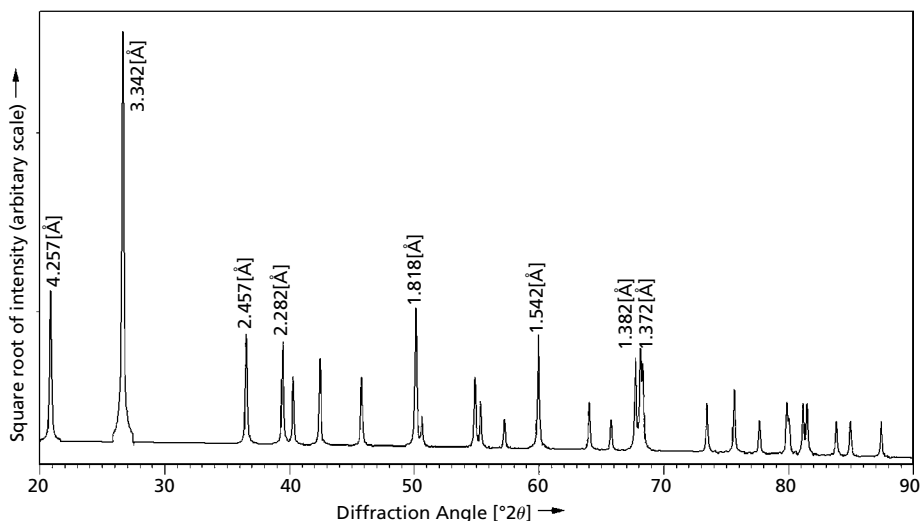


Fig. 10.4. An example of an X-ray diffractometer chart of intensity of the reflected beams (ordinate) vs 2θ angle (abscissa). The intensity scale is non-linear (square root) to emphasize the weaker reflections. The specimen is polycrystalline SiO_2 (quartz), $\text{CuK}\alpha_1$ radiation ($\lambda = 1.541 \text{ \AA}$). The d -spacings (\AA) of the reflections are indicated (compare with Figs 10.7 and 10.8). (Courtesy of Mr. D. G. Wright.).

There are two other ‘classical’ X-ray powder techniques of interest—the back reflection method in which the whole or part of the diffraction cones are recorded on flat film (an experimental arrangement identical to that for the Laue back reflection method) and the Debye–Scherrer technique in which a thin rod-shaped specimen or a powder in a capillary tube is set at the centre of a cylindrical camera.

The geometry of the back reflection powder method is shown in Fig. 10.5. The effective position of the source S is determined by the design of the collimator tube which passes through a hole in the centre of the film. In practice the divergence angle is very small, of the order 0.5° – 2° . Notice that, like the diffractometer, it is a semi-focusing method—all the reflected beams from the (flat) specimen surface focus approximately at the circumference of the focusing circle. However, the flat film can be placed only at one distance x from the specimen: if x is the focal distance of the high 2θ angle reflections as shown, it will not be at the focal distance of the lower 2θ angle reflections. In practice a ‘compromise’ value of x is chosen such that the diffraction rings of particular interest are most sharply focused.

The great advantage of the Debye–Scherrer method over the diffractometer (and to a lesser extent the Seeman–Bohlin method and its variants) is that only very small amounts of material are required for, say, insertion into a capillary tube.

The geometry and specimen–film arrangement in the Debye–Scherrer camera are shown in Fig. 10.6. The cylindrical specimen (a powder in a capillary tube or a cemented powder in the form of a little rod) is placed at the centre of a cylindrical camera. The strip of film may be fitted round the circumference of the camera in several ways: it may have

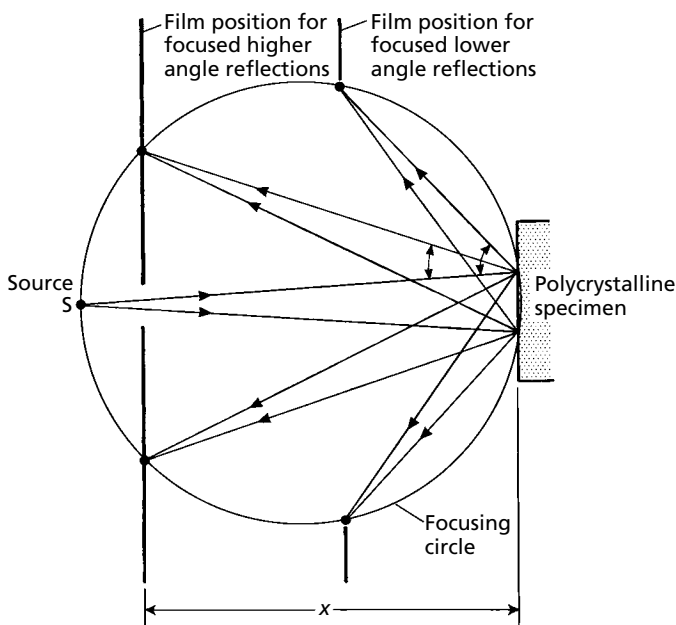
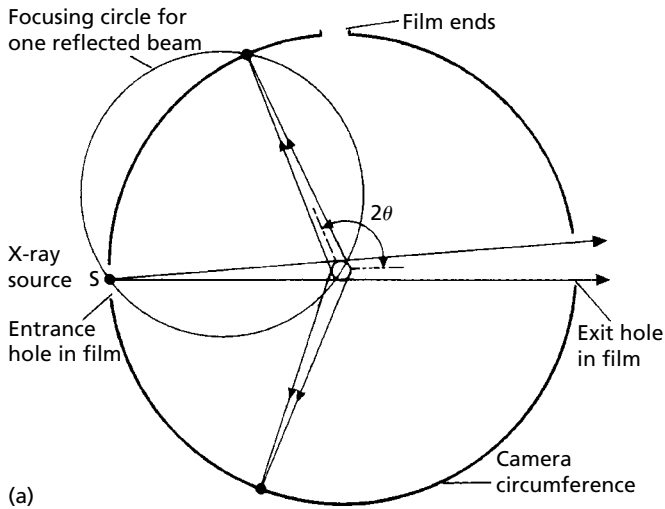


Fig. 10.5. The geometry of the back reflection X-ray powder method; the diverging X-ray beam from an (effective) source S passes through a hole at the centre of the film. The reflected beams for two reflections are shown. The film is shown placed at a specimen–film distance x so as to intercept the higher angle reflections such that they are sharply focused. In order to intercept the lower angle reflections such that they are sharply focused it would need to be moved closer to the specimen as indicated. In practice a ‘compromise’ value for x is chosen which is acceptable since the divergence angle, and the de-focusing of the incident beam, is small.

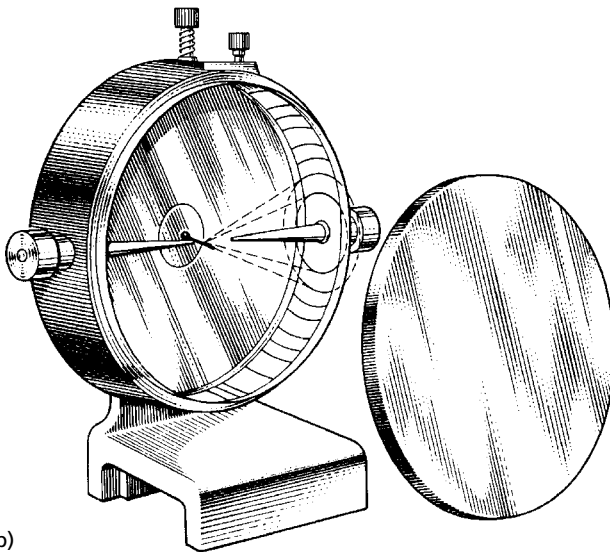
a single hole punched at its centre and so arranged to coincide with the ‘exit’ direction of the X-ray beam (the ends of the film being each side of the ‘entrance’ direction of the X-ray beam) or *vice versa*. However, the usual way is to punch two holes in the film, one to match the ‘entrance’ and the other to match the ‘exit’ directions of the X-ray beam, the two ends of the film now being at the ‘top’ or ‘bottom’ of the camera as shown. This ‘asymmetrical’ arrangement or ‘setting’ has the advantage that a complete range of 2θ angles—from 0° to 180° —may be recorded on one side of the film without a ‘cut-off’ occasioned by the presence of a film end. In this way accurate d_{hkl} -spacings may be determined and any effects of film shrinkage accounted for.

The position of the effective source S is determined by the design of the collimator. The focusing circle for a particular reflection is shown; however, this only represents the physical situation very approximately since the reflected beams arise to different extents from the whole volume of the specimen and the position of the source S and the focusing effect is by no means as precise as that drawn in Fig. 10.6.

An example of a Debye–Scherrer film (asymmetrical setting) is shown in Fig. 10.7. The $2\theta = 0^\circ$ and $2\theta = 180^\circ$ positions can be worked out exactly by determining



(a)



(b)

Fig. 10.6. (a) The geometry of the Debye-Scherrer camera; the reflected beams from a cylindrical specimen *tend* towards a focus on the film around the circumference of the camera and the focusing circle for a particular reflected beam is shown. In practice deviations from this idealized situation occur because the reflected beams originate with varying intensities from the whole volume of the specimen and the effective source S may not coincide with the circumference of the camera. (b) The camera with the light-tight lid removed showing the specimen at the centre, the collimator and receiving tube and the (low angle) X-ray diffraction rings on the film. The screws at the top are for locating and fixing the ends of the film (from *Manual of Mineralogy*, 21st edn, by C. Klein and C. S. Hurlbut Jr., John Wiley, 1993).



the centres of the 'exit' and 'entrance' rings, the distance between them on the film corresponding to 180° exactly. Hence the camera diameter does not need to be known, although in practice cameras are made with diameters 57.53 mm or 114.83 mm such that (and accounting for film thickness) the circumference is 180 mm or 360 mm. Hence for quick work the angles can simply read in terms of millimetres on the film.

It may be thought that the Debye–Scherrer method, as a film technique, has been supplanted by the diffractometer. This is by no means the case: the ability of examining very small amounts of material and the conversion of film data to digital data *via* the use of the microdensitometer has resulted in its use, for example, in Rietveld analysis (Section 10.6). In addition, film may be replaced by an array of position sensitive detectors in both X-ray and neutron diffraction techniques.

10.3 Some applications of X-ray diffraction techniques in polycrystalline materials

10.3.1 Accurate lattice parameter measurements

The accurate measurement of d_{hkl} -spacings is now largely carried out with the X-ray diffractometer using monochromatized ($K\alpha_1$) radiation, narrow divergence and receiving slit systems, internal calibration systems and peak profile measurement procedures. However, as shown below, it is the high 2θ angle reflections which are most sensitive to small variations in d_{hkl} -spacings and for this reason the Debye–Scherrer powder camera and back reflection flat film techniques in which 2θ angles up to nearly 180° can be recorded, are still used. By contrast, the largest 2θ angles measurable with a diffractometer are about 150° because the near approach and possible contact between the source and receiving slit assemblies.

Given the crystal system and the hkl values of the reflections, the lattice parameter(s) can be determined using the appropriate equation (Appendix A4.1). This procedure is clearly simplest for the cubic system in which the d_{hkl} -values depend only upon the one variable, a . In other systems several d_{hkl} -spacings need to be measured and the values inserted into simultaneous equations from which values of the lattice parameters are extracted.

Fig. 10.7. An example of a Debye–Scherrer X-ray film ($\text{CuK}\alpha$ X-radiation) for SiO_2 (quartz). S is the 'entrance' hole and O the 'exit' hole. The 'spotty' appearance of the rings arises because of the relatively coarse crystallite size in the specimen. At high 2θ angles (near the entrance hole) the $K\alpha_1/K\alpha_2$ doublets are resolved but at low 2θ angles (near the exit hole) they are unresolved. The streaks around the exit hole arise from the presence of residual 'white' X-radiation in the incident beam.

The sensitivity of change of the 2θ angle for a reflection with a change in d_{hkl} -spacing is a measure of the resolving power of the diffraction technique. The resolving power, or rather the limit of resolution, $\delta d/d$, can be obtained by differentiating Bragg's law with respect to d and θ (λ fixed), i.e.

$$\lambda = 2d \sin \theta$$

differentiating:

$$0 = 2d \cos \theta \delta \theta + 2 \sin \theta \delta d$$

hence

$$\delta d/d = -\cot \theta \delta \theta.$$

This equation may be 'read' in two ways. For a given value of $2\delta\theta$, which may be expressed in terms of the minimum resolved distance between two reflections on the film, chart, etc., for the smallest limit of resolution we want $\cot \theta$ values to be as small as possible; or, for a given value of $\delta d/d$, we want the angular separation of the reflections $2\delta\theta$ to be as large, and hence again $\cot \theta$ values to be as small as possible.

A glance at cotangent tables shows that $\cot \theta$ values are high at low θ angles and rapidly decrease towards zero as θ approaches 90° . Hence d_{hkl} -spacing measurements are most accurate using high-angle X-ray diffraction methods and least accurate with low-angle electron diffraction methods.

10.3.2 Identification of unknown phases

For powder specimens in which the crystals are randomly orientated, the set of d -spacings and their relative intensities serves as a 'fingerprint' (or 'genetic strand') from which the phase can be identified by comparison with the 'fingerprints' of phases in the *X-ray Powder Diffraction File*—a data bank of over 250,000 inorganic and 300,000 organic and organometallic phases. The File is administered by the International Centre for Diffraction Data (ICDD)—formerly the Joint Committee for Powder Diffraction Standards (JCPDS)—and new and revised sets of data are published annually in book form (replacing the original 5 inch by 3 inch cards) or as a computer database. In addition, there are published Indexes with the phases arranged alphabetically by chemical name, search manuals and abstracts from the File (including Indexes and Search Manuals) or Frequently Encountered Phases (FEP).

The entry for each phase in the File or computer database (which differ slightly in their layout) includes: file number, chemical formula and name, experimental conditions, physical and optical data (where known), references and the set of d -spacings (given in Å), their Laue indices and their relative intensities arranged in order of decreasing d -spacing. Finally, the ICDD editors assign a 'quality mark' to indicate the reliability of the data (e.g. a '*' indicates that the chemistry, structure and X-ray data of the phase is well characterized); or whether the X-ray data has been derived by calculation, rather

46-1045			★		
SiO₂			dÅ	Int	hk/
Silicon Oxide			4.2550	16	100
Quartz, syn			3.3435	100	101
Rad. CuKα ₁ λ 1.540598 Filter Ge Mono.d-sp Diff. Cut off Int. Diffractometer I/I _{cor} 3.41			2.4569	9	110
Ref. Kern, A., Eysel, W., Mineralogisch-Petrograph.Inst., Univ. Heidelberg, Germany, ICDD Grant-in-Aid, (1993)			2.2815	8	102
S.G. P3 ₂ 21 (154)			2.2361	4	111
a 4.91344(4) b c 5.40524(8) A Z 3 mp C 1.1001			2.1277	6	200
Ref. Ibid.			1.9799	4	201
D _x 2.65 D _m 2.66 SS/FOM F ₃₀ = 539(.002,31)			1.8180	13	112
εα nωβ 1.544 εγ 1.553 Sign + 2V			1.8017	<1	003
Ref. Swanson, Fuyat, Natl. Bur. Stand. (U.S.), Circ. 539,324(1954)			1.6717	4	202
Color White			1.6592	2	103
Integrated intensities. Pattern taken at 23(1) C.Low temperature quartz. 2θ determination based on profile fit method. O ₂ Si type. Quartz group. Silicon used as internal standard. PSC: hP9. TO replace 33-1161. Structure reference: Z.Kristallogr., 198 177(1992)			1.6083	<1	210
See following card.			1.5415	9	211
			1.4529	2	113
			1.4184	<1	300
			1.3821	6	212
			1.3750	7	203
			1.3719	5	301
			1.2879	2	104
			1.2559	3	302
			1.2283	1	220
			1.1998	2	213
			1.1978	<1	221
			1.1840	2	114
			1.1802	2	310
			1.1530	1	311
			1.1407	<1	204
			1.1145	<1	303
			1.0816	2	312
			1.0638	<1	400
			1.0477	1	105
			1.0438	<1	401
			1.0346	1	214
			1.0149	1	233
			0.9896	<1	115
			0.9872	<1	313
			0.9783	<1	304
			0.9762	<1	320
			0.9608	<1	321
			0.9285	<1	410
			0.9182	<1	322
			0.9161	2	403
			0.9152	2	411
			0.9089	<1	224
			0.9009	<1	006
			0.8972	<1	215
			0.8889	1	314
			0.8814	<1	106
			0.8782	<1	412
			0.8598	<1	305

Fig. 10.8. The Powder Diffraction File Card No. 46-1045, for quartz. The left-hand side gives crystallographic optical and physical information and the source of the data. The right-hand side lists the *d*-spacings, in descending order, with the strongest line assigned an intensity of 100. Formerly (up to set 24) the cards included along the top left edge the *d*-spacings of the three strongest lines and the largest *d*-spacing recorded in the pattern. (International Centre for Diffraction Data.)

than observed (a ‘c’ mark). Figure 10.8 shows an example of a Powder Diffraction File card, that for quartz, set number 46, card number 1045.

A comparison of an unknown phase with so many others is potentially a daunting task! It is greatly facilitated by a search procedure based on that first devised by J. D. Hanawalt in 1936 and now refined and speeded up using computer search procedures.

The phases are grouped together (into what is known as Hanawalt groups) according to the *d*-spacing of their strongest reflection. There are forty Hanawalt groups covering the whole range of *d*-spacings. For example, the strongest line of quartz (relative intensity 100) is that at 3.34 Å (Figs 10.4 and 10.8); quartz therefore lies in the Hanawalt group with *d*-spacings in the range from 3.39 to 3.32 Å (Fig. 10.9—first column). Within each Hanawalt group the patterns are listed in the second column in order of decreasing *d*-spacings of the second strongest line which for quartz is that at 4.26 Å; on reading down the list of patterns in the second column of the Hanawalt group a potential ‘match’ can be made with the second strongest line and then (from the number of possibilities available) final confirmation made with the *d*-spacings and intensities of the third, fourth etc. strongest lines in the subsequent columns. Figure 10.9 is from the Hanawalt Inorganic Search Manual showing some entries in the Hanawalt group 3.39–3.32 Å which includes that for quartz, File No. 46-1045.

In practice the procedure is by no means as straightforward as this. First, many minerals and metallic alloys give very nearly the same diffraction pattern because of the existence of solid solution ranges, which result in very small shifts in lattice parameter.

										3.39 – 3.32 (±.02)	
QM	Strongest Reflections					PSC	Chemical Formula	Mineral Name/Common Name		PDF#	I/I ₁
	3.40 _x	4.29 _x	4.09 _x	6.63 _x	4.82 _x	3.31 _x	2.67 _x	2.33 _x	o*144	ClF ₂ OBF ₄	26-235
	3.39 _x	4.29 _x	5.88 _x	3.12 _x	2.98 _x	2.30 _x	1.96 _x	1.78 _x	hP15	Li ₂ 33Fe _{0.67} S ₂	36-1089
	3.39 _x	4.29 _x	2.47 _x	2.31 _x	2.23 _x	2.14 _x	1.99 _x	1.83 _x	h**	BPO ₄	11-237
O	3.36 _x	4.29 _x	2.85 _x	5.60 _x	4.02 _x	2.58 _x	1.98 _x	1.90 _x		V _{0.87} Cr _{0.13} O _{2.17}	35-332
i	3.34 _x	4.29 _x	10.5 _x	2.64 _x	2.71 _x	5.27 _x	5.25 _x	3.79 _x	ol32	Na ₅ Ta ₃ O ₈ F ₃	25-871
	3.32 _x	4.29 _x	2.99 _x	2.87 _x	2.52 _x	4.70 _x	2.38 _x	2.30 _x		C ₅ Al(NO ₃) ₃	28-274
	3.31 _x	4.29 _x	3.68 _x	2.91 _x	2.34 _x	2.06 _x	1.99 _x	1.93 _x		Pu(OH)(CO ₃)*xH ₂ O	33-982
i	3.37 _x	4.28 _x	1.84 _x	1.55 _x	2.47 _x	2.31 _x	1.39 _x	2.14 _x	hP18	AlPO ₄	10-423
	3.35 _x	4.28 _x	3.71 _x	2.85 _x	2.17 _x	4.07 _x	3.03 _x	2.73 _x		K ₂ N ₂ V ₆ O ₂₁	20-1379
i	3.34 _x	4.28 _x	4.27 _x	3.38 _x	2.77 _x	2.33 _x	2.79 _x	2.32 _x	mp28	CsLiSeO ₄	29-411
	3.33 _x	4.28 _x	3.24 _x	4.58 _x	2.91 _x	2.37 _x	1.87 _x	4.95 _x	hP20.70	Cs _{0.35} V ₃ O ₇	30-385
	3.36 _x	4.27 _x	1.82 _x	2.28 _x	1.54 _x	2.46 _x	2.13 _x	1.37 _x	hP9	SiS ₂	47-1376
i	3.34 _x	4.27 _x	3.19 _x	2.70 _x	2.28 _x	4.91 _x	1.82 _x	3.13 _x	mp100	CaAl ₂ Si ₂ O ₈ *4H ₂ O	20-452
	3.30 _x	4.27 _x	3.71 _x	3.45 _x	3.92 _x	3.34 _x	3.27 _x	2.96 _x	ap26	KFeSi ₂ O ₈	16-153
i	3.38 _x	4.26 _x	4.16 _x	1.68 _x	6.70 _x	2.97 _x	2.86 _x	2.56 _x		Cs ₂ VCl ₄ *4H ₂ O	20-301
	3.37 _x	4.26 _x	4.18 _x	2.98 _x	8.56 _x	6.76 _x	3.49 _x	3.09 _x	mC40	Cs ₂ VCl ₄ *4H ₂ O	34-322
O	3.36 _x	4.26 _x	4.21 _x	2.86 _x	5.90 _x	5.55 _x	3.26 _x	2.94 _x		KAlH(P ₃ O ₁₀)	38-55
O	3.36 _x	4.26 _x	2.98 _x	5.95 _x	5.55 _x	4.02 _x	3.26 _x	2.87 _x		KCrHP ₃ O ₁₀	41-442
	3.34 _x	4.26 _x	4.33 _x	3.40 _x	3.38 _x	2.05 _x	4.89 _x	2.02 _x	op36	KNaSiF ₆	43-1313
	3.34 _x	4.26 _x	3.66 _x	2.61 _x	2.48 _x	1.80 _x	3.97 _x	3.05 _x	hP168	3PbCO ₃ *2Pb(OH) ₂ *H ₂ O	9-356
i	3.34 _x	4.26 _x	2.13 _x	7.40 _x	3.49 _x	2.58 _x	2.24 _x	2.21 _x	hP70	Ca ₃ Ge(SO ₄) ₂ (OH) ₆ *3H ₂ O	19-225
	3.34 _x	4.26 _x	2.13 _x	7.40 _x	2.57 _x	2.03 _x	3.49 _x	2.24 _x	hP70	Ca ₃ Mn ⁴⁺ (SO ₄) ₂ (OH) ₆ *3H ₂ O	20-226
O	3.33 _x	4.26 _x	4.24 _x	4.31 _x	2.89 _x	2.75 _x	3.88 _x	3.19 _x		K ₂ Ca(VO ₃) ₄	37-180
i	3.30 _x	4.26 _x	3.27 _x	3.65 _x	2.89 _x	2.30 _x	2.63 _x	2.32 _x		Sm ₂ O(CO ₃) ₂ *xH ₂ O	28-904
	3.30 _x	4.26 _x	2.89 _x	4.45 _x	3.14 _x	2.56 _x	3.89 _x	2.66 _x	mp16	CsO ₃	45-947
*	3.34 _x	4.26 _x	1.82 _x	2.46 _x	1.54 _x	2.28 _x	1.38 _x	2.13 _x	hP9	SiO ₂	46-1045
	3.31 _x	4.25 _x	4.09 _x	3.72 _x	2.98 _x	2.20 _x	1.93 _x	5.47 _x	o*66	ClPtOF ₆	26-415
	3.30 _x	4.25 _x	4.09 _x	3.67 _x	7.42 _x	5.47 _x	2.96 _x	1.91 _x	o*66	(ClF ₂ O)AsF ₆	26-117
	3.40 _x	4.24 _x	3.00 _x	5.72 _x	2.65 _x	2.85 _x	2.37 _x	2.00 _x	ti24	KAuF ₄	27-395
*	3.37 _x	4.24 _x	2.32 _x	2.12 _x	2.45 _x	1.84 _x	1.83 _x	1.54 _x	hP18	GaPO ₄	8-497
O	3.36 _x	4.24 _x	2.86 _x	5.90 _x	5.55 _x	3.26 _x	2.94 _x	6.60 _x		KAlH(P ₃ O ₁₀)	38-55
*	3.33 _x	4.24 _x	3.39 _x	2.64 _x	3.25 _x	2.60 _x	4.38 _x	3.44 _x	mp44	SrUO ₆ O ₁₈	38-1560
i	3.41 _x	4.23 _x	2.87 _x	2.49 _x	2.06 _x	1.99 _x	1.95 _x	1.93 _x	mC12	α-WP ₂	35-1467
	3.39 _x	4.23 _x	5.06 _x	3.45 _x	3.18 _x	3.05 _x	5.25 _x	3.76 _x	mC*	RbAl ₂ (H ₂ P ₃ O ₁₀)(P ₃ O ₁₂)	37-261
O	3.39 _x	4.23 _x	2.99 _x	2.89 _x	2.77 _x	5.93 _x	3.24 _x	4.75 _x		RbGaHP ₃ O ₁₀	34-1347
	3.38 _x	4.23 _x	3.83 _x	2.50 _x	3.10 _x	1.71 _x	3.31 _x	2.21 _x	mp62	K ₂ Mn(SeO ₄) ₂ *6H ₂ O	53-1151
O	3.37 _x	4.23 _x	3.46 _x	3.00 _x	2.13 _x	6.00 _x	2.69 _x	2.45 _x		CsSnFBrI	30-369
O	3.36 _x	4.23 _x	2.37 _x	2.29 _x	2.15 _x	1.90 _x	9.50 _x	3.95 _x		Al ₆ La ₂ Si ₅	41-734
	3.36 _x	4.23 _x	1.64 _x	2.72 _x	2.44 _x	2.23 _x	1.93 _x	3.14 _x		Mo ₂ O ₉ *xH ₂ O	21-574
	3.35 _x	4.23 _x	3.12 _x	3.43 _x	3.84 _x	3.75 _x	3.39 _x	3.37 _x		β-C ₂ Cl(SO ₄) ₂	28-288
i	3.32 _x	4.23 _x	1.88 _x	3.45 _x	2.76 _x	2.25 _x	2.12 _x	2.64 _x	op36	β-NaSrGaF ₆	44-1352
O	3.40 _x	4.22 _x	3.20 _x	3.14 _x	5.81 _x	3.62 _x	3.03 _x	2.64 _x		Na ₃ VO ₂ (SO ₄) ₂	41-175
	3.41 _x	4.21 _x	3.11 _x	2.75 _x	7.58 _x	5.60 _x	4.46 _x	3.31 _x		Na ₂ SbF ₃ SO ₄	28-1038
O	3.41 _x	4.21 _x	2.99 _x	3.24 _x	2.91 _x	2.77 _x	5.95 _x	4.77 _x		RbCrHP ₃ O ₁₀	41-443
O	3.40 _x	4.21 _x	3.30 _x	3.22 _x	6.97 _x	4.76 _x	3.11 _x	2.58 _x	a*15.54	UO ₃ *0.393H ₂ O	41-443
O	3.39 _x	4.21 _x	3.92 _x	2.78 _x	1.89 _x	3.78 _x	2.96 _x	2.08 _x		Pb ₂ Sb ₂ S ₆	36-94
O	3.34 _x	4.21 _x	3.15 _x	2.11 _x	2.71 _x	2.05 _x	4.73 _x	2.56 _x		Cs ₂ Zr ₂ (PO ₄) ₃	52-1181
	3.35 _x	4.21 _x	3.82 _x	2.95 _x	2.47 _x	2.34 _x	2.01 _x	1.99 _x		CsXeOF ₆	35-1267
O	3.30 _x	4.21 _x	3.40 _x	3.22 _x	6.97 _x	4.76 _x	3.11 _x	2.58 _x	a*15.54	UO ₃ *0.393H ₂ O	43-346
O	3.41 _x	4.20 _x	3.65 _x	2.77 _x	2.71 _x	2.96 _x	2.15 _x	4.00 _x		Tl ₂ Si ₂ S ₅	38-914

Fig. 10.9. Part of the Hanawalt Search Manual for Inorganic Phases, showing some entries in the Hanawalt Group 3.39–3.32 Å. The intensities of the reflections are indicated by subscripts $x = 100$, $9 = 90$, $8 = 80$, and so on. Notice that some patterns are entered in this Hanawalt Group according to their *second*-strongest or *third*-strongest lines; e.g. $K_2N_2V_6O_{21}$ (20-1379) or $RbGaHP_3O_{10}$ (34-1347) respectively. This is because they have intensities over 75% of that of the strongest line and may experimentally be identified as the strongest lines. (International Centre for Diffraction Data.)

Second, the crystals in the powder specimen may not be randomly orientated—the specimen may be textured or may show preferred orientation, which implies that the relative intensities of the reflections may be altered as compared with those in the File. Third, the unknown specimen may consist of more than one phase—and if they are in roughly equal proportions the strongest lines may be ‘mixed up’.

These problems are partly (but not wholly) circumvented by a series of ‘entry rules’, the details of which are given in the Search Manual. First, those patterns in which the d -spacing of the strongest reflection lies close to one of the boundary values of the Hanawalt group are entered in both groups—the one above and the one below. Second, those patterns in which the intensity of the second strongest reflection is greater than 75% of the intensity of the strongest (and in which there is therefore a strong possibility of the mis-identification of the strongest reflection) are entered twice; the second strongest reflection determining the Hanawalt group and the position in the group listed (as before) in accordance with the (decreasing) d -spacing of the second strongest reflection. Similar

rules apply to the third and fourth strongest reflections such that a pattern may be listed several times. Examples of such permutations are shown in Fig. 10.9.

10.3.3 *Measurement of crystal (grain) size*

This is based on the determination of β , the line broadening in the Scherrer equation (Section 9.3) and an estimate of K , the ‘shape’ correction factor (which does not differ significantly from unity). However, this is not a straightforward business because the *observed* broadening, β_{obs} , also includes ‘instrumental’ factors (see Section 9.3) such as detector slit width, area of specimen irradiated, possible presence of a $K\alpha_2$ component in the X-ray beam, etc. The contributions from these factors have to be ‘subtracted’ from the observed peak breadth (or, strictly speaking, they have to be deconvoluted from the peak). The usual procedure is to measure the instrumental broadening, β_{inst} , in a large-grained material in which grain size broadening is assumed to be negligible, and to determine β either by a simple subtraction, due to Scherrer, i.e. $\beta = \beta_{\text{obs}} - \beta_{\text{inst}}$, or by a subtraction of squares, due to Warren, i.e. $\beta^2 = \beta_{\text{obs}}^2 - \beta_{\text{inst}}^2$. In practice, attempts to measure ‘absolute’ grain sizes by X-ray diffraction are fraught with difficulty because of the presence of imperfections (particularly sub-grain boundaries), lattice strains, etc. which contribute to the broadening of the X-ray peaks.

10.3.4 *Measurement of internal elastic strains*

The elastic strains to be measured can be distinguished into those occurring on a ‘macro’ scale and those occurring on a ‘micro’ scale. Macroscale refers to the situation where the whole material is subject to some directional residual tension or compression; the resultant strains, which are manifested in terms of increases (tension) or decreases (compression) in the d_{hkl} -spacings are therefore also directional and the measured values vary with the orientation of the reflecting planes—those parallel to the stress axis for example suffering no change.

In order to measure such strains (and to determine the stress axis) in the diffractometer, the specimen needs to be rotated from the symmetrical (Bragg–Brentano) geometry as described above. In practice, measurements of peak shift are made for various settings of the specimen and from which the direction and magnitude of the stress can be extrapolated.

Microscale refers to the situation in which the directions (and magnitudes) of the internal strains vary from crystal to crystal. The subsequent elastic strains give rise, not to a shift, but to a broadening of the diffraction peaks from which an estimate of the micro-stress can be made. The relevant equation is that derived for the limit of resolution (Section 10.3.1), in which e , the elastic strain, is substituted for $\delta d/d$, i.e.

$$\epsilon = -\cot \theta \delta \theta.$$

Hence the broadening, β , expressed as the half-height peak width $2\delta\theta$, is:

$$\beta = -\frac{2\epsilon}{\cot \theta} = -2\epsilon \tan \theta.$$

Notice that this equation is very similar to the Scherrer equation for broadening arising from crystal size; the important difference being that in this case β varies as $1/\cot \theta$ or $\tan \theta$ and in the Scherrer equation β varies as $1/\cos \theta$ or $\sec \theta$. As in the case of grain size broadening (Section 10.3.3), the instrumental broadening, β_{inst} , measured for a stress-free material, must be subtracted from β_{obs} , the observed broadening for the micro-strained material. Having measured the strain ϵ , the stress may be determined by substituting the appropriate value of the Young modulus, E .

Finally, the elastic strain ϵ may be expressed in terms of the extension of reciprocal lattice points into ‘nodes’ just as we did for a crystal of finite thickness t (Section 9.3.1). Since

$$\epsilon = \frac{\delta(d_{hkl})}{(d_{hkl})} = \frac{\delta\left(\frac{1}{d_{hkl}^*}\right)}{1/(d_{hkl}^*)} = -\frac{\delta(d_{hkl}^*)}{(d_{hkl}^*)}$$

(remembering the differential $d\left(\frac{1}{x}\right) = -\frac{dx}{x^2}$) then the extension is

$$\delta(d_{hkl}^*) = -\epsilon d_{hkl}^* = -\frac{\epsilon}{d_{hkl}}$$

i.e. unlike the extension arising from crystal size in which every reciprocal lattice point is extended the same amount, $1/t$, in this case the reciprocal lattice points are more extended the further we go from the origin in reciprocal space.

10.4 Preferred orientation (texture, fabric) and its measurement

There are essentially two methods of recording preferred orientation: film methods which make use of flat-plate film cameras, and counter methods which make use of a special design of diffractometer called a *texture goniometer*. Film methods have the advantage that the cones of reflected beams from planes of different d_{hkl} spacings can be recorded ‘all at once’ so that you can see at a glance, from the varying intensities around the diffraction rings, whether the crystals are in random orientation or not. In practice the film may be set ‘behind’ the specimen as in Fig. 10.5 such that the cones of high-angle reflections are recorded (the back reflection X-ray method; or the film may be set ‘in front of the specimen such that the cones of low-angle reflections are recorded) the transmission X-ray method. In the latter case the specimen must be thin enough for the reflected beams to pass through with sufficient intensity to be recorded—which sets a practical limitation in the case of ‘bulk’ specimens which cannot be cut into thin sections.

However, film methods have the disadvantage that, except for the case of fibres, the data cannot easily be represented in a quantitative way—the varying intensities around the diffraction rings depend also on the orientation of the specimen with respect to the incident beam which means that several exposures need to be made and the results collated and the intensities analysed in terms of the ‘blackening’ of the films—a tedious business. In the case of fibres only one orientation and hence only one photograph is

needed—the fibre axis normally being set vertical and perpendicular to the direction of the (horizontal) incident beam.

In the texture goniometer the detector is set at a fixed 2θ angle to record the diffracted intensity from just one set of d_{hkl} planes. All the movement takes place at the specimen which can be rotated about two axes as described below such that the detector in effect scans a wide range of orientations of the selected d_{hkl} planes. The detector may then be re-set at another 2θ angle to record another set of d_{hkl} planes and the process repeated. It is therefore, in contrast to film methods, a sequential procedure but has the enormous advantage that the output from the detector can be represented in the form of pole figures or processed numerically to give what is known as an orientation distribution function (ODF) which provides a complete description of the texture or fabric of the material.

10.4.1 Fibre textures

Figure 10.10 shows the simple experimental set-up for the transmission X-ray method to record the low 2θ angle (highest d_{hkl}) reflections. The fibre, or reference direction is set vertical and perpendicular to the incident X-ray beam. Figure 10.11 is an example of the application of the technique in the study of polymers. Figure 10.11(a) shows the diffraction pattern of a thin section of an injection-moulded specimen of polypropene $n(\text{CH}_2\text{—CHCH}_3)$ which partially crystallizes on cooling from the melt; the diffraction rings are of uniform intensity which shows that the crystallites are in random orientation. Figure 10.11(b) is of the same material which has been plastically deformed in tension to a strain of about 500%. The diffraction rings are no longer continuous but consist of peaks of intensity which show that the crystallites now lie in a particular orientation with respect to the tensile axis. The diffraction pattern approaches that of a rotation or oscillation photograph of a single crystal (Fig. 9.17), the peaks of intensity lying in layer-lines perpendicular to the axis of rotation/oscillation. Given the structure and unit cell of polypropene and the $\{hkl\}$ reflections which occur, we can index the reflections

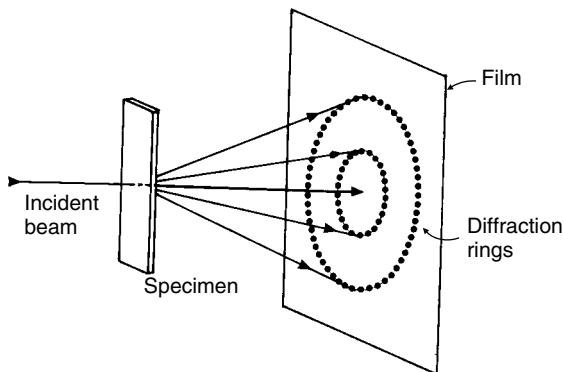


Fig. 10.10. Transmission X-ray powder method. The diffraction rings consist of reflections from many crystallites as indicated by the dots. Each ring corresponds to a cone of reflected beams of semi-angle 2θ .

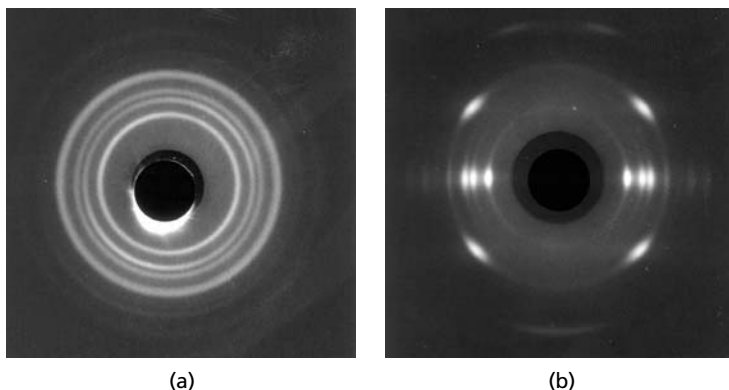


Fig. 10.11. Transmission X-ray photographs of polypropylene $n(\text{CH}_2\text{--CHCH}_3)$: (a) as-crystallized from the melt (crystallites in random orientation); (b) after $500^\circ/\text{a}$ plastic deformation in tension (crystallites orientated with the polymer chains along the (vertical) tensile axis). (Photographs by courtesy of Dr. J. Way.)

and hence determine which crystallographic direction is orientated along the tensile axis. Intuitively we may guess that the crystallites are orientated such that the polymer chains lie in the direction of the tensile axis and the demonstration that this is indeed the case is given in Exercise 10.4.

10.4.2 Sheet textures

The texture goniometer consists essentially of a cradle in which a flat-surface specimen (as in a diffractometer) can be rotated about two axes as indicated in Fig. 10.12(a), one of which, $\text{O} \dots \text{O}$ is normal to the specimen surface and the other $\text{B} \dots \text{B}$ lies in the specimen surface and in the plane containing the incident and diffracted beams (i.e. perpendicular to the direction $\text{A} \dots \text{A}$). In the ‘starting position’ the specimen is set in the symmetrical or Bragg-Brentano focusing arrangement as shown in Fig. 9.20(a) and all the reflected intensity received by the detector arises from the crystal planes lying parallel to the specimen surface. The specimen is then tilted a small angle β (say 5°) about the axis $\text{B} \dots \text{B}$. The reflected intensity received by the detector now arises from the crystal planes also tilted 5° to one side of the specimen surface. Note that this angle of tilt is *not* the same as the angle α in Fig. 9.20(b) which is in effect a tilt about the other direction $\text{A} \dots \text{A}$ in Fig. 10.12(a). The specimen is then rotated about the normal $\text{O} \dots \text{O}$; in a complete revolution of 360° the detector records the reflected intensity from the planes tilted in all directions at 5° to the specimen surface. Now the specimen is tilted about the axis $\text{B} \dots \text{B}$ say another 5° and again rotated 360° about its normal; the recorded intensity now arises from all the planes tilted 10° from the specimen surface—and so on.

Figure 10.12(b) shows the geometry involved for an angle of tilt β ; the diffracted intensity arises from the planes whose normals lie in a cone normal to the specimen surface of semi-apex angle β . The ‘vertical’ edge of the cone (in the plane of the incident

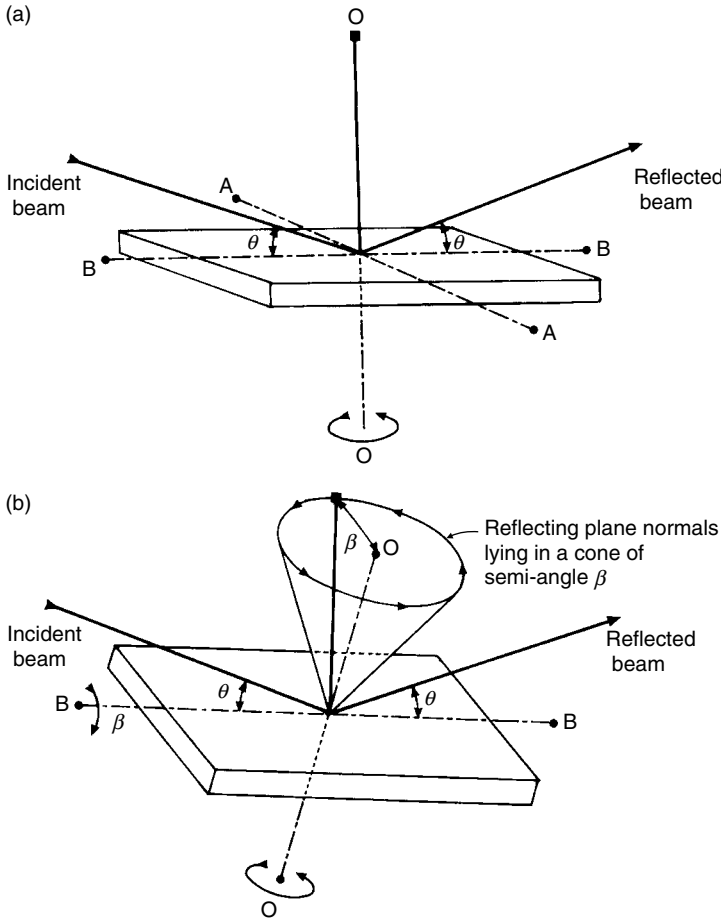


Fig. 10.12. The geometry of the texture goniometer, the specimen is rotated about the axis O...O normal to the specimen surface and tilted about the axis B...B lying in the specimen surface and in the plane containing the incident and diffracted beams, (a) indicates 'starting position' (reflecting plane normals perpendicular to specimen surface) and (b) at angle of tilt β (reflecting plane normals lying in a cone at angle β to specimen surface).

and diffracted beams) corresponds to the normals of the planes which are reflecting at any point during the 360° rotation.

Tilting about the axis B...B maintains the symmetrical Bragg–Brentano focusing geometry (unlike, as in Fig. 9.20(b), tilting about the other axis A...A) but clearly as β increases the incident and diffracted beams lie at an increasingly small 'glancing' angle to the specimen surface such that the practical limit of tilt is about 80° . Hence the planes which lie perpendicular to the specimen surface (normals lying in the specimen surface) cannot be recorded. This problem is overcome either by using a transmission method or by sectioning the specimen in another orientation.

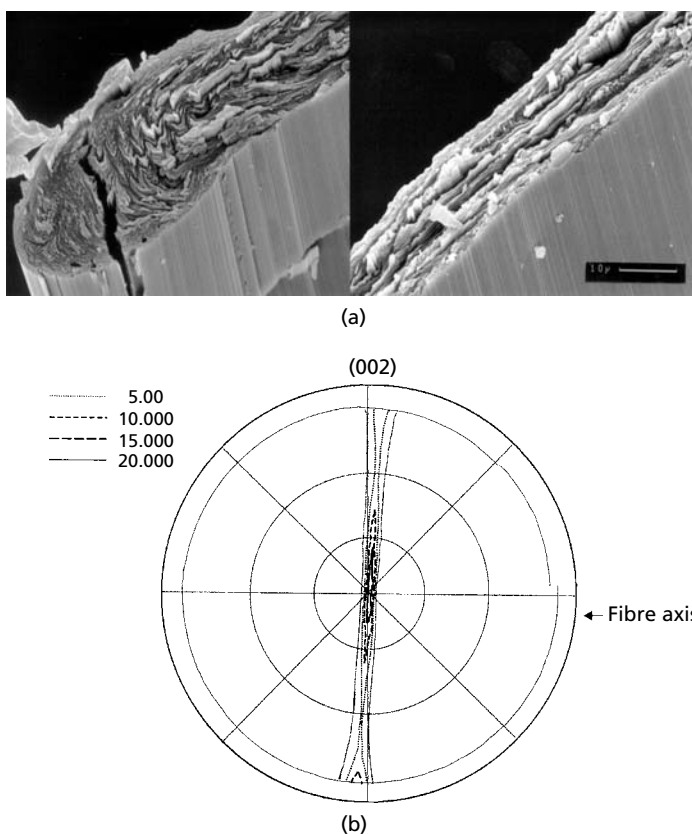


Fig. 10.13. (a) Graphitized carbon tape showing the orientations of the graphite layers at a fracture surface (left) at the edge of the tape and (right) in the centre (photograph by courtesy of Dr S. Lu and Professor B. Rand). (b) The corresponding pole figure, the plane of projection is the plane of the tape and the **fibre** or tape direction is as indicated. The pole figure extends to $\sim 80^\circ$ and the limit of the spiral is shown by the thin line. The intensity-contours are indicated in the legend.

In practice the mechanics of the texture goniometer are such that the specimen is tilted and rotated at the same time—say a 5° tilt for 360° rotation, such that the recorded intensity arises from planes lying in a spiral of 5° pitch. The data is then plotted in a stereographic projection—a pole figure (Section 12.5.3) and presented in terms of contours of intensity data. Finally, in order that the X-ray beam may sample as large an area as possible, the specimen is oscillated in its cradle, or shunted to and fro, by a mechanical device rather like the connecting-rod to the wheels in a steam engine. It is the one feature of the texture goniometer which students always notice first!

Figure 10.13(a) is a scanning electron micrograph of a graphitized carbon tape showing clearly the graphite layers lying parallel to the surface of the tape except at the edges where they ‘curl over’—but always lying parallel to the long direction of the tape. Figure 10.13(b) is the corresponding pole figure, the 2θ angle being set to record the

0002 graphite planes. They peak in the centre (the planes parallel to the surface of the tape) and also towards the transverse directions (the planes curled over at the edges). This is a nice example because the relationship between the pole figure and the micrograph can be visualized very easily. In most other materials the micrographs do not reveal the orientations of the reflecting planes at all and their orientations are only revealed in the pole figure.

10.5 X-ray diffraction of DNA: simulation by light diffraction

The 1952 X-ray photograph of deoxyribonucleic acid (DNA) is of such importance in the history of science that I have placed it, along with the 1912 X-ray photograph of zinc blende, at the very beginning of this book (p. xv). The caption indicates how some of the features of this pattern relate to the structure of DNA. We are, of course, unable to attempt a complete analysis of the positions and intensities of the diffraction spots from a structure of such complexity, but we can make some progress towards that goal by making use of the simple ideas about diffraction that we covered earlier in this book together with a simplified (two-dimensional) model of DNA itself.¹

Figure 10.14 shows a projection of a simplified DNA model showing schematically the two helical backbones of the phosphate groups (indicated by dots along the sine waves) and the equidistant planar bases (indicated by horizontal bars), $p = 3.4$ nm is the helical repeat distance; the two helices are separated by $3/8 p$ and the distance between the bases is $1/10 p$. The diameter of the helices is $0.6 p \approx 2.0$ nm.

We will now represent this structure in the simplest possible way—as a row of horizontal lines of length $0.6 p$ and separation p (Fig. 10.15(a)). The corresponding diffraction pattern (or optical transform) is shown in Fig. 10.16(a). It is produced in the same way as the patterns shown in Fig. 7.3 except that, in practice, the diffracting mask is made up not of one, but of many sets of such lines, irregularly spaced, so as to give sufficient diffracted light intensity. It is also made to such a scale that the distance p between the lines and the wavelength of laser light is in the same proportion to the actual helix repeat distance (3.4 nm) and typical X-ray wavelengths (~ 0.15 nm).

The vertical separation between the laterally-streaked spots is given by the simple diffraction grating equation (Section 7.4): $\sin \alpha_n = n\lambda/p$ and since $\lambda \ll p$, $\sin \alpha_n \approx \alpha_n$ and the spots are nearly equally spaced.

Now we will improve our model by inclining the lines at (approximately) the same angle as the ‘arms’ or the ‘zigs’ and ‘zags’ of the helices (Fig. 10.15(b)). The diffraction pattern from *one* of these again shows laterally-streaked spots with the *same* vertical

¹ The analysis which follows is largely based on the work of Prof. Amand Lucas and his colleagues of the University of Namur, Belgium, to whom I am very grateful. Their analysis entitled ‘Revealing the backbone structure of B-DNA from laser optical simulations of its X-ray diffraction diagram’ is published in the *Journal of Chemical Education* **76**, 378–83, 1999. It is also available from the authors as a videotape (together with a diffraction mask) entitled DNA—from light to life, and is also included in the Vega Science Film Series (Videotape VRS-7 ‘How X-rays cracked the structure of DNA’), available from the Vega Science Trust, University of Sussex, UK, BN1 3QJ and via the vega website; www.vega.org.uk.

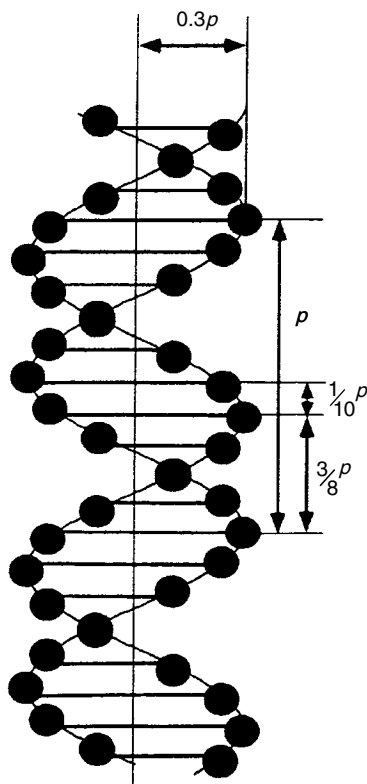


Fig. 10.14. A model of DNA showing schematically the two helical backbones of the phosphate groups (indicated by dots) and the equidistant planar bases (indicated by horizontal bars), $p = 3.4$ nm is the helical repeat distance, the two helices are separated by $3/8 p$ and the distance between the bases is $1/10 p$. The diameter of the helices is $0.6 p = 2.0$ nm (from A. A. Lucas, Ph Lambin, R. Mairesse and M. Mathot. *J. Chem. Educ.* **76**, 378, 1999).

separation but with maximum intensities in a direction perpendicular to the inclined lines (Fig. 10.16(b)). Clearly, for the arms of the helices inclined in the opposite sense the diffraction pattern will be mirror-related to that in Fig. 10.16(b) in a vertical line. Now we combine the two sets of lines to give a zig-zag pattern (Fig. 10.15(c)) which roughly represents the projection of a single helix; the resulting pattern (Fig. 10.16(c)) now shows (as expected) the two characteristic rows or arms of spots radiating out from the centre and the angle between them, which is the angle between the arms of the helices and can, together with the repeat distance p , be used to estimate the width of the helices, i.e. the diameter of the DNA structure. We may refine our model by representing the helix more properly as a sine wave but the resulting pattern is only changed in detail.²

² Examples of diffraction patterns of sine waves of various forms are given in the *Atlas of Optical Transforms* (see Chapter 7).

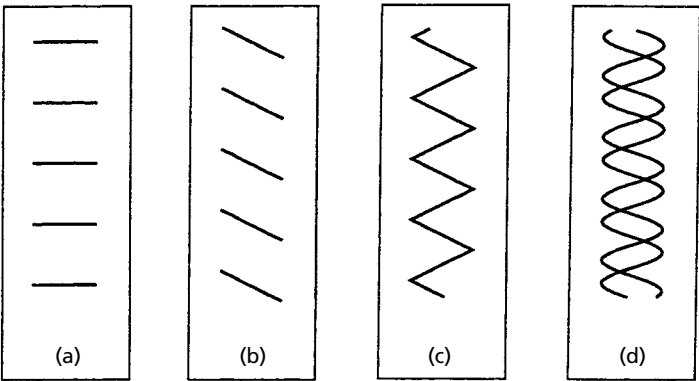


Fig. 10.15. Representational models of the DNA structure. (a) Lines spaced the helical repeat distance p and length $0.6 p$; (b) lines inclined at (approximately) the same angle as one of the arms of the helices; (c) a zig-zag pattern made by combining the two arms of the helices and roughly representing the single sine wave, in projection, of one of the helices; (d) two helices (represented as sine waves rather than zig-zags) separated by a distance $3/8 p$. (From A. A. Lucas *et al.* loc. cit.)

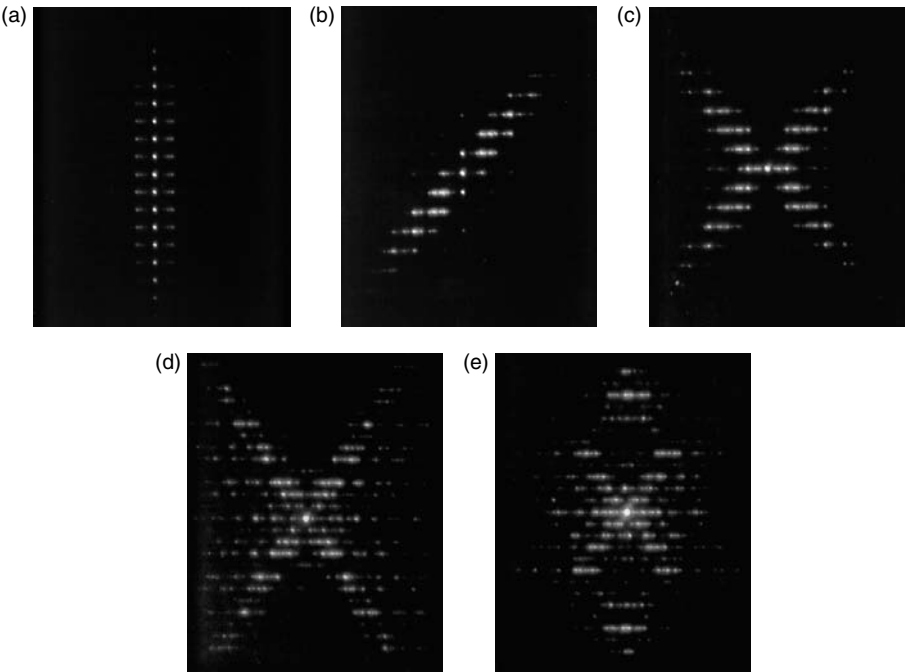


Fig. 10.16. The optical transforms or diffraction patterns corresponding to the models shown in Fig 10.15(a)–(d) and Fig 10.14: (a) from horizontal lines spacing p and length $0.6 p$; (b) from lines inclined as in one of the arms of the helices, the intensity maxima lie in a direction normal to the lines; (c) from two sets of lines (zig-zags) representing the sine-wave projection of a single helix; (d) from two sine waves separated by a distance $3/8 p$; and (e) from the double-helix model as represented in Fig. 10.14. (Photographs by courtesy of Prof. A. A. Lucas.)

Next, we combine two zig-zags or two sine waves separated by the distance $3/8 p$ (Fig. 10.15(d)). The diffraction pattern is similar, but with the crucial difference that there are gaps, or systematic absences, in the sequence of lines—the 4th (12th and 20th) lines are missing (Fig. 10.16(d)). We can very easily understand this by drawing a diffraction grating of slit separation p , working out the diffraction angles as in Section 7.4 and then considering the contributions to the diffracted intensities of a second set of slits separated by distance $3/8 p$. It is *precisely* the same procedure that we used to determine the diffracted amplitudes from a crystal with just two atoms per unit cell (Section 9.2 and Fig. 9.3(a)).

Figure 10.17(a) shows the geometry involved. Let f be the scattered amplitude from each slit and consider first the interference between the diffracted beams from the slits A---A---. Maxima occur when the path difference $x = n\lambda = p \sin \alpha_n \approx p\alpha_n$ and the amplitude per unit length p (or per unit cell) is f . Now consider slits B---B---. We only need consider the contribution of one such slit (i.e. in one cell), since what applies to one applies to all. The path difference between each A and B slit, $y = 3/8 x = 3/8 n\lambda$ and we can now construct the amplitude- or vector-phase diagrams for $n = 0, 1, 2, 3, 4 \dots$ The results, and corresponding intensities in terms of f^2 are shown in Fig. 10.17(b). The cyclic variations in intensities with zeros at $n = 4, 12, 20$, etc. are clear.

Figure 10.16(e) shows the diffraction pattern of the double helix with the phosphate groups and planar bases shown as in Fig. 10.14. Its similarity to well-defined X-ray diffraction patterns of DNA is remarkable, especially so since it was arrived at by such simple procedures.

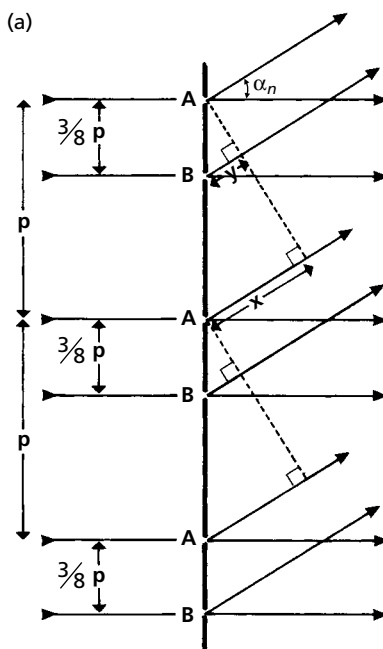


Fig. 10.17. (continued)

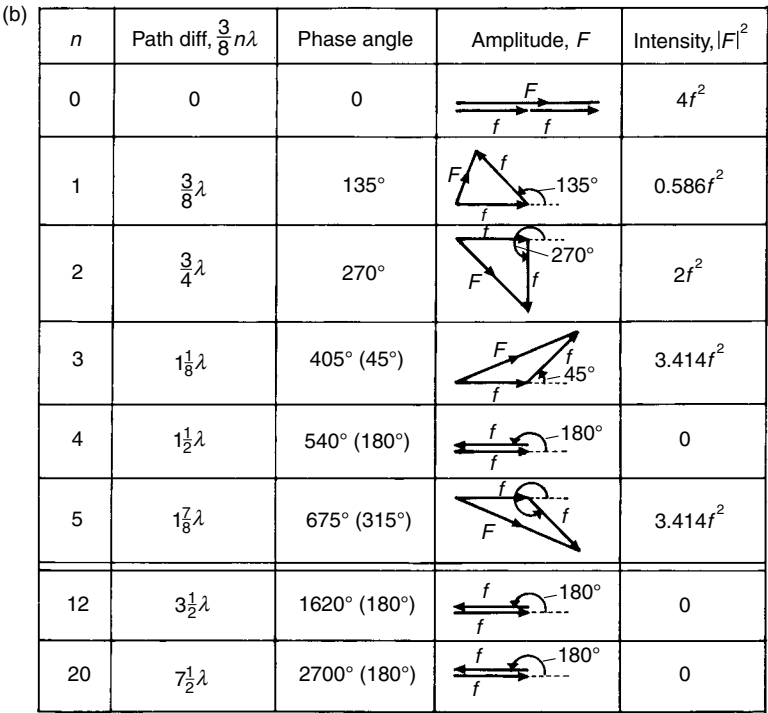


Fig. 10.17. (a) A diffraction grating of repeat distance p made up of two sets of slits A...A and B...B... separated by distance $3/8 p$. Maxima occur when the path difference $x = n\lambda = p \sin \alpha_n$. The amplitudes or intensities of the diffracted beams are modulated by interference between the waves diffracted at each pair of slits A and B. (b) The vector-phase diagram for values of $n = 0, 1, 2, 3, 4$, indicating zero intensity for $n = 4$ (and 12, 20, etc.).

However, there is a further problem to be solved. It was known (prior to 1952) that the sugar-phosphate groups of nucleic acids were *polar*; the sequence of phosphate groups along one direction is reversed in the opposite direction—in an analogous way as the sequence of Zn and S atoms along a $\langle 111 \rangle$ (polar) direction in zincblende (Section 4.7). How, therefore, are the two helices (Fig. 10.14) related; do the DNA backbones run in the same, or in opposite directions? Francis Crick showed that they in fact ran in *opposite* directions. The story is as follows³. As mentioned above, within living cells the DNA is surrounded by the high water content of the cell as in a B-DNA fibre.

³ Again, I am indebted to Professor Amand Lucas on whose paper, A-DNA and B-DNA: Comparing their Historical X-ray Fibre Diffraction Images, *Journal of Chemical Education* **85**, 737 (2008) I have largely based this brief account. Professor Lucas and his colleagues have also prepared (available on request) two slides; one consisting of nine optical masks for B-DNA and the other twelve optical masks consisting of the same nine masks for B-DNA plus two additional masks for A-DNA and one mask to disprove the co-oriented model of double-stranded DNA. The use of these masks, in demonstrating the relations between the structures and diffraction patterns of DNA, is explained in the paper.

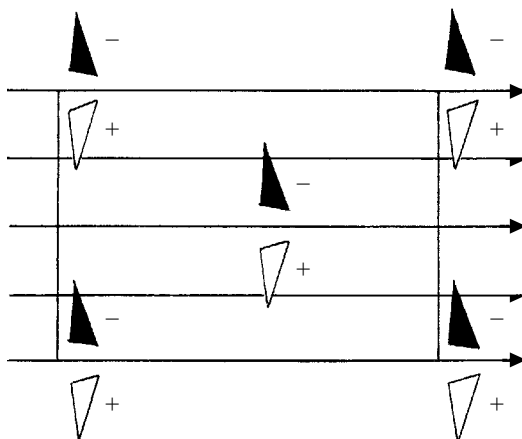


Fig. 10.18. A portion of a pattern based on space group $C2$. An (open) triangle at height + is turned over by the operation of a horizontal diad axis (double-headed arrows along the y -axis) to one at height— (black triangle). The pair of triangles is repeated by the C -face-centring lattice point. Screw diad axes (single-headed arrows) arise between the diad axes.

However, when the water content of the fibre is reduced, the strands shrink slightly, but more importantly, they pack together in nearly, but not quite, an hexagonal array (A-DNA). In order to achieve the most efficient packing, the helical ‘grooves’ of one strand locate into the ‘projections’ of the next—in just the same way that a bundle of ordinary screws (or threaded rods) pack together; the ‘tops’ of the threads of one screw fitting in to the ‘bottoms’ of the threads of the next. This results (in the case of A-DNA) in a C -face centred monoclinic, rather than an hexagonal unit cell. Gosling and Franklin determined the space group to be $C2$ (a ‘permissible’ space group—see Table 4.1): the only symmetry elements which the unit cell possesses are the diad (and screw diad) axes running perpendicular to the strands. Crick realized that, since the cell possessed diad symmetry, the DNA molecules must also possess diad symmetry and that the only way this could be achieved was for the polar backbones to run in opposite directions. This is readily seen in Fig. 10.18, the black and white triangles, related by diad symmetry, representing the opposite, or counter-oriented molecular chains. This deduction, arrived at by such simple crystallographic reasoning, was of crucial importance in guiding Watson and Crick in their model building of the structure of DNA.

10.6 The Rietveld method for structure refinement

Powder diffraction data has long been used to identify and characterize crystalline materials, particularly through the use and development of the *X-ray Powder Diffraction File* (Section 10.3.2). However, until the advent of the Rietveld method it was little used for the determination of all but the simplest of crystal structures largely on account of overlapping peaks and the consequent difficulty of accurately measuring integrated

intensities, this being the first step in determining the structure factors of the reflections which can be then used, as in single-crystal data, to solve or refine structures. This *peak profile fitting* procedure clearly only works for relatively simple structures which yield diffraction patterns with minimal peak overlap. One may say that the first such peak profile-fitting procedure was carried out (albeit with single crystals) by W. L. Bragg in 1913 who established, from relative peak intensities, the location of the S atoms in FeS₂ (Section 4.7, Fig. 4.16).

The Rietveld method, in contrast, does not measure, nor attempt to measure, integrated intensities as such but records the whole powder diffraction pattern: the measurement of intensity at each 2θ step constitutes a data point and the whole set of such data points is compared with those calculated. The calculation takes into account not only structural parameters (unit cell size, atom positions and occupancy factors) but also scale factors, background intensity coefficients and profile parameters describing peak shapes and widths. These parameters are then varied in a least-squares procedure until the calculated pattern best matches the observed pattern. The quantity R to be minimized is given by:

$$R = \sum_i w_i (Y_{io} - Y_{ic})^2$$

where Y_{io} is the observed intensity at step i , Y_{ic} is the calculated intensity and w_i is a weighting assigned to each step—the stronger the observed intensity (i.e. the smaller the counting error), the larger is w_i .

Such is the process of Rietveld refinement, but in order for it to be successful a large number of conditions, both theoretical and experimental, need to be met. First the ‘input’ structure (unit cell dimensions, atom positions, occupancy of atomic sites, etc.) needs to be a close approximation of that which is ultimately to be determined by the refinement—how close depends of course on the complexity of the structure. Then, as mentioned above, account must be taken of all the other factors which affect the observed intensities: fluorescence from the specimen, detector noise, thermal diffuse and incoherent scattering, scattering from the sample holder, beam collimator and slits and preferred orientation (Section 10.4). The Rietveld method is able to accommodate moderate amounts of preferred orientation, which may otherwise be difficult or impossible to eliminate (see point 3 below), by the inclusion of refining parameters which model the effect. In so doing preferred orientation may both be quantified and also removed as a confounding influence on the other variables.

The experimental conditions are no less demanding. They may be summarized as follows:

- (1) Accurate alignment of diffractometer (to ensure accurate 2θ values).
- (2) Correct positioning of specimen (both in the diffractometer and Debye–Scherrer arrangement).
- (3) Correct choice of Soller slits (which limit lateral beam divergence in the diffractometer) to avoid low-angle peak ‘tails’ in low- 2θ reflections.

- (4) Elimination (as far as possible) of preferred orientation effects; even the process of pressing a powder into a holder, or introducing it into a capillary tube, can give rise to preferred orientation.
- (5) Constant volume condition. In the Debye–Scherrer arrangement this is achieved automatically (except in the case of strongly-absorbing specimens). In the diffractometer it is achieved if the incident beam remains within the area of the specimen (a potential problem at low 2θ angles) and if the beam does not penetrate to the underlying holder (i.e. is regarded as ‘infinitely thick’). The constant volume condition arises because the area of specimen irradiated varies as $1/\sin\theta$ and the depth of operation varies as $\sin\theta$, hence the volume is independent of θ . Some diffractometers incorporate divergence slits which open out as 2θ increases—resulting in a gain in intensity, and hence reduced counting errors, at high 2θ angles but also an increase in irradiated volume which must be accounted for.
- (6) A powder particle size of $\sim 1\text{--}5\text{ }\mu\text{m}$; for sizes smaller than this line broadening needs to be taken into account and for sizes much larger than all crystallite orientations may not contribute equally to the intensity, a problem akin to preferred orientation.

All these considerations indicate the complexity of the computer programs required in a Rietveld refinement.

The technique was invented, and the first programs written, by Hugo M. Rietveld to refine structures recorded by neutron, rather than X-ray, diffraction. He records that when he first announced the techniques at the Seventh Congress of the IUCr in Moscow in 1966, ‘the response was slight, or rather non existent’.⁴ Since then it has become a major tool in structure determination, particularly since increasing computer power has led to its application in X-ray diffraction (where line profiles are more complex than those in neutron diffraction). Apart from being able to solve the structures of intrinsically-fine crystalline materials it has found particular application in, e.g., perovskites and superconductors in which the various structural forms arise from displacive transformations (see Section 1.11). It is also able to deal with multiphase specimens and to detect the presence of amorphous components.

The final word must come from Rietveld himself ‘... the method is not to be treated as a black box. One must be continually aware of the limitations, not only of this method, but in general of all least squares methods.’⁴

Exercises

- 10.1 Show, by simple geometrical reasoning, that in the X-ray monochromator (Fig. 10.2) the curved reflecting crystal planes should have a radius twice that of the focusing circle.
- 10.2 Show, by simple geometrical reasoning, that in the back-reflection X-ray powder photograph (Fig. 10.5), the reflections are most sharply focused when $R^2 = xy$ where R = the radius of the ring, x = the specimen–film distance and y = the distance of the (effective) source S behind the film.

⁴ H.M. Rietveld, ‘The early days, a retrospective view,’ in *The Rietveld Method* p. 39–42, ed. R.A. Young. IUCr/Oxford Science Publications, Oxford University Press, Oxford (1993).

- 10.3 Determine the d -spacings of the strongest low-angle reflections in the Debye–Scherrer film of quartz (Fig. 10.7) and check that they correspond (within the limits of experimental accuracy) with those indicated in Fig. 10.4 or listed in Fig. 10.8.
(Hint: the precise locations at which $2\theta = 0$ and 180° are *not* found from the centres of the holes in the film (which might be slightly displaced) but by determining the mid-points of the low-angle and high-angle reflections, respectively. The distance between these mid-points corresponds to an angle of 180° and the linear scale can be related to the angular scale and the 2θ values. Hence the d -spacings of the reflections can be found using Bragg’s law. (The film is taken using filtered $\text{CuK}\alpha$ radiation which includes both the $\text{K}\alpha_1$ and $\text{K}\alpha_2$ components. At low angles these are unresolved, $\lambda\text{CuK}\bar{\alpha} = 1.542 \text{ \AA}$, but at high angles they are resolved, $\lambda\text{CuK}\alpha_1 = 1.541 \text{ \AA}$, $\lambda\text{CuK}\alpha_2 = 1.544 \text{ \AA}$.)
- 10.4 Crystalline polypropene may be assigned a monoclinic unit cell with lattice parameters $a = 6.65 \text{ \AA}$, $b = 20.96 \text{ \AA}$, $c = 6.50 \text{ \AA}$ and $\beta = 99.3^\circ$ (see Section 4.8.2). The polymer chains are orientated along the c -axis. The table shows the d spacings, relative intensities and corresponding $hk0$, $hk1$ and $hk2$ indices (data from Natta, G., Corradini, P. and Cesari, M. (1956), *Rend. Acad. Naz. Lincei* **21**, 365).

$d/\text{\AA}$	$(hk0)$	Intensity [†]	$d/\text{\AA}$	$(hk1)$	Intensity [†]	$d/\text{\AA}$	$(hk2)$	Intensity [†]
6.21	110	s	4.14	111	m	3.06	022	mf
5.20	040	vs	4.06	131	s	3.05	112	mf
4.74	130	s	4.03	041	s	2.50	202	f
3.50	150	m				2.11	202	mf
3.46	060	m						
3.25	200	mf						
3.11	220	mf						

[†] Intensities: s = strong, v = very, m = medium, f = faint.

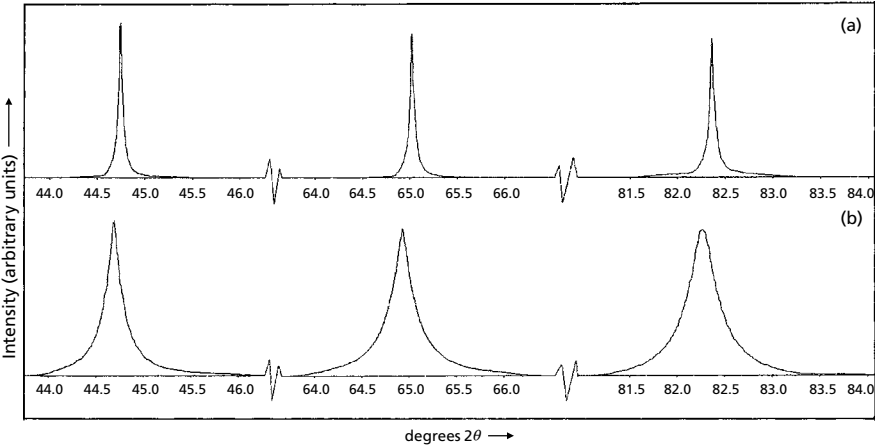


Fig. 10.19. Diffractometer charts ($\text{CuK}\alpha_1$ radiation, $\lambda = 1.541 \text{ \AA}$) showing the first three reflections for a steel specimen ($\alpha\text{-Fe}$, bcc) in (a) the annealed condition and (b) after heavy surface abrasion giving broadened and shifted X-ray diffraction peaks which arise from residual stresses on the micro- and macroscale and a reduction in crystallite size. (Data by courtesy of Mr D. G. Wright.)

Given that the X-ray photographs in Fig. 10.11 were taken with $\text{CuK}\alpha$ radiation ($\lambda = 1.542 \text{ \AA}$) and that the specimen-film distance (corrected for printing = 36 mm), index the reflections and show that in Fig. 10.11(b) the polymer chains are orientated along the tensile axis.

- 10.5 With reference to Fig. 10.19, determine β (expressed in radians) for each of the peaks from the half-height peak widths of the annealed (β_{Inst}) and abraded (β_{OBS}) specimens. On

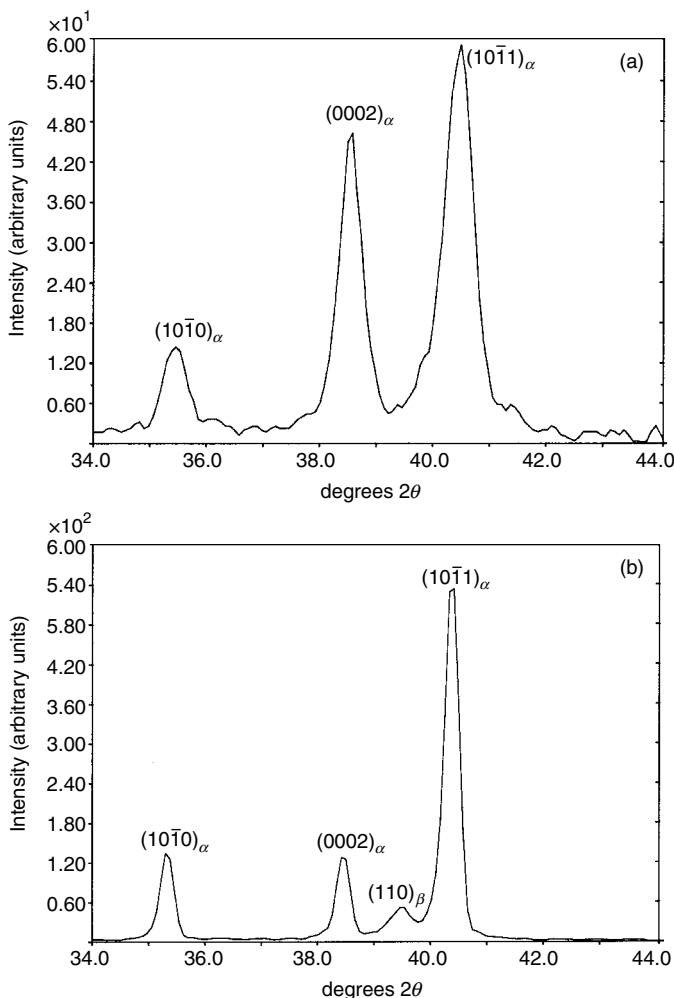


Fig. 10.20. Diffractometer charts ($\text{CuK}\alpha_1$ radiation, $\lambda = 1.541 \text{ \AA}$) showing the first three reflections for a titanium alloy (Ti-6% Al-4% V) powder specimen in (a) the mechanically milled condition and (b) following consolidation and heat treatment which gives rise to an increase in grain size and precipitation of the β phase (bcc) in the α phase (hexagonal) alloy matrix. (Data by courtesy of Mr D. G. Wright and Dr A. Brown.)

the assumption that the broadening arises solely from microstrain, determine the microstrain and hence residual stress given the Young modulus for iron $E = 207 \text{ GPa}$ (see Section 10.3.4).

- 10.6 With reference to Fig. 10.20, electron microscopy indicates that the grain size of the milled powder (a) is in the range 10–50 nm and that of the consolidated powder (b) is $5 \mu\text{m}$ and above. On the basis that the increased broadening in (a) arises solely as a result of the fine crystallite size, show that the X-ray data is consistent with the microscopical data.

Electron diffraction and its applications

11.1 Introduction

In Section 7.3 we discussed the wave- and particle-like characters of light which are linked by Planck's equation $E = hc/\lambda$; and also the wave-like character of moving particles which is linked to their mass and velocity by de Broglie's equation $\lambda = h/mv$. The common or 'linking factor' in both equations being Planck's constant $h = 6.63 \times 10^{-34}$ Js. In the case of neutrons (Section 9.7 and Exercise 9.3), it is the thermal conditions in the reactor which give rise to the neutron velocities, and hence mv values which, when substituted in de Broglie's equation, give wavelengths very similar to those for X-rays (Section 9.7). In the case of electrons in the transmission electron microscope the velocity and hence momentum mv of the electrons (m being relativistically corrected) depends on the accelerating voltage V and is determined by equating the potential energy eV (lost) where e is the charge on the electron with the kinetic energy $\frac{1}{2}mv^2$ (gained). The resulting λ values are very small (see Exercise 11.1), for example in a microscope operating at 300 kV, $\lambda = 1.97$ pm (0.0197 Å) and this of course is the basis of the high resolving power (or small limit of resolution) of the electron microscope in comparison with the light microscope as described in Section 7.5. Finally, it should be emphasized that de Broglie's equation applies to all moving particles, not just neutrons and electrons—including pieces of chalk thrown at inattentive students in lectures! However, as a simple calculation shows, the associated wavelengths are very small.

Whereas X-rays are scattered by the electrons in atoms, the incident electrons are primarily scattered by the protons in the nuclei, the scattering amplitude being proportional to Z . The electrons do, however, play a role insofar as they 'shield' the nuclei from the incident electrons by an amount proportional to f , the X-ray atomic scattering factor. Hence, the electron atomic scattering amplitude, f_e is proportional to $(Z - f)$. It is normally expressed as a scattering length (rather than a number like f) and the electron scattering intensities are thus expressed as areas or atomic scattering cross-sections.

The important consequence is that on average $f_e \propto \sqrt[3]{Z}$ (rather than $f \propto Z$ for X-rays) so that light elements scatter more strongly, in comparison to heavy elements, than X-rays. More important still the *amount* of scattering is much greater than for X-rays by a factor of 10^3 or 10^4 such that electron beams are attenuated much more rapidly. Hence in electron diffraction the dynamical interactions discussed in Section 9.1 are much more important than in X-ray diffraction and must always be taken into account in any attempt to relate observed electron beam intensities to atomic positions. There is, in electron

diffraction, no simple analogy to the structure factor equation for X-ray diffraction. (i.e. no simple way of relating atomic positions to diffracted beam intensities.)

The scattering described above is the dominant scattering process in the ‘thin foil’ ($\sim 1\text{ nm}$ – 100 nm) crystalline specimens used in transmission electron microscopy (TEM). It is described as an *elastic* scattering process because the scattered electrons lose no energy and therefore suffer no change in wavelength. It is the physical basis of the ‘spot’ electron diffraction patterns described in Sections 11.2 and 11.3.

There are in addition a number of *inelastic* scattering processes in which the incident electrons lose energy and therefore suffer a change in wavelength. They are of increasing importance in ‘thicker thin-foil’ specimens in TEM and the ‘bulk’ specimens used in scanning electron microscopy (SEM). We have already described some such inelastic scattering processes in Section 9.8; the large energy losses suffered by electrons as they enter the anode of an X-ray tube give rise to the continuous and characteristic X-radiation (Fig. 9.24). There are in addition several inelastic scattering processes which involve much smaller energy losses—thermal diffuse or phonon scattering, plasmon scattering, single valence electron scattering—the physics of which are described in the books on electron microscopy listed in Further Reading. The important point for us is that, since the energy losses are small, the wavelength changes are also small and such inelastically scattered electrons can then be elastically scattered, giving rise to Kikuchi patterns in the TEM and electron backscattered diffraction (EBSD) patterns in the SEM. The geometry of these diffraction patterns and their importance in the precise determination of crystal orientation are described in Section 11.5.

Finally, we should note, as with light microscopy, the importance of diffraction in relation to image formation and resolution. This is a very large topic which is introduced very briefly in Section 11.6.

11.2 The Ewald reflecting sphere construction for electron diffraction

Since electron wavelengths are *very much* smaller than the lattice parameters of crystals, which are normally in the region of 0.3 nm upwards, the diameter of the reflecting sphere is *very large* in comparison with the size of the unit cell of the reciprocal lattice. Referring to the reciprocal lattice sections in Figs 8.6 and 9.14(a) and (b) for example, for the case of electron diffraction, the centre of the reflecting sphere would be situated along the direction of the incident beam at a point far to the left of the origin of the reciprocal lattice, well beyond the left-hand edge of the paper.

The situation for a simple cubic crystal (as for Fig. 9.14(a)) is illustrated in Fig. 11.1, which shows again that part of the reciprocal lattice section perpendicular to the \mathbf{b}^* reciprocal lattice vector or y -axis (out of the plane of the paper) which lies close to the surface of the reflecting sphere, only part of which near the origin can be shown since its radius is so large. The incident electron beam is directed along the \mathbf{a}^* reciprocal lattice vector or x -axis and the centre of the reflecting sphere is far to the left of the diagram.

Close to the origin, 000 , the curvature of the sphere is so small that it approximates to a plane perpendicular to the direction of the electron beam and hence passes (in this section) very close to the 001 , 002 , 003 and $00\bar{1}$, $00\bar{2}$, $00\bar{3}$, reciprocal lattice points.

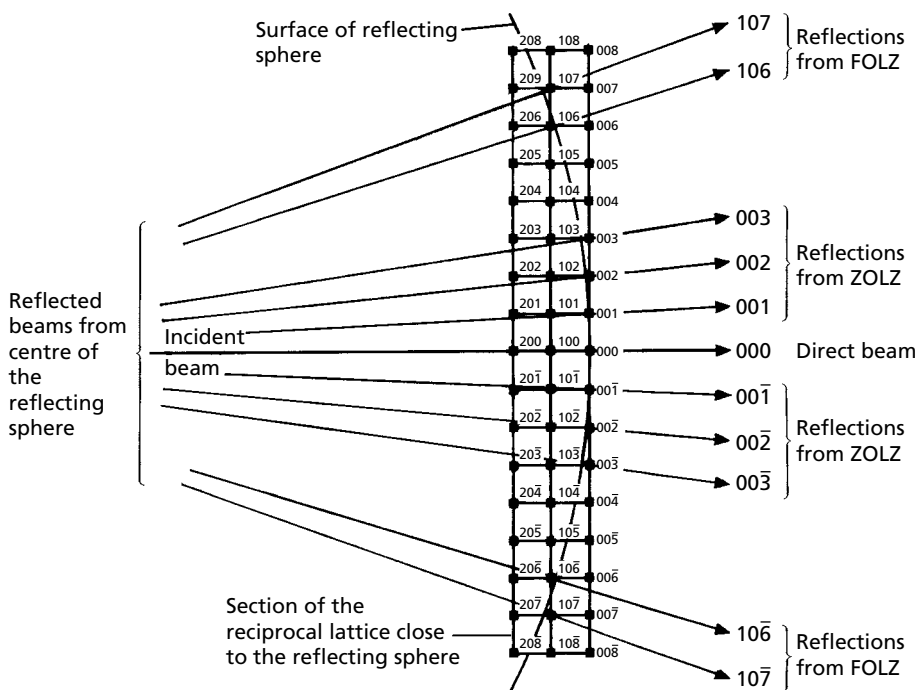


Fig. 11.1. The Ewald reflecting sphere construction for a simple cubic crystal in which the electron beam is incident along the \mathbf{a}^* reciprocal lattice vector (x -axis). The \mathbf{b}^* reciprocal lattice vector (y -axis) is perpendicular to the plane of the page. A section of the sphere (centre beyond the left-hand edge of the page) and the reflected beams passing at small angles from the centre of the sphere through the reciprocal lattice points in ZOLZ (giving spots close to the direct beam) and FOLZ (giving spots further away from the direct beam) are indicated.

Now in order for Bragg's law to be satisfied exactly, a reciprocal lattice point must intersect the Ewald reflecting sphere. However, since reciprocal lattice points are broadened into nodes (Section 9.3) they may be extended sufficiently to intersect the sphere and hence give rise to diffracted beams. This situation also arises in X-ray diffraction but to a lesser extent than in electron diffraction (a) because the reciprocal lattice points of the thin foil crystal sections used in electron microscopy are extended perpendicular to the foil surface and are therefore approximately parallel to the electron beam and (b) because thin foils are often slightly bent or 'buckled' such that the orientation of the electron beam varies slightly over the surface of the foil—i.e. it is never incident precisely along one crystallographic direction as indicated in Fig. 11.1.

Hence (referring again to Fig. 11.1), the reciprocal lattice points 001 , 002 , 003 , $00\bar{1}$, $00\bar{2}$, $00\bar{3}$ which lie in a reciprocal lattice row perpendicular to the electron beam direction all give rise to reflected beams, which are directed from the centre of the sphere (to the far left of the page) as indicated. Similar considerations apply to the reciprocal lattice row in the 'next layer above the page', i.e. the row through 010 (above 000), 011 , 012 ,

013, etc. and also the next layer below, i.e. through $0\bar{1}0$ (below 000), $0\bar{1}1$, $0\bar{1}2$, $0\bar{1}3$, etc. All of these reciprocal lattice points lie in the $(0kl)$ plane or section of the reciprocal lattice which is perpendicular to the electron beam direction. In summary, therefore, the reciprocal lattice points close to the origin, in the $(0kl)$ reciprocal lattice section perpendicular to the electron beam direction, give rise to reflected beams.

Since the diffraction angles are small (Fig. 11.1), the pattern of spots on the screen perpendicular to the beam corresponds to the pattern of reciprocal lattice points. Figure 11.2 shows this pattern of spots from the $(0kl)$ reciprocal lattice section grouped around the direct beam. For simplicity and clarity, only those reflected beams of type $00l$ (in the section perpendicular to the y -axis, Fig. 11.1) are indexed.

These diffraction spots are said to belong to the zero order Laue zone (ZOLZ for short) since they all arise from reciprocal lattice points in a section through the origin or, equivalently, they all arise from planes in a zone—the zone axis being parallel (or nearly parallel) to the electron beam direction.

The pattern of electron diffraction spots (for a particular incident beam direction) in the zero order Laue zone is identical to that in the zero level X-ray precession photograph (when the crystal is precessed by the appropriate angle about the same incident beam direction). This is seen by comparing Fig. 9.18(c) with Fig. 11.2. The far simpler set-up (a stationary crystal) in electron diffraction ‘works’ because of the ‘flatter’ (large

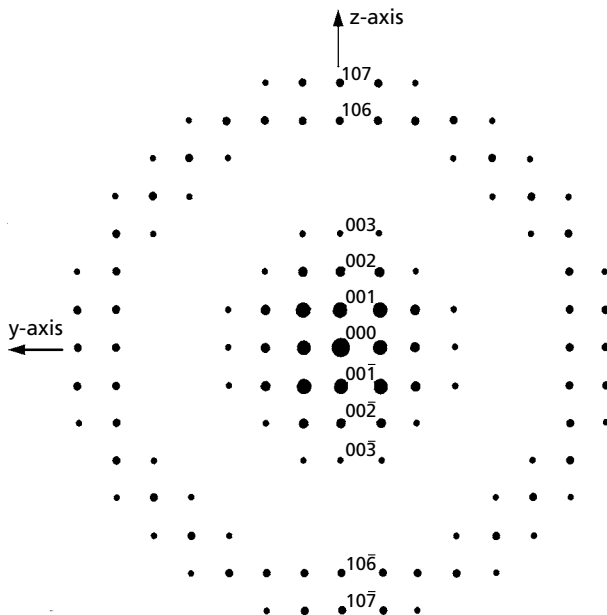


Fig. 11.2. The diffraction pattern on a screen perpendicular to the electron beam direction. The $0kl$ ZOLZ spots are grouped around the direct beam (centre spot) and the $1kl$ FOLZ spots are grouped roughly in a ring outside. Only the $h0l$ spots in the section perpendicular to the y -axis (Fig. 11.1) are indexed (compare with Fig. 9.18(c)).

diameter) Ewald reflecting sphere, the extension of the reciprocal lattice nodes and the slight buckling of the thin foil specimens—all of which serve to provide the requisite diffraction conditions without the necessity of precessing the specimen over a very much smaller angular range.

Referring again to Fig. 11.1, as we proceed along the surface of the reflecting sphere away from the origin, we begin to intersect the next row of reciprocal lattice points which does not pass through the origin. The reciprocal lattice points in this row which lie close to the sphere, i.e. 106 , 107 , $10\bar{6}$ and $10\bar{7}$ (and in the corresponding rows above and below the plane of the diagram, all of which lie in the $(1kl)$ section of the reciprocal lattice) will also give rise to diffraction spots as indicated. These spots, which lie outside those from the zero order Laue zone away from the centre of the pattern (Fig. 11.2) are said to belong to the first order Laue zone (FOLZ for short). Continuing outwards towards the edge of Fig. 11.1 we come to reciprocal lattice points in the second order Laue zone (SOLZ for short). These are just the first two in a series of higher order Laue zones (HOLZ for short).

11.3 The analysis of electron diffraction patterns

The analysis of electron diffraction patterns is essentially a process of identifying the reciprocal lattice sections which give rise to them. Several computer programs are now available (see Appendix 1) which generate reciprocal lattice sections, given as input data the lattice parameters, type of unit cell (and in some cases the space group and atomic positions) and the electron beam (zone axis) direction. Several examples showing the ZOLZ only are given in Fig. 11.3. Care must be exercised in using such data because a number of different electron diffraction patterns from different types of high-symmetry crystals have identical symmetry and only differ in scale. For example the $\langle 111 \rangle_{\text{fcc}}$ and $[0001]_{\text{hcp}}$ patterns shown in Figs 11.3(b) and (d) both consist of hexagonal patterns of points.

The first step in the analysis of electron diffraction patterns is measurement of the d -spacings. This is an easy matter. Figure 11.4 shows a set of reflecting planes at the Bragg angle θ (much exaggerated) to the electron beam. The diffracted beam, at angle $\theta + \theta = 2\theta$, to the direct beam, falls on the screen at a distance R from the centre spot. Figure 11.4 does not represent the *actual* ray paths in the electron microscope, which are of course determined and controlled by the lens settings: hence L , the camera length, is not the *actual* distance between the specimen and screen, but is a ‘projected’ distance which varies with the lens settings.

From Fig. 11.4, $\tan 2\theta = R/L$. Since θ is small, $\tan 2\theta \approx 2\theta$ (2θ of course being measured in radians). Similarly for Bragg’s law, $\sin \theta \approx \theta$ hence $\lambda \approx 2d_{hkl}\theta$. Eliminating θ from these equations we have:

$$d_{hkl} = \lambda L/R$$

where λL is known as the camera constant and which, like L , varies with lens settings in the microscope. The units of λL are best expressed in terms of the product of R , the distance measured on the screen (e.g. mm) and d_{hkl} (e.g. nm, Å or pm). Although the

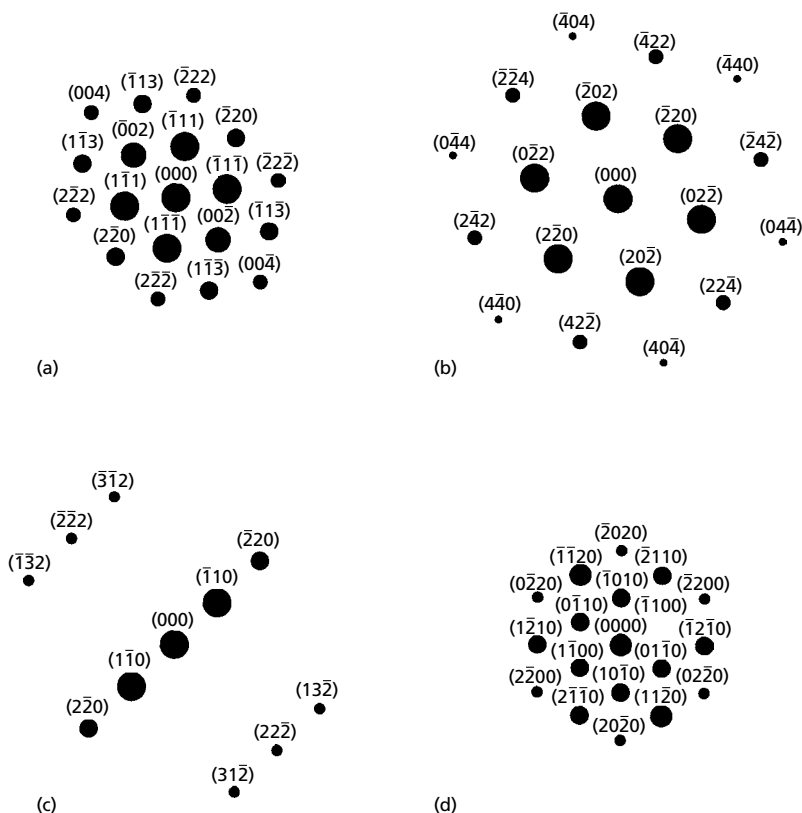


Fig. 11.3. Examples of the computer-generated diffraction patterns, drawn to the same scale ($\lambda L = 16.1 \text{ \AA mm}$). (a) Aluminium (fcc), zone axis = $\langle 110 \rangle$; (b) aluminium (fcc), zone axis = $\langle 111 \rangle$; (c) iron (bcc), zone axis = $\langle 112 \rangle$; (d) titanium (hcp), zone axis = $[0001]$.

ångström (\AA) is not an SI (Système International) unit, it is coherent with the SI system ($1 \text{ \AA} = 10^{-10} \text{ m}$) and still remains in widespread use in crystallography (a) because it is roughly equal to atomic diameters and (b) because X -ray d_{hkl} -spacing data in the *Powder Diffraction File* (see Section 10.3) is recorded in ångströms.

The accuracy with which the d_{hkl} -spacings can be measured is very limited because of the size or ‘diffuseness’ of the diffraction spots. Moreover the camera constant, λL , will only be known to a high degree of accuracy if a ‘standard’ specimen is used which gives a diffraction pattern with spots of accurately known d_{hkl} -spacings. Otherwise the small variations in lens settings from specimen to specimen and from day-to-day will limit the accuracy of λL values at best to three significant figures. Hence, as pointed out above, patterns which have identical symmetry but which only differ slightly in scale with respect to the d_{hkl} -spacings of the diffraction spots are not readily distinguished.

The spots may then be indexed by reference to tables of data such as are contained in the *Powder Diffraction File*, which show the (Laue) indices, hkl , corresponding to

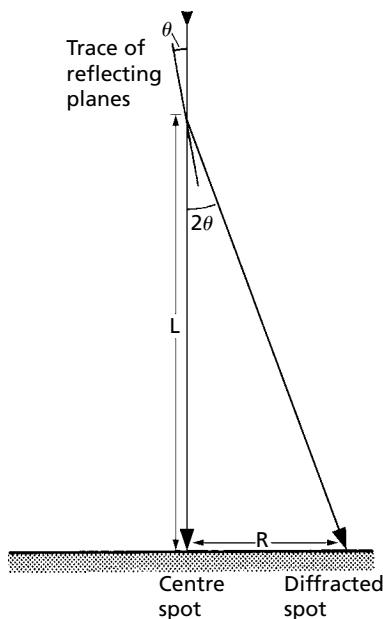


Fig. 11.4. Idealized representation of the direct and diffracted ray paths in the electron microscope between the specimen and the screen. L is the camera length and R is the distance between the centre spot (direct beam) and the diffracted spot.

the measured d_{hkl} -spacings. In doing so, a further step is required: the indexing must be such that the addition rule (Section 6.5.2) is satisfied. A given set or family of planes $\{hkl\}$ (which are invariably listed in data files simply as hkl —no brackets) will consist of a number of variants of identical d_{hkl} -spacings. For example, in the cubic system (see Section 5.4), there are six variants of the ‘plane of the form’ $\{100\}$, all of which have identical d_{hkl} -spacings. The procedure consists of *choosing* the appropriate variants such that the addition rule is satisfied. Consider, for example, Fig. 11.3(a). The four spots of identical d_{hkl} -spacings closest to the centre spot are all reflections from planes of the form $\{111\}$. The particular indices have been chosen such that the indices of the remaining spots are determined correctly. For example, $\mathbf{d}_{1\bar{1}1}^* + \mathbf{d}_{11\bar{1}}^* = \mathbf{d}_{002}^*$ and the zone axis, $[110]$, is found by cross-multiplication of any pair of these indices (see Sections 5.6.2 and 6.5.7), the ‘choice’ only needs to be made once, and having been made, all the other spots in the pattern can be indexed consistently by repeated application of the addition rule; again, with reference to Fig. 11.3(a), $\mathbf{d}_{1\bar{1}1}^* + \mathbf{d}_{002}^* = \mathbf{d}_{1\bar{1}3}^*$ and so on. The ‘choice’ is of course arbitrary: the number of different choices which can be made, all leading to a self-consistently indexed diffraction pattern, depends on the number of equivalent variants of the zone axis. In a cubic crystal there are twelve variants of the $\langle 110 \rangle$ direction, hence there are twelve ways in which a pattern like that of Fig. 11.3(a) can be indexed.

The availability of computer-generated diffraction patterns has greatly facilitated the indexing and verification of electron diffraction pattern analysis. However, it must

be said that many ‘useful’ diffraction patterns—i.e. those which may be of potential scientific interest, which have been obtained under conditions of experimental difficulty and which may consist of many spots from several crystals of varying degrees of visibility on the film—still require for their solution careful observation and measurement and an awareness of the possible occurrence of additional complicating factors such as double diffraction (see Appendix 6). Those books on electron diffraction techniques in Further reading provide a more detailed and thorough coverage of these topics.

11.4 Applications of electron diffraction

11.4.1 Determining orientation relationships between crystals

One of the greatest advantages of electron diffraction is the facility in the electron microscope of being able to select a particular area of the specimen and to vary the diameter of the beam to obtain diffraction patterns simultaneously from those phases of interest. Moreover, the reflections from the phases present may be distinguished by the technique of dark field imaging. Each electron diffraction pattern may be indexed according to the procedures described in Section 11.3. The orientation relationship(s) may then be given in terms of parallelisms between zone axes and planes.

Figure 11.5(a) shows an electron diffraction pattern of α -iron $a = 2.866 \text{ \AA}$ (bcc—strong reflections) in which are precipitated (or exsolved) particles of Fe_2TiSi , $a = 5.732 \text{ \AA}$ (fcc—weak reflections) in a single crystallographic orientation. It is obvious, simply by inspection or *looking*, that there is a clearly defined orientation relationship between the iron matrix and the precipitate and, because of the coincidence of many of the

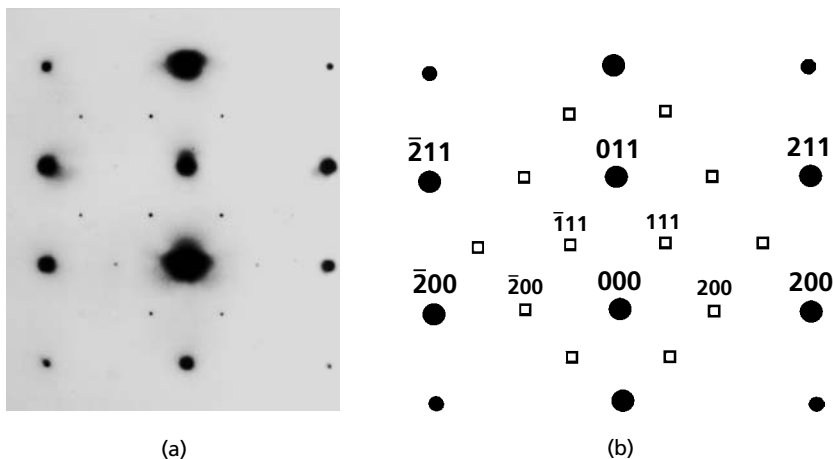


Fig. 11.5. (a) An electron diffraction pattern of α -iron (bcc, $a = 2.866 \text{ \AA}$: strong reflections) and Fe_2TiSi (fcc, $a = 5.732 \text{ \AA}$: weak reflections) in a single crystallographic orientation. The camera constant $\lambda L = 31.5 \text{ \AA mm}$. (b) The patterns indexed according to one (arbitrary) variant of the ‘cube–cube’ orientation relationship: $(200)_{\text{Fe}_2\text{TiSi}} \parallel (200)_{\alpha\text{-Fe}}$; $[0\bar{1}1]_{\text{Fe}_2\text{TiSi}} \parallel [0\bar{1}1]_{\alpha\text{-Fe}}$. (Photograph by courtesy of Dr. D. H. Jack.)

reflections, that the lattice parameters are related in some rational ratio. The d -spacings of the reflections may be measured (Section 11.3) and, given the lattice parameters and the conditions for reflection for the cubic F (fcc) and cubic I (bcc) lattices (Table A6.2), the reflections may be indexed. Figure 11.5(b) shows the patterns indexed according to one (arbitrary) variant of the orientation relationship. Note that the 200 Fe_2TiSi spot is *half* the distance (and therefore *twice* the d -spacing) of the 200 α -Fe spot from the centre; these planes are therefore parallel and the lattice parameter of Fe_2TiSi is twice that of α -Fe. Similarly, the 022 Fe_2TiSi reflection (by vector addition of $\bar{1}11$ and 111) is coincident with 011 α -Ti. The zone axes, obtained by cross-multiplication (Section 11.3), are both $[0\bar{1}1]$.¹ The orientation relationship may be specified by quoting the parallelisms:

$$(200)_{\text{Fe}_2\text{TiSi}} \parallel (200)_{\alpha\text{-Fe}}$$

$$[0\bar{1}1]_{\text{Fe}_2\text{TiSi}} \parallel [0\bar{1}1]_{\alpha\text{-Fe}}$$

This is known as the ‘cube-cube’ orientation relationship because it is equivalent to the statement that the x , y , z axes of both crystals are mutually parallel.

Other, more complicated, orientation relationships may be determined by the same simple approach, but to go from the parallelisms between the planes and zone axes observed for the particular patterns to the establishment of possible parallelisms between planes not observed in the patterns (i.e. those that are not (nearly) parallel to the electron beam direction), requires a knowledge of the stereographic projection (see Chapter 12).

11.4.2 Identification of polycrystalline materials

The *Powder Diffraction File* may be used to identify polycrystalline specimens from their electron diffraction patterns. However, its use is much more limited owing to the fact that the d -spacings of the diffraction rings can be measured to a much lower level of accuracy and only qualitative estimates can be made of their relative intensities. Hence the use of search procedures, as described in Section 10.3.2, is uncommon. Usually we have a fair idea as to what the specimen might be and make direct comparisons between the experimental data and that of ‘possible’ patterns in the File. Exercise 11.4 gives an example of this in the case of a single-crystal electron diffraction pattern.

Figure 11.6 gives an example of an electron diffraction ‘ring’ pattern from a fine-grained polycrystalline thin foil specimen of aluminium. It is, in effect, the superposition of many single-crystal patterns. Notice the variations in intensity and the sequence of spacings of the rings. Aluminium can immediately be recognized as having the fcc structure since the rings occur in the characteristic sequence ‘two-together’, ‘one-on-its-own’, ‘two-together’, etc. (see Note 3, Table A6.2). Hence the rings may simply be indexed ‘by inspection’, i.e.

$$111,200, \quad 220, \quad 311,222, \quad 400, \quad 331,420.$$

¹ The *order* of cross-multiplication is important; one should read *anticlockwise*. E.g. for the α -iron diffraction spots write down (211) as the first line in the memogram and then (011) as the second line. This gives (for the usual right-handed axial system) the zone axis direction *upwards* (i.e. anti-parallel to the electron beam which is much easier to deal with when plotting the data on a stereographic projection (Chapter 12)).

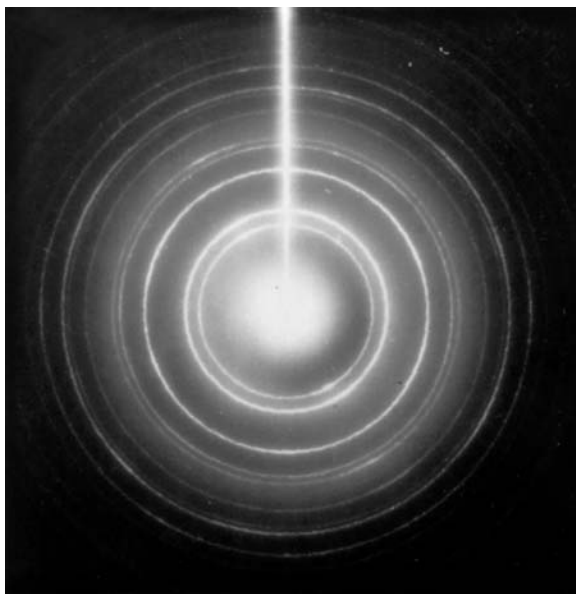


Fig. 11.6. An electron diffraction pattern of polycrystalline aluminium, showing varying intensities of the diffraction rings and the sequence of ring spacings characteristic of the fcc structure.

11.4.3 Identification of quasiperiodic crystals

In Section 4.8 we showed how quasiperiodic crystals or crystalloids could nucleate and grow without any long range translational symmetry and that their existence was first recognised from the ten-fold symmetry of their electron diffraction patterns. Figure 11.7 shows the first observed such electron diffraction pattern of a nodule-like phase in a rapidly quenched Al-25 wt.% Mn alloy. Such a ten-fold pattern does not however constitute sufficient evidence for quasiperiodicity since multiply-twinned crystals (consisting of 10 twin-related segments radiating out from a central point rather like the slices of a cake) can also give rise to such ten-fold patterns. Nor is this a remote possibility and some alloy systems may exhibit quasiperiodic crystals or multiply-twinned crystals (the microcrystalline state) depending upon heat treatment. For example the $\text{Al}_{65}\text{Cu}_{20}\text{Fe}_{15}$ alloy gives twinned microcrystals when slowly cooled from the melt which on heating transform to quasiperiodic crystals.²

There are two ways in which these quasiperiodic and multiply-twinned states may be distinguished. First the evidence from microscopy: twin boundaries and the changes in orientation of lattice fringes at twin boundaries may be observed by high resolution electron microscopy—which constitutes firm evidence for the microcrystalline phase. Second, the fine detail of the spots in the electron diffraction patterns: the segments or ‘slices of cake’ in multiply-twinned crystals are not *perfectly* related by five-fold

² *Quasicrystals: A Primer* by C. Janot, Clarendon Press, Oxford, 1992.

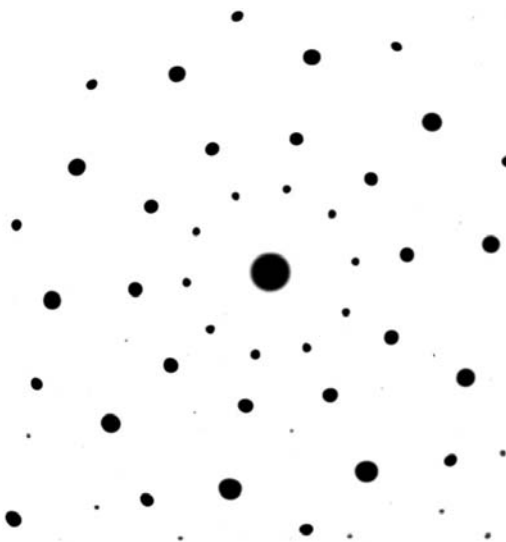


Fig. 11.7. Electron diffraction pattern of the first observed icosahedral particle in an Al-25 wt.% Mn alloy, April 1982. (Photograph by courtesy of Prof. D. Shechtman.)

symmetry; there is some misalignment which results in spots of a triangular ‘shape’ (i.e. made up of a group of little sub-spots) rather than the clear and distinct single spots of Fig. 11.7. Other, more complicated five-fold patterns of spots may also arise. It is not surprising that the first reported occurrences of quasiperiodic crystals were greeted with considerable scepticism throughout much of the crystallographic community.

11.5 Kikuchi and electron backscattered diffraction (EBSD) patterns

11.5.1 Kikuchi patterns in the TEM

We first consider the trajectories, or paths, of the inelastically scattered electrons within the specimen (Section 11.1). These occur over a range of angles, the scattering being most intense at small angles to the incident beam and decreasing at larger angles, giving in effect a ‘pear-shaped’ distribution of intensity as shown schematically in the upper part of Fig. 11.8. This distribution of intensity around the incident electron beam (the centre spot) is shown in the lower part of Fig. 11.8. Such a distribution is only observed in practice in ‘thicker’ specimens (in the range 200 nm upwards) and in which the amount of inelastic scattering is significant. It is almost entirely absent in the thin foil specimens from which the electron diffraction patterns shown in Figs 11.5(a), 11.17, 11.18 and 11.19 were obtained.

Now we describe the elastic scattering, or Bragg reflection, of the weakly inelastically scattered electrons that have suffered negligible changes in wavelength. Consider a specimen in which a set of hkl planes is at an angle to the incident beam slightly smaller

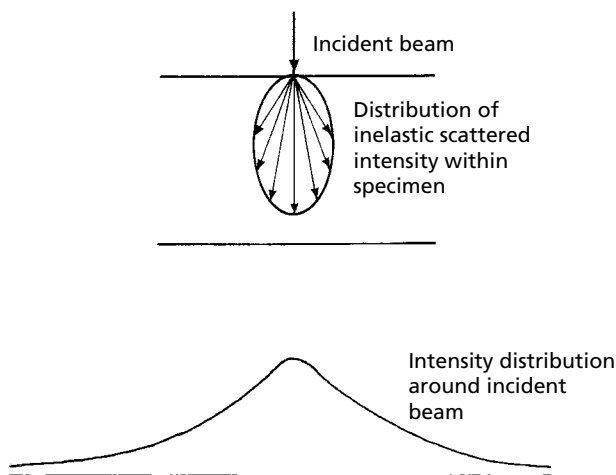


Fig. 11.8. The distribution of inelastic scattered intensity within a specimen and (below) the distribution intensity around the incident (unscattered) electron beam.

than the Bragg angle (Fig. 11.9(a)). No reflection of the incident beam, or given the extension of the reciprocal lattice point (Section 11.2), only a weak reflection of the incident beam occurs. However, those inelastically scattered beams which are incident to the planes at the Bragg angle are reflected. Figure 11.9(a) shows two such beams, AB and AC, AB being more intense than AC since the inelastic scattering angle is smaller. Beam AB is reflected to D (solid line), giving an increase in intensity; at the same time it is attenuated in the direction to E (dotted line) giving a reduction in intensity. A similar reflection (solid line) and attenuation (dotted line) occurs for AC. However, because beam AC is weaker the overall effect will still be an increase in intensity at D and a decrease in intensity at E. Now these peaks are not spots but are sections through cones of intensity which intersect the reflecting sphere to give nearly straight lines running parallel to the reflecting planes, i.e. perpendicular to the plane of the paper. These—the ‘light’ and ‘dark’ Kikuchi lines—are shown in the plane of the diffraction pattern in Fig. 11.9(b). Also shown is the (weak) hkl diffraction spot and the *downwards* projected trace of the planes which lies half-way in between the Kikuchi lines (dashed line). The angle between the Kikuchi lines is 2θ and thus they have the same separation R as the distance between the centre spot and hkl diffraction spot.

From Fig. 11.9(a) two angles are of interest; ϕ , the deviation of the planes from the exact Bragg angle, and ρ , the deviation of the planes from exact parallelism with the incident beam. These angles may be determined by measuring the distance a_K (from the dark Kikuchi line to the centre spot) and a_t (from the trace of the planes and the centre spot). Given the camera length L (Fig. 11.4), then $\phi = a_K/L$ and $\rho = a_t/L$.

The geometry may also be represented in terms of the Ewald reflecting sphere construction, Fig. 11.10. \mathbf{k} and \mathbf{k}_0 are the vectors representing the directions of the diffracted

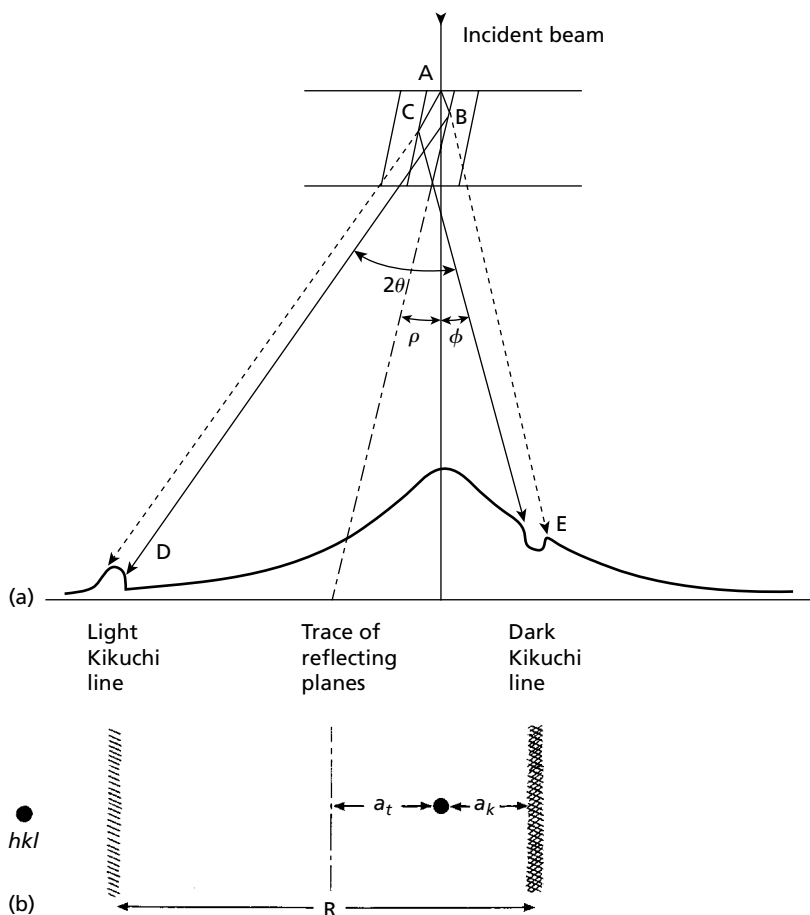


Fig. 11.9. (a) A crystal with a set of planes at an angle to the incident beam slightly smaller than the Bragg angle. AB and AC show two inelastically scattered beams (see Fig. 11.8) which are incident to the planes at the Bragg angle and which are partly reflected (solid lines) and partly attenuated (dotted lines) resulting in light (electron excess) and dark (electron deficient) Kikuchi lines, shown in plan in (b) together with the diffraction and centre spots and the projected trace of the reflecting planes.

and direct beams and $\mathbf{g}_{hkl} (\equiv \mathbf{d}_{hkl}^*)$ is the reciprocal lattice vector for the reflecting planes (see footnote, page 198, Section 8.3). The hkl reciprocal lattice point lies outside the sphere and the vector \mathbf{s} (closely parallel to \mathbf{k} and \mathbf{k}_0) represents the deviation of \mathbf{g}_{hkl} from the exact Bragg condition, the modulus of which is given by $|\mathbf{s}| = \phi |\mathbf{g}_{hkl}|$. Now we see the value of Kikuchi lines in establishing the precise orientation of the reflecting planes: as we (say) rotate the crystal clockwise, the pair of Kikuchi lines move to the left and at the exact Bragg angle ($\phi = 0$), the dark Kikuchi line passes through the centre spot and the bright Kikuchi line passes through the diffraction spot. Similarly, when the crystal is

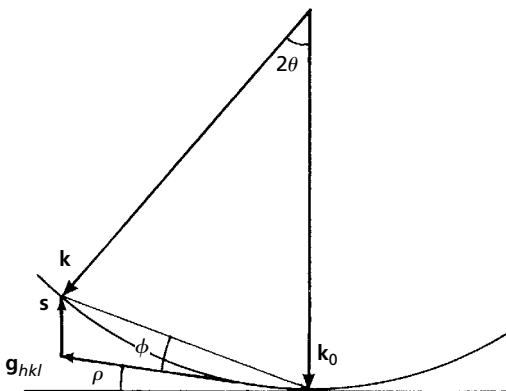


Fig. 11.10. The Ewald reflecting sphere construction for a set of hkl planes at an angle to the incident beam (vector \mathbf{k}_0) slightly smaller than the Bragg angle. The reciprocal lattice vector \mathbf{g}_{hkl} lies outside the sphere and the vector \mathbf{s} represents the deviation from the exact Bragg condition. ϕ is the deviation angle of the planes from the exact Bragg angle and ρ the deviation of the planes from exact parallelism with the incident beam.

rotated such that the planes are exactly parallel to the incident beam, the Kikuchi lines will be at equal distances each side of the centre spot.³

In practice we may see many Kikuchi lines—as many pairs as there are diffraction spots (Fig. 11.11). However, just two pairs of lines, and two diffraction spots, are sufficient to determine the orientation of the crystal with respect to the incident electron beam direction. Figure 11.12 shows a pattern with two spots, $h_1k_1l_1$ and $h_2k_2l_2$ and their associated Kikuchi lines; half way in between which are drawn the downwards projected traces of the planes (dashed lines). The downwards direction of the zone axis $[\bar{u}\bar{v}\bar{w}]$ lies at the intersection of the traces as shown; the *upwards* direction $[uvw]$ (i.e. anti-parallel to the electron beam) lies on the opposite side of the centre spot and is found by cross-multiplication of the indices as described in the footnote on p. 281. The angle η between $[uvw]$ and the centre spot, 000, is simply found by measuring the distance P , again using the relationship $\eta = P/L$.

The pattern of Kikuchi lines also reflects the symmetry of planes in a crystal and ‘maps’ may be created showing the patterns of lines for different crystal orientations. Figure 11.13 shows one such map for an fcc crystal centered on $[001]$, the four-fold symmetry of which is clearly evident. Note that the spacings of the pairs of lines correspond to the reciprocal lattice spacings; 200 and 020 passing through the centre being the narrowest, then 220, $2\bar{2}0$, and so on. The value of such maps is that they provide a means of tilting the specimen into any desired orientation: one simply ‘moves along’ a pair of lines (like railway lines!) to bring the desired zone axis to the centre of the projection.

³ In this situation the (simplified) explanation of Kikuchi line contrast given above breaks down. A more detailed analysis shows that the lines are still observed.

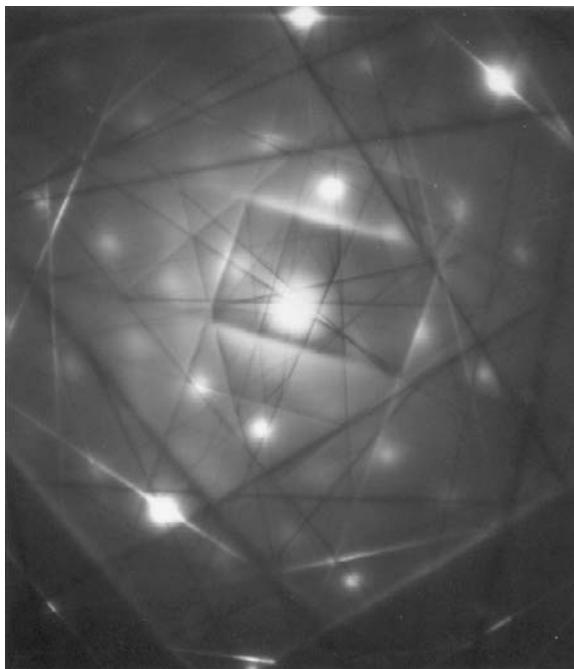


Fig. 11.11. An electron diffraction pattern of an austenitic stainless steel (fcc) showing diffraction spots and Kikuchi lines. (Photograph by courtesy of Dr P.M. Champness and Professor G.W. Lorimer.)

11.5.2 *Electron backscattered diffraction (EBSD) patterns in the SEM*

The geometry of the formation of EBSD patterns is analogous to that of Kikuchi patterns except that the incident electron beam is at a small angle, typically $\sim 20^\circ$, to the specimen surface. Only those electrons inelastically-elastically scattered from depths some 10–20 nm below the specimen surface (depending on the specimen, incident beam energy and angle) emerge from the specimen to be recorded on a phosphor screen and a CCD camera. Hence EBSD is essentially a surface technique and any surface damage or distortion must be removed by careful preparation techniques. An example of an EBSD pattern is shown in Fig. 11.14. The orientation analysis is of course carried out by computer software. The great value of EBSD is that it can be used to determine the orientations of crystals in a specimen and therefore the misorientations and nature of the boundaries between them. The beam is scanned across the specimen surface and the crystal orientation is measured at each point—the resulting map reveals the constituent crystal morphology, orientations and boundaries. The resolution depends of course on the diameter of the incident beam and interaction volume—at present, under favourable conditions, resolutions of 10–20 nm are obtainable. The crystal orientations may also be presented in the form of a *pole figure* in an analogous way to the X-ray pole figures described in Section 12.5.3. They are in fact complementary techniques: X-rays record

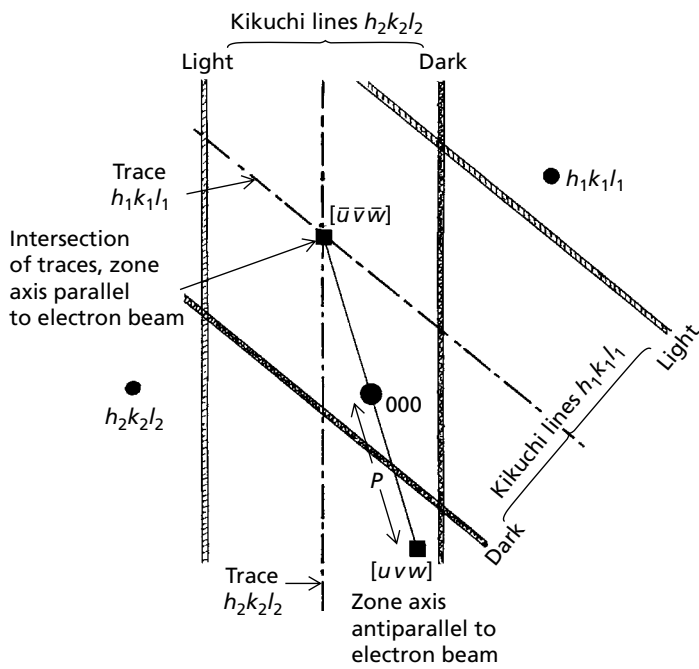


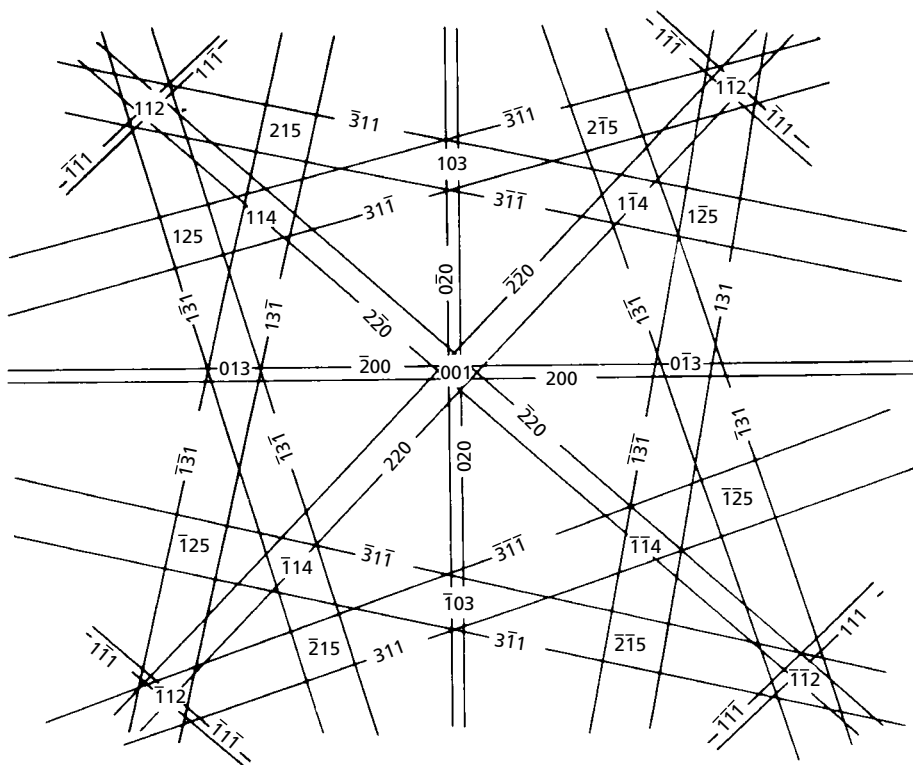
Fig. 11.12. Determination of the exact orientation of a crystal from a spot-Kikuchi line electron diffraction pattern. The *downwards* zone axis, $[\bar{u}\bar{v}\bar{w}]$, lies at the intersection of the projected traces of the reflecting planes $h_1k_1l_1$ and $h_2k_2l_2$. The angle η of the zone axis $[uvw]$ to the incident beam direction is given by $\eta = P/L$.

the reflections non-sequentially from one set of planes in a larger volume (area and depth) of the specimen.

EBSD is also complementary to the Laue X-ray diffraction technique (Section 9.4); again in the X-ray technique the X-rays penetrate into a much greater depth in the specimen (typically 5–20 μm) compared to the 10–20 nm of EBSD.

11.6 Image formation and resolution in the TEM

The Abbe criterion for image formation, discussed in Section 7.5, applies equally to light and electron microscopy. Electron wavelengths are very much smaller (4 pm for 100 kV instruments) than atomic dimensions, but atomic resolution (perhaps the ultimate goal in microscopy) is limited by the severe spherical aberration of electron (electromagnetic) lenses which limits numerical aperture (NA) values to the order of 0.01. Using the equation $a = 0.5\lambda/\text{NA}$ gives a limit of resolution of 2\AA —a dimension of the same order as atomic dimensions and interatomic spacings. The development of higher kV instruments (smaller λ) and improvements to the corrections (for spherical aberration and



astigmatism) in electron lenses have reduced this limit to about 1 Å. However, to obtain such Abbe or high resolution images is not a simple matter—neither experimentally nor theoretically. First the specimen must be very thin (of the order 2–20 nm) in order that the inelastic scattering processes described in Section 11.5 are negligible. Second, the specimen must be carefully orientated such that the electron beam is precisely parallel to a prominent zone axis—and of course there are no Kikuchi lines to help guide us! Under such conditions several diffracted beams are excited which then pass through the objective aperture to interfere to form the image. However, there is never an exact one-to-one correspondence between the atomic structure in the specimen and the image, the contrast of which depends upon the amount of defocus of the objective lens and the fact that higher-angle reflections are excluded by the objective aperture and which would otherwise refine the fine detail in the image. Hence, it is standard practice to compare the observed images (obtained at different amounts of defocus) with those obtained by computer simulation. However, despite these problems ‘high resolution’ TEM images

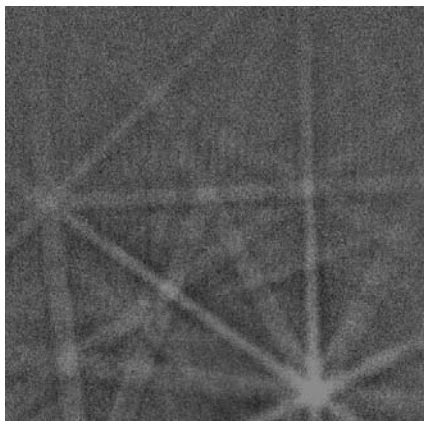


Fig. 11.14. An EBSD pattern of a β (bcc) titanium alloy, a $\langle 111 \rangle$ zone axis is at the lower right hand corner. (Photograph by courtesy of Dr E. Merson.)

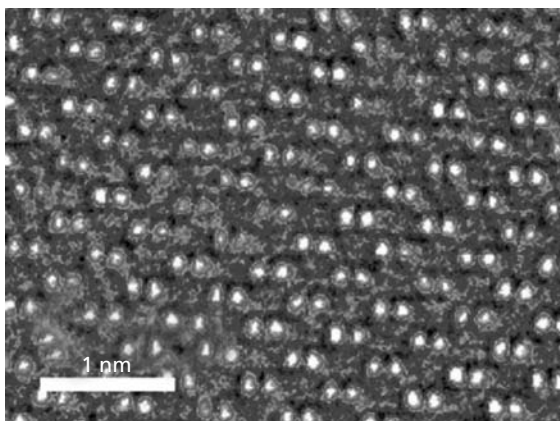


Fig. 11.15. A high resolution TEM 'dumbbell' image of germanium; the electron beam is aligned along a $\langle 110 \rangle$ direction in the crystal (diamond-cubic structure). (Photograph by courtesy of TEAM, a collaborative programme between Argonne National Laboratory, CEOS, FEI Company, Frederick Seitz Materials Laboratory, Lawrence Berkeley National Laboratory's National Center for Electron Microscopy, Oak Ridge National Laboratory. TEAM homepage: <http://ncem.lbl.gov/TEAM-project/index.html>.)

are being routinely obtained in which the peaks of intensity clearly correspond to atom positions. Figure 11.15 shows such a high resolution TEM of germanium which has the diamond cubic structure (Fig. 1.36(a)). The electron beam is aligned precisely along a $\langle 110 \rangle$ direction in the crystal and in this orientation the germanium atoms appear to be arranged in pairs—the so-called 'dumbbell' structure. So, here we see atoms: how delighted Robert Hooke would have been to actually see his 'bullets' (Fig. 1.1 in this book).

There are, however, other, no less important, modes of image formation available in the electron microscope which occur when only one beam—either the direct beam (bright field mode) or one diffracted beam (dark field mode) passes through an objective aperture of small numerical aperture. In the bright field mode the contrast arises from the varying attenuation of the direct beam through different regions of the specimen; the attenuation arising as a result either of inelastic or of elastic scattering (or more generally a combination of the two). The former case gives rise to *mass-thickness contrast* because the amount of inelastic scattering depends on the thickness of the specimen and the variations in atomic number and density of the various atomic species present. The latter case gives rise to *diffraction contrast* which arises from variations in elastic scattering, or Bragg reflection, of the incident beam. The subject is not simple because, as noted on p. 206 (Section 9.1) we have to take account of the dynamical interactions between the direct and reflected, re-reflected, etc. beams. The result of these interactions is a ‘to-and-fro’ or pendulum-type swing of energy between the direct and diffracted beams as they progress down through the specimen, the periodicity of which is called the extinction distance. Hence the tapered edges of specimens, or inclined grain boundaries, show light and dark ‘thickness’ fringes corresponding to the depths at which (in bright field mode) the direct beam has a maximum or minimum intensity.

Diffraction contrast may be illustrated by two simple examples. Figure 11.16(a) shows a thin metal specimen which is slightly bent or distorted—a very common situation. Hence the planes across the surface are at slightly different angles to the incident beam: when they are close to, or at, the exact Bragg angle, reflection occurs and hence in these regions the direct beam is attenuated. When the direct beam is used to form the image (bright field mode) these regions result in diffuse, dark lines called *Bragg contours*. Correspondingly, when the diffracted beam is used to form the image the Bragg contours appear bright. The contrast from crystal defects arises in a similar way. For example, Fig. 11.16(b) shows an edge dislocation in a specimen; note that around the ‘extra’ half plane the planes are bent or curved, the distortion decreasing further away from the

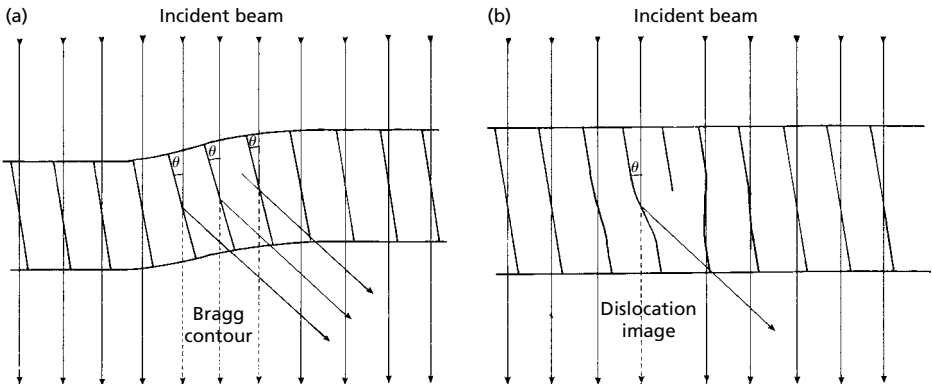


Fig. 11.16. Diffraction contrast image formation. The origin of (a) Bragg contours in a slightly-bent metal thin foil and (b) from the bending of planes around an edge dislocation.

dislocation. If the curvature is such as to bring the planes to the Bragg angle (as is shown in Fig. 11.16(b)), reflection of the incident beam will occur and thus the dislocation is imaged. Note that we do not image the dislocation as such, we only image, or record, the bending of the planes one side, or the other, of the dislocation.

Exercises

- 11.1 Using de Broglie's equation, derive a simple equation for the (non-relativistically corrected) wavelength λ of electrons in the electron microscope in terms of m , e (electron mass and charge) and V the microscope accelerating voltage. Given the following values of m (rest mass) $= 9.11 \times 10^{-31}$ kg, e (electron charge) $= 1.6 \times 10^{-19}$ C, and h (Planck constant) $= 6.63 \times 10^{-34}$ Js, determine λ for $V = 10$ kV, 100 kV and 1 MV.
- 11.2 Figure 11.17 is an electron diffraction pattern of a thin crystal of aluminium (fcc, $a = 0.4049$ nm (4.049 Å)) taken using an electron microscope operating at 100 kV, and shows diffraction spots from the ZOLZ (zero order Laue zone) only. Given the electron wavelength $\lambda = 0.0037$ nm (0.037 Å) and the camera length $L = 688$ mm, index the diffraction spots and determine the zone axis of the diffraction pattern. (*Note:* In face-centred lattices, reflections from the planes for which h, k and l are *not* all odd or all even integers are forbidden.)
- (*Hint:* Refer to Table A.6.2 listing the indices $\{hkl\}$ and d -spacings of the allowed reflecting planes. Determine the d_{hkl} -spacings of the diffraction spots in the pattern (see Section 11.3)

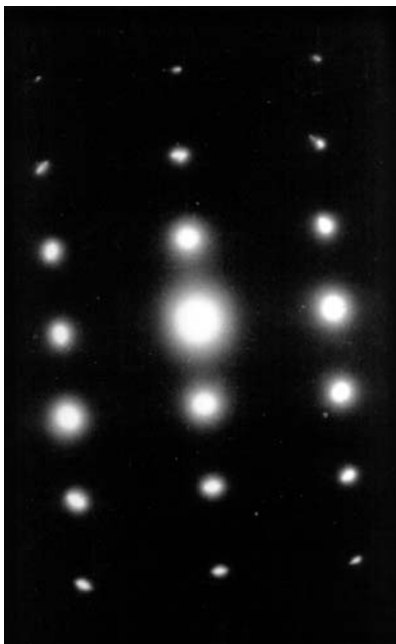


Fig. 11.17. An electron diffraction pattern (ZOLZ) of a fcc crystal. The camera length L (adjusted for the print size) is 688 mm (see Exercise 11.2).

and hence, using the table, find their indices $\{hkl\}$. Using the addition rule in Section 6.5.2, assign a consistent set of indices hkl to the diffraction spots and hence find their common zone axis using the equation in Section 6.5.7.)

- 11.3 In an electron diffraction experiment the bcc crystal described in Exercises 9.1 and 9.2 is irradiated in the $[100]$ (or \mathbf{a}^*) direction with an electron beam of wavelength 0.002 nm (0.02 \AA). Find the reciprocal lattice points which lie close to the sphere in the ZOLZ (zero order Laue zone) and FOLZ (first order Laue zone).

(Hint: Using the same reciprocal lattice scale as in Exercises 9.1 and 9.2, it will be found that a very large sheet of paper and very large compasses are needed to draw the complete reflecting sphere! However, a sketch of the surface of the sphere near the origin will suffice. In electron diffraction, sections of the reciprocal lattice perpendicular to the electron beam (i.e. normal to the $[100]$ or \mathbf{a}^*) direction are most convenient. Draw the section through the origin 000 containing the $0kl$ reciprocal lattice points (i.e. the ZOLZ), and the section containing the $1kl$ reciprocal lattice points (i.e. the FOLZ) (see also Fig. 6.8(a)). Estimate the regions of these reciprocal lattice sections, and hence the reciprocal lattice points, which are close to the surface of the reflecting sphere.)

- 11.4 Figure 11.18 is an electron diffraction pattern of a particle which has been extracted from a nitrided chromium-containing steel. It is one of three possible compounds, CrN , Fe_3C or $(\text{Cr,Fe})_7\text{C}_3$. The d_{hkl} -spacings and indices of the lowest angle reflections are given below.⁴ Given $\lambda L = 38.3\text{ \AA mm}$, identify the compound and index the diffraction pattern.

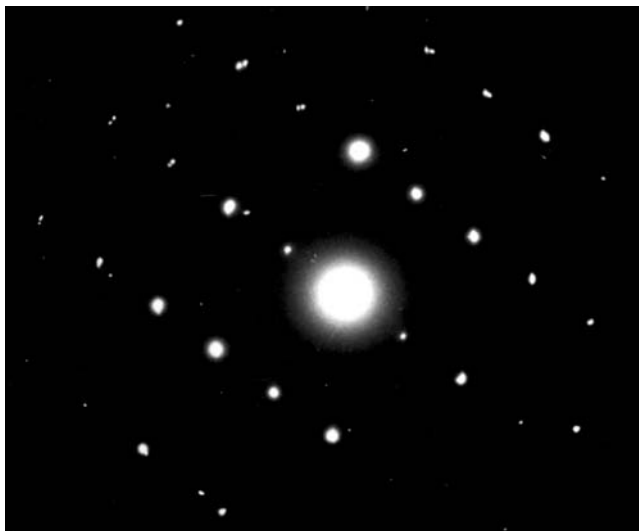


Fig. 11.18. An electron diffraction pattern (ZOLZ) of a particle extracted from a nitrided chromium-containing steel. The camera constant λL (adjusted for print size) is 38.3 \AA mm (see Exercise 11.4).

⁴ Data for CrN from the ICDD Powder Data File (11–65), for Fe_3C and $(\text{Cr,Fe})_7\text{C}_3$ from *Interpretation of Electron Diffraction Patterns*, 2nd edn, 1972 by K. W. Andrews, D. J. Dyson and S. R. Keown, Adam Hilger (1972).

CrN(fcc)		Fe ₃ C(orthorhombic)		(Cr,Fe) ₇ C ₃ (hexagonal)	
$a = 4.14 \text{ \AA}$		$a = 4.524 \text{ \AA}$		$a = 13.982 \text{ \AA}$	
		$b = 5.088 \text{ \AA}$		$c = 4.506 \text{ \AA}$	
		$c = 6.741 \text{ \AA}$			
$d_{hkl} / \text{\AA}$	hkl	$d_{hkl} / \text{\AA}$	hkl	$d_{hkl} / \text{\AA}$	hkl
2.39	111	6.742	001	12.108	01 $\bar{1}$ 0
2.07	200	5.088	010	6.991	11 $\bar{2}$ 0
1.46	220	4.524	100	6.054	02 $\bar{2}$ 0
1.25	311	4.061	011	4.576	12 $\bar{3}$ 0
1.20	222	3.757	101	4.506	0001
1.04	400	3.381	110	4.223	01 $\bar{1}$ 1
0.950	331	3.371	002	4.036	03 $\bar{3}$ 0
0.926	420	3.022	111	3.878	11 $\bar{2}$ 1
0.845	422	2.810	012	3.615	02 $\bar{2}$ 1
0.800	511	2.703	102	3.495	1340
		2.544	020	3.358	13 $\bar{4}$ 0
		2.387	112	3.211	12 $\bar{3}$ 1
		2.380	021	3.027	0440
		2.262	200	3.006	03 $\bar{3}$ 1
		2.247	003	2.777	2350
		2.218	120	2.767	22 $\bar{4}$ 1
		2.107	121	2.692	1341
		2.067	210	2.642	14 $\bar{5}$ 1
		2.031	022	2.512	0441
		2.013	103	2.421	0550
		1.976	211	2.364	2351
		1.872	113	2.330	2360
		1.588	130	2.288	2460

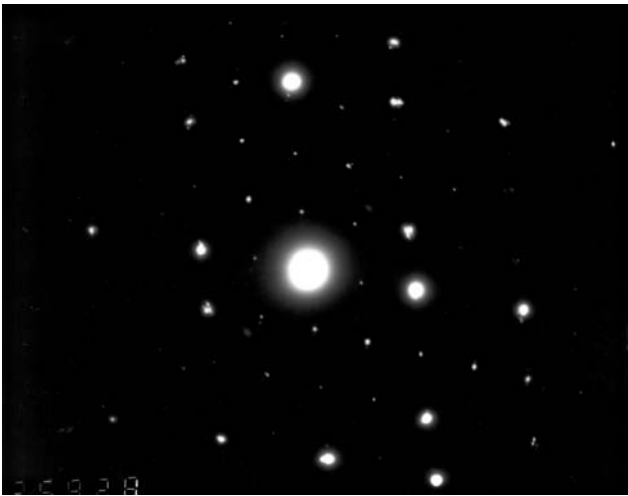


Fig. 11.19. A selected area electron diffraction pattern of a thin foil of a quenched and tempered steel showing reflections from Fe₃C precipitates in a single crystallographic orientation (weak spots) and two twin-related orientations of the ferrite (α -Fe) matrix (strong spots). (Photograph by courtesy of Dr. D. H. Jack.)

- 11.5 Given the lattice parameter of aluminium $a = 4.041 \text{ \AA}$, find the camera constant in Fig. 11.6.
- 11.6 Figure 11.19 is a selected area electron diffraction pattern of a thin foil of a steel (Fe, 1.3% Mn, 0.5% Mo, 0.7% Ni, 0.2% Cr, 0.2% C) which has been quenched from 1300°C and tempered at 615°C . The microstructure consists of a matrix of tempered martensite (α -Fe, bcc) and particles of cementite, iron carbide, Fe_3C . The pattern includes α -Fe (strong spots) and Fe_3C (weak spots). Index the patterns and determine the orientation relationship between α -Fe and Fe_3C . The camera constant $\lambda L = 36 \text{ \AA mm}$.
(Hint: A list of d_{hkl} -spacings for α -Fe should be worked out given $a_{\alpha\text{-Fe}} = 2.866 \text{ \AA}$ and given the condition for allowed reflections for the Cubic I lattice (Table A6.2). The d_{hkl} -spacings for Fe_3C are given in Exercise 11.4. Notice that the α -Fe pattern also consists of two twin-related variants (see Fig. 7.17(a) for the analogous case in the diffraction of light.)
- 11.7 Draw the diamond-cubic pattern of germanium atoms in a $\langle 110 \rangle$ projection (see Fig. 1.36(a)) and show that the pattern corresponds precisely with the high resolution TEM ‘dumbbell’ image (Fig. 11.15). Given that the lattice parameter a of germanium is 0.566 nm , calculate the separation of the tetrahedrally coordinated atoms and their apparent ‘dumbbell’ separation in the $\langle 110 \rangle$ projection.

The stereographic projection and its uses

12.1 Introduction

In Chapter 6 we showed how both the orientations and the d_{hkl} spacings of planes could be represented in terms of reciprocal lattice vectors and how these vectors could be used to determine the angles between planes and to specify zones and zone axes. We now need a method of representing the planes or faces in a crystal ‘all at once’ so that we can recognize the zones to which they belong and determine the angles between them without the need for repetitive calculations. The ‘crystal drawings’ such as Fig. 5.7 are obviously inadequate in this respect; half of the crystal faces are ‘hidden from view’ and we can only recognize zones with difficulty by looking for the parallel lines of intersections between the (visible) faces. The stereographic projection provides an important method of overcoming these difficulties. It is similar to the reciprocal lattice construction in that in both cases planes or faces are represented by their *normals*.

The stereographic projection is a very ancient geometrical technique; it originated in the second century A.D. in the work of the Alexandrian astronomer Claudius Ptolemy who used it as a means of representing the stars on the heavenly sphere. The original Greek manuscript is lost, but the work comes down to us in a sixteenth-century Latin translation from an Arabic commentary entitled *The Planispherium*. The stereographic projection was first applied to crystallography in the work of F. E. Neumann* and was further developed by W. H. Miller.*

The geometry of the stereographic projection may be described very simply. First, the crystal is imagined to be at the centre of a sphere (the stereographic sphere); the normals to the crystal faces are imagined to radiate out from the centre and to intersect the sphere in an array of points. Each point on the sphere therefore represents a crystal face or plane (and is labelled with the appropriate Miller index) just as a ‘point’ on the surface of the Earth represents a town or city. The (angular) distance between two points is equal to the angle between the corresponding planes and is determined in the same way that we find the angular distance between, say, Bangkok and New York: we take our private aeroplane and, uninhibited by Traffic Control, fly in a *great circle* between the two. Lines of longitude are simply special cases of great circles which pass through the north and south poles, the angular distances between the poles being of course 180° . Lines of latitude are called *small circles* and represent different angular distances from

* Denotes biographical notes available in Appendix 3.



Fig. 12.1. A portion of the surface of the Moon (south at top); above centre is the crater *Tycho* (from which the bright rays radiate) and above this, and seen increasingly foreshortened, is the large crater *Clavius* and smaller craters towards the edge. (Photographed at Mount Wilson Observatory, USA.)

the north and south poles. The largest small circle is the equator which is also a great circle 90° from the north and south poles.

The second step is to find a method of representing this three-dimensional information in two dimensions. One method is to project all the points on the surface of the sphere by parallel lines on to a flat disc called the plane of projection—in the same way as we see in effect all the features on the surface of the Moon, Fig. 12.1. This has the disadvantage that features near the edge of the Moon are seen foreshortened or ‘edge on’ and that craters, which we know to be circular, are seen as elliptical in shape. The geometry is shown in Fig. 12.2(a), the point of view being taken, in ‘Earth’ terms, from above the north pole. Five points 15° , 30° , 45° , 60° and 75° from the north pole are shown and it is easily seen how equal angles are represented by *smaller distances* as we move out from the centre. However, in the stereographic projection we *do not* project the points on the surface of the sphere in this way but rather project them to the *south pole* as shown in Fig. 12.2(b). Now the distortion is, as it were, the other way round, equal angles are represented by *larger distances* as we move out from the centre. However, the stereographic projection has one very important geometrical advantage and that is that circles on the surface of the sphere appear as circles, not ellipses, in the plane of projection. The geometry is shown

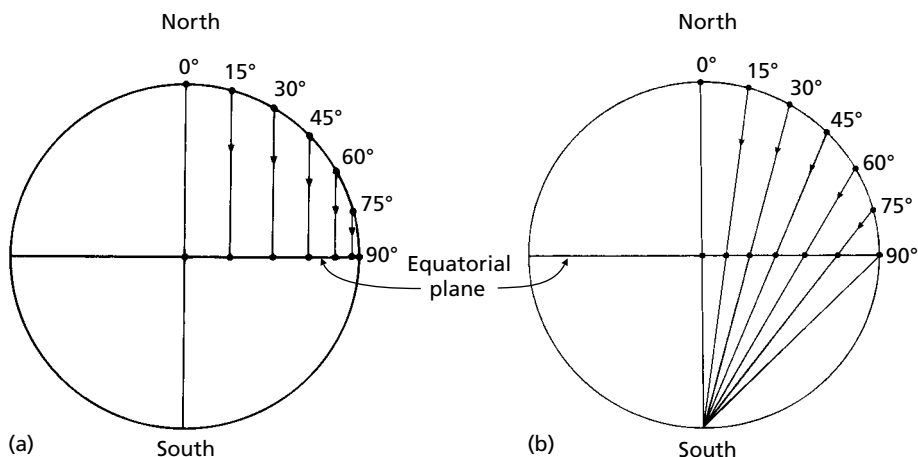


Fig. 12.2. A cross-section of the Earth perpendicular to the equator (the plane of projection) with the north pole at the top and the south pole at the bottom, and points on the surface of the Earth at equal angles 15° , 30° , 45° , 60° , 75° and 90° from the north pole. Viewed from a point a long distance above (as we see the surface of the Moon) the points project on to the equatorial plane as shown in Fig. 12.2(a). However, in the stereographic projection the points are projected to the south pole as in Fig. 12.2(b).

in Fig. 12.3(a). Here a circle in the northern hemisphere (a small circle) is centred about O; all the points on this small circle are at equal angles from O (just as all the points on a line of latitude are at equal angles from the north and south poles). All the points on the circle are projected, as shown, to the south pole giving a cone—not a cone like an ice-cream cone of circular cross-section but one of elliptical cross-section. However, in any such elliptical cone there are two circular cross-sections inclined at equal angles to the axis of the cone, one of which is the circle on the sphere and the other of which lies in the plane of projection (the proof of this is left as Exercise 12.1). Figure 12.3(b) shows a plan view of the equatorial plane, or the stereographic projection of the small circle. Notice that O', the projection of the centre of the circle is displaced towards the centre of the projection and does not coincide with the point of a drawing-compass. This follows from the fact, pointed out above, that in the projection equal angles are not represented by equal distances.

Figures 12.2 and 12.3 show the construction for points in the northern hemisphere. For points in the southern hemisphere we project instead to the north pole and represent the intersections of the lines with the plane of projection by small unfilled circles instead of dots.

Hence, in summary, and to return to our crystal, the stereographic projection consists of an array of points and circles, called **stereographic poles** or simply **poles** representing plane normals in the northern and southern hemispheres respectively and each labelled with the appropriate Miller index of the crystal face they represent.

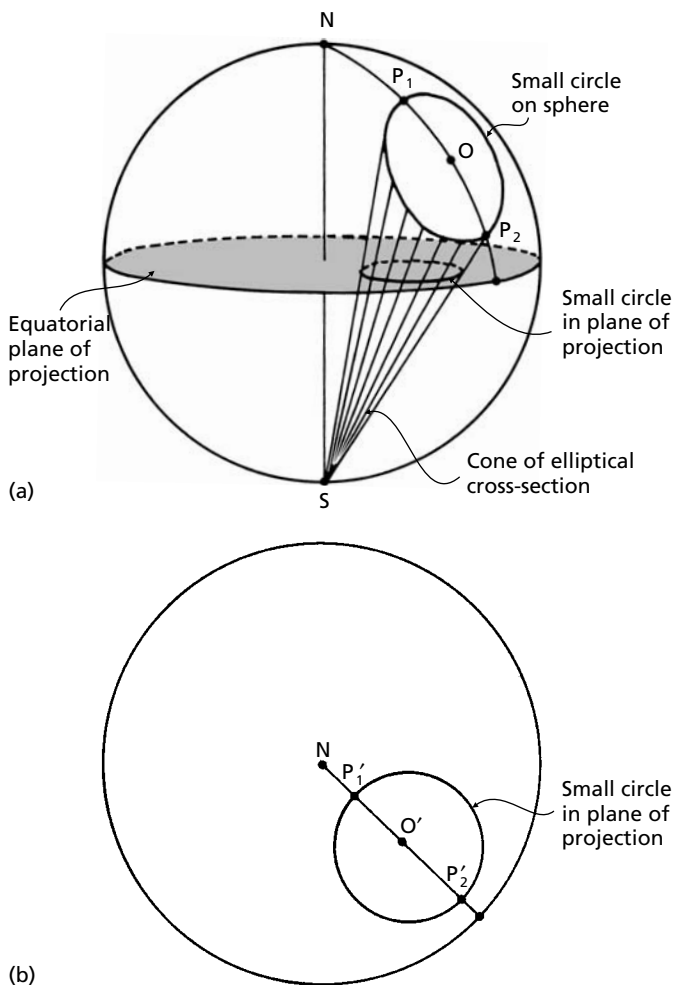


Fig. 12.3. (a) The geometry of the stereographic projection of a small circle (or Moon-crater); all the points on the circle are at equal angles to the centre O. The cone outlined by the lines of projection to the south pole is elliptical in cross-section but its intersection with the equatorial plane of projection is again a circle (see Exercise 12.1). P₁ and P₂ are two points on the small circle on the same line of longitude (great circle through the north pole) which passes through the origin O. (b) The equatorial plane, stereographic projection, or simply stereogram, of the small circle. Notice that the projected points P'₁ and P'₂ are *not* equidistant from the projected centre of the small circle O'; this follows because equal angles are not represented by equal distances (see Fig. 12.2(b)).

12.2 Construction of the stereographic projection of a cubic crystal

Figure 12.4 shows a cubic crystal at the centre of the stereographic sphere with {100}, {110} and {111} faces and oriented for easy 'Earth' reference with the z-axis in the

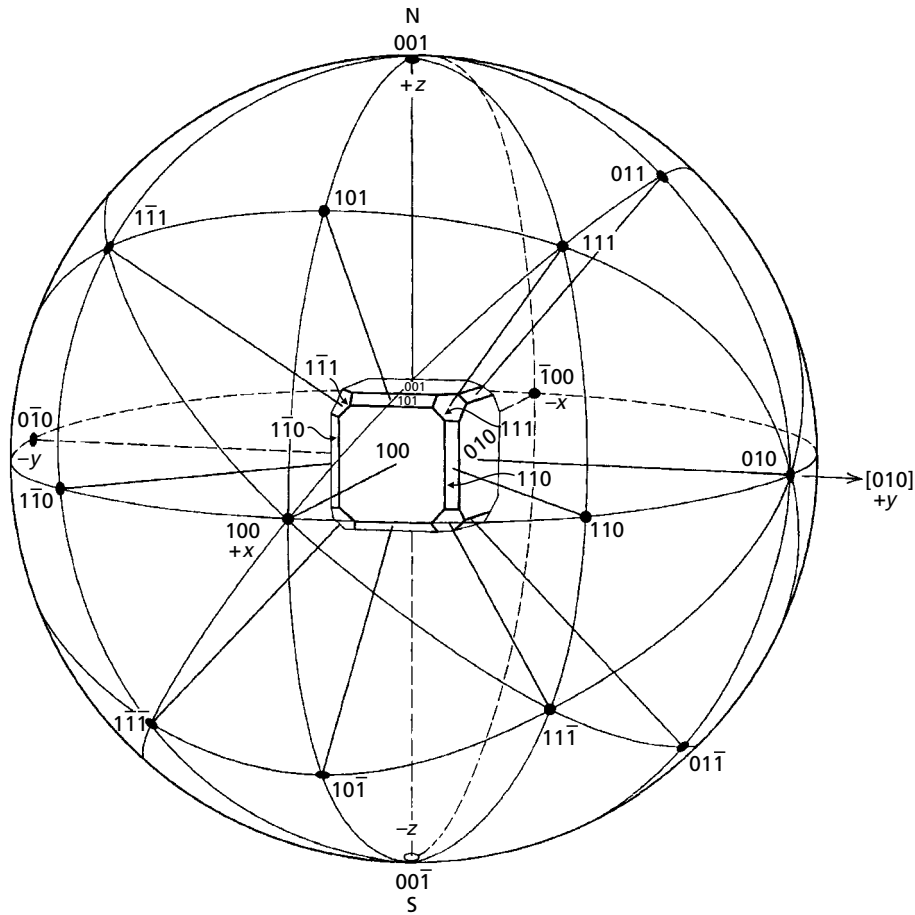


Fig. 12.4. A cubic crystal showing faces of the form {100}, {110} and {111} at the centre of the stereographic sphere with face normals intersecting the surface of the sphere. Zones are shown as great circles (diametral sections) on the sphere, the zone axis being normal to the diametral section. (From *Manual of Mineralogy*, 21st edn, by C. Klein and C. S. Hurlbut Jr; John Wiley, 1993.)

direction of the north pole and the x and y axes in the equatorial plane (the stereographic plane of projection). The normals to the crystal faces are shown and their intersections with the sphere labelled with their $\{hkl\}$ indices. The great circles on the sphere represent zones. For example, planes or faces $(00\bar{1})$, $(10\bar{1})$, (100) , (010) and (001) all lie in the $[010]$ zone and their normals lie on a great circle—a line of longitude which passes through the north and south poles. Similarly, planes or faces (010) , (111) , (101) , $(\bar{1}\bar{1}1)$ and $(0\bar{1}0)$ all lie in the $[\bar{1}01]$ zone and their normals all lie on a great circle in this case inclined at 45° to the north and south poles.

Figure 12.5 just shows the poles of planes in the equator and in the northern hemisphere with the crystal and great circles omitted (to avoid the confusion of too many

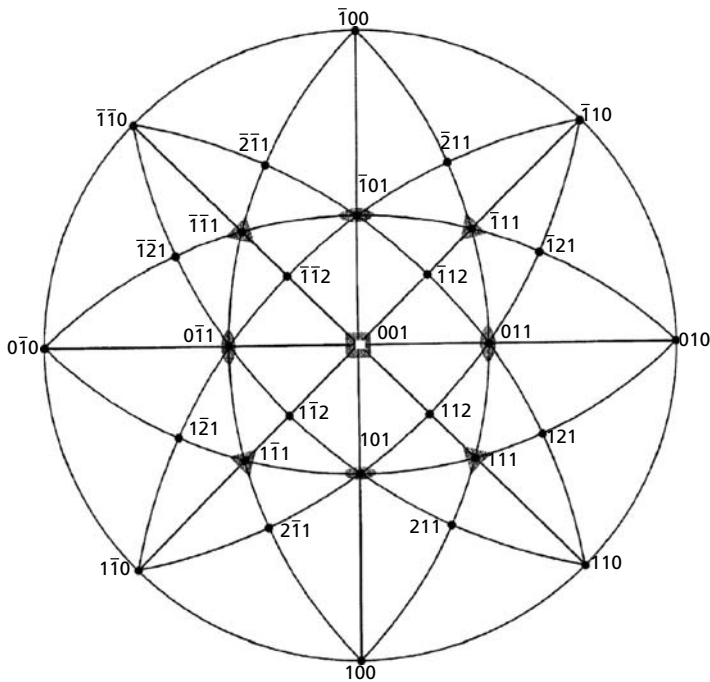


Fig. 12.6. A plan view of the stereographic plane of projection (the stereogram) showing the stereographic poles of the faces of the crystal in Fig. 12.4 and including both those faces ‘hidden from view’ in Fig. 12.4 and also additional faces (such as, for example, (112)) not drawn in Fig. 12.4. Great circles on the sphere project as the arcs of circles in the plane of projection.

those ‘hidden from view’ such as $(\bar{1}11)$ and also ones not shown in the drawing of the crystal in Fig. 12.4. For example (112) lies at the intersection of the zone through (101) and (011) and also the zone through (111) and (001); i.e. by use of the addition rule (Section 5.6.4) $(101) + (011) = (112)$ and $(111) + (001) = (112)$. Clearly, by drawing more great circles and using the addition rule, planes of higher $\{hkl\}$ values can be located (Exercise 12.2).

Finally, we must now consider the points lying in the southern hemisphere where the projection lines are made to the north pole and their intersections with the plane of projection represented by small unfilled circles. These need not be shown as such in Fig. 12.6 because clearly, for this orientation of the crystal (z -axis or (001) at the centre), a plane such as $(10\bar{1})$ is coincident with (but ‘underneath’) the plane (101).

12.3 Manipulation of the stereographic projection: use of the Wulff net

We now need a ‘stereographic graph paper’ in order to locate stereographic poles, zones and zone axes. One such is the *polar net* (Fig. 12.7) which shows great circles like lines

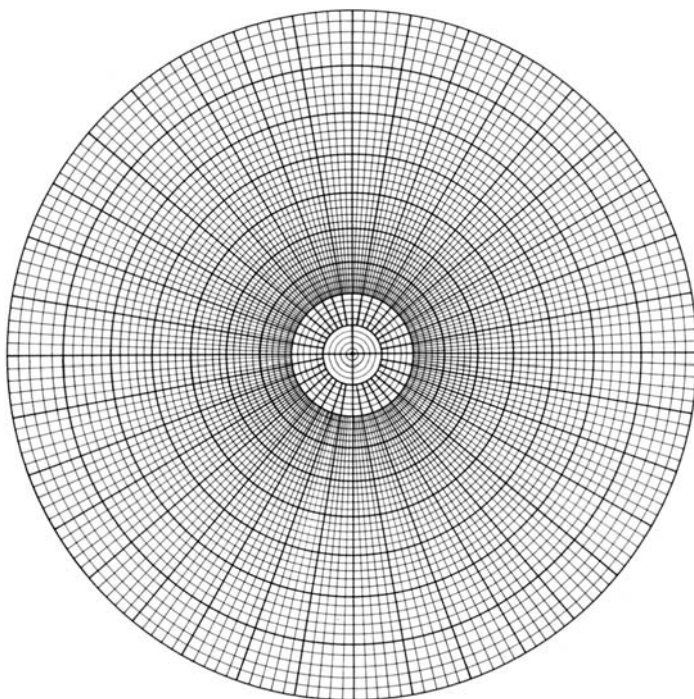


Fig. 12.7. The polar net.

of longitude and small circles like lines of latitude. This net is not very useful. Instead we use the net devised by G. V. Wulff* (Fig. 12.8) which is, in effect, the polar net rotated through 90° ; the great circles all pass through diametral points A...A in the plane of the projection ('top' and 'bottom' of Fig. 12.8) and the small circles are at increasing angles to these points, i.e. each small circle represents the loci of points at equal angles to a point like 0 in Fig. 12.3 where 0 is now located in the plane of the projection. But the Wulff net is rotatable (about a pin in the centre) and the diametral points A...A or axis of the net may be centered along the x -axis, or the y -axis (90° rotation) or indeed any direction in the plane of the projection.

The use of the Wulff net is best explained by way of some examples. Suppose we wish to find the angle between planes $h_1k_1l_1$ and $h_2k_2l_2$ (Fig. 12.9) (or, in Earth terms, between New York and Bangkok). We rotate the Wulff net until $h_1k_1l_1$ and $h_2k_2l_2$ lie on the *same* great circle as shown (full line) and the angle between them is simply 'read off' from the divisions between the small circles which intersect at 90° . The dashed

* Denotes biographical notes available in Appendix 3.

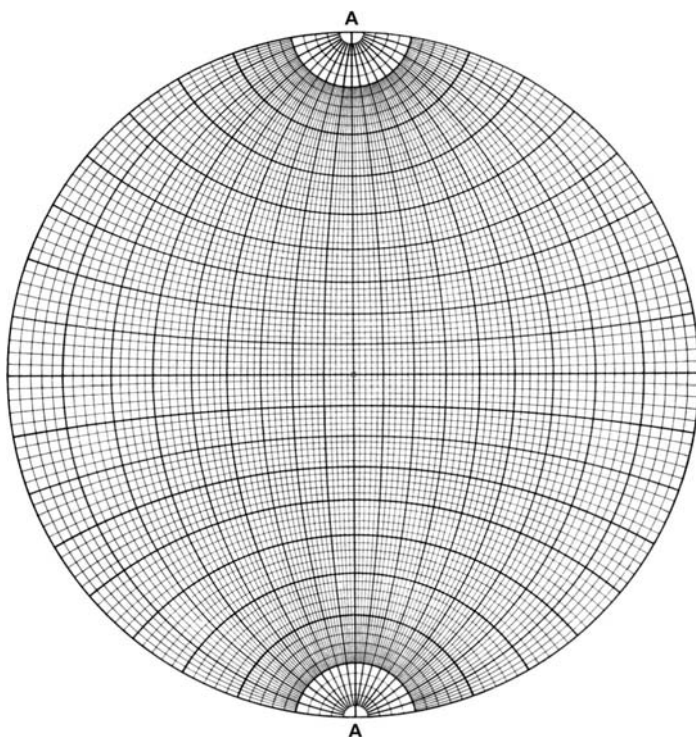


Fig. 12.8. The Wulff net (which may be rotated about the centre of the stereographic projection such that the 'axis' A...A lies in any direction).

line, symmetrical about the centre, is the continuation of the great circle in the southern hemisphere and the angle, say, between $h_2k_2l_2$ and $h_3k_3l_3$ is found by continuing the small-circle division-counting round the edge. The opposite direction of a plane normal, say $h_1k_1l_1$, is found by drawing a line through the centre (arrowed line in Fig. 12.9); the two poles, $h_1k_1l_1$ and $\bar{h}_1\bar{k}_1\bar{l}_1$ being related by a centre of symmetry. Finally, the zone axis is the direction 90° to all points in the zone as indicated by the point ZA.

Small circles may be used to locate poles in the stereographic projection given their α , β and γ angles to the x , y and z axes (Exercise 12.3). They may also be used to find the positions of the poles when the crystal is rotated away from its 'standard' orientation (z axis along the north pole—Fig. 12.6) to some other orientation. Suppose we wish to rotate the crystal to bring (112) to the centre. The angle of rotation (the angle between (001) and (112)) is 35.3° and the axis of rotation is the $[1\bar{1}0] - [\bar{1}10]$ direction. The Wulff net is orientated such that the small circles are centered along this axis (A...A, Fig. 12.10) and all the poles rotated 35.3° around their respective small circles, the angle of rotation being calibrated by the intersections of the great circles.

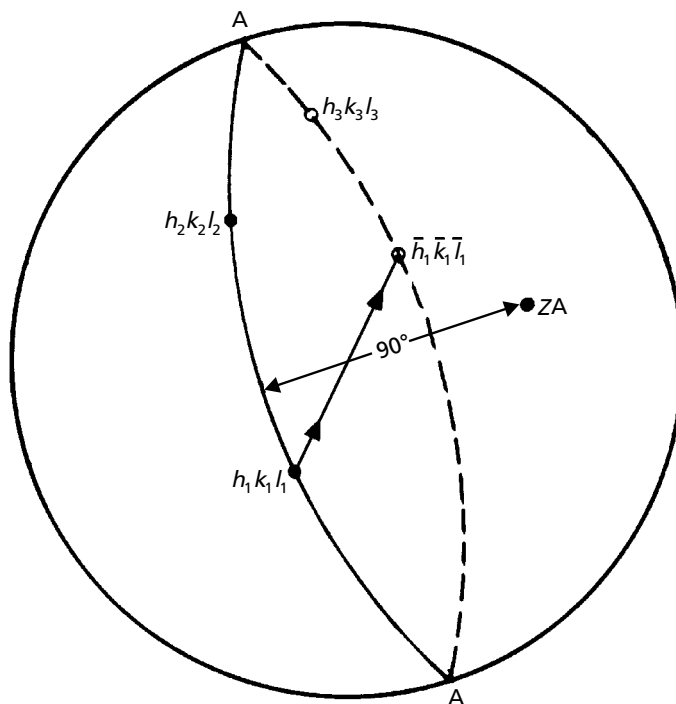


Fig. 12.9. Use of the Wulff net: to find the angle between two planes $h_1k_1l_1$ and $h_2k_2l_2$ in the northern hemisphere, the Wulff net is rotated until the poles lie on the same great circle (solid line, axis along $A \dots A$); the angle between the poles is calibrated by the intersections of the small circles. The dashed line represents the continuation of this great circle in the southern hemisphere on which lies the pole $h_3k_3l_3$. The pole $\bar{h}_1\bar{k}_1\bar{l}_1$ is related to $h_1k_1l_1$ by a centre of symmetry indicated by the arrowed line. ZA indicates the zone axis of the zone in which all these poles lie.

12.4 Stereographic projections of non-cubic crystals

Stereographic projections of triclinic, monoclinic and trigonal crystals appear to be rather complicated because the crystal axes in these systems are not orthogonal; we will not consider them further. Stereographic projections of hexagonal crystals in the 'standard' orientation (i.e. the z -axis or (0001) in the centre and the x , y and u axes in the plane of the projection) are, like those of cubic crystals, easily visualized—the hexagonal symmetry of the pattern of poles is immediately evident. Similarly with orthorhombic (and tetragonal) crystals, except that in these cases, as compared to cubic crystals, the $\{110\}$ planes are no longer at 45° to the $\{100\}$ planes; the angles must be calculated from the a , b and c lattice parameters. Furthermore, as shown in Section 5.5, in non-cubic crystals plane normals and directions with the same numerical indices are not, except in special cases, parallel to each other. For example, in hexagonal crystals a plane normal such as (10 $\bar{1}$ 0) is parallel to the direction [10 $\bar{1}$ 0] but a plane normal such as (10 $\bar{1}$ 1) is not parallel to the direction [10 $\bar{1}$ 1]. In orthorhombic crystals a plane normal such as (100) is parallel to the direction [100] but a plane normal such as (110) is not parallel

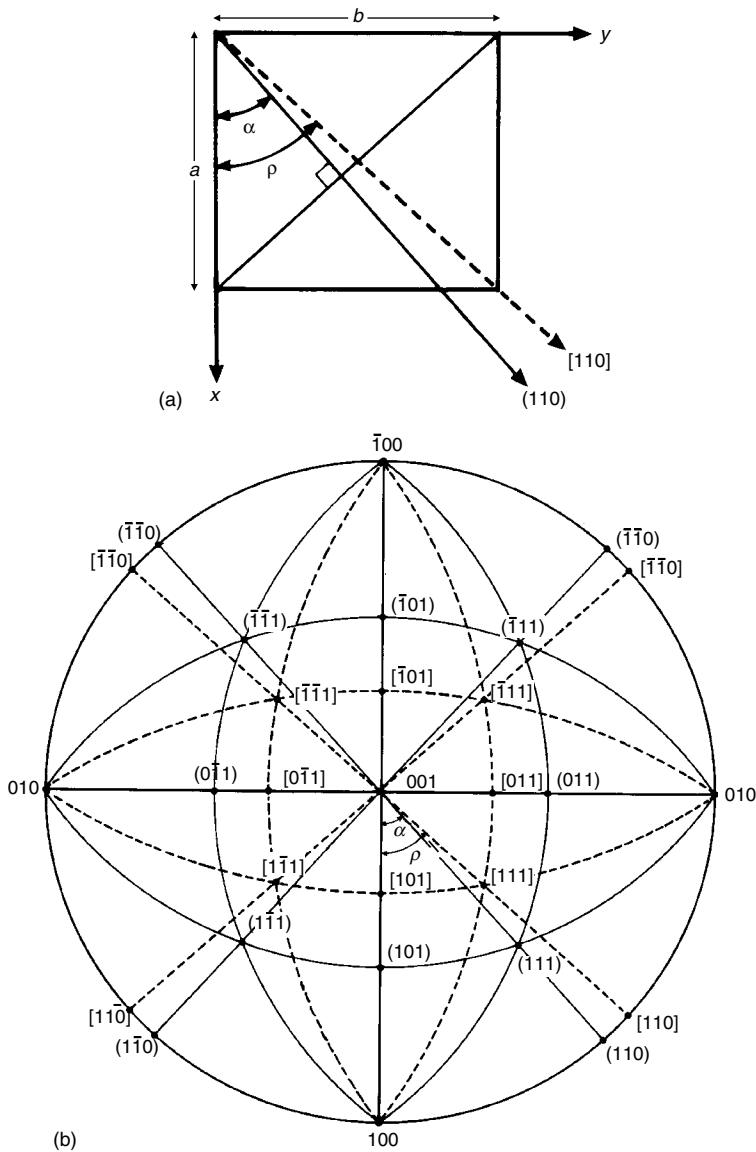


Fig. 12.11. (a) Plan view (perpendicular to the z axis) of an orthorhombic crystal (cementite, Fe_3C) showing the angles α and $\rho = (90^\circ - \alpha)$ of the (110) plane normal (full line) and $[110]$ direction (dashed line) to the x -axis respectively. (b) The 'composite' stereographic projection showing two sets of great circles through the $\{hkl\}$ poles (full lines) and the $[uvw]$ directions (dashed lines).

12.5 Applications of the stereographic projection

12.5.1 Representation of point group symmetry

In Chapter 4 we discussed the point group symmetry elements—mirror planes, centres, rotation and inversion axes of symmetry. We can represent the operation of these symmetry elements very easily with the stereographic projection by first placing a single pole (representing a single face) in a *general position* in the projection (i.e. not on an axis or mirror plane) and then seeing how it is repeated by the action of the symmetry elements present. In this way all the 32 point groups can be built up.

Figure 12.12(a) shows a pole reflected in a ‘vertical’ mirror plane m (indicated by a heavy line) and Fig. 12.12(b) shows a pole reflected by a mirror plane in the plane of the projection—one pole being in the ‘northern’ hemisphere and its reflection (an open

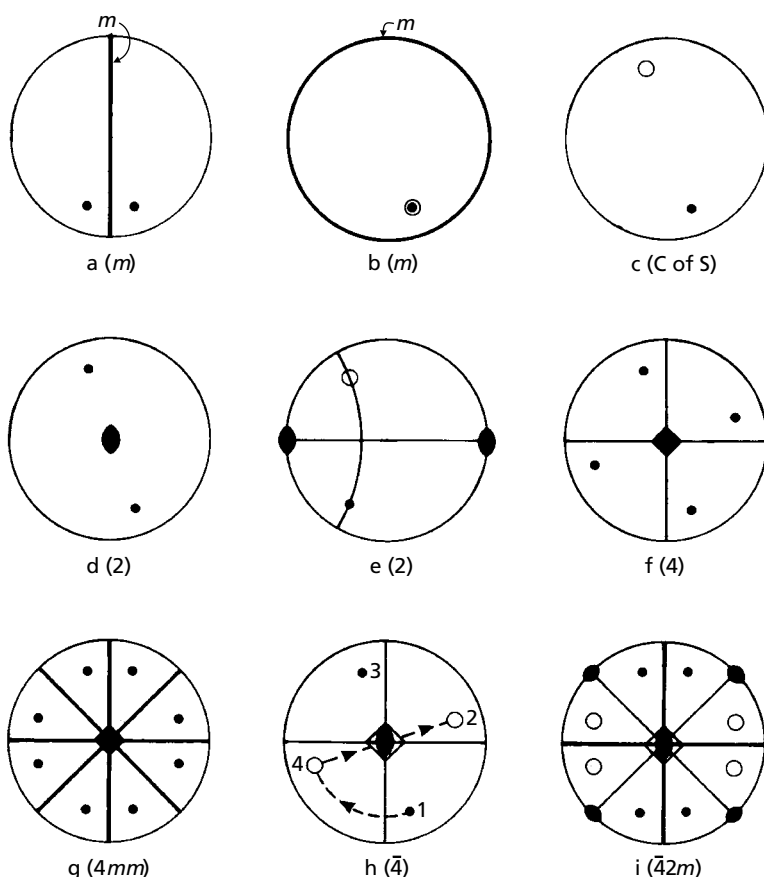


Fig. 12.12. Stereographic projections showing the operation of some point group symmetry elements as indicated. Light lines indicate ‘guidelines’ for locating the poles, heavy lines indicate mirror planes.

circle) in the 'southern' hemisphere below. Fig. 12.12(c) shows the operation of a centre of symmetry and Figs. 12.12(d) and (e) show the operation of a diad axis—a 'vertical' diad as in (d) or a 'horizontal' diad (in the plane of projection) as in (e); the rotation is 180° about a small circle centred along the diad axis giving one pole in the upper hemisphere, and one in the lower hemisphere as shown.

Figure 12.12(f) shows the operation of a 'vertical' tetrad giving a four-fold pattern of poles (the light lines may be regarded as 'guidelines' in making the drawing). When one of these guidelines is made into a mirror plane the resulting pattern of poles is given in Fig. 12.12(g). Notice that the tetrad symmetry not only generates mirror planes at 90° but an additional set at 45° as well (see Section 2.3).

Figure 12.12(h) shows the operation of the inversion tetrad axis of symmetry. The procedure is as follows: starting with the pole marked 1, rotate 90° and invert through the centre (dashed and arrowed lines) to give the next position of the pole marked 2. Then repeat to give poles marked 3 and 4. Notice that the pattern of poles (two 'above' and two 'below') includes the operation of a diad axis, hence the symbol for the inversion tetrad axis includes the diad symbol. Finally, Fig. 12.12(i) shows the pattern of poles when a 'vertical' mirror plane is added, which generates not only a 'horizontal' mirror plane at 90° but also two sets of diads at 45° as indicated. This point group $\bar{4}2m$ represents the symmetry of urea or a tennis ball (Fig. 4.6).

Figure 12.13 shows the pattern of poles for a cubic crystal with minimum symmetry (point group 23) and maximum symmetry (point group $m\bar{3}m$). The principal symmetry elements are the four equally-inclined triad axes around which the poles rotate like points round the centre of a small circle (Fig. 12.3). In Fig. 12.13(a) the great circles drawn in are all 'guidelines' as in, e.g. Fig. 12.12(f), and around each triad are a set of three poles—two 'above' and two 'below'. Notice that the diad axes are 'automatically' generated along the x , y and z axes. Figure 12.13(b) shows the holosymmetric point group $m\bar{3}m$; all the great

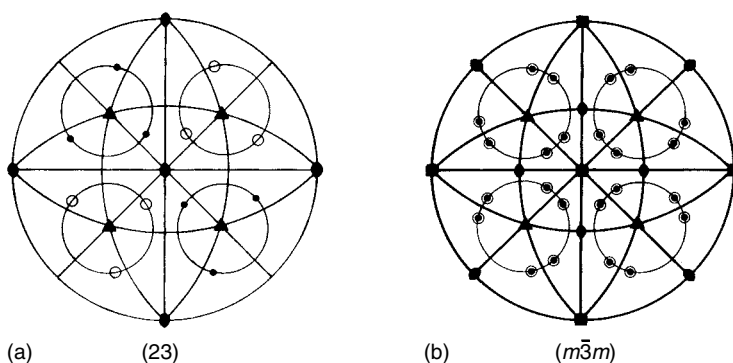


Fig. 12.13. Stereographic projections of cubic crystals (a) point group 23 and (b) point group $m\bar{3}m$. The principal symmetry elements are the four equally-inclined triad axes around which the poles are distributed around small circles centred on these axes. In (a) the only additional symmetry elements are the diad axes along the x , y and z -axes, whereas in (b) these become tetrads; There are also six further diads along $\langle 110 \rangle$ directions and all the great circles become mirror planes (heavy lines).

circles now correspond to mirror planes, the x , y and z axes correspond to tetrads, the $\langle 110 \rangle$ directions correspond to diads and the triads include a centre of symmetry, hence the symbol $\bar{3}$. These symmetry elements are indicated in the stereographic projection of the cubic crystal shown in Fig. 12.6.

Figures 12.12 and 12.13 show 11 of the 32 point groups. It will help your understanding of symmetry to draw stereographic projections of all the 32 point groups (see Table 3.1) and thereby you will appreciate more fully the relationships between them.

12.5.2 Representation of orientation relationships

The study of solid state transformations in which new crystals nucleate and grow within, or at the boundaries of, parent crystals is of major importance in materials and earth sciences. Our interest as crystallographers is not so much with the mechanisms of the transformations and the conditions which give rise to them but rather with the fact or observation that in almost all cases the planes and directions in the parent and product phases bear definite relationships to each other and that such relationships may provide evidence of the nature of the transformation processes.

That such relationships arise may be seen almost intuitively from the simplest of examples—as we saw in Section 1.5. When iron transforms from its high-temperature ccp form to its low temperature bcc form, a closest-packed $\{110\}$ plane in the bcc structure (Fig. 1.9(b)) is parallel, or closely parallel, to a close-packed $\{111\}$ plane in the ccp structure (Fig. 1.4) and a pair of close-packed directions ($\langle 111 \rangle$ in bcc, $\langle 110 \rangle$ in ccp) are also parallel, or closely parallel. Hence, the orientation relationship may be stated in terms of (i) parallelism of planes and (ii) parallelism of directions within these planes, i.e.

$$(111)_{\text{ccp}} \parallel (110)_{\text{bcc}}$$

$$[\bar{1}\bar{1}0]_{\text{ccp}} \parallel [1\bar{1}1]_{\text{bcc}}$$

Similarly, when cementite, Fe_3C , precipitates as fine particles within ferrite (the interstitial solid solution, α , of carbon in bcc iron), then under certain conditions the orientation relationship which occurs is given as:

$$(001)_{\text{Fe}_3\text{C}} \parallel (112)_{\alpha}$$

$$[010]_{\text{Fe}_3\text{C}} \parallel [\bar{1}10]_{\alpha}$$

However, such statements of ‘parallelisms’ do not immediately tell us what *other* planes and directions in the two phases may be parallel (or nearly parallel) to each other, nor do they immediately specify the angles between the two sets of crystal axes—except in the very simplest cases such as the ‘cube–cube’ orientation relationship between α -iron and Fe_2TiSi (Fig. 11.5) where the diffraction pattern clearly shows that the crystal axes of these two phases are parallel.

The stereographic projection provides a graphical way of analysing the relationships between planes and directions in two phases. For example, if we place the cubic stereogram with the (112) plane in the centre (Fig. 12.10) over the stereogram of the cementite

crystal with (001) in the centre (Fig. 12.11(b)) and rotate them until the $[100]_{\text{Fe}_3\text{C}}$ and $[110]_{\alpha}$ directions (at the edge, i.e. in the plane of the projection) coincide, then we can see, across the whole composite projection, the orientation relationships between the crystal axes and other planes and directions. Furthermore, it may well be (and usually is) the case that the zones we observe in our electron diffraction patterns of the two phases may well be those out of the plane of projection and we may check the occurrence of the orientation relationship by a trial-and-error process of tracing round great circles in the composite projection and seeing whether or not the plane normals of the two phases occur at the observed angles to each other. The diffraction pattern in Fig. 11.5 provides a very simple example. The cube–cube orientation relationship is simply represented by two cubic stereograms in the ‘standard’ orientation with the x , y and z axes parallel and with the added proviso that for α -Fe (bcc) the planes which reflect are those for which $h + k + l$ is even and for Fe_2TiSi (fcc), h , k , l are all odd or all even. The angles between the two sets of planes may be checked by tracing round the great circles with the common $[0\bar{1}1]$ zone axis.¹

12.5.3 Representation of preferred orientation (texture or fabric)

Pole figures (see Section 10.4), are in effect stereographic ‘contour maps’, the positions of the ‘hills’ or ‘peaks’ in the maps showing the orientations of a particular set of crystal planes and the ‘height’ and ‘steepness’ of the hills showing the extent or degree of preferred orientation from a random distribution. In materials science the plane of projection is normally set parallel to the surface of the metal sheet, in Earth science it is normally set horizontal with the points of the compass around the edge.

The geometry of pole figures is best understood by way of a simple example. Let us suppose that in a rolled sheet of a polycrystalline cubic metal the $\{100\}$ planes of all the crystallites lie closely, but not perfectly, parallel to the sheet surface and that the $\langle 100 \rangle$ directions lie closely parallel to the rolling direction (this texture, incidentally, occurs in rolled and recrystallised sheets of iron–silicon alloys used for transformer cores). The pole figure for the $\{100\}$ planes will appear as shown in Fig. 12.14(a)—the $\{100\}$ plane normals cluster at the centre (i.e. normal to the sheet surface) and also along the rolling and transverse directions giving contoured ‘peaks’ in these positions as shown. Now suppose that the crystallites still remain aligned such that the $\langle 100 \rangle$ directions lie closely parallel to the rolling direction but that the $\{100\}$ planes are more randomly orientated with respect to the surface of the sheet. The pole figure will appear as in Fig. 12.14(b)—the contour lines representing the distribution of the $\{100\}$ plane normals are now spread out towards the transverse directions. This pole figure corresponds closely to that for graphitized carbon tapes (Fig. 10.13(b)) which shows the orientations of the graphite layers.

Pole figures may be prepared for any set of planes. For example the $\{111\}$ pole figure corresponding to the texture shown in Fig. 12.14(b) would consist of peaks of intensity as

¹ A more detailed description of the use of stereographic projections in the analysis of orientation relationships, with step-by-step examples, may be found in my article on *Stereographic Techniques*, Module 9.17 in *Procedures in Electron Microscopy* (eds A. W. Robards and A. J. Wilson), John Wiley, 1993.

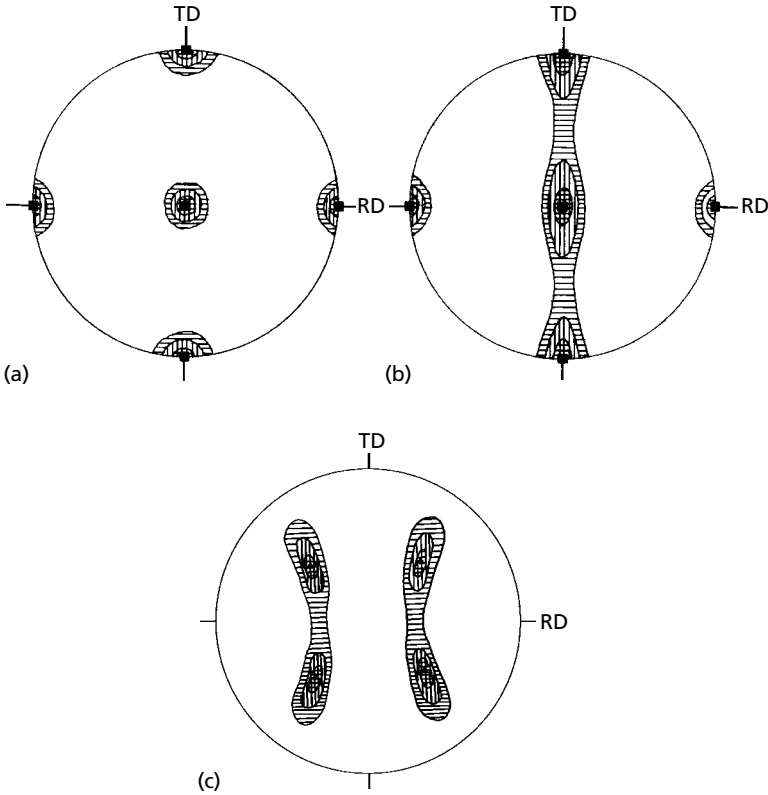


Fig. 12.14. (a) A $\{100\}$ pole figure in which the $\{100\}$ planes lie closely parallel to the sheet surface and the $\langle 100 \rangle$ directions lie closely to the rolling direction (RD) and transverse direction (TD). The successive levels of shading correspond to the contours of the orientations of plane normals and directions. (b) A similar pole figure to (a) except that the $\{100\}$ planes are more randomly distributed about the rolling direction—the peaks are extended across the transverse direction. (c) A pole figure of the same texture as (b) but now showing the orientations of the $\{111\}$ planes.

shown in Fig. 12.14(c). Pole figures may be prepared in practice by a number of experimental techniques—by the use of the texture goniometer as described in Section 10.4, by recording backscattered electron diffraction patterns in the scanning electron microscope (see Section 11.5.2) or by recording the orientation of individual grains in thin sections in the light microscope. In general the textures observed are rather more complicated than those of the simple examples described above and may consist of two or more *components*, i.e. two or more sets of planes and directions may be aligned to a greater or lesser extent parallel to the plane of the sheet and along the rolling direction respectively. For example, Fig. 12.15(a) shows the $\{111\}$ pole figure of heavily cold rolled copper in which the texture may be described as $(123)[41\bar{2}]$ and $(146)[21\bar{1}]$ where the indices refer to the planes orientated parallel to the rolling plane and the direction symbols refer to the directions orientated along the rolling direction. Finally, Fig. 12.15(b) is a pole figure

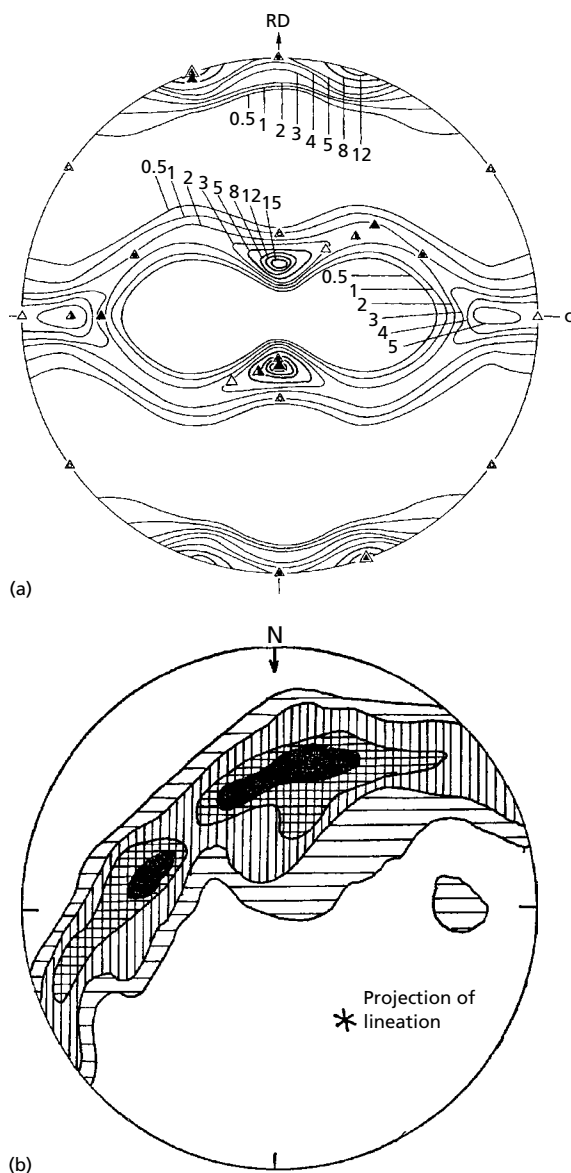


Fig. 12.15. (a) A {111} pole figure for heavily cold rolled copper, rolling direction RD vertical (from H. Hu and S. R. Goodman, *Trans. AIME*, **227**, 627, 1963). (b) A pole figure with contours shaded as in Fig. 12.14, showing the orientations of the c -axes (or 0001 planes) of the quartz grains in a metamorphosed psammite rock. These lie in a zone with a zone axis approximately parallel to the lineation of the rock (from *Introduction to Geology* by H. H. Read and Janet Watson, Macmillan, 1968).

(or petrofabric diagram²) showing the orientations of the *c*-axes of the quartz grains in a metamorphosed psammite rock. They lie, as can be seen, roughly in a great circle, the zone axis of which is closely parallel to the direction of lineation or structural long direction of the rock.

Exercises

- 12.1 Prove that the stereographic projection of a small circle on the stereographic sphere is again a circle. (*Hint*: this is an exercise in Euclidean geometry.)
- 12.2 Use the Wulff net to prepare a projection of a cubic crystal with (001) in the centre as in Fig. 12.6. Find, by drawing in additional great circles, the positions of the (212) and ($\bar{3}\bar{3}2$) planes, measure their angles α , β and γ to the *x*, *y* and *z* axes and hence check that the ratios of their direction cosines $\cos \alpha : \cos \beta : \cos \gamma$ are in the ratios of *h* : *k* : *l* in each case (see Section 5.5).
- 12.3 Two planes in a cubic crystal make the following angles to the crystal axes

	<i>x</i> -axis	<i>y</i> -axis	<i>z</i> -axis
Plane A	+36.5°	+57.5°	+74.5°
Plane B	−48.2°	−70.5°	+48.2°

Find the positions of these planes on a standard projection from the common intersections of small circles centred about the *x*, *y* and *z*-axes, and determine their Miller indices. Using the Wulff net measure the angles between: Plane A and Plane B; Plane A and ($\bar{1}\bar{1}1$); Plane B and (101); Plane B and ($\bar{1}01$).

- 12.4 Using sketch stereograms as in Fig. 12.12, show that (a) $\bar{2} \equiv$ a perpendicular mirror plane; (b) $\bar{3} \equiv 3 +$ a centre of symmetry, and (c) $\bar{6} \equiv 3 +$ a perpendicular mirror plane.

² Petrofabric (or fabric) diagrams may also be represented on *equal area projections* which are, of course, much used in earth science and geography since they show, for example, the sizes of materials in their correct proportions. ‘Equal area graph paper’ consists, like the Wulff net, of intersecting small and great circles, but these are not arcs of circles and do not appear to intersect at 90°. The geometry of equal-area projection is more complicated than that of the stereographic projection. For example, referring to Fig. 12.2, we need to project the points on the sphere 15°, 30°, etc. from the north pole such that they make *equal* divisions along the equatorial plane, and this cannot be done by projecting lines down to a single point.

Fourier analysis in diffraction and image formation

13.1 Introduction—Fourier series and Fourier transforms

In many areas of physics we encounter physical events, characteristics or properties which repeat at regular intervals and which may be represented by waveforms of various shapes and complexity. Perhaps the most familiar examples are the sound waves produced by musical instruments, where the waveforms represent air pressure variations and the repeat distance or wavelength represents the frequency or pitch of the fundamental note. Figure 13.1 shows three such waveforms; the characteristic ‘sound’ of each instrument is related to the shape of the waveform in each case. Another example is a simple diffraction grating which has a waveform consisting of flat-topped peaks (corresponding to the light from the slits) with dark regions in between (Fig. 13.7(a) below). Such waveforms are called *periodic functions* and are also of great importance in crystallography because, as we shall see below, crystal structures can be represented in terms of periodic variations of *electron density*, the density peaking at the atom positions and falling to low values in between.

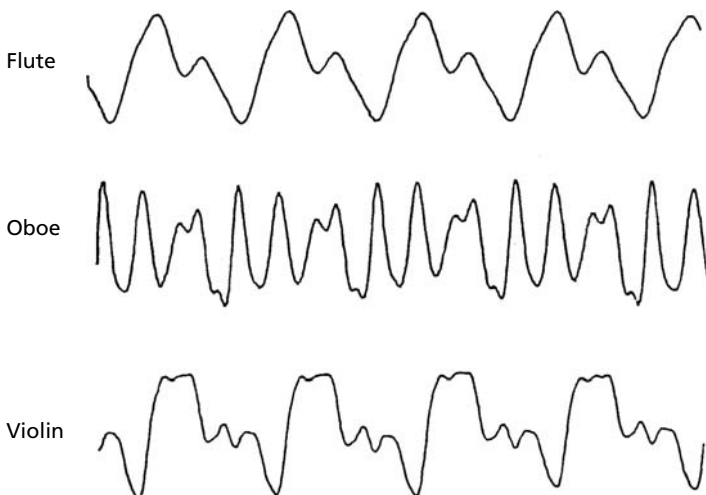


Fig. 13.1. Examples of waveforms of musical instruments (from *Measured Tones* by I. Johnston, Adam Hilger (Institute of Physics), Bristol, 1989).

Jean Baptiste Fourier* showed that any periodic waveform or function could be analysed in terms of a series of cosine or sine waveforms (or, more generally, a series of exponential functions). First, a 'constant' term (representing, in sound waves, the undisturbed air pressure or, in crystals, a uniform 'sea' of electrons); then a term with a wavelength or repeat distance corresponding, in sound, to the fundamental note, or in a crystal to the lattice repeat distance, then a term of half the wavelength (or twice the frequency) corresponding, in sound, to the first harmonic, and so on. Each of these cosine or sine waves is defined by its amplitude and phase—the phase representing the displacements of the waves with respect to each other.

The process of analysing a complex waveform into a series of such components is called *Fourier analysis*. Conversely, the generation of a complex waveform from such components is called *Fourier synthesis*. Figure 13.2 shows two examples in which the complex waveforms (a) and (b) are synthesized from, or analysed into, three terms: a constant term, a fundamental term and a first harmonic term. Notice that in (a) there is a phase difference between the component waves which gives rise to the synthesized asymmetrical waveform whereas in (b) there is zero (or a 180° phase difference depending as to where you take the origin) which gives rise to the symmetrical waveform. In crystallography (a) corresponds to electron density variations in a crystal without a centre of symmetry whereas (b) corresponds to a crystal with a centre of symmetry (or a mirror plane or diad axis normal to the direction in which the electron density is measured).

The amplitude A versus distance x of a periodic function is represented mathematically by a Fourier series:

$$A = A_0 + A_1 \cos \left(2\pi 1 \left(\frac{x}{a} \right) - \alpha_1 \right) + A_2 \cos \left(2\pi 2 \left(\frac{x}{a} \right) - \alpha_2 \right) + \cdots \\ + A_n \cos \left(2\pi n \left(\frac{x}{a} \right) - \alpha_n \right)$$

i.e.

$$A = \sum_{n=0}^{n=N} A_n \cos \left(2\pi n \left(\frac{x}{a} \right) - \alpha_n \right)$$

where a is the repeat distance, the amplitudes A_1, A_2, \dots, A_n are called the Fourier coefficients and $\alpha_1, \alpha_2, \dots, \alpha_n$ are the phase angles. The Fourier series may equally well be written in terms of sines or, more generally, exponential terms, but in cases where the waveform is symmetrical (as in crystals with a centre of symmetry or a simple diffraction grating and in which the phase angles are zero or 180°) we shall find the cosine form more convenient: a cosine is a symmetrical function, i.e. $\cos x = \cos(-x)$ whereas a sine is an asymmetrical function, i.e. $\sin x = -\sin(-x)$. Hence the Fourier series may be written:

$$A = A_0 + A_1 \cos 2\pi 1 \left(\frac{x}{a} \right) + A_2 \cos 2\pi 2 \left(\frac{x}{a} \right) + \cdots + A_n \cos 2\pi n \left(\frac{x}{a} \right)$$

* Denotes biographical notes available in Appendix 3.

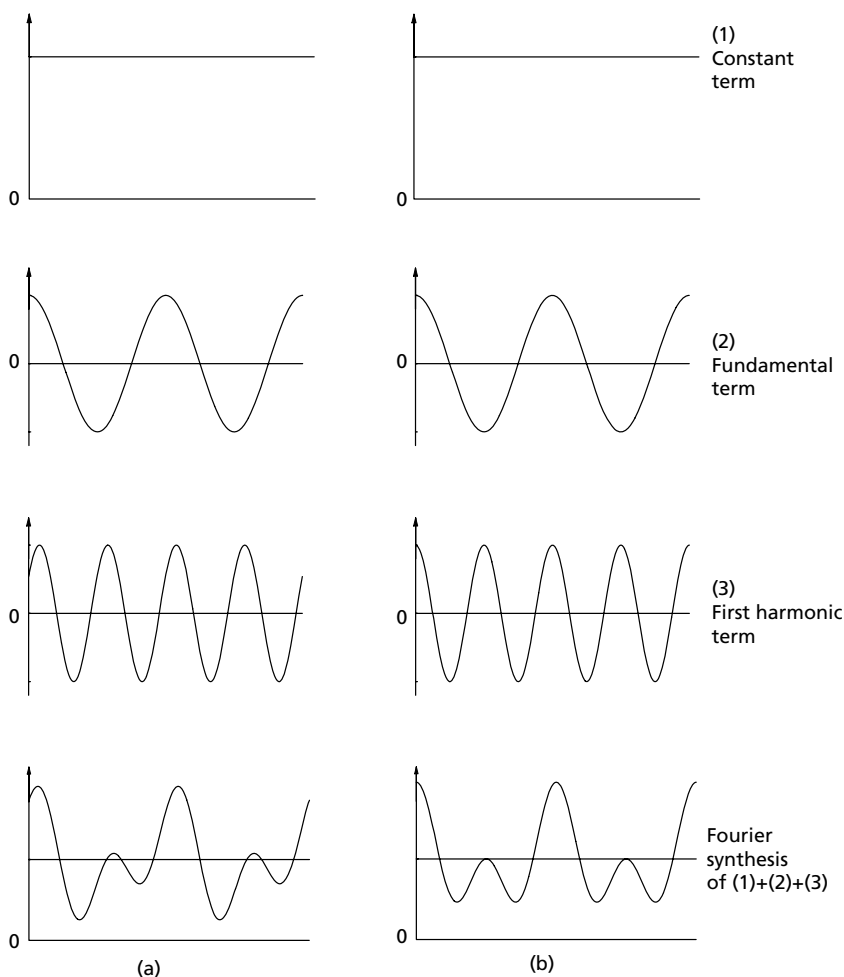


Fig. 13.2. Fourier synthesis of a complex waveform from three components: a constant term (1), a fundamental term (2) and a first harmonic (3). The asymmetrical waveform in (a) arises from the phase difference between the fundamental term and first harmonic. (Courtesy of Mr D.G. Wright.)

i.e.

$$A = \sum_{n=0}^{n=N} A_n \cos 2\pi n \left(\frac{x}{a} \right).$$

The first term A_0 represents, in effect, a wave of infinite wavelength (in sound the undisturbed air pressure), the second a wave of amplitude A_1 , and wavelength a (in sound the fundamental note), the third a wave of amplitude A_2 and wavelength $a/2$ (in sound the first harmonic), and so on. The Fourier coefficients A_0, A_1, A_2 , etc. may also

be represented as components on a frequency scale A_0 (zero frequency), A_1 (frequency $2\pi/a$), A_2 (frequency $4\pi/a$), and so on.

Finally, there is a very important development in Fourier analysis (though not envisaged by Fourier himself) and that is that it can also be applied to *non-periodic* functions such as a single sound pulse or the distribution of light from a single slit or aperture. This may be done by envisaging a non-periodic function as, in effect, a periodic function with a fundamental repeat distance that approaches infinity. In this case the Fourier coefficients, represented as components on a frequency scale, approach closer and closer together (the frequency differences become smaller and smaller) until they merge together. The envelope of all the merged-together Fourier coefficients is called the *Fourier transform* and is treated mathematically as an integral, rather than a summation of the Fourier series for a periodic function. As we shall see, the diffraction pattern from a single slit or aperture (expressed as an amplitude, rather than an intensity distribution) and the Fourier transform are synonymous.

13.2 Fourier analysis in crystallography

In our derivation of the structure factor F_{hkl} (Section 9.2), we considered the atoms to be discrete scattering centres, the atoms being located at specific points in the unit cell denoted, for the n th atom, by the fractional coordinates $(x_n \ y_n \ z_n)$. The atomic scattering factor f_n was derived by considering the interference of all the waves scattered by the z electrons in the atom and then the structure factor F_{hkl} was obtained by considering the interference of all the scattered waves from all the atoms in the unit cell. Hence we obtained the relation:

$$F_{hkl} = \sum_{n=0}^{n=N} f_n \exp 2\pi i (hx_n + ky_n + lz_n).$$

We are now going to determine F_{hkl} starting, as it were, from a different standpoint. Since it is the electrons which scatter X-rays then we are really detecting the distribution, or variation in the ‘density’ of electrons throughout the unit cell, the electron density being greatest at the atom centres and falling to low values in between. In short we have a three-dimensional periodic variation in electron density, the variation being repeated (as for the lattice) from cell to cell.

It is not easy to represent such electron density variations in three dimensions except for the simplest crystals. It is much easier to represent the *projection* of electron density on to one face of the cell—just as we represented crystal structures in terms of projections or plans (Section 1.8). Figure 13.3 shows a ‘classic’ example: a projection on the (010) face of the monoclinic mineral diopside, $\text{CaMg}(\text{SiO}_3)_2$. Figure 13.3(a) shows the atom positions and Fig. 13.3(b) the corresponding electron density ‘contour map’—the peaks corresponding to the heavy, overlapping Ca and Mg atoms and the diffuse ‘ridges’ in between corresponding to the distribution of the lighter O and Si atoms.

We now need to replace the atomic scattering factor f_n in the equation by an equivalent electron-density term. Let ρ_{xyz} be the electron density (number of electrons per unit volume) at *distance* coordinates xyz in the unit cell. We use these coordinates in preference

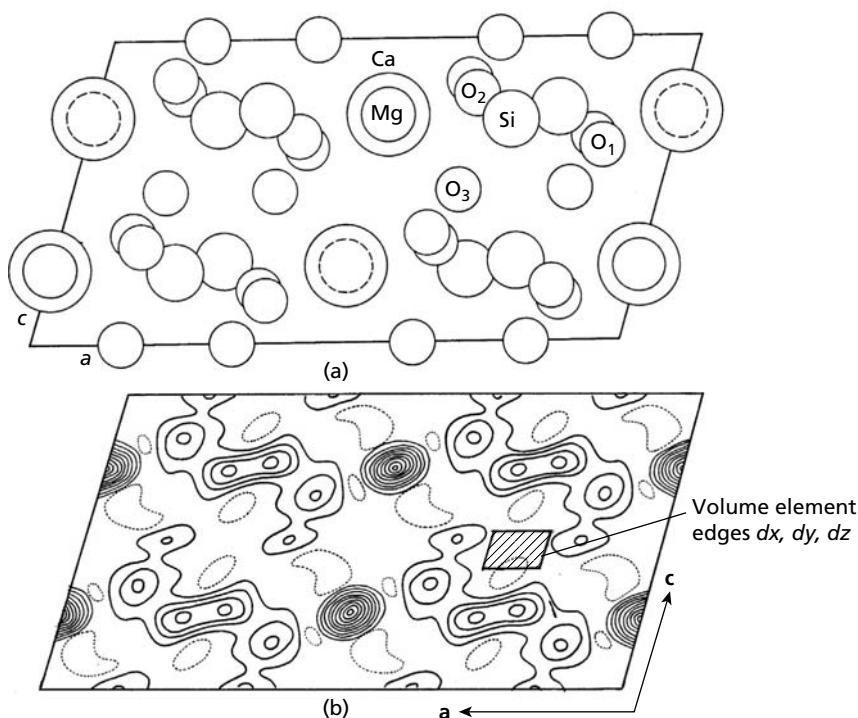


Fig. 13.3. (a) Projection of the atom positions in diopside, $\text{CaMg}(\text{SiO}_3)_2$, on to the (010) face and (b) the corresponding electron density 'contour map'. Also indicated is a volume element dV , at distance coordinates xyz and edge-lengths dx, dy, dz . (Adapted from W.L. Bragg, *Zeitschrift für Kristallographie* **70**, 475, 1929.)

to the *fractional* coordinates used in Chapter 9, i.e. x (fractional) = x (distance)/ a and similarly for y and z . Now we outline a small volume element with edges dx, dy, dz parallel to the unit cell axes a, b, c as indicated in Fig. 13.3(b). Let dV be the volume of this element and V the volume of the unit cell. The *ratio* dV/V equals the *ratio* $dx dy dz / abc$, whence $dV = \frac{V}{abc} dx dy dz$ (for orthogonal axes of course $dV = dx dy dz$).

The number of electrons in the volume element is simply $\rho_{xyz} dV = \frac{V}{abc} \rho_{xyz} dx dy dz$ which we now replace for f_n in the structure factor equation. However, since ρ_{xyz} is a continuous function we must also replace the summation by a triple integral, i.e. along all three axes. Hence the structure factor equation becomes:

$$F_{hkl} = \frac{V}{abc} \int_0^a \int_0^b \int_0^c \rho_{xyz} \exp 2\pi i \left[h \left(\frac{x}{a} \right) + k \left(\frac{y}{b} \right) + l \left(\frac{z}{c} \right) \right] dx dy dz.$$

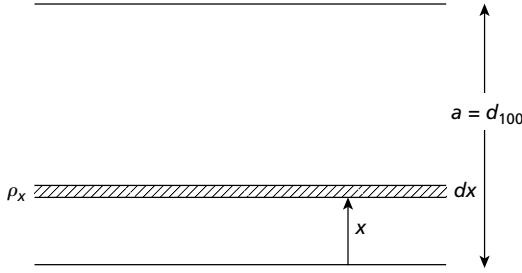


Fig. 13.4. Representation of electron density as a 'slab' of thickness dx parallel to one set of lattice planes of spacing (repeat distance) a .

In order to proceed further with this equation we need to express the electron density ρ_{xyz} in terms of a three-dimensional Fourier series. However, without loss of principle, we shall carry out the analysis in one dimension (corresponding to reflections from one set of crystal planes) and also for a crystal with a centre of symmetry in which the phase angles of the Fourier components are all zero or 180° (i.e. the signs of the Fourier coefficients are all + or -).

Consider Bragg reflection from one set of lattice planes (100) with a spacing $a (= d_{100}$ for orthogonal axes), Fig. 13.4. As we know it is a consequence of Bragg's law (Fig. 8.3) that the interference conditions for the scattered waves are the same irrespective of the positions of the atoms parallel to the planes. Referring to the simple example in Fig. 9.2(b) the atom f_1 may be located anywhere along the dashed line; the phase angle ϕ_1 is solely determined by the component of \mathbf{r}_1 perpendicular to the planes. Hence (Fig. 13.4) we can only specify the electron density, ρ_x , in the x -direction and must therefore replace the volume element with a 'slab' or 'layer' of thickness dx and nominal unit area. The number of electrons in the slab is then simply $\rho_x dx$.

We now express ρ_x in terms of a one-dimensional Fourier series:

$$\rho_x = A_0 + A_1 \cos 2\pi 1 \left(\frac{x}{a} \right) + A_2 \cos 2\pi 2 \left(\frac{x}{a} \right) + \cdots + A_n \cos 2\pi n \left(\frac{x}{a} \right)$$

$$\rho_x = \sum_{n=0}^{n=N} A_n \cos 2\pi n \left(\frac{x}{a} \right).$$

Now we write the structure factor equation for F_{h00} for a crystal with a centre of symmetry and also using distance coordinates instead of fractional coordinates:

$$F_{h00} = \sum_{n=0}^{n=N} f_n \cos 2\pi h \left(\frac{x_n}{a} \right).$$

Substituting f_n by $\rho_x dx$ and replacing, as before, the summation by an integral (ρ_x is a continuous function) we have:

$$F_{h00} = \int_{x=0}^{x=a} \rho_x \cos 2\pi h \left(\frac{x}{a} \right) dx.$$

Then, substituting for ρ_x and interchanging the integral and summation signs we have:

$$F_{h00} = \sum_{n=0}^{n=N} \int_{x=0}^{x=a} A_n \cos 2\pi n \left(\frac{x}{a}\right) \cos 2\pi h \left(\frac{x}{a}\right) dx.$$

Now, remembering the trigonometrical identity:

$$\cos A \cos B = \frac{1}{2} [\cos (A + B) + \cos (A - B)]$$

we have:

$$F_{h00} = \frac{1}{2} \sum_{n=0}^{n=N} A_n \left[\int_{x=0}^{x=a} \cos 2\pi (n + h) \left(\frac{x}{a}\right) dx + \int_{x=0}^{x=a} \cos 2\pi (n - h) \left(\frac{x}{a}\right) dx \right].$$

Now, since n and h are integers the integrals express the total area for one complete cycle of the cosine curve and are thus zero since the areas above and below zero cancel out *except* for the cases where $(n + h)$ and $(n - h)$ are zero, in which case the integrals are $\int_{x=0}^{x=a} \cos 0 dx = a$.

Hence, the equation reduces as follows:

$$\text{When } h = n = 0; \quad F_{000} = \frac{1}{2} A_0 [a + a] = A_0 a$$

$$\text{When } n = h; \quad F_{h00} = \frac{1}{2} A_h [0 + a] = A_h a/2$$

$$\text{When } n = -h; \quad F_{\bar{h}00} = \frac{1}{2} A_{\bar{h}} [a + 0] = A_{\bar{h}} a/2.$$

This is a profound result, first envisaged by W.H. Bragg in 1915. It shows that each Fourier coefficient is equal (apart from the scaling factor a) to the corresponding structure factor. In the general case, where the structure factors are complex numbers, so also are the Fourier coefficients and for reflections hkl the relations are written $F_{hkl} = V A_{hkl}$ where V is the volume of the unit cell.

We may now rewrite the Fourier series equation for ρ_x substituting for $A_0 = (1/a)F_{000}$, $A_h = (2/a)F_{h00}$ and $A_{\bar{h}} = (2/a)F_{\bar{h}00}$ and summing for both positive and negative values of h :

$$\rho_x = \frac{1}{a} \sum_{h=-N}^{h=+N} F_{h00} \cos 2\pi h \left(\frac{x}{a}\right)$$

and for the general three-dimensional case:

$$\rho_{xyz} = \frac{1}{V} \sum_h \sum_k \sum_l F_{hkl} \exp 2\pi i \left[h \left(\frac{x}{a}\right) + k \left(\frac{y}{b}\right) + l \left(\frac{z}{c}\right) \right].$$

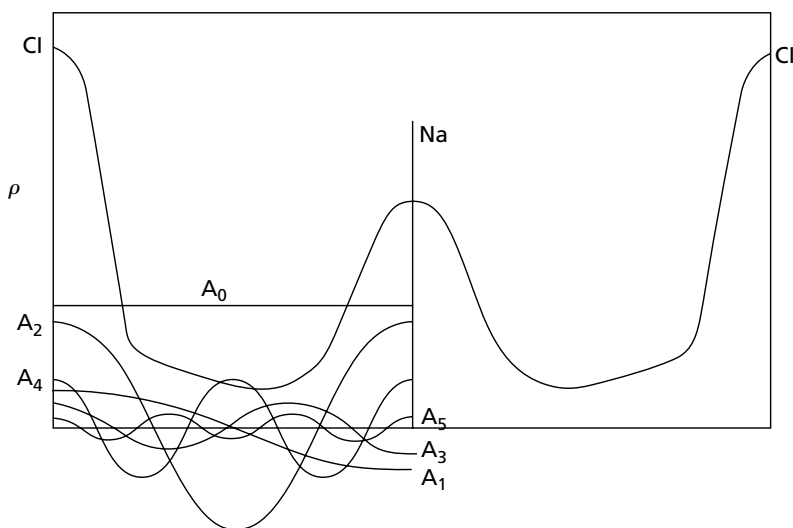


Fig. 13.5. The variation in electron density ρ normal to the (111) planes in NaCl. On the left are shown the Fourier components A_0, \dots, A_5 , each of which correspond to the structure factors $F_{000}, F_{111}, \dots, F_{555}$. (Adapted from *X-ray Analysis of Crystals* by J.M. Bijvoet, N.H. Kolkmeier and C.H. MacGillivray, Butterworths, London, 1951.)

Figure 13.5 shows a one-dimensional Fourier synthesis of the electron density perpendicular to the (111) planes of NaCl which consist of alternate layers of Na and Cl atoms. The electron density, which is symmetrical about both Na and Cl atoms, is the sum of five components, A_0, \dots, A_5 with coefficients corresponding to $F_{000}, 2F_{111}, \dots, 2F_{555}$. For h, k, l all even $F_{hkl} = 4(f_{\text{Cl}} + f_{\text{Na}})$ and for h, k, l all odd $F_{hkl} = 4(f_{\text{Cl}} - f_{\text{Na}})$. Hence, using f vs. $\sin \theta/\lambda$ data from the *International Tables* the F_{hkl} values and hence the values of the Fourier coefficients can be determined.

This of course is a simple case because all of the structure factors are real and positive (origin at a Cl atom). Notice that the electron-density curve lies equally above, and below, the A_0 term which represents a uniform ‘sea’ of electron density.

Hopefully, it is now easy to see how atoms are located at the intersecting maxima of electron density waves from different sets of reflections. Figure 13.6 shows just two waves, $F_{020} \cos 2\pi 2(y/b)$ and $F_{300} \cos 2\pi 3(x/a)$ (where a and b are the cell edge lengths) and (below) their sum and projection as a contour map. Even at this low level of resolution the locations of the atom centres are evident.

For crystals without a centre of symmetry, in which the structure factors are complex numbers and their relative phases are unknown, we need to make use of further mathematical tools, the principal of which is the *Patterson function* which does not specify the location of atoms, but rather the distribution of vectors, representing the distances between them. However, this topic, and the determination of crystal structures in general, are beyond the scope of this book.

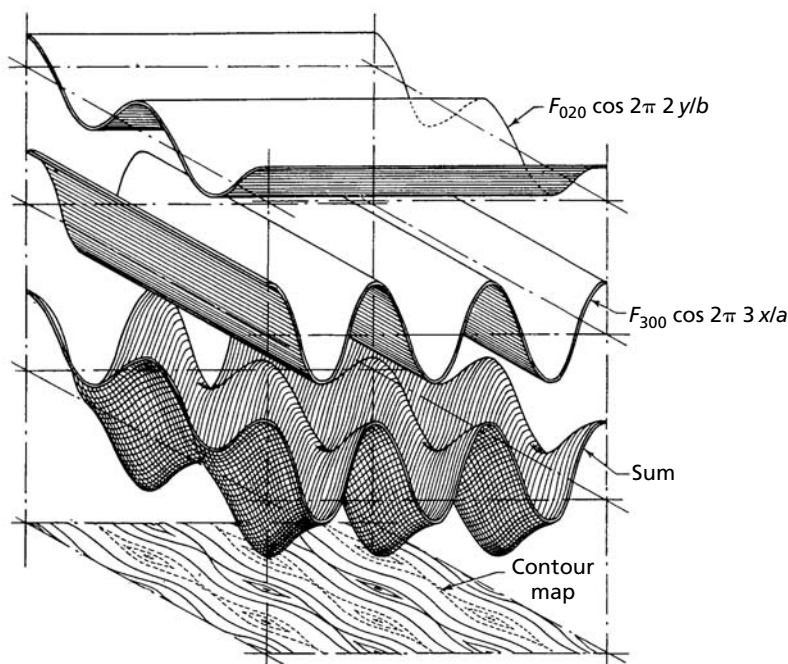


Fig. 13.6. A two-dimensional contour map synthesized from just two Fourier components (upper curves) and their sum (lower curve). Even at this low level of resolution the contour map shows discrete maxima (from *X-ray Crystal Structure* by D. McLachlan, McGraw-Hill Book Company, 1957.)

13.3 Analysis of the Fraunhofer diffraction pattern from a grating

Figure 13.7(a) shows the 'square top' waveform representing the amplitude of light emerging from a grating consisting of six slits ($N = 6$), width d and spacing a , illuminated by an incident plane wave normal to the grating. Figure 13.7(b) shows the corresponding diffraction pattern. First, we recapitulate the simple analysis given in Section 7.4.

- (1) The envelope of the pattern (dashed curve) corresponds to the intensity profile for a single slit with minima at $\sin \alpha$ angles $1^\lambda/d, 2^\lambda/d, 3^\lambda/d$, etc.
- (2) The principal maxima correspond to the conditions for constructive interference between the slits at $\sin \alpha$ angles $1^\lambda/a, 2^\lambda/a, 3^\lambda/a$, etc.
- (3) The minima of the subsidiary maxima correspond to the conditions for destructive interference for the whole grating considered as a single slit of width $6a$, i.e. at $\sin \alpha$ angles $1^\lambda/6a, 2^\lambda/6a, 3^\lambda/6a$, etc.

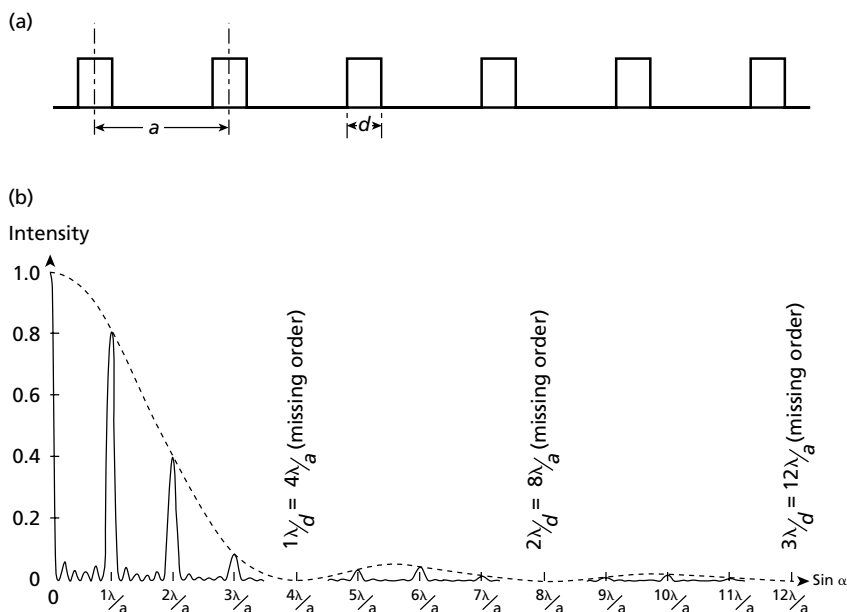


Fig. 13.7. (a) The ‘square-top’ waveform representing the amplitude of light from a diffraction grating consisting of six slits, width d and spacing a and ratio $a/d = 4$. (b) The corresponding diffraction pattern. Note the fourth, eighth, etc. ‘missing orders’ and the number $(6 - 2) = 4$ of the subsidiary maxima between the principal maxima (adapted from *Geometrical and Physical Optics* by R.S. Longhurst, 2nd edn, Longmans, London, 1967.)

- (4) For the given ratio, $a/d = 4$, the first, second, etc. minima of the single slit envelope correspond to the angles of the fourth, eighth, etc. principal maxima (sometimes called ‘missing orders’).

It is easy to see the effects of changing the variables d (slit width), a (slit spacing) and N (number of slits). As d increases the single slit profile (dashed line) becomes narrower. As N increases the principal maxima become narrower, i.e. ‘sharper’ and the subsidiary maxima both increase in number ($N - 2$) and decrease in intensity. As a increases the principal maxima become closer together and the ratio a/d determines the missing orders.

As we have seen in Section 13.2, the amplitudes of the diffracted beams each correspond to a Fourier coefficient of the Fourier analysis of the periodic variation in electron density in a crystal. Precisely the same analysis applies to the amplitudes of the diffracted beams from a grating: they each correspond to a Fourier coefficient of the Fourier analysis of the square-topped waveform. Furthermore, if we take the origin at, say, the centre of a slit, the Fourier coefficients are real (as with the example of NaCl, Fig. 13.5), with signs $+$ (zero phase angle) or $-$ (180° phase angle). Hence, we now have to determine the amplitudes of the diffracted beams as a function of the angle α (rather than simply determining the angles for either destructive or constructive interference). We do this by means of *amplitude–phase diagrams*; first for a single slit and then for a grating of N slits.

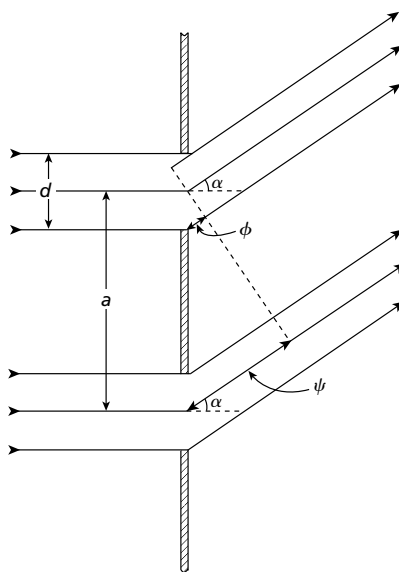


Fig. 13.8. A diffraction grating indicating the path difference $d/2 \sin \alpha$ (phase difference ϕ) between a Huygens wavelet at the centre and either edge of a slit and the path difference $a \sin \alpha$ (phase difference ψ) between the slits.

Single slit width d (Fig. 13.8)

When $\alpha = 0$, all the Huygens wavelets are in phase and their sum, a straight line, has amplitude, say A_0 (Fig. 13.9(a)). Now consider the situation at angle α . Taking the centre of the slit as the origin, the path difference, PD, between the wavelet at the centre of the slit and those at the edge is $d/2 \sin \alpha$ and the phase difference $\phi = 2\pi/\lambda(\text{PD}) = \pi d/\lambda \sin \alpha$; $+\phi$ for the wavelet at the lower edge and $-\phi$ for the wavelet at the top edge. The amplitude–phase diagram is now the arc of a circle, length A_0 , as shown in Fig. 13.9(b) with the phase differences $+\phi$ and $-\phi$ indicated. The resultant amplitude is given by A , the chord of the circle. From the geometry $A_0 = r2\phi$ and $A = r2 \sin \phi$ where r is the radius of the circle. Hence $A = A_0 \frac{\sin \phi}{\phi}$. This function, $\frac{\sin \phi}{\phi}$, occurs so commonly in optics that it is given a special name, $\text{sinc} \phi$ (pronounced sink ϕ). Its operation can be seen in Fig. 13.9. As ϕ (or α) increases, the arc of the circle ‘winds up’ until $\phi = \pi$ (or $\sin \alpha = \lambda/d$) at which point $A = 0$ (Fig. 13.9(c)). Then, as ϕ increases further it ‘winds on itself’ and the resulting amplitude A is reversed in sign (Fig. 13.9(d)), and so on.

The function, $\text{sinc} \phi$, plotted vs. $\sin \alpha$ to the right and vs. ϕ to the left is shown in Fig. 13.10 (solid line) together with its square (dashed line), representing the intensity distribution from a single slit.

N slits, width d , spacing a (Fig. 13.8)

The path difference, PD, between corresponding points between adjacent slits is $a \sin \alpha$ and the phase difference $\psi = 2\pi/\lambda(\text{PD}) = \frac{2\pi a}{\lambda} \sin \alpha$. Again, when $\alpha = 0$, all the

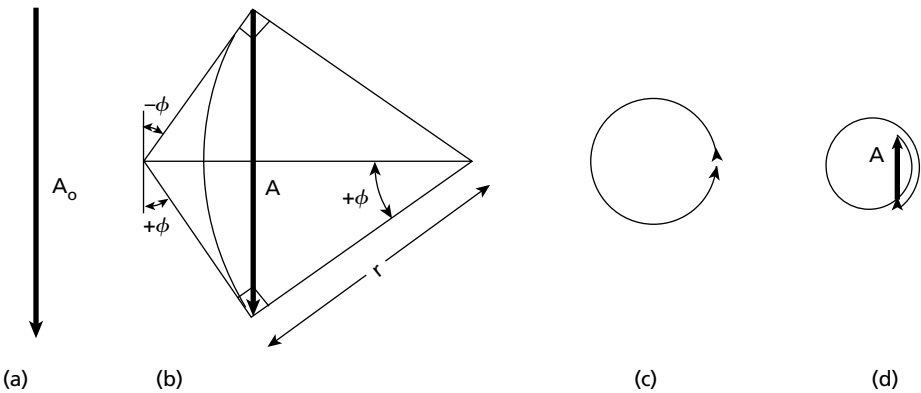


Fig. 13.9. The amplitude–phase diagram for a single slit: (a) $\alpha = 0$; all the Huygens wavelets are in phase; (b) for phase difference $\pm\phi$ between the wavelet at the centre and those at the edges of the slit; (c) for phase difference $\phi = \pi$, the amplitude A is zero; (d) for $\phi > \pi$, the amplitude A is reversed in sign.

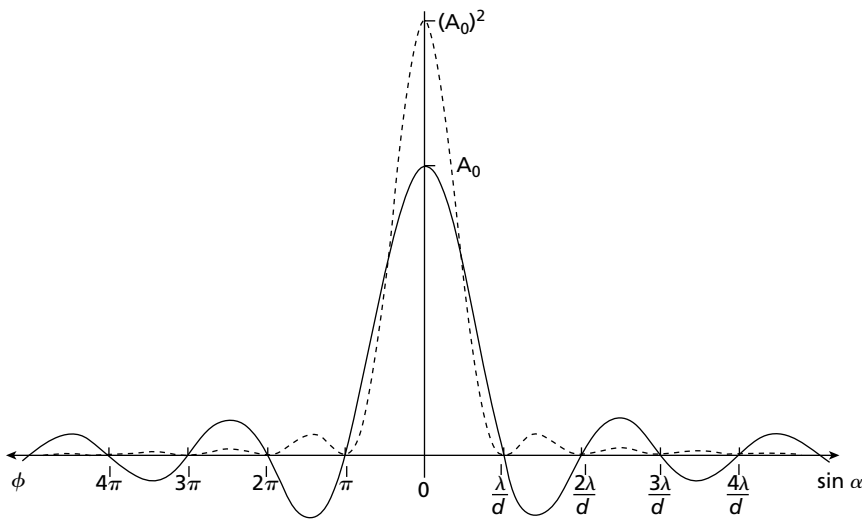


Fig. 13.10. The function $A_0 \sin c\phi$ vs. $\sin \alpha$ (plotted to right) or vs. $\phi = \frac{\pi d}{\lambda} \sin \alpha$ (plotted to left) representing the amplitude distribution from a single slit (or aperture) (solid line) and its square representing the intensity (dashed line). In this example $A_0 = 1.5$. (Courtesy of Mr D.G. Wright.)

slits scatter in phase and the amplitude $A_T = A_0$. At angle α we again construct an amplitude–phase diagram—but not as before as the arc of a circle of constant length, but as a series of chords, each of amplitude A and differing in phase by ψ (Fig. 13.11). For each chord $A/2 = R \sin \psi/2$ where R is the radius. For N chords half the total angle is

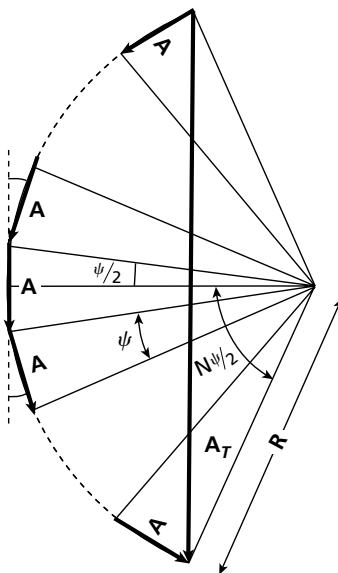


Fig. 13.11. The amplitude-phase diagram for a grating of N slits and for phase difference ψ between the slits, total amplitude $= A_T$. Note that (unlike the single slit) the series of chords (the arc of the circle-dashed line) is not of constant length.

$N\psi/2$ and $A_T/2 = R \sin N\psi/2$. Substituting for R and A we have:

$$A_T = A_0 \frac{\sin \phi}{\phi} \cdot \frac{\sin N\psi/2}{\sin \psi/2} \quad (\phi = \pi d / \lambda \sin \alpha, \psi = 2\pi a / \lambda \sin \alpha \text{ and } \psi/\phi = 2a/d).$$

The first term in this expression is called the *single-aperture term* and the second is called the *grating term*. In computing the amplitude, A_T , and intensity, $(A_T)^2$, distributions the equation may be simplified by using only two variables, ϕ and N , and a given ratio of slit spacing/slit width, a/d ; i.e. $\sin N\psi/2 = \sin N\phi a/d$ and $\sin \psi/2 = \sin \phi a/d$, hence

$$A_T = A_0 \frac{\sin \phi}{\phi} \cdot \frac{\sin N\phi a/d}{\sin \phi a/d}.$$

For $N = 6$ and $a/d = 4$ this function is shown in Fig. 13.12(a) and its square, representing the intensity distribution for the diffraction grating, is shown in Fig. 13.12(b) below. Notice that the phases of the amplitudes of the diffraction maxima alternate between $+$ and $-$ (Fig. 13.12(a)) but that this phase information is lost in the intensity distribution (Fig. 13.12(b), which corresponds of course to the experimental intensity profile of Fig. 13.7(b)).

Figure 13.12(c) shows the effect of increasing the number of slits, N , from 6 to 20. The principal maxima are now sharper and the subsidiary maxima are now greater in number but much reduced in intensity. Finally, Fig. 13.12(d) shows the effect of increasing a/d , from 4 to 10 and for $N = 4$. The principal maxima approach closer together and, as pointed out above, merge into one continuous function when a/d approaches infinity.

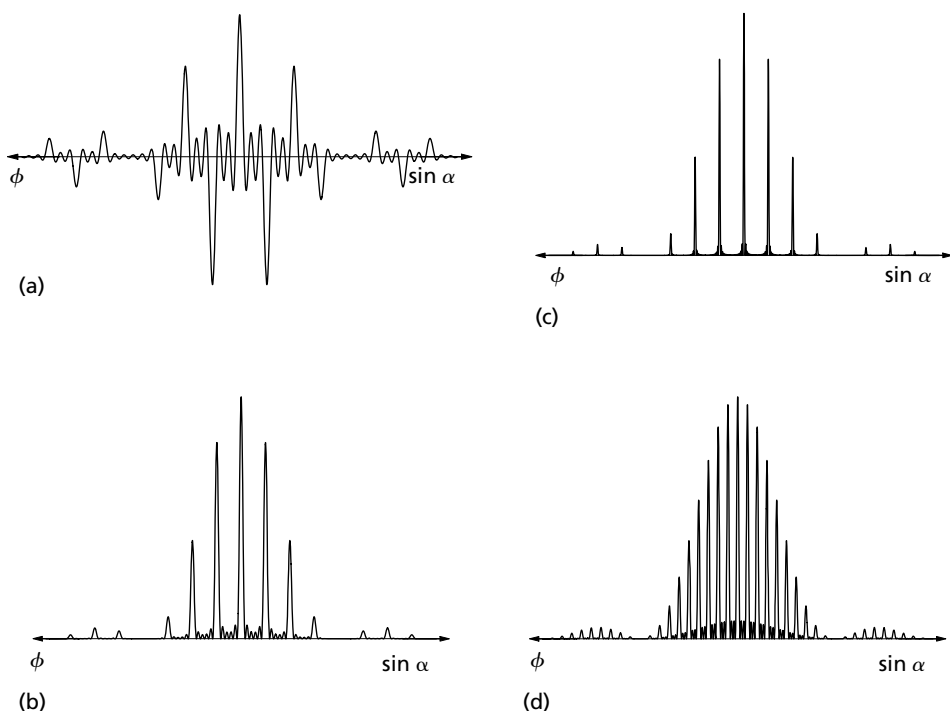


Fig. 13.12. (a) The amplitude distribution A_T for a grating with $N = 6$ slits and $a/d = 4$, and (b) the corresponding intensity distribution $(A_T)^2$. (c) The effect on the intensity distribution of increasing the number of slits to 20—the principal maxima are sharper and the subsidiary maxima are insignificant. (d) The effect of increasing a/d to 20 ($N = 4$)—the principal maxima approach closer together. (Courtesy of Mr D.G. Wright.)

13.4 Abbe* theory of image formation

The formation of an image in a microscope may be considered to be carried out by the objective lens in two stages. First, the lens collects some (not all) of the parallel wavetrains resulting from the diffraction and interference of light across the grating into a series of diffraction peaks (sometimes called ‘spectra’) situated in the back focal plane. In this sense the objective lens performs a Fourier analysis of the light emanating from the grating as shown diagrammatically in Fig 13.12(a). A screen placed here records their positions and intensities (Fig 13.12(b)) or the diffraction peaks may be observed by simply removing the microscope eyepiece and observing the back focal plane either directly or with the aid of a close-focused telescope.¹

* Denotes biographical notes available in Appendix 3.

¹ Phase contrast and polarized-light microscopes often incorporate a *Bertrand lens* below the eyepiece which when ‘flipped in’ allows observation of the back focal plane directly.

The wavetrains emanating from the diffraction peaks then spread out and interfere to form a set of interference fringes in the image plane—in short the objective lens then performs a Fourier synthesis of the amplitude distribution of the light in the back focal plane, the amplitudes of the zero, first, second, etc. diffraction peaks or spectra corresponding to the zero, first, second etc. Fourier coefficients. And the greater the number of terms included in the Fourier synthesis, i.e. the greater the number of diffracted beams intercepted by the objective lens, the closer does the image correspond to the amplitude distribution across the grating. Figure 13.13(a)–(d) shows the evolution of the image of a diffraction grating with a ‘square-top’ waveform with $a/d = 4$ (as in Fig. 13.7(a)) synthesized with an increasing number of Fourier terms.

This two-stage image formation process may also be understood in simple terms by making use of Abbe’s ‘classic’ representation of image formation (Fig. 13.14). A plane wave (Fraunhofer case) incident normally on the narrow-line grating **G** is diffracted and the diffracted beams are collected and focused by the objective lens **L** to give a series of diffraction peaks or spectra situated in the back focal plane of the objective lens. Three such spectra are shown in Fig. 13.14, the zero order S_0 and the first orders S_1 and S'_1 each side. The waves then ‘spread out’ and interfere in the image plane. The wavefronts are shown on the right of Fig. 13.14; each (curved) line may be considered to represent the ‘crest’ of the waves. Where all three intersect, at I_1 , I_2 and I_3 , we have complete constructive interference and these interference maxima reproduce the periodicity of the grating—in short the line-spacing of the grating is resolved in the image plane. It is not a ‘perfect’ image because half-way in between I_1 , I_2 and I_3 we see that the two waves from S_1 and S'_1 interfere constructively but that from S_0 interferes destructively giving ‘subsidiary’ maxima of one-third the amplitude (and one-ninth the intensity) of the maxima at I_1 , I_2 and I_3 . (Such subsidiary maxima are also evident in Fig. 13.13(a)–(c).)

Figure 13.14 may also be used to see the effect of ‘blocking off’ one or more of the waves emanating from S_0 , S_1 and S'_1 . If we ‘block off’, say S'_1 then again we have interference maxima at I_1 , I_2 and I_3 and the amplitude distribution will be a simple cosine curve, again reproducing the periodicity of the grating. If we ‘block off’ any two, say S_1 and S'_1 , then clearly there will be no interference in the image plane but just (for a narrow slit grating) a uniform distribution of light—the periodicity of the grating is not resolved. Finally (and this is an important case), if we ‘block off’ the zero order, S_0 , then we have constructive interference (for the waves from S_1 and S'_1) at I_1 , I_2 and I_3 and half-way in between giving a (cosine curve) of periodicity *twice* that of the grating.

In order to demonstrate his theory of image formation (which was by no means immediately accepted, particularly by the English amateur microscopists), Abbe devised a special slide carrying diffraction gratings—the *Diffraktionsplatte*—together with a device enabling diaphragms to be inserted into the objective lens back focal plane to prevent (i.e. ‘block off’) some parts of the diffraction pattern from contributing to the image. This equipment was included in the Zeiss catalogue in 1878 and was available intermittently until the 1960s. Abbe’s demonstrations have since been extended by Dr P.J. Evennett,² examples of which are shown in Figs 13.15 and 13.16.

² P.J. Evennett, Abbe and the development of the modern microscope, *Proc. Roy. Micros. Soc.*, **31**, 283 (1996).

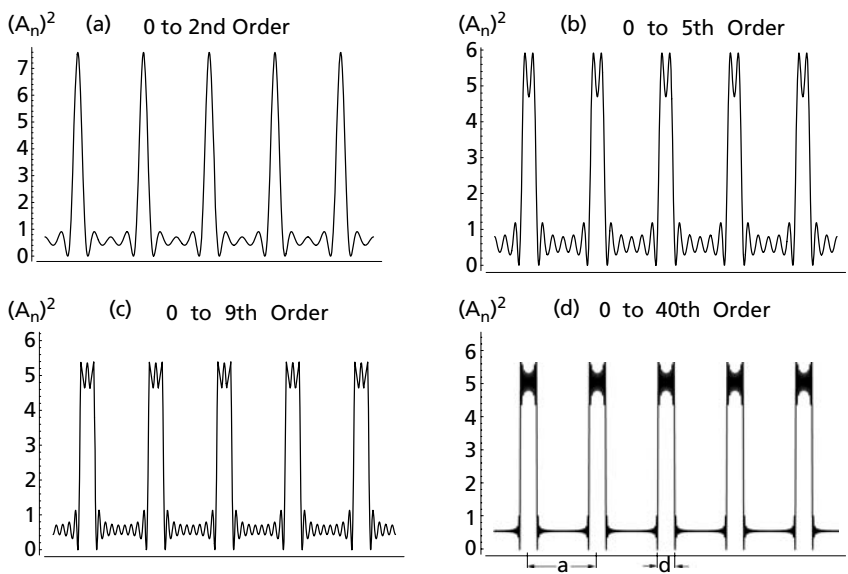


Fig. 13.13. The image of a diffraction grating with a ‘square-top’ waveform (as in Fig. 13.7(a)), $a/d = 4$ synthesized with an increasing number of Fourier terms (a)–(d). (Courtesy of Mr D.G. Wright.)

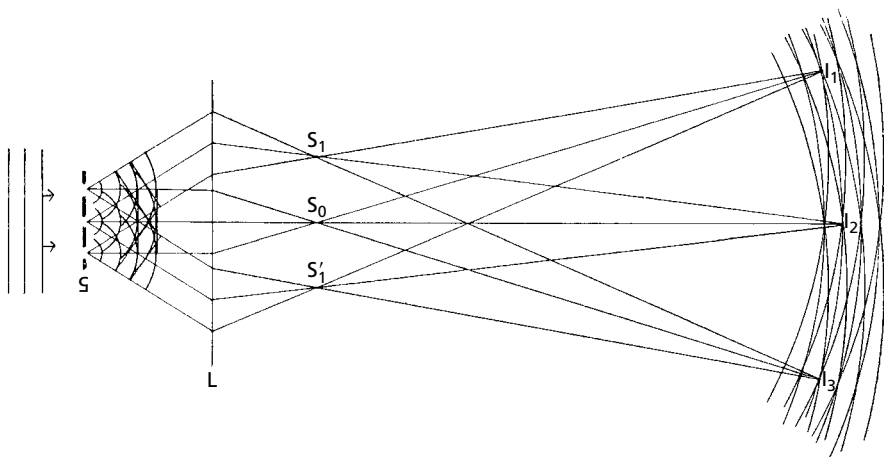


Fig. 13.14. Abbe’s representation of image formation in a microscope. A plane wave (left) incident upon a narrow-slit grating G is diffracted and the sets of parallel diffracted beams are intercepted and focused by the objective lens L to give diffraction peaks (or spectra) S_0 , S_1 and S'_1 situated in the back focal plane, the light from which interferes to give maxima I_1 , I_2 and I_3 in the image plane (see text).

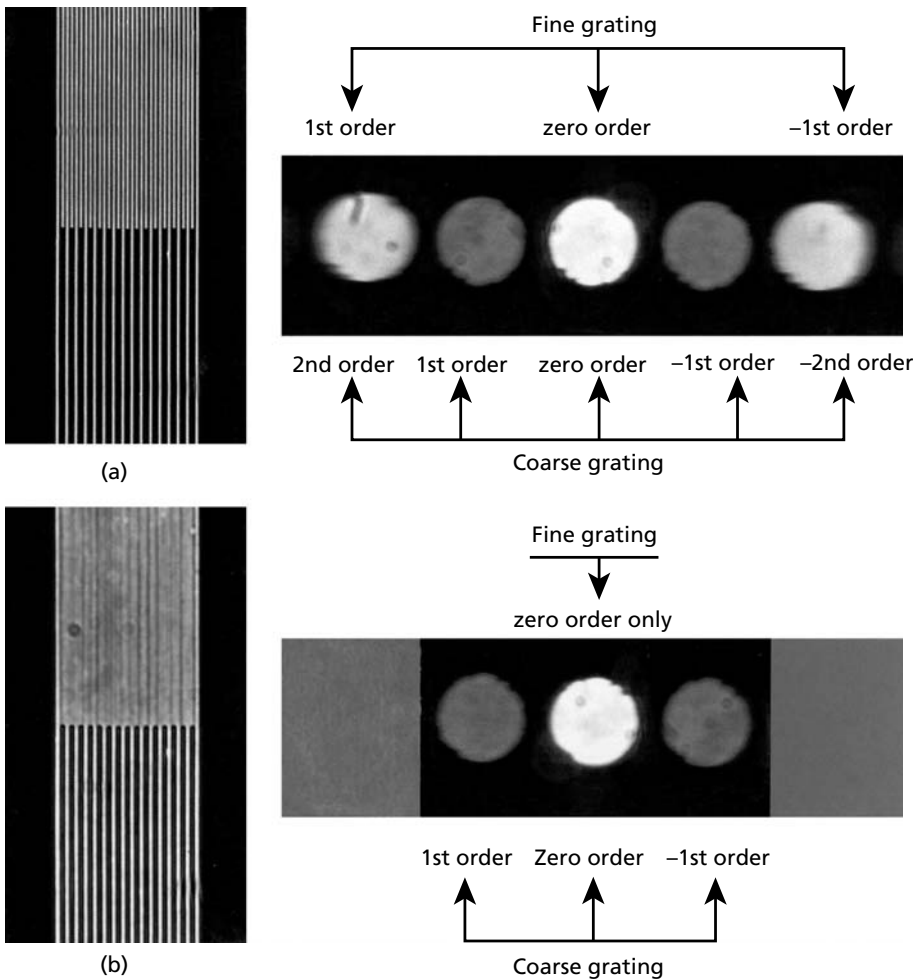


Fig. 13.15. (a) The image of a diffraction grating consisting of coarse and fine line spacings and the corresponding diffraction pattern. (b) The image showing loss of resolution of the fine lines when the first-order diffraction spots are excluded by a slit-diaphragm. (Courtesy of Dr P.J. Evennett.)

Figure 13.15(a) shows the image of a diffraction grating with regions with two line spacings and the corresponding diffraction pattern taken from both regions with the diffraction spots labelled accordingly. When a wide-slit diaphragm is inserted as in Fig. 13.15(b) the first-order spots from the fine grating do not contribute to the image and the lines are not resolved. Similarly, Fig. 13.16(a) shows the image of a square cross-grid grating and its associated diffraction pattern (see also Figs 7.1 and 7.3). When a slit diaphragm is inserted as in Figs 13.16(b) and (c), the periodicity is only resolved in the direction normal to the lines of the diffraction spots—and the spacing of the lines

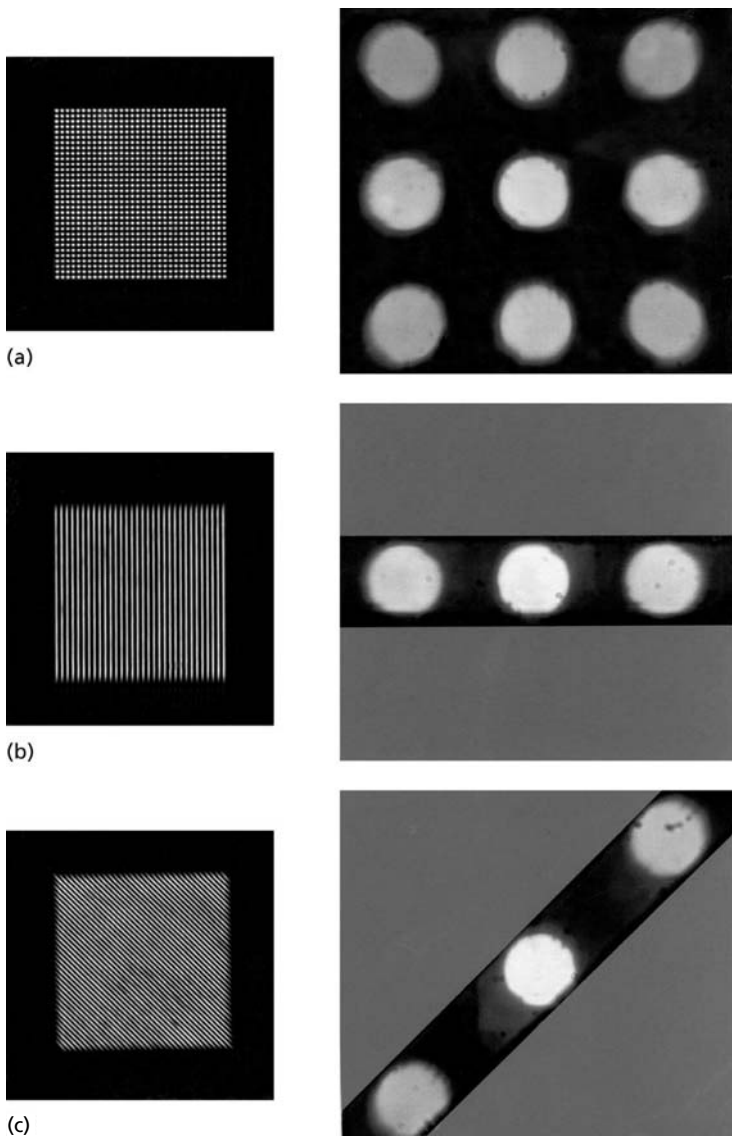


Fig. 13.16. (a) The image of a square cross-grid grating and the corresponding diffraction pattern. (b) and (c) The periodicity of the grating is only resolved in the direction normal to the line of diffraction spots which contribute to the image. (Courtesy of Dr P.J. Evennett.)

is of course inversely proportional to the spacings of the diffraction spots. We have, in short, the relationship between the lattice and the reciprocal lattice. How simple it all is!

Appendix 1

Computer programs, models and model-building in crystallography

Computer programs now contribute a significant ‘learning resource’ in crystallography since, unlike the illustrations in books, images of crystal structures, lattices and space groups can be created and orientated at will such that a student can more readily appreciate the dispositions of atoms and symmetry elements. The same applies to the three-dimensional construction of the Ewald reflecting sphere and reciprocal lattice in providing an understanding of the geometry of diffraction. Moreover, some computer programs make use of anaglyphs such that the images appear to ‘emerge’ from the screen as three-dimensional objects when viewed with the appropriate left and right eye filter spectacles.

It might be supposed therefore that such computer programs have superseded models as a learning resource. I believe that this is not the case: what is missing is the *tangible* element, the enhancement of understanding brought about by the link between hand and eye. In short, models provide the basis for crystallographic *object lessons*. And by models I do not only mean the crystal-model building kits which are commercially available but the simpler ones which you can make yourself from cardboard or plastic spheres or even such everyday objects as clothes pegs, tennis balls or plant stems which provide the very first lessons in understanding symmetry.

Listed below are (1) a selection of computer programs which are of value in learning crystallography (though many include also much more advanced material) and (2) some suggestions for model-building and a list of suppliers of model-building kits.

A1.1 Computer programs in crystallography

The International Union for Crystallography (IUCr) maintains a website with links to many others. Its URL is:

(IUCR) <http://www.iucr.org/>

Useful links are to the American Crystallographic Association (ACA), the British Crystallographic Association (BCA), Crystallography World-Wide (CWW) and the European Crystallographic Association (ECA) whose URLs are:

(ACA) <http://www.hwi.buffalo.edu/ACA/>

(BCA) <http://bca.cryst.bbk.ac.uk/BCA/index.html>

(CWW) <http://www.iucr.org/cww-top/crystal.index.html>

(ECA) <http://area.ba.cnr.it/eca/>

The following list provides brief descriptions of some programs currently available.

Ca. R. Ine Crystallography, version 3.1 and 4.0 by Cyrille Boudias and Daniel Monceau, CIRIMAT Laboratory, CNRS INPT UPS, ENSIACET, 31077 Toulouse, France, distributed by C Sellier, Centre de Transfert UTC BP 50149, 60200 Compiègne. Tel. 03 44 23 45 30, e-mail: christine.sellier@utc.fr

CARINE CRYSTALLOGRAPHY software is distributed in two versions (both on the same disk). The new version (4.0) is focused on 3D modelling of crystals, including surfaces and interfaces. The 3.1 version is used for simple rendering and for simulation and analysis. CaRIne 3.1 exposes in a clear way the relationships between different geometrical representations of crystals and brings them together in a user friendly interface: stereographic projections, X-ray diffraction on powders, reciprocal lattices in 3D and 2D and (*hkl*) plane-based calculation lists. All the unit cells created with the 4.0 version can be sent directly to the 3.1 version via the [Send to CaRIne 3.1] command. Daniel Monceau also edits the 'E-materials' website: <http://e-materials.ensiacet.fr/>.

Crystallographica by A R Renshaw, Oxford Cryosystems, 3 Blenheim Office Park, Long Hanborough, Oxford OX29 8LN, UK, e-mail: AlexRenshaw@oxfordcryosystems.co.uk.

CRYSTALLOGRAPHICA runs under any version of Windows including 3.1, 95, 98, NT, 2000, XP and Vista and is available free from www.crystallographica.com. The package includes structure and reciprocal lattice displays, powder simulation, graphing (including common X-ray data formats) and a unique crystallographic scripting language, all supported by comprehensive help and numerous example scripts and structures. See also Crystallographica—a software toolkit for crystallography, *J. Appl. Cryst.*, **30**, 418 (1997).

CrystalMaker by David C Palmer, CrystalMaker Software Ltd., Centre for Innovation and Enterprise, Begbroke Science Park, Sandy Lane, Yarnton, Oxford, OX5 1PF, UK, e-mail: info@crystalmaker.com.

CRYSTALMAKER is a program for building, displaying and manipulating crystal and molecular structures, including real-time photo-realistic graphics and 'out-of-the-screen' three-dimensional displays. CrystalMaker allows visualization of massive structures (millions of atoms), with fast bond and polyhedra generation and the display of thermal ellipsoids. New features include the ability to seamlessly browse multiple structures in the same window and generate animations and movies (e.g. showing structural changes resulting from temperature or pressure). The program supports a wide range of data formats, exports high-resolution graphics in a wide range of formats, plus Quick-Time movies and VR objects—and works with the 'SingleCrystal' and 'CrystalDiffract' diffraction software.

CrystalMaker is available in two versions: for Mac (a 'universal binary' application that runs natively on the new Intel-based Macs, as well as the older PowerPC-based Macs), and for Windows computers running XP or Vista. The software is applicable in the areas of materials science, solid-state physics, chemistry, earth sciences and crystallography.

Crystals by David Watkin, Chemical Crystallography Department, University of Oxford, Oxford, OX1 3TA, UK, e-mail: david.watkin@chem.ox.ac.uk.

CRYSTALS is available without charge for non-commercial use from the web server xtl.chem.ox.ac.uk. It provides all the basic and advanced facilities needed for crystal structure determination, plus a visualization window which continuously displays the structure and a graphics module for manipulating and drawing the structure. A 'guide' leads the user through all the stages of a normal crystal structure analysis and the manual is included as Postscript files and as browsable html. The distribution kit includes versions of SHELXS, SIR92 and Superflip (with the author's permissions). Tutorials and data are included for a number of demonstration structures. A scripting interface enables the program to be customized as a teaching aid, and two extensible examples are included.

Introduction to Crystallography and Diffraction by Anne Fretwell and Peter Goodhew, University of Liverpool, Liverpool, L69 3BX, UK, e-mail: goodhew@liv.ac.uk

INTRODUCTION TO CRYSTALLOGRAPHY is part of (one module of 18) a CD-ROM which covers the basics of materials science and related subjects at undergraduate level, viz Crystals, 2-D and 3-D Crystallography, Crystal Structures and Indexing Directions and Planes. Embedded multiple choice questions and interactive simulations and a comprehensive glossary are included.

DIFFRACTION runs live on the web from the MATTER site and includes geometry, the Ewald sphere, structure factors, electron approximations, etc. The best URL for both programs is the root MATTER site at www.matter.org.uk.

!Polynet, !Polysymm and !Stellate by Kate Crennell, 'Fortran Friends', PO Box 64, Didcot, Oxon, OX11 0TH. Website: <http://fortran.orpheusweb.co.uk/poly/prodip.htm>

THESE POLYHEDRA PLOTTING PROGRAMS can run on RISCOS systems or on PCs under the Virtual Acorn emulator. They show the construction and symmetries of the Platonic and Archimedean solids and their duals and some of their stellations. For details see the website above, from which demonstration copies of the software may be freely downloaded. Free copies of plans to cut out and construct 3D models are also available to make space-filling models and examples of each of the crystal classes.

A1.2 Crystallography models, model-building and suppliers

The use of crystal models in the teaching or exposition of crystallography has a long history, the first perhaps being the terracotta models of Rome de L'Isle (1783). Later, comprehensive sets in wood were made by geological suppliers, particularly by the German firm of Krantz. Glass, aluminium, paper and card have also been used. Some of the strangest and most intriguing crystal models were those made by William Barlow. His workshop is said to have resembled a toy factory with thousands of balls of various sizes and colours and plaster dolls' hands which he arranged in frameworks to demonstrate enantiomorphism and space group symmetry. Unfortunately, toy suppliers, unlike their Victorian forebears, are today unwilling or unable to provide dolls' hands for such crystallographic purposes.

Cardboard/paper models of polyhedra are very easily constructed. 'Ready-made' templates are available on the BCA website and also in several **Tarquin Publications** (99

Hatfield Road, St Albans, AL1 4JL, UK; www.tarquinbooks.com), e.g. *Make Shapes*, books 1 and 2 by Jenkins and Wild; *Paper Polyhedra in Colour* by Jenkins and Bear; *Geodesic Domes* by van Loon and the classic text *Mathematical Models* by Cundy and Rollett. By making collections of polyhedra and glueing them together you can see, in a very direct way, those which are space-filling and those which are not. You can also represent twinned and multiply-twinned crystals. Figure A1.1 shows an interesting example. Each tetrahedron represents a ccp crystal, the faces of which correspond to the $\{111\}$ twin planes. The twinning angle across each face is 70.53° and the total angle for the five twins is $70.53^\circ \times 5 = 352.65^\circ$, i.e. very close to 360° . Such a multiply-twinned ccp crystal shows ‘pseudo-pentagonal’ symmetry—not to be confused with the pentagonal symmetry of quasicrystals (see Section 4.9).

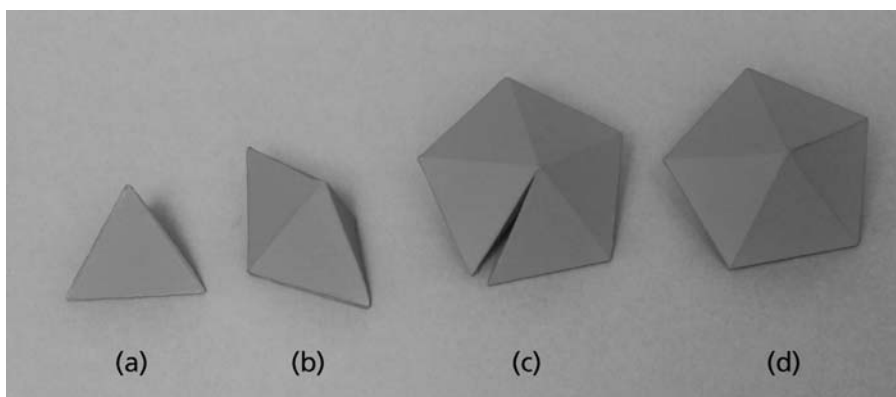


Fig. A1.1. (a) The faces of the tetrahedron correspond to the $\{111\}$ twin planes in a ccp crystal; (b) a singly-twinned crystal; (c) a multiply-twinned crystal (five twins) showing pseudo-pentagonal symmetry. By a small distortion of the model the pentagonal symmetry of a quasicrystal (d) is obtained.

Plastic (polystyrene) sphere models of the ccp and hcp metal structures may be made by glueing spheres together to form close-packed hexagonal layers and then stacking them together in the ABCABC... and ABAB... sequences. The insertion of smaller (e.g. plasticine) spheres shows the sizes and distribution of the interstitial sites. The more complex stacking sequences (e.g. in SiC (Fig. 1.27) or of the oxygen atoms in Al_2O_3) can also be demonstrated. The bcc metal structure is best made by making layers of the closest-packed $\{110\}$ planes (Fig. 1.9(b)) and stacking them in the ABAB... sequence, atoms in each layer being located at the ‘saddle-points’ of the layer below. Notice that the layer-separation is reduced if the layers are slipped into the recesses each side of the saddle-points, giving a more closely packed but no longer cubic structure.

Childrens’ wooden building bricks come in a variety of shapes—cubes, tetragonal, hexagonal and orthorhombic prisms—and (apart from building castles), may be used to represent the 32 point groups (monoclinic and triclinic models must be home-made).

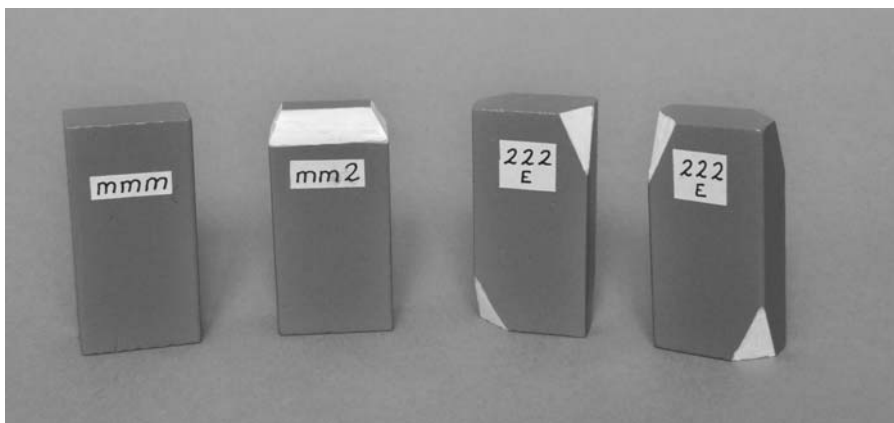


Fig. A1.2. Models showing the symmetries of the three orthorhombic point groups: mmm , $mm2$ and 222 . Note the two enantiomorphic forms of point group 222 .

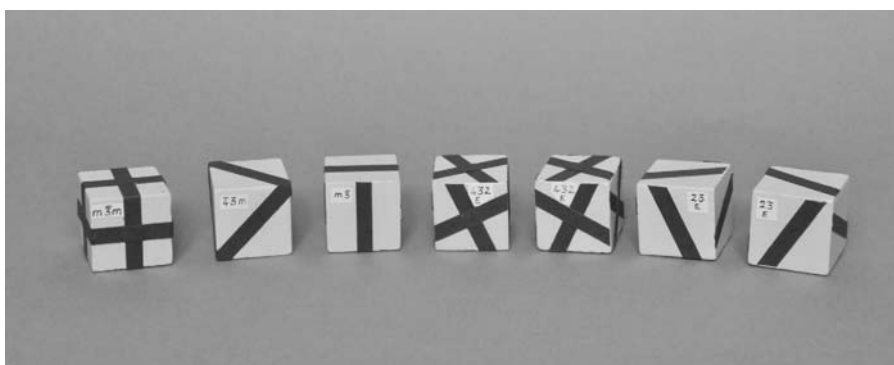


Fig. A1.3. Models showing the symmetries of the five cubic point groups $m\bar{3}m$, $\bar{4}3m$, $m\bar{3}$, 432 and 23 . Note the two enantiomorphic forms of point groups 432 and 23 .

The plain models represent the holosymmetric point groups; those of lower symmetry may be made by cutting-off appropriate corners and edges (as shown in Fig. A1.2 for the three orthorhombic point groups) or by marking the faces (as shown in Fig. A1.3 for the five cubic point groups). Bricks may also be cut across a non-mirror plane and the two halves then rotated 180° to show the geometry of twinning. Clearly, many beautiful multiply-twinned crystals can be created in this way.

Model-building kits and complete models are obtainable from a number of suppliers of which the following is a selection.

Cochranes of Oxford Ltd., 29 Groves Yard, Shipton Road, Milton under Wychwood, Chipping Norton, Oxford, OX7 6JP, UK; <http://www.cochranes.co.uk> makes Orbit™ and Minit™ molecular model kits based on plastic atom centres colour-coded according

to the element which are joined together with plastic tubes of the appropriate lengths. The scale of the Orbit™ system is $30\text{ mm} = 1\text{ Å}$ when used for organic and inorganic chemistry and typically $12\text{--}25\text{ mm} = 1\text{ Å}$ for crystal structures. For the smaller-scale Minit™ system the scale is typically $10\text{--}15\text{ mm} = 1\text{ Å}$. Also available are larger-scale Unit™ molecular models in which the atoms are joined together with rigid aluminium or flexible vinyl tubes.

Miramodus Limited (formerly Beevers Miniature Models Unit), c/o School of Chemistry, West Mains Road, Edinburgh, EH9 3JJ; <http://www.miramodus.com> produces crystal models for display and teaching on the scale of $1\text{ cm} = 1\text{ Å}$. Coloured PMMA balls are individually drilled and connected with stainless steel rods to give accurate and attractive models of any crystal or molecular structure. Models can be made to individual requirements, including mounting for gifts or presentations and are suitable for museum-quality displays. Rods and balls can also be supplied for self-assembly.

Spirling Enterprises Ltd., Billingshurst, West Sussex, RH14 9EZ, UK; <http://www.molymod.com> makes the Molymod™ molecular model system. The colour-coded atom centres are joined together with flexible mushroom-shaped links. A wide range of sets for building organic and inorganic molecular models is available as well as DNA (and RNA) model kits in which abstract-shaped parts are designed to represent the bases, sugar and phosphate groups of the double helix.

3-D Molecular Designs, 2223 North 72nd Street, Wauwatoza, WI 53213, USA; <http://3DMolecularDesigns.com> make molecular and crystal models in which the atoms or molecules are held together by internal magnets. These models simulate, for example, the hydrogen bonding and polarity of water molecules in the structures of liquid water and ice.

Appendix 2

Polyhedra in crystallography

In this Appendix the crystallographic and geometrical properties of the polyhedra which are introduced and briefly described in this book are summarized. The word comes from the Greek meaning many (poly) faces or planes (hedra). The (simpler) polyhedra are simply described by their number of faces as indicated below. It is curious that only the hexahedron has a ‘simple’ name—the cube.

Polyhedron names

For the simpler polyhedra the prefix indicates the number of faces. Those of importance in crystallography are: tetra (4), penta (5), hexa (6), octa (8), deca (10), dodeca (12), icoso (20), icosidodeca (32). Further prefixes indicate the shapes of the faces themselves and/or their symmetry, e.g. pentagonal or rhombic dodecahedra (polyhedra with twelve pentagonal or rhombic (diamond shaped) faces respectively), or trapezohedra (polyhedra in which the twelve rhombic faces are arranged in hexagonal symmetry). Further prefixes such as triakis or pentakis indicate that plane triangular or pentagonal faces are replaced by a group of three or five faces respectively. Thus a triakis tetrahedron has twelve (4×3) faces, and so on.

Truncation

Many polyhedra are described as ‘truncated’ which simply means ‘cutting off the corners’ of a polyhedron—and the truncated polyhedron thus created depends on ‘how much’ of the corners are cut off. As shown in Fig. A.2.1(a)–(c) the truncated cube, cubeoctahedron and truncated octahedron are created by cutting increasing amounts off the cube corners. Alternatively, we could ‘start off’ with an octahedron and obtain the same polyhedra by again cutting off the corners as shown in Fig. A.2.1(d)–(f). Truncation can also be applied to the newly-created corners and edges: the possibilities are almost endless and a whole series of polyhedra, with many faces of different shapes and sizes (and with rather long descriptive names) can be created. The process has its analogy in the beautiful patterns of faces which can develop in crystal growth.

Duality

Polyhedra of identical symmetry are said to be dual if the faces of one correspond to the corners (or vertices) of the other and vice versa. Thus the cube and octahedron are duals: the eight vertices of the cube correspond to the eight faces of the octahedron and,

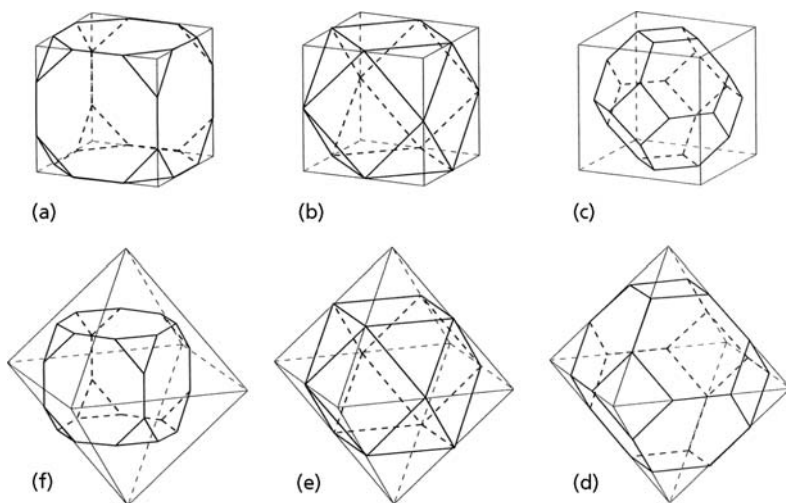


Fig. A2.1. Alternative truncation procedures to create a truncated cube, cubeoctahedron and truncated octahedron. (a) \rightarrow (b) \rightarrow (c) successive truncation of a cube; (d) \rightarrow (e) \rightarrow (f) successive truncation of an octahedron. (From *Polyhedra* by Peter R. Cromwell, Cambridge University Press, Cambridge, 1999.)

conversely, the six vertices of the octahedron correspond to the six faces of the cube. Similarly, the pentagonal dodecahedron and icosahedron are duals. The tetrahedron is *self-dual*: the four vertices of one correspond to the four faces of the other and vice versa.

Classification of polyhedra

There is an enormous number of polyhedra, including beautiful star-shapes with re-entrant faces. However, those of most importance in crystallography are the Platonic and Archimedean polyhedra, deltahedra, coordination and space-filling (Voronoi) polyhedra and Brillouin zones. These groupings are of course not mutually exclusive.

(A) The five perfect (regular) polyhedra or Platonic solids

These polyhedra (Fig. A.2.2) each have identical faces and edges of equal length. The vertices and faces of each circumscribe and inscribe respectively the surface of a sphere.

The tetrahedron has cubic point group symmetry $\bar{4}3m$ and the octahedron and cube have the full (holosymmetric) cubic point group symmetry $4/m\bar{3}2/m \equiv m\bar{3}m$. The icosahedron and pentagonal dodecahedron both have point group symmetry $2/m\bar{3}5$ —the symmetry possessed by quasicrystals, buckminsterfullerene and some viruses. Of all the Platonic polyhedra, only the cube is space-filling.

These solids were known to the Ancient Greeks and were clearly identified and described by Theaetatus of Athens (d. 369 BC). They were considered by Plato to constitute the fundamental building-blocks of matter: fire (tetrahedron), solid (cube), air (octahedron), liquid (icosahedron) and the universe or cosmos itself (pentagonal

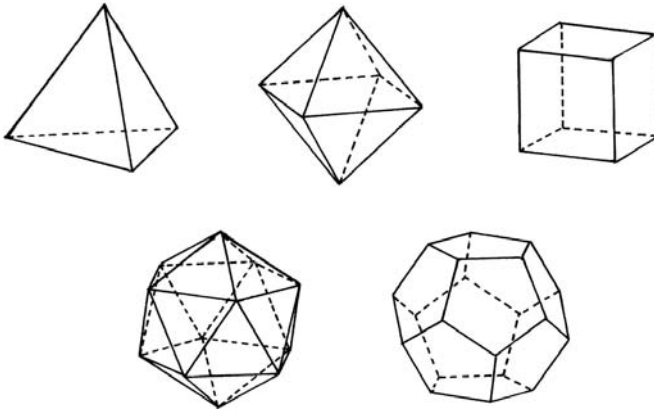


Fig. A2.2. The five perfect polyhedra or Platonic solids: tetrahedron, octahedron, cube, icosahedron, pentagonal dodecahedron.

dodecahedron). Hence, they are attributed to him, instead of (more properly) to Theaetatus.

The notion that the Platonic solids had a cosmic significance was taken up by Johannes Kepler in his first book *Mysterium Cosmographicum*, 1596, in which he attempted to show that the ratios of the diameters of the (circular) orbits of the then-known six planets corresponded with the ratios of the inscribed and exscribed diameters of the spheres of the five perfect solids. Thus the ratios of the diameters of the inscribed and exscribed spheres for an octahedron correspond to the orbits of Mercury and Venus; that for an icosahedron the orbits of Venus and Earth, and so on. In short he attempted to explain or model the orbits of the planets in purely geometrical terms. The model failed of course, even in Kepler's time, by observation and calculations of greater precision on the ellipticity of the planetary orbits.

(B) The thirteen semi-regular or Archimedean Polyhedra

In these polyhedra, the discovery of which is attributed to Archimedes, every face is a regular polygon as in the Platonic polyhedra but the faces may be of different kinds—two kinds in the case of ten of the polyhedra and three kinds in the remaining three. Around each vertex the faces are arranged in the same order, the edges are of equal length and all the polyhedra are inscribable in a sphere. A complete list is given in Table A.2.1 and those of particular crystallographic interest are shown in Fig. A.2.3.

We owe the (rather long) names of these polyhedra to Kepler, and as indicated, they may be obtained by truncation of the corresponding Platonic solids—either a simple truncation of the vertices as shown for example in Fig. A.2.1, or a more complex truncation of the newly created vertices or edges. For example the truncated cubeoctahedron (also known as the great rhombicuboctahedron) and the (small) rhombicuboctahedron are obtained by truncating the cubeoctahedron in two different ways. The last two polyhedra, described by the curious word 'snub', are not derived simply by a process

Table A2.1 The Archimedean polyhedra

No.	Name	No. and shapes of faces	Point group symmetry
1	Truncated tetrahedron	4 hexag, 4 triang	$\bar{4}3m$
2	Truncated cube	8 triang, 6 oct	$m\bar{3}m$
3	Truncated octahedron	6 square, 8 hexag	$m\bar{3}m$
4	Truncated dodecahedron	20 triang, 12 decag	$\bar{2}/m\bar{3}5$
5	Truncated icosahedron	12 pentag, 20 hexag	$2/m\bar{3}5$
6	Cubeoctahedron	8 triang, 6 square	$m\bar{3}m$
7	Icosidodecahedron	20 triang, 12 pentag	$2/m\bar{3}5$
8	Truncated cubeoctahedron (great rhombicubeoctahedron)	12 square, 8 hexag, 6 oct	$m\bar{3}m$
9	(small) rhombicubeoctahedron	8 triang, 18 square	$m\bar{3}m$
10	Truncated icosidodecahedron	30 square, 20 hexag, 12 decag	$2/m\bar{3}5$
11	Rhombicosidodecahedron	20 triang, 30 square, 12 pentag	$2/m\bar{3}5$
12	Snub cubeoctahedron	32 triang, 6 square	432
13	Snub icosidodecahedron	80 triang, 12 pentag	235

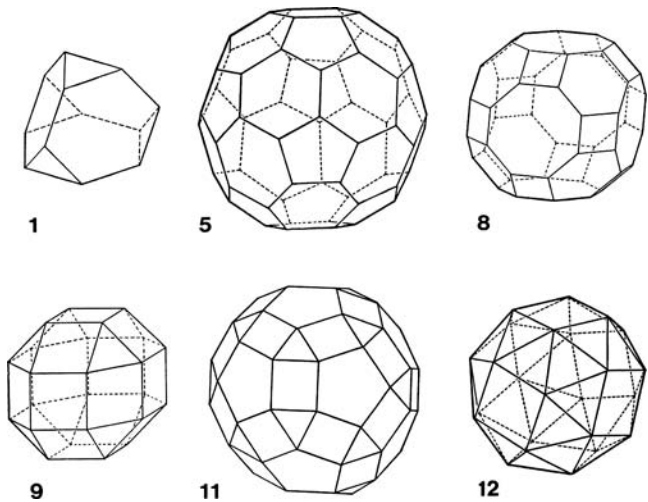


Fig. A2.3. Six of the thirteen Archimedean polyhedra, Nos. 1, 5, 8, 9, 11, 12 (see Table A.2.1). Figure A.2.1 shows Nos. 2, 3, 6. (From *Mathematical Models* by H.M. Cundy and A.P. Rollett, 2nd edn, Clarendon Press, Oxford, 1961 reprinted by Tarquin Publications, St Albans, 2006.)

of truncation, but also involve a ‘twist’ or rotation, which destroys mirror planes and centres of symmetry. Hence, they occur in two enantiomorphic forms. It should be noted that the point group symmetry 432 of the snub cubeoctahedron is not known to occur in any inorganic crystal (see pp. 38 and 103).

Of these thirteen polyhedra, only the truncated octahedron (the Voronoi polyhedron for the cubic I lattice) is space-filling (Fig. 3.9). The pattern of faces in the truncated icosahedron corresponds to that of C_{60} (see Section 1.11.6). The duals of the Archimedean polyhedra have the same symmetry. They are perhaps of less interest, except for the dual of the cubeoctahedron which is a rhombic dodecahedron (the space-filling Voronoi polyhedron for the cubic F lattice (Fig. 3.8(a))) and that of the icosidodecahedron which is a rhombic triacontahedron (Fig. A.2.4). The ratios of the lengths of the long and short diagonals of the rhombic or diamond-shaped faces are not the same: for the rhombic dodecahedron it is $\sqrt{2} : 1$ and for the rhombic triacontahedron it is $\sqrt{5} + 1 : 2$ or $1.618 : 1$ —the Golden ratio (see Section 2.9).

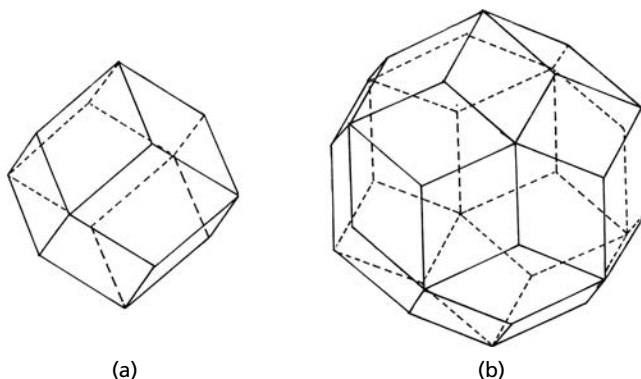


Fig. A2.4. (a) Rhombic dodecahedron and (b) rhombic triacontahedron. (a) is the space-filling polyhedron for the cubic F lattice and also the coordination polyhedron for the cubic I lattice.

(C) *The eight deltahedra*

In these polyhedra all the faces are equilateral triangles (Greek Δ). Three (the tetrahedron, octahedron and icosahedron) are also Platonic polyhedra. The remaining five have 6, 10, 12, 14 and 16 faces. Two, the triangular and pentagonal dipyrramids with 6 and 10 faces, are shown in Fig. A.2.5. Their duals are triangular and pentagonal prisms respectively.

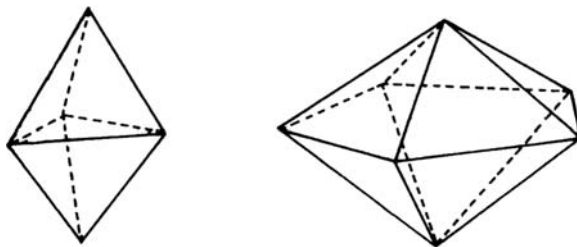


Fig. A2.5. Two of the eight deltahedra: the triangular and pentagonal dipyrramids.

(D) Coordination and space-filling polyhedra (Voronoi polyhedra or Dirichlet domains)

Coordination polyhedra, which represent the pattern of atoms or lattice points surrounding an atom or lattice point, should be clearly distinguished from the domains (Voronoi polyhedra or Dirichlet domains) which define the environment around an atom or lattice point and which are always space-filling (see Section 3.4). A vertex of a coordination polyhedron corresponds to the face of the corresponding domain, but the polyhedra are not necessarily duals.

They are duals, for example, in the cubic *F* lattice in which the coordination polyhedron is a cubeoctahedron (Fig. A.2.1(b) and (e)) and the space-filling polyhedron is a rhombic dodecahedron (Fig. A.2.4(a)) but not in the case of the cubic *I* lattice in which the coordination polyhedron is a rhombic dodecahedron¹ and the space-filling polyhedron is a truncated octahedron.

The procedure for constructing the space-filling Voronoi polyhedra for lattices is described in Section 3.4. For crystal structures consisting of only one kind of atom²—e.g. the simple cubic, bcc, fcc and hcp metal structures the procedure is the same. For structures consisting of more than one kind of atom the procedure is to construct the space-filling polyhedron around one kind of atom and its nearest neighbours *of the same kind*.³ The atoms of other kinds are then shown as occupying the appropriate vertices of the space-filling polyhedron.

A few examples will make this clear. In the NaCl structure the space-filling polyhedron around a Cl atom is a rhombic dodecahedron and the Na atoms are situated at the six vertices of the polyhedron where four edges (or faces) meet, as shown in Fig. A.2.6(a) (the same pattern occurs of course if the space-filling polyhedron is constructed around an Na atom).

In the NiAs or α -Al₂O₃ structures in which the As or O atoms are (closely) hexagonal close packed the space-filling polyhedron is a trapezohombic dodecahedron. In NiAs the Ni atoms are situated at all six vertices where four edges (or faces) meet (Fig. A.2.6(b)) and in α -Al₂O₃ the Al atoms are situated at four such vertices (Fig. A.2.6(c)).

Coordination polyhedra also determine the radius ratios of interstitial sites, e.g. between the atoms in metals as described in Section 1.6 or between close-packed oxygen anions. The data are summarized in Table A.2.2 which includes the interstitial sites delineated by squares and triangles.

Table A.2.3 lists the coordination and space-filling polyhedra for some simple structures.

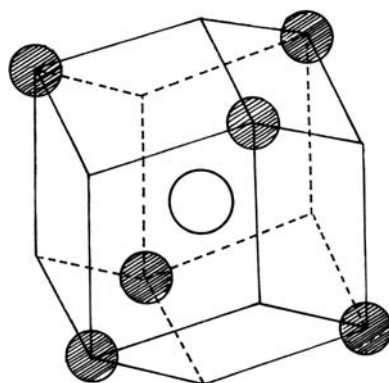
(E) Brillouin zones

Brillouin zones are 'nests' of polyhedra in *k*-space (reciprocal space with the scale factor 2π). Their surfaces represent the directions and wavelengths (or wavenumbers) of free

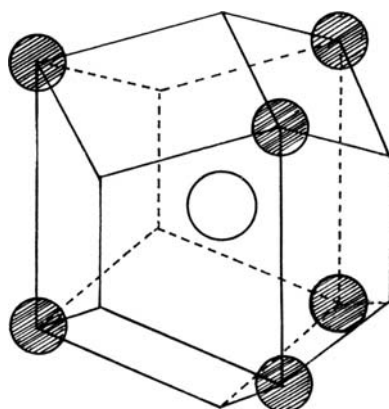
¹ The eight 'obtuse' vertices correspond to the lattice points at the corners of the cell and the six 'acute' vertices correspond to the lattice points at the centres of neighbouring cells as indicated in Fig. A.2.4(a)

² The term 'atom' encompasses charged species, i.e. both cations and anions.

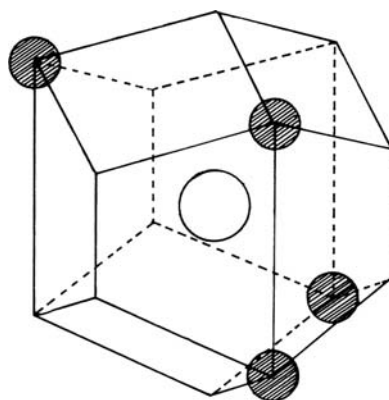
³ E.W. Gorter. Classification representation and prediction of crystal structures of ionic compounds. *J. of Solid State Chem.* **1**, 279 (1970).



(a)



(b)



(c)

Fig. A2.6. Space-filling polyhedra for (a) the NaCl structure, (b) the NiAs structure and (c) the α -Al₂O₃ structure.

Table A2.2 Coordination polyhedra for interstitial sites and radius ratios

Structure type	Co-ordination polyhedron around interstitial site	Radius ratio
Simple cubic	Cubic	0.732
	Square	0.414
Cubic close packed	Octahedral	0.414
	Square	0.414
	Tetrahedral	0.225
	Triangular	0.155
Hexagonal close packed	Octahedral	0.414
	Tetrahedral	0.225
	Triangular	0.155
Body centered cubic	'Distorted' octahedral	0.154
	'Distorted' tetrahedral	0.291
Simple hexagonal	Triangular prism	0.528
	Triangular	0.155

Table A2.3 Coordination and space-filling polyhedra

Structure/lattice type	Co-ordination polyhedron	Space-filling polyhedron
cubic <i>P</i> (simple cubic)	octahedron (square dipyramid)	cube (dual)
cubic <i>F</i> (fcc)	cubeoctahedron	rhombic dodecahedron (dual)
cubic <i>I</i> (bcc)	rhombic dodecahedron	truncated octahedron
hexagonal <i>P</i> (simple hexagonal)	hexagonal dipyramid	hexagonal prism (dual)
hexagonal close-packed (hcp)	hexagonal cubeoctahedron	trapezorhombic dodecahedron (dual)
NaCl (structure type)	octahedron, Na around Cl or Cl around Na	rhombic dodecahedron, with Na or Cl at the 6 vertices where 4 edges meet
CsCl (structure type)	cube, Cs around Cl or Cl around Cs	cube, with Cs or Cl at the 8 vertices
NiAs (structure type)	trigonal prism, Ni around As	trapezorhombic dodecahedron, with Ni atoms at the 6 vertices where 4 edges meet
$\alpha\text{-Al}_2\text{O}_3$	tetrahedron (distorted), Al around O	trapezorhombic dodecahedron, with Al atoms at the 4 of the 6 vertices where 4 edges meet
CaF ₂ and Li ₂ O (fluorite and anti-fluorite structure types)	cube, F or Li around Ca or O tetrahedron, Ca or O around F or Li	rhombic dodecahedron, with F or Li at the 8 vertices where 3 edges meet cube, with Ca or O situated at 4 of the 8 vertices forming a tetrahedron

electrons in crystals which are Bragg-reflected by the lattice planes. The first, innermost Brillouin zone corresponds to the reflections from the planes of largest *d*-spacing, the

next Brillouin zone corresponds to reflections from the planes of next largest spacing, and so on.

The first Brillouin zone is equivalent to the Voronoi polyhedron or Wigner–Seitz cell for the corresponding reciprocal lattice. For example, for the cubic F lattice, for which the corresponding reciprocal lattice is cubic I , it is a truncated octahedron.

The constructional procedure for Brillouin zones may be illustrated for a cubic P (simple cubic) lattice with a cell edge length a and for which the corresponding reciprocal (k -space) lattice is also cubic P with a cell edge length $\frac{2\pi}{a}$ (Fig. A.2.7).

Consider electrons travelling in the $\mathbf{x}^*\text{--}\mathbf{y}^*$ plane reflected from lattice planes parallel to the \mathbf{z}^* axis. In order of decreasing d_{hkl} -spacing (or increasing \mathbf{d}_{hkl}^* spacing) these are 100, 110, 200, 210, ... Consider an electron with wavevector \mathbf{k} as indicated:

$$k = |\mathbf{k}| = \frac{2\pi}{\lambda}.$$

For reflection from the 100 planes, the corresponding value of k is found by substituting for λ in Bragg's law

i.e.
$$k = \frac{2\pi}{\lambda} = \frac{2\pi}{2a \sin \theta} = \frac{2\pi}{a} \cdot \frac{1}{2 \sin \theta}$$

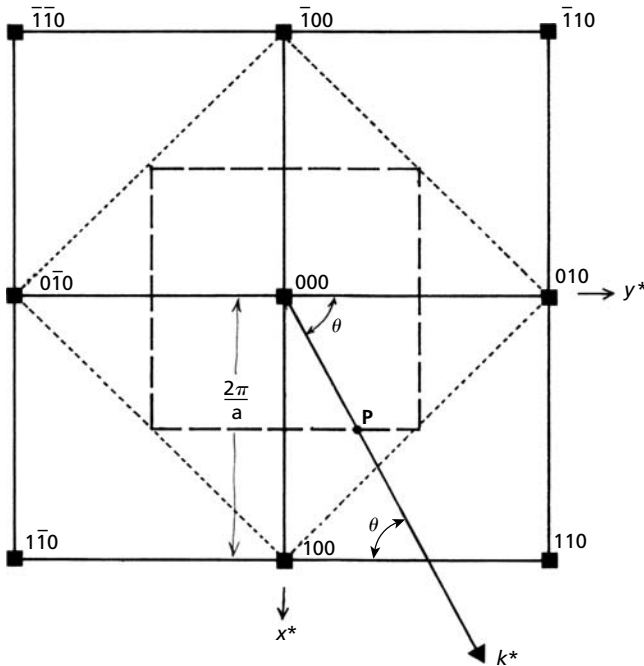


Fig. A2.7. Construction for the first Brillouin zone for a cubic P lattice. θ is shown for reflection from the 100 planes.

which value is indicated by point P. The locus of P, for all values of θ , and for reflections from the 010, etc. planes, gives rise to the outline of the first Brillouin zone, as indicated by the dashed lines. In three dimensions the Brillouin zone is a cube.

The second Brillouin zone arises from reflections from the 110 planes and, proceeding as before, the corresponding values of \mathbf{k} are indicated by the dotted lines. In three dimensions this second Brillouin zone is a rhombic dodecahedron (like the first Brillouin zone for the cubic I reciprocal lattice).

Appendix 3

Biographical notes on crystallographers and scientists mentioned in the text

Ernst Abbe 1840–1905

Abbe's father was a mill worker in Eisenach, Germany, and it was his employers who provided the scholarships which enabled Abbe to proceed from High School to study physics at the Universities of Jena and Göttingen. In 1863 Abbe achieved his ambition of becoming a lecturer at Jena, but his career may be said to commence in 1866 when he began his long and fruitful collaboration with Carl Zeiss. As a theoretician he established the relation between the aperture and the limit of resolution of a lens (the equation is engraved on his memorial at Jena); as an optical designer he invented the apochromatic objective lens (made possible with the new glasses developed by the Schott glassworks); and as an industrialist he and Zeiss developed systematic microscope production on a large scale.

In 1876 he was made a partner in the Carl Zeiss firm and became the sole owner following the death of Zeiss in 1888. In 1891 he created the Carl Zeiss Foundation whose charter was used in Prussia as a model for progressive social legislation.

George Biddell Airy 1801–92

Airy's life was characterized, to a remarkable degree, by a determination to succeed and meticulous organization: he made a record of everything that he wrote, with dates, and discarded not the merest note or receipt. His entry to Cambridge in 1819, which was largely facilitated by a wealthy uncle in Colchester, provided him with the opportunity to break away from a modest parental background and thence his career developed rapidly. He was appointed Lucasian Professor of Mathematics in 1826, Plumian Professor of Astronomy in 1828 and Astronomer Royal in 1835, a post he filled for 46 years and which entirely fitted his temperament. He largely re-equipped the Greenwich Observatory and transformed it into a highly efficient Institution—but at a price: it provided no centre for the training of innovative scientific minds and the discoveries of John Herschel and John Couch Adams were made elsewhere. Airy was, in effect, the prototype of the modern government scientist and played a major role in the development of institutional science in Victorian England. He designed (with the lawyer, Edmund Beckett Denison) the clock for the new Palace of Westminster—it had to be redesigned in 1852 when it was discovered that the interior walls had been made too small—but its continued functioning almost without interruption for over 140 years is a measure of their achievement.

Airy calculated the magnitude of the image formed by a telescope objective of a star—a point source of light—and thereby laid the foundations for the theory of the resolving power of optical instruments. He was knighted in 1872, having refused that honour three times previously on the grounds that he couldn't afford the fees.

William Thomas Astbury 1898–1961

Astbury was born in Longton in Staffordshire, England, one of the 'five towns' of the pottery manufacturing industry in what was then called the 'Black Country'. His family was poor, but Astbury's success in winning scholarships provided him with an excellent early education and entry into Jesus College, Cambridge, which would otherwise have been beyond his reach. His initial studies in mathematics and physics were interrupted by the First World War, during which time he served with the X-ray unit of the Royal Army Medical Corps. On his return to Cambridge, through the influence of Arthur Hutchinson, Demonstrator in Mineralogy, he studied in addition chemistry, mineralogy and the newly emerging science of X-ray crystallography pioneered by the Braggs. Arthur Hutchinson indeed was the 'source' of many of the crystals first studied by the Braggs which he 'borrowed' (without permission) from the Mineralogical Museum.

In 1921 Astbury joined W.H. Bragg's newly formed research group at University College, London and in 1923 moved with the group to the Royal Institution where (together with Kathleen Yardley) he developed the first space group tables to help determine, from X-ray evidence, to which of the 230 space groups a crystal belongs. W. H. Bragg thought them unnecessary—all that was needed was common sense. Astbury replied that not everyone has common sense. However, the major direction of his life's work, in macromolecular structures, came about as a result of a request from Bragg in 1926 that he take some X-ray photographs of fibres which Bragg wished, if possible, to use in one of his Royal Institution lectures. This was typical of Bragg's subtle way of directing research—to simply ask for help on some particular topic. Astbury was so successful in applying X-ray techniques to the study of cellulose, silk and wool fibres that in 1928 Bragg recommended him for the post of Lecturer in Textile Physics and Director of the Textile Physics Research Laboratory at Leeds University which, particularly through the work of J. B. Speakman, was pre-eminent in the study of the physical and chemical properties of fibres. Here he made rapid progress in distinguishing the fully-extended chain structures characteristic of cellulose and silk (the simplest polypeptide protein structure) and the much more complex protein structure, keratin—the basic material not only of wool and hair fibres but also of nails horn and quills. He showed, in wool, that the keratin polypeptide chains occurred in two forms, a folded form, which he called α -keratin and an extended form, β -keratin, a discovery of enormous scientific and technological importance in understanding the extensibility of wool fibres and in the processing of woollen fabrics. He disseminated this information in a series of University Extension lectures in 1932 and which formed the basis of his book *Fundamentals of Fibre Structure* (Oxford University Press, 1933).

Astbury proposed a model for α -keratin in which the amino acid peptide links were folded in the form of hexagons, parallel to the chain axis and perpendicular to the cross-linking side arms. This model was superseded in 1951 by Pauling's α -helix model but

it did nevertheless represent the first attempt to model a protein chain structure in which specific linkages held the polypeptide chains in a characteristic conformation.

In 1935, together with a research student, Florence Ogilvy Bell, Astbury began to study the structure of nucleic acids and in 1938 together they published the first X-ray diffraction photograph (or fibre diagram) of a nucleic acid and attempted, unsuccessfully, to interpret its structure.

In 1945 Astbury was appointed to the new Chair of Biomolecular Structure at Leeds which he occupied until his early death in 1961.

As a pioneer it was perhaps inevitable that Astbury should see his own work superseded. His great legacy is his early stimulation to so many others in the field of molecular biology.

Johannes Martin Bijvoet 1892–1980

Bijvoet was born and brought up in an old waterside house in the centre of Amsterdam. He recalls that his wish to become a chemist arose from the excellent teaching at his secondary school, where the emphasis was on understanding rather than rôle learning. As a result (and also having passed the then rigorous examinations in Latin and Greek required for university entrance) he entered Amsterdam University in the years preceding the First World War. Here the emphasis was on routine analytical chemistry, which gave him much less satisfaction.

During the war, Bijvoet, like all young men of his age, was conscripted for the military service, but since the Netherlands was a non-combatant nation, it was simply a period of enforced idleness which Bijvoet used 'to study quietly thermodynamics and statistical mechanics'—an indication perhaps of his serious attitude to life.

Bijvoet's move to the area of crystallography arose from the excitement aroused by Bragg's model of NaCl, a model which was by no means accepted by the professorial staff at the University, including his own supervisor, as an adequate representation of the structure. However, these objections had a happy consequence in that it was decided that X-ray investigations should be undertaken in which Bijvoet would have a leading role.

However, despite sound progress made in the solution of crystal structures, the 'chemists' remained unconvinced. Bijvoet recalls a 'painful memory' of a visit by W. H. Bragg in which in despair at the persistent hackneyed arguments against the results of X-ray analysis, Bragg 'raised his arms up to heaven'. Even after Bijvoet's appointment in 1928 as lecturer in crystallography and thermodynamics he records that he 'passed through a time of struggle for the *raison d'être* of X-ray analysis'.

In 1939 Bijvoet was appointed to the Chair of Chemistry at the van't Hoff Laboratory of the University of Utrecht, a post which the previous holder, Ernst Cohen, was forced, as a Jew, to vacate and who, despite his support for Germany following the First World War, was later to be killed by the Nazis.

It was at Utrecht, in the years 1949–1951, that Bijvoet and his colleagues, made their most outstanding contribution to X-ray crystallography: the use of anomalous scattering to determine absolutely (and not relatively) the right and left handed forms of enantiomorphic crystals—a fulfilment, in a sense, of van't Hoff's work of 1874 on tetrahedrally bound carbon in organic crystals. The experimental work, carried out with

crystals of sodium rubidium tartrate, was of great difficulty. Exposures of over 100 hours were needed, using an improvised X-ray tube with a zirconium target and a 'freakish' pump which had to be watched continuously.

Bijvoet was closely involved in the establishment of the International Union of Crystallography in 1946 and became President in 1951. He retired to Winterswijk, a rural district of the Netherlands, in 1962.

William Barlow 1845–1934

Following an inheritance from his father, Barlow, one of the last great English amateurs in science, took up the study of crystallography in his early thirties and attempted to relate the properties of crystals to the packing arrangements of their constituent atoms. He collaborated with W. J. Pope at Cambridge and guessed (correctly) the structure of the alkali halides. His mathematical ability and developing interest in symmetry enabled him to extend the methods of Bravais and Sohncke to find the 'symmetrical groupings to fit the forms and compositions of a variety of different substances' but he did not publish his derivation of the 230 space groups until 1894, three years after Fedorov and Schoenflies, of whose work he almost certainly had no prior knowledge.

William Henry Bragg 1862–1942

W.H. Bragg was born in Westward, Cumberland. At the age of seven, following his mother's death, he went to live first with an Uncle in Market Harborough, Leicestershire and then to a boarding school in the Isle of Man. In 1881, he won a scholarship at Trinity College, Cambridge to read mathematics; he graduated as a 'Third Wrangler' in Part I of the mathematical tripos in 1884 and obtained a first class in Part II in 1885. On the basis of this remarkable mathematical achievement in the same year he was appointed Professor of Mathematics and Physics at the University of Adelaide. The story goes that some friends pointed out that he did not know any physics. 'Ah', said Bragg 'but the boat takes ten weeks to reach Australia, plenty of time to read up on the subject.'

For nearly twenty years, Bragg immersed himself in the affairs of the University, developed his clear teaching style but did little serious research. It was only in 1903, at the age of 41, that he identified a research area suited to his particular gifts—the problems of radioactive emission, the ionization of gases and the nature of X-rays which he considered to be 'corpuscular' in nature. His rapidly growing reputation resulted in election to the Royal Society in 1907 and, in the same year, Bragg was offered the Cavendish Chair of Physics in the University of Leeds, a post which he took up in 1909.

The contrast between Leeds and Adelaide could not have been more great: his Australian wife, Gwen, was particularly appalled by Leeds, the dirt and smoke, the rows of back-to-back houses and the poor rickety children. It was no better in the University; Bragg was restricted by the syllabus, found the students inattentive and also found himself in a losing battle with his corpuscular theory of X-rays and γ -rays. However, he derived support from Arthur Smithells, Professor of Chemistry, from Ernest Rutherford at Manchester and not least from the emerging scientific abilities of his elder son,

Lawrence. Gwen immersed herself in social work for poor children and for the family there were weekends spent in the beautiful surrounding Dales countryside.

In June and July 1912, Laue's two papers announcing the diffraction of X-rays were presented at meetings of the Bavarian Academy of Sciences. They were published in late August, but even before then word 'got around' it did so to the Braggs during a family holiday at Cloughton, a village on the Yorkshire coast, by way of a letter from Lars Vegard, a former colleague, who enclosed a photograph which he had obtained from Laue. Laue's photograph clearly showed the wave nature of X-rays but both father and son were reluctant to abandon the corpuscular theory and on their return to Leeds, attempted to interpret the patterns in terms of corpuscles travelling along 'avenues' between the atoms. This work resulted in a letter to *Nature* in October 1912, authored solely by W.H. Bragg. It represents the last attempt to 'save' the corpuscular theory. Thereafter, the wave theory was unquestioned.

Bragg's significant achievement at this time was the design and construction in the Leeds physics workshops in the winter of 1912–1913 of the X-ray spectrometer and it was this instrument that enabled him and Lawrence to make the first determinations of crystal structures, for which work they were jointly awarded the Nobel Prize in 1915.

Bragg records how he and Lawrence worked together in the physics laboratory far into the night and it is near impossible to disentangle the relative contributions of father and son. Certainly Lawrence's deep physical insight and his exploitation of the law of reflection that bears his name was of primary importance. But set against this is Bragg's foresight, expressed in the Bakerian lecture to the Royal Society in 1915, that the series of spectra (reflections) from a given set of crystal planes represented a series of harmonic terms which could be analysed by Fourier methods—a notion of profound importance in crystallography which awaited some ten years before it could be exploited in crystal structure determination.

In 1915 Bragg accepted the Quain Chair of Physics and University College London but only took up the post in 1918, following secondment for research at the Admiralty during the course of the War. At University College he assembled and encouraged a remarkable team of researchers—W.T. Asbury, G. Shearer, A. Muller, K. Yardley—and made the first attacks on the structure of organic crystals (by tacit agreement Lawrence, then at Manchester, worked on inorganic, mainly mineral and silicate, crystals).

In 1919 Bragg was invited to give the Christmas lectures 'to a Juvenile Auditory' at the Royal Institution, continuing a long-standing tradition that had begun with Michael Faraday. The lectures, subsequently published as 'The World of Sound', show his powers of simple exposition and his affection for young people (he dedicated the book 'to Peggy, Gwendy and Phyllis who discussed with me so many things in this book as we walked to school in the mornings').

It was perhaps as a result of these lectures that Bragg was elected in 1923 to the headship of the Royal Institution and the title, *inter alia* of Fullerian Professor of Chemistry. Bragg was by now the distinguished icon of British science, he was elected to the Order of Merit in 1931, yet in spite of his heavy administrative duties continued to attract to the Institution younger scientists such as J.D. Bernal who maintained Britain's leading role in X-ray crystallography. His book *The Universe of Light* (1933) was based on his 1931 Royal Institution Christmas lectures.

In 1935, at the age of 73, Bragg was elected to the Presidency of the Royal Society, a post he held until 1940. It was a difficult time for him, the gathering clouds of war and the administrative duties taxed his strength. His daughter, Gwendoline, records seeing on one occasion how wearily he looked up from his papers. ‘Daddy, need you work so hard’ she cried, and he answered simply ‘I must dear, I’m always afraid they’ll find out how little I know.’

William Lawrence Bragg 1890–1971

W. L. Bragg, the elder son of W. H. Bragg and Gwendoline Bragg (née Todd) was born in Adelaide, Australia. He attended St Peter’s Collegiate School there and enrolled at Adelaide University at the early age of 15, achieving a first class degree in mathematics before coming to England with his family in 1909. He immediately entered Trinity College, Cambridge and within a year again achieved a first class in Part I of the Mathematics Tripos. For Part II he made the momentous decision to switch from Mathematics to Natural Sciences—a decision perhaps prompted by his father. He now began to acquire his knowledge of optics which was to be of such seminal importance in his later discoveries, from C. T. R. Wilson, his most influential teacher (whose lectures were the best, and whose delivery was the worst!).

In June 1912, Bragg graduated with a first class degree and immediately began research at the Cavendish Laboratory under the supervision of Professor J. J. Thomson. It was a hopeless time for him, there was very little apparatus available, virtually no workshop facilities and he made no progress with his research project (on ionic mobility) at all. However, all this was to shortly change. In order, perhaps, to escape from the frustrations of the Cavendish Laboratory, in August 1912 he joined his family on their summer holiday and where he heard from his father the first news of Laue’s discovery, of the scattering of X-rays by crystals which clearly showed the wave nature of X-rays.

The first ‘breakthrough’ was made by Bragg following his return to Cambridge in October. He noticed that the spots were elliptical in shape—and this was just the shape one would expect of the X-rays were effectively *reflected* from sheets of atoms in the crystal. Moreover he realized, following the ideas of William Pope, Professor of Chemistry at Cambridge, that if the atoms in Laue’s zinc blende crystals were packed in the form of a face-centred cubic, rather than a simple cubic pattern, he was able to explain the positions of all the spots in the Laue photographs. Bragg announced his interpretation in a paper ‘The diffraction of short electromagnetic waves by a crystal’ read to the Cambridge Philosophical Society on 11th November 1912 and which included for the first time the Bragg law in embryonic form $n\lambda = 2d \cos \theta$ (where θ is the complement of θ subsequently used).

How was it that a twenty-two year old student succeeded where all the ‘best brains’ of Europe had failed? Genius certainly, but perhaps a genius whose mind was not encumbered with complicated theory and which rather drew on simple optical ideas. There is a story recounted by R.W. James, a later close colleague. At a meeting of English and German students at Leipzig in 1931 it did not go unnoticed by the German delegates that, in comparison with their own rigorous education, there was a distinct lack of training in

mathematics and physics among the English. 'Tell me', confided one of James's German colleagues, 'how does Bragg discover things? He doesn't know anything.'

In comparison to the Cavendish Laboratory, his father's laboratory at Leeds was much better equipped, in particular the availability of an X-ray spectrometer, with which father and son carried out their joint researches in the summer and autumn of 1913. The notebook in which they recorded their observations is now held in the Brotherton Library at Leeds University and in its closely-pencilled pages one can recognize the data which resulted in a stream of papers in which the structures of ZnS, NaCl, KCl, FeS₂, sulphur, diamond, CaCO₃ and the calcite series of crystals, the spinels and CaF₂ were all wholly or partially determined and for which father and son were jointly awarded the Nobel Prize in 1915.¹

At the outbreak of war, Bragg enlisted with the Royal Artillery and was posted to France in August 1915. It was from here, in the closing weeks of 1915, that the news reached him both of the Nobel Prize and also the death of his younger brother, Bob, in the Gallipoli landings.

In 1919 Bragg was appointed to the Langworthy Chair of Physics at Manchester, a post vacated by Ernest Rutherford. It was a tough assignment: the mainly ex-servicemen students had little time for authority and in Bragg's lectures little short of hooliganism prevailed. However, by 1921 this difficult transitional phase was over: he was elected Fellow of the Royal Society, became married, solved the structure of α -quartz and in 1923 broke what he later called the 'sound barrier' in X-ray analysis in his analysis of the structure of aragonite, in which he made explicit use of space group theory for the first time. He also pioneered the use of Fourier methods in the analysis of diopside and beryl and studied the structures of metals and alloys.

At this time Bragg and his father made a tacit agreement to divide their work on crystal structure determination: Bragg would work on inorganic structures and the father, then at University College, London, would work on organic structures. Many years were to elapse before Bragg became involved, as Cavendish Professor, in organic structures, but as early as 1935, cognisant of the work of Astbury at Leeds, he realized that the structures produced by living matter were the most interesting field of all.

In 1937 he left Manchester to become Director of the National Physical Laboratory (NPL)—a socially but perhaps not a scientifically, prestigious appointment. Bragg (and certainly his wife) never overcame their disparaging view of life in the north of England, the (then) black and smoky Manchester in particular. He mentioned that 'the students are rather rough diamonds, as indeed they must be when one considers their circumstances'.

The appointment at NPL was short-lived. Even before Bragg took it up, Rutherford died and in 1938 Bragg was offered, and accepted, the Cavendish Chair of Experimental Physics at Cambridge. Almost immediately the Second World War intervened and Bragg was primarily involved in war work such that his tenure only commenced in earnest when the war was over. Even so, Bragg pursued the analogies between light and

¹ *The Bragg Notebook: A Commentary and Interpretation.*

<http://www.leeds.ac.uk/library/spcoll/bragg-notebook/> Written by Christopher Hammond; edited by Diana Joyce, Jane Saunders and Catherine Robson; website designed and developed by Matt Taylor and Tom Grahame.

X-ray diffraction in the analysis of crystal structures (his so-called ‘fly’s eye’ and ‘X-ray microscope’ techniques). But most significant of all was his support, from 1939, of the work of Max Perutz, an Austrian refugee who had been working with J. D. Bernal on the structure of haemoglobin. It seemed an entirely impossible task; haemoglobin clearly had a far more complicated structure than anything then known but it is a measure of Bragg’s willingness to take chances that, as he said ‘some intuition led me to think that this line of research must be pursued’. Bragg’s support led, in 1947 to the establishment of the Medical Research Council Unit on the molecular structures of biological systems and ultimately to the solution of the structure of haemoglobin and myoglobin in 1960 by Perutz and Kendrew and the structure of DNA in 1953 by Watson and Crick. There is no doubt that this Nobel prize-winning work owed its origin to Bragg’s willingness ‘to take chances’.

Bragg resigned the Cavendish Chair in 1953 to take up the post of Director and Fullerian Professor in the Royal Institution. Since the days of his father, the Institute had declined to a point where almost no research was done at all. Bragg set about a major programme of reform; he assembled what was to become a prestigious research group on biological structures and in addition to the long-standing Christmas lectures revived the programme of afternoon schools’ lectures, which were far more enthusiastically received than his university lectures. When asked why (as with his father) he had such an easy rapport with school children his explanation was simple ‘we enjoy the same things’. He records that the period 1960–1966 was ‘the happiest time of my life’: a family atmosphere prevailed at the Royal Institution and the only thing lacking, for Bragg, was a garden. In 1966, the year of his retirement, Bragg was awarded the Copley Medal of the Royal Society—its highest award—and a year later was made a Companion of Honour. But the anticipated peace of his retirement was soon to be shattered when he received the first draft of Watson’s book *The Double Helix*, which he himself had encouraged Watson to write many years previously and which now, in view of its scurrilous remarks (even on Bragg himself) provoked widespread hostility. Bragg had always had a high regard for Watson’s imaginative and brilliant ideas (whereas Crick did all the talking!); perhaps he also felt an affinity for Watson, who, like himself, had arrived in England very much as an outsider. But Bragg recognized the value of this personal record and on condition of the removal of some of the most offending passages agreed to write a supportive foreword.

Auguste Bravais 1811–63

Bravais was born in Annonay in France, studied mathematics in Paris and became a naval cadet in Toulon, which enabled him to participate in explorations to Algeria and the North Cape. He was appointed Professor of Physics at the École Polytechnique in 1845, and his interest in the relationships between the external forms and internal structures of crystals led to the derivation of the fourteen space lattices in 1848, published in his famous *Memoire sur les systèmes formés par des points distribués régulièrement sur un plan ou dans l’espace* (1850)—work which was partly based on Frankenheim’s fifteen ‘nodal’ lattice types. However, constant application to a wide range of studies which aroused his curiosity led, in 1857, to a breakdown of his health.

Martin Julian Buerger 1903–86

Buerger was born in Detroit, USA, and studied mining engineering at the Massachusetts Institute of Technology, specializing after graduation in research in mineralogy. It was during this time that he attended, in 1927, a course of lectures on X-ray diffraction given by W. L. Bragg, as a result of which Buerger realized that in order to understand the chemical and physical properties of crystals it was necessary to know their structures. Hence began his life-long work in X-ray crystallography, not only in the solving of crystal structures but in the invention of the equi-inclination Weissenberg camera, the precession camera and the writing of several well-known textbooks, the earliest of which *X-Ray Crystallography* is, like Bragg's *The Crystalline State: Volume 1, A General Survey*, a classic which is still current today.

Buerger was closely associated with the founding of the International Union of Crystallography and was a member of the Commission for the International Tables from its establishment in 1948.

Peter Joseph William Debye 1884–1966

Debye was born in Maastricht in the Netherlands, was educated at Aachen and Munich and held a number of Chairs in Physics before becoming Director of the Kaiser Wilhelm Institute for Theoretical Physics 1935–40. He then emigrated to the USA in 1940, becoming Professor of Chemistry at Cornell University.

Debye was primarily a theoretician concerned with the application of physical methods to molecular structure and is best known for his work of specific heat, electrolysis and the electron diffraction of gases. He was a member of staff in the Institute of Experimental Physics at the University of Munich at the time that Laue carried out his famous X-ray diffraction experiments. His development of a technique and camera (with P. H. Scherrer) for the investigation of X-ray diffraction from powders was made at the University of Göttingen in 1915.

Paul Peter Ewald 1890–1985

Ewald, a posthumous child, was brought up by his mother, Clara Philippson Ewald, a renowned portrait painter; they travelled widely and Ewald learned English and French at an early age. He graduated from the Königlichches Victoriagymnasium in Potsdam in 1905 and spent a short time studying chemistry at Cambridge before returning to the University of Göttingen in 1906. Ewald's interests then moved from chemistry to mathematics; he transferred to the University of Munich to attend the courses of lectures given by Sommerfeld on hydrodynamics.

The story of Ewald's thesis topic is given in Section 8.1 and it is clear that Ewald deserves greater recognition for his contribution to the interpretation of X-ray diffraction patterns than he has hitherto been accorded—unlike Laue or the Braggs he was not awarded a Nobel Prize. Yet his doctor's thesis of 1912, which he discussed with Laue, contained within it the basis of the 'reciprocal lattice and reflecting sphere construction' analysis of the geometry of (X-ray) diffraction which is equivalent to Bragg's law. Indeed,

it was only after reading Laue, Friedrich and Knipping's published papers that Ewald realized the relevance of his own approach and, in particular, the applicability of the formula in his thesis which he had brought to the attention of Laue but which in fact he (Laue) had not used.

During the First World War, Ewald became a field X-ray technician in the northern Russian Front but had sufficient time to publish, from 1916 onwards, a series of papers on crystal optics and dynamical theory. In 1921 he became first Professor of Theoretical Physics in the University of Stuttgart and then Rector in 1932. It was an inauspicious time: only one year after his inaugural address, in which he pleaded for the pursuit of social and political harmony, he was forced, by a Nazi Party decree, to resign his Rectorship because his wife was Jewish and he part-Jewish himself. The increasing persecution and corruption of the objective academic ideals of German science by the Nazi Party forced him in 1937 to leave Germany for England with the support of W. L. Bragg. He lived in Cambridge with his family in a financially precarious situation until 1939 when he became Professor of Theoretical Physics in the Queens University in Belfast. In 1949 he became Professor of Physics at the Polytechnic Institute of Brooklyn, and although he remained in the USA for the rest of his life he never gave up his British citizenship.

The International Union of Crystallography was founded in 1947 largely through Ewald's initiative, with W. L. Bragg as President and he himself as Vice-President. It was, in a sense, a fulfilment of those ideals for which he had pleaded twenty-five years previously.

Evgraph Stepanovich Fedorov 1853–1919

Son of an army engineer, Fedorov attended military school in Kiev and became, in turn, a combat officer and member of the revolutionary underground. His first ideas on the derivation of the 230 space groups were contained in his book *The Elements of Configurations*, started in 1879, when he was 26 years old but not published until 1885. His complete derivation of the space groups was circulated in 1890 to his friends (including Schoenflies) as a series of preprints but was not published until 1891, shortly before Schoenflies' independent derivation.

Jean Baptiste Joseph Fourier 1768–1830

Fourier, son of poor parents who died when he was nine, attended the military school in his home town of Auxerre, France, where his great mathematical ability was first recognized. As a young man he was caught up in the Revolution; he was imprisoned both by Robespierre (being released only as a result of Robespierre's execution in 1794) and, subsequently, by the counter regime, ironically as a supporter of Robespierre.

Fourier's administrative and political talents were recognized by Napoleon who made Fourier secretary of the newly formed Institut d'Egypte, but after Napoleon's fall he found himself out of favour with Louis XVIII and was not elected a member of the Academie Francaise until 1827.

Fourier's main achievements lie in his development of the mathematical techniques applied to the diffusion of heat and (what are now called) Fourier series and Fourier integrals. He also made substantial contributions to the theory of equations, linear inequalities, and probability.

Frederick Charles Frank 1911–1998

Frank was born in Durban, South Africa. His parents were English and the family returned to England, to Abbots Farm in Suffolk, when Frank was just ten weeks old. His early schooling was at the village of Denham Abbots, then Ipswich Grammar School from which he won, in 1929, an Open Scholarship to Lincoln College, Oxford, to read chemistry. Having achieved a first class degree in 1933 he switched to research in engineering, gaining the DPhil degree in 1937, and then went on to do two years' research in physics at the Kaiser Wilhelm Institute für Physik in Berlin. It was this wide educational background (and fluency in German) which was to be of such value to him in his later wide-ranging research from the physics and properties of crystals to geophysics and continental drift.

At the outbreak of World War II, Frank joined the Chemical Defence Research Establishment at Porton Down in Wiltshire—but in view of his experience was 'head-hunted' by R. V. Jones to join him in Scientific Intelligence in the Air Ministry. Then followed a remarkably fruitful six-years' partnership, vividly described in Jones' book *Most Secret War* (1978) and in which he pays tribute to Frank's acute powers of observation and interpretation—perhaps the most spectacular being his identification, near Bruneval on the French coast, of the paraboloid antenna of the much-sought Würzburg 53 cm radar and which was captured intact in a British parachute raid in 1942.

Immediately following the war, Frank was involved in secretly recording conversations among ten eminent German scientists detained at Farm Hall, near Cambridge. The transcripts, of enormous historical interest, were eventually released in 1992 and published, with notes and in introduction by Frank, as *Operation Epsilon: The Farm Hall Transcripts* (1993).

In 1946, Professor Nevill Mott, Director of the H. H. Wills Physics Laboratory in the University of Bristol invited Frank to examine problems associated with the deformation and growth of crystals. Here Frank was spectacularly successful and contributed largely to the subject now known as physical metallurgy. He showed how, during deformation, dislocations (the line-defects in crystals) could be continuously generated (Frank–Read sources); he identified different types (Frank partial and Frank sessile dislocations) and showed how crystal growth could be explained in terms of (screw) dislocations intersecting growth surfaces. From here he moved to polymeric materials and described the chain-folded structures of polymer crystals and the linear defects, for which he coined the term *disclinations*, which occur in single crystals. These physical intuitions extended to geophysics; island arcs for example being simply explained by analogy with the shape of a dimple in a squashed ping-pong (table tennis) ball.

Frank was elected Fellow of the Royal Society in 1954, was its Vice-President 1967–69 and received the Copley Medal, the Society's premier award, in 1994. He became

Head of the Physics Department at Bristol in 1969 and was knighted soon after his retirement in 1977.

Frank was a man with a strong sense of duty and social conscience, which extended from his tireless help to young research students to his membership of the ‘Pugwash’ movement, which strove to alert nations to the dangers of nuclear weapons proliferation.

Moritz Ludwig Frankenheim 1801–69

Frankenheim was born and educated in Brunswick and the University of Berlin, where he was appointed lecturer in 1826. He was subsequently appointed Professor of Physics at Breslau, a post which he held until 1866. It was in a work of 1835 that he showed there could be only fifteen ‘nodal’, i.e. space lattice types, which much later (1856) he corrected to fourteen configurations, 8 years after Bravais’ derivation of the fourteen space lattices.

Rosalind Elsie Franklin 1920–58

Rosalind Franklin was born in London into a prosperous upper middle class Jewish family. She was one of five children (three brothers and a younger sister) and followed a Franklin family tradition in being educated at St. Paul’s Girls’ School where she was a Foundation Scholar. By the age of 15 she had no doubts that she wanted to be a scientist (which was a new departure away from her cultural background) and in 1938 won an Exhibition (a scholarship) to Newnham College, Cambridge. Her studies were affected by the outbreak of war when many of the university staff were seconded to the war effort and in 1941 she graduated, to her disappointment and against expectations, with a second, rather than a first class degree. However, she was awarded a Research Scholarship at Newnham College which she held for a year before being appointed as a Research Officer at the British Coal Utilization Research Council—a youthful organization where she established her reputation as a research scientist and for her work there was awarded the PhD degree by Cambridge University in 1945. In 1947 she was appointed Chercheur in the Laboratoire Centrale des Services Chimique de l’Etat in Paris and it was here that she developed X-ray diffraction techniques in the analysis of carbon structures—work which has partly laid the foundations to a whole new materials technology. In 1951 she decided it was time to return to England and on the basis of her expertise in a difficult area of X-ray analysis was appointed to a Newall and Turner Research Fellowship in the Medical Research Council Unit at King’s College, London to work on DNA—the elucidation of the structure of which was widely recognized as being a matter of paramount importance. It has, indeed, been represented as a race between competing laboratories and individuals, but if so it was a race which could not be won by one group alone but rather with the inputs from various individuals. Franklin’s great contribution was her meticulous experimental work, and cautious, unspeculative but well-founded deductions. Together with a research student, Raymond Gosling, who, under M. H. F. Wilkins’ direction had obtained diffraction patterns of DNA which showed a high degree of crystallinity, she demonstrated the effect of varying humidity on the crystal structure of DNA and in 1951 showed that the B-form (that which occurs under conditions

of high humidity) had a structure consistent with a helical conformation and that the phosphate groups of the amino acids must lie on the outside, rather than the inside, of the chains. Her photograph of DNA, which was crucial in demonstrating the correctness of Crick and Watson's model in 1953, was taken with Gosling over the weekend of 1 May 1952.

In the last five years of her life, before her untimely death from cancer, she worked in the Crystallography Laboratory at Birkbeck College London, where she discovered the structure of the tobacco mosaic virus.

Joseph Fraunhofer 1787–1826

Fraunhofer was the eleventh child of a poor master glazer in Straubing, Germany, who, after the early death of his parents and an unsatisfactory apprenticeship, joined the optical instrument workshop of a scientific instrument maker in Munich in 1806. Here his versatility as experimental scientist, optical instrument technician and glassmaker laid the foundations of the pre-eminence of the German optical instrument industry which was to be consolidated with such success by Otto Schott, Carl Zeiss and Ernst Abbe later in the century. It was a result of his investigations into the optical properties of glass that Fraunhofer discovered that the solar spectrum was crossed by many fine dark lines (some of which William Wollaston had first noticed in 1802), thereby laying the foundations of spectrometry. Following the work of Thomas Young he made the first quantitative study of diffraction and found the reciprocal relationship between the separation of the lines in diffraction gratings and the dispersion of light. In 1823, three years before his death from tuberculosis, he was appointed to the post of director of the Physics Museum of the Bavarian Academy of Sciences.

Augustin Jean Fresnel 1788–1827

Fresnel was born in Broglie, France, and grew up in a stern Jansenist home environment. In 1804 he entered the Ecole Polytechnique in Paris, his intended career being in civil engineering; from there he entered the Ecole des Ponts et Chaussees, graduating in 1809. His first big job as a civil engineer was the construction of the Imperial Highway to link France and Italy through the Alpine Pass of Col Montgenevre.

Fresnel's interests in optics and the nature of light appear to have begun in about 1814, but were stimulated in 1815 when he was suspended from his engineering work because of his opposition to Napoleon's return to France from exile in Elba—a period of enforced leisure during which time Fresnel was under police surveillance. However, in 1823 he became a member of the French Academy of Sciences and in 1824 was appointed to the lighthouse commission in France and developed the echelon lens which bears his name.

Like Thomas Young, but working entirely independently, Fresnel advocated and elaborated on the wave theory of light, though it is not known to what extent he was familiar with the ideas of Christiaan Huygens. Like Young, he introduced the principle of interference, drawn from analogy with his work on acoustics, publishing the results of his experiments on the diffraction and interference of light in 1815.

Fresnel collaborated closely with François Arago in studies on the polarization phenomena of light and followed Young in the realization that light waves must be transverse rather than longitudinal. For most of his short life Fresnel suffered severe ill-health; he was awarded the Rumford Medal of the Royal Society shortly before his early death.

Richard Buckminster Fuller 1895–1983

Richard Buckminster Fuller was born in Milton, Massachusetts, into a patrician New England family—his great-great-grandfather was the Massachusetts delegate at the Federal Constitutional Assembly that created the USA. He broke from family tradition by failing to graduate from Harvard and was packed off to work in a cotton mill in Canada. In 1917 he enlisted with the United States Navy which first provided him with experience of engineering design and organization. The death of his young daughter from influenza in 1922 was a turning-point in his life; he developed an obsession with the role of damp and bad housing on public health and founded a company to develop his ‘Stockade Building System’—a method of cheaply building walls from cement and wood shavings. However, the company collapsed in 1927. Thereafter followed a strange and crucial period of his life, ‘the year of silence’ when he refused to speak to anyone, not excepting his wife, but consumed books and articles on mathematics, science, engineering and architecture with a compulsive and almost destructive inner energy. It was a time when the inventiveness of his mind took root—an inventiveness subsequently expressed in a welter of ideas, proposals and projections throughout the rest of his life which it is difficult, if not impossible, to assess. Certainly he was far ahead of his time in his advocacy of a ‘world design science’ to avoid ecological catastrophe and the invention of the geodesic dome was a major engineering design achievement; however these must be set against so much else of his work and ideas which now seem merely fanciful and which he would tirelessly express in presentations and lectures of up to four hours at a stretch!

The initial outcome of the year of silence was ‘4-D’ (meaning four-dimensional thinking) in time as well as space. It was the first of many terms or words coined by Buckminster Fuller to express ideas or concepts for which the English language was then deficient; the most well-known of which are *Synergy*, or *Dymaxion*, the latter a word not invented by Buckminster Fuller himself but by the public relations department of a Chicago department store (the ‘spin doctors’ of the time) and made up of the words he most frequently used—‘dynamic’, ‘maximum’ and ‘ion’. It was Buckminster Fuller’s favourite adjective which he applied to light-weight, easily erectable houses, towers (stacks of Dymaxion houses) and, most famous of all, the Dymaxion car of 1933–4, a hoped-for breakthrough in automobile design which would lift the industry out of the depression.

The geodesic dome was largely the outcome of Buckminster Fuller’s work with the Design Class of Black Mountain Art School, North Carolina, from 1948. The Patent was applied for in 1951 and granted in 1954; it represented the last turning-point in his life from failed entrepreneur to visionary designer. The basic structural design has been applied to simple tent-like structures to radomes and, following the success of the

dome covering the Ford Motor Company's building in Dearborn, Michigan, has become an accepted architectural form. The use of his name to describe the newly-discovered carbon structures was made after his death.

René-Just Haüy 1743–1822

The son of a poor weaver, Haüy received a classical and theological education at the College de Navarre in Paris and was ordained in 1770. His *Essai d'une théorie sur la structure des cristaux* of 1784 laid the foundation for the mathematical theory of crystal structure. In 1793 he proposed that there were six 'primary forms'—a parallelepiped, rhombic dodecahedron, hexagonal dipyrmaid, right hexagonal prism, octahedron and tetrahedron. In the *Traité de Minéralogie* of 1801 these were further divided, which led to the notion of 'molécules intégrantes'. Haüy survived the Revolution and was made Honorary Canon of Notre Dame in 1802.

Carl Heinrich Hermann 1898–1961

Formal structure theory, following the derivation of the 230 space groups by Fedorov, Schoenflies and Barlow, remained dormant even in the early years of crystal structure analysis by X-rays, largely because of the inconvenient and difficult notation then used. Hermann's great contribution (carried out initially independently of Mauguin) was to simplify the notation for the symmetry elements and space groups, making the theory much more accessible. Hermann was also instrumental in the preparation of the *Strukterberichte (Structure Reports)* from 1925 to 1937. He was a member of the Society of Friends and after the Second World War (during which he was jailed for listening to BBC broadcasts) he was appointed Professor of Crystallography at Marburg, a post he held until his death.

Norman Fordyce McKerron Henry 1909–83

N. F. M. Henry was born at Grangemouth, Stirlingshire and was brought up in Aberdeen where his father was a master at the Grammar School. He read geography at Aberdeen University and in 1934 entered the newly founded Department of Mineralogy and Petrology at Cambridge University and St. John's College which was to become, to a great extent, the focus of his life.

Henry's research interests lay in the fields of X-ray crystallography and reflected light microscopy and, although he published few papers, the two books *The Interpretation of X-ray Diffraction Photographs and the Microscopic Study of Opaque Minerals* which he co-authored have been instrumental in the wide dissemination of these subjects. Indeed, he and his colleagues introduced the subject of crystallography to a greater number of students than at any other university. As a teacher Henry presented an image of formality and dryness, but even undergraduates could recognize the humour and generosity that lay underneath. He conducted tutorials two at a time, passing from group to group (with perhaps time for a cigarette in between), setting problems and expecting the solutions to be ready at the next visitation: a simple and most effective technique.

Henry played a major role in the work of the International Union of Crystallography where his knowledge of European languages and cultures did much to establish an atmosphere of goodwill and collaboration. He edited (with Kathleen Lonsdale) the first volume of the *International Tables for X-ray Crystallography*, a task entirely fitted to his rigorous standards and painstaking scholarship.

In 1960 he was elected a Fellow of St. John's College, was made Steward (1961–9) in recognition of his knowledge of food and wine and was elected Praelector or 'college-father' in 1971 where again his support and concern for his younger colleagues found full expression.

Johann Friedrich Christian Hessel 1796–1872

Hessel was born and educated at Nuremberg but spent most of his professional life as Professor of Mineralogy and Mining Technology at Marburg. He was the first to show (in 1830) that only two-, three-, four- and six-fold axes of symmetry can occur in crystals and that considerations of symmetry lead to the thirty-two crystal classes. However, his work was unrecognized by his contemporaries and remained so until long after his death.

Robert Hooke 1635–1703

Hooke attracted the attention of Robert Boyle at Oxford and it was through his mechanical skill that he made a success of Boyle's air pump. He became a Fellow of the Royal Society and held the post of 'Curator of Experiments' from 1662 until the end of his life. It was in this capacity that Hooke was solicited by the Council of the Royal Society to prosecute his microscopical observations in order to publish them and was also charged to bring in at every meeting one microscopical observation at least. Hooke more than fulfilled this onerous obligation and, in doing so, caused the great capability of the microscope to be realized in England. The fruit of his work, *Micrographia, or Some Physiological Descriptions of Minute Bodies made by Magnifying Glasses, with Observations and Inquiries Thereupon*, was printed in 1665. In his book the word 'cell', so important in biology, was first applied to describe the porous structure of cork.

Albert Wallace Hull 1880–1966

Albert W. Hull was born in Connecticut and studied Classics at Yale University. However, he became increasingly interested in physics and after a period teaching modern languages, returned to Yale and completed, as it were, his educational transition by the award of a doctorate in 1909. After a further period of teaching (this time physics), he joined the General Electric Research Laboratory at Schenectady where he discovered (independently of Debye and Scherrer) the powder diffraction technique. Hull's later achievements were in the fields of electronics (principally the invention of the Thyratron) and what is now called materials (principally the development of metal-glass vacuum seals). He was elected President of the American Physical Society in 1942.

Christiaan Huygens 1629–95

Huygens was born in The Hague, studied at the University of Leiden and Breda and became one of the founding members of the French Academy of Sciences. He made important contributions to dynamics and showed that a pendulum which describes a cycloid (rather than the arc of a circle) is exactly isochronous and succeeded in inventing and constructing a pendulum clock based on this principle. He also made major contributions to observational astronomy and was the first to describe Saturn's rings correctly.

Huygens' greatest achievement was his development of the wave theory of light described in his *Traite de Lumiere* (1690). The notion of action at a distance was abhorrent to him; in his view space is pervaded by particles (the ether), light being the effect of the disturbance of the particles—that of one particle being transmitted to the next and so on. The net effect is a wave spreading out from the point of origin, each point in the wavefront being the source of secondary wavelets. Huygens was thereby able to explain refraction and reflection and to predict (correctly) that the velocity of light decreased in passing from a rarer to a denser medium—whereas Newton's corpuscular theory required the denser medium to attract the corpuscles of light and therefore increase its velocity. However, because the waves were conceived as being longitudinal, rather than transverse, he could not satisfactorily explain double refraction.

The problem of double refraction constituted one of Newton's objections to the wave theory of Huygens for 'Pressions and Motions', as he says in *Opticks*, 'propagated from a shining body through a uniform medium must on all sides be alike', whereas experiment had shown that the 'Rays of Light have different properties in their different sides'—a clear presentiment of the idea of polarization. The other, even more serious objection, was that without the concept of interference, Huygens' wave theory could not explain the most obvious character of a light beam, namely rectilinear propagation. It was not until the work of Fresnel and Young at the beginning of the nineteenth century that the wave theory of light was finally established.

Johannes Kepler 1571–1630

The turmoil of Kepler's life is in strong contrast to his belief in the existence of a mathematical harmony underlying the Universe, the search for which was the guiding inspiration of his life's work. He was born in Württemberg in Germany and in 1594 was appointed teacher of mathematics at the seminary at Gratz. Here he encountered the work of Nicolaus Copernicus and published his first book (*Mysterium Cosmographicum*, 1596), in which he tried to show that the orbits of the planets were determined by the nesting, one within the other, of Plato's five regular solids—cube, tetrahedron, dodecahedron, icosahedron and octahedron. Forced, as a Lutheran, to leave Gratz, he joined Tycho Brahe in Prague under the patronage of the emperor Rudolph II, a fruitful but uneasy collaboration. Here Kepler discovered the first two of the three laws of planetary motion which were to be of such importance to Newton, wrote a major work on optics, discovered the second new star visible to the naked eye since antiquity and prepared his astronomical tables, against a background of the social unrest of the Thirty Years' War and continual lack of financial support from the emperor.

In 1611 civil war broke out in Prague, the emperor was forced to abdicate and Kepler's young son and wife died. He moved to Linz, remarried in 1613, and had to face his mother's trial for witchcraft in Württemberg. At Linz he published *Harmonices Mundi* (1619) which contains his third law.

On completion of the astronomical (Rudolphine) tables, Kepler moved to Sagan in Silesia under the patronage of Imperial General Wallenstein. He died of a fever at Ratisbon in the unsuccessful quest of 12 000 florins owed to him by the emperor.

Alexander Isaakovich Kitaigorodskii 1914–1985

Kitaigorodskii was born in Moscow into a professional family background: his father was a distinguished chemical engineer and one of the creators of devitrified glasses. In his early education at home Kitaigorodskii became fluent in French (the then polite language of the Russian aristocracy and professional classes) and learnt German and some English. He also became a skilled, indeed prize-winning dancer. In short, his childhood seems to have been little affected by the political and social turmoil of the times.

On leaving secondary school at the age of sixteen he worked in the laboratory of a metallurgical (steelmaking) plant in the Urals and there found both the time and opportunity to acquire a knowledge of physics and mathematics at sufficient depth not only to allow him to enter the Physics Department of Moscow University directly into the third year but also contribute to the teaching of students. His biographers assert that he achieved this knowledge 'completely by himself',² but it is difficult to believe that he had no teacher nor mentor to encourage him. One thinks of the near-parallel case of Harry Brearley, the discoverer of stainless steel, working in the laboratory of the Sheffield steelmaking firm of Thomas Firth and Sons and becoming a skilled analyst through the encouragement of the Head of the Laboratory.

On graduating in 1935, Kitaigorodskii commenced research on the X-ray diffraction of amino acids in the Biophysics Division of the Institute of Experimental Medicine, gaining his PhD degree in 1939. During the second world war he was Head of the Physics Department of an armaments plant in the City of Ufa in the Urals. In 1944 he returned to Moscow to work in the Institute of Organic Chemistry of the Soviet Academy of Sciences.

In these years Kitaigorodskii developed his ideas concerning the packing arrangements of organic molecules in crystals, the first fruit of which was the subject of his DSc thesis *Arrangement of molecules in crystals of organic compounds* which he defended in the Institute of Physical Problems. This famous Institute of the Soviet Academy of Sciences has a remarkable history. Its founder was Peter Kapitza, a Soviet citizen who had yet been long resident in England (and hence eligible for election as a Fellow of the Royal Society) and who in 1930 had been appointed as Head of the Royal Society's Mond Laboratory at Cambridge. On a visit to his home country in 1934, Kapitza was 'detained' by the Authorities, but in order that his work could continue, the equipment at

² Yu. T. Struchkov and E. I. Fedin. Alexander Kitaigorodsky his life and scientific activity, *Acta Chimica Hungarica* **130** (2), 159 (1993).

Cambridge was purchased by the Soviet Government to equip the new and prestigious Institute. From 1946 (the year of Kitaigorodskii's DSc thesis) until 1955, Kapitza was under house arrest for refusing to take part in nuclear weapons development.

In 1954, Kitaigorodskii moved to the Institute of Organoelement Compounds where he remained until his death although he was never elected to a University professorship.

Kitaigorodskii's work on the geometry of the packing of organic molecules and his elucidation of the space groups for closest, limitingly and permissible close packing became widely recognized through the English translation of his book *Organic Chemical Crystallography* (1961). It is in his later book *Molecular Crystals and Molecules* (1973) that the limitations of the geometrical approach became apparent: Kitaigorodskii assumed that molecules were rigid objects, undeformed by crystal forces and that variations in bond lengths were spurious. This of course is not the case, but at the time such variations were within the experimental error of the equipment then available to him.

Towards the end of his life, Kitaigorodskii was allowed to travel abroad and amazed his hosts not only by his science but by his convivial and outgoing nature—his dancing skills developed into water-skiing and ice-skating! But despite being awarded the D. I. Mendeleev (1949) and E. S. Fedorov (1967) prizes of the Soviet Academy of Sciences, he was never himself elected an Academician—doubtless a consequence of his irreverent attitude even to the Academy itself. Of his life's work he should have the last word. Not long before his death he was asked which of his achievements in science he considered the most important. 'I've shown', he replied 'that a molecule is a body. One can take it, one can hit with it—it has mass, volume, hardness. I followed the ideas of Democritus.'

Max von Laue 1879–1960

Max Laue (the title 'von' appears after his father was raised to the hereditary nobility in 1914) was born in Pfaffendorf near Koblenz. He was educated at the University of Berlin and, as a pupil of Max Planck, obtained his doctorate in 1903 for a thesis on the interference of light between plane parallel plates.

In 1909 he became *Privatdozent* in the Institute for Theoretical Physics in the University of Munich under Arnold Sommerfeld. He was an early 'convert' to Einstein's special theory of relativity and wrote the first monograph on the subject.

Laue's intuition (that the regular arrangement of atoms in a crystal might give rise to an interference effect if the waves travelling through were of a wavelength of the same order as the atom or 'resonator' spacing) almost certainly stems from a meeting with P.P. Ewald in January 1912. Ewald was completing his doctorate thesis and wished to discuss some of his conclusions with Laue. Laue encountered strong disbelief amongst his colleagues of a significant outcome of such a diffraction experiment on the grounds that the thermal vibration of the atoms would obscure any diffraction maxima. However, he persevered, and with the assistance of Walter Friedrich (an assistant of Sommerfeld) and Paul Knipping (who had just finished his thesis under Röntgen), the famous experiment on a copper sulphate crystal which 'happened to be in the laboratory' was carried out.

Laue recalls in his *Autobiography* the very time and place when the idea for a mathematical explanation of the spots in the photograph taken by Friedrich and Knipping came

to him: 'I was plunged in deep thought as I walked home along Leopold-strasse just after Friedrich showed me this picture. Not far from my own apartment at Bismarckstrasse 22, just in front of the house at Siegfriedstrasse 10, the idea for a mathematical explanation of the phenomena came to me . . . I had to re-formulate Schwers's theory of diffraction by an optical grating so that it would be valid, if iterated, also for a cross-grating. I needed only to write down the same equation for a third time, corresponding to the triple periodicity of the space lattice, in order to explain the new discovery.'

The new discovery, and Laue's analysis (in terms of a three-dimensional diffraction grating), which Einstein referred to as one of the most beautiful in physics, led to the award of the Nobel Prize for Physics in 1914. But unlike the Braggs, who were awarded the Nobel Prize in 1915, Laue did not pursue crystal structure determination since his main interests lay towards the 'great general principles' of Physics.

In 1919 Laue returned to the University of Berlin to be near his mentor, Max Planck, and in 1921 was elected a member of the Prussian Academy of Sciences. He protested against the Nazi Party's persecution of Einstein: at his opening address on 18 September 1933 to the Physics Congress held in Würzburg he drew the parallel between Galileo, champion of the Copernican World View, and Einstein, the founder of relativity theory; just as Galileo had won out against the church's prohibition so also would Einstein win out against the proscriptions of National Socialism. However, Laue was unable to stem the tide of Nazi infiltration into German Science; he was increasingly 'sidelined', his advice and judgement were no longer asked for and in 1943 he took early retirement from teaching and moved away from Berlin to Württemberg-Hohenzollern. After the war he was briefly interned in England and until his death took a major role in the rebuilding of German science and its institutions.

Kathleen Lonsdale 1903–71

Kathleen Yardley was born in Newbridge, S. Ireland, the youngest in a family of ten children. In 1908 the Yardley family moved to England in view of the unsettled state in Ireland. As a schoolgirl Kathleen showed her remarkable aptitude for physics and mathematics; at the age of 16 she won a scholarship to Bedford College for Women and in 1922 came top of the class list, as a result of which the examiner, W. H. Bragg, offered her a place in his research team first at University College and then at the Royal Institution—a team which then consisted of some of the brightest stars in X-ray crystallography. In 1927 she married Thomas Lonsdale and moved with him to Leeds when he took up a post in the Textile Department. It was a short but formative period in her life: she proved that the benzene molecule was planar, established her position as a leading X-ray crystallographer and also showed that it was possible to combine the roles of a scientist and a wife and mother. Her recollections of Leeds—the food bargains which could be obtained (and can still be obtained today) in the closing-time auctions at the Leeds market—are evocative. In 1929 she returned to London as W. H. Bragg's research assistant and remained with him at the Royal Institution until his death in 1942. Her early upbringing was strict Baptist, but by degrees she became a member of the Society of Friends, a vegetarian and a pacifist. These latter ideals led to her imprisonment for a short time in 1943 in Holloway Prison which was another positive formative influence in her life.

Kathleen Lonsdale (and Marjory Stephenson) were the first women to be elected Fellows of the Royal Society (22 March 1945). It was only subsequently that she was appointed to a university post, and became involved in teaching, first as Reader (1946) and then as Head (1949) of the Department of Crystallography at University College, London. However, perhaps her most enduring achievement was her leading role in the preparation of the *International Tables for X-ray Crystallography* as General Editor 1948–63 and as joint editor (with N. F. M. Henry) of the first volume, published in 1952.

To the end of her life her social conscience and concern for what is now called women's liberation was unwavering. She wrote in 1957 the Penguin Special *Is Peace Possible?* and in 1971 the broadsheet 'Women Scientists—Why so Few?'

Charles Mauguin 1878–58

Mauguin's early career expectation was that of a teacher in a teacher's training college, but he quickly developed an interest in mathematics and natural philosophy and commenced his scientific work in the field of organic chemistry. His interest in crystallography probably stems from a course of lectures given by Pierre Curie which he attended in 1905. Mauguin was one of a small group of crystallographers who, in 1933, undertook the publication of the International Tables, and it is his symbolism of the 230 space groups (worked out in collaboration with C. H. Hermann) which is now in almost universal use.

Helen Dick Megaw (1907–2002)

Helen Megaw was born in Dublin in 1907 into a distinguished and well-connected Northern Irish family—her father was a Leading Ulster politician. The family moved to Belfast in 1921 just before the partition of Ireland, but Helen continued her education in England—at Roedean School in Brighton. It was here that her interest in science, and crystallography in particular, was stimulated by her reading the Braggs' book *X-ray and Crystal Structure*.

She briefly returned to Northern Ireland to study at the Queen's University, Belfast, but in 1926 returned to England with a scholarship to read natural sciences at Girton College, Cambridge (then an all-female college). By a happy chance one of her chosen subjects was mineralogy and she achieved a first class in Part I of the Tripos examination. But in Part II (physics) she failed to achieve a first class. This was the second happy chance because it effectively debarred her from beginning research in the Cavendish Laboratory; instead she went to see Arthur Huthcinson of the Department of Mineralogy (who many years previously had provided the Braggs with crystals) and through his good offices began research with J.D. Bernal. Her subject was the structure of ice and Megaw identified the 'oscillating' hydrogen bonding between oxygen atoms. For this work 'Megaw Island' in the Antarctic was named after her.

But in 1934, the year she was awarded her PhD, the country was in a state of depression and jobs in research were virtually non-existent. So, from 1925 to 1943 she taught physics at high-flying girls' schools in Bedford and Bradford.

However, in 1943 she joined Philips Research Laboratories at Mitcham and by another happy chance began to study the structure of barium titanate (samples of which had been sent to Philips from the USA by mistake). This was the beginning of her life's work on the perovskite structures which she continued briefly with Bernal at Birkbeck College (1945) and finally at the Cavendish Laboratory and Girton College (1946 until her retirement in 1972).

In 2000, at the age of 93, Helen Megaw received an Honorary Degree of the Queen's University.

William Hallowes Miller 1801–80

Miller was educated in St. John's College, Cambridge, where, in 1829, he became a Fellow. In 1839 he published *A Treatise on Crystallography*, in which he made the fundamental assertion that crystallographic reference axes should be parallel to possible crystal edges. His system of indexing was based on a 'parametral' plane making intercepts a , b and c on such axes [i.e. (111)]; a plane making intercepts a/h , b/k and c/l was assigned the (integral) indices (hkl). Although the algebraic advantages of this system were immediately apparent to his contemporaries (and were quickly adopted), their full significance was not fully appreciated until Bragg's and Ewald's interpretation of X-ray diffraction.

Franz Ernst Neumann 1798–1895

Neumann was born in Joachimsthal (now Jáchymov in the Czech Republic) and was brought up by his grandparents (his mother, a divorced Countess, being unable to marry his father who was from a lower social class). He showed an early aptitude for mathematics and attended the Berlin Gymnasium after which, at the age of 16, he volunteered to serve in the Prussian Army. He was wounded in the Battle of Ligny (the forerunner to Waterloo) in 1815.

Neumann's contributions to mineralogy and crystallography, which represent a relatively small part of his life's work, arose through his collaboration with his friend and mentor C. S. Weiss. He introduced and developed the stereographic projection in the study of crystals and extended Weiss' work on zones in publications of 1823 and 1830. He was appointed curator of the Mineral Cabinet at the University of Berlin in 1823.

Although throughout his long life Neumann made many original contributions to optics, heat and electrodynamics (for which he was awarded the Copley Medal of the Royal Society in 1887), he was chiefly remembered by his contemporaries as an inspiring teacher. He was also a firm Prussian patriot and supported Bismarck's policy for the unification of Germany.

Isaac Newton 1642–1727

'Nature was to him an open book, whose letters he could read without effort.'

A. Einstein. Foreword to Newton's Opticks

Isaac Newton was born, a premature and posthumous child, at Woolsthorpe Manor in Lincolnshire. He was educated at the King's School, Grantham, and was admitted to Trinity College, Cambridge, in 1661. It is while he was an undergraduate that he seems to have made his first acquaintance with optics; he read the works of Kepler and Descartes and from about 1663 was involved in the construction and performance of telescopes and the observation of lunar crowns and haloes. In the summer of 1665 he went home to Woolsthorpe Manor to escape the plague and remained there until April 1667, except for a three-month visit to Cambridge from March 1666. It was during this time that Newton says of himself 'I was in the prime of my age for invention and minded Mathematicks and Philosophy more than at any time since.' These two years of intellectual achievement—the formulation of the binomial theorem and the differential and integral calculus, the theory of colours and of universal gravitational attraction—together with the two years (1685–86) during which he composed the *Principia*, have never been surpassed.

Newton's first paper to the Royal Society (published in 1672), in which he showed that ordinary white light is a mixture of rays of every variety of colour, received such a hostile reception from Robert Hooke that it made Newton cautious of publishing his work; the *Principia* or the *Mathematical Principles of Natural Philosophy* itself was not published until 1687 and then largely due to the encouragement of Edmund Halley. It immediately brought to Newton enormous prestige, a place in society and public affairs but thereafter little more science.

The *Opticks* was not published until 1704, a year after the death of Robert Hooke, Newton's most pertinacious antagonist. Further editions came out in 1717, 1721 and 1730, the last being 'corrected by the Author's own hand'. In this great work Newton states that his 'design in this book is not to explain the Properties of Light by Hypothesis but to propose and prove them by Reason and Experiments'. However, there are many comments suggestive of a deeper penetration into the nature of light than exact knowledge could then achieve, including the notion of interference, for in attempting to explain the colours of thin films Newton describes the passage of light as being made up of 'alternate fits of easy Reflection and easy Transmission'.

The greatest interest in the *Opticks* lies in the *Queries*, in which Newton speculates on the nature of light. The question form may have been used to allay criticism that he was departing from his dictum 'hypotheses non fingo' (I frame no hypotheses), but all are couched in the negative 'Do not Bodies act upon Light at a distance?' A negatively phrased question suggests or implies a positive answer; 'do *not* bodies act upon light at a distance?' Is not Newton implying that the answer must be in the affirmative?

Shoji Nishikawa 1884–1952

Nishikawa was born in Hachioji near Tokyo where his father was a prosperous and well-established merchant of silk textiles. However, he was brought up and educated in Tokyo itself, entering the Faculty of Science at Tokyo University and completing the undergraduate degree course in Physics in 1910. As a young man he was shy and modest (personal characteristics which were to remain with him for most of his life),

but of his scientific ability there was no doubt. It was therefore a natural progression for him to continue at the University as a postgraduate student where he commenced a research project in the area of radioactivity. His change of direction into the area of X-ray crystallography arose from a visit, either by chance, or perhaps in view of his scientific insight, to the laboratory of Torahiko Terada in 1913. Terada, like the Braggs in England, on hearing the news of the discovery of X-ray diffraction by Laue, Friedrich and Knipping, immediately began experiments on single crystals of rock-salt and other minerals. His unique contribution at the time was to visually record the movements, as the crystal was rotated, of the diffraction spots on a fluorescent screen which he interpreted (like W. L. Bragg) as arising from reflections from the crystal planes. There can be little doubt that he arrived at this conclusion independently since it appears unlikely, given the problems of communication with Japan, that he would have known of W. L. Bragg's November 1912 Cambridge Philosophical Society paper in which the Bragg law in the embryonic form $\lambda = 2d \cos \theta$ was first announced (θ being the complement of the θ angle subsequently used). In the event Nishikawa, encouraged by Terada, commenced X-ray diffraction studies, principally on fibrous materials, asbestos and gypsum, and published the earliest X-ray fibre patterns. This work was extended to lamellar materials, talc and mica, thin sheets of rolled and annealed metals and finely-powdered materials, rock-salt, quartz and corundum. Again, independently of W. L. Bragg, he determined the crystal structure of spinel in 1915.

In 1917 the Institute of Physical and Chemical Research of the University of Tokyo was established, one of the first acts of which was to send Nishikawa first to join R. W. G. Wykoff at Cornell University and then, after the end of the war, to join W. H. Bragg at University College, London. On his return to Tokyo in 1920 he organized, and led, the Nishikawa Laboratory, the work of which was seriously interrupted by an earthquake in 1923.

In 1924 Nishikawa married Kiku Ayai, was appointed Professor of Physics and gave largely inaudible (but otherwise excellent) lectures to undergraduates. As with Terada it might be said that he suffered from the then lack of communication from abroad; he was forced to abandon his nearly completed structural analysis on aragonite and α -quartz on finding that W. L. Bragg (1924) and W. H. Bragg and R. E. Gibbs (1925), respectively, had already solved these structures. However, following the discovery of electron diffraction in 1927 by G. P. Thomson and A. Reid in England and Davisson and Germer in the USA, he was instrumental in his guidance to his pupil, Seishi Kikuchi, in the discovery of what are now known as Kikuchi lines. Nishikawa's last statesmanlike act, long after his retirement, was to secure for Japan membership of the International Union of Crystallography.

Louis Pasteur 1822–95

Pasteur is perhaps best remembered for his work in microbiology and immunology and, in particular, the practical applications—the discovery of vaccines, the treatments for rabies and anthrax, silkworm disease, etc. His work in crystallography was confined to the early years of his scientific career. Beginning in about 1847 (shortly after completing his dissertation in physics), he began a series of investigations into the relations between

optical activity, crystalline structure and chemical composition in organic compounds. His guiding principle was that optical activity was somehow associated with life; that whereas enantiomorphic crystals or molecules produced in the laboratory, or of mineral origin, occurred in equal quantities of left- and right-handed forms, those of organic origin—from plants or animals—were always of one form. The origin of life it seemed was bound up with an original asymmetric chemical synthesis. Hence Pasteur believed that molecular asymmetry was an essential characteristic of the chemistry (and biology) of life.

Pasteur's demonstration that the optically inactive (or racemic) paratartronic acid was composed of equal amounts of two optically active forms of opposite senses was made on crystals of sodium-ammonium paratartrate. In using these, and in separating out the two forms, he was perhaps fortunate, as in no other compounds is the relationship between crystal structure and molecular asymmetry so straightforward; also, the distinctive 'hemihedral' crystalline forms of these compounds occur only under certain conditions of crystallization. From this he was led to study asparagine and its derivatives (aspartic acid and the aspartates, malic acid and the malates).

Linus Carl Pauling 1901–1994

Pauling was born in Portland, Oregon, USA. His childhood, following the death of his father, was a difficult one, but he was encouraged by an early school teacher, Pauline Geballe, who recognized his clearly emerging scientific abilities. Years afterwards, as the recipient of two Nobel prizes, he revisited, at a school reunion, his old teacher who had been such an influence on him.

After graduating from Oregon Agricultural College with high honours, Pauling enrolled not in one of the well-established 'Ivy League' Universities of the USA but in the fledgling California Institute of Technology at Pasadena: 'Caltech' was to be Pauling's Alma Mater for another forty years. His advisor was Roscoe Dickinson who had introduced X-ray diffraction techniques from England and Pauling determined the structures of microcline and labradorite, gaining his PhD degree in 1925. Thence the nature of the chemical bond dominated his interest: he realized early on that the newly emerging field of quantum mechanics was relevant to the problems with which he was concerned. From 1926 Pauling made extended visits to Europe to make contact with the leading figures of European science: Arnold Sommerfeld in Munich, Niels Bohr in Copenhagen and W.L. Bragg in Manchester. It was during this time that he developed his 'rules' for the solution of crystal structures, first enunciated in a paper of 1928 and which were eventually to be encapsulated in his great book *The Nature of the Chemical Bond and the Structure of Molecules and Crystals*, which was first published in 1939. Pauling's presentation of his rules, as solely the fruit of his own chemical insight, was the source of friction with W.L. Bragg whose analyses of the structures of minerals, silicates in particular, involved, in effect, an application of the first three rules and whose work and contribution received scant acknowledgement. It was not the only such occasion: Pauling's undoubted brilliance (and perhaps his own feeling of superiority and/or lack of recognition of the contributions of others) led to difficult relations with many of his fellow scientists.

In 1932, armed with the first of a series of large grants from the Rockefeller Foundation, Pauling abandoned the analysis of inorganic compounds and entered the field of biology and medicine—a major phase in his life's work that was ultimately to lead to the 'α-helix' model for the structure of proteins. Pauling's initial work was on haemoglobin and led, from 1936, to his long collaboration with Robert Corey.

During the war years 1940–1945, Pauling virtually abandoned scientific work and became involved with political and social issues which initially stemmed from his outrage at the treatment of Japanese-American citizens and the vilification of his doctor—an outspoken communist whose treatment in 1941 for a serious illness certainly saved Pauling's life. After the war, Pauling became a strong supporter of the Peace Movement, an advocate of rapprochement with the Soviet Union and an opposer of nuclear weapons, activities which during the McCarthy era stigmatized him as a security risk and which led to the withdrawal of his passport in 1952.

The story of Pauling's discovery of the α-helix protein structure is a curious one. He recalls that during a visit to Oxford as a visiting Professor in 1948 he was laid up in bed with a bad cold. Sick of reading detective stories he drew pictures of amino-acid molecules on pieces of paper, folding the papers in such a way as to achieve the correct bond angles and then fitting them together to form a helix—a helix with the unexpected property that the successive turns of the helix did not correspond with an integral number of amino acid residues. On his return to Caltech he set a senior fellow, Herman Branson, with the problem of finding possible helical structures and Branson, largely independently, came up with two solutions—the α and γ helices. The discovery of the α-helix was formally announced at a congress in Stockholm in 1951. It did not go down well at first with the English scientists—Astbury, Perutz and Bragg—because it contravened their innate feeling that the turns of the helix should correspond with an integral number of amino acid residues.

In 1952, W. T. Astbury organized a Discussion Meeting on the Structure of Proteins at the Royal Society, to which of course Pauling was invited as a principal speaker. But without a passport, he was unable to attend and a colleague, Edward Hughes, had to deputize on his behalf.

The great opus of Pauling's scientific work was recognized with the award of his first Nobel Prize for Chemistry in 1954. His second Nobel Prize, for Peace, was announced on 10th October 1963, the same day as the announcement of the (partial) Test Ban Treaty for which Pauling had campaigned so hard.

William Jackson Pope 1870–1939

Pope's major scientific work was in the field of organic chemistry. He was educated at Finsbury Technical College and the City and Guilds of London Institute in Kensington; in 1908 he was appointed Professor of Chemistry at Cambridge at the early age of 38. His crystallographic work extends over the period 1906–10 when, in collaboration with W. Barlow, he developed models of crystal structures based on the close-packing of ions or atoms of different sizes—models which were to prove so valuable to the Braggs in their analyses of crystal structures.

Jean Baptiste Louis Rome de L'Isle 1736–90

Rome de L'Isle, the son of a cavalry officer, was born in Gray in France. In 1756 he joined the Royal Corps of Artillery and Engineering and travelled to Pondicherry in the French East Indies. When Pondicherry was seized by the English in 1761 he was taken prisoner and transported to China where he remained until 1764 when he returned to France. He first studied mineralogy and in 1767 he was asked to prepare a catalogue of a collection of mineral 'curiosities'. In doing so he followed the method of Linnaeus (the great Swedish botanist) in emphasising the importance of crystalline form in mineralogical description. In 1772 he published *Essai de cristallographie* and in 1783 his major work *Cristallographie*. Here he identified 450 'crystalline forms' and characterized the cube, regular octahedron, parallelipiped, rhomboidal octahedron and dodecahedron. In the course of measuring the angles between the faces of terracotta (clay) crystal models using a contact goniometer, he recognized the constancy of interfacial angles.

Rome de L'Isle's great contribution, through his experimental work, was to establish crystallography as the firm basis for the study of minerals although he did not follow (and was critical of) Haüy's notion of 'molecules integrantes'.

Wilhelm Conrad Röntgen 1845–1923

Röntgen was born in Lennep, a small town near Remscheid in the Rhine province of Germany. His father was a prosperous cloth merchant and both parents came from established Lutheran Rhineland families. When Röntgen was aged three, the family moved to Appeldoorn in Holland. During his boyhood Röntgen showed no special aptitudes and his education was interrupted as a result of being expelled from school for refusing to name a fellow pupil who had been involved in some misdemeanour. He entered Utrecht Technical School (rather than University) in 1862 and then went on to study mechanical engineering at Zurich Polytechnic, gaining the PhD degree in 1869.

By this time Röntgen's academic ability, and moreover his outstanding practical experiment skills, were evident. In 1871 he became assistant to Professor August Kundt in the University of Würzburg and moved with him to Strasbourg before being himself appointed in 1879 to the Chair of Physics at the University of Geissen—a post he held until 1888 despite the offer of Chairs at the prestigious Universities of Jena and Utrecht. However, in 1889 he returned to Würzburg as Professor of Physics: perhaps the atmosphere of that old Bavarian town suited his own reticent personality—for Röntgen shunned all public engagements. He worked almost entirely alone in the laboratory such that there should be no disturbance to his concentration and developed acute powers of observation which undoubtedly led to his discovery of X-rays on 8th November 1895.

Röntgen was experimenting with discharge (cathode ray) tubes and the action of the rays in generating fluorescence in crystals and luminescence in gases—hardly a 'hot topic' since such tubes had been developed by William Crookes some twenty years earlier. Röntgen had enclosed the tube in a light-tight cardboard box and noticed that every time the induction coil discharged through the tube, a crystal of barium platinocyanide, lying on a nearby table, gave a flash of fluorescence. Röntgen, ever cautious, did not

immediately announce his discovery, but in a feverish bout of work found that the rays (which, not knowing their nature, he called X-rays), originated from where the cathode rays fell on the glass walls of the tube; that they were neither refracted, reflected nor diffracted (from optical gratings), were more heavily absorbed by denser elements and blackened photographic plates. On 22nd December he took the famous radiograph of his wife's hand and on 28th December communicated his observations to the Physical and Medical Society of Würzburg which he followed up by sending friends and colleagues reprints of his paper as New Year gifts. On 5th January 1896 the news of these amazing rays which could reveal the living skeleton broke around the World and on 15th January, Röntgen received a Royal Summons from the young Kaiser Wilhelm II to demonstrate his discovery at the Royal Palace in Berlin (a summons which, of course, he could not refuse), following which he was immediately awarded the Prussian Order of the Crown, Second Class. Further honours followed. In 1896, jointly with Lenard, he was awarded the Rumford Medal of the Royal Society and in 1901 the first Nobel Prize for Physics; at the presentation ceremony Röntgen declined to give the expected lecture.

Röntgen's discovery is an example of serendipity in science as well as a testament to his observational and experimental skills. For X-rays were being generated long before 1895. As early as 1879 Crookes complained of fogged photographic plates and Goodspeed and Jennings in Philadelphia in 1890 noted a 'peculiar' blackening of photographic plates after a demonstration with a Crookes discharge tube. Finally, we should record that Röntgen's other great achievement was to detect and measure the (very weak) magnetic effects, predicted by Maxwell's theory, when a dielectric is moved between charged condenser plates.

Alexei Vasilievich Shubnikov 1887–1970

Shubnikov's childhood in Moscow was one of great poverty, a family of six children being raised by his mother following the early death of his father. In 1906 Shubnikov attended a 'popular' course in crystallography given by G.V. Wulff and following his enrolment in 1908 at the State University, became Wulff's devoted pupil and assistant. At this time the seeds of the Russian Revolution were already being sown: in 1911 Wulff, Shubnikov and many of the academic staff resigned in protest against the reactionary policy of the Minister (of Education) Lev A. Kasso and transferred to the Shaniavskii People's University from which Shubnikov graduated in 1912. He was seriously wounded in 1914 and spent the remaining war years on non-combat duty as a chemist, working during his free time on geometrical crystallography and corresponding with Fedorov. In 1918 he returned to the People's University as Wulff's assistant but the political circumstances of the time—the isolation from Western Europe and the almost complete lack of equipment—made it impossible to do any serious research work. However, by 1927 the situation had eased and Shubnikov was 'sent' to Germany and Norway to gain first hand experience of X-ray analysis and where he met many of the leading figures of German science. He recalls asking Laue to show him the laboratory where he (Laue) investigated crystal structures and being amazed to find that Laue did not have a laboratory at all!

In 1925 Wulff died and Shubnikov took up a position in the Mineralogical Museum of the Soviet Academy of Science in Leningrad where he set up an X-ray diffraction facility and also studied piezoelectricity in quartz, work which entailed the full use of his great experimental skills. This work was severely interrupted in 1934 when the government transferred the Academy to Moscow and again in 1941 when the crystallography laboratory was evacuated to the Urals. It was during this time that Shubnikov developed the idea of ‘antisymmetry’ (surely an unsatisfactory and potentially misleading word) which rather means the unification of opposite concepts – plus and minus, black and white, etc., initially an abstract field of crystallography which has later found wide application in the study of magnetic and other properties of crystals.

John William Strutt, third Baron Rayleigh 1842–1919

Like his near contemporary the geologist and microscopist Henry Clifton Sorby, Lord Rayleigh (as he became when he succeeded to his father’s title in 1873) had the leisure and financial resources to devote his life to science. His early life was dogged by ill health; in 1865 he graduated in mathematics at Cambridge and remained there until 1872 when he went to Egypt for a period of convalescence. It was not, however, a period of idleness; he wrote his classic book *The Theory of Sound* on a houseboat on the Nile.

On his return to England he built his own private laboratory and carried out most of his work there except for a short period (1879–1884) when he was Cavendish Professor of Experimental Physics at Cambridge.

Rayleigh’s main contributions to science were in optics and acoustics; his work on the scattering of light by small particles led to the explanation of the blue colour of the sky and his work on the density of gases led to the discovery of argon.

Paul Hermann Scherrer 1890–1969

Scherrer was born at St. Gall, Switzerland. During his education his interests moved away from commercial topics towards natural history, first to botany and then to mathematics and physics. In 1913 he entered the University of Göttingen and became a member of Debye’s research group. The stimulus for the investigation of polycrystalline specimens appears to have come from Debye although the construction of the cylindrical camera was due to Scherrer. With it, Debye and Scherrer took the first X-ray powder photographs (of lithium fluoride) in 1915. A very similar method was devised in 1917 by Albert W. Hull at the General Electric Laboratories, USA.

In later years Scherrer was active in the foundation of the European Centre for Nuclear Research (CERN). He was also prolific teacher and brought to his lectures a considerable element of showmanship.

Arthur Schoenflies 1853–1928

Schoenflies was born in Landsberg an der Warte, now in Poland. He studied mathematics at Berlin and became successively high school teacher, Associate Professor of

Mathematics (at Göttingen), Professor (at Königsberg) and Rector at the University at Frankfurt. He extended the work of Sohncke on periodic discrete groups by taking into consideration rotation–reflection and inversion axes of symmetry, adding another 165 to Sohncke’s sixty-five groups. The work was completed in his book *Kristall-systeme und Kristallstruktur*, published in Leipsig in 1891, a few months after Fedorov’s paper.

William Bradford Shockley 1910–89

William Shockley was born in London to American parents and moved to California (with them) in 1913. He was educated at the California Institute of Technology and Massachusetts Institute of Technology and, after war service with the U.S. Navy’s Submarine Warfare Operations Research Group, became a supervisor in the semiconductor research group at Bell Telephone Laboratories in New York. There, in 1947, together with John Bardeen and Walter Brattain, he discovered the principle of the point contact transistor and then went on to develop the junction transistor. This may be said to be the starting point of the electronic transformation of the latter part of the twentieth century, which was recognized by the award of the Nobel prize for Physics, jointly with Bardeen and Brattain, in 1956.

Shockley then left ‘Bell Labs’ to set up the Shockley Semiconductor Corporation in California and from 1963 became Professor of Engineering at Stanford University.

The latter part of his life was clouded by controversy because of his uncompromisingly held views on dysgenics, i.e. retrogressive evolution through the excessive reproduction of the genetically disadvantaged, and for which, as one example of his increasing isolation, the University of Leeds refused to confirm his nomination for an Honorary Doctorate.

Leonhard Sohncke 1842–97

Sohncke was born in Halle, Germany, where his father was Professor of Mathematics at the University. Like his father he followed an academic career, being appointed to a succession of professorships in physics, firstly at Halle and at the end of his career at the Technische Hochschule in Munich. Sohncke considered the possible arrays of points which have identical environments but not necessarily in the same orientation (as in the definition of Bravais lattices), and arrived at sixty-five of the possible 230 space groups. He published his findings in 1867, while he was professor of Physics at the Technische Hochschule in Karlsruhe, and used cigar-box models by way of illustrations.

Nicolaus Steno (Niels Stensen) 1638–86

Stensen (Steno being the Latinized form of his name) was born in Copenhagen where his father, a goldsmith, kept a shop close to the famous Round Tower. He studied medicine at the University of Copenhagen and carried out anatomical researches in Florence, ultimately being appointed Royal Anatomist in Denmark in 1672.

Stensen combined his medical and anatomical career with an interest in minerals, metals, the refraction of light, telescopes and microscopes which presumably stemmed

both from boyhood associations in his father's shop and also from his later travels in Italy where he became acquainted with the works of Kepler and Galileo. He published in Florence in 1669 the *Prodromum* (i.e. an advance notice) to a treatise on solid bodies naturally enclosed in other solids—a work in which he outlined the principles of geology. This was translated into English by Henry Oldenberg, Secretary of the Royal Society, and re-published in London in 1671. In this work Stensen shows that crystals grow by external deposition on faces already laid down and not (as was then supposed by analogy with plants) by the absorption of fluids and the deposition of material from within. The *Law of the Constancy of Interfacial Angles*, for which he is best known, is illustrated in just one figure and stated in two sentences. In the latter part of his life Stensen's strongly held religious beliefs led him to renounce scientific research.

Gustav Heinrich Johann Apollon Tammann 1861–1938

Tammann can be regarded as a pioneer physical metallurgist in the light of his work in metallography and the study of solid-state chemical reactions. He was born in Yamburg (now Kingisepp) in Russia and, after a career as a lecturer at Charlottenburg and Leipzig, was chosen to head the newly formed Institute at Göttingen in 1903. It was here that he began his studies on metallic compounds, the crystal structures and mechanical properties of metals and alloys, and the general problems of the mechanisms of plastic deformation and work hardening in terms of crystallographic slip and crystalline rearrangements. He continued to work on these problems until shortly before his death, applying his ideas at the same time to the flow of ice.

Georgy Fedoseevich Voronoi 1868–1908

Voronoi was born in Zhuravka, Russia, into an academic family—his father was Superintendent (a sort of Government Inspector) of the Gymnasiums in towns in Southern Ukraine. His mathematical ability was apparent from an early age; he attended the Gymnasium at Priluka, graduated in mathematics in the University of St. Petersburg in 1889 and was appointed Professor of Pure Mathematics in the University of Warsaw at the early age of 26. Voronoi's main interests were in the Theory of Numbers, for which he planned a series of memoirs—a series cut short by his early death. It was in the second of these that he established the possible methods of filling n -dimensional Euclidean space with identical non-intersecting convex polyhedra (Voronoi polyhedra or parallelepipeds), all of which possessed contiguous boundaries—an analysis which extended the work of his near contemporary, Fedorov.

Wilhelm Eduard Weber 1804–91

Weber was Professor of Physics at Göttingen from 1831 for most of his professional life and worked in collaboration with Gauss on magnetic phenomena. His main achievements were the introduction of a logical system of units for electricity, related to the fundamental units of mass, length and time and also the connection between electromagnetic phenomena and the velocity of light—a connection which was later thoroughly

worked out by Maxwell. Weber was also one of the ‘Göttingen Seven’ who, in 1837, lost their university posts because of their opposition to the autocracy of King Ernst August of Hanover.

Christian Samuel Weiss 1780–1856

After studying medicine at Leipzig, Weiss switched to chemistry and physics, becoming Professor of Physics there in 1808. In 1810 he was appointed Professor of Physics at the newly established and prestigious University of Berlin, a post which he held until his death. Weiss developed the idea of crystal axes, from which he was able to distinguish crystal systems by the ways in which crystal faces were related to such axes. He also formulated the concept of a zone: originally conceived as a direction of prominent crystal growth, the term was defined as a collection of crystal faces parallel to a line—the zone axis; from this concept the zone law was derived.

Georg (Yuri Viktorovich) Wulff 1863–1925

Georg Wulff (the name he used in his German-language publications) was born in Nezhin in the Ukraine. He published his first papers (on the morphology and physical properties of crystals) in 1883 and 1884 whilst still a student at Warsaw University. In 1907 he was appointed Professor of Crystallography at Moscow University, a post which he held until his death. He proposed what has become known as the Wulff net (the stereographic projection of a sphere orientated with the polar ‘north-south’ axis in the plane of projection rather than perpendicular to it) in 1909.

Wulff’s contribution to X-ray crystallography was his demonstration of the geometrical equivalence of Laue’s diffraction and W. L. Bragg’s reflection interpretation of X-ray diffraction. The equation which he derived in 1913³ is equivalent to that which W. L. Bragg presented in the previous year;⁴ in both cases the equation is expressed in the form $n\lambda = 2d \cos \Theta$ where $\Theta = (90 - \theta)$. On this basis some writers link Wulff’s name with Bragg’s—the Bragg-Wulff equation. However, the present form of the equation was first given in a later joint paper by W. H. and W. L. Bragg⁵ and it was of course the Braggs who made the first great leap forward in crystal structure analysis.

Thomas Young 1773–1829

Young was an infant prodigy who could read at the age of 2 and at the age of 14 knew Latin, Greek, French and Italian, and had begun to study several ancient languages—Hebrew, Chaldean, Syriac and the like—linguistic knowledge that he put to use in his contribution to the translation of the text of the Rosetta stone. Young intended to take up a medical career and commenced his education in 1793 at St. Bartholomew’s Hospital, moving from there to Edinburgh, Göttingen and Cambridge. He was elected a Fellow of

³ Phys. Zeitschrift (15 Mar. 1913) Vol. 14, p. 217.

⁴ Proc. Cam. Phil. Soc. (11 Nov. 1912) Vol. 17, pp. 43–57.

⁵ Proc. Roy. Soc. A (17 April 1913) Vol. 88, pp. 428–438.

the Royal Society as early as 1794 for his explanation on how the ciliary muscles of the eye change the shape (and focal length) of the lens.

Young's great contribution to science was his revival in 1800–04 of Huygens' wave theory of light, to which he added the concept of interference to explain rectilinear propagation and the diffraction phenomena at single or double slits or pinholes and in which he was closely shadowed by the work of Fresnel in France. In England Young was strongly attacked because he questioned the hegemony of Newton, but his work quickly won acceptance in the USA and Europe. Young was also first to suggest (in a letter to François Arago in 1816) that light might be propagated as a transverse wave, thus accounting for polarization and meeting the main objection of Newton. Regrettably, Young did not live to witness Foucault's demonstration, in 1850, that the speed of light was less in water than in air—the crucial experiment which distinguished between the corpuscular and wave theories.

Young was also active in many other fields. His name comes down to us through his work on the elastic behaviour of solids as the constant of proportionality (E) in Hooke's law, called Young's (or latterly Young) modulus.

Appendix 4

Some useful crystallographic relationships

In Sections A4.1–A4.3 the rather lengthy expressions for the triclinic system are omitted.

A4.1 Interplanar spacings, d_{hkl} (see Section 6.5.4)

Orthorhombic:

$$\frac{1}{d_{hkl}^2} = \frac{h^2}{a^2} + \frac{k^2}{b^2} + \frac{l^2}{c^2}.$$

(Tetragonal: $a = b$; cubic: $a = b = c$.)

Hexagonal:

$$\frac{1}{d_{hkl}^2} = \frac{4}{3} \left(\frac{h^2 + hk + k^2}{a^2} \right) + \frac{l^2}{c^2}.$$

Rhombohedral:

$$\frac{1}{d_{hkl}^2} = \frac{(h^2 + k^2 + l^2) \sin^2 \alpha + 2(hk + kl + hl)(\cos^2 \alpha - \cos \alpha)}{a^2(1 - 3 \cos^2 \alpha + 2 \cos^3 \alpha)}.$$

Monoclinic:

$$\frac{1}{d_{hkl}^2} = \frac{1}{\sin^2 \beta} \left(\frac{h^2}{a^2} + \frac{k^2 \sin^2 \beta}{b^2} + \frac{l^2}{c^2} - \frac{2hl \cos \beta}{ac} \right).$$

A4.2 Interplanar angles, ρ , between planes $(h_1 k_1 l_1)$ of spacing d_1 and $(h_2 k_2 l_2)$ of spacing d_2 (see Section 6.5.5)

Orthorhombic:

$$\cos \rho = \frac{(h_1 h_2 / a^2) + (k_1 k_2 / b^2) + (l_1 l_2 / c^2)}{\sqrt{[(h_1^2 / a^2) + (k_1^2 / b^2) + (l_1^2 / c^2)][(h_2^2 / a^2) + (k_2^2 / b^2) + (l_2^2 / c^2)]}}.$$

(Tetragonal: $a = b$; cubic: $a = b = c$.)

Hexagonal:

$$\cos \rho = \frac{h_1 h_2 + k_1 k_2 + \frac{1}{2}(h_1 k_2 + h_2 k_1) + (3a^2/4c^2)l_1 l_2}{\sqrt{\{(h_1^2 + k_1^2 + h_1 k_1 + (3a^2/4c^2)l_1^2)[h_2^2 + k_2^2 + h_2 k_2 + (3a^2/4c^2)l_2^2]\}}}$$

Rhombohedral:

$$\cos \rho = (a^4 d_1 d_2 / V^2) [\sin^2 \alpha (h_1 h_2 + k_1 k_2 + l_1 l_2) + (\cos^2 \alpha - \cos \alpha) (k_1 l_2 + k_2 l_1 + l_1 h_2 + l_2 h_1 + h_1 k_2 + h_2 k_1)].$$

Monoclinic:

$$\cos \rho = \frac{d_1 d_2}{\sin^2 \beta} \left[\frac{h_1 h_2}{a^2} + \frac{k_1 k_2 \sin^2 \beta}{b^2} + \frac{l_1 l_2}{c^2} - \frac{(l_1 h_2 + l_2 h_1) \cos \beta}{ac} \right].$$

A4.3 Volumes of unit cells (see Section 6.5.6)

Orthorhombic:

$$V = abc.$$

(Tetragonal: $a = b$; cubic: $a = b = c$.)

Hexagonal:

$$V = (\sqrt{3}/2)a^2 c = 0.866a^2 c.$$

Rhombohedral:

$$V = a^3 \sqrt{(1 - 3 \cos^2 \alpha + 2 \cos^3 \alpha)}.$$

Monoclinic:

$$V = abc \sin \beta.$$

A4.4 Angles between planes in cubic crystals (variants between 100 and 221) (see Section 6.5.5)

100	100	0.00	90.00	
	110	45.00	90.00	
	111	54.74		
	210	26.56	63.43	90.00
	211	35.26	65.90	
	221	48.19	70.53	
110	110	0.00	60.00	90.00
	111	35.26	90.00	
	210	18.43	50.77	71.56
	211	30.00	54.74	73.22 90.00
	221	19.47	45.00	76.37 90.00

111	111	0.00	70.53				
	210	39.23	75.04				
	211	19.47	61.87	90.00			
	221	15.79	54.74	78.90			
210	210	0.00	36.87	53.13	66.42	78.46	90.00
	211	24.09	43.09	56.79	79.48	90.00	
	221	26.56	41.81	53.40	63.43	72.65	90.00
211	211	0.00	33.56	48.19	60.00	70.53	80.40
	221	17.72	35.26	47.12	65.90	74.21	82.18

A4.5 Relationships between zones and planes (see Section 6.5.3)

For a plane (hkl) which lies in a zone $[uvw]$:

$$hu + kv + lw = 0.$$

For a plane (hkl) which lies in a zone $[UVTW]$:

$$hU + kV + lW = 0.$$

For a lattice point with coordinates $[uvw]$ which lies in the n th (hkl) plane from the origin:

$$hu + kv + lw = n.$$

For a plane (hkl) which lies in the; zones $[u_1v_1w_1]$ and $[u_2v_2w_2]$:

$$h = (v_1w_2 - v_2w_1); \quad k = (w_1u_2 - w_2u_1); \quad l = (u_1v_2 - u_2v_1).$$

For a zone $[uvw]$ which contains the planes $(h_1k_1l_1)$ and $(h_2k_2l_2)$:

$$u = (k_1l_2 - k_2l_1); \quad v = (l_1h_2 - l_2h_1); \quad w = (h_1k_2 - h_2k_1).$$

Appendix 5

A simple introduction to vectors and complex numbers and their use in crystallography

A5.1 Scalars, vectors, tensors

In science—and, of course, everyday life—we are concerned with different types of quantities as well as quantities of the same type but of different size or magnitude. In many cases the quantities are independent of direction—mass for example, or volume or temperature. Such quantities, which can be represented by points on scales, are known as **scalars** and are denoted algebraically in familiar italic type— m for mass, t for time, x and y for unknown (scalar) quantities and so on. In many other cases, quantities are direction dependent, or, in other words, in order to specify the quantity completely the direction as well as the magnitude of the quantity needs to be described. Such quantities are called **vectors** and are denoted algebraically by printing in bold type—**a**, **b**, **x**, **y**, etc. In handwriting wavy underlining is substituted for bold type, i.e. \underline{a} , \underline{b} , \underline{x} , \underline{y} , etc.

Velocity is an everyday example of a vector quantity—we need to specify not only the speed of an object but the direction in which it is travelling. A motor car travelling 50 km h^{-1} due north has the same speed as a motor car travelling 50 km h^{-1} due east, but their velocities are different—one has a velocity of 50 km h^{-1} *north* and the other has a velocity of 50 km h^{-1} *east*. The velocities may be represented as vectors by arrows—one pointing north and one pointing east. The lengths of the arrows or vectors gives the speed—the greater the speed the longer the arrows. In the above case (50 km h^{-1}), the arrows are of equal length.

Heat and electrical current flow, electrical and magnetic fields are examples of vector quantities of interest in crystal physics, but in geometrical crystallography we are invariably concerned with vectors which denote displacements: for example the displacement from one corner of a unit cell to the next, or the displacement from one atom to another. Crystal axes or directions are examples of such displacement vector quantities. In Fig. 5.1 (p. 132) the directions and lengths of the edges of the unit cell are all denoted by the vectors **a**, **b**, and **c**. In the special case of cubic crystals (Fig. 3.1, p. 85) these vectors are all at 90° (orthogonal) and are also the same length, but they are *not* identical vectors because they ‘point’ in different directions.

The ‘length’ of a vector is called its **modulus**. In the case of the motor car the modulus of the velocity is the speed. The modulus of a vector is written in two ways, either in italic type, a (denoting that it is a scalar quantity), or with the heavy type vector symbol bracketed between straight vertical lines thus: $|\mathbf{a}|$. Hence $|\mathbf{a}| = a$.

In Fig. 3.1 the moduli a , b , and c of the unit cell vectors for the fourteen Bravais lattices are indicated. In the case of cubic (or rhombohedral) crystals, the unit cell edge lengths, or moduli, are all identical and are represented (for all three axes) by a . Hence $|\mathbf{a}| = |\mathbf{b}| = |\mathbf{c}| = a$ (as in Fig. 3.1).

Scalars and vectors are particular types of quantities which are known in general as **tensors**. There are other, more complicated types of tensors which are of importance in crystal physics because they are able to describe properties such as conductivity or stress which vary not only with the direction of the applied field or force but also with the orientation of the crystal. ‘Everyday’ examples of tensors (other than scalars or vectors) are not easy to provide, but the following, perhaps rather contrived example, may illustrate the ideas involved.

Consider rainwater flowing down a corrugated roof. The flow of water (a vector) is obviously down the roof, parallel to the corrugations and parallel also to a vector representing the inclined component of the gravitational field. The effective ‘conductivity’ may simply be regarded as the quantity that relates these two parallel vectors. Now consider a (badly made) roof in which the corrugations are set at an angle. The water will partly run sideways, along the ‘preferred direction’ of the corrugations and will partly flow downwards over from one corrugation to the next. The overall water flow will lie in a direction somewhere between the lines of the corrugations and downwards. In this case the effective gravitational field vector and the water flow vector are not parallel, and in estimating the effective conductivity of the roof, both the ‘downwards’ and ‘sideways’ components of the water flow need to be taken into account.

In crystals the ‘corrugations’ may be loosely regarded as preferred or easy directions of, say, heat or electrical flow. The conductivity of the crystal is the quantity which relates one vector (heat or electrical flow) to another vector (temperature or electrical field gradient). As indicated in the example above these vectors may not, except in special cases, be parallel and in general a total of nine terms or components¹ are required in order to specify the conductivity completely.

Conductivity is called a second-rank tensor property. There are, in addition, third-rank tensor properties (e.g. piezoelectricity) which are specified by 27 components and fourth-rank tensor properties (e.g. elasticity) which are specified by 81 components. Scalars, which are specified by one term or component are, in this classification, called zero-rank tensors and vectors which are, as shown below, specified by three components are called first-rank tensors.

A5.2 Resolving vectors into components and vector addition

Consider the (displacement) vector \mathbf{r} drawn in Fig. A5.1 which is outlined in a (two-dimensional) lattice with the unit cell vectors \mathbf{a} and \mathbf{b} . Note that all these vectors have a common origin.

¹ These components are not all independent: their number is greatly reduced by symmetry considerations. For further information on tensors, see J. F. Nye, *Physical Properties of Crystals*, Clarendon Press, Oxford, Second Edition 1985.

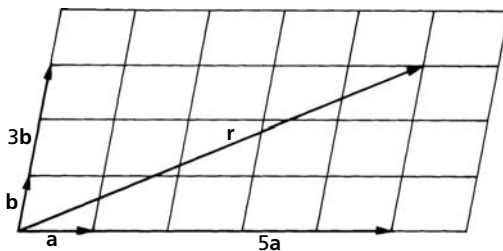


Fig. A5.1.

The vector \mathbf{r} may be resolved into its components in the directions of the unit cell vectors \mathbf{a} and \mathbf{b} . These components, $5\mathbf{a}$ and $3\mathbf{b}$, are drawn in Fig. A5.1. Added together they give \mathbf{r} , i.e. $\mathbf{r} = 5\mathbf{a} + 3\mathbf{b}$.

In vector analysis in general, cubic or Cartesian axes are chosen, and the unit cell vectors are labelled \mathbf{i} , \mathbf{j} , \mathbf{k} rather than \mathbf{a} , \mathbf{b} , \mathbf{c} . Also, the moduli of \mathbf{i} , \mathbf{j} , \mathbf{k} are unity and they are known as **unit vectors**. The general symbol for a unit vector is \mathbf{n} , i.e. $|\mathbf{n}| = 1$.

A5.3 Multiplying vectors—scalar products and vector products

There are two ways in which vectors can be multiplied, namely, the scalar product and the vector product, the general significance of which go beyond the scope of this book. We will consider only the multiplication of displacement vectors.

The scalar (or ‘dot’) product $\mathbf{a} \cdot \mathbf{b}$ may be thought of as ‘representing’ the product of the moduli of the vectors resolved in the direction of one or other of the vectors. For example (Fig. A5.2), if the angle between the vectors, drawn from a common origin, is θ , the resolved component of the modulus of \mathbf{b} along the \mathbf{a} direction is $b \cos \theta$. Hence $\mathbf{a} \cdot \mathbf{b} = ab \cos \theta$. The same result applies if \mathbf{a} is resolved along the direction of \mathbf{b} .

If one of the vectors is a unit vector—say in Fig. A5.2 $\mathbf{a} = \mathbf{n}$ —then the scalar product $\mathbf{n} \cdot \mathbf{b} = b \cos \theta$ (since $|\mathbf{n}| = 1$): it is simply the modulus of \mathbf{b} resolved along the direction of the unit vector \mathbf{n} . The scalar product may therefore be thought of as a ‘shorthand’ means of resolving the vectors along different directions.

Clearly, the maximum value of the scalar product occurs when the vectors are parallel ($\theta = 90^\circ$) and the minimum value, zero, occurs when they are at right angles ($\theta = 90^\circ$). The scalar product of a vector multiplied by itself is simply the modulus squared, i.e. $\mathbf{a} \cdot \mathbf{a} = |\mathbf{a}||\mathbf{a}| = a^2$.

The vector (or ‘cross’) product $\mathbf{a} \times \mathbf{b}$ may be thought of as ‘representing’ the area outlined by two vectors. In Fig. A5.3 the area outlined by the vectors \mathbf{a} and \mathbf{b} is $ab \sin \theta$. But there is more: the area may represent a crystal plane or surface, the **orientation** of which also needs to be specified. The orientation of the surface may be specified by the direction normal to it, i.e. perpendicular to the page. Let the unit vector along this direction be \mathbf{n} ; then $\mathbf{a} \times \mathbf{b} = (ab \sin \theta)\mathbf{n}$.

In general, the vector product is expressed as $\mathbf{a} \times \mathbf{b} = \mathbf{c}$, where \mathbf{c} is perpendicular to \mathbf{a} and \mathbf{b} and $|\mathbf{c}| = ab \sin \theta$. The largest value of \mathbf{c} occurs when \mathbf{a} and \mathbf{b} are at right angles

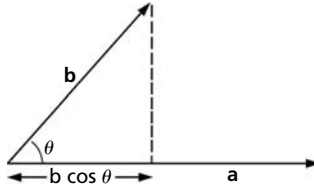


Fig. A5.2.

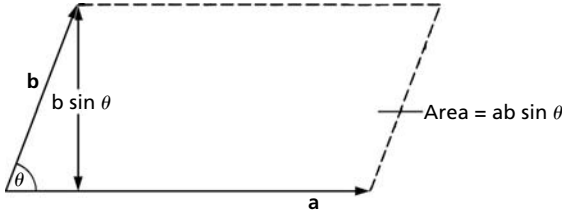


Fig. A5.3.

and the smallest value, zero, occurs when they are parallel. Finally, the vector product involves the use of a sign convention: the vector \mathbf{c} or \mathbf{n} is perpendicular to the plane defined by \mathbf{a} and \mathbf{b} but can have one of two directions, i.e. with reference to Fig. A5.3, it can be 'up' from the page or 'down'. One vector must have a + sign and the opposite must have a - sign. The sign convention is as follows. Consider in Fig. A5.3 an (ordinary) right-handed screw coming out of the page (i.e. parallel to \mathbf{c} or \mathbf{n}) through the common origin of \mathbf{a} and \mathbf{b} . If we 'screw' from \mathbf{a} to \mathbf{b} the screw will move 'upwards' and this upwards direction is the direction or sense of \mathbf{c} . If we screw in the opposite direction, from \mathbf{b} to \mathbf{a} , the screw will move downwards. Hence, the order of the multiplication of vectors is important and leads to the **anticommutative law** for the vector product:

$$\mathbf{a} \times \mathbf{b} = -(\mathbf{b} \times \mathbf{a}).$$

A5.4 Multiplication of vectors in terms of components

Calculations are generally made easier if vectors are expressed in terms of their components on a Cartesian axis system with unit vectors, $\mathbf{i}, \mathbf{j}, \mathbf{k}$ at right angles. In this case $\mathbf{i} \cdot \mathbf{i} = 1, \mathbf{i} \cdot \mathbf{j} = 0, \mathbf{i} \times \mathbf{i} = 0, \mathbf{i} \times \mathbf{j} = \mathbf{k}$, and similarly for the other combinations of \mathbf{i}, \mathbf{j} and \mathbf{k} .

Writing

$$\mathbf{a} = (a_1\mathbf{i} + a_2\mathbf{j} + a_3\mathbf{k}) \quad \text{and} \quad \mathbf{b} = (b_1\mathbf{i} + b_2\mathbf{j} + b_3\mathbf{k}).$$

The scalar product

$$\begin{aligned} \mathbf{a} \cdot \mathbf{b} &= (a_1\mathbf{i} + a_2\mathbf{j} + a_3\mathbf{k}) \cdot (b_1\mathbf{i} + b_2\mathbf{j} + b_3\mathbf{k}) \\ &= a_1b_1\mathbf{i} \cdot \mathbf{i} + a_1b_2\mathbf{i} \cdot \mathbf{j} + \dots \\ &= (a_1b_1 + a_2b_2 + a_3b_3) \end{aligned}$$

(all the other terms cancel because $\mathbf{i} \cdot \mathbf{i} = 1$ and $\mathbf{i} \cdot \mathbf{j} = 0$, etc.)

The vector product

$$\begin{aligned}\mathbf{a} \times \mathbf{b} &= (a_1\mathbf{i} + a_2\mathbf{j} + a_3\mathbf{k}) \times (b_1\mathbf{i} + b_2\mathbf{j} + b_3\mathbf{k}) \\ &= a_1b_1(\mathbf{i} \times \mathbf{i}) + a_1b_2(\mathbf{i} \times \mathbf{j}) + \dots \\ &= (a_2b_3 - b_2a_3)\mathbf{i} + (a_3b_1 - b_3a_1)\mathbf{j} + (a_1b_2 - b_1a_2)\mathbf{k}\end{aligned}$$

(all the other terms cancel because $\mathbf{i} \times \mathbf{i} = 0$ and $\mathbf{i} \times \mathbf{j} = \mathbf{k}$, etc.).

The vector product may be expressed in matrix form as a determinant:

$$\mathbf{a} \times \mathbf{b} = \begin{vmatrix} \mathbf{i} & \mathbf{j} & \mathbf{k} \\ a_1 & a_2 & a_3 \\ b_1 & b_2 & b_3 \end{vmatrix}.$$

A5.5 Volumes of unit cells in vector notation

The volume of a unit cell defined by vectors \mathbf{a} , \mathbf{b} , and \mathbf{c} is ‘the area of the base times the height’.

The ‘area of the base’ is $(\mathbf{a} \times \mathbf{b}) = (ab \sin \theta)\mathbf{n}$. The ‘height’ is the component of \mathbf{c} resolved in the direction of the normal \mathbf{n} (Fig. A5.4), i.e. the height $= \mathbf{n} \cdot \mathbf{c} = c \cos \phi$. Hence the volume $V = (\mathbf{a} \times \mathbf{b}) \cdot \mathbf{c}$. It is a scalar quantity. The vectors \mathbf{a} , \mathbf{b} , \mathbf{c} in this equation may be ‘cycled’ but the sequence must be maintained, i.e.

$$V = (\mathbf{a} \times \mathbf{b}) \cdot \mathbf{c} = \mathbf{a} \cdot (\mathbf{b} \times \mathbf{c}) = (\mathbf{c} \times \mathbf{a}) \cdot \mathbf{b}, \text{ etc.}$$

If the sequence is reversed, i.e. $(\mathbf{b} \times \mathbf{a}) \cdot \mathbf{c}$, then a negative volume results. In practice this can occur if a left-handed set of axes are substituted, inadvertently or otherwise, for a right-handed set.

The reciprocal unit cell \mathbf{a}^* , \mathbf{b}^* , \mathbf{c}^* can be derived from the ‘direct’ unit cell \mathbf{a} , \mathbf{b} , \mathbf{c} in a similar way as outlined in Section 6.5.6. Note that the relationships

$$\mathbf{a}^* = \frac{\mathbf{b} \times \mathbf{c}}{V} \text{ etc.}$$

are valid for the primitive unit cells for any axis system.

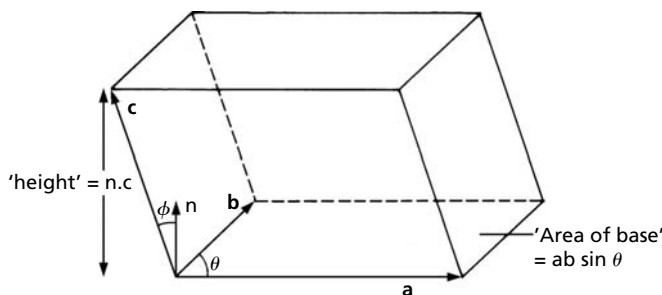


Fig. A5.4.

A5.6 Representing vectors by complex numbers: the Argand diagram

The sum of a number of vectors $\mathbf{a} + \mathbf{b} + \mathbf{c} + \dots$ may be simply obtained graphically by adding them 'top to tail' as shown in Fig. A5.5. In the case where the vectors represent the atomic scattering factors, f , for the atoms in the motif, the sum is the structure factor F_{hkl} .

However, although graphical procedures are very instructive in that they clearly show the physical principles involved, they are also very clumsy and do not readily lend themselves to analytical procedures. We need therefore an alternative method of representing vectors and the method we adopt is that of representing vectors as complex numbers.

A complex number, z , is a number which has two parts of the form

$$z = x + iy$$

where x and y are real numbers and $i = \sqrt{-1}$. The first part, x , is called the real part of the complex number and the second part, iy , is called the imaginary part. These two parts can be represented graphically on what is known as an Argand diagram—a graph in which the horizontal axis (abscissa) represents x , the real part and the vertical axis (ordinate) represents iy , the imaginary part (Fig. A5.6).

The complex number z is represented on the Argand diagram by the point $\mathbf{P}(x, y)$ and the length $OP = r = \sqrt{x^2 + y^2}$ is called the **modulus** of the complex number z (or simply 'mod z ' or $|z|$). Hence (from Fig. A5.6) the complex number z can be written in the form:

$$z = r \cos \phi + ir \sin \phi$$

where r (the modulus) and ϕ (the angle) are known as polar coordinates. This expression can further be written in exponential form (Euler's formula); $\cos \phi + i \sin \phi = \exp i\phi$ and $\cos \phi - i \sin \phi = \exp -i\phi$, i.e. $z = r \exp i\theta$.

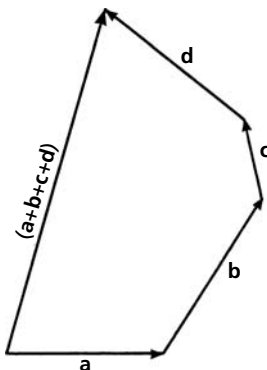


Fig. A5.5.

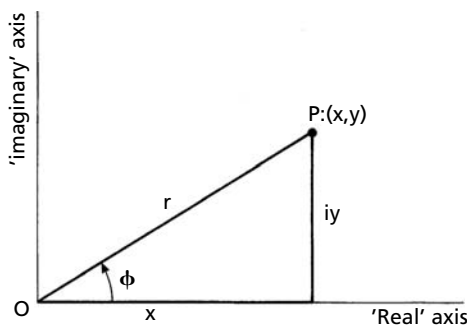


Fig. A5.6.

This representation of complex numbers in exponential form by means of the polar coordinates r and ϕ allows us to add, subtract and carry out other mathematical operations upon them without having to resort to rulers and graph paper.

For example, the addition of complex numbers, $z_1 + z_2 + \dots$ is simply given by:

$$z_1 + z_2 + \dots = r_1 \exp i\phi_1 + r_2 \exp i\phi_2,$$

or:

$$z_1 + z_2 + \dots = r_1 \cos \phi_1 + r_2 \cos \phi_2 + \dots + i(r_1 \sin \phi_1 + r_2 \sin \phi_2 + \dots)$$

(sum of 'horizontal' components) + i (sum of 'vertical' components).

This is the procedure used to find the structure factor F_{hkl} , the sum of all the atomic scattering factors, f , for the atoms in the motif.

The complex conjugate of a complex number, symbol z^* is one which has the same modulus r , but a negative angle ϕ , i.e.

$$z^* = r \cos \phi - ir \sin \phi = r \exp -i\phi.$$

The complex conjugate can be used, for example to determine the modulus r of a complex number, i.e.

$$z \cdot z^* = r \exp i\phi \cdot r \exp -i\phi = r^2.$$

Appendix 6

Systematic absences (extinctions) in X-ray diffraction and double diffraction in electron diffraction patterns

A6.1 Systematic absences

In X-ray diffraction (and also, except for the complication of double diffraction, in electron diffraction) the intensities of reflections from certain planes with Laue indices hkl are zero. Such reflections are said to be *forbidden* or *extinguished* or, better, *systematically absent* since they arise from the centring of the unit cell and /or the presence of translational symmetry elements—glide planes and screw axes. The identification of systematic absences is very useful since it provides the ‘first step’ in crystal structure determination.

The subject may be best introduced by considering the diffraction of light from a wide slit diffraction grating (Sections 7.4 and 13.3). In the diffraction of light extinctions or ‘missing orders’ occur for certain ratios of the slit spacing a and the slit width d . For example, referring to Fig. 7.7 or 13.7, if the slit width d is set equal to one-third of the slit spacing a , then the zero order minimum of the central peak from a single slit coincides with the angle of the third order diffracted peaks $n = \pm 3$. These peaks (and subsequently the sixth, ninth etc. order peaks) are therefore of zero intensity (i.e. extinguished). Other sets of systematic absences may be derived for other combinations of a and d —the most important being that when $d = \frac{1}{2}a$ (see Exercise 7.2).

Systematic absences in crystals may be derived in two ways: either by a consideration of the geometrical consequences arising from the use of centred, rather than primitive, unit cells and the presence of glide planes and screw axes, or by application of the structure factor equation. The former approach is the proper one, since systematic absences arise solely as a consequence of the architecture of crystals—but the latter approach is a useful means of gaining practice and familiarity with the structure factor equation. We will start with both approaches for an fcc crystal.

Consider Fig. A6.1 which shows the unit cell vectors **a**, **b**, **c** for the conventional fcc unit cell and the unit cell vectors **A**, **B**, **C** for (one variant) of the primitive rhombohedral unit cell. The origin is drawn at the front left-hand corner to help make clear the shape of the rhombohedral cell.

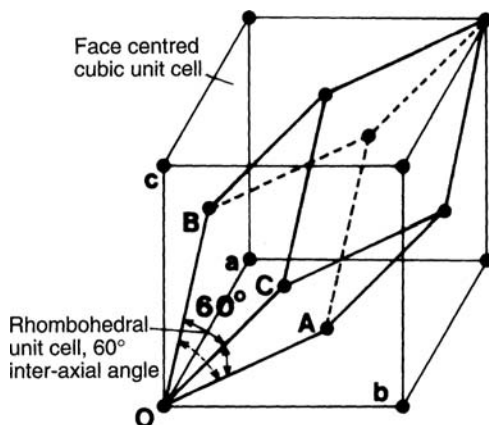


Fig. A6.1.

Writing down the transformation equations for unit cell vectors or axes (see Section 5.8):

$$\mathbf{A} = \frac{1}{2}\mathbf{a} + \frac{1}{2}\mathbf{b} + 0\mathbf{c}$$

$$\mathbf{B} = \frac{1}{2}\mathbf{a} + 0\mathbf{b} + \frac{1}{2}\mathbf{c}$$

$$\mathbf{C} = 0\mathbf{a} + \frac{1}{2}\mathbf{b} + \frac{1}{2}\mathbf{c}.$$

Now, as shown in Section 5.8, Miller indices transform in the same way as unit cell vectors. Hence if (HKL) and (hkl) are the Miller indices of a plane referred to the primitive and fcc unit cells, respectively:

$$H = \frac{1}{2}h + \frac{1}{2}k + 0l \quad 2H = h + k$$

$$K = \frac{1}{2}h + 0k + \frac{1}{2}l \quad \text{or} \quad 2K = h + l$$

$$L = 0h + \frac{1}{2}k + \frac{1}{2}l \quad 2L = k + l.$$

Now H, K, L are all integers, odd or even; hence $2H, 2K, 2L$ are all *even* integers, from which it follows that $(h + k), (h + l), (k + l)$ are also all even integers.

An even integer is either the sum of two even integers, or two odd integers, but not mixed. Hence, for each identity, h, k, l are either all odd or all even integers. In other words the lattice planes from which reflections occur are those for which h, k, l are all even or all odd integers. When h, k, l are mixed (some odd, some even) the Miller index (hkl) describes a set of planes which are not lattice planes since they do not all pass through lattice points.

Now let us derive the same result using the structure factor equation applied to an fcc crystal with an identical atom (atomic scattering factor f) at each of the four lattice points in the cell. The $(u_n v_n w_n)$ fractional coordinate values of these atoms are:

$$(000), \left(\frac{1}{2} \frac{1}{2} 0\right), \left(\frac{1}{2} 0 \frac{1}{2}\right), \left(0 \frac{1}{2} \frac{1}{2}\right).$$

Hence,

$$F_{hkl} = f \exp 2\pi i(h0 + k0 + l0) + f \exp 2\pi i\left(h\frac{1}{2} + k\frac{1}{2} + l0\right) \\ + f \exp 2\pi i\left(h\frac{1}{2} + k0 + l\frac{1}{2}\right) + f \exp 2\pi i\left(h0 + k\frac{1}{2} + l\frac{1}{2}\right).$$

Simplifying, and remembering that since the cell is centrosymmetric the sine components in the exponents vanish:

$$F_{hkl} = f(1 + \cos \pi(h + k) + \cos \pi(h + l) + \cos \pi(k + l)).$$

Now, $\cos \pi$ (even integer) = +1 and $\cos \pi$ (odd integer) = -1. The value of F_{hkl} will depend on whether h, k, l are all even, all odd or mixed. It is easily seen that if they are all even or all odd $F_{hkl} = 4f$ and if they are mixed $F_{hkl} = 0$.

The conditions for systematic absences from body- and base-centred lattices can be derived in the same ways: either by referring the lattice to a primitive unit cell or by applying the structure factor equation. For example, for a body-centred cubic crystal with identical atoms at (000) and $\left(\frac{1}{2} \frac{1}{2} \frac{1}{2}\right)$

$$F_{hkl} = f \exp 2\pi i(h0 + k0 + l0) + f \exp 2\pi i\left(h\frac{1}{2} + k\frac{1}{2} + l\frac{1}{2}\right) \\ = f(1 + \cos \pi(h + k + l)).$$

Hence when $(h + k + l) = \text{even integer}$ $F_{hkl} = 2f$ and when $(h + k + l) = \text{odd integer}$ $F_{hkl} = 0$.

Systematic absences for glide planes and screw axes may be derived in the same way; an example of each will suffice to show the principles involved.

Figure A6.2 shows a (monoclinic) crystal with a c -glide plane in the xz plane or (010) plane (the plane of the paper). The action of the c -glide is to translate any atom, atomic scattering factor f , with fractional coordinates (uvw) to $\left(u\bar{v}\left(\frac{1}{2} + w\right)\right)$. Substituting

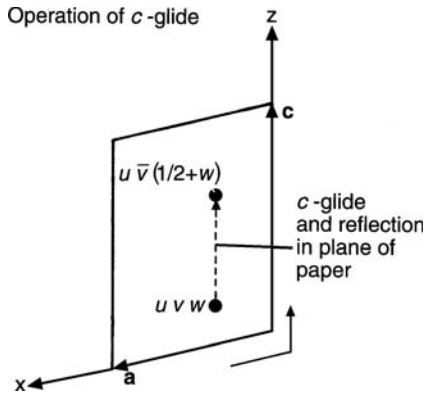


Fig. A6.2.

these two values in the structure factor equation:

$$F_{hkl} = f \exp 2\pi i(hu + kv + lw) + f \exp 2\pi i \left(hu + k\bar{v} + l \left(\frac{1}{2} + w \right) \right).$$

Consider the $h0l$ reflections ($k = 0$), i.e. the reflections in the zone whose axis is perpendicular to the glide plane (010)

$$\begin{aligned} F_{h0l} &= f \exp 2\pi i(hu + lw) + f \exp 2\pi i(hu + lw) \exp 2\pi i \frac{1}{2} l \\ &= f \exp 2\pi i(hu + lw) [1 + \exp \pi i l]. \end{aligned}$$

When $l = \text{odd integer}$, $\exp \pi i l = -1$ and $F_{h0l} = 0$. This then gives the condition for systematic absences for the $h0l$ planes; systematic absences occur when l equals an odd integer and, correspondingly, reflections occur when l equals an even integer. Clearly, for a -glide in the (010) plane reflections occur when h equals an even integer.

Figure A6.3 shows a (monoclinic) crystal with a screw diad axis, 2_1 along the y -axis, the action of which is to translate an atom with fractional coordinates (uvw) to $\left(\bar{u} \left(\frac{1}{2} + v \right) \bar{w} \right)$. Proceeding as before:

$$F_{hkl} = f \exp 2\pi i(hu + kv + lw) + f \exp 2\pi i \left(h\bar{u} + k \left(\frac{1}{2} + v \right) + l\bar{w} \right)$$

consider the $0k0$ reflections ($h = l = 0$) i.e. reflections arising from planes perpendicular to the screw axis.

$$\begin{aligned} F_{0k0} &= f \exp 2\pi i(kv) + f \exp 2\pi i \left(k \frac{1}{2} + kv \right) \\ &= f \exp 2\pi i(kv) [1 + \exp \pi i k]. \end{aligned}$$

When $k = \text{odd integer}$, $\exp \pi i k = -1$ and $F_{0k0} = 0$ and reflections only occur from $0k0$ planes when k equals an even integer. This result can also be seen intuitively: the action of the screw diad axis repeats the atomic layers at spacings equal to half the **b** lattice repeat distance.

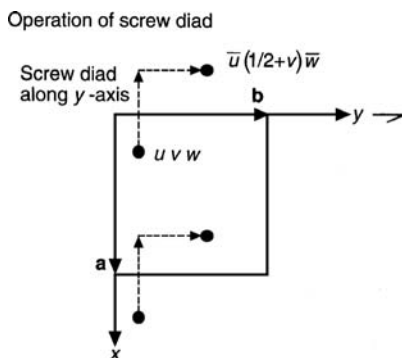


Fig. A6.3.

Table A6.1 lists the extinction criteria for lattices and translational symmetry elements. n and d are the symbols for diagonal glide planes where the translations are along two axes in the plane, each of which are half the unit cell repeat distance for an n glide plane and a quarter of the unit cell repeat distance for a d glide plane (d stands for ‘diamond glide’). In summary, Table A6.1 shows that lattices affect all reflections, glide planes affect only reflections which lie in the zone whose axis is perpendicular to the glide plane and screw axes affect only the reflections from planes perpendicular to the screw axis.

Table A6.2 lists the reflecting planes in cubic P , I , F and diamond-cubic crystals in order of decreasing d_{hkl} -spacing. For cubic crystals $d_{hkl} = a/\sqrt{N}$ where a = the lattice parameter and $N = (h^2 + k^2 + l^2)$. The conditions for reflection for a diamond-cubic crystal are h, k, l are all odd or all even integers (since a diamond-cubic crystal has an fcc lattice) with the additional condition that $(h + k + l)$ is either an odd integer or an integer which is an even multiple of 2 (see Exercise 9.5, p. 241).

A6.2 Double diffraction

In electron diffraction the presence of face- or body-centring lattice points also gives rise to systematically absent reflections just as in the case of X-ray diffraction (the first group in Table A6.1). However, reflections which are systematically absent in X-ray diffraction as a result of the presence of translational symmetry elements (glide planes and screw axes, Table A6.1) may, and usually do, occur in electron diffraction patterns. This is known as double diffraction and occurs because the intensities of the diffracted beams may be comparable with that of the direct or undiffracted beam—a consequence of the dynamical interactions between the direct and diffracted beams. The effect, in terms of the geometry of the electron diffraction pattern, is that a strong diffracted beam can behave, as it were, as the direct beam and the whole pattern is in effect shifted so as to be centred about the diffracted beam. In the case of electron diffraction patterns from centred lattices all the spots are coincident and no new ones arise; but in most other cases new ones arise in positions in which the diffraction spots should be systematically absent. A simple example—that of electron diffraction from the hcp structure—will make this clear.

In the hcp structure the relevant translational symmetry element is the screw hexad 6_3 (Fig. 4.10) which describes the symmetry of the sequence of A and B layer atoms (Fig. 1.5(b)). Consider the conditions for constructive interference for Bragg reflections from the A layers of atoms, i.e. the (0001) planes with interplanar spacing $d_{0001} = c$. When the path difference (PD) is 1λ (constructive interference), the path difference between the interleaving A and B layers of atoms, interplanar spacing $d_{0002} = c/2$ is $\frac{1}{2}\lambda$, which is the condition for *destructive* interference; hence the 0001 reflection is (systematically) absent. Second-order reflection from the (0001) planes (PD = 2λ) corresponds to the first-order reflection from the (0002) planes (PD = 1λ). Continuing in this way it turns out that 000 l reflections where l is odd are systematically absent, as shown in Table A6.1. The same result may be found by applying the structure factor equation to the (0001), (0002), (0003), etc. planes, as in Example 4, Section 9.2: when l is odd the atomic scattering factors for the A and B layer atoms are equal and opposite.

Now let us draw a commonly observed hcp electron diffraction pattern from the $[\bar{1}2\bar{1}0]$ zone (Fig. A6.4), showing the systematically absent reflections 0001, 000 $\bar{1}$, 0003, 000 $\bar{3}$

Table A6.1 Extinction criteria for lattices and symmetry elements

Lattice or symmetry element type	Symbol	Class of reflections	Condition for presence
Lattice type:		hkl	
primitive	P		none
body-centred	I		$h + k + l = 2n$
centred on the C face	C		$h + k = 2n$
centred on the A face	A		$k + l = 2n$
centred on the B face	B		$h + l = 2n$
			h, k, l
centred on all faces	F		all = n (odd) or all = $2n$ (even)
rhombohedral, obverse	R		$-h + k + l = 3n$
rhombohedral, reverse	R		$h - k + l = 3n$
Glide plane (001)	a b n d	$hk0$	$h = 2n$ $k = 2n$ $h + k = 2n$ $h + k = 4n$
Glide plane (100)	b c n d	$0kl$	$k = 2n$ $l = 2n$ $k + l = 2n$ $k + l = 4n$
Glide plane (010)	a c n d	$h0l$	$h = 2n$ $l = 2n$ $h + l = 2n$ $h + l = 4n$
Glide plane (110)	c b n d	hhl	$l = 2n$ $h = 2n$ $h + l = 2n$ $2h + l = 4n$
Screw axis c	$2_1, 4_2, 6_3$ $3_1, 3_2, 6_2, 6_4$ $4_1, 4_3$ $6_1, 6_5$	$00l$	$l = 2n$ $l = 3n$ $l = 4n$ $l = 6n$
Screw axis a	$2_1, 4_2$ $4_1, 4_3$	$h00$	$h = 2n$ $h = 4n$
Screw axis b	$2_1, 4_2$ $4_1, 4_3$	$0k0$	$k = 2n$ $k = 4n$
Screw axis $[110]$	2_1	$hh0$	$h = 2n$

(n = odd integer, 2n = even integer etc.)

Table A6.2 Reflecting panes (\checkmark) in cubic P , I , F and diamond-cubic crystals.

N	hkl	cubic P	cubic I	cubic F	Diamond cubic
1	100	\checkmark			
2	110	\checkmark	\checkmark		
3	111	\checkmark		\checkmark	\checkmark
4	200	\checkmark	\checkmark	\checkmark	
5	210	\checkmark			
6	211	\checkmark	\checkmark		
7	—				
8	220	\checkmark	\checkmark	\checkmark	\checkmark
9	300/221	\checkmark			
10	310	\checkmark	\checkmark		
11	311	\checkmark		\checkmark	\checkmark
12	222	\checkmark	\checkmark	\checkmark	
13	320	\checkmark			
14	321	\checkmark	\checkmark		
15	—				
16	400	\checkmark	\checkmark	\checkmark	\checkmark
17	410	\checkmark			
18	330/411	\checkmark	\checkmark		
19	331	\checkmark		\checkmark	\checkmark
20	420	\checkmark	\checkmark	\checkmark	

Note 1. There are no squares of three numbers which add up to 7, 15 etc. This means that there are ‘gaps’ in the sequence of reflections for cubic P crystals, i.e. ‘line 7’, ‘line 15’ etc. are missing.

Note 2. Cubic I crystals show a uniform sequence of reflections (with no ‘gaps’ as in cubic P crystals).

Note 3. Cubic F crystals show a characteristic sequence of lines: ‘two-together’, ‘one-on-its-own’, ‘two-together’ etc.

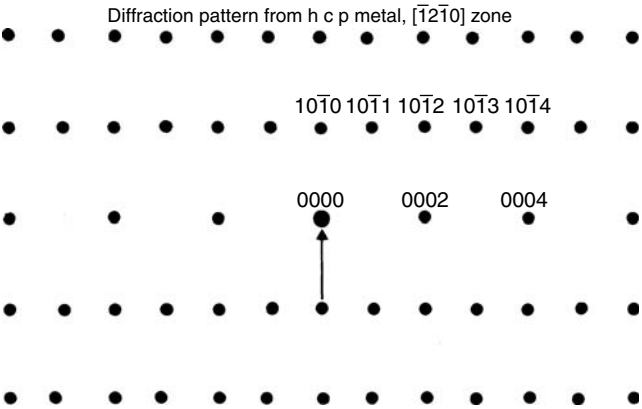


Fig. A6.4.

etc. in the row through the origin.¹ Now suppose that the (strong) $10\bar{1}0$ reflected beam acts as it were as the direct beam: the whole pattern will, in effect, be shifted from the origin 0000 to $10\bar{1}0$ as shown by the arrow and spots will now appear in the systematically absent positions. The same result will be obtained for other choices of strong diffracted beams—as can easily be seen by making a tracing paper overlay in Fig. A6.4 and shifting the origin to the positions of different diffracted spots.

Double diffraction can also occur in situations in which the electron diffraction spots of two (or more) crystals are present in the pattern. In such cases the double-diffracted spots which appear may correspond to no d -spacing in either crystal—and are probably the biggest cause of the frustrated electron microscopists' 'unindexable' patterns. Figure A6.5 indicates the geometry involved. Here, two (high order) patterns are shown consisting of widely separated rows (indicated by filled and open circles). The strong spots in the rows through the origin may act in effect as the direct beam, generating additional double diffraction spots in the positions marked by the letter d . The pattern *appears* to be from a relatively simple low-order zone—but of course it is not, and is either unindexable or (worse) may be indexed incorrectly. An example of the latter case

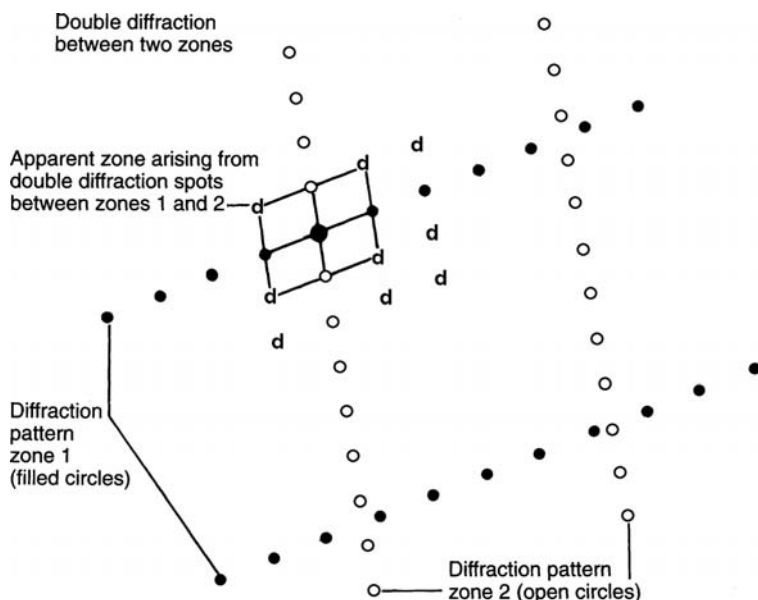


Fig. A6.5.

¹ Systematic absences also occur in every *third* row (not shown in Fig. A6.4). These arise because the A-layer and B-layer atoms are in special equivalent positions in the hexagonal unit cell (see Section 4.6). This leads to the conditions for hkl : if $h - k = 3n$, $l = 2n$, i.e. in the third row the $30\bar{3}1, 30\bar{3}3$, etc. reflections are systematically absent. These conditions are given in the table in Fig. 4.14, space group $P6_3/mmc$, for the special equivalent positions for hcp structures denoted by the Wyckoff letters c and d .

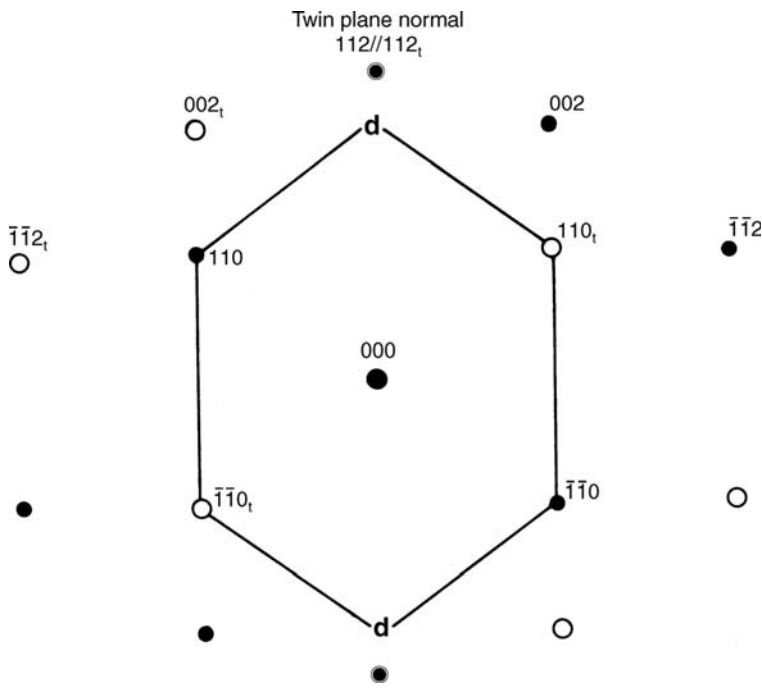


Fig. A6.6.

is that of the electron diffraction patterns from twin-related plates or laths of ferrite (bcc) which occur in the microstructures of some structural steels.

Figure A6.6 shows the spots (indicated by filled and open circles) for two bcc [110] zones twin-related in the (112) plane. Double diffraction between these twin-related zones gives rise to the spots marked **d** (i.e. $\mathbf{d}_{110}^* + \mathbf{d}_{110_T}^* = \mathbf{d}_d$ where $(110)_T$ is the twin-spot of (110)). The presence of these additional spots indicates a pattern in which the spots outline an ‘elongated’ hexagon, as indicated, which is precisely the same shape as for an fcc $\langle 110 \rangle$ zone—the four bcc $\{110\}$ spots closer to the centre spot being identified as fcc $\{111\}$ spots and the two double-diffraction spots further away being identified as fcc $\{200\}$ spots. Since in steels d_{110} (ferrite) is closely similar to d_{111} (austenite), then this pattern may be misinterpreted as a $\langle 110 \rangle$ austenite zone—leading to the erroneous conclusion that this phase is present at the ferrite twin boundary.

Answers to exercises

Chapter 1

- 1.1 Figure E1.1 shows a tetrahedron of height h and edge-length equal to the interatomic spacing a . The 'B layer' atom lies above the centre of the triangle formed by three 'A layer' atoms. The distance AC is $\frac{2}{3}a \cos 30^\circ = a/\sqrt{3}$. Hence from a right-angled triangle ABC $h^2 = a^2 - \frac{1}{3}a^2$ whence $h = \sqrt{2/3}a$. Hence $c/a = 2h/a = 2\sqrt{2/3} = 1.633$. The centre of the tetrahedron above the triangular base (denoted by X in Fig. E1.1), is obtained by projecting a bisector from any edge, e.g. AB to X . $\cos x = h/a$ and $BX = a/2 \cdot \frac{1}{\cos x} = a/2 a/h = a^2/2h$ and since $a = \sqrt{3/2}h$, $BX = \frac{3h^2}{2.2h} = \frac{3}{4}h$ or $CX = 1/4h$: i.e. the centre of a tetrahedron is at $1/4$ of its height.
- 1.2 As can be seen in Figure 1.13(d), the tetrahedron of four A atoms is not regular but has four shorter edges of length $a\sqrt{3}/2$ and two longer edges of length a . However, unlike the octahedral interstitial site all four A atoms are equidistant from the interstitial X atom at the centre of the tetrahedron. The geometry is best appreciated with reference to a plan view (Fig. E1.2) showing two bcc cells and one tetrahedral interstitial site which lies, by symmetry, at height $\frac{1}{4}a$ in the common cell face. The distance from the centre of the tetrahedron to any corner is $\sqrt{(a/2)^2 + (a/4)^2} = a\sqrt{5}/4 = r_X + r_A$. The closest distance between A atoms is along the direction of the body-diagonal of the cube, i.e. $2r_A = 1/2\sqrt{3}a$. Hence $r_X + r_A = a\sqrt{5}/4 = r_A\sqrt{5/3} = 1.291r_A$ whence $r_X = 0.291r_A$.
- 1.3 The interstitial site is at the centre of a triangular prism of height and side-length $2r_A$ (Fig. E1.3). The interstitial atom X at height r_A is equidistant from all six corners of the prism. Hence, proceeding as in Exercise 1.1, $AC = \frac{2}{3}2r_A \cos 30^\circ = r_A 2/\sqrt{3}$, and $AX = \sqrt{4/3 r_A^2 + r_A^2} = r_A\sqrt{7/3}$. Hence $AX = r_X + r_A = 1.528r_A$ whence $r_X = 0.528r_A$.

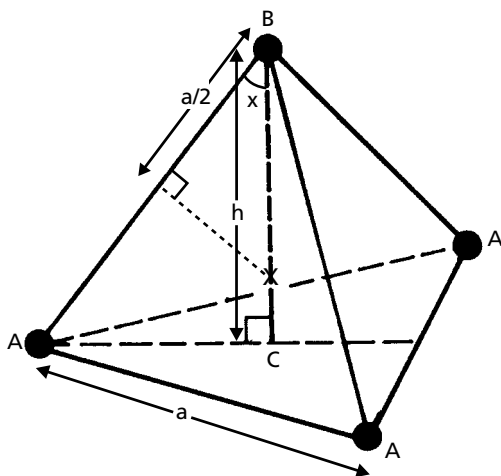


Fig. E1.1.

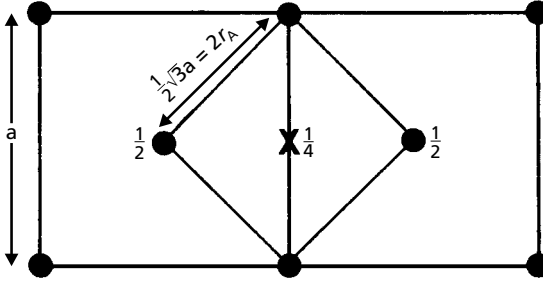


Fig. E1.2.

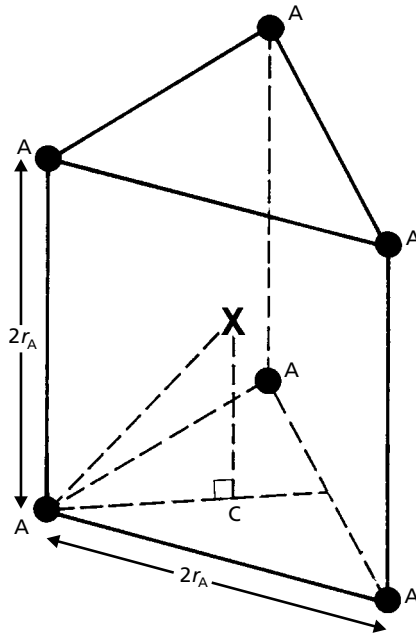


Fig. E1.3.

- 1.4 (a) In the ccp structure there are four sets of close-packed planes and six close-packed directions and in the hcp structure only one set of close-packed planes and three close-packed directions.
- (b) In the bcc structure there are six sets of closest-packed planes and four close-packed directions.
- 1.5 In the ccp structure each close-packed plane contains three close-packed directions, i.e. three slip systems share a common close-packed plane. As there are four sets of close-packed planes in the ccp structure there are therefore twelve slip systems. In the bcc structure each closest-packed plane contains two close-packed directions, i.e. two slip systems share a

common closest-packed plane. As there are six sets of closest-packed planes in the bcc structure there are therefore also twelve slip systems.

- 1.6 The atomic coordinates are (000) (for all the layer' atoms situated at the corners of the unit cell), and *either* $\left(\frac{1}{3}\frac{2}{3}\frac{1}{2}\right)$ *or* $\left(\frac{2}{3}\frac{1}{3}\frac{1}{2}\right)$ for the 'B layer' or the 'C layer' atom within the cell, depending upon the arbitrary choice made between these two possible (B or C) sites.
- 1.7 For B6 (carborundum II) the stacking sequence is ABCACBA... giving a six-layer unit cell repeat distance. In the Frank notation this is $\Delta\Delta\Delta\nabla\nabla\nabla\dots$, i.e. an inversion every three layers (rather than an inversion every layer in B4 and an inversion every two layers in B5).
For B7 (carborundum I) the stacking sequence is ABACBCACBABCBA... giving a fifteen-layer unit cell repeat distance. In the Frank notation this is $\Delta\nabla\nabla\nabla\Delta\Delta\nabla\nabla\nabla\Delta\Delta\nabla\nabla\nabla\Delta\dots$, i.e. inversions every two and three layers alternately.
- 1.8 Fault an A layer to a B layer as in Fig. 1.20(a)–(b). Then fault *not* the C layer in Fig. 1.20(b) but the A layer *above* which becomes a B layer; all the layers above are re-labelled $B \rightarrow C$ and $C \rightarrow A$ as before. Again, fault the next A layer above to become a B layer and repeat as before. The stacking sequence is clearly CBCB..., i.e. the hcp stacking sequence.
- 1.11 The sequence is: $\Delta\Delta\nabla\nabla\Delta\Delta\nabla\nabla$ (a four-layer repeat).

Chapter 2

- 2.1 There are twice as many mirror lines in $p3m1$ and the triads lie at the intersections of all of them; in $p31m$ half the triads are not intersected by mirror lines.
- 2.2 The lattice type is $p3m1$ (refer to your drawings or Question 2.1).
- 2.3 The lattice type is $p2$ —i.e. the pattern has identical symmetry to Fig. 2.7; it is based on the oblique plane lattice, *not* a rectangular plane lattice (primitive or centred) because there are no mirror lines of symmetry present.
- 2.4 The lattice type is pg . The glide lines run vertically through the back heels of the black men and the raised hands of the white men.
- 2.5 A $4'$ axis with vertical and horizontal m' lines and diagonal m lines (see Fig. 2.11).
- 2.6 The one-dimensional lattice types (Fig. 2.23) are:
(a) $p112$ (b) $p112$ (c) $p112$
(d) $p112$ (e) $pmm2$ (d) $pmm2$
(g) $p1a1$ (h) $p111$ (i) $p112$.
- 2.7 Figure 2.24(b) is counterchange plane group $p2g'g'$.
- 2.8 There are three such counterchange patterns based upon $pma2$ ($p2mg$) as shown in Fig. E2.8.

Chapter 3

- 3.1 (a) is orthorhombic C ; (b) is not a Bravais lattice because the points *do not* all have an identical environment [see the two-dimensional examples, Figs 2.2(b) and (c)]; (c) is orthorhombic P (two primitive cells are drawn together).
- 3.2 (a) is orthorhombic P (relocate the origin at $x'y'z'$); (b) is orthorhombic I (relocate the origin at $0\frac{1}{2}0$); (c) is orthorhombic C (relocate the origin at $00z'$; the motif is two atoms, one of each type).
- 3.3 For $\alpha > 90^\circ$ it is a 'distorted' truncated octahedron (i.e. rectangular, rather than square faces and unequal-sided hexagonal faces) and for $\alpha < 90^\circ$ it is a 'distorted' rhombic dodecahedron (i.e. with 12 faces of unequal-shaped diamonds). See Fig. 3.7(d) and (e).

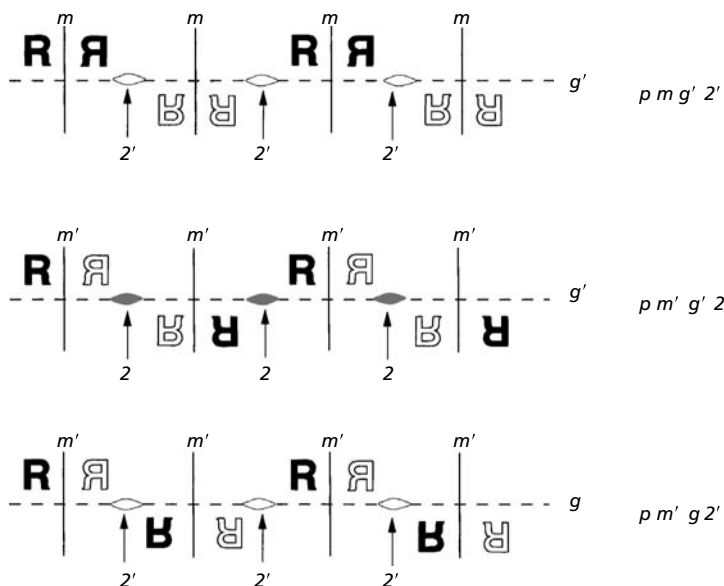


Fig. E2.8.

Chapter 4

4.2	Structure	Bravais lattice	Motif
	NaCl	Cubic F	(Na and Cl)
	CsCl	Cubic P	(Cs and Cl)
	Diamond	Cubic F	(C and C)
	ZnS (sphalerite)	Cubic F	(Zn and S)
	ZnS (wurtzite)	Hexagonal P	(2Zn and 2S)
	Li_2O (or CaF_2)	Cubic F	(2Li and 1O)
	CaTiO_3	Cubic P	(1Ca, 1Ti, and 3O).

NB: in ferroelectric crystals the distortions which occur at the Curie temperature and below change the Bravais lattice from Cubic P to Tetragonal P to Orthorhombic P and to Rhombohedral with decreasing temperature.

Chapter 5

- 5.1 In fcc crystals the slip planes are $\{111\}$, slip directions are $\langle 110 \rangle$.
In bcc crystals the slip planes are $\{110\}$, slip directions are $\langle 111 \rangle$.
- 5.2 $[2\bar{3}\bar{1}]$, i.e. $2.1 + 3.1 + 1.5 = 0$.
 (321) , i.e. $3.1 + 2.\bar{1} + 1.\bar{1} = 0$.
- 5.3 Triclinic, none; monoclinic, (010) and $[010]$; tetragonal, (001) and $[001]$; $(hk0)$ and $[hk0]$.
- 5.4 $(4\bar{1}\bar{1})$; $(\bar{2}\bar{3}1)$; $[\bar{1}211\bar{4}]$; $[3\bar{3}1]$ (or, their opposites, e.g. (411) , etc.).
- 5.5 (a) $d_{101} = 375$ pm; $d_{100} = 452$ pm; $d_{111} = 302$ pm; $d_{202} = 188$ pm.
(b) $\alpha = 48.1^\circ$; $\beta = 53.5^\circ$; $\gamma = 63.4^\circ$.

(c) $p = 61.8^\circ$; $q = 58.0^\circ$; $r = 45.3^\circ$.

α, β, γ are not identical to p, q, r because the (111) plane normal is not parallel to the [111] direction in orthorhombic crystals. These directions are only parallel in the case of cubic crystals.

5.6 Writing planes as row matrices (Section 5.8);

$$\text{Cubic } I : (HKL) \Leftrightarrow (hkl) \begin{pmatrix} \frac{1}{2} & \frac{\bar{1}}{2} & \frac{1}{2} \\ \frac{1}{2} & \frac{1}{2} & \frac{\bar{1}}{2} \\ \frac{\bar{1}}{2} & \frac{1}{2} & \frac{1}{2} \end{pmatrix}$$

$$\text{Cubic } F : (HKL) \Leftrightarrow (hkl) \begin{pmatrix} \frac{1}{2} & 0 & \frac{1}{2} \\ \frac{1}{2} & \frac{1}{2} & 0 \\ 0 & \frac{1}{2} & \frac{1}{2} \end{pmatrix}.$$

The answers you obtain will depend upon your particular choices of **A, B, C** and **a, b, c**—but they will be the same form as those given above. The reverse transformations for planes are given by the inverse of the matrix in each case. Note that each matrix and its inverse also gives the transformation for direction symbols $[UVW] \Leftrightarrow [uvw]$ when these are written as column matrices (see for example, Section 5.8). Finally, check that your determinants are positive ($\frac{1}{2}$ for Cubic *I*, $\frac{1}{4}$, for Cubic *F* in the examples above). A *negative* value means that you have inadvertently chosen a left-handed axial system to describe one or other of the unit cells.

5.7 $[001] = [0001]$; $[010] = [\bar{1}2\bar{1}0]$; $[210] = [30\bar{3}0] = [10\bar{1}0]$; $[110] = [11\bar{2}0]$.

5.8 The direction $[UVTW]$ is $[4\bar{3}\bar{1}1]$ and the plane $(hkil)$ is $(14\bar{3}1)$ (or their opposites).

5.9 Figure E5.9 shows traces of planes (0002), (10 $\bar{1}$ 1), etc. lying in the $[\bar{1}2\bar{1}0]$ zone axis (normal to the page). We require $\tan x = \tan 60^\circ = c/a \cos 30^\circ$ i.e. $c/a = \tan 60^\circ \cdot \cos 30^\circ = 3/2 = 1.5$.

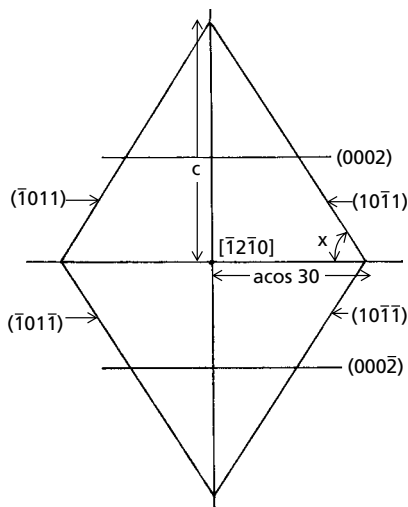


Fig. E5.9.

Chapter 6

- 6.1 These reciprocal lattice sections all consist of hexagonal arrays of reciprocal lattice points, those closest to the origin representing the $\{10\bar{1}0\}$ planes (hexagonal lattice), $\{110\}$ planes (cubic I lattice) and $\{220\}$ planes (cubic F lattice).
- 6.2 Check your answers with the equations given in Appendix 4.
- 6.3 Yes.
- 6.4 $r_{uvw}^* = \left| \frac{1}{\mathbf{r}_{uvw}} \right| = 0.149 \text{\AA}^{-1}$

Chapter 7

- 7.1 The unit cells of the net are ‘skew’, like that for the monoclinic crystal (Fig. 6.4(c)) or the net (Fig. 7.1(d)). The (reciprocal lattice) unit cells of each twin orientation indicated by circles and squares are shown in Fig. E7.1. The vertical row of spots through the origin and perpendicular to the twin plane is common to both twin orientations and the spots are unstreaked. Similarly, in every third row spots are common to both twin orientations and are also unstreaked. This arises because one-in-three of the points in the net have the same position, or are *coincident* in both twin orientations. Streaking, or the extension of the reciprocal lattice points normal to the twin plane, increases as the twin thickness decreases, *except* for those reciprocal lattice points common to both orientations.
- 7.2 The angles at which the second, fourth etc. maxima occur, i.e. $2(\lambda/a)$, $4(\lambda/a)$, etc., coincide with the angles at which the zero order, first order etc. minima occur, i.e. $(1\lambda/d)$, $2(\lambda/d)$. Hence alternate peaks or maxima in the diffraction pattern are missing.

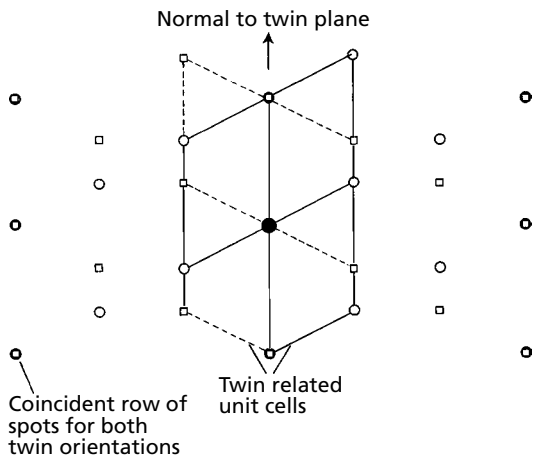


Fig. E7.1.

Chapter 8

- 8.1 α_n , the angle between the direct and diffracted beams, is equal to 2θ (see Fig. E8.1); the planes are inclined to the diffraction grating such that they make equal angles with the incident and reflected beams. Hence $d_{hki} = a \cos \theta$. Substituting for θ and d_{hki} in the equation

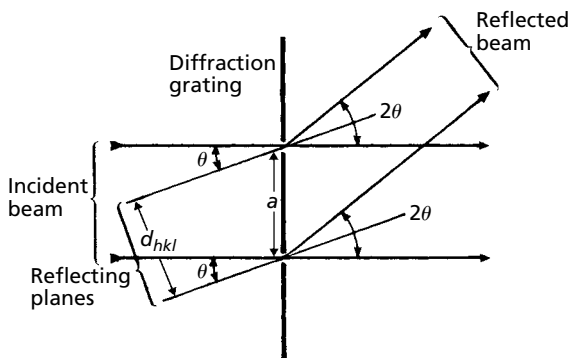


Fig. E8.1.

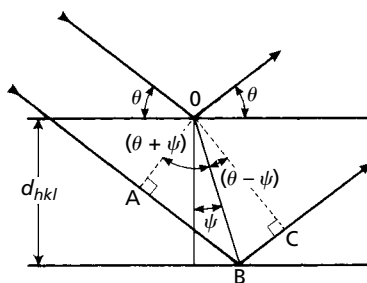


Fig. E8.3.

$n\lambda = a \sin \alpha_n$ gives $n\lambda = (d_{hkl} / \cos \theta) \sin 2\theta = (d_{hkl} / \cos \theta) 2 \cos \theta \sin \theta = 2d_{hkl} \sin \theta$ —
i.e. Bragg's law.

8.2 $d_{110} = 0.2027$ nm; $d_{200} = 0.1433$ nm; and $d_{211} = 0.1170$ nm. Planes whose d -spacings are smaller than $\lambda/2 (= 0.1146$ nm) do not satisfy Bragg's law since the maximum possible value of θ is 90° .

8.3 Let the angle Ψ and distance OB be as shown in Fig. E8.3. Then $AB = OB \sin(\theta + \Psi)$ and $BC = OB \sin(\theta - \Psi)$. Summing and expanding the sine terms:

$$(AB + BC) = OB \sin \theta \cos \Psi + OB \cos \theta \sin \Psi + OB \sin \theta \cos \Psi - OB \cos \theta \sin \Psi.$$

Hence, cancelling and substituting $OB \cos \Psi = d_{hkl}$:

$$(AB + BC) = 2OB \sin \theta \cos \Psi = 2d_{hkl} \sin \theta;$$

i.e. the path difference is independent of the value of Ψ .

Chapter 9

9.1 Bragg's law is satisfied for the planes $(2\bar{2}0)$, $(3\bar{1}0)$, (400) , (310) , (220) (in the $hk0$ section); $(4\bar{1}1)$, $(4\bar{1}\bar{1})$, (301) , (411) , $(41\bar{1})$ (in the $hk1$ and $hk\bar{1}$ sections) and $(3\bar{1}2)$,

$(3\bar{1}\bar{2})$, (202) , $(2\bar{0}\bar{2})$, (312) , $(31\bar{2})$ (in the $hk2$ and $hk\bar{2}$ sections). The (larger) reflecting sphere does not extend beyond the $hk2$ and $hk\bar{2}$ sections.

9.2 Bragg's law is satisfied for the planes (420) , $(4\bar{2}0)$, (220) and $(2\bar{2}0)$.

9.3 Let v be the root mean square velocity of the neutrons. Hence, the kinetic energy $\frac{1}{2}mv^2 = 3/2kT$. The wavelength λ is given by de Broglie's equation $\lambda = h/mv = h/\sqrt{3mkT}$. Substituting the values of h , m , k and $T = 373$ K gives $\lambda = 1.33 \times 10^{-10} \text{ m} = 1.33 \text{ \AA}$.

9.4 The reflection condition for the cubic F lattice is h, k, l are all odd or all even and $F_{hkl} = 4f$ (Appendix 6). For f we substitute the values for Zn and S, using the exponential form since ZnS is non-centrosymmetric (point group $43m$):

$$\begin{aligned} F_{hkl} &= 4 (f_{\text{Zn}} \exp 2\pi i (h0 + k0 + l0) + f_{\text{S}} \exp 2\pi i (h/4 + k/4 + l/4)) \\ &= 4 \left(f_{\text{Zn}} + f_{\text{S}} \exp \pi i \frac{(h+k+l)}{2} \right). \end{aligned}$$

Hence, when

$$\begin{aligned} (h+k+l) &= 4n, & F_{hkl} &= 4(f_{\text{Zn}} + f_{\text{S}}) \\ (h+k+l) &= 4n+2, & F_{hkl} &= 4(f_{\text{Zn}} - f_{\text{S}}) \\ (h+k+l) &= 2n+1, & F_{hkl} &= 4(f_{\text{Zn}} \pm if_{\text{S}}). \end{aligned}$$

9.5 For the origin at the centre of symmetry the atomic coordinates are $\pm (\frac{1}{8} \frac{1}{8} \frac{1}{8})$, hence

$$F_{hkl} = 4 \cdot 2f_c \cos 2\pi (h/8 + k/8 + l/8) = 8f_c \cos \pi/4 (h+k+l)$$

which gives the condition that when

$$(h+k+l) = 4n+2, \quad F_{hkl} = 0$$

in addition to the condition for a cubic F lattice that $F_{hkl} = 0$ when h, k, l are mixed (see Table A6.2).

9.6 For f we substitute the values for f_{Cl} at (000) and f_{Na} at $(\frac{1}{2} 0 0)$ (equivalent to $(0 \frac{1}{2} 0)$ or $(0 0 \frac{1}{2})$).

$$\begin{aligned} F_{hkl} &= 4 (f_{\text{Cl}} \exp 2\pi i (h0 + k0 + l0) + f_{\text{Na}} \exp 2\pi i (h^{1/2} + l0 + k0)) \\ &= 4 (f_{\text{Cl}} + f_{\text{Na}} \exp \pi i h). \end{aligned}$$

Hence when h, k, l all odd $F_{hkl} = 4(f_{\text{Cl}} - f_{\text{Na}})$

when h, k, l all even $F_{hkl} = 4(f_{\text{Cl}} + f_{\text{Na}})$.

9.7 Simply measure the distances, r , of the $hk1$ and $hk2$ layer lines from the $hk0$ layer line. Figure E9.7 shows the Ewald sphere. The $hk0$, $hk1$, $hk2$, etc. reflections lie in the layer lines, spacing \mathbf{c}^* as indicated, where $\frac{1}{|\mathbf{c}^*|} = c$, the lattice repeat distance.

From Fig. 9.7, $\tan 2\theta = r/30 \text{ mm}$ and $\sin 2\theta = |\mathbf{c}^*| \frac{1}{1/\lambda} = \lambda/c$

For the $hk1$ layer line r (corrected for scale factor) = 9.1 mm, whence $c = 5.31 \text{ \AA}$.

For the $hk2$ layer line r (corrected for scale factor) = 21.3 mm, whence $c/2 = 2.66 \text{ \AA}$, $c = 5.32 \text{ \AA}$.

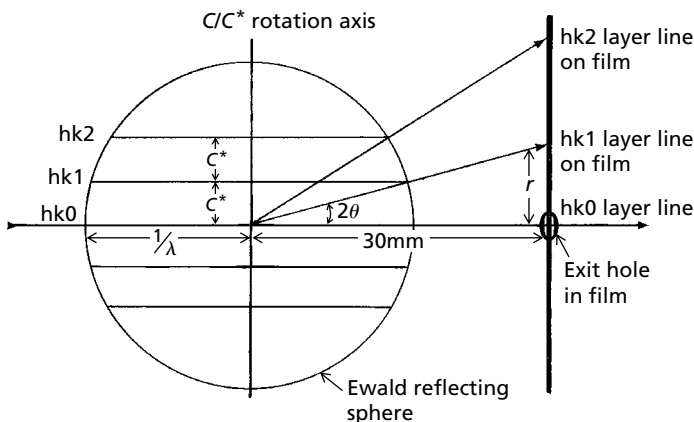


Fig. E9.7.

Chapter 10

- 10.4 The rings in both Figs 10.11(a) and (b) have the same diameters and hence show the same sequence of d -spacings. The diameters of the rings represent a 4θ (not 2θ) angle, hence $\tan 2\theta = \text{radius of ring/specimen film distance}$, from which, and using Bragg's law, the d -spacings can be determined. Referring to the table, the sequence of indices is (110), (040), (130) (the first three strong reflections in the zero layer-line in Fig. 10.11(b)), (111), (131) (the weaker reflections in the first layer-lines above and below) and (022), (112) (the very faint reflections in the second layer lines).

Since the reflections in the zero layer-line are all of type $\{hk0\}$, they have a common zone axis $[001]$ which is parallel to the tensile axis and the direction of the polymer chains.

- 10.5 The 2θ angles and d -spacings of the peaks in (a) should first be checked to confirm that they correspond to the 110, 200 and 211 reflections for α -Fe ($a = 2.866 \text{ \AA}$). The half-height peak widths (measurable only to a limited accuracy) give $\beta (= \beta_{\text{obs}} - \beta_{\text{inst}})$ values ≈ 0.004 , 0.006 and 0.008 respectively which give residual stress values ($\sigma = \frac{1}{2}E \cot \theta$) in the range $1.10 \sim 0.92 \text{ GPa}$. These are considerably greater than the yield stress of mild steel indicating that a large component of the broadening arises from a reduction in crystallite size.
- 10.6 The β values for the peaks are determined in the same way as for Exercise 10.5. Substituting these values into the Scherrer equation $\beta = \lambda/t \cos \theta$ gives grain size (t) values in the range $35\text{--}50 \text{ nm}$. Notice also the small peak shifts; these arise from variations in the α lattice parameters as a result of a change in vanadium concentration following precipitation of the vanadium-rich β phase.

Chapter 11

- 11.1 The equation to be derived follows from the discussion in Section 11.1. Since $eV = \frac{1}{2}mv^2$, then $\sqrt{2meV} = mv$. Substituting in de Broglie's equation gives $\lambda = h/\sqrt{2meV}$. The numerical values obtained by substituting the m , e and V values are 10 kV: 12.2 pm (12.2 pm); 100 kV: 3.88 pm (3.70 pm); 1 MV: 1.22 pm (0.87 pm). The relativistically corrected values are in brackets, from which it is seen that the differences between the values are insignificant at 10 kV, significant at 100 kV and very significant at 1 MV.

- 11.2 The zone axis of the pattern is $\langle 112 \rangle$. The particular variant obtained depends upon the variants of the indices chosen to index the pattern consistently.
- 11.3 This problem is essentially the same as that for the simple cubic crystal as shown in Figs 11.1 and 11.2, except that the cubic P reciprocal lattice is replaced by the cubic F reciprocal lattice (for a cubic I crystal—see Section 6.4). In the ZOLZ $0kl$ and FOLZ $1kl$ the reflecting planes are those for which $(h + k + l) = \text{an even number}$ (see Fig. 6.8(a)).
- 11.4 The diffraction pattern is from Fe_3C (cementite) and is indexed in Fig. E11.4. Notice that the pattern is *not* rectangular, but slightly skew. Since the structure is orthorhombic the order of the indices hkl may not be changed; only their signs may be changed, e.g. the allowed permutations of 103 are: $\bar{1}03$, $10\bar{3}$, 103 , $\bar{1}0\bar{3}$.

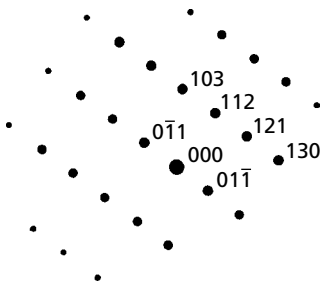


Fig. E11.4.

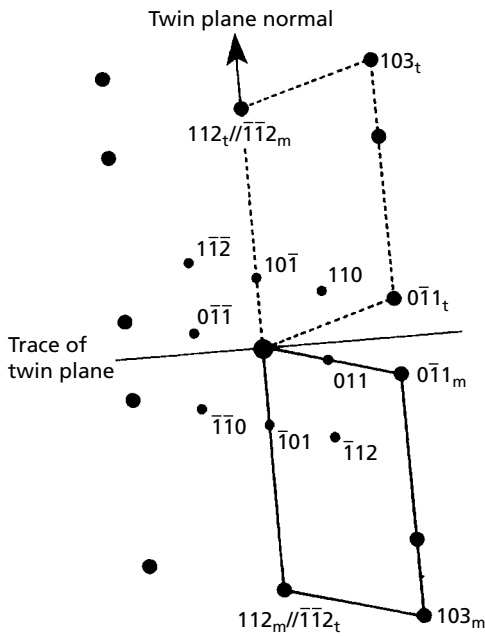


Fig. E11.6.

- 11.5 In Fig. 11.6 the camera constant $\lambda L = 27\text{\AA}$ mm.
- 11.6 The diffraction patterns may be indexed as shown in Fig. E11.6. The ‘matrix’ α -Fe orientation is outlined by solid lines and the twin orientation by dashed lines. The trace of the twin plane and the twin plane normal are indicated (compare with the twin-related unit cells in the optical diffraction pattern as shown in the answer to Exercise 7.1). The reflections for matrix (m) and twin (t) orientations are indexed such that (e.g.) $0\bar{1}1_t$ is related to $0\bar{1}1_m$ by reflection in the twin plane. The Fe_3C reflections may be indexed as shown, giving the orientation relationship between the α -Fe (matrix) and Fe_3C as:

$$(011)_{\text{Fe}_3\text{C}} \parallel (0\bar{1}1)_{\alpha\text{-Fe}} \quad \text{and} \quad (\bar{1}01)_{\text{Fe}_3\text{C}} \parallel (112)_{\alpha\text{-Fe}}.$$

For the zone axes, obtained by cross multiplication (see Section 5.6.2):

$$[\bar{1}1\bar{1}]_{\text{Fe}_3\text{C}} \parallel [3\bar{1}\bar{1}]_{\alpha\text{-Fe}}.$$

- 11.7 Figure E11.7(a) shows a $[001]$ projection of the diamond-cubic structure and the traces (dashed lines) of the (220) planes, the atoms in successive planes being denoted by the \bullet and \blacksquare symbols; separation = $\sqrt{3}/4$ (0.566 nm) = 0.245 nm. Figure E11.7(b) shows the $\langle 110 \rangle$ projection and the ‘dumbbell’ (circled) pattern of atoms; spacing (in projection) = $1/4(0.566\text{nm}) = 0.142\text{ nm}$. *Note:* Fig. E11.7(b) rotated 90° with respect to Fig. 11.15.

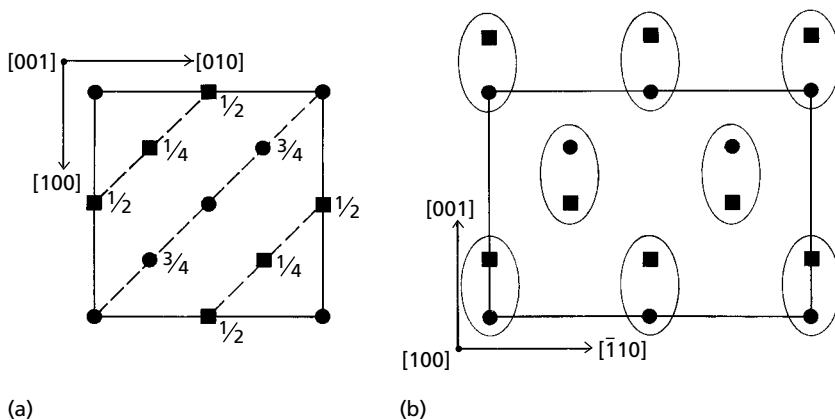


Fig. E11.7.

Chapter 12

- 12.1 Figure E12.1 shows a ‘vertical’ section with the axis of the cone of elliptical cross-section marked OS as in Fig. 12.3(a) and at angle x to the N–S direction. The tangent to the circle (heavy line), which is parallel to the small circle on the sphere, is also tilted at this angle x to the axis of the cone since the angle at the centre of the circle is $2x$ (Euclid, Proposition 20, p. 201). Since the two circular sections must, by symmetry, be inclined at equal and opposite angles to the axis of the cone OS, then the other circular section, indicated by the other heavy line, is parallel to the plane of the stereographic projection.

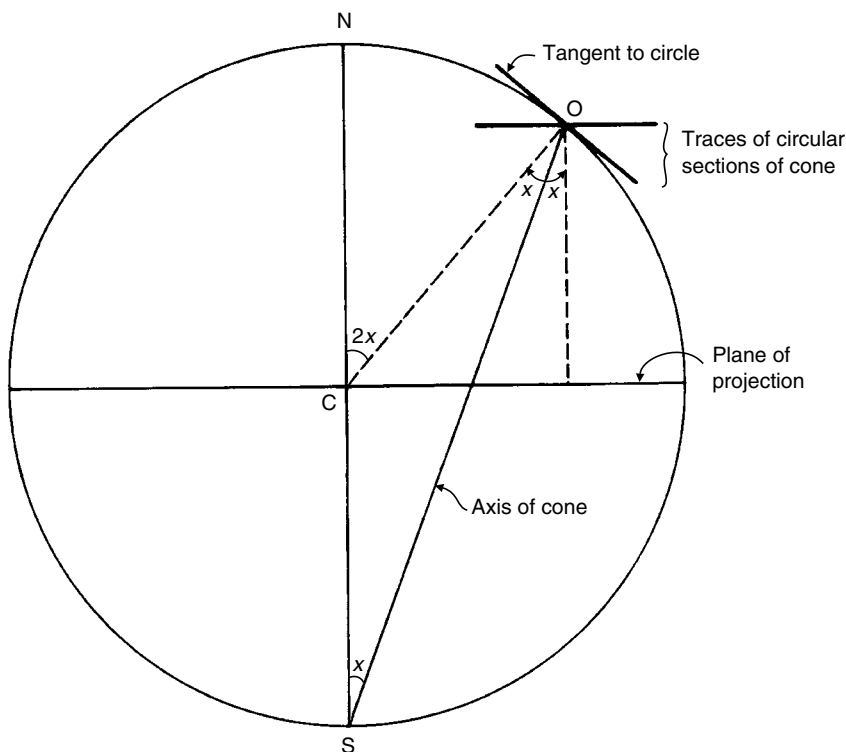


Fig. E12.1.

- 12.2 The α , β and γ angles of the (212) plane to the x , y and z axes are 48° , 71° and 48° , hence the direction cosines $\cos \alpha$, $\cos \beta$ and $\cos \gamma$ are 0.67, 0.33 and 0.67. The ratios between these direction cosines are equal to the ratios between the Miller indices, i.e. 2:1:2. The α , β and γ angles of the $(\bar{3}\bar{3}2)$ plane are -50° , -50° and 65° ; hence the direction cosines are -0.64 , -0.64 , 0.42 which are equal to the ratios $\bar{3} : \bar{3} : 2$.
- 12.3 For plane A, using the Wulff net with its axis A...A along the x -axis, draw in the small circle 36.5° from the $+x$ -axis; this small circle represents the locus of all planes which lie 36.5° from the $+x$ -axis. Now rotate the Wulff net 90° so that its axis A...A lies along the y -axis and draw in the small circle 57.5° from the $+y$ -axis. The two points of intersection of the small circles both in the northern and southern hemispheres (i.e. above and below the plane of projection) show the two possible positions of plane A. Finally, draw in the small circle (the 'line of latitude') at 74.5° from the $+z$ -axis. The three small circles all intersect at the point in the northern hemisphere and hence give the position of plane A (see Fig. E12.3).

The position of plane B is found by the same procedure except that a—sign indicates that the small circle is drawn from the—(minus)—axis.

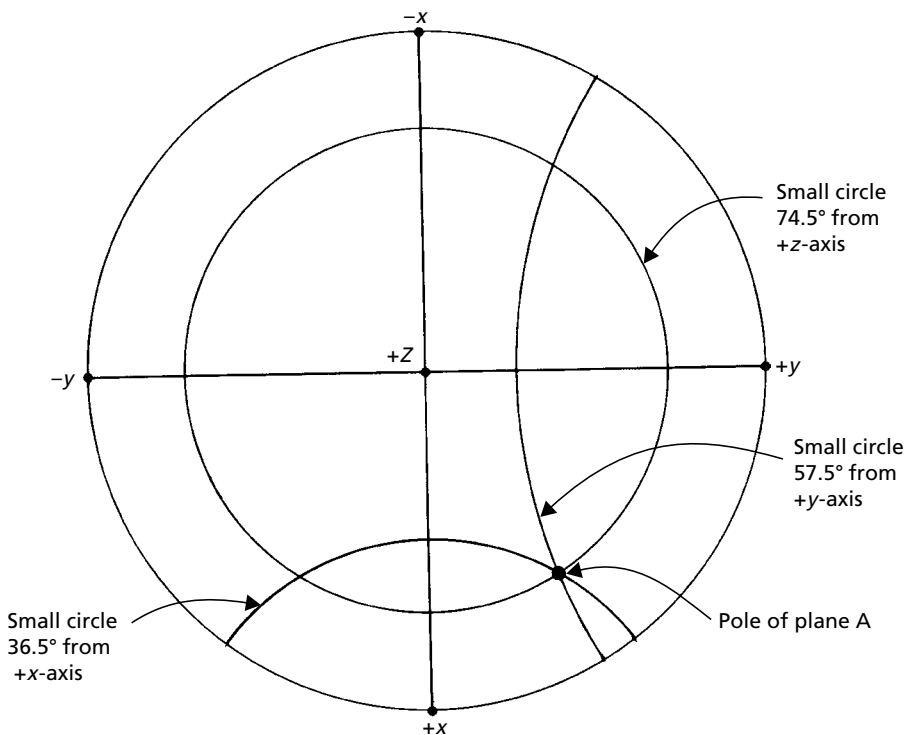


Fig. E12.3.

To find the Miller indices of planes A and B, write down the direction cosines of the angles to the x , y and z -axes respectively and express these as the ratios of whole numbers, i.e.

Plane A	+36.5°	+57.5°	+74.5°
direction cosines:	+0.804	+0.537	+0.267
ratios:	3 :	2 :	1

Hence the Miller index of plane A is (321) .

Similarly, the Miller index of plane B is $(\bar{2}\bar{1}2)$.

The angles between the planes are found by rotating the Wulff net until each pair of planes lie in the same great circle.

Plane A and plane B : 121°

Plane A and $(\bar{1}\bar{1}1)$: 126°

Plane B and (101) : 90°

Plane B and $(\bar{1}01)$: 19°

Further Reading

Introductory books on crystallography

- Bhadeshia, H. (1987). *Worked Examples in the Geometry of Crystals*. The Institute of Materials, London.
- Glazer, A. M. (1987). *The Structures of Crystals*. Adam Hilger, Bristol.
- Holden, A. and Morrison, P. (1982). *Crystals and Crystal Growing*. MIT Press.
- Kennon, N. F. (1978). *Patterns in Crystals*. John Wiley, New York.
- Steadman, R. (1982). *Crystallography*. Van Nostrand Reinhold, Wokingham.
- Windle, A. (1977). *A First Course in Crystallography*. G. Bell and Sons Ltd, London.

Books on two-dimensional patterns and symmetry

- Grünbaum, B. and Shephard, G. C. (1989). *Tilings and Patterns: An Introduction*. W. H. Freeman, New York.
- Hann, M. A. and Thomson, G. M. (1992). *The Geometry of Regular Repeating Patterns*. The Textile Institute, Manchester.
- Jackson, L. (2008) *From Atoms to Patterns: Crystal Structure Designs from the 1951 Festival of Britain*. Richard Dennis Publications, The Old Chapel, Shepton Beauchamp, Somerset, UK.
- Jones, Owen (1856). *The Grammar of Ornament*. Day and Son, London, reprinted (1986) by Studio Editions, London.
- MacGillavry, C. H. (1976). *Symmetry Aspects of M. C. Escher's Periodic Drawings*. Published for the I.U.Cr. by Bohn, Scheltema and Holkema, Utrecht. Re-issued as *Fantasy and Symmetry: the Periodic Drawings of M. C. Escher*. Abrams, New York.
- Shubnikov, A. V. and Koptsik, V. A. (1974). *Symmetry in Science and Art* (English translation, ed. David Harker). Plenum Press, New York and London.

Books mainly concerned with crystal structure and symmetry

- Buerger, M. J. (1970). *Contemporary Crystallography*. McGraw-Hill, New York.
- Buerger, M. J. (1971). *Introduction to Crystal Geometry*. McGraw-Hill, New York.
- Evans, R. C. (1964). *An Introduction to Crystal Chemistry* (2nd edn). Cambridge University Press, Cambridge.
- Janot, C. (1992). *Quasicrystals: A Primer*. Oxford Science Publications, Clarendon Press, Oxford.
- McKie, D. and McKie, C. (1986). *Essentials of Crystallography*. Blackwell Scientific Publications, Oxford.
- Phillips, F. C. (1963). *Introduction to Crystallography* (3rd edn). Longmans, London.
- Vainshtein, B. K. (1981). *Modern Crystallography I: Symmetry of Crystals, Methods of Structural Crystallography*. Springer-Verlag, Berlin, Heidelberg, and New York.

Books which cover, generally in more detail, structural crystallography, symmetry, X-ray and electron diffraction techniques from the standpoint of the chemist, geologist, materials scientist or physicist

- Allen, S. M. and Thomas, E. L. (1999). *The Structures of Materials*. John Wiley, Chichester and New York.
- Bacon, G. E. (1962). *Neutron Diffraction* (2nd edn.). Oxford University Press, Oxford.
- Barrett, C. S. and Massalski, T. B. (1980). *The Structure of Metals* (3rd edn). Pergamon, Oxford.
- Brown, P. J. and Forsyth, J. B. (1973). *The Crystal Structure of Solids*. Arnold, London.
- Bunn, C. W. (1967). *Chemical Crystallography* (2nd edn). Oxford University Press, Oxford.
- Dent-Glasser, L. S. (1977). *Crystallography and its Applications*. Van Nostrand Reinhold, New York.
- Giacovazzo, C., Monaco, H. L., Artioli, G., Viterbo, D., Ferraris, G., Gilli, G., Zanotti, G. and Catti, M. (2002). *Fundamentals of Crystallography*. IUCr Texts on Crystallography 7, 2nd edn. Ed. C. Giacovazzo. International Union of Crystallography/Oxford Science Publications. Oxford University Press, Oxford.
- Glusker, J. P., Lewis, M. and Rossi, M. (1994). *Crystal Structure Analysis for Chemists and Biologists*. VCH Publishers, New York.
- Hahn, T. (ed.) (1985), 3rd edn (1993). Brief Teaching Edition of Volume A of the *International Tables for Crystallography*. Kluwer Academic Publishers, Dordrecht, Boston, and London.
- Hargittai, M. and Hargittai, I. (2008). *Symmetry Through the Eyes of a Chemist* (3rd edn). Springer, New York and London.
- Kelly, A., Groves, G. W. and Kidd, P. (2000), revised edn. *Crystallography and Crystal Defects*. John Wiley, Chichester and New York.
- Klein, C. and Hurlbut, C. S., Jr. (1993). *Manual of Mineralogy* (21st edn). John Wiley, New York.
- McKie, D. and McKie, C. (1974). *Crystalline Solids*. Nelson London.
- Nye, J. F. (1985). *Physical Properties of Crystals: Their Representation by Tensors and Matrices*. Oxford University Press, Oxford.
- Putnis, A. (1992). *An Introduction to Mineral Sciences*. Cambridge University Press, Cambridge.
- Smith, J. V. (1982). *Geometrical and Structural Crystallography*. John Wiley, New York.
- Verma, A. R. and Srivastava, O. N. (1982). *Crystallography for Solid State Physics*. Wiley Eastern, New Delhi.
- Wells, A. F. (1984). *Structural Inorganic Chemistry* (5th edn). Oxford Science Publications, Oxford.
- Whittaker, E. J. W. (1981). *Crystallography for Earth Science (and other solid state) Students*. Pergamon, Oxford

Books on optics and the diffraction of light

- Harburn, G., Taylor, C. A. and Welberry, T. R. (1983). *Atlas of Optical Transforms*. Bell & Hyman Ltd. London (first published in 1975 by G. Bell and Sons Ltd).
- Hecht, E. (1998). *Optics* (3rd edn). Addison-Wesley, London.
- Jenkins, F. A. and White, H. E. (1976). *Fundamentals of Optics* (4th edn). McGraw-Hill, New York.
- Lipson, S. G. and Lipson, H. (1981). *Optical Physics*. Cambridge University Press, Cambridge, London, New York, Sydney.

- Robinson, P. C. and Bradbury, S. (1992). *Qualitative Polarized Light Microscopy*. Royal Microscopical Society Handbook No. 09. Oxford University Press/Royal Microscopical Society.
- Smith, F. G. and Thomson, J. H. (1988). *Optics*. John Wiley and Sons Ltd., Chichester, New York, Brisbane, Toronto, Singapore.
- Steward, E. G. (1989). *Fourier Optics*. Ellis Horwood Ltd., Chichester.
- Taylor, C. A. (1978). *Images: a Unified View of Diffraction and Image Formation with all Kinds of Radiation*. Wykeham Publications, London and Basingstoke.
- Wood, E. A. (1977). *Crystals and Light* (2nd edn). Dover Publications, New York.

Books on X-ray diffraction and X-ray crystallography

- Azaroff, L. V. (1968). *Elements of X-ray Crystallography*. McGraw-Hill, New York.
- Bijvoet, J. M., Kolkmeier, N. H., MacGillavry, C. H. (1951). *X-ray Analysis of Crystals*. Butterworths Scientific Publications, London.
- Blow, D. (2002). *Outline of Crystallography for Biologists*. Oxford University Press, Oxford.
- Bragg, W. H. and Bragg, W. L. (1966). *The Crystalline State*, Vol. 1. *A General Survey* by W. L. Bragg. G. Bell and Sons Ltd, London.
- Buerger, M. J. (1942). *X-ray Crystallography*. John Wiley, New York.
- Clegg, W. (1998). *Crystal Structure Determination*. Oxford University Press, Oxford, New York and Tokyo.
- Cullity, B. D. and Stock, S. R. (2001). *Elements of X-ray Diffraction* (3rd edn). Prentice-Hall, Upper Saddle River, New Jersey.
- Henry, N. F. M., Lipson, H. and Wooster, W. A. (1961). *The Interpretation of X-ray Diffraction Photographs* (2nd edn). Macmillan, New York.
- Ladd, M. F. C. and Palmer, R. A. (2003). *Structure Determination by X-ray Crystallography*. 4th edn. Kluwer-Plenum Press, New York.
- Rhodes, G. (1993). *Crystallography Made Crystal Clear*. Academic Press, New York.
- Woolfson, M. M. (1997). *An Introduction to X-ray Crystallography* (2nd edn). Cambridge University Press, Cambridge.

Books on electron diffraction techniques

- Brandon, D. and Kaplan, W. D. (2001). *Microstructural Characterisation of Materials*. John Wiley and Sons, Chichester and New York.
- Champness, P. M. (2001). *Electron Diffraction in the Electron Microscope*. Royal Microscopical Society Handbook No. 48, Bios Scientific Publishers/Royal Microscopical Society, Oxford.
- Dyson, D. J., Andrews, K. W. and Keown, S. R. (1971). *Interpretation of Electron Diffraction Patterns* (2nd edn). Hilger and Watts, London.
- Edington, J. W. (1975). *Electron Diffraction in the Electron Microscope*. Monograph 2. Practical Electron Microscopy in Materials Science. Philips Technical Library, Macmillan, London.
- Goodhew, P. J., Humphreys, F. J. and Beanland, T. F. (2001). *Electron Microscopy and Analysis* (3rd edn). Taylor and Francis, London and New York.
- Loretto, M. H. (1994). *Electron Beam Analysis of Materials* (2nd edn). Chapman and Hall, London.
- Thomas, G. and Goringe, M. J. (1979). *Transmission Electron Microscopy of Materials*. Wiley, Chichester and New York. Reprinted by Tech books, 4012 Williamsburg Court, Fairfax, Virginia 22032.

Williams, D. B. and Carter, C. B. (1996). *Transmission Electron Microscopy: A Textbook for Materials Science*. Plenum Press, New York and London.

Books of Reference

The *International Tables for Crystallography* is the republication of the *International Tables for X-ray Crystallography*. The volumes are listed below.

International Tables for X-ray Crystallography

Volume I: *Symmetry Groups* (1952)

Volume II: *Mathematical Tables* (1959)

Volume III: *Physical and Chemical Tables* (1962)

Volume IV: *Revised and Supplementary Tables to Volumes II and III* (1974)

Published for the International Union of Crystallography by the Kynoch Press, Birmingham, England.

International Tables for Crystallography

Volume A: *Space Group Symmetry*. Hahn, T. (ed.) (1983, corrected reprint of 5th edn., 2005). Brief Teaching edn. (1985, 5th edn. 2005)

Volume B: *Reciprocal Space*. Shmueli, U. (ed.) (1993, 2nd edn. 2001)

Volume A1: *Symmetry Relations between Space Groups*. Wondratschek, H. and Müller, U. (eds.) (2004)

Volume C: *Mathematical, Physical and Chemical Tables*. Wilson, A. J. C. and Prince, E. (eds.) (1992, 3rd edn. 2004)

Volume D: *Physical Properties of Crystals*. Authier, A. (ed.) (2003)

Volume E: *Sub-Periodic Groups*. Kopský, V. and Litvin, D. B. (eds.) (2002)

Volume F: *Crystallography of Biological Macromolecules*. Rossmann, M. G. and Arnold, E. (eds.) (2001)

Volume G: *Definition and Exchange of Crystallographic Data*. Hall, S. R. and McMahon, B. (eds.) (2005)

Formerly published for the International Union of Crystallography by Kluwer Academic Publishers, Dordrecht, Boston and London and latterly by Springer-Verlag, Heidelberg, Germany and Secaucus, USA. Also published on-line from the IUCr website.

The X-Ray Powder Diffraction File is published by the International Centre for Diffraction Data (ICDD) (the Joint Committee for Powder Diffraction Standards, JCPDS), 12 Campus Boulevard, Newtown Square, PA 19073-3273, USA. It is updated as sets are added at approximately yearly intervals, together with the following manuals.

Alphabetical Indexes: Inorganic Phases

Hanawalt Search Manual: Inorganic Phases

Organic and Organometallic Phases Search Manual

Indexes and Search Manual: Frequently Encountered Phases.

Books on, or including, the stereographic projection

Barrett, C. S. and Massalski, T. B. (1980). *The Structure of Metals* (3rd edn). Pergamon, Oxford.

Cullity, B. D. and Stock, S. R. (2001). *Elements of X-ray Diffraction* (3rd edn). Prentice-Hall, Upper Saddle River, New Jersey.

Hammond, C. (1993). *Stereographic Techniques*, Module 9.17 in *Procedures for Transmission Electron Microscopy*, eds Robards, A. and Wilson, A. J. John Wiley, Chichester and New York.

- Johari, O. and Thomas, G. (1969). *The Stereographic Projection and its Applications*. Techniques for Metals Research, Vol. 2A. Interscience Publishers, New York.
- Krawitz, A. D. (2001) *Introduction to Diffraction in Materials Science and Engineering*. John Wiley and Sons, New York.
- Moon, J. R. (1978). *Worked Examples in Stereographic Projections*. Institute of Metallurgists Monograph No. 2. The Institute of Metals, London.

Books of general or historical interest

- Aste, T. and Weaire, D. (2000). *The Pursuit of Perfect Packing*. Institute of Physics Publishing, Bristol.
The authors recount the story of the problem of the densest packing of identical spheres and many others which have to do with packing things together—from atoms in crystals, soap bubbles in foams to the structure of the Giant's Causeway; together with brief accounts of the lives of the scientists who devoted themselves to these problems.
- Bragg, W. H. and Bragg, W. L. (1966). *The Crystalline State*, Vol. 1. *A General Survey* by W. L. Bragg. G. Bell and Sons Ltd, London.
A book which shows the clarity and incisiveness of Bragg's scientific method. It is so well written that it remained in print, substantially unrevised from its first publication in 1933, for nearly forty years. Even today very little is 'out of date' and it contains much material which is not adequately covered at the same level elsewhere.
- Bragg, W. L. (1975). *The Development of X-ray Analysis*, edited by Phillips, D.C. and Lipson, H. G. Bell and Sons, London.
A book published four years after Bragg's death; a summary in effect of his life's work, written in a simple and engaging fashion.
- Bunn, C. (1964). *Crystals, their Role in Nature and in Science*. Academic Press, New York and London.
A book very much in the same category as A. F. Wells (1968) (see below) but with an even wider range of subject matter (including speculations on crystals and the origin of life) to appeal to the general scientific reader.
- Crick, F. (1989). *What Mad Pursuit: A Personal View of Scientific Discovery*. Weidenfeld and Nicolson, London. Reprinted by Penguin Books, London, 1990.
A book which should be read together with J. D. Watson's *The Double Helix*; written much later, it provides in retrospect a more balanced, but no less personal, account of the discovery of the structure of DNA and its aftermath.
- Cundy, H. M. and Rollett, A. P. (1961). *Mathematical Models* (2nd edn). Oxford University Press, Oxford. Reprinted by Tarquin Publications, St. Albans (2006).
This book not only includes clear descriptions of polyhedra and how to construct them but also describes mechanical and models for logic and computing—a compendium of information not to be found elsewhere.
- Ewald, P. P. and numerous crystallographers (1962). *Fifty Years of X-ray Diffraction*. Published for the International Union of Crystallography by N. V. A. Oosthoek's Uitgevers-maatschappij, Utrecht.
An invaluable source-book which describes the beginnings of X-ray diffraction, the growing field and development of schools of crystallography throughout the world, and the personal reminiscences and memoirs of those who participated. One of the strongest

impressions is that of an international community of scientists which transcended the barriers of nationality, politics and war.

Hargittai, M. and Hargittai, I. 3rd edn. (2008). *Symmetry Through the Eyes of a Chemist*. Springer, New York and London.

A book which transcends the usual subject barriers and which draws illustrations and analogies from a wide range of sources. It also bridges the gap between a popular book on patterns and symmetry and a textbook on 'the third dimension' in chemistry.

Lima de Faria, J. (Editor) (1990). *An Historical Atlas of Crystallography*. Kluwer Academic Publishers, Dordrecht.

A very comprehensive historical survey of the development of geometrical, physical and chemical crystallography and crystal structure determination—topics which are covered in most histories of science in a fragmentary manner. Special features of the book are the beautifully presented 'time maps' of crystallography, the title pages of important works and a bibliography on the history of crystallography.

Lipson, H. (1970). *Crystals and X-rays*. Wykeham Publications (London) Ltd.

An excellent introduction to X-ray diffraction, largely treated historically and with reference to the diffraction of light and microscopy. Crystal structure analysis is also described in a very clear and simple manner.

Newton, I. (1979). *Opticks or A Treatise of the Reflections, Refractions, Inflections and Colours of Light*. Dover Publications, New York, based on the Fourth Edition, London, 1730. Published by G. Bell and Sons Ltd. in 1931.

First published in 1704, Newton's *Opticks* is one of the most readable of all the great classics of physical science; in simple language Newton describes his famous experiments with colours, lenses, reflection and diffraction of light, the colours of rainbows and soap bubbles. This (Dover) edition has a foreword by Albert Einstein, a preface by I. Bernard Cohen and an introduction by Sir Edmund Whittaker.

Thompson, D'Arcy Wentworth (1942). *On Growth and Form: A New Edition*. Cambridge University Press. Reprinted by Dover Publications, New York 1992.

A classic book, first published in 1917, which provides in many ways a unique perspective on the evolution of biological structures and processes in terms of their physical and mathematical aspects. It is also a major work of literature. An abridged edition, edited by J. T. Bonner, was first issued by Cambridge University Press in 1961.

Watson, J. D. (1968). *The Double Helix: A Personal Account of the Discovery of the Structure of DNA*. With a Foreword by Sir Lawrence Bragg. Weidenfeld & Nicolson, London, and Penguin Books, Harmondsworth (1970).

A book which has become notorious for its lop-sided treatment of the other scientists in the UK and USA whose work also contributed to the discovery of the structure of deoxyribonucleic acid (DNA)—but which should not detract from Watson and Crick's great achievement in recognizing that the helices ran in opposite directions and the crucial idea of base-pairing.

Wells, A. F. (1968). *The Third Dimension in Chemistry*. Clarendon Press, Oxford.

A very scholarly work, with a much wider range of subject matter than its title suggests: it includes elegant descriptions of polygons and plane nets, polyhedra and the symmetry of crystals from a broad scientific and historical framework.

Weyl, Hermann (1952). *Symmetry*. Princeton University Press, Princeton, NJ.

A book in the same mould as *On Growth and Form*, Weyl expresses symmetry as *harmony of proportions* and shows that it is one of the ideas by which mankind throughout the ages has tried to create order, beauty and perfection in the world.

IUCr Commission on Crystallographic Teaching: Teaching Pamphlets

The aim of this series of pamphlets, edited by C. A. Taylor and first published in 1981, is to produce a collection of short statements, each dealing with a specific topic at a specific level. They are listed below and may be downloaded from the IUCr website.

First Series

- 1 *A Non-Mathematical Introduction to X-ray Diffraction*. C. A. Taylor
- 2 *An Introduction to the Scope, Potential and Applications of X-ray Analysis*. M. Laing
- 3 *Introduction to the Calculation of Structure Factors*. S. C. Wallwork
- 4 *The Reciprocal Lattice*. A. Authier
- 5 *Close-Packed Structures*. P. Krishna and D. Pandey
- 6 *Pourquoi les Groupes de Symétrie en Cristallographie*. D. Weigel
- 7 *Crystal Structure Analysis using the 'Superposition' – and 'Complementary' – Structures*. L. Höhne and L. Kutchabsky
- 8 *Anomalous Dispersion of X-rays in Crystallography*. S. Caticha-Ellis
- 9 *Rotation Matrices and Translation Vectors in Crystallography*. S. Hovmöller
- 10 *Metric Tensor and Symmetry Operations in Crystallography*. G. Rigault

Second Series

- 11 *The Stereographic Projection*. E. J. W. Whittaker
- 12 *Projections of Cubic Crystals*. I. O. Angell and M. Moore
- 13 *Symmetry*. L. S. Dent Glasser
- 14 *Space Group Patterns*. W. M. Meier
- 15 *Elementary X-ray Diffraction for Biologists*. J.P. Glusker
- 16 *The Study of Metals and Alloys by X-ray Powder Diffraction Methods*. H. Lipson
- 17 *An Introduction to Direct Methods. The Most Important Phase Relationships and their Application in Solving the Phase Problem*. H. Schenk
- 18 *An Introduction to Crystal Physics*. E. Hartmann
- 19 *Introduction to Neutron Powder Diffractometry*. E. Arzi

Third Series

- 20 *Crystals – A Handbook for School Teachers*. E. A. Wood
- 21 *Crystal Packing*. A. Gavezzotti and H. Flack
- 22 *Matrices, Mappings and Crystallographic Symmetry*. H. Wondratschek

Index

Note: Illustrations are indicated by italic page numbers, footnotes are indicated by the letter n

- α -alumina, space-filling polyhedron for 345
- Abbe criterion (for limit of resolution)
 - in the electron microscope 288
 - in the light microscope 185, 186, 187
- Abbe, Ernst 184, 185, 349
- Abbe theory of image formation 328–32, 330, 331, 332
- absorption factor (in X-ray diffraction) 206n
- addition rule 140, 140, 159, 279
- Airy, George Biddell 180, 349–50
- Airy disc 180–3, 182, 183, 184
- Alhambra, the 72–3
- aluminium
 - structure of 6
 - electron diffraction patterns of 278, 282
- aluminium boride (AlB_2), structure of 17, 17
- aluminium oxide (Al_2O_3), structures of 34
- alternating (rotation-reflection axes) 74–5, 104
 - relation to inversion axes 104
- amplitude-phase diagrams
 - for a single slit 325, 326
 - for N slits 325–8, 327
- angles (between planes) 160–1, 382–3
 - table for cubic crystals 383–4
- ångström (\AA) units, use of in X-ray and electron diffraction 253, 254, 255, 278
- anisotropy (of crystal properties) 104–6
- anomalous scattering (of X-rays) 213–4, 213, 214
- answers (to exercises) 401–13
- antifluorite structure 19, 20
- antiphase domain boundaries 234
- α -polonium, structure of 9
- α -quartz, enantiomorphous forms of 110, 110
- applications of X-ray and electron diffraction techniques
 - detection of ordering 236
 - determination of crystal orientation 221–2, 222, 283–8, 285, 287, 288, 289, 290
 - determination of orientation
 - relationships 280–1, 280
 - identification of unknown phases 253–6, 281–3
 - measurement of crystal (grain) size 256
 - measurement of internal (elastic) strains 256–7
 - measurement of lattice parameters 252–3
 - measurement of preferred orientation 258–62, 259, 261
- approaches (to the study of crystal structures) 55–6
- Archimedean (semi-regular) polyhedra 50, 127, 341–3, 342
- Argand diagram (representation of complex numbers) 390–1, 391
- asparagine 98, 107
- Astbury, William Thomas 350–1
- atactic polymers 125
- α -tetrakaidodecahedron 94
 - in epidermal cells 95, 95
- Atlas of Optical Transforms* 171, 263n
- atomic coordinates 19, 207, 319
- atomic radii, variations in 14–15
- atomic scattering factor (amplitude)
 - for electrons, f_e 273
 - for neutrons 236, 237
 - for X-rays, f 203, 204
- Aulonia hexagona* 52
- austenite (solid solution of C in ccp Fe) 18
- axial distances 85
- back focal plane (of light microscope) 328–9, 330
- back reflection X-ray diffraction techniques
 - Laue method 221–3, 222
 - powder method 249, 250
- barium titanate, structures of 31–33, 32
 - displacive transformations in 33
 - domains in 32
 - ferroelectric effect in 32, 105
- Barlow, William 111, 352
 - derivation of space groups of 111
- base-centred lattices 85, 86–7
- base (unit cell) vectors 133
- Bertrand lens (for light microscope) 328n
- Bijvoet, Johannes Martin 214, 351–2
- biographical notes 349–81
- body-centred cubic (cubic *I*) lattice 86
 - (conventional) unit cell of 85, 86
 - primitive (rhombohedral) unit cell of 86
 - reciprocal lattice unit cell of 156–8, 157
- body-centred cubic (bcc) structure 10
 - closest packed planes in 10
- body-centred lattices 85, 87
- bonding
 - in inorganic crystals 27–9
 - in organic crystals 121
- border (or frieze) patterns 65, 70, 83
 - systematic identification of 71
- boron nitride, structures of 53
- Bragg, William Henry 192, 352–4
 - Universe of Light, the* 353
- Bragg, William Lawrence 192, 354–6
- Bragg-Brentano focusing geometry 230, 230, 247, 247, 260
- Bragg contours (in electron microscopy) 291, 291
- Bragg equation (in light diffraction) 187, 187

- Bragg's law
 and Fourier analysis 320
 derivation of 196–8, 196, 197
 equivalence to Laue equations 198
 in electron diffraction 277–8, 279
 in light diffraction 187–8, 187
 origin of 192
 use of Laue indices in 138
 vector notation for 197, 197
- Bragg notebook, the 355n
- Bravais, Auguste 84, 356
- Bravais (space) lattices 84–90
 table of 91
 symmetries of 86–90
 unit cells of 85
- Brillouin zones 158, 344, 347–8, 347
- broadening of X-ray reflected beams
 crystal size factor 217–8, 217
 crystal (lattice) strain factor 256–7
 instrumental factor 215, 219n, 256
- de Broglie's equation 172
- Buckminster fullerenes 48, 50, 51
- Buerger, Martin Julian 226, 357
- caesium chloride (CsCl)
 Bravais lattice for 118
 space group for 119
 structure of 12, 13, 209
- calcite (CaCO_3) 3
 bonding in 27
 rhombohedral structure of 28
- calcium fluoride (CaF_2 , fluorite)
 Bravais lattice for 118
 space group for 119
 structure of 16, 19
- Cambridge Structural Database 123
- camera constant (for the electron microscope) 277
- camera length (for the electron microscope)
 277, 279
- camera
f-number of 183
 limit of resolution of 183, 183
- carbon, structures of 46–53
 diamond 47, 48
 graphite 47, 49
 fullerenes 48–52, 51
 nanotubes 52, 53
- carborundum (SiC)
 stacking sequences in 33, 34, 35
 tetrahedral structure types 33, 34
- cementite (Fe_3C)
 electron diffraction pattern of 294
 stereographic projection of 306, 307
- centre of symmetry 100, 101, 102
- centrosymmetric point groups, table of 91
- chiral molecules 103
- chirality
 in amino acids 106–7
 in deoxyribonucleic acid (DNA) 106–7
- clathrates 129
- close-packed hexagonal arrays (of atoms) 4, 4
- close-packed structures 6, 7
- close packing of spheres 1
- closest-packed planes (in bcc structures) 10, 10
- clustering (in alloy structures) 234
- cobalt, structures of 23
- cobalt-copper multilayer specimen, low angle
 X-ray diffraction trace of 231, 232
- cobalt-gold multilayer specimen, high angle
 X-ray diffraction trace of 231, 232
- coherence, conditions for in light
 diffraction 173–4, 174, 184n
- coherence length 206n, 220–1
- complex numbers, vector representation of 390–1, 391
- computer programs in crystallography 333–5
- constancy of interfacial angles, Law of 1, 99
- copper-gold alloys, ordering in 234–5, 235
- copper-zinc alloy, ordering in 234, 235, 236
- counterchange (black-white) patterns 65, 68, 70–3
 point groups 68, 72
 symmetry elements 68, 70–1, 72
- coordination of Bravais lattice points 90
- coordination polyhedra, linking rules 29–31, 30
- corundum ($\alpha\text{-Al}_2\text{O}_3$), stacking sequence in 34
- covalent bonding 27–8
- cristaballite (SiO_2)
 α and β structures of 43–4
 space groups for 117, 118
- crystal classes (point groups) 99
 notation for 102–4
 table of 91, 213
- crystal habit 3, 97
- crystalline state, nature of 1–4
- crystalloids *see* quasiperiodic crystals
- crystal plans or projections 19–21, 20
- crystal models, suppliers of 335–8
- crystal size, measurement of 216–9, 219n, 256
- crystal structure determination 204–7, 206n, 318–23, 319, 320, 322, 323
 corollary with diffraction grating 204–6
 phase problem in 215, 320, 322
- crystal symmetry, properties related to 104
- crystal systems 89–90
 Bravais lattices for 90
 table of 91
- cubic close-packed (ccp) structure 6
 crystal plan of 19, 20
 interstitial sites in 11–12, 12
 unit cells of 8–9
- cubic crystal system
 point groups (crystal classes) in 103, 337
 stereographic representation (of point groups)
 309–10, 309
- cubic crystals
 angles between planes, table of 383–4
 Miller indices and zone axis symbols for 136

- point group symbols for 103
- stereographic projections of 299–302, 300, 302
- cubic (Bravais) lattices 85–6, 85, 86
 - geometrical relationships between 86, 86
 - reciprocal lattices of 157, 157
 - space-filling polyhedra for 90
- cubic space groups 119–120
- cultures (relationship to symmetry and patterns) 65, 66
- cyclosilicates 39, 40
- ‘Daedalus’ (D.E.H. Jones) 48, 52
- Debye, Peter Joseph William 243, 357
- Debye-Scherrer X-ray diffraction
 - powder method 249–52, 251, 252
- deoxyribonucleic acid (DNA)
 - effect of humidity on structure 121
 - space group for 267, 267
 - structure simulation by light diffraction of 262–7, 263, 264, 265, 266
- X-ray photograph of xv
- diad (two-fold) axis of symmetry 56, 75, 76, 99
- diamond (rectangular centred) lattice 62, 63
- diamond
 - bonding in 27
 - space group for 120
 - structures of 47, 48
- diffraction and interference 173–4
- diffraction contrast (in the electron microscope) 291–2, 291
- diffraction grating
 - image of 329–32, 330, 331, 332
 - with a limited number of slits 180, 182
 - with narrow slits 175–7, 175, 177
 - with wide slits 178–9, 177
- diffraction grating and Fourier analysis 323–8, 324, 325, 327, 328, 330
- diffraction grating equation 176, 179–80, 326–7
- grating term 327
- relationship to Bragg’s law 187–8, 187
- single aperture term 327
- diffractometer X-ray powder method *see* X-ray diffractometer
- Diffractionsplatte* 329
- diopside 318
 - electron density map of 319
- direction (zone axis) symbols 132–3
- Dirichlet domains *see* Voronoi polyhedra
- dislocations 25
 - imaging of in the electron microscope 291, 291
- disordered crystals 234
- displacive phase transformations
 - in barium titanate 33
 - in deoxyribonucleic acid (DNA) 121
 - in silica 43
- dog-tooth spar (calcite) 3, 3
- domain boundaries (long-range order) 234
- domains (in barium titanate) 32, 32
- double diffraction
 - and ‘unindexable’ electron diffraction patterns, 399, 399
 - effect on systematically absent reflections 396
 - in electron diffraction patterns of the hcp metal structure 396, 398, 399, 399n
 - in electron diffraction patterns of twin-related crystals 399–400, 400
 - origin of 396
- Double Helix, The* 204, 356
- duality (in polyhedra) 339–40, 344
- dynamical theory
 - in electron diffraction 273
 - in X-ray diffraction 205, 206
- elastic scattering processes 274, 283, 287
- electron backscattered diffraction (EBSD)
 - patterns 287–8, 290
- electron density 315, 318, 319, 320, 322
- electron diffraction
 - comparison with light and X-ray diffraction 165
 - Ewald reflecting sphere construction for 274–6, 275
- electron diffraction patterns 276–7, 276
- analysis of 277–8, 278, 279
- electron diffraction techniques
 - identification of polycrystalline specimens 281–2, 282
 - identification of quasiperiodic crystals 282–3, 283
 - orientation relationships between crystals 280–1, 280
- electron scattering amplitude (f_e) 273
- Elements of Euclid* 244–5
 - relation to X-ray focusing geometry 245–6, 245
- embrittlement (in iron and steel) 4
- enantiomorphism
 - in α and β quartz structures 44, 44
- enantiomorphous crystal structures 43, 106, 107
- enantiomorphous screw axes of symmetry 109, 110
- enantiomorphous point groups 120
 - in cubic system 337
 - in orthorhombic system 337
 - table of 91
- enantiomorphous space groups 118, 120
- equal area projection 314n
- Escher, M.C. 72, 81, 82
- Euler’s formula (for complex numbers) 390–1, 391
- Ewald, Paul Peter 193, 357–8
- Ewald reflecting sphere construction
 - and broadening of diffracted beams 217–9, 218
 - derivation of 198–202, 199, 200
 - and electron diffraction 274–6, 275
 - and Laue technique 201, 201
 - for monoclinic crystal 200, 200, 201
 - and oscillation method 223–4, 224
 - for planes deviating from Bragg angle 284–6, 285, 286

- Ewald reflecting sphere construction (*Cont.*)
 and precession method 226–9, 227, 228, 229
 and rotation method 225, 226
 for a single set of planes 198–202, 199, 200, 201
 and X-ray diffractometer 230–1, 230, 233
- Ewald's synthesis 198–202, 199, 200, 201
- eye, the optical properties of 189
- extinction criteria, tables of allowed reflections 397, 398
- extrinsic stacking faults 21, 22
- fabric *see* texture
- face-centred cubic (cubic *F*) lattice 85, 86
 primitive (rhombohedral) unit cell of 86, 86
 reciprocal lattice unit cell of 156–8, 157
 unit cells of 86, 86, 392–3, 393
- face-centred cubic (fcc) structure 16
 distinction between ccp structure 16
- face-centred orthorhombic lattice 85, 87
 unit cell of 85
- faulting *see* stacking faults
- Fedorov, Evgraph Stepanovich 111, 358
 derivation of space groups of 111
- ferric oxide (Fe_2O_3), structures of 36–7
- ferrihydrate ($\text{Fe}_5(\text{OH})_8\text{H}_2\text{O}$), structure of 37
- ferrite (interstitial solid solution of C in bcc Fe) 17
- ferritin molecule 37
 protein shell of 38
- ferroelectricity 32–3
- ferromagnetic materials 234
- ferroso-ferric oxide (Fe_3O_4) 36
- ferrous oxide (FeO) 35
- Festival (of Britain) Pattern Group* 73, 73n
- Fibonacci series of numbers 80
- fibre textures 258–9, 258
- Fifty Years of X-ray Diffraction* 193
- first order Laue zone 275, 276, 277
- five-fold (pentad) rotation axis 61
- five plane lattices 61–3, 62
- flow diagrams, for identification of
 one-dimensional plane lattices 65, 71
 two-dimensional plane lattices 64–5, 69
- fluorite (CaF_2) structure of 19, 20
- f*-number (for camera lens and eye) 183, 188
 relation to numerical aperture 188
- focusing circle (X-ray diffractometer) 246, 247
- focusing X-ray diffraction geometry 245–6,
 245, 246
- focusing X-ray diffraction methods 246–8,
 246, 247
- forbidden reflections *see* systematic absences
- four-fold (tetrad) rotation axis 58
- Fourier, Jean Baptiste Joseph 316, 358–9
- Fourier analysis 315–8, 315, 317
 in crystallography 318–23, 319, 320, 322
 in microscopy 328–9, 330
- Fourier coefficients 316, 318
 relation to amplitudes of diffracted beams 321, 324
- Fourier series 316, 320–1
- Fourier synthesis 316–8, 317
 in crystallography 322, 322
 in microscopy 328–9, 330
- Fourier transform 318
- Frank, Frederick Charles 21, 359–60
- Frank notation (for stacking sequences) 21–3, 34
- Frankenheim, Moritz Ludwig 84, 360
- Franklin, Rosalind Elsie xv, 360–1
- Fraunhofer, Joseph 176, 361
- Fraunhofer diffraction 176
- Fraunhofer diffraction patterns
 for a single slit 177, 178–9, 178, 325, 326
 for a grating, many (N) slits 175–81, 177, 181,
 325–8, 327, 328
- Fresnel, Augustin Jean 172, 361–2
- Fresnel diffraction 176
- Friedel's law 212
- Friedrich, Walter xiv, 192
- From Atoms to Patterns* 349n
- Fuller, Richard Buckminster 48, 362–3
- fullerenes, structures of 48–52, 51
- general equivalent positions (in space groups)
 113–4
- geodesic dome 49, 128
- geodesics 49n
- geometrical relationships
 addition rule 140, 159
 angle between planes 160–1, 382–3
 d_{hkl} -spacings of lattice planes 160
 plane parallel to two directions 161
 reciprocal (and direct) lattice unit cell
 vectors 158, 158, 161
 Weiss zone law (zone equation) 139, 159, 160
 zone axis for two planes 161
- geometry of X-ray diffraction
 Bragg's analysis 196–8, 196, 197
 Ewald's synthesis 198–202, 199, 200, 201
 Laue's analysis 193–5, 194, 195
- germanium, high resolution image of 290, 290
- glide line of symmetry 63–4, 63
- glide plane of symmetry 76, 76, 108
 systematic absences arising from 394–5, 394
- goethite ($\alpha\text{-FeO.OH}$), structure of 37
- gold, ccp structure of 6
- golden mean (or ratio) 80
- grain size, measurement of 256
- Grammar of Ornament*, the 71
- graphene layers (nets) 47, 50, 52, 53
- graphite
 bonding in 28
 space groups for 120
 structures of 47, 49
- Greninger net 221n
- habit 3, 97–8, 97, 98
- haematite ($\alpha\text{-Fe}_2\text{O}_3$), structure of 37

- Hanawalt groups 254
 Hanawalt search procedure 254–5, 255
 hard sphere model (for crystal structures) 4, 17
 Haiiy, René-Just 3, 363
 Essai d'une Theorie sur la Structure des Cristaux (1784) 3
 Henry, Norman Fordyce McKerron 111, 363–4
 Hermann, Carl Heinrich 111, 363
 Hermann-Mauguin space group symbols 112
 Hessel, Johann Friedrich Christian 99, 364
 hexad (six-fold) axis of symmetry 58, 102
 hexagonal arrays (of atoms)
 constructing ccp and hcp structures from 5–6, 5
 hexagonal close-packed (hcp) structure 5–6, 7
 interstitial sites in 14
 relation to hexagonal lattice 118
 space group for 115, 117
 unit cell of 7
 hexagonal crystal system
 indexing in 141–3, 141
 point groups (crystal classes) in 103
 hexagonal (Bravais) lattice 87, 85, 87
 unit cells of 141, 141
 hexagonal (plane) lattice 62, 63
 high order Laue zone 277
 holosymmetric crystal classes 103–4
 honeycomb, structure of 47n
 Hooke, Robert 1, 364
 Micrographia (1665) 1, 2
 Hooke's sketches of atom packing 2
 Hull, Albert Wallace 243, 364
 Huygens, Christian 172, 365
 Traite de Lumiere (1690) 356
 Huygens' wavelets 173, 175, 175, 178, 178
 hydrogen bonds 121

 ice, crystal structures of 45, 46
 icosahedral packing 128, 128
 relation to cuboctahedral packing 127, 129–30
 icosahedral structures in metallic alloys 128
 icosahedron 50, 51, 341
 image formation (in the light microscope) 184–8,
 185, 328–32, 330
 image formation (in the transmission electron
 microscope) 288–92
 conditions for high-resolution (Abbe)
 images 289–90, 290
 diffraction contrast (bright and dark field) 291,
 291
 mass-thickness contrast 291
 incoherent illumination (in the light microscope)
 184–5, 184
 conditions for 184n
 incommensurate (Penrose) tilings 77–8, 79
 indexing
 for hexagonal/trigonal crystal systems 141
 for lattice directions (zone axes) 132–3
 for lattice planes 133–6
 inelastic scattering processes
 in the scanning electron microscope 287
 in the transmission electron microscope 283,
 274
 inorganic compounds, non-stoichiometry in 29
 insilicates 39, 40
 arrangement of SiO₄ tetrahedra in 42, 43
 instrumental broadening (in X-ray diffraction) 256
 integrated intensity (reflection) 220
 International Centre for Diffraction Data (ICDD)
 253
International Tables for (X-ray) Crystallography
 111, 322
 International Union for Crystallography (IUCr) 333
 interplanar angles 382–3
 table of for cubic crystals 383–4
 interplanar (d_{hkl}) spacings, table of for cubic
 crystals 382
 interstices
 between plane arrays of atoms 4
 in bcc structure 14, 15
 in ccp structure 11–12, 12
 in hcp structure 14
 in simple cubic structure 12–13, 13
 in simple hexagonal structure 14
 interstitial compounds 17
 interstitial sites, table of 346
 interstitial solid solutions 17, 233
 interstitial structures 11–18
 intrinsic stacking faults 21–2, 22
 inverse spinel structure (of Fe₃O₄) 36
 inversion axes of symmetry 101–2
 ionic (heteropolar) bonds 27
 ionic structures 27–8
 iron sulphide (pyrites, FeS₂)
 space group for 119
 structure of 119–20
 iron and steel
 fracture appearance of 4
 hardness of 17–8
 phase transformations in 10
 iron oxy-hydroxides 37
 iron oxides 35–7
 iron pyrites
 space group for 119
 structure of 119–20, 119
 irrational numbers 79–80, 80n
 isotactic polymers 125

 Jones, D.E.H. (Daedalus) 48, 52

 Keissig fringes (in X-ray diffraction) 231, 232, 233
 Kelvin, Baron (W Thomson) 93, 94n
 Kepler, Johannes 1, 341, 365–6
 Mysterium Cosmographicum (1596) 365
 Strena Seu de Nive Sexangula (1611)
 Harmonices Mundi (1619) 77, 78

- Kikuchi patterns in electron microscopy 283–7,
284, 285, 286, 287
analysis of 284–6, 285, 286
'map' 286, 288
- Kitaigorodskii, Alexander Isaakovich 122–3,
366–7
and close-packing of organic molecules 122–4,
123, 124
- Knipping, Paul xiv, 192
- Krystallos* (Greek: ice) 44
- lattice 56
definition of 57
three-dimensional (Bravais) types of 84–8,
85, 86
two-dimensional types of 56–8
- lattice directions (zone axes) 132
- lattice planes
families of 133, 134
indexing of 133–4, 133
in relation to Bragg's law 138
parallel to two directions 140
spacings (d_{hkl}) of 137–8, 160
- lattice points 56, 86, 90
and reciprocal lattice points 150
- lattice unit cell vectors 132–3, 132
- Laue, Max von 192, 367–8
- Laue cones 194, 195
- Laue equations 193–5, 194, 195
- Laue-Friedrich-Knipping experiment xiv
- Laue indices 114, 137–8
relationship to Miller indices 138
relationship to reciprocal lattice vectors 156
- Laue point groups 213
table of 213
- Laue (X-ray diffraction) method 201, 201,
221–3, 222
X-ray photograph of zinc blende xiv
- Laue zones 230
- Law of constancy of interfacial angles 1, 99
- Law of rational indices 135–6
- layer lines (in X-ray diffraction) 224, 225, 226
- layer (two sided) symmetry 73–77
- layer (two sided) symmetry groups 73–6, 76
as sub-groups of space groups 74
in relation to the packing of molecules 122
in woven textiles 74, 75, 76–7, 76n
- lepidocrocite (γ -Fe.O.OH), structure of 37
- light
coherence, scattering and interference 172–4,
174
diffraction of 165–71, 168, 169
interference of 173–5
nature of 172–3
- light diffraction
corollary with X-ray and electron
diffraction 165, 166, 204, 206, 231
from a circular aperture 179–80
from a single slit 178–9, 178
geometry of 174–8, 175, 177
observations using a laser 170, 171
observations using nets 167–9, 168, 169
limit of resolution *see* resolving power
line broadening in X-ray diffraction *see* broadening
of X-ray reflected beams
lithium oxide (Li_2O) antifluorite structure
of 19–20, 20
Bravais lattice for 118
long chain polymer molecules, crystal structures
of 124–5
polyethylene (polyethene) 125, 125
polypropylene (polypropene) 126, 126
long range ordering 234
in the Cu-Au alloy system 234, 235
in the Cu-Zn alloy system 234, 235
- Lonsdale, Kathleen 47, 368–9
and *International Tables for X-ray Diffraction*
111
- Lonsdaleite 47, 48
- Lorentz-polarization factor 206n
- low angle Bragg reflections 231
for cobalt-copper multilayer specimen 232, 233
- MacKay, A.L. 77
De nive quinquangula 77
icosahedral packing of spheres 128
magnetic materials, ordering in 234
'map scales' for direct and reciprocal lattices 152
maghemite (γ - Fe_2O_3), structure of 34, 36
magnetite (Fe_3O_4), inverse spinel structure of 36
matching rules (Penrose tiling) 79
- Mauguin, Charles 111, 369
(and Hermann) space group symbols 112
- Megaw, Helen 73, 369–70
- 'Memograms' (for geometrical relationships)
to find Miller-Bravais indices 143
to find plane parallel to two directions 140
to find Weber symbols 143
to find zone axis along the intersection of two
planes 139
- metal carbides, structures of 17, 17
- metals, deformation of 21, 23–5
- metallic bond 27
- microscope (electron), limit of resolution
of 288–90, 290
- microscope (light), limit of resolution of 184–8,
184, 185, 188
- Miller, William Hallows 134, 370
- Miller-Bravais indices (for hexagonal structures)
141, 141
- Miller indices 133–6
in cubic crystals 136
distinction between Laue indices 138
in non primitive cells 135
transformation of 143–6, 144
- mirror (reflection) line of symmetry 56
- mirror (reflection) plane of symmetry 76, 101, 101
- mirror-rotation axis of symmetry 71, 75

- model building 5, 337–8
- molécules integrantes* 3
- molecule: concept of in inorganic compounds 28–9
- monad (one-fold) axis of symmetry 58
- monoclinic crystal 85, 87
 - reciprocal lattice unit cell for 152, 154–6, 154, 155, 156
- monoclinic crystal system
 - point groups (crystal classes) in 103
 - space-filling polyhedron for 92
- monoclinic lattices 85
- moon craters, appearance of 297–8, 297
- mosaic structure 220–1, 220
- motif 56, 56, 58–60
 - symmetries of 59, 60, 61–4
- multilayer specimens, X-ray diffraction of 229–33, 232
- multiplicity factor 206n
- nature of crystalline state 1–5
- nanotubes, structures of 52, 53
- nesosilicates 39, 40
- Neumann, Franz Ernst 296, 370
- neutron diffraction 236
 - in Rietveld refinement technique 269
- neutron radiograph 237
- Newton, Isaac 172, 370–1
 - Opticks* (1704) 173
- Newton's laws 198
- nickel arsenide (NiAs, niccolite)
 - space-filling polyhedron for 345
 - structure of 18
- Nishikawa, Shoji 371–2
- non-centrosymmetric point groups 105
 - table of 91
- non-enantiomorphous point groups, table of 91
- non-periodic patterns and tilings 61, 77–80, 78, 79
- non-polar (molecular) layers 122, 124
- non-stoichiometry (in inorganic compounds) 29
- numerical aperture (NA)
 - of the eye 189
 - of a microscope 188
 - relation to f -number 188
- oblique lattice 57, 57, 62
- octahedral interstitial sites
 - in bcc structure 14, 15
 - in ccp structure 11, 12
- one-dimensional (border) patterns 65, 70, 83
 - systematic identification of 71
- one-fold (monad) rotation axis 58
- On Growth and Form* 52, 419
- optical transformations (diffraction patterns) 167, 171
- optical activity
 - in enantiomorphous crystals 106, 109
 - in liquids 110–11
- optic axis 106
- ordering in crystals 234
 - detection of 235
- organic compounds
 - crystal structures of 121–6
 - space groups for 121
 - stability of 121
- organic molecules
 - close (and closest) packing of 122–3, 123
 - layer symmetry groups of 122, 124
- orientation relationships
 - from electron diffraction patterns 280–1, 280
 - stereographic representation of 310–1
- orthohexagonal unit cell 141, 143
- orthorhombic crystal system 89, 89, 98
 - point groups (crystal classes) in 91, 98, 103, 337
- orthorhombic lattices 85, 87
- oscillation (X-ray diffraction) method 223–5, 224, 225
- oxides of iron 35–7
- oxy-hydroxides of iron 37
- partial dislocations 25, 34
- partial slip (in ccp metals) 23, 24
- Pasteur, Louis 106, 372–3
 - chirality of molecules 106, 107
- Patterson function 322
- Pauling, Linus Carl 373–4
- Pauling's rules 30
- Penrose tiling 77–8, 79, 80
- pentad (five-fold) axis of symmetry 61
- pentagonal dodecahedron 49, 51
- pentagonal symmetry 61, 128–9, 129
- periodic function 315–7, 317
- perovskite: coordination polyhedra in 30
- perovskite structures 20, 21, 31–3, 32
- petrofabric (texture) diagrams 314n
- phase problem (in crystal structure determination) 204, 215
- phyllosilicates 39, 41
- piezoelectricity 105
- Planck's equation 172
- plane indices *see* Miller indices
- plane lattices 61–3, 62, 153
 - reciprocal plane lattices of 153
- plane patterns (groups) 64–5, 66, 67
 - symbols for 64, 66
 - systematic identification of 64, 69
- plane point groups 59, 59, 60
- Platonic solids (polyhedra) 49, 51, 340–1, 341
- point groups, table of 91
 - occurrence (of crystal classes) 103–4
- point group symbols 102, 103
- point group symmetry
 - of cubic crystals 89, 89, 98, 98, 337
 - of orthorhombic crystals 89, 89, 98, 99, 337
 - table of 91
- polar axes 105, 120
- polar (molecular) layers 122, 124
- polar net 302, 303
- polar point groups 91, 105

- pole figures
 - determination of 259–61, 260, 261, 311–3, 312, 313
 - of cold-rolled copper 312, 313
 - of graphitised carbon tape 261–2, 261
 - of psammite rock 312–4, 313
- polyethylene (polyethene) crystal structure of 125, 125
- polyhedra, classification of
 - Archimedean 341–2, 342
 - coordination 29–31, 343–4, 346
 - regular (Platonic) 340–1, 341
 - space-filling 343, 346
- polyhedron names 337
- polymer molecules – long chain 124–6
- polypropylene (polypropene) isotactic crystal structure of 126, 126
 - X-ray fibre patterns of 258–9, 259
- polytypes (of silicon carbide) 33, 34, 35
 - 'Poor Common Salt' 29
- Pope, William Jackson 55, 374
- Powder Diffraction File* 253–6, 254, 255, 278
- powder (X-ray diffraction) methods
 - back-reflection (flat film) 249–50, 250
 - Debye-Scherrer 249–52, 251, 252
 - diffractometer *see* X-ray diffractometer
 - Seeman-Bohlin (Hägg-Guinier) 246
- precession (X-ray diffraction method)
 - compared with electron diffraction 276–7
 - Ewald reflecting sphere construction for 226–9, 227, 228
 - zero level photograph (of tremolite) 229
- preferred orientation (texture, fabric)
 - fibre textures 258, 258, 259
 - sheet textures 259–62, 260, 261
- primitive cell, definition of 63
- primitive rhombohedral unit cells
 - of cubic *F* lattice 86
 - of cubic *I* lattice 86
- principal maxima (in light diffraction) 180–1, 181, 323
- pyrites *see* iron sulphide
- pyroelectricity 105
- quartz (SiO₂)
 - development of faces in 90, 100
 - enantiomorphous forms of 109, 110
 - Hanawalt Search Manual* listing for 255
 - optical properties of 109–10
 - Powder Diffraction File* card for 254
 - structures of 43, 44
 - X-ray diffraction from 248, 249, 252
- quasiperiodic crystals (or crystalloids) 61, 126–30
 - in 63% Al–25% Cu–11% Fe 129
 - in Al₇₀ Pd₂₁ Mn₉ 130
- radius ratios of interstitial sites 11–15, 344, 346
- Rayleigh, Baron (JW Strutt) 183, 377
- Rayleigh criterion (for limit of resolution in the light microscope) 183–4, 184
- reading list (Further Reading) 414–20
- reciprocal lattice, construction of 150–5
- reciprocal lattice nodes 217–9, 218
- reciprocal lattice planes 161–3, 162
 - relationship to (direct) lattice vectors 162, 162
- reciprocal lattice points 151, 152, 154, 155, 156
- reciprocal lattice unit cells 154–6, 154, 155, 156
 - for cubic crystals 156–8, 157
 - for a monoclinic crystal 154–6, 154, 155, 156
 - referred to rhombohedral axes (primitive cells) 158
- reciprocal lattice vectors 150–2, 151, 152
 - as components of reciprocal lattice unit cell vectors 156
 - symbolism for in X-ray and electron diffraction 164
- reciprocal lattice unit cell vectors 154–5
- reconstructive phase transformation 43
- rectangular (plane) lattice 57, 57
- rectangular *c* (diamond, plane) lattice 62, 63
- reflecting conditions, tables of
 - for lattices and translational symmetry elements 397
 - for cubic structures 398
- reflecting sphere construction *see* Ewald reflecting sphere construction
- reflection-glide symmetry *see* glide line of symmetry; glide plane of symmetry
- reflection indices *see* Laue indices
- reflection symmetry *see* mirror line of symmetry; mirror plane of symmetry
- relationships between planes and zones 384
- rel-rods (extension of reciprocal lattice points) 219
- resolving power of optical instruments
 - of a camera or telescope 182–4, 182, 183, 188
 - limited by diffraction 181–2
 - of a microscope 184–8, 184, 185
 - of the eye 189, 189
- resolving power of X-ray diffraction
 - techniques 253
- rhombic dodecahedron 92, 94, 343, 343
- rhombic triacontahedron 343, 343
- rhombohedral lattice 87, 87
 - indexing for 141–2, 141
 - transformation matrices for trigonal crystals 146–7
- rhombohedral unit cells 85, 87, 87
 - for the cubic *F* lattice 86–7, 87
 - for the cubic *I* lattice 86–7, 87
 - of the ccp structure 8
- Rietveld method for structure refinement 267–9
 - experimental conditions for 268–9
- rock-crystal (α -quartz) 44
- Rome de l'Isle Jean Baptiste Louis 3, 375
 - Cristallographie* (1783) 3
- Röntgen, Wilhelm Conrad 237, 375–6

- rotation-reflection (mirror-rotation) axes
 - of symmetry 72, 74–5
 - relationship to inversion axes 104n
- tetrad rotation-reflection axis 72, 74, 77
- rotation method (in X-ray diffraction) 225–6, 226
- rotatory polarisation (optical activity) 106, 109, 110–1
- satellite reflections 231
- scalars 385
- Scherrer, Paul Hermann 243, 377
- Scherrer equation 216–9, 217
- Schoenflies, Arthur 111, 377–8
 - derivation of space groups of 111
- screw axes of symmetry 75, 76, 108, 108
 - enantiomorphous forms of 109, 109
 - symbols for 108
- Seeman-Bohlin X-ray camera 246
- self-consistency in indexing electron diffraction patterns 279
- semi-focusing X-ray diffraction methods 247, 248–9, 250, 251
- seven one-dimensional groups 65, 70, 83
 - ‘flow diagram’ for identification of 71
- seventeen plane groups 64–5, 66, 67
 - ‘flow diagram’ for identification of 69
- Shechtman, D (quasiperiodic crystals) 127
- sheet textures 259–62, 260, 261
- Shockley, William Bradford 25, 378
- Shockley partial dislocations 24, 25
- short range order 234
- Shubnikov, Alexei Vasilievich 73, 376–7
- silica structures 43–4, 44
- silicate structures 37–43, 40, 41, 42
- silicon carbide (carborundum, SiC) 33–4, 33
 - Frank notation for 34
 - polytypes (structures of) 35
- simple cubic (cubic *P*) lattice 85
- simple cubic structure 9, 9
 - interstitial sites in 12, 13
- simple hexagonal structure 6, 7
 - interstitial sites in 14
- simple monoclinic (monoclinic *P*) lattice 85, 90
 - space filling polyhedron for 90, 92, 92
- simple ionic and covalent structures 18–19
- sinc function 325, 326
- six-fold (hexad) rotation axis of symmetry 58
- slip systems (in metal deformation) 23–5, 24
- snowflake 1, 46
- sodium chloride (NaCl), structure of 16, 18, 28–9, 118
 - co-ordination polyhedra in 30
 - electron density variation in 322, 322
 - space-filling polyhedron for 345
- sodium rubidium tartrate 352
 - enantiomorphous analysis of 214
- software suppliers (computer programs in crystallography) 333–5
- Sohnke, Leonhard 111, 378
- Sohnke groups 111
- sorosilicates 39, 40
- space-filling polyhedra 90–3, 93, 94, 343–4
- space groups 111–8
 - asymmetric unit of pattern in 112
 - general equivalent positions in 113
 - Hermann-Mauguin notation for 111–2
 - special positions in 113
 - Wyckoff letters for 113
- space groups, examples of
 - C*2 (No. 5) 267, 267
 - P*2₁/*c* (No. 14) 114, 115
 - P*ba2 (No. 32) 113
 - P*4₁2₁2 (No. 92) 117
 - P*6₃/*mmc* (No. 194) 116
- space groups for organic molecular packing 121
 - table of 125
- space groups for some inorganic structures 119–20
- space groups, frequency of occurrence of 120–1
- space lattice *see* Bravais lattice
- spinel (AB₂X₄) structure 36, 36
- square arrays 4, 4
 - constructing ccp and simple cubic structures from 9, 9
- stacking faults, Frank notation for 21–2
- stacking faults, occurrence of
 - in close-packed structures 6
 - in crystallisation and deformation 21, 23, 24
 - in twinning 21–6
- stacking fault energy 23
- stacking sequence
 - in carborundum (SiC) structures 33, 34
 - in corundum (α -Al₂O₃) structures 34
 - for bcc structure 10
 - for ccp and hcp structures 6
- steel, hardness of 17–18
- Steno, Nicolaus (Stensen, Niels) 1, 378–9
- stereographic poles 288
- stereographic projection 296–314
 - addition rule, use of 301–2
 - great circles in 296–7, 300, 300, 301, 302, 304
 - for cubic crystals 299–302, 300, 301, 302
 - for hexagonal crystals 305
 - for orthorhombic crystals 305–7, 307
 - origin of 296
 - projection geometry of 297–9, 297, 298, 299
 - rotation of 304, 306
 - small circles in 296–8, 299, 304
 - Wulff net, use of 302–5, 304, 305
- stereographic representation of
 - orientation relationships 310–11
 - point group symmetry 308–10, 308, 309
 - preferred orientation 311–4, 312, 313
- stoichiometry (in iron oxides) 35
- structure factor (*F*_{*hkl*})
 - definition of 203
 - derivation of equation 207–9, 208
 - for anomalous scattering 213–4, 213, 214
 - and Fourier analysis 318–23

- structure factor equation, applications to
 - a bcc metal structure 210
 - a crystal with a centre of symmetry 210
 - CsCl structure 209, 209
 - an hcp metal structure 210–11, 211, 212
 - a non-centrosymmetric crystal structure 212, 213
 - Cu₃Au structure 235, 235
 - CuZn structure 235, 236
- subsidiary maxima (in light diffraction) 180–1, 181, 323, 329, 330
- substitutional solid solutions 233
- superlattice formation 234
- suppliers
 - of computer programs in crystallography 333–5
 - of model-building kits 338
- Symmetry Aspects of M.C. Escher's Periodic Drawings* 81, 82
- symmetry and crystal habit 97–9
- symmetry elements, self-consistency of 88–9
- symmetry in art and design 65, 68, 70–3
- synchrotron X-ray generation 239
- syndiotactic polymers 125
- systematic absences (in X-ray diffraction) 392–6
 - for a crystal with a glide plane of symmetry 394–5, 394
 - for a crystal with a screw axis of symmetry 395–6, 395
 - for the cubic *F* lattice 393–4
 - for the deoxyribonucleic acid (DNA) model structure 265, 266
 - for the cubic *I* lattice 394
 - for the hcp structure 396, 398, 399, 399n
- table (of allowed reflections) for cubic structures 398
- table (of allowed reflections) for lattices and translational symmetry elements 397
- Tamman, Gustav Heinrich Johann Apollon 55, 379
- tartaric acid
 - enantiomorphous (crystal) forms of 110
 - molecule 107
 - optical activity in 106
- tectosilicates 39, 41
- telescope
 - limit of resolution of 182–4, 182, 183, 188
 - radio telescope 189–90
- temperature factor 206n
- ten (plane) point groups 59, 59, 60
- tennis ball, point group symmetry of 102
- tensors 385–6
- tetrad (four-fold) axis of symmetry 58, 101
- tetrad rotation-reflection axis of symmetry 74, 74, 75
- tetragonal crystal system 103
 - point groups (crystal classes) in 103
- tetragonal lattices 87–8
 - unit cells for 88
- tetrahedral interstitial sites
 - in bcc structure 14, 14
 - in ccp structure 11, 12
 - in hcp structure 14
- tetrahedral structure types 33, 34, 35
- texture (preferred orientation)
 - origin of 244
 - in cold rolled copper 312, 313
 - in graphitised carbon tape 261–2, 261
 - in polypropylene (polypropene) 258–9, 259
 - in psammite rock 312–4, 313
- texture, measurement of
 - in flat plate camera 258, 258
 - in goniometer 258–61, 260
- texture, representation of 311–4
 - orientation distribution function (ODF) 258
 - photographic (flat plate camera) 259
 - pole figures 261, 312, 313
- three-fold (triad) axis of symmetry 58
- tiling (plane patterns) 61
- titanium hydrides, TiH, TiH₂ and nitride, TiN
 - cubic *F* Bravais lattices for 118
 - structures of 16–17, 16
- transformation: cubeoctahedral \rightleftharpoons icosahedral
 - packing 127–8, 127, 129–30
- transformations in crystal structures
 - bcc \rightleftharpoons ccp; bcc \rightleftharpoons hcp 10
 - ccp \rightleftharpoons hcp 23
 - in barium titanate 33
 - in silica 43
- transformation matrices
 - for Miller indices 143–5
 - for trigonal crystals with rhombohedral lattices 146–7, 147
 - for zone axis symbols 145–6
 - inversion procedure for 147–8
- transition alumina structures 34
- translational symmetry elements
 - glide lines 63–4, 63
 - glide planes 108
 - screw axes 75, 76, 108–9, 108
- triad (three-fold) axis of symmetry 58
- triclinic crystal system 90
 - point groups (crystal classes) in 90
- triclinic lattice 85, 87
- tridymite (SiO₂), α and β structures of 43
- trigonal crystal system 89
 - point group (crystal classes) in
- trigonal crystals
 - indexing in 141–3
 - lattices of 89, 143
- transformation matrices for 143–4, 146–7
 - unit cells for 89, 146
- truncation (in polyhedra) 339, 340
- truncated icosahedron 50, 51, 342
- truncated octahedron 92, 93, 340, 342
- twin axis 25
- twinned crystals 21–5, 22, 24
 - electron diffraction pattern of 400
 - examples of 26, 336

- stacking sequence (in close-packed structures) 22, 22
- two-dimensional (plane) patterns and groups 64–5, 66, 67
 - systematic identification of 64, 69
- two-dimensional symmetry elements 58–61
 - glide lines 63, 63
 - mirror (reflection) lines 56, 59, 63
 - rotational axes 58–61, 59, 60
- two-fold (diad) axis of symmetry 56
- unit cells
 - base vectors for 132, 133
 - for the 14 Bravais lattices 85
 - for the bcc structure 10, 10
 - for the ccp structure 6, 7, 9
 - for the hcp structure 6–9, 7
 - for the simple hexagonal structure 6, 7
- unit cell, choices of
 - for cubic lattices 86, 86
 - for hexagonal and rhombohedral lattices 87, 87
 - for plane lattices 57, 62
- units (Système International) 278
- useful crystallographic relationships
 - angles between planes in cubic crystals 383–4
 - interplanar angles 382–3
 - interplanar (d_{hkl}) spacings 382
 - relationships between planes and zones 384
 - volumes of unit cells 383
- van der Waals bond 28, 121
- vector components 388–9
- vector modulus 385, 390–1, 391
- vector notation for unit cell volume 389, 389
- vector-phase diagrams 208, 208
- vector product 387–8, 388
- vector quantities 104
- vectors 385–9
 - addition of 390, 390
 - and scalars and tensors 385–6
 - multiplication of 387–9
 - representation by complex numbers 390–1
 - resolution into components 386–7
- virus structures 128
- Voronoi Georgy Fedeesovich 92, 379
- Voronoi (space-filling) polyhedra 92, 92, 93, 158, 343–4, 343, 347
- water, structures of 44, 45
- wavetrain 173–4, 174
 - in Abbe theory of image formation 328, 330
- Weber, Wilhelm Eduard 142, 379–80
- Weber (zone axis) symbols 141–3
- Weiss, Christian Samuel 139, 380
- Weiss zone law (zone equation) 139, 159–60, 160
 - for Weber symbols 142–3
- Weissenberg X-ray method 202
- ‘white’ X-radiation 238, 239
 - in Laue method 201, 201, 221–2, 222
- Wigner-Seitz cells *see* Voronoi polyhedra
- woven textiles, symmetries of 74–6, 74, 75
 - plain weave 73, 74, 76–7
 - twill weave 73, 75, 76
- Wulff, Georg (Yuri Viktorovich) 303, 380
- Wulff net 302–5, 304, 305
- wurtzite (ZnS) structure 18, 33, 34
 - space group for 115
- Wustite (FeO) structure 35
- Wyckoff letters 113, 399n
 - for hcp metal structure 210
- X-ray diffraction
 - Bragg’s interpretation of 196–8, 196, 197
 - Ewald’s interpretation of 198–201, 199, 200, 201
 - Laue’s interpretation of 193–5, 194, 195
- X-ray diffraction broadening factors
 - grain size and shape 217–9, 217, 256
 - instrumental 256
 - internal elastic strain 256–7
- X-ray diffraction – corollary with light and electron diffraction 165–6, 204, 206, 231
- X-ray diffraction methods
 - Laue method 201, 201, 221–3, 222
 - oscillation method 223–5, 224, 225
 - precession method 226–9, 227, 228, 229
 - rotation method 225–6, 226
- X-ray diffraction spots, elliptical shapes of xiv
- X-ray diffractometer 247–9
 - and reciprocal space 230
 - asymmetrical specimen setting 247, 248
 - chart for quartz 248, 249
 - focusing circle of 247
 - semi-focusing geometry of 247, 248
 - symmetrical (Bragg-Brentano) focusing geometry of 247, 247
- X-ray diffractometer applications
 - detection of ordering 233–4
 - identification of unknown phases 253–6
 - measurement of internal elastic strain/stress 248, 256–7
 - measurement of grain size 256
 - measurement of lattice parameters 252–3
 - multilayer analysis 229–33, 232
- X-ray photographs
 - of deoxyribonucleic acid (DNA) xv
 - of zinc blende xiv
- X-ray Powder Diffraction File 253–6, 254
 - file cards 253–4, 254
 - Hanawalt groups 254–5, 255
 - Hanawalt search procedure 253–5, 255
- X-ray recording techniques 240
- X-ray tubes 238
 - characteristic wavelengths 239, 239
 - generation of X-rays in 238–9
- Young, Thomas 172, 380–1

- Zeiss, Carl 184, 329
- zero-order Laue zone 276–7, 276
- zinc blende (sphalerite, ZnS)
 - Bravais lattice for 118, 120
 - coordination polyhedron of 30
 - Laue photograph of xiv
 - polymorphs of 18
 - space group for 120
 - structure of 33, 34
- zone, definition of 131
- zone axis
 - at the intersection of two planes 139, 161
 - vector representation of 133
- zone axis (direction) symbols 132
 - for cubic crystals 136
 - for hexagonal crystals (Weber symbols) 142
 - transformation of 145–6
- zone equation (Weiss zone law) 139
 - for Miller-Bravais axes 142, 143
 - for reciprocal lattice planes 163